NASA CR-191004

1992 Research Reports

NASA/ASEE Summer Faculty Fellowship Program

John F. Kennedy Space Center
and
University of Central Florida

1992 RESEARCH REPORTS

NASA/ASEE SUMMER FACULTY FELLOWSHIP PROGRAM

JOHN F. KENNEDY SPACE CENTER

UNIVERSITY OF CENTRAL FLORIDA

EDITORS:

Dr. Loren A. Anderson
Associate Professor of Engineering
University of Central Florida

Ms. Carol Valdes
Systems Training and Employee Development Branch
John F. Kennedy Space Center

PREPARED FOR:

John F. Kennedy Space Center
Merritt Island, Florida

NASA Grant NGT-60002 Supplement: 8

Contractor Report No. CR-191004

September 1992

PREFACE

This document is a collection of technical reports on research conducted by the participants in the 1992 NASA/ASEE Summer Faculty Fellowship Program at Kennedy Space Center (KSC). This was the eighth year that a NASA/ASEE program has been conducted at KSC. The 1992 program was administered by the University of Central Florida in cooperation with KSC. The program was operated under the auspices of the American Society for Engineering Education (ASEE) with sponsorship and funding from the Office of Educational Affairs, NASA Headquarters, Washington, D.C. The KSC program was one of nine such Aeronautics and Space Research Programs funded by NASA Headquarters in 1992. The basic common objectives of the NASA/ASEE Summer Faculty Fellowship Program are:

a. To further the professional knowledge of qualified engineering and science faculty members;

b. To stimulate an exchange of ideas between participants and NASA;

c. To enrich and refresh the research and teaching activities of participants' institutions; and,

d. To contribute to the research objectives of the NASA centers.

The KSC Faculty Fellows spent ten weeks (June 1 through August 7, 1992) working with NASA scientists and engineers on research of mutual interest to the University faculty member and the NASA colleague. The editors of this document were responsible for selecting appropriately qualified faculty to address some of the many problems of current interest to NASA/KSC. A separate document reports on the administration aspects of the 1992 program. The NASA/ASEE program is intended to be a two-year program to allow in-depth research by the University faculty member. In most cases a faculty member has developed a close working relationship with a particular NASA group that has provided funding beyond the two-year limit.

TABLE OF CONTENTS

1992 NASA/ASEE SUMMER FACULTY FELLOWSHIP PROGRAM

JOHN F. KENNEDY SPACE CENTER
UNIVERSITY OF CENTRAL FLORIDA

USE OF CYCLIC CURRENT REVERSAL POLARIZATION VOLTAMMETRY FOR INVESTIGATING THE RELATIONSHIP BETWEEN CORROSION RESISTANCE AND HEAT-TREATMENT INDUCED VARIATIONS IN MICROSTRUCTURES OF 440C MARTENSITIC STAINLESS STEELS

PREPARED BY: Dr. John R. Ambrose

ACADEMIC RANK: Associate Professor

UNIVERSITY AND DEPARTMENT: University of Florida
Department of Materials Science and Engineering

NASA/KSC

DIVISION: Materials Science Laboratory

BRANCH: Failure Analysis and Materials Evaluation

NASA COLLEAGUE: Coleman J. Bryan

DATE: July 24, 1992

CONTRACT NUMBER: University of Central Florida
NASA-NGT-60002 Supplement: 8

ACKNOWLEDGEMENTS

I would like to express my appreciation for again being selected to participate in the 1992 NASA/ASEE Summer Faculty Fellowship program, to Loren Anderson [University of Central Florida] and Carol Valdes [NASA] for their capable administration of the program, and to my NASA colleagues Cole Bryan and Rupert Lee for their assistance and encouragement. In many ways, this second year was more fulfilling then the first - it was surely more challenging. I thank Lewis MacDowell for the opportunity to use his equipment and see how our tex money goes to buy the kind of equipment the State of Florida chooses not to supply its universities with - also for his help in that critical stage of data transfer. To Steve McDanels, my thanks for your SEM work; to Scott Murray, our all to few trips outside the O & C building were always welcome. And to Peter Marciniak and the rest of the endangered wildlife on Merritt Island...thanks for letting me be a part of your day.

ABSTRACT

Software for running a cyclic current reversal polarization voltammagram has been developed for use with a EG&G Princeton Applied Research Model 273 potentiostat/galvanostat system. The program, which controls the magnitude, direction and duration of an impressed galvanostatic current, will produce data in ASCII format which can be directly incorporated into commercial spreadsheets [Lotus, Quattro] for graphical representation of CCRPV voltammograms.

The program was used to determine differences in corrosion resistance of 440C martensitic stainless steel produced as a result of changes in microstructure effected by tempering. It was determined that tempering at all temperatures above 400°F resulted in increased polarizability of the material, with the increased likelihood that pitting would be initiated upon exposure to marine environments.

These results will be used in development of remedial procedures for lowering the susceptibility of these alloys toward the stress corrosion cracking experienced in bearings used in high pressure oxygen turbopumps used in the main engines of space shuttle orbiters.

SUMMARY

1. Description and rationale of the cyclic current reversal polarization voltammetry technique are presented.

2. Development of a program with which a commercial potentiostat can be menu driven, using a PC to run the experiment, to acquire and to process the data.

3. The technique and experimentation procedure were tested against alloys whose microstructure had been changed by heat treatment. Results will be used to develop other, more effective, heat treatment procedures.

TABLE of CONTENTS

LIST OF ILLUSTRATIONS

20 750 temper, comparison of 5th cathodic cycles for groups 1-3.

21 1000° temper - comparison of 5th cathodic cycles for groups 1-3.

22 1250 temper - comparison of 5th cathodic cycles for groups 1-3.

1.0 INTRODUCTION

There have been a number of occurrences of stress corrosion cracking [SCC] failures of AISI 440C cryogenic bearing races, a component of Pratt and Whitney high pressure oxygen turbopumps [HPOTP] used in the main engines of the space shuttle orbiter main engines. Stress Corrosion Cracking is a localized corrosion phenomenon involving propagation of cracks through the cross-section of a material due to the interaction of an applied or residual stress upon exposure to certain environments. Failures appear to result from a synergistic interaction of three variables, namely:

1. **Surface Finish [roughness] produced by grinding,**
2. **"Non-Optimal" microstructure produced by quenching and**
3. **Susceptibility of this alloy composition toward chloride induced environmental fracture.**

A number of fabrication modifications which change these particular variables have been shown to result in extended service life or time to failure [TTF]. Since selection of an alternate material is out of the question at this point in time, attention has focussed on procedures which increase the time to failure for the material.

One possibility would be to increase SCC resistance by increasing the temperature used in tempering the martensitic microstructure produced during the quench from the austenization temperature. The beneficial aspects of this procedure involve a minimization of "...residual quench tensile stresses while producing a less brittle martensite." [quotation from Pratt-Whitney audio-visual presentation AVA376070 901005]. However, the effect of this variation with respect to corrosion resistance has yet to be resolved. It should be emphasized that true SCC susceptibility is determined by electrochemical/mechanical testing methodology. However, the standard test methodology - slow strain rate testing - is a prohibitively long test. The question is - can an accelerated electrochemical test procedure which has successfully been used to differentiate between degrees of susceptibility to SCC possess sufficient sensitivity to determine the effectiveness of these remedial fabrication procedures?

1.1 THEORETICAL BASIS for PROPOSED EXPERIMENTAL PROCEDURE

Measurement of degree of polarization which result from impressed current is not a new technique, having been used for some time as an analytical chemistry technique - chronopotentiometry, stripping voltammetry, etc. It has not been

used to any great extent in corrosion science applications. It would seem, however, to be most appropriate in measuring the behavior of a material in response to flow of current across the metal/environment interface. By impressing a constant [galvanostatic] current between an inert electrode [platinum counter] and the material being characterized [working electrode], the potential change or polarization can be measured as a function both of time and of the amplitude of the impressed current. In order to simulate "natural" conditions, the current direction should be regularly reversed in order to develop concentrations of both kinds of reaction products at the metal interface - anodic and cathodic. Thus evolves the name of the technique - **"CYCLIC CURRENT REVERSAL POLARIZATION VOLTAMMETRY"** or **CCRPV**. The experimental variable to be measured will be the rate of change in material potential, or "polarization rate".

Cyclic Current Reversal Polarization Voltammetry [CCRPV]

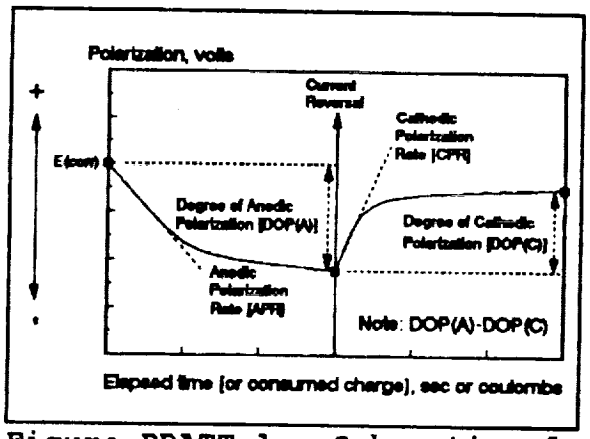

Figure PRATT-1 - Schematic of a single cycle CCRPV sweep and associated interpretive parameters.

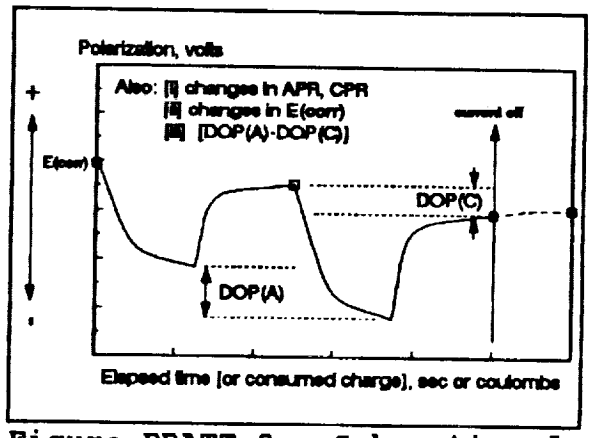

Figure PRATT-2 - Schematic of multiple CCRPV cycles and interpretive output parameters.

The experimental methodology for the CCRPV technique is quite simple, utilizing a conventional potentiostat in the galvanostatic mode coupled to a square wave signal generator and an oscilloscope for measuring polarization kinetics. This polarization rate output for both single and multiple cycles contains a variety of types of information which relates directly to the corrosion process [Figures PRATT-1 and PRATT-2]. The various output parameters which will be utilized in determination of electrolyte corrosivity are discussed below.

Degree of polarization [DOP] is given by the magnitude of potential shift [polarization] associated with a particular direction of impressed current flow - i.e. for an anodic impressed galvanostatic pulse, the degree of anodic polarization

[DOP(A)] is given by:

$DOP(A) = E_h - E_s$, where E_h = the potential of the working electrode at the end of a given current pulse, and

E_s = the potential at the start of the current pulse.

A large value for DOP(i) indicates the presence of a large resistive component in the current path between counter [auxiliary] and working electrodes. Although consistent with the occurrence of a protective surface barrier layer, a large electronic resistance does not, by itself, guarantee equivalent corrosion resistance. First, passivity is usually associated with ionic resistance of insoluble corrosion products. Secondly, large degrees of electronic resistance can often result in dielectric breakdown of passive layers with associated high localized corrosion rates - e.g. pitting above pitting potentials, etc.

Anodic and Cathodic Polarization Rates [APR and CPR], determined from polarization v. time plots, are directly related to changes in resistance toward charge transfer [metal dissolution (A) or plating (C)] rates and to kinetics of insoluble film growth (A) or dissolution (C). Normally, these processes may be distinguished using Rotating Ring-Disc voltammetry techniques. However, in the proposed experimentation, only progressive changes in polarization kinetics will be used as a quantitative measure for stability of the system. Any potential arrests occurring during the polarization transient can be related to the electrochemical reactions responsible for the consumption of current by associating the potential arrest with a variation in the kinetics of a particular Redox process.

E_s potentials, particularly progressive shifts in rest potentials are directly related to variations in corrosion potential E_{corr}. Although variations in corrosion potential have often been considered as "irreproducible" behavior by the uninitiated, these shifts are, in fact, associated with an irreversible component of the total polarization which occurs in response to the passage of current. The direction and magnitude of these E_s potentials can be related to the process[es] responsible for their occurrence by comparing their behavior in response to changes in other experimental variables - i.e. solution flow rate, amplitude and frequency of current pulses, etc.

System stability [or, alternatively, system corrosivity] can be estimated by associating progressive changes in one or more of these parameters with changes in the subject material - with surface roughness or microstructure, for example. We have demonstrated that austenitic stainless steels found to be sensitive to pitting or to intergranular stress corrosion

cracking were easily polarized with but a few current reversal cycles to potentials above a critical value for initiation of pits. For these stainless steels, onset of pitting - and presumably SCC crack initiation as well - was signalled by an abrupt decrease in polarization once this critical value was exceeded. This procedure was also effective in correlating a decreased pitting resistance with the amount of retained delta ferrite in the weldments of 316L austenitic stainless steels.

We should be reminded that susceptibility to SCC is determined by mutually inclusive electrochemical and mechanical factors - breakdown of passivity is one factor. However, the mechanical factor cannot be ignored. What we are assuming here is that the material is intrinsically susceptible - 440C martensitic stainless steel will eventually fail by SCC. We are will be trying to determine whether remedial fabrication methodology [1] affects resistance to passivity breakdown and [2] whether such change in resistance can be detected by our proposed experimental protocol. The "bottom line" will be - can a "calibration curve" of sorts be constructed which demonstrates a some direct relationship between a processing variable [e.g. surface polishing, "pancake" forging or temperature induced microstructural alteration] and a measure of localized corrosion resistance.

1.2 CRITERIA for CORROSION SUSCEPTIBILITY EVALUATION

Polarization in response to current flow can be of three types, individually or in combination:

i. a potential drop across an ohmic resistance. This polarization is characterized by a V=IR response, and is virtually time independent - i.e. instantaneous polarization with application of current. Capacitance or interfacial charging processes are included in this category as is the voltage drop across the electrolyte between the working and counter electrodes.

ii. polarization due to the resistance to charge transfer across the electrified interface - i.e. so-called "Tafel" overvoltage. This kind of polarization is characterized by a logarithmic dependence upon current flow - the "Tafel Equation":

$$\ln[I] - \pm\left[\frac{\eta_i}{\beta_i}\right]$$

where n_i = degree of polarization produced by current I
and β_i = charge transfer resistance.

iii. the potential drop across an insoluble reaction product or film which forms at the metal/electrolyte interface. The degree of polarization is a function of the resistivity of the reaction product, the polarization rate is a function of the nucleation/growth kinetics of the deposition process. It is this polarization process with which we will be most interested.

A schematic representation of the polarization extremes - polarization resistance during active metal dissolution versus IR resistance across an insoluble corrosion product - is shown in Figure 3.

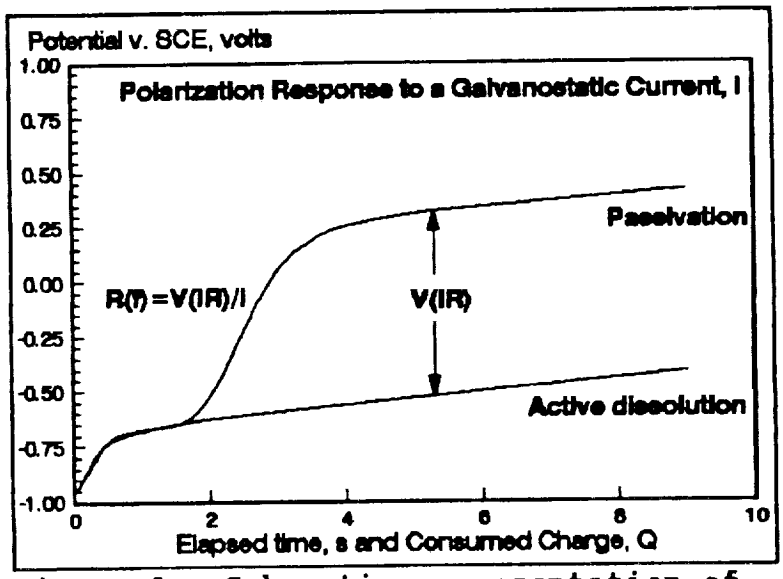

Figure 3 - Schematic representation of limiting cases in polarization behavior - metal dissolution v. insoluble corrosion product.

Under conditions of repetitive current reversal, any change in either degree or in rate of polarization signifies changes in the one of the three processes enumerated above. Of the three, only the third should provide any significant contribution. Thus, by evaluating such changes, we should be able to establish criteria for evaluating the environmental stability of a particular material in a given environment.

As "protective" films grow on bare or air-formed film covered metal substrates, there should be a regular increase in degree of polarization with each consecutive anodic cycle. Furthermore, the degree of polarization should progressively decrease as well, if the protective film is becoming more and more protective. Any change in this trend will be interpreted as an indication of development of instability in the system - a loss in ability of the system to resist the corrosive actions of the environment. We shall find, however, that with passive alloys like stainless steels, too high an electrical resistance leads to onset of pitting.

1.3 PROPOSED EXPERIMENTAL PROTOCOL

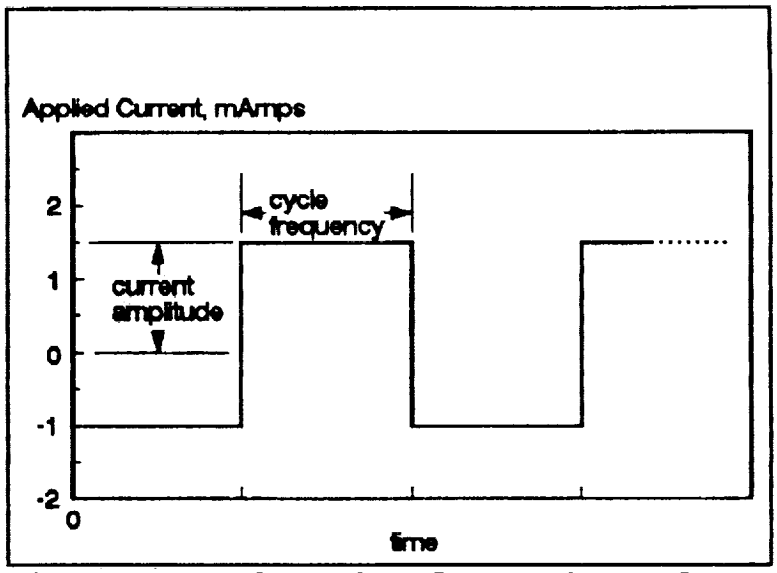

Figure 4 - Schematic of Experimental Procedure with respect to the RCRV control variables.

The CCRPV procedure requires that both magnitude of impressed current as well as its magnitude be specified - both these variables represent critical operating controls [Figure 4]. It would appear that current levels should correspond to maxima experienced during actual service exposure. However, this is not an easy selection to make. Cathodic currents seldom exceed the maximum for cathodic reduction of dissolved oxygen - about 10^{-3} amperes/cm^2 on steel surfaces. With concentration polarization, this value is reduced by several orders of magnitude - the 1 mA value represents an upper limit. Similarly, the duration of the current pulse represents the coulombic charge increment allowed to flow during the transient. Too short a time, and the system will not have time to respond or to polarize. Too long a period and the system will have changed too much - environmental compositions will have changed far in excess of realistic values. After considerable experimentation in c/5 natural seawater [natural seawater containing about 0.1 M Cl^- ion] resulted in a =/- 6.25 μA current applied for 5 seconds. Finally, the total number of cycles to be included in the experiment had to be decided upon. Variation in this operating parameter is determined by what is necessary in order to get some idea of where the stability of the system is heading. Too few cycles and a clear direction is not obtained. Unfortunately, there was insufficient time for testing of optimum current/frequency/duration values.

In order to facilitate data acquisition and analysis, it was decided to develop a software program for use in running CCRPV experimentation on equipment in use in the NASA-KSC corrosion testing facilities. The procedure involved modification of commercial software prepared by Princeton Applied Research Corporation, the manufacture of the Model 273 potentiostat used in this research. Alteration of their CPCOM.T program was accomplished and is included in Appendix A at the end of this report.

2.0 EXPERIMENTAL - MATERIALS and EQUIPMENT

2.1 Material

All experimentation was performed using specimens of 440C martensitic stainless steel provided by Pratt-Whitney Corporation of West Palm Beach, Florida. The nominal composition for this alloy is provided in Table I.

Table I - Elemental Composition for 440C Martensitic Stainless Steel Alloy Selected for this Study.

C	Mn	Si	Cr	P	S	Others
0.95-1.20	1.00	1.00	16.0-18.0	0.04	0.03	0.70 Mo

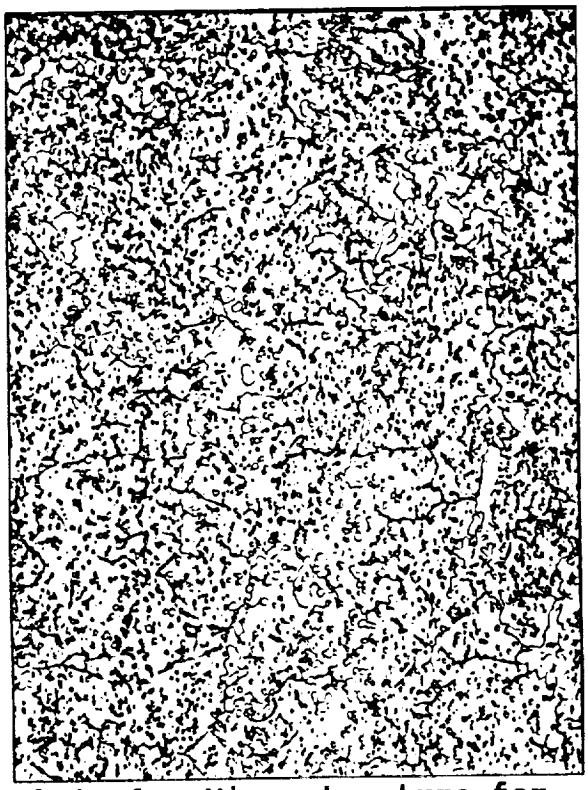

Photo 1 - Microstructure for PW#1, 400°F temper, super picral etch, 500x.

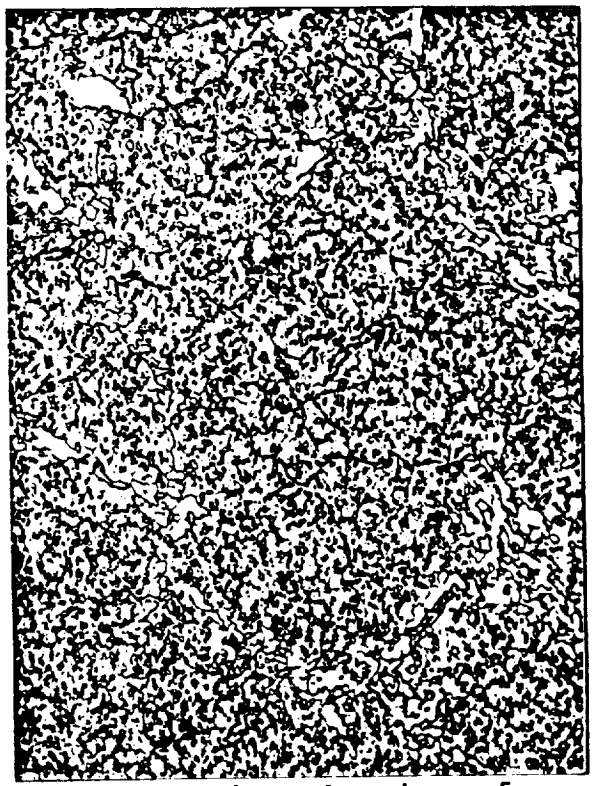

Photo 2 - Microstructure for PW#5, 750F Temper, super picral etch, x500.

Photo 4 - Microstructure for PW#6, 1000F Temper, super picral etch, x500.

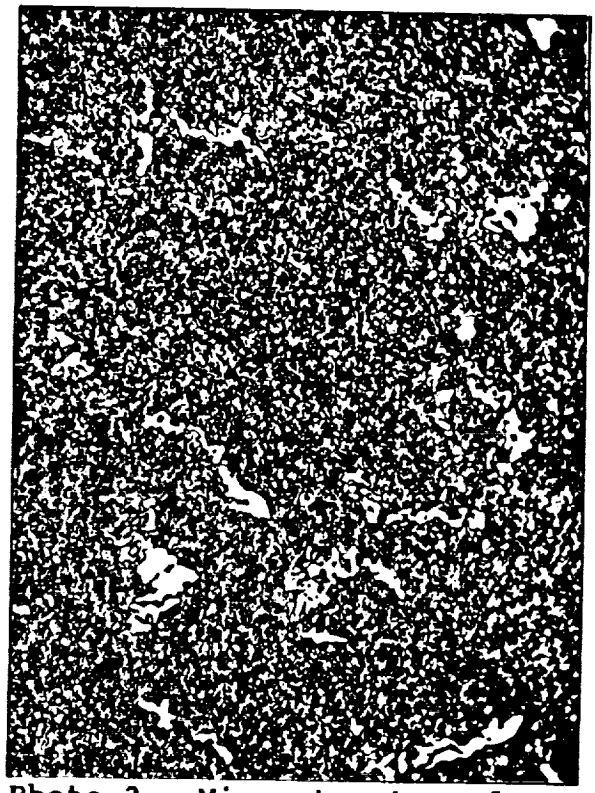

Photo 3 - Microstructure for PW# 7, 1250F temper, super picral etch, x500.

Duplicate specimens tempered at four different temperatures were received and their microstructures characterized. For each duplicate specimen set, one specimen was analyzed metallographically, while the other was used in the as-received condition for the electrochemical experimentation. When performing subsequent experiments, specimens were repolished according to the same procedure used for the metallographic specimens. Shown in Photos 1-4 are photomicrographs of specimen surfaces produced by mechanical rotary polishing through a series of silicon carbide metallographic polishing papers, 1 micron diamond paste on nylon cloth, finished with 0.3 and 0.05 micron alumina on felt. Etching was accomplished with a super picral etching medium.

Microstructures are consistent with conventional heat treatments described in the literature [Appendix B]. Of particular relevance to us will be the relative distributions of the primary carbide phase [large blocky light-colored phase] and secondary carbide phase [small circular light-colored phased] within the martensite matrix. Note that the primary carbide phase, produced during the initial quench from

the austenitizing temperature - therefore supposedly independent of tempering temperature, does appear to be somewhat different in the four tempers [Figures 5-8].

All experiments were performed in natural seawater, diluted with distilled water to a 1:5 concentration - approximately equal to a 0.1 M Cl^{-1} concentration. Solutions were stagnant, making no attempt to change the air saturated condition.

2.2 Equipment

The electrochemical cell used was a standard Greene cell furnished by EG&G Princeton Applied Research - counter electrodes [2] were graphite. 5/8-inch diameter, 3/16-inch thick specimens were designed to fit a standard PAR specimen holder in the PAR specimen holder. Electrochemical experimentation was performed using a PAR Potentiostat/galvanostat Model 273 in combination with an AT clone PC. Software was, as previously stated, an adaptation of PAR "Headstart, version 1.0, software.

2.3 Experimental Procedure

Following mounting in the cell specimen holder, specimens were placed in the electrochemical cell to which diluted seawater had already been added and allowed to stabilize for 10 minutes. Readings of open circuit [corrosion] potential were made immediately after placing in the cell, and at the 5 and 10 minute marks. After the stabilization interval, the CCRPV program was initiated. Following the 5 anodic/5 cathodic cycle sequence, the system was allowed to stabilize again for 10 minutes, with E_{corr} measurements made again at 5 minute intervals. Two more groupings of CCRPV perturbations were performed, following the same experimental protocol - a total of three groups of 5 current reversal sequences. Following the experimental procedure, the specimen was removed from the cell, and from the holder, cleaned, dried and retained for further experimentation.

Data was collected in a ASCII format, transferred to a standard LOTUS spreadsheet, collated and plotted. Named graphs were reprocessed using Lotus FREELANCE software, saved as TIFF files for incorporation into the WORDPERFECT, v. 5.1 text used in the writing of this report.

3.0 EXPERIMENTAL RESULTS and DISCUSSION

In Table II are listed the variations in corrosion or rest potentials which were recorded before and after each CCRPV group.

Table II - Corrosion Potential Data

Grp#	time	PW# 1	PW# 5	PW# 6	PW# 7
1	-10	-223	-227	-312	-260
	-5	-164	-244	-	-308
	0[b]	-161	-278	-406	-285 [?]
	0[a]	-153	-284	-421	-248
	-5	-175	-302	-451	-295
	-10	-181	-321	-476	-289
2	0	-170	-331	-483	-209
	-5	-185	-342	-501	-289
	-10	-188	-353	-	-
3	0	-177	-337	-507	-209
	-5	-190	-367	-517	-294
	-10	-192	-	-	-

Two features are evident: [1] There is a generalized progression in E_{corr} toward more negative values both before and after CCRPV runs; [2] There is a progressive shift in E_{corr} toward more negative values following CCRPV from group to group of CCRPV cycles. Such shifts could be due to either cathodic concentration polarization [diffusion limited O_2 transport], to increases in anodic current density [passivity breakdown or pitting] or to both. It would appear that small changes in corrosion potential, on the order of 20-30 mV, are probably due to concentration polarization, while relatively larger changes [50-100 mV] are probably associated with passivity breakdown.

With respect to CCRPV experimentation, results will be treated in terms of the following comparisons between heat treatments:

[1] Degree and rate of polarization for the 1st anodic cycle during the 1st group.
[2] Degree and rate of polarization for the five anodic cycles within the 1st group for each temper.
[3] Degree and rate of polarization for 1st anodic cycle of each group for each temper.
[4] Same data treatment for the cathodic cycles [3 comparison classifications].

Anodic Polarization Behavior

In Figure 5 are plotted the 1st anodic cycles of group for the 4 subject tempers in this study - 400, 750, 1000 and 1250°F - as a function of the square root of time. The fact that polarization kinetics would be linear with respect to $t^{\frac{1}{2}}$ is significant in that the cause of the polarization - an electric resistance to the flow of current - is being limited by what appears to be diffusion control. Fick's 2nd Law for chemical diffusion would show the same order of reaction kinetics. Notice that in Figure 5, only the polarization of the 400°F temper is linear with respect to $t^{\frac{1}{2}}$. This implies that the interfacial resistance developing in response to the flow of anodic current is being limited by diffusion of some species - if an anodic film is providing this resistance, its growth rate os being limited by the transport of some specie [or species] to or from the specimen/solution interface. Not only do the other three tempers not display diffusion limited kinetics, but their polarization rates are much higher. Except for specimen #6, the 1000°F temper, there would have been a direct correlation between polarization rate and degree of polarization and tempering temperature, with the higher temperatures producing higher DOP's and DOP rates. As it is, there appears to be a direct correlation between relative amount of primary carbide in the alloy microstructure [Photos 1-4] and polarization kinetics. It should be noted that the 1000° temper specimen, when removed from the cell, was found to be severely pitted. Occurrence of pitting during a CCRPV scan produces ambiguous results because the majority of the current flows out of the pits on the surface, a relatively small area. The remainder of the surface will show a disproportionate amount of polarization - thus the relative position of the 1000 temper as compared to the other three. The occurrence of pits on the surface of the 1000° temper is shown in Photo 5. Note that incidence of pitting is in proximity to primary carbide deposits within the alloy microstructure.

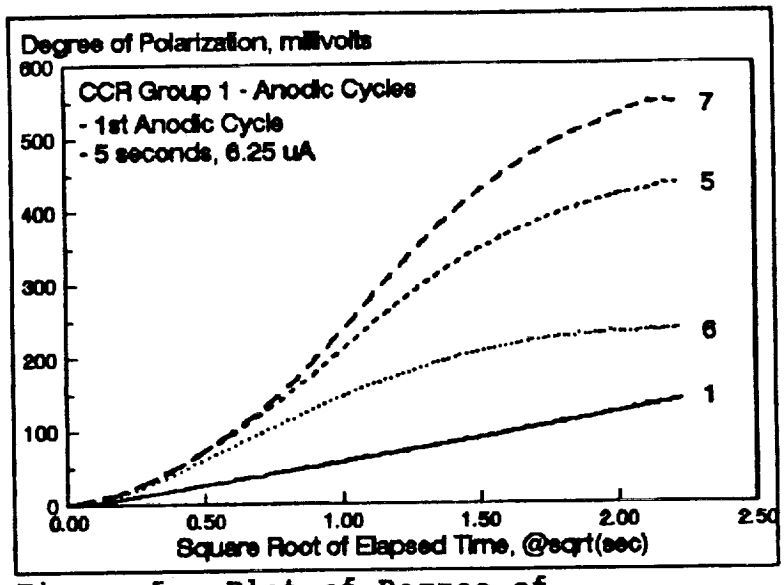

Figure 5 - Plot of Degree of Polarization [V(t)-V(o)] v. $t^{\frac{1}{2}}$ for all 4 440C tempers - 1st anodic cycle, 1st CCRPV group.

Comparing anodic behavior within the first CCRPV group, we see

that, although there is a slight [3-5 mV] increase in degree of polarization [DOP] from 1st to 5th cycle for the 400° temper,

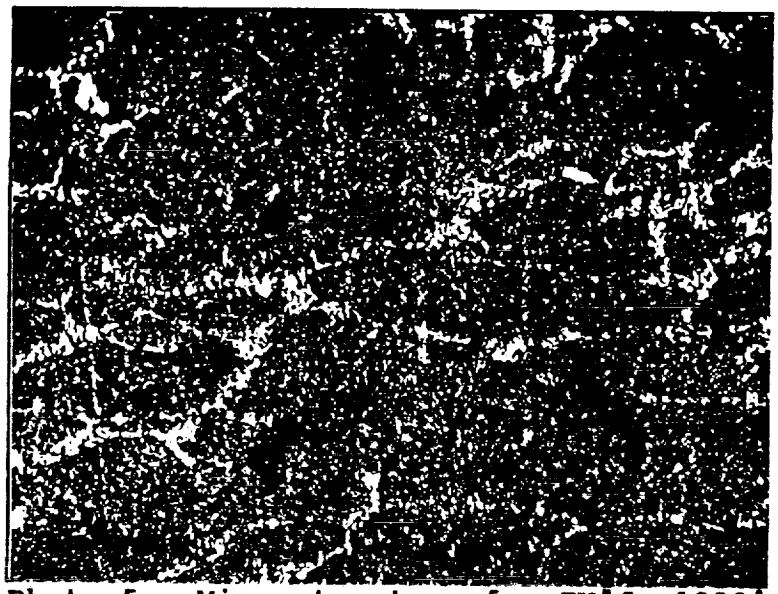

Photo 5 - Microstructure for PW#6, 1000° temper, after CCRPV run. Note dark areas which correspond to pits.

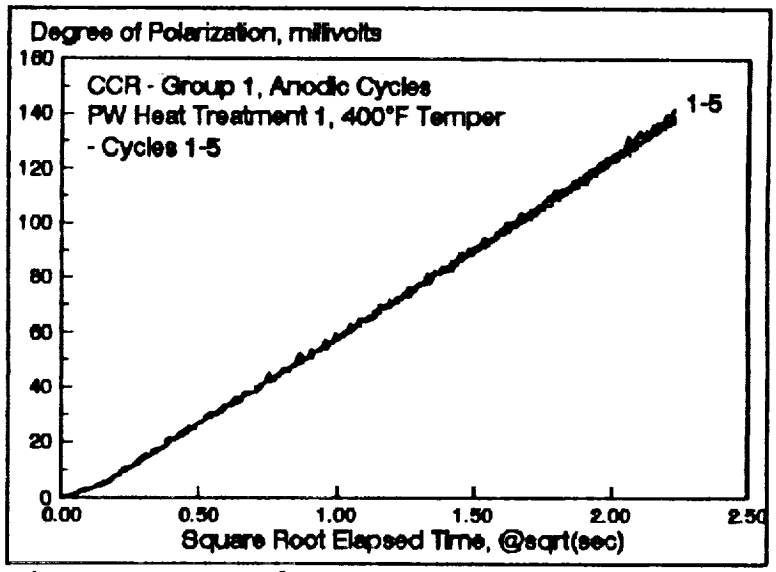

Figure 6 - 400° temper, group 1 anodic cycles.

there is no change in the delta DOP - the change in polarization from the beginning to the end of any given cycle - nor in the polarization rate [Figure 6]. The other three tempers do not

display the same constancy, with variations in both delta DOP and polarization rate - the 1000° temper, as you might have suspected, shows the most pronounced change [Figures 7-9].

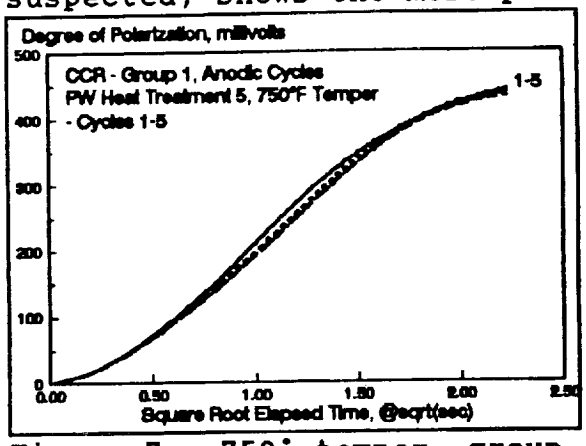

Figure 7 - 750° temper, group 1 anodic cycles.

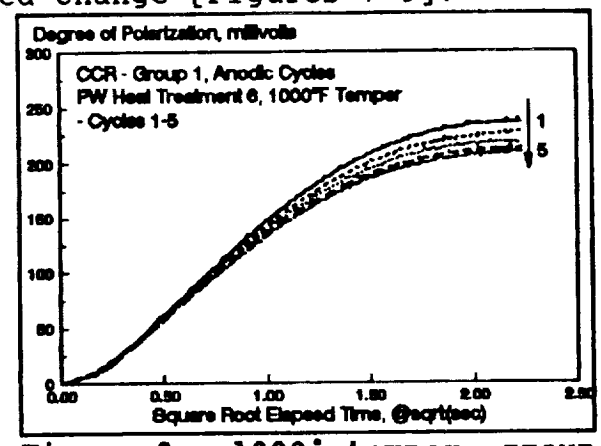

Figure 8 - 1000° temper, group 1 anodic cycles.

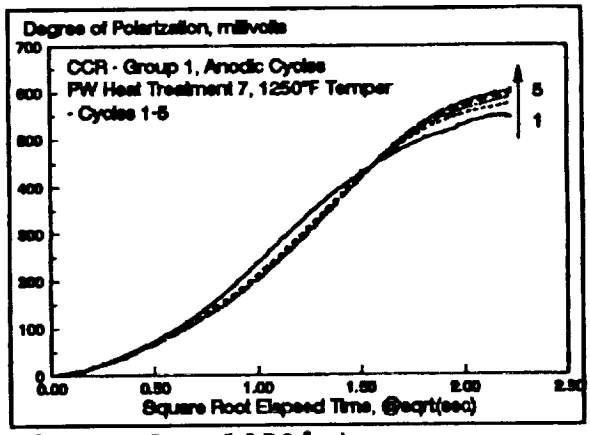

Figure 9 - 1250° temper, group 1 anodic cycles.

The consequences of cathodic polarization are shown in the Figure 10-14 series. It is important to note that although cathodic polarization does not, in itself, cause corrosion - just the opposite is true. Metals are not supposed to corrode under impressed cathodic current - that, after all, is the basis for "cathodic protection". However, cathodic polarization contributes to compositional changes in the solution adjacent to the metal surface - specifically, in the case of dissolved molecular oxygen reduction, to increases in interfacial alkalinity or pH. At the very least, this pH change tends to offset acidity produced by the hydrolysis of metal cations produced by anodic dissolution of metal atoms. The synergistic interaction of both anodic and cathodic reaction products contributes to the production and maintenance of insoluble corrosion product layers at metal/solution interfaces - to passive behavior. Thus, in a very real sense, the results of the first cathodic polarization cycle will affect what happens during the immediately preceding anodic cycle, and so on.

Cathodic polarization behavior follows the same pattern established for anodic behavior - increases in tempering temperature result in an increase in both cathodic DOP and in cathodic polarization rates [Figure 10]. Note again, that in the

case of the 400° temper, that polarization appears to follow diffusion limited mass transport kinetics while the others do not. For whatever it is worth, both anodic and cathodic polarization can be linearized by plots delta DOP as a function of t^x where x can have values between 0.600 and 0.750. The mechanistic significance in terms of what process or processes control has yet to be established.

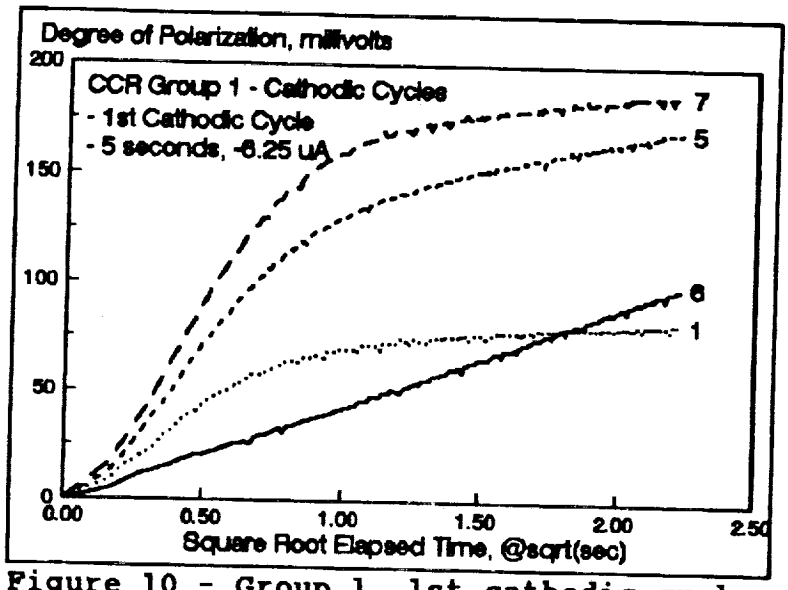

Figure 10 - Group 1, 1st cathodic cycles for 400°, 750°, 1000° and 1250° tempers.

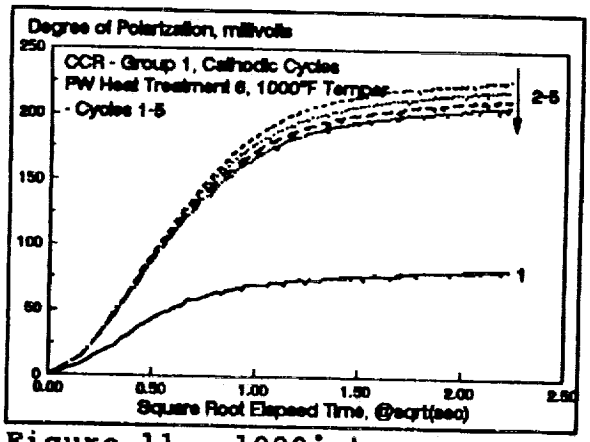

Figure 11 - 1000° temper, group 1 cathodic cycles.

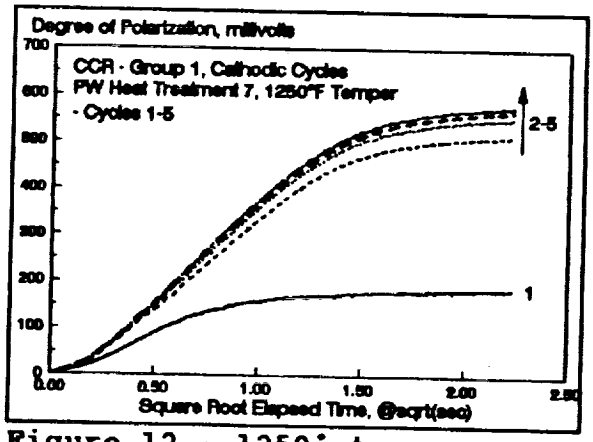

Figure 12 - 1250° temper, group 1 cathodic cycles.

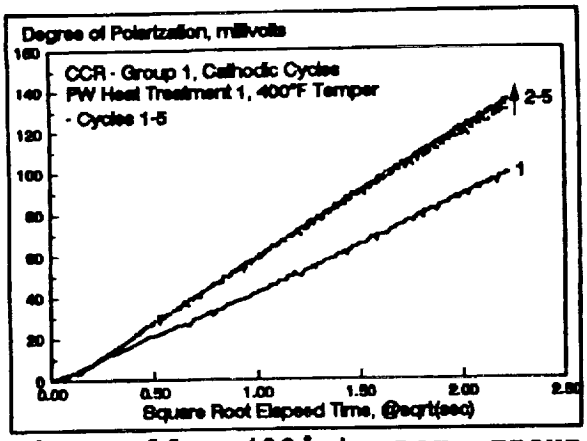

Figure 13 - 400° temper, group 1 cathodic cycles.

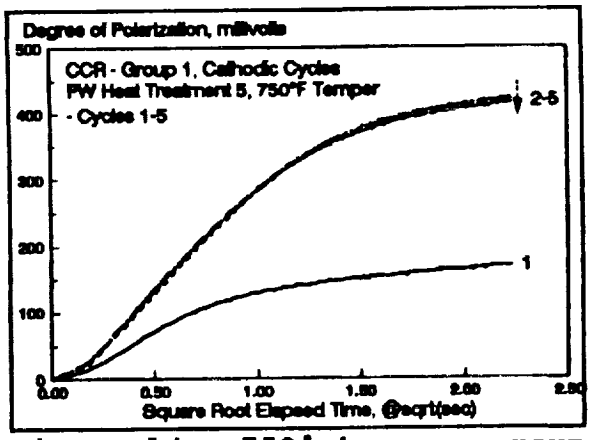

Figure 14 - 750° temper, group 1 cathodic cycles.

When comparing the 5 cathodic cycles for group 1, it is immediately obvious that the 1st cycle is different than all others - both in a lower DOP and polarization rate. Why this behavior during the 1st cycle is not clear - perhaps the change from bulk interfacial pH [about 8.5] is most pronounced during the 1st cycle. It is also possible that any corrosion product produced during the subsequent anodic cycle is never completely removed during later cathodic cycles. Whatever, the difference is there. It is also interesting to note, that except for our 1000° temper anomalous behavior, there appears to be a regular increase in cathodic polarizability with increasing tempering temperature. Whatever is changing about the microstructure is clearly making the cathodic reduction process more difficult, requiring increasing voltages to be induced in response to our -6.25 μA impressed current level [Figures 10-14].

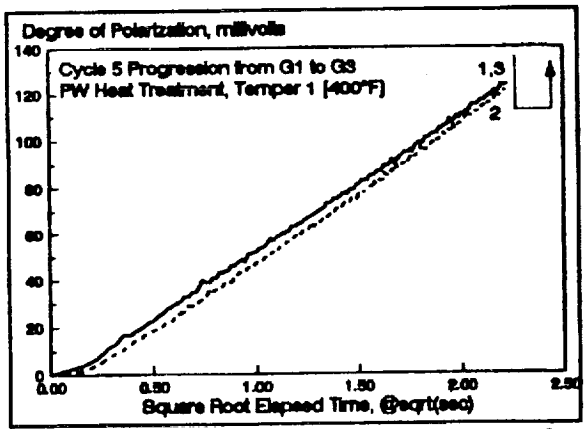

Figure 15 - Comparison of 5th anodic cycles in groups 1-3 for temper 400°.

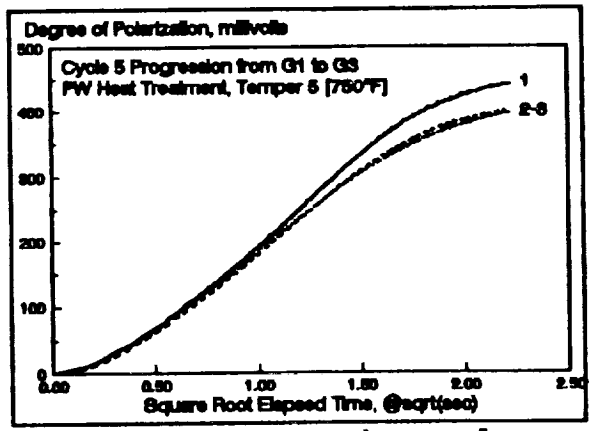

Figure 16 - Comparison of anodic cycles for groups 1-3 for temper 750°.

When comparing 5th anodic cycles for groups 1-3 [Figures 15-18], we notice that the 400° and 750° tempers show virtually no change in polarization behavior [Figures 15 and 16].

For the 1000 and 1250°F tempers, however, there are variations. The 1000°F temper material, which fails to repassivate during cathodic cycles, shows a large drop in anodic polarizability from the 5th cycle in group 1 to the 5th cycle in

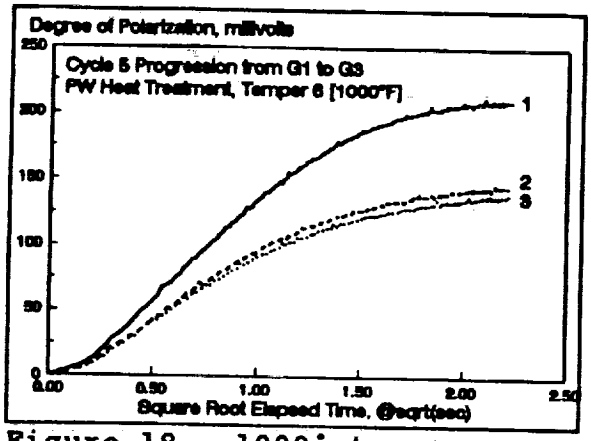

Figure 18 - 1000° temper, comparison of 5th anodic cycles for groups 1-3.

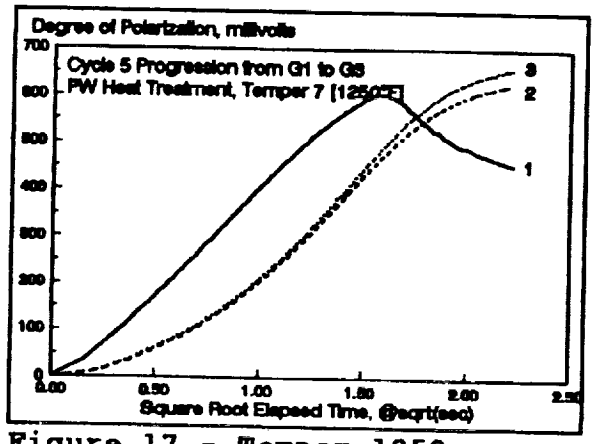

Figure 17 - Temper 1250, comparison of 5th anodic cycles, groups 1-3.

group 2, with little change through group 3. It is interesting to compare this behavior with that of the 1250 temper, which suffers breakdown at the tend of the 5th cycle [maxima in anodic polarization] but repassivates and shows no loss in corrosion resistance through groups 2 and 3.

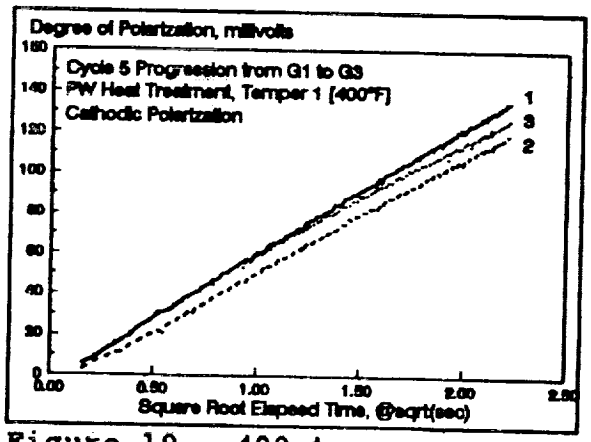

Figure 19 - 400 temper, comparison of 5th cathodic cycles, groups 1-3.

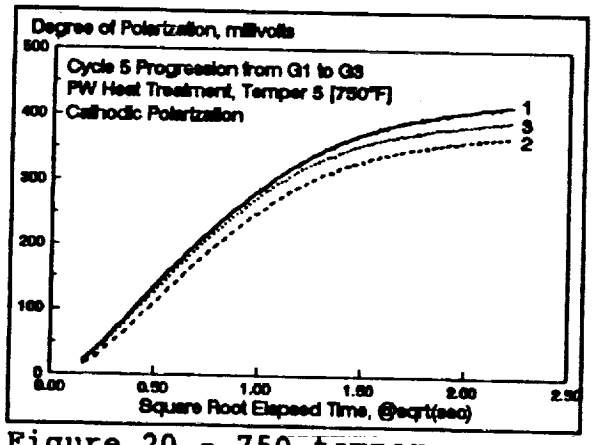

Figure 20 - 750 temper, comparison of 5th cathodic cycles for groups 1-3.

Looking at progressive changes in cathodic polarization behavior, the results again seem to parallel anodic behavior. As Figures 19 and 20 show, little variation in 5th cycle cathodic behavior occurs from group 1 to 3 for either the 400 or 750 temper alloys. Likewise, there is little effect on the reaction order either. Cathodic polarization rates obey $t^{\frac{1}{2}}$ kinetics throughout the exposure period.

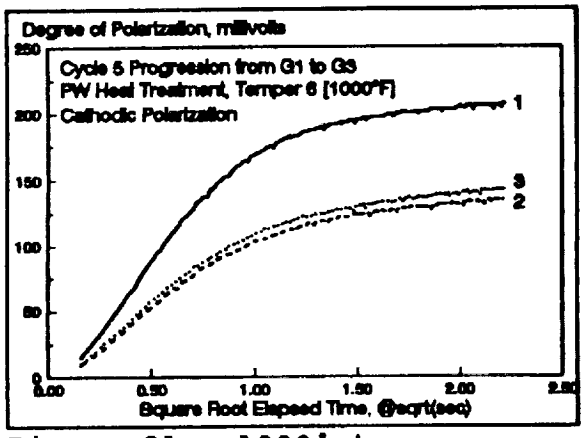

Figure 21 - 1000° temper - comparison of 5th cathodic cycles for groups 1-3.

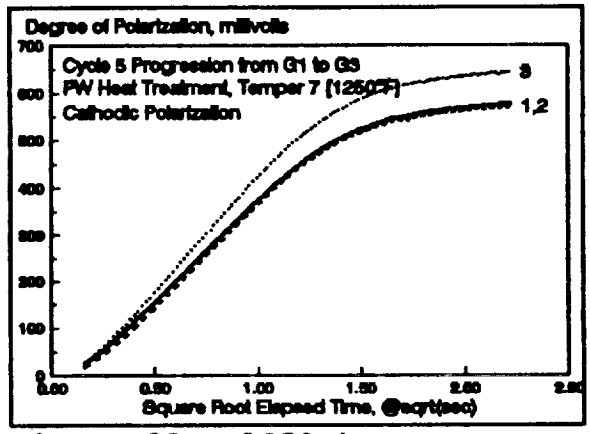

Figure 22 - 1250 temper - comparison of 5th cathodic cycles for groups 1-3.

Finally, variations in cathodic polarization behavior for the 1000 and 1250° tempers also parallel their anodic counterparts.

4.0 CONCLUSIONS

The **CYCLIC CURRENT REVERSAL POLARIZATION VOLTAMMETRY** technique offers a simple, inexpensive method for distinguishing, even quantifying the relationship between alloy microstructure and localized corrosion resistance. The study presented here utilizes the tempering temperature as a variable - increases in this temperature for tempering of martensite is supposed to alter the carbide/ferrite fraction of the microstructure and increase alloy toughness. What happens to the corrosion resistance was then the subject of this research.

Increasing the tempering temperature results in a greater resistance to both anodic and cathodic polarization - the consequences appearing to adversely affect corrosion resistance. Although an increase in temperature where the unstable martensite to stable dispersions of carbide in ferrite transformation occurs should result in changes within the secondary carbide/ferrite microconstituent, this is not apparent. Rather, there appears to be little change in the carbide/ferrite microconstituent and an increase in the relative amount of the primary carbide phase at the prior austenite grain boundaries. Just why this increase should result in boundary layers which afford greater resistance to passage of electric current is not clear, but there is no question that the 1000°F temper displays an extremely poor resistance to onset of pitting than does its 400° counterpart.

5.0 RECOMMENDATIONS FOR FUTURE WORK

Although the technique appears to be sensitive to variations in microstructure, it will be necessary to quantify relationships a bit more. For instance, what are the specific causes for changes in the various CCRPV output parameters? What would changes in temperature, dissolved oxygen concentration, solution pH, salinity, etc. produce?

Secondly, Pratt and Whitney are interested in determining the effect of other microstructural modifications - namely, quenching in oil with development of a high carbon "white layer" on the material surface. Oil quenches will result in less severe residual stresses being incorporated into the alloy. In order to eliminate any negative consequences of the "white layer", the effect of nickel plated surfaces prior to austenization are to be evaluated. These tests, a continuation of the work begun this summer, will be finished at the University of Florida during the coming academic year.

6.0 APPENDICES

6.1 Appendix A - CCRPV menu [CCRPVCOM]

```
*****************************************************************
      DCL '           M273 DEFAULT PARAMETERS
      I/E -4  '       100 uA FULL SCALE CURRENT OUTPUT
      MODE 1 '        GALVANOSTATIC MODE
      BIAS 0 '        NO OFFSET, CURRENT=0 AT START
      MR 2 '          8000 COUNTS=2V ON MOD DAC
      MM 2 '          ARBITRARY WAVEFORM MODE
      SCV 2 '         SOURCE CURVE #2
      DCV 0  '        DESTINATION CURVE #0
      FP 0;LP 2000 '  2000 POINTS FROM 1ST TO LAST POINT
      TMB 25000 '     50 SECOND RUN
      S/P 1 '         ONE READING PER POINT
      PAM 0 '         NO AVERAGING
      INITIAL 0 0 '   ZERO CURRENT 1ST POINT
      VERTEX 1 -500 'A STEP OF 1/8 X FULL SCALE CURRENT RANGE
      VERTEX 199 -500 '
      VERTEX 200 500 '  CURRENT REVERSAL [- TO +]
      VERTEX 399 500 '
      VERTEX 400 -500 '
      VERTEX 599 -500 '
      VERTEX 600 500
      VERTEX 799 500 '
      VERTEX 800 -500 '
      VERTEX 999 -500 '
      VERTEX 1000 500 '
      VERTEX 1199 500 '
      VERTEX 1200 -500 '
      VERTEX 1399 -500 '
      VERTEX 1400 500 '
      VERTEX 1599 500 '
      VERTEX 1600 -500 '
      VERTEX 1799 -500 '
      VERTEX 1800 500 '
      VERTEX 1999 500 '
      VERTEX 2000 -500 '
      ASM '         ASSEMBLE ARB WAVE FORM INTO SCV
      SIE 2 '       POTENTIOMETRY-MEASURE POTENTIAL
      INTRP 0 '     CLEAN STEP
      EGAIN 5 '     2.000 VOLT FULL SCALE POTENTIAL MEASUREMENT
      NC '          PRELOAD MOD DAC WITH 1ST POINT IN ARB WAVEFORM
      CELL 1 '      TURN CELL ON
      P 5 '         PAUSE 5 SECONDS AT CURRENT = 0
      TC '          TAKE CURVE
      WCD;CELL 0 'CELL OFF AFTER CURVE DONE
      GOSUB 51000:    STOCK SUBROUTINE - TRANSFERS DATA
      GOSUB 52000:       STOCK SUBROUTINE - STORES DATA
*****************************************************************
```

6.0 APPENDICES

6.2 Appendix B - Microstructures and Heat Treatments for 440C

"Heat Treater's Guide - Standard Practices and Procedures for Steel, Paul M. Unterweiser, ASM, Metals Park, 1982 [pp 438-9]

440C

Chemical Composition. AISI and UNS: Nominal. 0.95 to 1.20 C, 1.00 Mn max, 0.040 P max, 0.030 S max, 1.00 Si max, 16.00 to 18.00 Cr, 0.75 Mo max

Similar Steels (U.S. and/or Foreign). UNS S44004; AMS 5618, 5630; ASTM A276, A314, A473, A493, A580; FED QQ-S-763; MIL SPEC MIL-S-862; SAE J405 (51440 C); (W. Ger.) DIN 1.4125; (Jap.) JIS SUS 440C

Characteristics. Highest hardness of hardenable stainless steels. Good corrosion resistance, particularly in hardened and tempered condition. Quenched in oil or air. Can be martempered. Can be full, process, or isothermal annealed. Magnetic in all conditions. Low machinability. Used for bearings, nozzles, valve parts, and wear parts of pumps

Forging. Start forging at 1900 to 2150 °F (1040 to 1175 °C). Do not forge below 1750 °F (955 °C). Cool slowly from finishing temperature. Anneal

Recommended Heat Treating Practice

Normalizing. Do not normalize

Annealing. Can be process, isothermal, or full annealed:

- *Process anneal* in subcritical temperature range of 1250 to 1400 °F (675 to 760 °C) for hardness of 98 HRB to 23 HRC. Use clean, rectified salt bath or an atmosphere that is compatible with this temperature range. Soaking and softening time depend on section size of the work. Air cool
- *Isothermal anneal* by heating to 1550 to 1650 °F (845 to 900 °C). Cool slowly to 1275 °F (690 °C). Hold for 4 hr. Hardness, approximately 25 HRC
- *Full anneal* at 1550 to 1650 °F (845 to 900 °C). Cool at a rate not faster than 30 to 40 °F (17 to 22 °C) per hour to 1100 °F (595 °C), after which cooling rate does not affect hardness. Avoid decarburization. Can use atmospheric protection in the form of a vacuum, the inert gases argon or helium (both expensive), or nitrogen. All should have dew point below −60 °F (−51 °C). For endothermic-generated atmosphere, hold dew point in the 0.95 to 1.20 carbon range for the annealing temperature used. Annealed hardness, 98 HRB to 25 HRC. Full annealing, expensive and time consuming, should not be used except as required for subsequent forming or difficult specialized metal cutting operation

Hardening. Atmospheric protection rules for annealing apply to hardening. Parts must be completely clean and free of oil and shop contamination. Thermal conductivity is significantly lower than that of carbon and alloy steels. High stresses during rapid heating may cause warpage and cracking in delicate or intricate parts. Preheat at 1400 to 1450 °F (760 to 790 °C), only long enough to equalize temperature in all sections. Extremely delicate or intricate parts would benefit from an additional prior preheat at 1000 °F (540 °C). Austenitize at 1850 to 1950 °F (1010 to 1065 °C). Use upper end of range for larger sections or where maximum corrosion resistance and strength are required. Soaking time of 30 to 60 min is adequate for sections up to ½ in. (13 mm). Allow an additional 30 min for each additional inch or fraction thereof. Double soaking time if parts have been full or isothermal annealed. If process annealed above 1300 °F (705 °C), increase soaking time by about 50%. Quench in oil or air. Oil preferred, because it guarantees maximum corrosion resistance and ductility. Martempering in hot oil or salt is suitable because of high hardenability. As-quenched hardness, approximately 60 to 62 HRC minimum

Stabilizing. For minimum retained austenite and maximum dimensional stability, use subzero treatment at −100 ± 20 °F (−74 °C). This should incorporate continuous cooling from the austenitizing temperature

Tempering. Temper at 325 °F (165 °C) or higher, for minimum hardness of 60 HRC. Temper at 375 °F (190 °C), for 58 HRC minimum; at 450 °F (230 °C), for 57 HRC minimum; and at 675 °F (355 °C), for hardness approximately 52 to 56 HRC. Double tempering beneficial. Cool to room temperature between tempers

Nitriding. Can be nitrided to case depth of 0.008 in. (0.203 mm) in 48 hr. For further information, see type 410

Recommended Processing Sequence

- Forge
- Anneal
- Rough machine
- Stress relieve
- Finish machine
- Preheat
- Austenitize
- Quench
- Stabilize (not mandatory, but beneficial)
- Temper
- Final grind to size
- Nitride (if required)

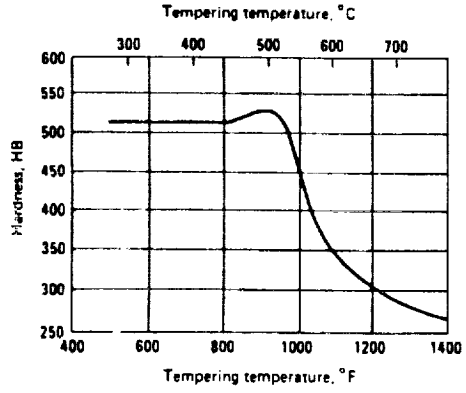

440C: Hardness Versus Tempering Temperature. Composition: 1.020 to 1.044 C, 0.40 to 0.48 Mn, 0.017 to 0.019 P, 0.010 to 0.011 S, 0.18 to 0.31 Si, 16.90 to 17.18 Cr, 0.24 to 0.54 Ni, 0.50 to 0.64 Mo. Heat treated at 1700 °F (925 °C), 1 hr. Oil quenched at 150 to 200 °F (66 to 94 °C). Double stress relieved at 350 °F (175 °C), 15 min. Water quenched. Tempered 2 hr. Heat treated, 0.550-in. (14-mm) round. Tested, 0.505-in. (12.8-mm) round. (Source: Republic Steel)

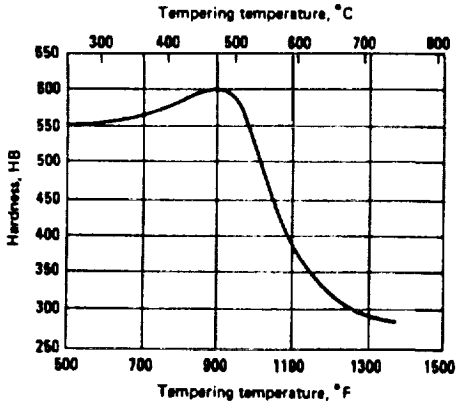

440C: Hardness Versus Tempering Temperature. Composition: 1.02 C, 0.48 Mn, 0.017 P, 0.011 S, 0.18 Si, 16.90 Cr, 0.54 Ni, 0.64 Mo. Heat treated at 1900 °F (1040 °C), 2 hr. Oil quenched at 150 to 200 °F (66 to 94 °C). Double stress relieved at 350 °F (175 °C), 15 min. Water quenched. Tempered 2 hr. Heat treated, 0.385-in. (9.78-mm) round. Tested, 0.375-in. (9.53-mm) round. At 500 to 1000 °F (260 to 540 °C). Also, heat treated, 0.550-in. (14-mm) round. Tested, 0.505-in. (12.8-mm) round. At 1100 to 1400 °F (295 to 760 °C). (Source: Republic Steel)

440C: Microstructures

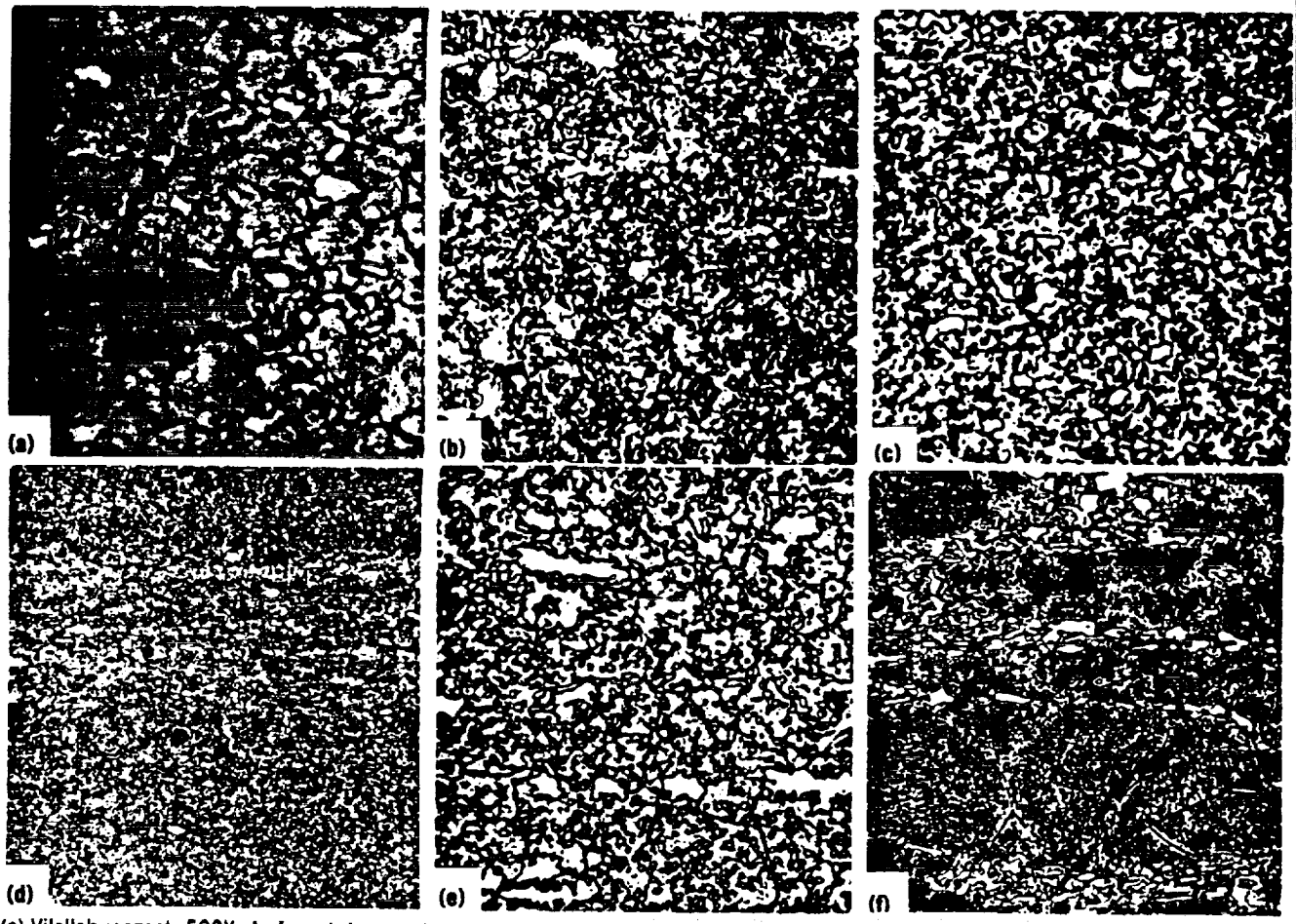

(a) Vilella's reagent, 500X. As forged. Large primary carbide particles. Heavy carbide precipitation at grain boundaries. Secondary carbide particles. Matrix predominantly retained austenite. (b) Vilella's reagent, 500X. Forging annealed at 1600 °F (870 °C). Furnace cooled to 200 °F (94 °C) in 48 hr. Air cooled. Large particles of primary and spheroidized particles of secondary carbide. Ferrite matrix. (c) Vilella's reagent, 500X. Forging hardened by austenitizing at 1850 °F (1010 °C), 1 hr. Air cooled. Tempered at 450 °F (230 °C), 2 hr. Large primary and tempered secondary carbide particles. Martensite matrix. (d) Vilella's reagent, 100X. Forging, hardened and tempered. Band of carbide segregation. Dispersed carbide particles. Tempered martensite matrix. Microhardness indentations (black). Shows relative hardness of carbide particles and matrix. (e) Super picral, 500X. Bar, preheated at 1400 °F (760 °C), ½ hr. Austenitized at 1875 °F (1025 °C), ½ hr. Air cooled to 150 °F (66 °C). Double tempered at 800 °F (425 °C), 2 hr each. Primary and secondary carbides, light islands and particles. Tempered martensite matrix. (f) Vilella's reagent, 200X. Bar, austenitized at 1850 to 1925 °F (1010 to 1050 °C). Oil quenched. Tempered at 375 °F (190 °C). Segregated stringers of primary carbide (light) and dispersed secondary carbide particles. Tempered martensite matrix. (Source: *Metals Handbook*, 8th ed., Vol 7, American Society for Metals, 1972)

N93-19392

1992 NASA/ASEE SUMMER FACULTY FELLOWSHIP PROGRAM

JOHN F. KENNEDY SPACE CENTER
UNIVERSITY OF CENTRAL FLORIDA

HYDROGEN LEAK DETECTION IN THE SPACE SHUTTLE

PREPARED BY:	Dr. Ronald G. Barile
ACADEMIC RANK:	Professor
UNIVERSITY AND DEPARTMENT:	Florida Institute of Technology Chemical Engineering Department
NASA/KSC	
DIVISION:	Engineering Design Lab
BRANCH:	Instrumentation & Hazardous Gas
NASA COLLEAGUE:	Ric Adams
DATE:	August 31, 1992
CONTRACT NUMBER:	University of Central Florida NASA-NGT-60002 Supplement: 8

ACKNOWLEDGEMENTS

Every person below was a terrific help to me. This summer was a wonderful experience because of them.

The NASA persons who conceived and directed the project:
Ric Adams, who guided me with skill and patience, and his managers, Bill Helms and Dave Collins.

Other NASA persons who kindly gave of their time on a daily basis to help me along:
Bill Larson, Greg Hall, and Curtiss Ihlefeld.

The Boeing Haz Gas Lab personnel who put in a major amount of time and made all my computer and experimental work possible:
Larry Lingvay, Guy Naylor, Rich Hritz, Curt Lampkin and Terry Hammond.

Florida Tech Chemical Engineering student who did the last month's experiments and data reduction:
Dan Diolosa.

The Transducer Lab, Optics Lab and other Boeing personnel who helped substantially and loaned important equipment:
Drew Schmidt, Dick Deyoe, Jerry Mason, and Dr. Bob Youngquist.

Engineering Development and Test:

Stu Gleman, who is always happy to help by inventing a circuit or a gadget.

The KSC library staff gave efficient and kindly support.

The UCF administrators:
Dr. Loren Anderson and Carrie Stiles, courteous and capable.

THANKS!

ABSTRACT

This study focuses on a helium gas jet flowing into room air. Measurements of helium concentration and velocity in the jet-air mixture are reported. The objective is to learn about jet characteristics so that dynamically similar hydrogen leaks may be located in the space shuttle. The hazardous gas detection system (HGDS) in the mobile launch pad uses mass spectrometers to monitor the shuttle environment for leaks. The mass spectrometers are fed by long sample tubes which draw gas from the payload bay, mid body, aft engine compartment and external tank. The overall purpose of this study is to improve the HGDS, especially in its potential for locating hydrogen leaks.

A rapid-response leak detection experiment was designed, built, and tested, following on the work done in this program last summer. The apparatus included a Perkin Elmer MGA-1200 mass spectrometer and air velocity transducer, both monitored by a Macintosh IIFX computer using LabVIEW software. A jet of helium flowing into the lab air simulated a gas leak. Steady helium or hydrogen-nitrogen jets were logged for concentration and velocity, and the power spectral density of each was computed.

Last year, large eddies and vortices were visually seen with Schlieren imaging, and they were detected in the time plots of the various instruments. The response time of the MGA-1200 was found in the range of 0.05 to 0.1 sec. Pulsed concentration waves were clearly detected at 25 cycles per sec. by spectral analysis of MGA data. No peaks were detected in the power spectrum, so in the present study, 10 Hz bandwidth-averaged power levels were examined at regular frequency intervals. The practical consequences of last year's study: sampling frequency should be increased above the present rate of 1 sample per second so that transients could be observed and analyzed with frequency response methods.

Many more experiments and conditions were observed in this second summer, including the effects of orifice diameter, jet velocity, sample tube design, radial effects, vertical flow, and low hydrogen concentration (1%). A frequent observation was

that the power spectrum, calculated from the Fourier transform of concentration fluctuations, gives a separate piece of information from concentration. Many of the tests suggest that power is high where mixing occurs at the helium-air interface. This fact is apparently independent of the concentration level, which could be high or low, but depends on the sample location relative to the jet (leak) origin. Whereas, high concentration may be due to a strong leak far away or a small leak close to the sample tube. If the power is low for any concentration level, this would signify helium is arriving at the sample tube by diffusion, not chaotic mixing caused by the jet interaction with air. The practical result is to propose a modification of the HGDL mass spectrometer data sampling and software so that sampling rates could be capable of observing at least 25 Hz fluctuations.

SUMMARY

This study focuses on helium and hydrogen-nitrogen jets flowing into lab air. The technical goal is to learn about how leak jets break up and mix with air. Such information may be applied to analysis of helium signature tests or hydrogen leaks from the main propulsion system in the space shuttle. The hazardous gas detection system (HGDS) in the mobile launch pad uses mass spectrometers fed by long gas sampling tubes to monitor the payload bay, mid body, aft engine compartment and external tank. The mass spectrometers continuously assay the shuttle environment for hydrogen, helium, oxygen and argon. The overall purpose of this study is to improve the HGDS, especially in its potential for precisely locating gas leaks.

The motivation for this work is the difficulty experienced in the past when hydrogen leaks were discovered using the HGDS. The number of sample tubes is too small, i.e., five total, too give a detailed prediction of leak source and specific location. As it exists presently, the system can distinguish only broad areas such as payload bay, midbody, aft compartment, etc.

Last year the HGDS was reviewed and pre-existing leak data was analyzed for transients to determine if the concentration-time data had any . Spectral analysis was performed on earlier data measured at the OPF and in the Hazardous Gas Detection Lab. Then, a rapid-response leak detection experiment was designed, built, and tested. The apparatus included a Perkin Elmer MGA-1200 mass spectrometer, an air velocity transducer, and a pressure transducer, all monitored by a Macintosh IIFX computer using LabVIEW software. A jet of helium flowing into the lab air simulated a gas leak. Schlieren imaging and video recordings were also employed to study the flow phenomena. Experiments on leak jet character-ization included velocity, pressure and concentration profiles and in particular on spectral analysis of these signals. Steady and pulsed jets were logged for concentration, velocity, and pressure, and the power spectral density was computed for each observation.

The LabVIEW software performed well in both analysis of earlier data and in real-time data acquisition and reduction. The air velocity transducer (TSI) and the pressure transducer

(Rosemount) were capable of measuring rapid transients in helium jet phenomena, and they have the versatility and potential to be applied to leak detection and location. Particular emphasis was centered on large eddies and vortices in the jet-air mixing zone. Large eddies and vortices were visually seen with Schlieren imaging, and they were detected in the time plots of the various instruments. The response time (63.2%) of the MGA-1200 was found in the range of 0.05 to 0.1 sec. Pulsed concentration waves were clearly detected at 25 cycles per sec. by spectral analysis of MGA data. For certain, the MGA was fast enough to detect transients such as hydrogen or helium eddies in the time trace data, if sampled at 50 Hz. Spectral analysis showed some evidence of correlated power in the 0.1 to 20 Hz. region, but visual and transient concentration observations indicated that eddy shedding from the leak jet was somewhat irregular in time. Thus, such events did not correlate well as definite peaks in power spectral density plots. One practical consequence of that study was to suggest that the backup HGDS sampling frequency should be increased above the existing rate of 1 sample per second.

The second year study focused on a refined spectral analysis of concentration and velocity data. The basic apparatus was reassembled in the configuration described above. LabVIEW software was extended to include band width averaging at selected central frequencies, e.g., 10 Hz bandwidths at center frequencies of 5, 10, 15 Hz, etc. Three sample tube designs were studied, two orifice types, gas flows of 3.64 to 14.56 SLM using 99.999% helium or 1% hydrogen in nitrogen. Concentration and spectral density were obtained at various axial lengths downstream from horizontal jets, including the centerline and various radial positions to the side and above the jet axis. Flow obstructions were also placed into the jet axis downstream from the origin. The general result is that concentration and power calculated from concentration fluctuations give distinct information about where the sample tube is relative to the leak jet origin. In the vicinity of the leak origin, one finds high or low concentration depending on the leak strength and the purge gas rate. But, in this region there is likely to be peaks in power independent of the concentration. Thus, mass

spectrometers should be operated at a high sampling rate, e.g., 25 Hz, so that power may be determined. This would result in greater capability to detect gas leaks and infer the leak location.

TABLE OF CONTENTS

LIST OF ILLUSTRATIONS

Figure

I INTRODUCTION

In the space shuttle, hydrogen and oxygen are the main engine propulsion gases, as well as the fuel-cell power system gases. Leaks of these gases may be found in the aft fuselage, the mid body, and other areas. Various forms of leak detection equipment are employed in and around the shuttle wherever hazardous materials are present. The hazardous gas detection system (HGDS) uses mass spectrometers fed by long gas sampling tubes to monitor the payload bay, mid body, aft engine compartment, and external tank. The mass spectrometers in the HGDS monitor the environment for hydrogen, helium, oxygen, nitrogen and argon.

This study will focus on helium jets in the lab which are intended to represent a typical leak during tests of the main propulsion system (MPS). Helium signature tests are routinely performed to determine the shuttle's MPS integrity. These tests, involving pressurization of the MPS with GHe and monitoring for helium leaks with the HGDS, are scheduled at the launch pad previous to the start of countdown. Hydrogen or oxygen leaks may still occur during tanking operations after the helium signature test is acceptable. These would be detected by either catalytic hydrogen detectors situated outside in the tank-piping system, or by the prime, backup, or external tank (HUMS) mass spectrometers sampling around and in the shuttle. By studying jets with a mass spectrometer using frequency response techniques, new understanding gained will lead to better methods for detecting and locating leaks in the MPS.

Main Goals of the Two-Summer Study:

1. Assess the present HGDS and analyze earlier leak data to determine if leak data has frequency information which can lead to pinpointing the leak location .
2. Design, build, and test a rapid-response leak detection experiment which focuses on leak characterizaton including velocity, pressure and concentration profiles and in particular on rapid fluctuations and spectral analysis of these variables.
3. For a longer-term objective: Predict an improved placement of sample tubes and improved data analysis for special tests so that leak locations can be pinpointed.

II BACKGROUND

2.1 PRESENT SYSTEM DEFINITION

The hazardous gas detection system at KSC is a mix of UTI (quadrupole) and Perkin Elmer (fixed sector) mass spectrometers. They monitor the shuttle and tail service mast (both prime and backup HGDS), and the external tank (HUMS). Gas samples are drawn through 0.18-in. ID tubes to mass spectrometers situated 100 to 200 ft. away inside the mobile launch platform. Five gas samples are sequentially assayed for hydrogen, helium, oxygen, nitrogen and argon. The five samples arrive in separate tubes: three from the shuttle, one from the tail service mast, and one from the external tank.

Sample gases are drawn from the shuttle interior into 0.23-in. ID SS tubes distributed in the aft area. The payload bay and mid body tubes are located just aft of the 1307 bulkhead. Four tubes which sample the payload bay purge are connected through tees into one tube which is routed through the umbilical disconnect panel (UDP, line 2). Two SS tubes which sample the mid body purge are connected into one tube leading to the UDP (line 4). The pair of aft sample tubes are mixed together and routed to the UDP. The aft sample tubes are located several feet aft of the 1307 BH at the #9 vent doors, thus the aft sample could reflect upstream leaks from the MB and PLB.

A 180-lb/min. nitrogen purge is flowing at the pad when the cryogenic propellants are loaded into the vehicle. Both hydrogen and oxygen flow inside separate piping systems from the tail service mast to the shuttle aft compartment to the external tank. Before loading cryogens, a test is done by injecting helium in this piping system, the main propulsion system (MPS), with air purge on the outside (1). Hence, leaks in the cryogenic piping can be detected via helium tests before loading cryogens, and by hydrogen and oxygen detection during and after these are loaded on board. Due to safety considerations, the present study was done primarily with helium, although hydrogen can be easily implemented in future work.

2.2 EARLIER KSC WORK RELATED TO HAZARDOUS GAS DETECTION

In 1990, Schleier studied gas leaks of helium, nitrogen, and

argon by flowing the gases through a slightly cracked gate valve (2). Using helium at 68 psig and 105 sccm as the reference condition, flows of helium, nitrogen, and argon correlated well as predicted vs. observed flows. Mehta characterized a turbomolecular-pumped magnetic sector mass spectrometer in 1988 working with the HGDL (3). The model was Perkin Elmer MGA-1200, the same type which is employed in the present study (H2S2). Linearity, precision, drift, detection limits and accuracy were found to be acceptable for quantitative analytical determination of hydrogen, helium, oxygen and argon in nitrogen or helium background gases. The 90% rise times for pulse inputs were on the order of one-half second.

One-second pulse of nitrogen into helium put into the Perkin Elmer 17" disconnect mass spectrometer resulted in an 84% peak on nitrogen and a total dead and lag time of less than 0.1 sec on the upswing (4). The downswing started about 0.2 sec late, and took another 0.8 sec. to drop to zero. A one-second pulse of helium into nitrogen rose quickly to 98% in less than 0.1 sec., but it did not fall off from 98% until 3 sec. and it zeroed after another second (4 sec. total). A recent internal HGDL study (5) on noise in MGA-1200 reported that the unfiltered 60-cycle and related harmonic rms noise level was on the order of 100 mV. Part One of the present study, completed in summer 1991 (6), is reviewed in the present document.

2.3 LITERATURE SURVEY OF JETS

Last summer, a wide-ranging review of jets, mass spectrometers, gas leaks, etc., was presented (6). The survey below focuses on earlier and new references which pertain to frequency and mixing phenomena.

A survey of jet literature was performed because a gas leak behaves similarly to a jet with regard to velocity decay, pressure profile, concentration decay, sonic waves, etc. The fluctuations seen in mass spectrometer test data are reminiscent of vortices or large scale eddies which form at the edge of the jet-air mixing zone (7-12). These swirling structures, which travel with the jet at roughly the local centerline velocity, could give rise to the type of concentration fluctuations which are observed in MS tests of concern here.

A small laminar or turbulent fluid stream issuing into a large region containing the same or similar fluid at rest is termed a free (submerged) jet, Fig.1 (top) (13). For a laminar free jet, there is an orderly pumping action by the jet, resulting in both lateral and axial motion in the surrounding fluid. The difference in velocity between a free jet and its surroundings generates a diffusion (mixing) region characterized by large scale eddies. Vortices occur in the interface region between the central jet core and the surrounding fluid. Vorticity (need Defn) tends to agglomerate, forming large-scale eddies, which grow by entraining fluid from the surroundings and by pairing--the basic mechanism or the growth of the shear mixing layer. While eddy motion is similar to molecular motion, there are important differences. Turbulent movement depends on the general (directed) motion and requires a continuous supply of energy to maintain it, while molecular motion does not. The source of energy which supports the eddies is the directed kinetic energy of the jet which eventually is transformed to kinetic energy of turbulence. The turbulence, in turn, decays irreversibly through viscous shear.

The free jet spreads because of shear at its boundaries, and the total flow crossing successive normal planes increases because of entrainment of the surrounding fluid, Fig. 1 (middle) (14). Of course, continuity must be satisfied, thus the increasing flow area requires a decreasing jet velocity. The mixing region, emanating from the solid boundary of the jet, progresses both inward and outward with respect to the jet axis as a function of axial distance. However, close to the exit plane of the jet there exists a region called the potential cone or core which is not disturbed by the large eddies. Downstream from the potential cone, the entire central portion of the jet is filled with large-scale eddies (once the diffusion has reached the axis) and the flow is fully established.

The momentum of a jet issuing from a circular orifice is:

$$Mo = (rho * Ao * Vo) * Vo.$$

where rho = density
Ao = orifice area
Vo = velocity at orifice.

To a good approximation, momentum is conserved, thus, the

product (rho x Vo) must remain constant by the jet area expanding and the velocity slowing down as it flows downstream. Dynamic similarity or similarity solutions generally apply to the free jet. This predicts the result that dimensionless profiles of mean velocity in the diffusion (mixing) region must be defined by the same functional form at all sections normal to the flow (Fig. 1, bottom) (14):

$$Vx/Vmax = f(N)$$

where

$N = l^*/g(x)$

l^* = radial coordinate measured out from the edge of the mixing region

$g(x)$ = arbitrary measure of radial extent of diffusion region (similarity).

Practically, similarity means that all velocity profiles of a given flow field will fall on one single curve. Three simple results of various studies are:

1. $g(x) = C * x$.
2. Vmax (centerline)/Vo = xc/x, where xc is the length of the central core.
3. The data for f(N) is reasonably fit by the error function.

Measurements of the mixing of two coaxial hydrogen-air jets are reported by Chriss (15), including centerline decay and radial profile shapes of composition, velocity, and total enthalpy. The striking result is that velocity and composition decay almost identically on dimensionless plots. These plots verify that velocity profiles fit the similarity condition, but in addition the concentration profiles also have this property. Becker et al. (7) worked with an air-air jet marked with oil smoke. Turbulent concentration fluctuations of the nozzle gas diffusing into the stagnant gas were on the order of 25% of the centerline value (lateral distance from centerline about 1/3 of jet radius). Heat transfer and flow measurements including frequency and intermittency data are given by Chua and Antonia (8). Turbulent fluctuations ranged from 10Hz for large peaks to 100 Hz for small variations.

Detailed analysis of shuttle hydrogen leaks are given by Seymour (16) on the STS-35 scrub-3 hydrogen leak analysis. The study featured a transient model of the aft compartment H2 concentration. The basic time constant of the aft compartment purge flow is about 90 sec. Some of the major conclusions were: the leak did not exist at ambient temperature, the engine prevalve 2 was the most likely leak location, at least 80% of leakage came from the engine 2 prevalve, the scrub-2 leak area was twice that of scrub 3 and consistent with the known engine 3 prevalve detent cover seal leakage, and leak area changes cannot be inferred from concentration changes without employing an analysis similar to that used in the study, i.e., the compartment model. The above work may be more readily understood by referring to MPS diagrams for propellant flow, etc. (17,18).

III APPARATUS AND PROCEDURE

3.1 LabVIEW SOFTWARE

LabVIEW programs (VI's) written by Larry Lingvay (Boeing HGDL) were used to get and analyze helium leak data. The data were stored in files such as MacPaint and as tab-delimited text files. The latter could be read by other LabVIEW software such as *Band Width Integrator* and *Data Display VI*. The software used in this project along with their functions are:

1. Super Spectrum Analyzer (SSA)--Collect helium concentration data, calculate the average over one or more seconds, take power spectrum of concentration data, display plots of concentration and power. Similarly, other gases could be measured by switching VI controls. The air velocity transducer (AVT) was also connected to SSA, on channel 5. A data file is generated which is read into Multifile Integrator (below).

2. Analog Mass Spec--Collect hydrogen, helium, nitrogen, oxygen and argon data at 1 sec. intervals as in IHUMS system.

3. Multifile Integrator--Take power spectrum vs. frequency data from SSA-generated files and integrate at several center frequencies, e.g., 5, 10, 20, 40, etc., for 10 Hz band widths. Each file is measured at a different length or position in the jet.

4. Data Multiplot Display--Plot integrated power data vs. length for various center frequencies.

3.2 APPARATUS AND DATA ACQUISITION

The apparatus and data system were similar to last year. Changes included new sample tube designs and new experimental configurations. A helium leak was simulated in the HGD Lab by a pure helium stream (KSC grade) flowing from the lab-service panel through 1/32-in. ID stainless steel tubing, and exiting through a small nozzle or a 1/4-in. ID Tygon tube. The gas exited the nozzle from a circular orifice, 0.05 cm. diameter, recessed in a short tube, 0.5 cm long and 0.4 cm. diameter (sonic orifice). In effect, the jet was actually emerging from the 0.05-cm. tube at or below local sonic velocities, depending

on the upstream pressure.

A schematic drawing of the equipment used in the HGDL is shown in Fig. 2. A Rosemount pressure transducer was used to measure pressure fluctuations in the jet field (Minneapolis, MN). This device is capable of measuring pressure from 22 to 32 inches of mercury absolute. Velocity and its fluctuations were detected by a TSI Inc. air velocity transducer (AVT) with a range of 0 to 10,000 fpm (St. Paul, MN). These probes were mounted on a small vise which was placed at various measured locations in relation to the jet origin.

The jet stream representing the leak was measured and controlled by a Sierra Instruments 840 SideTrak mass flow meter/controller. The instrument was calibrated for nitrogen gas flow, but was correctable to helium gas by multiplying the reading by 1.453 (for units of standard liters per minute, SLM). An independent check on the frequency response of velocity and concentration measurements was provided by installing in the leak jet a mechanical chopper used in optical experiments.

A Perkin Elmer MGA-1200 (H2S2) mass spectrometer was employed as the gas analyzer. The helium jet was sampled with a 15-ft length of 1/32-in ID stainless steel tubing with a crimp at about 3 inches downstream from the sample orifice. This tube, *ST1*, was connected directly to the porous plug at 200 Torr in the MS evacuated area, and as such it was pumped directly with the MGA roughing pump Samples were taken at various locations downstream from the jet origin normally in the horizontal direction, *x* (x=axial, y=lateral-horizontal, z=vertical). Data were taken with this tube between 7-13-92 and 7-24-92. Later, the same tube minus the crimped region, became a 14.5-ft. length of 1/32-in. ID SS capillary tubing, which was fitted to the MGA inlet valve #3. This tube, *ST2*, was also pumped by roughing pump as with ST1. The crimp was cut off due to plugging, as manifested by slow sample tube response and recovery. Flow resistance in valve #3 was sufficient to provide enough pressure drop so that the vacuum system was not overloaded. The measured time constant of this second tube was about 0.08 sec.

After a few trial runs, ST2 was found to be inappropriate for lab air measurements. A third change (*ST3*, on 8-7-92) employed the 14.5-ft 1/32-in ID tube connected directly into the heated

MGA valve #1, with a vacuum pump at the valve outlet. In this way, flow in the sample tube remained high, with a small leak sample drawn off a tee to the mass spec. This insured that the transit time through the sample tube was high, but the pressure to the mass spec remained low. (The big pressure drop in the sample line occurred in capillary tube downstream from the valve.) The sampling dead time was a few seconds.

All sensors were fed into a National Instruments data acquisition board (NB-MIO-16XL-42) plugged into a MacIntosh IIFX computer. A VI called *Super Spectrum Analyzer* sampled, plotted and analyzed the data from each sensor. The analysis routine was to sample during a given time window with a specified period of samples, e.g., 1 or 2 sec., for a specified band width of typically 100 Hz. The mean concentration was computed, and the time traces of concentration and power spectrum were plotted, all in the LabVIEW panel. Then, the frequency data were integrated (offline) about selected center frequencies for 10 Hz band widths by a VI called *Multifile Integrator*. Data generated in *Multifile Integrator* were then displayed by *Data Multiplot Display* as average power vs. jet axial length, x, as a function of several center band frequencies.

3.3 PROCEDURE

Set gas flow, put sample tube and/or AVT in vise at specified location. Calibrate mass spec zero and span gas, run LabVIEW, store data in file, save paint file of LabVIEW screen. Run data analysis VIs, create plots of concentration and power spectra.

IV RESULTS AND DISCUSSION

4.1 SIMULATED HELIUM LEAKS

The experimental variables were helium jet flow rate, 3.64, 7.28, and 14.56 SLM; jet orifice either sonic orifice or 1/4 in.-ID Tygon tube; sample tubes ST1, ST2, and ST3; various axial positions from 1/16 to 36 in.; and, radial positions at fixed x; horizontal, cylindrical bar obstruction, 3/4-in. diameter, 3/4" downstream from jet; jet orientation to gravity was usually horizontal, but vertical up flow was also observed with/without fan-driven crossflow.

4.1.1 SAMPLE TUBE 1. Experiments using sample tube 1 (ST1) were run between 7-13-92 and 7-24-92. Individual experiments are discussed below in order of the run date.

7-13-92 Fig. 3a shows the percent helium and the hand-averaged power due to concentration fluctuations at several frequencies versus axial length downstream. For this slow flow, 3.64 SLM (3,640 SCCM) helium, the concentration of helium falls very quickly from 100% at the jet origin to 2.5% at x = 6". (At this rate, the helium exits the 0.4 cm diameter orifice into air at 1035 FPM.) In contrast, the power at 5 Hz rises up from -31 near the jet to -4 at x = 3 and 6 in. downstream (relative log scale units, analogous to dB if the concentration were in volts). Higher frequencies, also shown on Fig. 3a, follow the same trend with a power peak in the 3 to 6 in. range. There is also evident a progressive downward trend of power as frequency increases in steps to 100 Hz. The background air in the lab has a flat power spectrum of -60 to -80 for all frequencies between 5 and 100 Hz. Figs. 3b and 3c show the concentration record and power vs. frequency during the above runs which were 1 second in duration. Average helium concentration during this period is noted on the individual traces at various *x* values.

7-16-92 to 7-24-92 A series of runs was observed with 1/4-in. ID Tygon tubing as the jet orifice. The helium flow was 3.64 SLM or 412 FPM issuing from the tube. A plot of percent helium and power versus length for Tygon is remarkably similar to the sonic orifice plot, Figs. 4 and 3a, respectively. A replicate run is shown in Fig. 4b. The key differences between the sonic orifice and the Tygon are 1) the Tygon orifice produces a slower

jet which decays in concentration faster, i.e., within 3 inches, and 2) the power peak for Tygon occurs closer to the origin, 1 in. instead of 3 to 6 in. as with the sonic orifice. The helium flow was subsequently doubled to 7.28 SLM (824 FPM) and doubled again to 14.56 SLM (1650 FPM) in order to show the effect of flow rate on these phenomena. A combined plot is shown in Fig. 5. As expected, higher flow stretches out the concentration profile to higher values downstream. The power peaks move downstream and are flattened as flow rate is increased. Fig. 6 shows the effect of two different orifice types at the same flow rate. The sonic orifice has an area of 0.00196 sq. cm. at the smallest point compared to the tygon tube which is 0.317 sq. cm. in cross section. Thus, there is an initial velocity ratio of 162 for the sonic orifice vs. the Tygon tube. This physical difference gives rise to similar sharp concentration drops within 6 in. downstream, but the power signatures are much different.

4.1.2 SAMPLE TUBE 2. With the crimp removed, this sample tube seemed more responsive. However, it was used only two days because its connecting valve arrangement was not providing enough pressure drop prevent saturation of the turbomolecular vacuum pump.

8-4-92 Again at 3.64 SLM helium flow with the sonic orifice, there was a pronounced power peak in the vicinity of 6 inches downstream, Fig. 7. The concentration profile was stretched out downstream to give higher concentration of helium, possibly due to the new sample tube arrangement. For example, the jet was 4.4% helium at 12 in. downstream, as opposed to 0.84% at the same location using ST1.

A mechanical-optical chopper was inserted into the jet at x=1 in. in order to introduce a known frequency of concentration variation. The jet was sampled at about x=3 in. The chopper was set at 25 and 15 Hz. Both settings gave pronounced power peaks at the respective frequencies. The former concentration and power curves are shown in Fig. 8.

4.1.3 SAMPLE TUBE 3. This change slowed the apparent response by a small amount. The response time was checked using a paper card to block the sample tube and then quickly remove it. A time trace of concentration showed that the response time

constant (63.2% of total rise) was about 0.16 sec, still a fast response.

8-7-92 A series of experiments was designed to show concentrations and power of oxygen and nitrogen from the surrounding air along with the usual helium record. Concentrations of these gases are shown in Fig. 9, top. Note this figure has only three *x* locations, but it shows that the data are basically consistent, i.e., helium drops off to zero percent at 24 in., oxygen rises to 21%, and nitrogen rises similarly. However, nitrogen is 5 to 10% low due to a mass spectrometer calibration anomaly. Fig. 9 also shows the power level for these gases versus *x*. The nitrogen power is about ten relative units above helium, and the helium power is about 5 units above oxygen. Although helium concentration is low at 12 in., the power level persists at a high value, showing decoupling of concentration and power.

8-11-92 This experiment extended the previous run of 8-7-92, with the inclusion of the air velocity transducer (AVT) to measure an approximate local velocity. Helium and oxygen concentrations, and stream velocity are plotted in Fig. 10. The velocities at small distances downstream are low by 10 percent or less due to the error introduced by measuring a helium-air stream with an air-calibrated AVT. This error becomes negligible past x=10 in. where helium falls to a few percent. The AVT power at 5 Hz does not have a peak downstream like concentration. This was not due to limitations in frequency response of the AVT, however. This instrument was observed by the author to have very fast response, at least capable of seeing 20 Hz waves, last year (6). The AVT, oxygen and helium power traces in Fig. 10 clearly indicate although helium is rapidly diluting and oxygen is climbing, the power levels are similar and actually are reversed for these gases (helium is higher).

8-12-92 All conditions were repeated from 8-11-92 except the helium flow was doubled to 7.24 SLM. Fig. 11 shows the effect of flow on concentration and velocity. Higher velocity stretches the jet out downstream so that concentration is elevated by a few percent at 10 in. The velocity effect is more pronounced. Fig. 12 shows the difference between helium power and AVT power at 7.28 SLM. The effect of flow on power at 5 Hz

may be ascertained by comparing Figs. 10 and 12. Helium power is similar close to the origin, but it remains elevated at 24 in. and beyond when the velocity is higher.

8-13-92 This run repeated the experiment of 8-11-92 at 3.64 SLM with the additional feature of including radial measurements for three *x* locations. Data were observed on the horizontal plane to the right (*+y*, looking downstream) of the jet plane. Concentration profiles in Fig. 13 clearly show how the jet spreads out by the increase in helium concentration laterally as the jet moves downstream. The power levels present a similar picture where the high power levels downstream indicate intense concentration fluctuations for x=6 in. at y=0.125 to 1 in., and for x=12 in. at y=0.125 to 3 in. Again, power and concentration have different trends with *x*, e.g., at x=6 in.

8-14-92 Similar to 8-13-92, this series was designed to show the effect of *+z* variations at 2, 4, and 6 in. above the jet. Fig. 15 shows that the jet is spread considerably in the vertical direction at x=12 in., where a concentration peak occurs. The power peaks occur at different locations.

8-17-92 For 3.64 SLM helium flow, a run was made using a horizontal, 3/4-in. diameter aluminum cylinder to block the jet. The cylinder was placed with its center at x=1 in. Concentration and power were observed at 6 *x* locations for 4 *z* values between 0.5 and 6 inches, Fig. 16. An interesting feature of these data is that power and concentration do not follow analogous curves. For example, at x=6 in., the percent helium for z=0, 0.5, and 1 in. are all much reduced from their upstream values, but their power levels are similar. This means that power gives a separate piece of information from concentration. It suggests that power is high where mixing occurs at the helium-air interface, whereas high concentration may be due to a strong leak far away or a small leak close by but with the sample tube outside of the flow and mixing area. The latter case would signify helium is arriving at the sample tube by diffusion, not chaotic mixing caused by the jet interaction with air. Comparison with Fig. 3a (5 Hz, no obstruction) shows that near the obstruction, power levels are similar, but downstream the power is very low in the wake of the obstruction. Elevated concentration levels are seen above the jet in the wake of the

obstruction, but these are absent in Fig. 15 (no obstruction).

8-18-92 This run was like 8-17-92, but with a double helium flow of 7.28 SLM, Fig. 17. Doubling the flow reduces the near-field concentration by a factor of two (around x=6 in.), but helium concentration is ten times higher than for the slower flow at x=12 in. Also at x=12 in., power remains high while concentration falls off rapidly.

8-25-92 to 8-27-92 These runs include a replicate of earlier helium experiments at 3.64 SLM GHe, sonic orifice, but with 1% hydrogen in nitrogen as the gas jet at 2.5 SLM, using ST3 (note that this needs to be rerun at 3.64 SLM); and, vertical upflow with and without crossflow provided by a small fan. At final writing, results were not available, but will be communicated privately to Ric Adams.

4.1.4 OTHER EXPERIMENTS. This study was prompted in part by strongly fluctuating data obtained in earlier experiments in the HGDL and in helium signature tests. For example, data from a shuttle MPS LO2 helium signature test are shown in Fig. 18. These data are sampled at about 1 sec. rate and show puzzling fluctuations. To shed some light on this problem, pure helium was flown directly to ST1 at atmospheric pressure, indicated as % helium. Fig. 18 shows these in the middle for comparison including both helium and nitrogen concentrations at 1-sec. intervals (nitrogen leaked in). The bottom of this figure shows stagnant lab air analysis, percent nitrogen and oxygen. All of these figures look similar, suggesting that the fluctuations may be inherent in the mass spectrometer. There is no other apparent reason for the concentrations to vary when the gas is directed at the sample tube without any flow or mixing phenomena present.

V CONCLUSIONS AND RECOMMENDATIONS

Conclusions

* The helium jet behaves as predicted from the literature in terms of rapid concentration and velocity decay, and the lateral spread of mass and momentum.
* The great majority of runs showed that local concentration and power levels were independent. Typically, power had peaks in regions where concentration was rapidly decaying.
* The effect of orifice size was to increase velocity at constant flow for a smaller orifice resulting in stretched-out concentration profiles and higher power traces.
* Sample tube design has a reasonably strong effect. All three tubes had time constants less than 0.2 sec., the last (ST3) having the largest of 0.13 to 0.16 sec. A small bore gives the advantage of a short transit time without damping frequency information.
* AVT power kid not correlate well with concentration power despite the rapid response capability of the AVT.
* Radial measurements indicated a distinction between concentration and power also.

Recommendations

* One practical consequence of this study is to suggest that the backup HGDS sampling frequency should be increased above the present rate of 1 sample per second.
* Also, it would be interesting to do tests like the above using two or more mass spectrometer sample tubes at different locations. These could be monitored sequentially by switching a solenoid valve between tubes. Then, spectral analysis of different tube locations would be analyzed for transient events pointing to the leak location. Such a system could be implemented with the present HGDS sample tubes in the shuttle.

REFERENCES

1. Bilardo, V. J., Jr., and Izquierdo, F., "Development of the Helium Signature Test for Orbiter Main Propulsion System Revalidation Between Flights," AIAA 25th Aerospace Sciences Meeting, Jan., 1987.

2. Schleier, H., "Correlation of Leak Rates of Various Fluids with the Leak Rate of an Inert Gas in the Same Configuration," NASA/ASEE Summer Faculty Fellowship Program, 308-338, 1990.

3. Mehta, N. K., "Characterization of a Turbomolecular-Pumped Magnetic Sector Mass Spectrometer," NASA/ASEE Summer Faculty Fellowship Program, KSC/UCF, 1988.

4. Kachnic, J., and Raisin, P., "The 17" Disconnect Mass Spectrometer with Turbomolecular Turbo Pump," Internal Report from Boeing to Dave Collins, NASA-KSC, DL-ESS-24, 4-12-88.

5. Hazardous Gas Detection Lab, Internal Report, "Overview of MGA-1200 Electrometer Card Testing," 1990.

6. Barile, R. G., "Hazardous Gas Leak Analysis in the Space Shuttle," NASA/ASEE Summer Faculty Fellowship Program, KSC/UCF, 1991.

7. Becker, H. A., Hottel, H. C., and Williams, G. C., "The Nozzle Fluid Concentration Field of the Round Turbulent Free Jet," J. Fluid Mech., 30, 285-303 (1967).

8. Chua, L. P., and Antonia, R. A., "Flow Reversal and Intermittency of a Turbulent Jet," AIAA J., 27, (11), 1494-1499 (1989).

9. Ghoniem, A. F., Chen, D. Y., and Oppenheim, A. K., "Formation and Inflammation of a Turbulent Jet," AIAA J., 24, (2), 224-229 (1986).

10. Lam, K. M., and Ko, N. W. M., "Investigation of Flow Structures of a Basic Annular Jet," AIAA J., 24, (9), 1488-93 (1986).

11. Birch, A. D., Brown, D. R., Dodson, M. G., and Thomas, J. R., "The Turbulent Concentration Field of a Methane Jet," J. Fluid Mech., 88, (3), 431-449 (1978).

12. Yule, A. J., "Observations of Late Transitional and Turbulent Flow in Round Jets," in Turbulent Shear Flows, Durst (Editor), Univ. Park, PA, Apr. 18-20, 1977.

13. Schlichting, H., Boundary Layer Theory, McGraw-Hill, 1960.

14. Benedict, R. P., "The Flow Field of a Free Jet," in R. B. Dowdell, Ed., Flow-Its Measurement and Control in Science and Industry, Vol. 1, ISA, 1974.
15. Chriss, D. E., "Experimental Study of Turbulent Mixing of Subsonic Axisymmetric Gas Streams," Arnold Engineering Development Center, AEDC-TR-68-133, Aug. 1968.
16. Seymour, D., "STS-35 Scrub 3 Hydrogen Leak Analysis," NASA TM-103548, July, 1991.
17. "MPS-2102, Main Propulsion System Workbook," Advanced Training Series, JSC-ATS-MPS-2102, July, 1983.
18. "Integrated System Schematic, Main Propulsion System," Orbiter Vehicle, V572-941099, Rockwell International Corp., Space Div.

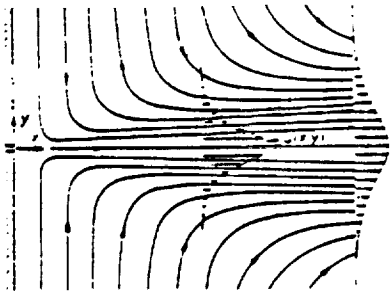

Stream-line pattern for a circular laminar jet

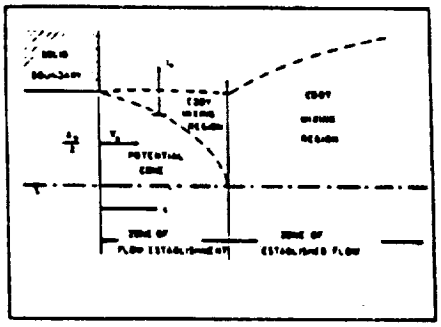

General flow field of a free jet.

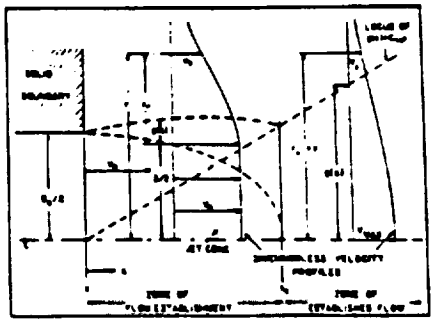

Three dimensional free jet flow field.

Figure 1. Jet review.

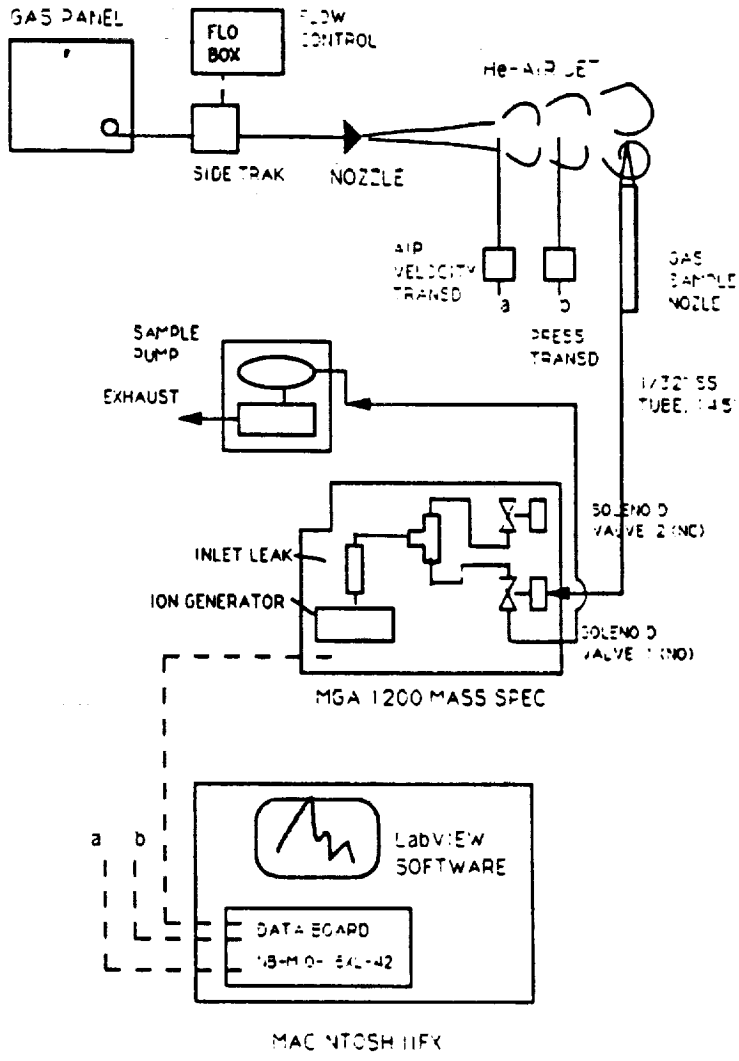

Figure 2. Present apparatus showing sample tube 3 arrangement

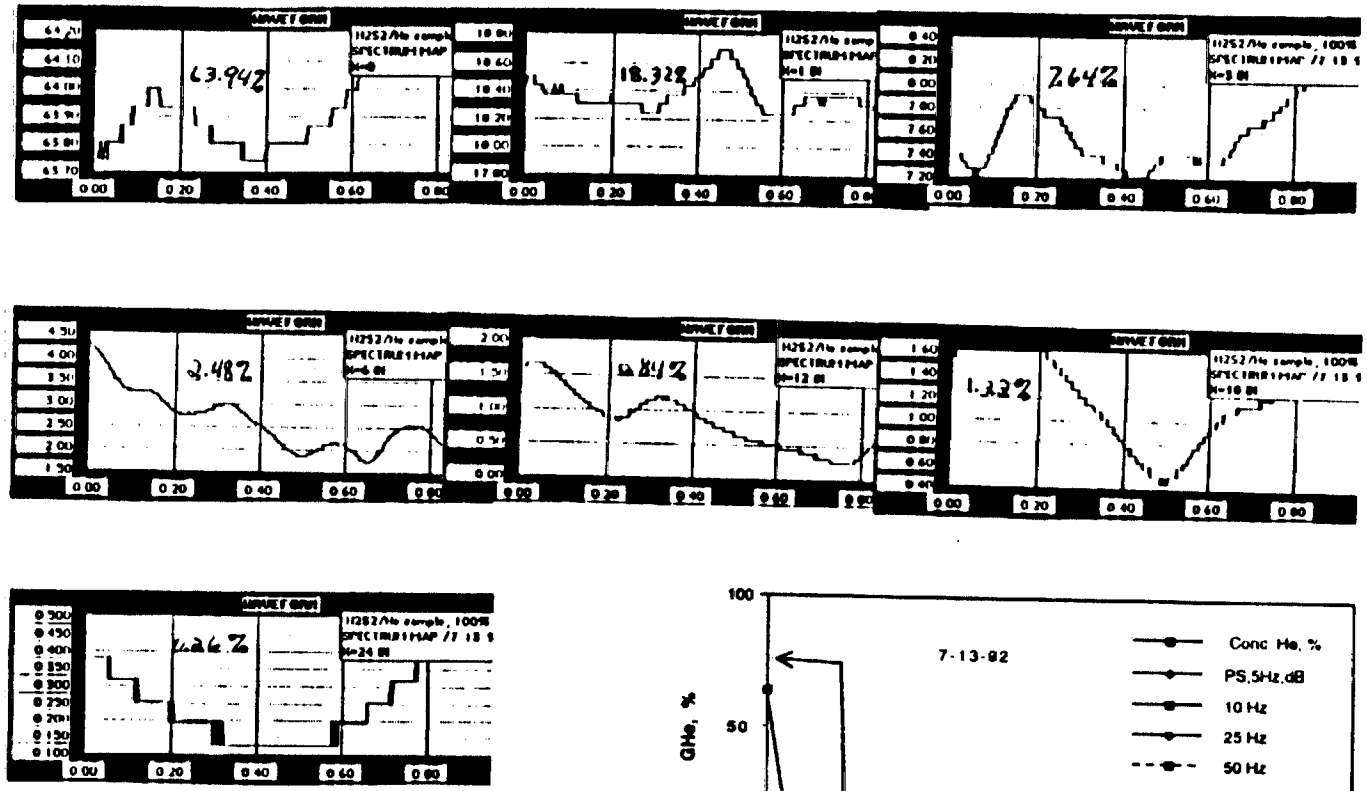

Figure 3b. GHe concentration vs. time, sec., at 7 values of x, 0 to 24 in.

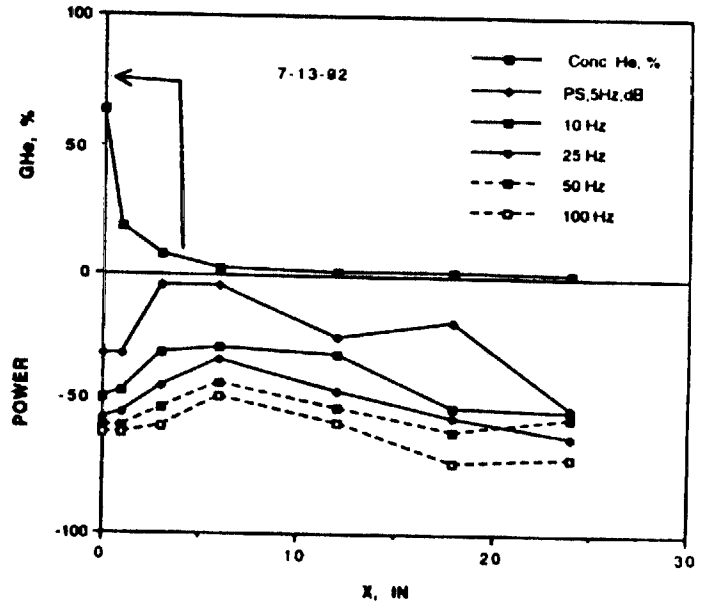

FIGURE 3a. GHe CONCENTRATION AND POWER VS. X. SONIC ORIFICE JET, 3.64 SLM, ST1.

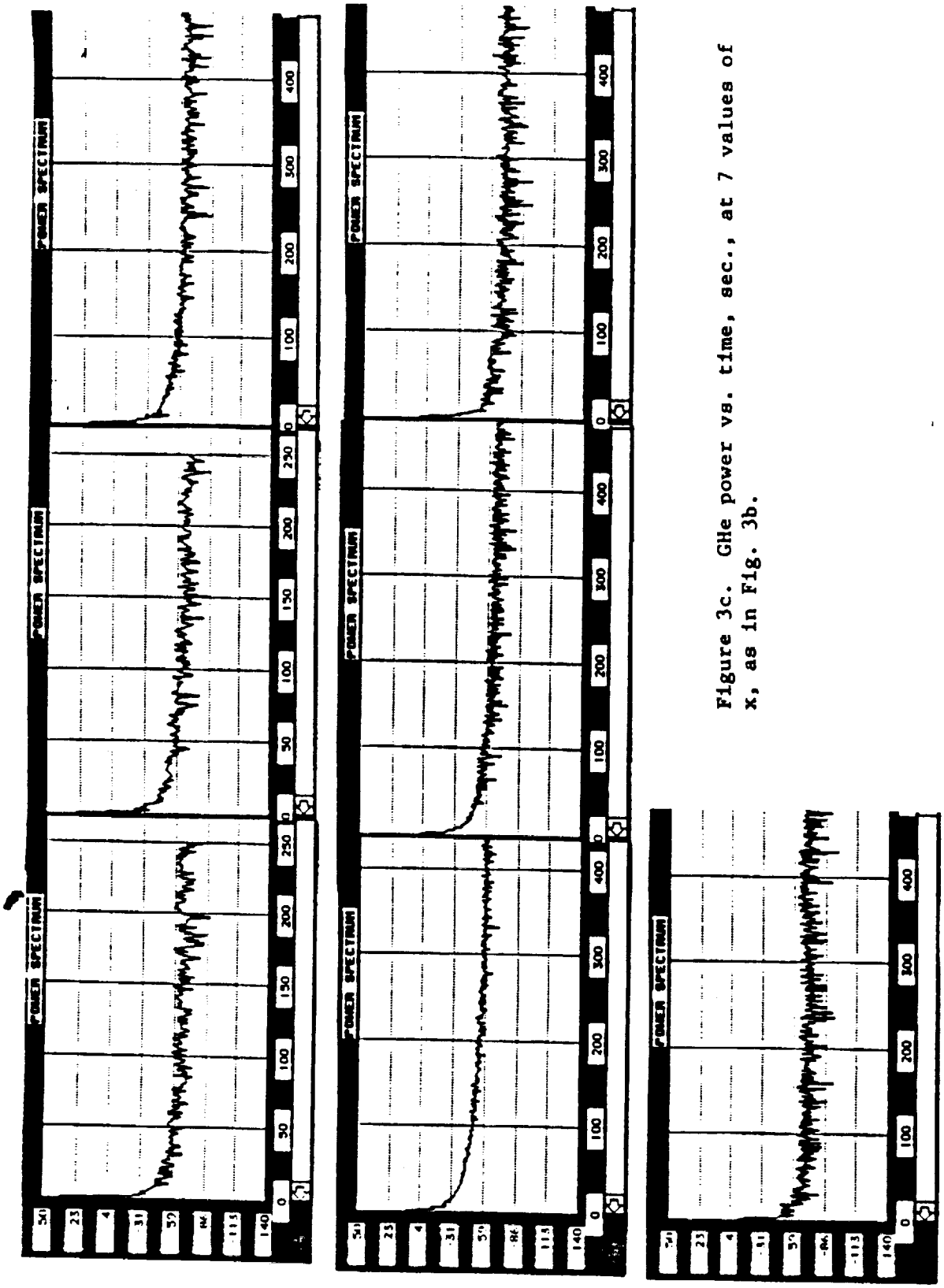

Figure 3c. GHe power vs. time, sec., at 7 values of x, as in Fig. 3b.

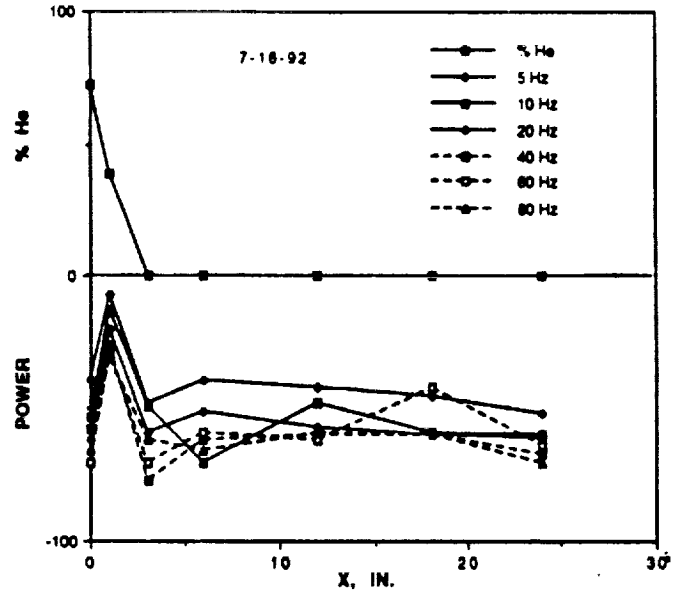

FIG. 4a. GHe CONCENTRATION AND POWER VS. X. TYGON TUBE JET, 3.64 SLM, ST1.

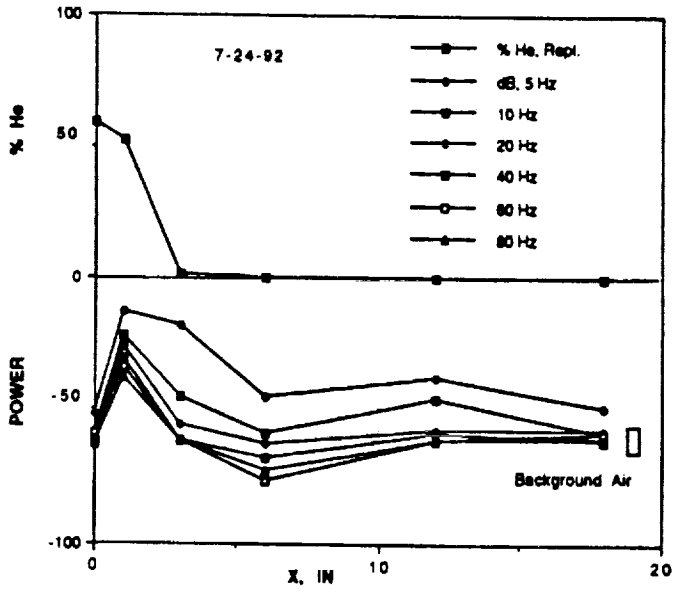

FIG. 4B. GHe CONCENTRATION AND POWER VS. X.
1/4 IN. TYGON TUBE JET, 3.64 SLM, REPLICATE

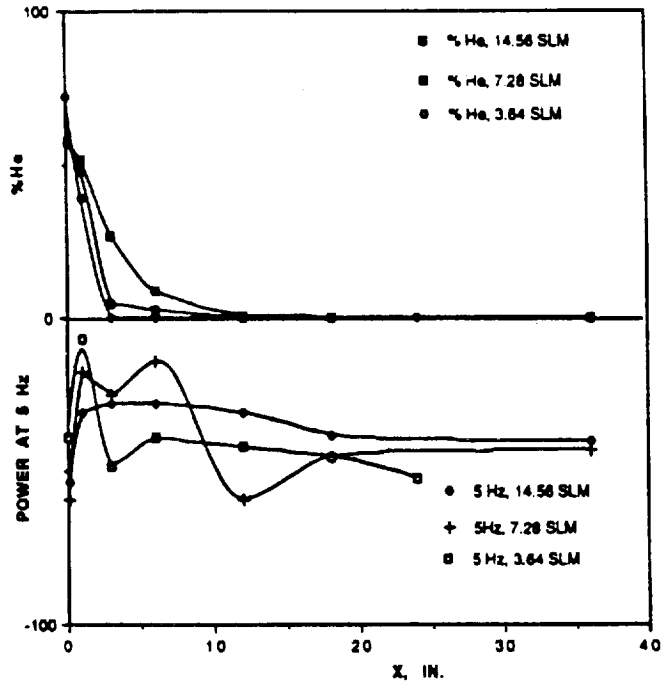

FIGURE 5. HELIUM CONCENTRATION VS. LENGTH, TYGON TUBE AT 3 FLOWS (ST1). 3.64, 7.28, 14.56 SLM GHe

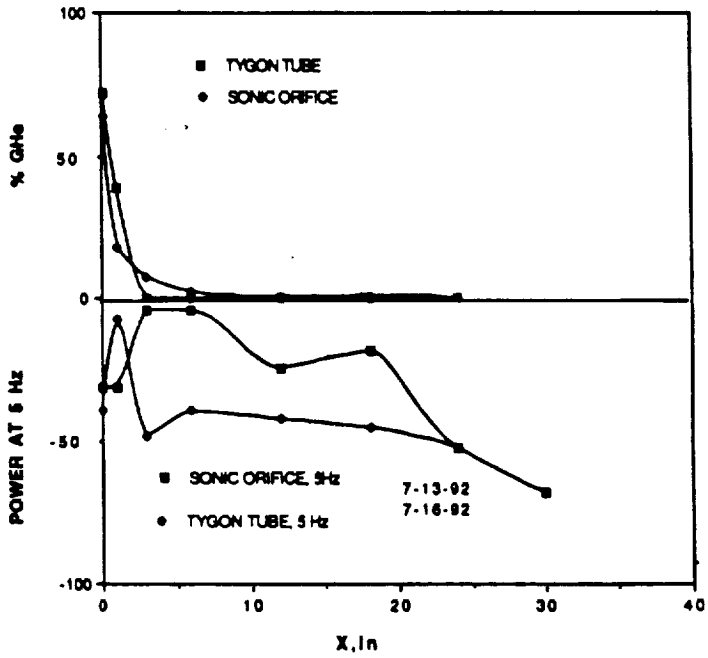

FIGURE 6. HELIUM CONCENTRATION AND POWER VS. X. COMPARISON OF SMALL (S.O.) AND LARGE (TYGON) ORIFICE AT 3.64 SLM.

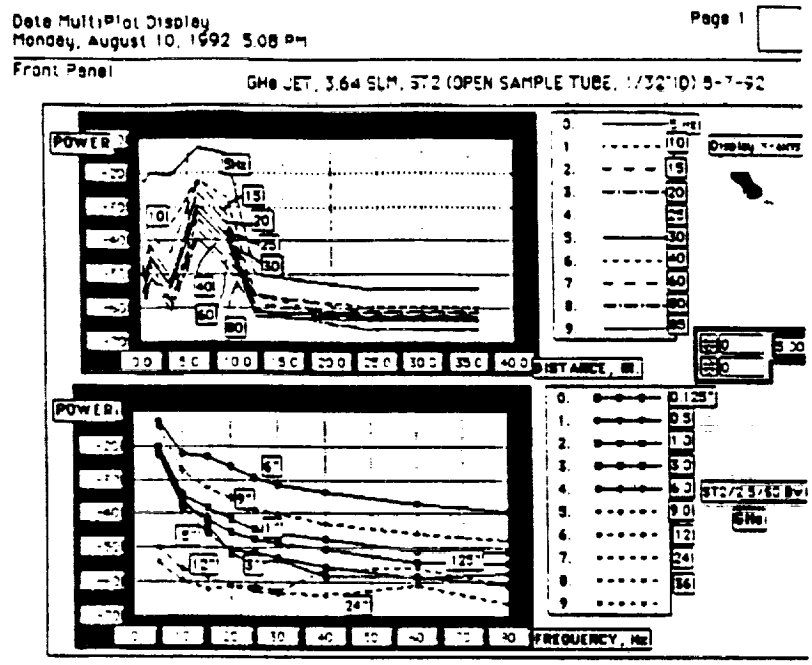

Figure 7. Power vs. length and frequency. Power is 10Hz bandwidth-averaged at center frequencies shown on top graph.

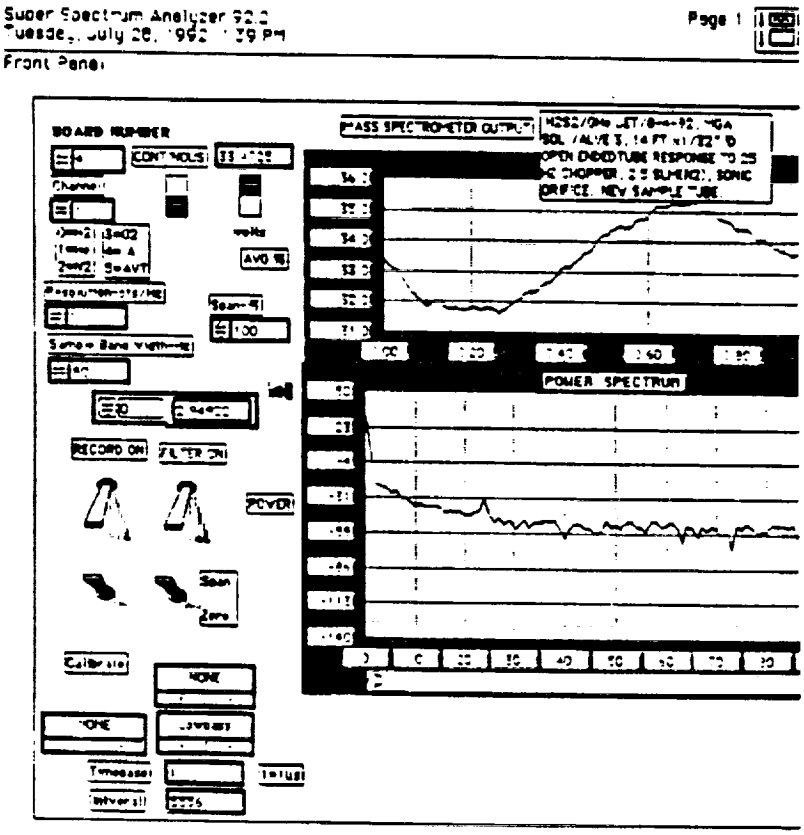

Figure 8. Mechanical chopper at 35Hz placed in jet stream 3 in. from orifice.

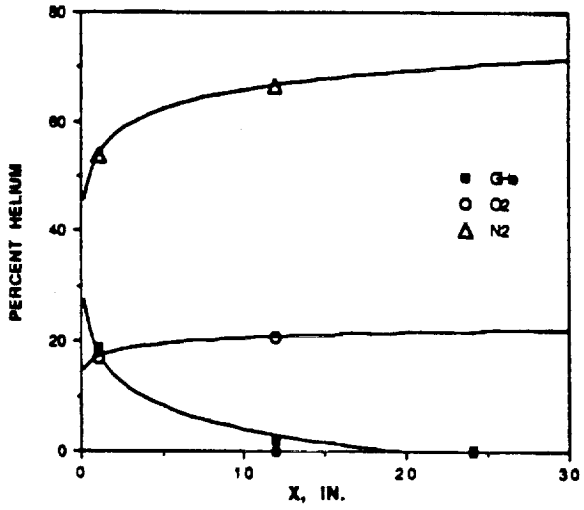

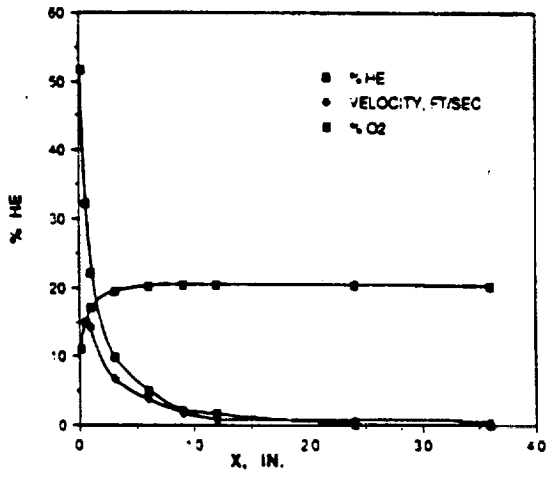

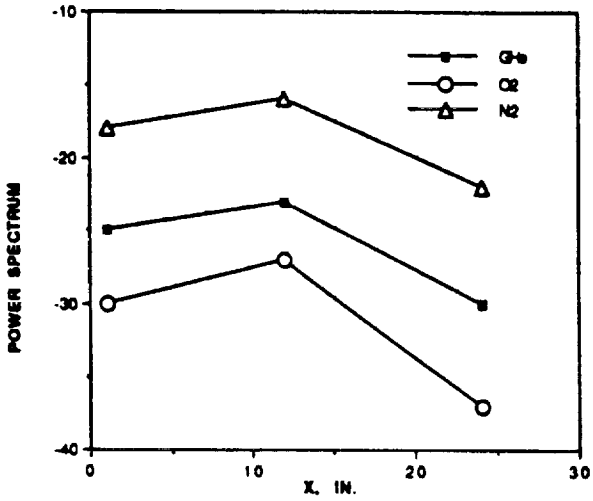

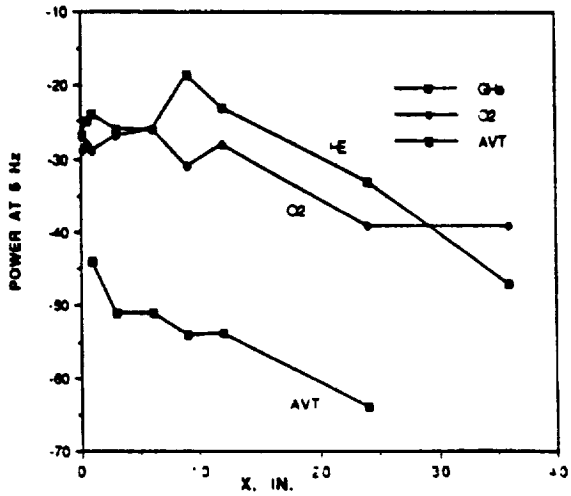

FIGURE 9. CONCENTRATION AND POWER @ 5hz vs DISTANCE. COMPARISON OF GHe, O2, & N2. ST3/SO/ 3.64 SLM GHe.

FIGURE 10. VELOCITY AND POWER AT 5Hz VS X. COMPARISON OF GHe, O2, AND AVT ST3. SONIC ORIFICE. 3.64 SLM GHe.

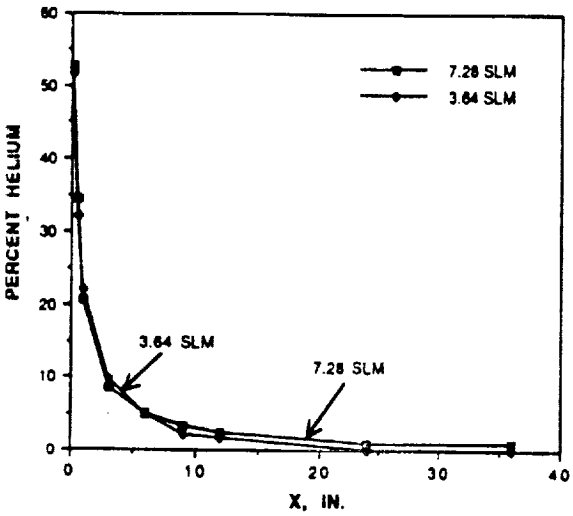

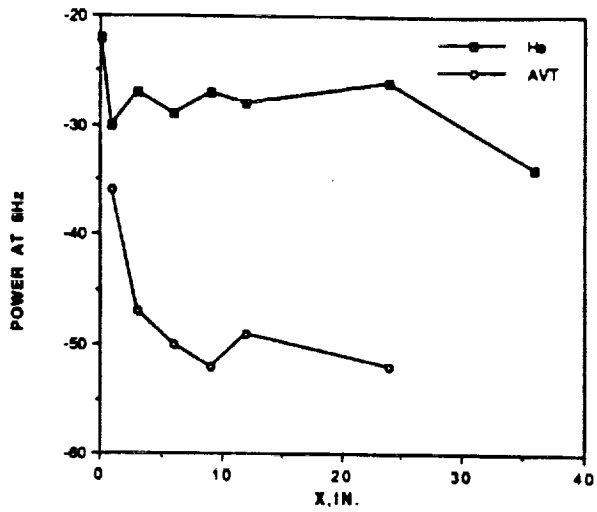

FIGURE 12. POWER AT 5 HZ VS. LENGTH. COMPARISON OF GHe & AVT DATA. ST3, SONIC ORIFICE, 7.28 SLM. GHe

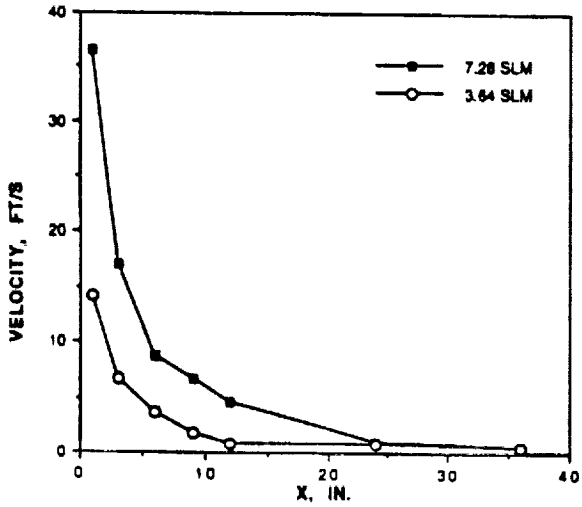

FIGURE 11. CONCENTRATION AND VELOCITY VS DISTANCE. COMPARISON OF 3.64 & 7.28 SLM GHe. ST3 SONIC ORIFICE.

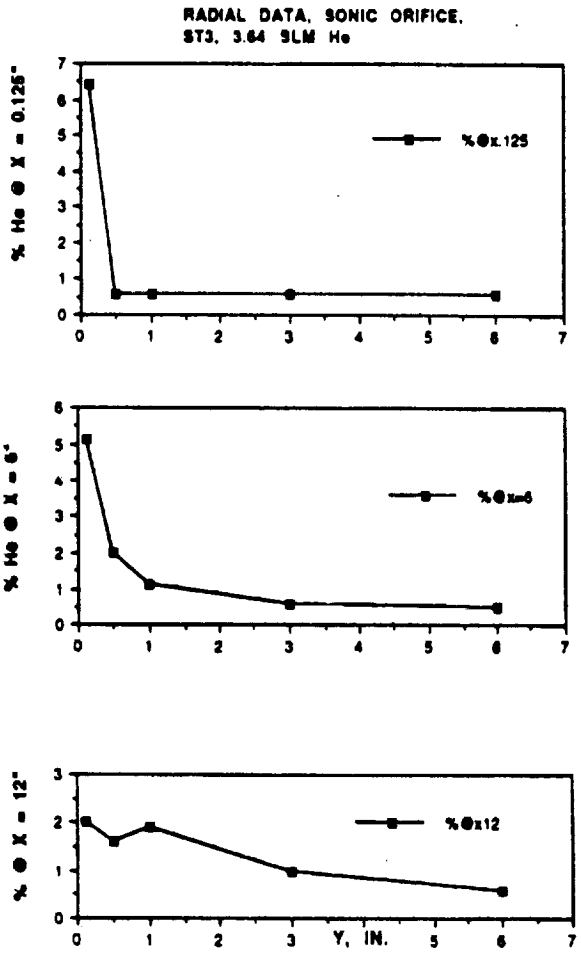

Figure 13. Helium concentration at three x values vs. radial coordinate y.

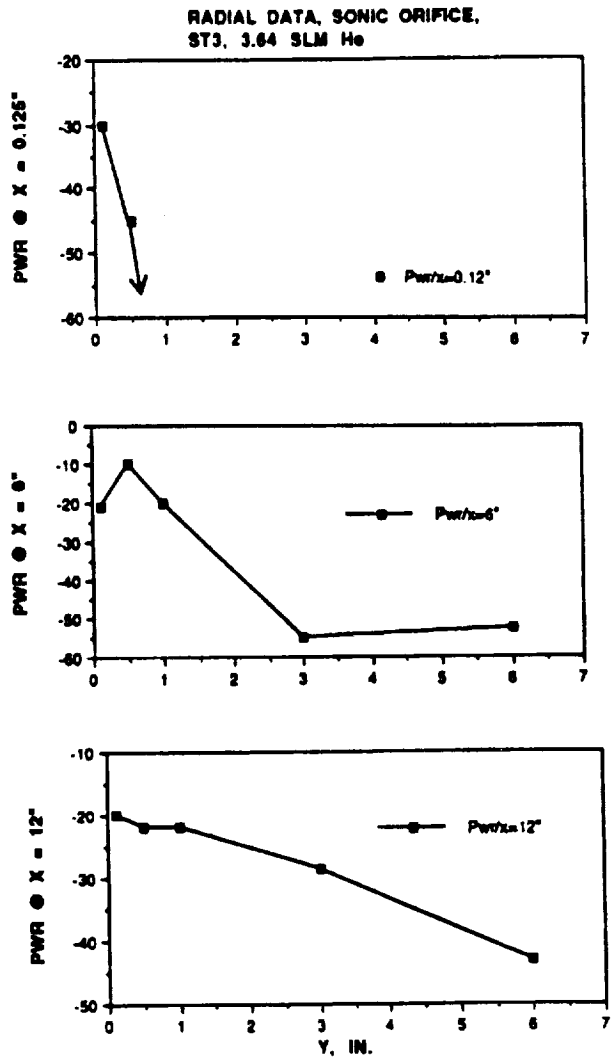

Figure 14. Power at 5 Hz, three x values, vs. y.

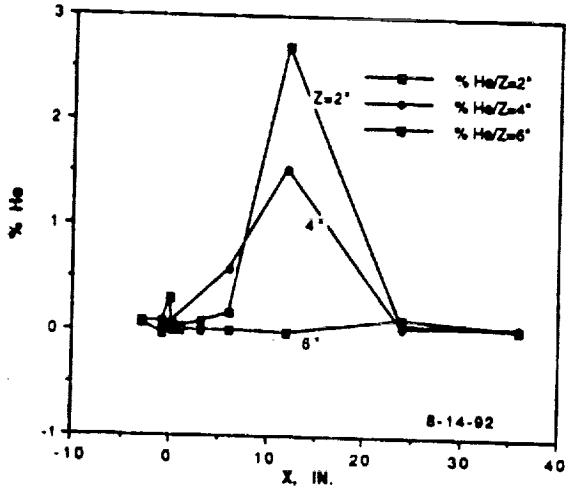

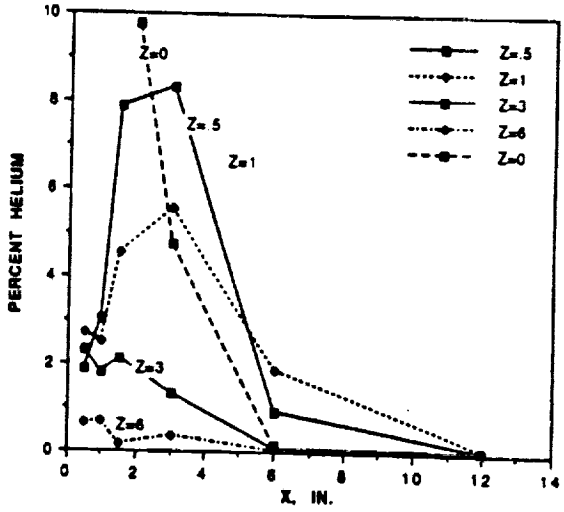

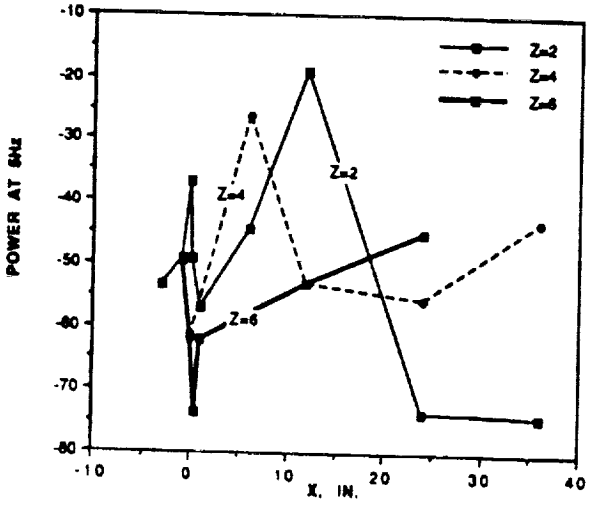

FIGURE 15. CONCENTRATION AND POWER AT 5 Hz VS. LENGTH. ST3. SONIC ORIFICE. 3.64 SLM GHe.

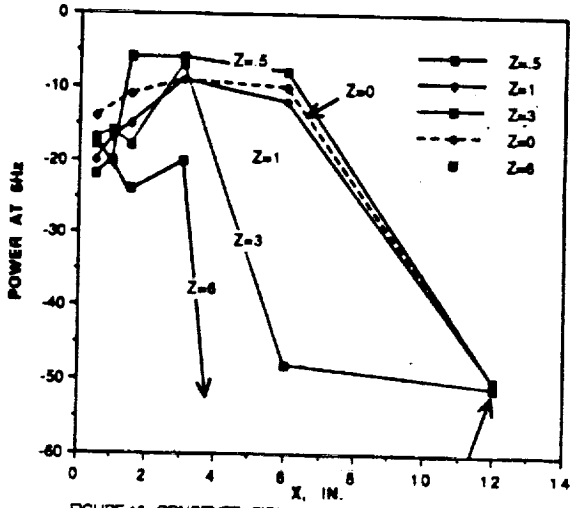

FIGURE 16. CONCENTRATION AND POWER VS LENGTH. HORIZONTAL CYLINDER OBSTRUCTION AT X = 1 IN. ST3. SONIC ORIFICE. 3.64 SLM GHe.

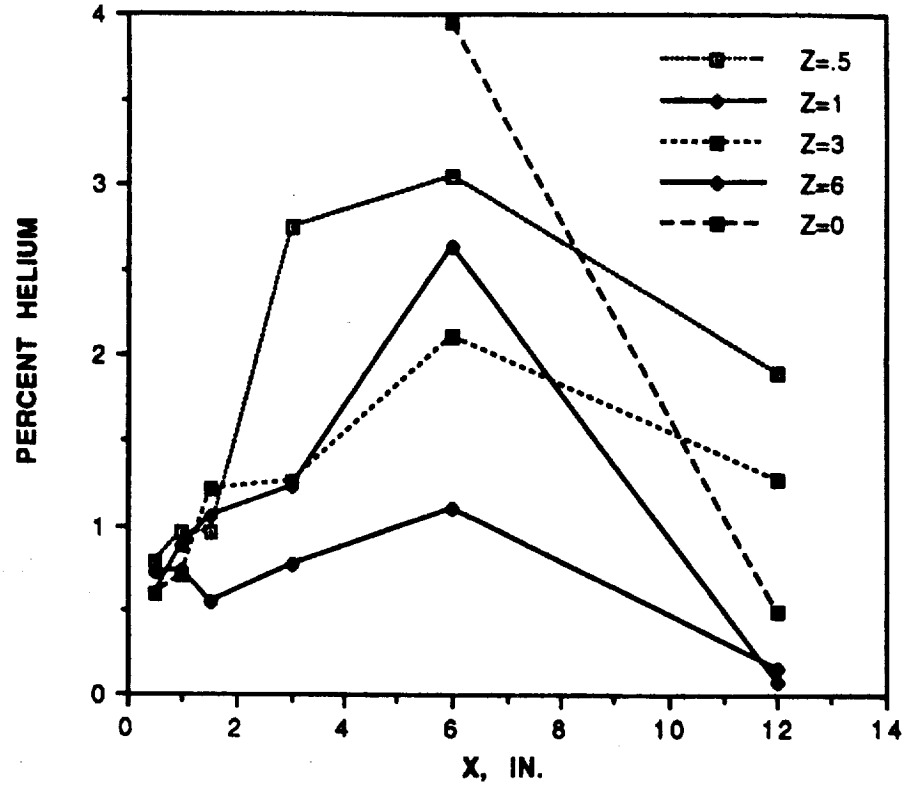

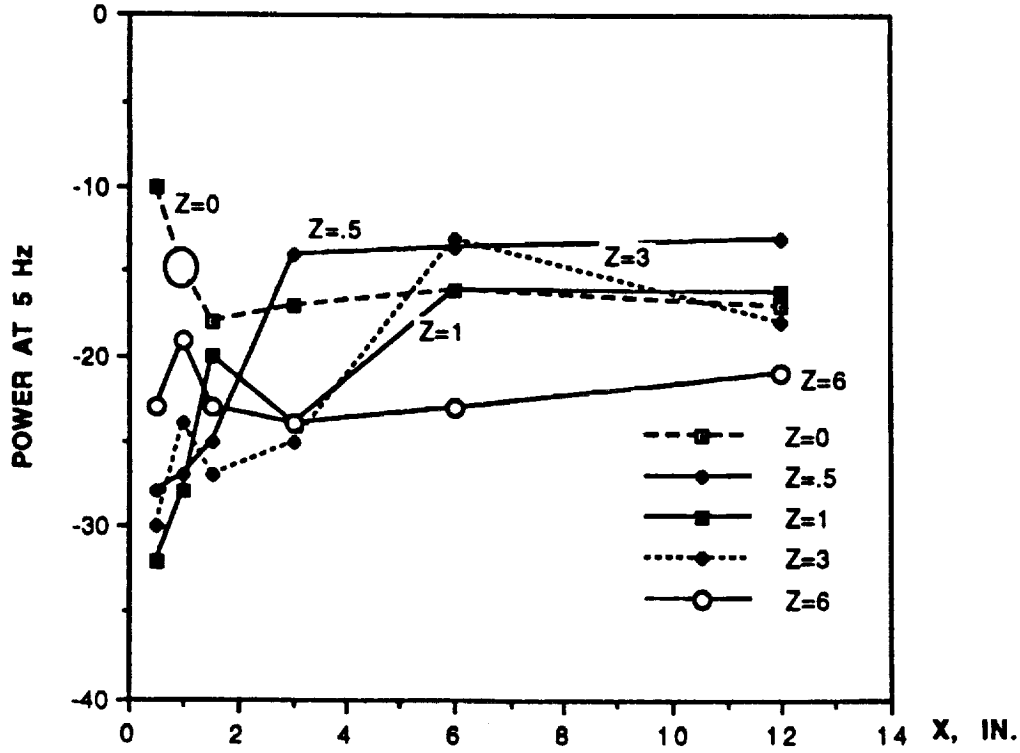

FIGURE 17. CONCENTRATION AND POWER VS. LENGTH.
HORIZONTAL CYLINDER OBSTRUCTION AT X=1 IN.
ST3, SONIC ORIFICE, 7.28 SLM GHe.

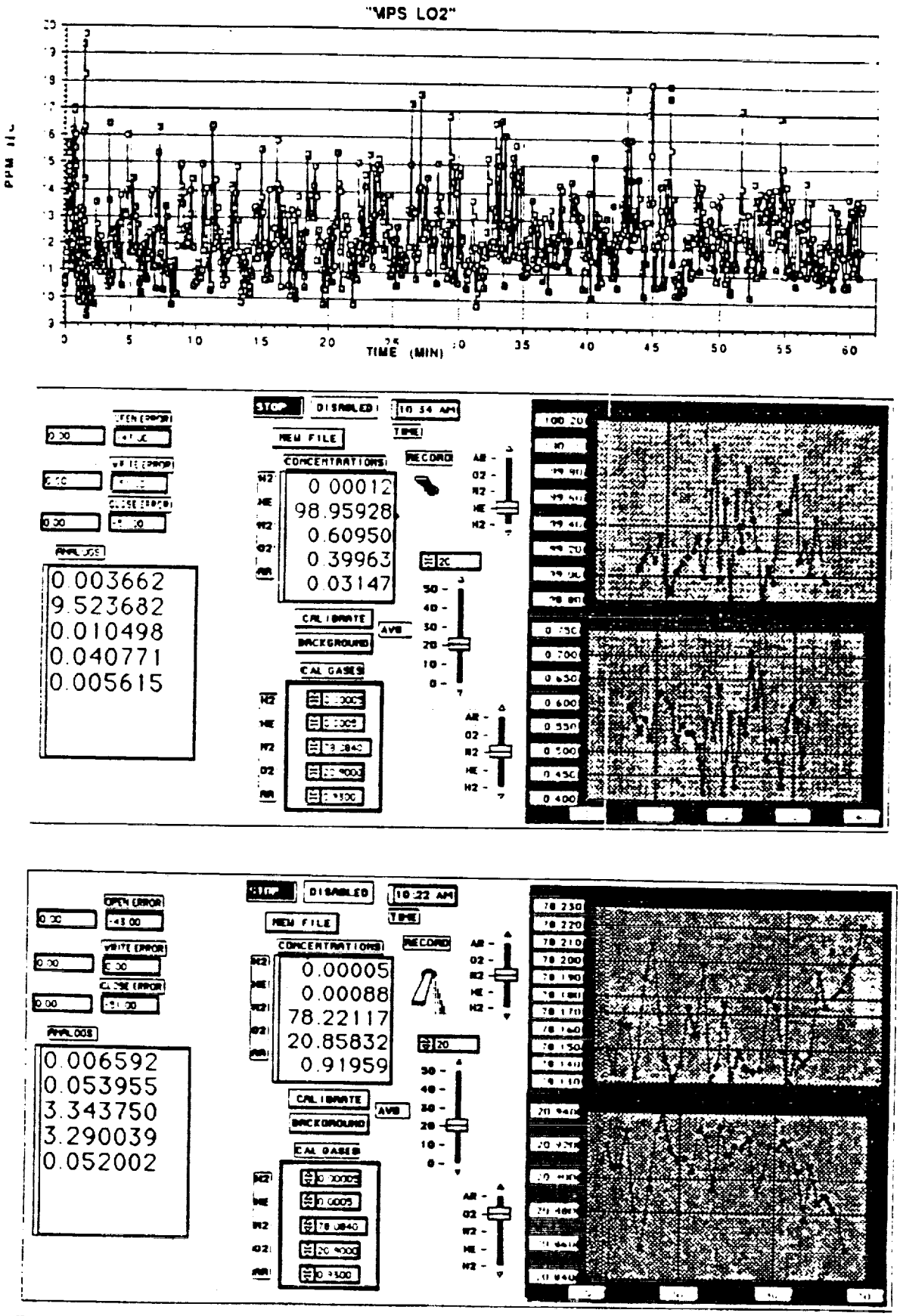

Figure 18. Top: helium (ppm) signature test in shuttle MPS; middle: helium (%) stream direct to mass spectrometer vs. time, sec.; bottom: stagnant lab air (%) vs. time, sec.

N93-19393

1992 NASA/ASEE SUMMER FACULTY FELLOWSHIP PROGRAM

JOHN F. KENNEDY SPACE CENTER
UNIVERSITY OF CENTRAL FLORIDA

KINEMATIC ANALYSIS OF THE ARID MANIPULATOR

PREPARED BY:	Dr. Keith L. Doty
ACADEMIC RANK:	Professor
UNIVERSITY AND DEPARTMENT:	University of Florida Department of Electrical Engineering
NASA/KSC	
DIVISION:	Mechanical Engineering Directorate
BRANCH:	Special Projects (RADL)
NASA COLLEAGUE:	Willis Crumpler Bill Jones Eduardo Lopez
DATE:	August 7, 1992
CONTRACT NUMBER:	University of Central Florida NASA-NGT-60002 Supplement: 8

ACKNOWLEDGEMENTS

The author gratefully acknowledges the support of the University of Central Florida faculty and staff along with the Boeing and NASA staffs whose diligence and kindness make the NASA Faculty Fellowship program at the Kennedy Space Center so efficient and productive. Particular thanks to Willis Crumpler, Bill Jones, Eduardo Lopez, Gabor Tamasi, Todd Graham and Carol Valdez of NASA; Ron Remus, Joe Looney, Jose Lago and Brian Yamauchi of Boeing and Loren Anderson and Kari Stiles of the University of Central Florida. A special thanks to my office mate, Carl Latino of Oklahoma State University, for stimulating discussions and all-around good fellowship.

ABSTRACT

This paper develops the forward and inverse position kinematics of the ARID manipulator and also its forward velocity kinematics.

TABLE OF CONTENTS

1. INTRODUCTION

The kinematic structure of the ARID manipulator lends itself to simple forward and inverse kinematics analysis. The purpose of this paper is to fully document and verify an existing analysis. The symbolic software package *MATHEMATICA* was used to produced and verify the equations presented here. In the analysis to follow, the standard Devenit-Hartenberg kinematic parameters of the ARID were employed.

2. ARID FORWARD KINEMATICS

Table 2.1 lists the Devenit-Hartenberg kinematic parameters for the ARID robot.

Table 2.1 : Kinematic Parameters for the ARID Robot

Joint	d	θ	a	α	Joint Limits
1 p	d_1	θ_1	a_1	0°	[0*inches*, 718*inches*]
2 r	0	θ_2	a_2	0°	[4° , 112°]
3 r	0	θ_3	a_3	0°	[102° , 148°]
4 r	0	θ_4	0	0°	[-16° , -117°]

Table 2.2 lists the nominal values of the link lengths and the fixed angle θ_1. The distance $l + a_4$ computes the tool-end-point along the x-axis of the tool-frame whose origin is located at the flange.

From the DH-parameters of the ARID robot listed in Table 2.1, the four link transforms compute to

$$L_1 = \begin{bmatrix} c_1 & -s_1 & 0 & a_1 c_1 \\ s_1 & c_1 & 0 & a_1 s_1 \\ 0 & 0 & 1 & d_1 \\ 0 & 0 & 0 & 1 \end{bmatrix}, \quad L_2 = \begin{bmatrix} c_2 & -s_2 & 0 & a_2 c_2 \\ s_2 & c_2 & 0 & a_2 s_2 \\ 0 & 0 & 1 & 0 \\ 0 & 0 & 0 & 1 \end{bmatrix},$$

$$L_3 = \begin{bmatrix} c_3 & -s_3 & 0 & a_3 c_3 \\ s_3 & c_3 & 0 & a_3 s_3 \\ 0 & 0 & 1 & 0 \\ 0 & 0 & 0 & 1 \end{bmatrix}, \quad \text{and} \quad L_4 = \begin{bmatrix} c_4 & -s_4 & 0 & 0 \\ s_4 & c_4 & 0 & 0 \\ 0 & 0 & 1 & 0 \\ 0 & 0 & 0 & 1 \end{bmatrix}. \quad (2\text{-}1)$$

Table 2.2 Nominal Values of ARID Kinematic Parameters

Parameter	Theoretical Value	Measured Value	Units
a_1	$\sqrt{66.37^2 + 48.28^2}$ = 82.0727	82.3	*inches*
a_2	45.00	45	*inches*
a_3	35.00	35	*inches*
$1 + a_4$		35.75	*inches*
s_1	$\frac{48.28}{a_1} = 0.588259$		
c_1	$\frac{66.37}{a_1} = 0.808673$		
θ_1	36.0335°	35.2053°	Degrees

The forward kinematics transform of the ARID equals

$$^0T_4 = L_1 L_2 L_3 L_4 \quad (2\text{-}2)$$

which reduces to

$$ {}^{0}T_4 = \begin{bmatrix} c_{1234} & -s_{1234} & 0 & a_1 c_1 + a_2 c_{12} + a_3 c_{123} \\ s_{1234} & c_{1234} & 0 & a_1 s_1 + a_2 s_{12} + a_3 s_{123} \\ 0 & 0 & 1 & d_1 \\ 0 & 0 & 0 & 1 \end{bmatrix} \qquad (2\text{-}3) $$

If the ARID axes are not parallel, this model will produce erroneous results. A second paper will address the development of a error-model for the ARID kinematics.

3. ARID END FRAME JACOBIAN

The Jacobian of the ARID relates the joint-rates $\dot{\mathbf{q}} = [\, \dot{d}_1 \quad \dot{\theta}_2 \quad \dot{\theta}_3 \quad \dot{\theta}_4 \,]^\tau$ to the frame-velocity $\mathbf{V} = [v^\tau \;\; \omega^\tau]^\tau$ of the end-frame,

$$ \mathbf{V} = \mathbf{J}\, \dot{\mathbf{q}}. \qquad (3\text{-}1) $$

The Jacobian of the ARID computes to

$$ {}^{4,0}\mathbf{J}_4 = \begin{bmatrix} 0 & a_2 s_{34} + a_3 s_4 & a_3 s_4 & 0 \\ 0 & a_2 c_{34} + a_3 c_4 & a_3 c_4 & 0 \\ 1 & 0 & 0 & 0 \\ 0 & 0 & 0 & 0 \\ 0 & 0 & 0 & 0 \\ 0 & 1 & 1 & 1 \end{bmatrix} \qquad (3\text{-}2) $$

The leading superscript *4* means that this Jacobian is expressed in frame F_4 while the *0* indicates the motion is that of the end-frame relative to the base frame F_0 of the ARID.

The Tool-Center-Point

The tool-center-point vector (**tcp**), expressed in the end-effector-frame F_4 for this robot, equals, by definition,

$$^4\mathbf{tcp} = [24\ \textit{inches} \quad 0 \quad 0\ ]^T = 24\ \mathbf{x}. \tag{3-3}$$

Hence, the base-frame expression of the tool-center-point vector equals

$$\begin{bmatrix} ^0\mathbf{tcp} \\ 1 \end{bmatrix} = \mathbf{H} \begin{bmatrix} ^4\mathbf{tcp} \\ 1 \end{bmatrix}. \tag{3-4}$$

The ARID base-frame expression of the **tcp** position, therefore, equals

$$^0\mathbf{tcp} = \mathbf{p} + \mathbf{R}\ ^4\mathbf{tcp}. \tag{3-5}$$

The ARID base-frame velocity of the **tcp**, therefore, equals

$$\mathbf{v}_{tcp} = \dot{\mathbf{p}} + \omega \times \mathbf{R}\ ^4\mathbf{tcp} = \mathbf{R}(\ ^{4,0}\mathbf{v}_4 + ^{4,0}\omega_4 \times 24\ \mathbf{x}), \tag{3-6}$$

where

$$^{4,0}\mathbf{V}_4 = \begin{bmatrix} ^{4,0}\mathbf{v}_4 \\ ^{4,0}\omega_4 \end{bmatrix} = {}^{4,0}\mathbf{J}_4\ \dot{\mathbf{q}}. \tag{3-7}$$

In general, the middle expression in (3-6) can be used to compute the velocity of any point fixed in the end-frame F_4.

4. ARID INVERSE POSE KINEMATICS

Specify the pose of the end-effector frame at the ARID flange by the homogeneous matrix **H**,

$$\mathbf{H} = \begin{bmatrix} n_x & b_x & t_x & p_x \\ n_y & b_y & t_y & p_y \\ n_z & b_z & t_z & p_z \\ 0 & 0 & 0 & 1 \end{bmatrix} \tag{4-1}$$

where $\mathbf{p} = [p_x \quad p_y \quad p_z]^\tau$ is the position of the flange center-point and

$$\mathbf{R} = \begin{bmatrix} n_x & b_x & t_x \\ n_y & b_y & t_y \\ n_z & b_z & t_z \end{bmatrix} \tag{4-2}$$

is the rotation matrix that rotates the base-frame of the robot into a frame parallel to the tool-frame. Equivalently, **R** transforms a vector expressed in the end-effector-frame coordinates into the same vector expressed in the robot base-frame coordinates. The inverse position kinematics problem is to solve for the joint variables given **H**. This means solving the matrix equation

$$^0\mathbf{T}_4 = \mathbf{H} \tag{4-3}$$

Solving for the Sum of the Three Revolute Joint Angles

Unless **R** a rotation about the *z-axis* , $t_z = 1$, no joint variable set will satisfy (4-3). Given that $t_z = 1$, $^0\mathbf{T}_{4[1,1]} = \mathbf{H}_{[1,1]}$, $^0\mathbf{T}_{4[2,1]} = \mathbf{H}_{[2,1]}$ implies

$$c_{1234} = n_x \qquad \text{and} \qquad s_{1234} = n_y \,. \tag{4-4}$$

Hence,

$$\theta_2 + \theta_3 + \theta_4 = atan2[n_y, n_x] - \theta_1. \tag{4-5}$$

The known value of θ_1 in Table 2.2 provides the additional information to compute the sum of the last three joint angles.

Solving for the Prismatic Displacement of Joint One

The value of the prismatic joint follows immediately from ${}^0T_4\,[3,4] = H_{[3,4]}$,

$$p_z = d_1. \tag{4-6}$$

Next, we solve for θ_3.

Solving for the Angle of Joint Three

Define the known, translated position vector $\tilde{p} = [\tilde{p}_x \;\; \tilde{p}_y \;\; \tilde{p}_z]^T$,

$$\tilde{p}_x := p_x - a_1 c_1, \qquad \tilde{p}_y := p_y - a_1 s_1, \qquad \text{and} \qquad \tilde{p}_z := p_z. \tag{4-7}$$

The equalities ${}^0T_4\,[1,4] = H_{[1,4]}$ and ${}^0T_4\,[2,4] = H_{[2,4]}$ imply

$$\tilde{p}_x = a_3 c_{123} + a_2 c_{12} \tag{4-8}$$

$$\tilde{p}_y = a_3 s_{123} + a_2 s_{12} \tag{4-9}$$

The previous two equations constitute the well-known elbow equations. Squaring both equations and adding yields the kinematic equation

$$c_3 = \frac{\tilde{p}_x^2 + \tilde{p}_y^2 - a_2^2 - a_3^2}{2\, a_2\, a_3}, \tag{4-10}$$

which has two solutions,

$$\theta_3 = \pm atan2[\sqrt{1 - c_3^2}, c_3], \tag{4-11}$$

or, equivalently,

$$\theta_3 = \pm\cos^{-1}\left[\frac{\tilde{p}_x^2 + \tilde{p}_y^2 - a_2^2 - a_3^2}{2\, a_2\, a_3}\right], \tag{4-12}$$

as long as the constraint

$$-1 \le \frac{\tilde{p}_x^2 + \tilde{p}_y^2 - a_2^2 - a_3^2}{2 \cdot a_2 \cdot a_3} \le 1, \qquad (4\text{-}13)$$

or, equivalently,

$$(a_2 - a_3)^2 \le \tilde{p}_x^2 + \tilde{p}_y^2 \le (a_2 + a_3)^2, \qquad (4\text{-}14)$$

is satisfied.

Equation (4-14) expresses the geometric constraints that the manipulator cannot reach out past the sum of its link lengths and no closer than the difference. The reachable *work space*, is contained in an envelope consisting of an annular ring with inner radius of $|a_2 - a_3|$ and outer radius of $a_2 + a_3$. When the end-point is on the inner radius, $cos\ \theta_3 = -1$ and on the outer boundary, $cos\ \theta_3 = 1$. On these boundaries there is only one solution for $\cos \theta_3$ in (4-12). The constraints on θ_3 prevents the ARID robot from reaching either the inner or outer boundaries. No position in the ARID work space violates either conditions. In the workspace on the orbiter, only the positive solution $\theta_3 > 0$ is considered.

Solving for the Angle of Joint Two

With joint angle θ_3 determined, θ_2 can be computed from (4-8) and (4-9) by expanding the trigonometric terms using the sum of angles formulas and collecting the s_2 and c_2 terms to form the simultaneous equations:

$$\begin{bmatrix} \tilde{p}_x \\ \tilde{p}_y \end{bmatrix} = \begin{bmatrix} -a_3 \cdot s_3 & a_2 + a_3 \cdot c_3 \\ a_2 + a_3 \cdot c_3 & a_3 \cdot s_3 \end{bmatrix} \cdot \begin{bmatrix} s_2 \\ c_2 \end{bmatrix}. \qquad (4\text{-}15)$$

Relation (4-15) is a linear algebraic system of equations in s_2 and c_2. Solutions exist to (4-15) provided the determinant of the matrix is non-zero,

$$\begin{vmatrix} -a_3 \cdot s_3 & a_2 + a_3 \cdot c_3 \\ a_2 + a_3 \cdot c_3 & a_3 \cdot s_3 \end{vmatrix} = -[a_2^2 + a_3^2 - 2 \cdot a_2 \cdot a_3 \cos(\pi - \theta_3)] = -[\tilde{p}_x^2 + \tilde{p}_y^2] \neq 0$$

Thus, as long as the position vector $\tilde{\mathbf{p}}$ of the end-frame has at least one of its planar components non-zero, $\tilde{p}_x^2 + \tilde{p}_y^2 \neq 0$, the system of equations (4-15) is invertible,

$$\begin{bmatrix} s_2 \\ c_2 \end{bmatrix} = \frac{-1}{\tilde{p}_x^2 + \tilde{p}_y^2} \begin{bmatrix} a_3 \cdot s_3 & -a_2 - a_3 \cdot c_3 \\ -a_2 - a_3 \cdot c_3 & -a_3 \cdot s_3 \end{bmatrix} \cdot \begin{bmatrix} \tilde{p}_x \\ \tilde{p}_y \end{bmatrix} \qquad (4\text{-}16)$$

One cannot be sure that (4-16) is valid unless, $s_2^2 + c_2^2 = 1$. This constraint can be proven to be satisfied whenever a solution to θ_3 exists. Finally, to obtain θ_2, compute

$$\theta_2 = \text{atan2}\left[-a_3 \cdot s_3 \cdot \tilde{p}_x + (a_2 + a_3 \cdot c_3) \cdot \tilde{p}_y,\ (a_2 + a_3 \cdot c_3) \cdot \tilde{p}_x + a_3 \cdot s_3 \cdot \tilde{p}_y\right]. \qquad (4\text{-}17)$$

Each value of θ_3 in (4-17) determines a unique value of θ_2.. In the ARID robot only the positive solution for θ_3 is used, hence, only one value of θ_2 requires computing.

ARID Robot Inverse Pose Kinematic Summary

Table 4.1 summarizes the inverse kinematics analysis for the ARID robot. The first column supplies the equations needed to solve for the joint variables in terms of the configuration variables and the DH-parameters. The second column states the *natural kinematic constraints* which must be satisfied in order for the solution to be valid. Natural kinematic constraints indicate geometric relationships between and amongst the DH-parameters and configuration variables that must be satisfied, independent of joint range limits or link interference. For purposes of theoretical analysis, therefore, joint variables range over all the real numbers. In the ARID, for example, the solution $d_1 = p_z$ is always theoretically valid, even though the solution is not *realizable* when p_z exceeds the physical length of the robot track. The inverse solutions to the ARID manipulator that satisfy the natural kinematic constraints must be checked to determine if the computed values of the joint variables fall within the physical joint limits dictated for the ARID. Those solutions which do satisfy the joint limits are said to be *realizable* by the manipulator. Refer to Table 2.2 for joint limits of the ARID robot.

Table 4.1 Inverse Solution to the ARID Manipulator

Joint Variable Solution	Theoretical Kinematic Constraints for Solution
$d_1 = p_z$	None
$\theta_3 = \pm\cos^{-1}\left[\dfrac{\tilde{p}_x^2 + \tilde{p}_y^2 - a_2^2 - a_3^2}{2 \cdot a_2 \cdot a_3}\right]$	$(a_2 - a_3)^2 \le \tilde{p}_x^2 + \tilde{p}_y^2 \le (a_2 + a_3)^2$
$\theta_2 = \text{atan2}\,[-a_3 \cdot s_3 \cdot \tilde{p}_x + (a_2 + a_3 \cdot c_3) \cdot \tilde{p}_y,$ $(a_2 + a_3 \cdot c_3) \cdot \tilde{p}_x + a_3 \cdot s_3 \cdot \tilde{p}_y]$	$(a_2 - a_3)^2 \le \tilde{p}_x^2 + \tilde{p}_y^2 \le (a_2 + a_3)^2$
$\theta_4 = \text{atan2}\,[n_y, n_x] - (\theta_1 + \theta_2 + \theta_3)$	$t_z = 1$

5. CONCLUSION

The nominal ARID forward position and velocity kinematics have been developed, as well as the forward velocity kinematics. A follow-up paper will develop a kinematics error-model for calibrating the ARID.

REFERENCES

1. Doty, K.L [1992] Class Notes.

2. Paul, R.P [1981], *Robot Manipulator: Mathematics, Programming and Control*, MIT Press, Cambridge, Mass.

N93-19394

1992 NASA/ASEE SUMMER FACULTY FELLOWSHIP PROGRAM

JOHN F. KENNEDY SPACE CENTER
UNIVERSITY OF CENTRAL FLORIDA

CALIBRATION OF THE ARID ROBOT

PREPARED BY:	Dr. Keith L. Doty
ACADEMIC RANK:	Professor
UNIVERSITY AND DEPARTMENT:	University of Florida Department of Electrical Engineering
NASA/KSC	
DIVISION:	Mechanical Engineering Directorate
BRANCH:	Special Projects (RADL)
NASA COLLEAGUE:	Willis Crumpler Bill Jones Eduardo Lopez
DATE:	August 7, 1992
CONTRACT NUMBER:	University of Central Florida NASA-NGT-60002 Supplement: 8

ACKNOWLEDGEMENTS

The author gratefully acknowledges the support of the University of Central Florida faculty and staff along with the Boeing and NASA staffs whose diligence and kindness make the NASA Faculty Fellowship program at the Kennedy Space Center so efficient and productive. Particular thanks to Willis Crumpler, Bill Jones, Eduardo Lopez, Gabor Tamasi, Todd Graham and Carol Valdez of NASA; Ron Remus, Joe Looney, Jose Lago and Brian Yamauchi of Boeing and Loren Anderson and Kari Stiles of the University of Central Florida. A special thanks to my office mate, Carl Latino of Oklahoma State University, for stimulating discussions and all-around good fellowship.

ABSTRACT

The author has formulated a new, general model for specifying the kinematic properties of serial manipulators. The new model kinematic parameters do not suffer discontinuities when nominally parallel adjacent axes deviate from exact parallelism. From this new theory the author develops a first-order, lumped-parameter, *calibration-model* for the ARID manipulator. Next, the author develops a calibration methodology for the ARID based on visual and acoustic sensing. A sensor platform, consisting of a camera and four sonars attached to the ARID end frame, performs calibration measurements. A calibration measurement consists of processing one visual frame of an accurately placed calibration image and recording four acoustic range measurements. A minimum of two measurement protocols determine the kinematics calibration-model of the ARID for a particular region: assuming the joint displacements are accurately measured, the calibration surface is planar, and the kinematic parameters do not vary rapidly in the region. No theoretical or practical limitations appear to contra-indicate the feasibility of the calibration method developed here.

TABLE OF CONTENTS

Keith L. Doty
NASA Faculty Fellow

1.0 PROJECT DESCRIPTION

Parameter and assembly tolerances and non-rigid-body effects due to link and joint flexion and thermal expansion introduce errors into the tool pose at the end-effector of a robot. Accounting for the various sources of kinematic error by means of a lumped, first-order model allows one to compensate for pose errors at different configurations. By calibrating the robot at discrete poses, designated *calibration poses* , in the region of its workspace where it will see service, one increases the robot's overall accuracy at those poses. The error-model will then permit interpolation between calibration poses to increase the accuracy of the robot at non-calibration poses.

The primary goal of this project is to increase the operational accuracy of the ARID robot through calibration and adjustments in the ARID control software.

Success in calibration hinges on the performance of the the following tasks,

1. Develop an appropriate kinematics model of the ARID robot to account for the observed end-frame positioning errors.
2. Identify a measurement technique for accurately determining the poses of the ARID robot.
3. Determine the critical calibration poses for measurement.
4. Measure ARID positioning errors at the critical calibration poses..
5. Develop, interface and test a computer program that will use experimentally measured data to compensate for ARID's inaccuracies.

Points 4 and 5 are not addressed in this paper.

2.0 SUMMARY OF PROGRESS

During this program the author has

1. Formulated a kinematics model for calibration,
2. Developed a calibration methodology for the ARID
3. Measured the angular error about the x- and y-*axes* of the ARID end-frame for a variety of configurations. This effort is given in another report [1].

Work yet to be done,

1. Complete the derivation of the ARID calibration-model and devise a methodology for solving for the error parameters.
2. Configure the Perceptics NuVision system and write C-code to perform the required blob analysis on the proposed calibration square.
3. Design and configure a calibration sensor-platform consisting of a camera and four sonar sensors.
4. Write software to acquire visual and acoustic data from the sensor platform.
5. Implement the calibration algorithms in software.
6. Test the calibration sensor-platform on a calibration square lying on a microscopically flat table.
7. Compute the ARID calibration model from calibration measurements.
8. Test and verify the derived calibration model.

In the next section, the author develops a general calibration model with general applicability.

3. KINEMATICS MODEL FOR CALIBRATION

A lumped kinematics model for calibration has been devised. The lumped-parameter calibration model is given in Table 3.1. The parameters found in the table are defined in Fig. 3.1. This model's parameters do not depend on the common normal between two axes, hence, the calibration parameters do not suffer the discontinuities incurred by the Denavit-Hartenburg parameters with nominally parallel axes.

Table 3.1 : Calibration Kinematic Parameters for the ARID Robot

Joint	d	θ	β	a	α	Joint Limits
1 p	d_1	θ_1	β_1	a_1	α_1	[0*inches*, 718*inches*]
2 r	0	θ_2	β_2	a_2	α_2	[4° , 112°]
3 r	0	θ_3	β_3	a_3	α_3	[102° , 148°]
4 r	0	θ_4	0°	0	0°	[-16° , -117°]

The angle parameters θ, β, α, will be called the *joint-angle, link pitch and link twist* , respectively. The parameter d is the *link offset* and a the *link length* . These parameters are determined as follows.

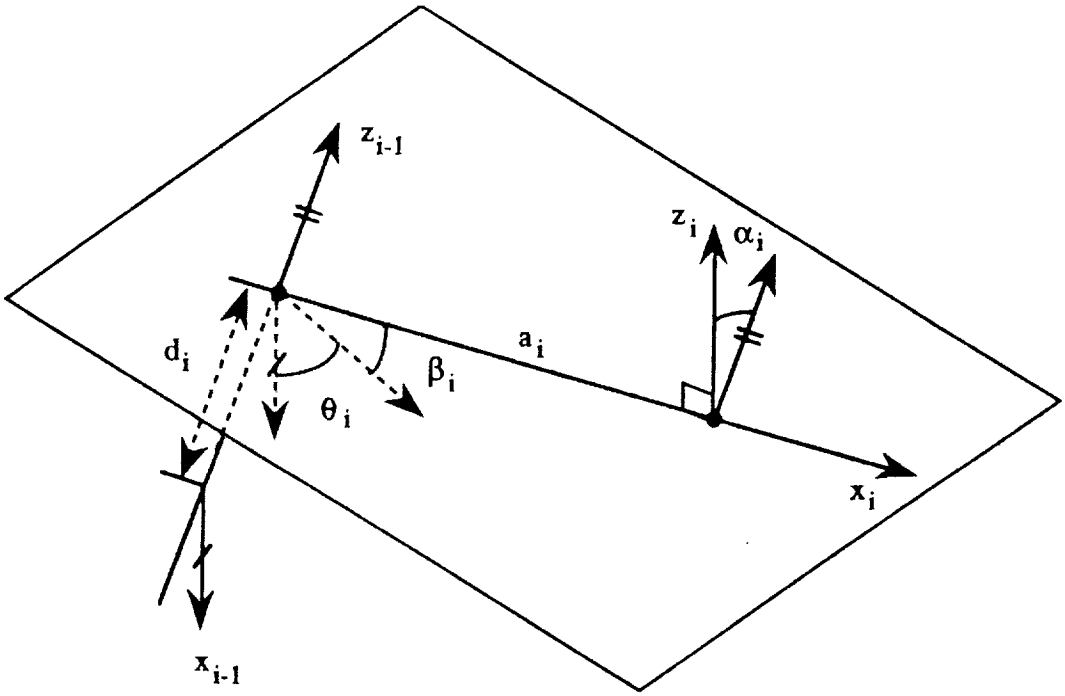

Figure 3.1 Calibration-model kinematic parameters between adjacent joint axes of a serial manipulator.

Draw a perpendicular line from the origin of frame F_{i-1} to the z_i *-axis* with $d_i = 0$. The intersection of this perpendicular line with the z_i *-axis* defines the origin of the next link frame, F_i . The length of this perpendicular line equals a_i . For revolute joints d_i always equals zero. For prismatic joints, d_i equals the joint displacement. Thus, for revolute joints, this model has the same number of parameters as the DH-model, namely, four. With prismatic joints, however, this model requires a fifth parameter, the link offset d_i .

The angle θ equals the amount of rotation about the z_{i-1} *-axis* required to make the z_{i-1} *-axis* , the x_{i-1} *-axis* and the line a_i coplanar. Rotating β_i about the new *y-axis* aligns the new *x-axis* to the line a_i . Translation along the line a_i moves the frame to the origin of F_i . To finish the alignment, twist the moving frame *z-axis* about the line a_i by the angle α_i to align it with the z_i *-axis* .

In summary, the sequence of coordinate transformations between successive joint frames to generate the link transformation $\mathbf{L}_i$ consists of the following:

Revolute Joint:

$$\mathbf{L}_i := \text{Rotate}(z, \theta_i)\ \text{Rotate}(y, \beta_i)\ \text{Translate}(x, a_i)\ \text{Rotate}(x, \alpha_i)$$

Prismatic Joint:

$$\mathbf{L}_i := \text{Translate}(z, d_i)\ \text{Rotate}(z, \theta_i)\ \text{Rotate}(y, \beta_i)\ \text{Translate}(x, a_i)\ \text{Rotate}(x, \alpha_i)$$

The link transform, therefore, computes to

$$\mathbf{L}_i := \begin{bmatrix} \mathbf{R}_i & \mathbf{l}_i \\ 0\ 0\ 0 & 1 \end{bmatrix}, \tag{3-1}$$

where

$$\mathbf{R}_i = \begin{bmatrix} c_{\beta i}\, c_{\theta i} & c_{\theta i}\, s_{\alpha i}\, s_{\beta i} - c_{\alpha i}\, s_{\theta i} & c_{\alpha i}\, c_{\theta i}\, s_{\beta i} + s_{\alpha i}\, s_{\theta i} \\ c_{\beta i}\, s_{\theta i} & c_{\alpha i}\, c_{\theta i} + s_{\alpha i}\, s_{\beta i}\, s_{\theta i} & -c_{\theta i}\, s_{\alpha i} + c_{\alpha i}\, s_{\beta i}\, s_{\theta i} \\ -s_{\beta i} & c_{\beta i}\, s_{\alpha i} & c_{\alpha i}\, c_{\beta i} \end{bmatrix} \tag{3-2}$$

and

$$\mathbf{l}_i := \begin{bmatrix} a_i\, c_{\beta i}\, c_{\theta i} \\ a_i\, c_{\beta i}\, s_{\theta i} \\ d_i - a_i\, s_{\beta i} \end{bmatrix} \tag{3-3}$$

The full forward kinematics ${}^0\mathbf{T}_4$ for the ARID equals

$${}^0\mathbf{T}_4 = \mathbf{L}_1\, \mathbf{L}_2\, \mathbf{L}_3\, \mathbf{L}_4\ . \tag{3-4}$$

Symbolic computation of the complete expression for ${}^0\mathbf{T}_4$ probably exceeds practical requirements. Since each link twist α_i and link pitch β_i lie close to zero, second-order and higher terms in these variables may be ignored. ${}^0\mathbf{T}_4$ will be computed only to first order terms in the α_i and β_i . This computation

appears in Section 3.2. Before continuing further, it will be instructive to define the various coordinate frames involved in this report.

3.1 Identifying the Various Coordinate Frames

Figure 3.2 indicates the relative orientation of the principle coordinate frames discussed in this report. The camera frame is defined at the lens center and the image frame on the image plane. Each calibration square on the calibration strip defines a calibration frame. The ARID base frame follows from the standard link frame definitions. Motion along the ARID base frame *z-axis* , therefore, corresponds to moving along the Orbiter's *x-axis*. To simplify the ensuing discussions, the term *ARID* in this report refers to the ARID on the Orbiter's starboard side.

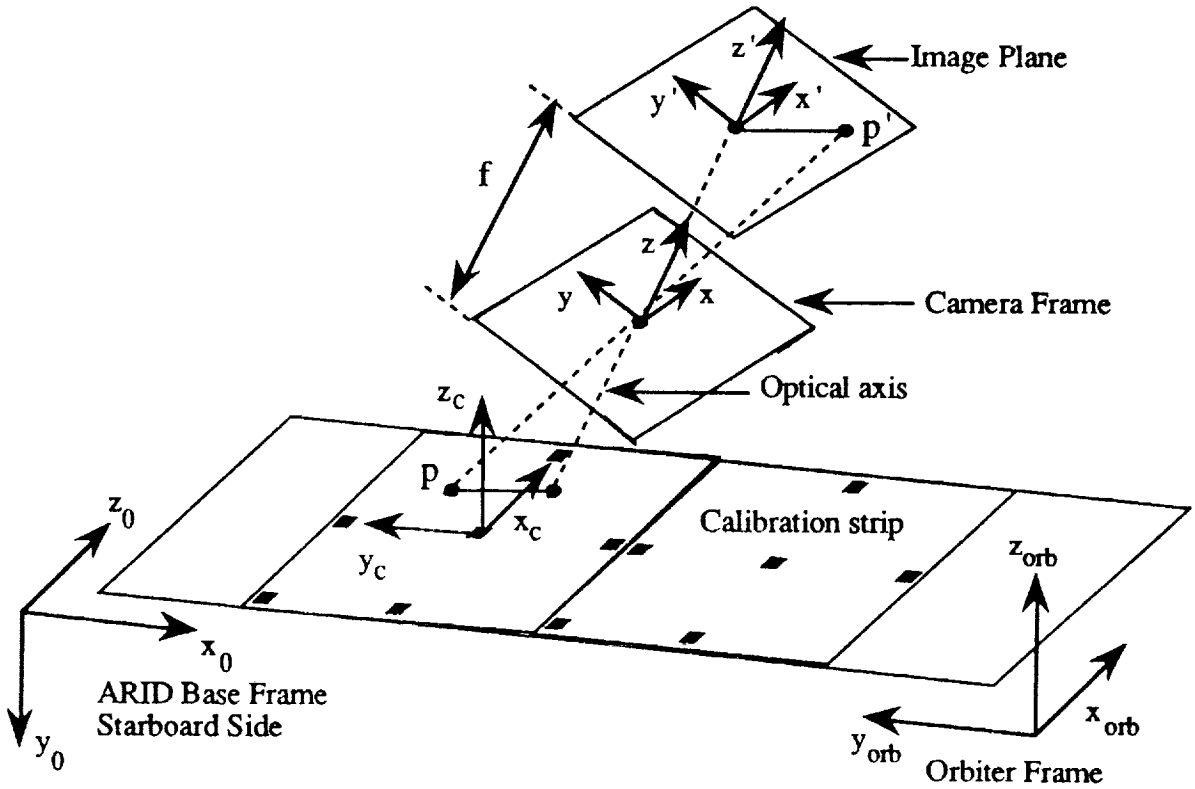

Figure 3.2 Depiction of the image, camera, calibration, ARID and Orbiter frames.

From Fig. 3.2 one determines that the rotation ${}^0\mathbf{R}_{orbiter}$,

C-2

$$ {}^{0}\mathbf{R}_{\text{orbiter}} = \begin{bmatrix} 0 & -1 & 0 \\ 0 & 0 & -1 \\ 1 & 0 & 0 \end{bmatrix}, $$

transforms Orbiter coordinates into Starboard-ARID base frame coordinates.

3.2 First-Order Calibration Model for the ARID

For manipulators where adjacent joint axes are nominally parallel, the link parameters α_i and β_i will be approximately zero. To first order,

$s_{\beta i} := \sin(\beta_i) \approx \beta_i$, $s_{\alpha i} := \sin(\alpha_i) \approx \alpha_i$, $c_{\beta i} := \cos(\beta_i) \approx 1$, $c_{\alpha i} := \cos\alpha_i) \approx 1$,

and $s_{\alpha i}\, s_{\beta i} \approx 0$. With these approximations the link transform rotation becomes

$$ \mathbf{R}_i = \begin{bmatrix} c_{\theta i} & -s_{\theta i} & \beta_i c_{\theta i} + \alpha_i s_{\theta i} \\ s_{\theta i} & c_{\theta i} & -\alpha_i c_{\theta i} + \beta_i s_{\theta i} \\ -\beta_i & \alpha_i & 1 \end{bmatrix} \tag{3-5} $$

and

$$ \mathbf{l}_i := \begin{bmatrix} a_i c_{\theta i} \\ a_i s_{\theta i} \\ d_i - \beta_i a_i \end{bmatrix} \tag{3-6} $$

Suppose links one and two have nominally parallel joint axes, then the first-order approximation of

$$ \mathbf{L}_1 \mathbf{L}_2 = \begin{bmatrix} \mathbf{R}_1 \mathbf{R}_2 & \mathbf{R}_1 \mathbf{l}_2 + \mathbf{l}_1 \\ 0\ 0\ 0 & 1 \end{bmatrix}, \tag{3-7} $$

consists of

$\mathbf{R}_1 \mathbf{R}_2 =$

$$\begin{bmatrix} c_{12} & -s_{12} & \beta_2 c_{12}+\alpha_2 s_{12}+\beta_1 c_1+\alpha_1 s_1 \\ s_{12} & c_{12} & \beta_2 s_{12}-\alpha_2 c_{12}+\beta_1 s_1-\alpha_1 c_1 \\ -\beta_1 c_2+\alpha_1 s_2-\beta_2 & \beta_1 s_2+\alpha_1 c_2+\alpha_2 & 1 \end{bmatrix} \quad (3\text{-}8)$$

and

$$\mathbf{R}_1 \mathbf{l}_2 + \mathbf{l}_1 = \begin{bmatrix} a_2 c_{12} + a_1 c_1 + d_2(\beta_1 c_1+\alpha_1 s_1) \\ a_2 s_{12} + a_1 s_1 + d_2(\beta_1 s_1-\alpha_1 c_1) \\ d_1 + d_2 + a_2(-\beta_1 c_2+\alpha_1 s_2-\beta_2) - \beta_1 a_1 \end{bmatrix} \quad (3\text{-}9)$$

Since the joint axes of the ARID are all nominally parallel, its first order calibration model may be computed using the general results in (3-8) and (3-9) to assist in the calculation of ${}^0\mathbf{T}_4 = \mathbf{L}_1 \mathbf{L}_2 \mathbf{L}_3 \mathbf{L}_4$. The results equal

$${}^0\mathbf{T}_4 = \begin{bmatrix} c_{1234} & -s_{1234} & \varepsilon_1 & a_1 c_1 + a_2 c_{12} + a_3 c_{123} \\ s_{1234} & c_{1234} & \varepsilon_2 & a_1 s_1 + a_2 s_{12} + a_3 s_{123} \\ \varepsilon_3 & \varepsilon_4 & 1 & d_1 + \varepsilon_5 \\ 0 & 0 & 0 & 1 \end{bmatrix} \quad (3\text{-}10)$$

where the first-order error terms $\varepsilon_1, \varepsilon_2, \varepsilon_3, \varepsilon_4, \varepsilon_5$ are given by

$$\varepsilon_1 = \beta_4 c_{1234} + \alpha_4 s_{1234} + \beta_3 c_{123} + \alpha_3 s_{123} + \beta_2 c_{12} + \alpha_2 s_{12} + \beta_1 c_1 + \alpha_1 s_1 \quad (3\text{-}11a)$$

$$\varepsilon_2 = \beta_4 s_{1234} - \alpha_4 c_{1234} + \beta_3 s_{123} - \alpha_3 c_{123} + \beta_2 s_{12} - \alpha_2 c_{12} + \beta_1 s_1 - \alpha_1 c_1 \quad (3\text{-}11b)$$

$$\varepsilon_3 = -\beta_1 c_{234} + \alpha_1 s_{234} - \beta_2 c_{34} + \alpha_2 s_{34} - \beta_3 c_4 + \alpha_3 s_4 - \beta_4 \quad (3\text{-}11c)$$

$$\varepsilon_4 = \beta_1 s_{234} + \alpha_1 c_{234} + \beta_2 s_{34} + \alpha_2 c_{34} + \beta_3 s_4 + \alpha_3 c_4 + \alpha_4 \quad (3\text{-}11d)$$

$$\varepsilon_5 = d_1 + a_3(-\beta_1 c_{23} + \alpha_1 s_{23} - \beta_2 c_3 + \alpha_2 s_3 - \beta_3) + a_2(-\beta_1 c_2 + \alpha_1 s_2 - \beta_2) - \beta_1 a_1 \quad (3\text{-}11e)$$

Equation (3-11) may be written more succinctly,

$$\varepsilon = \mathbf{E}\,\psi\,, \tag{3-12}$$

where

$$\varepsilon := [\varepsilon_1\ \varepsilon_2\ \varepsilon_3\ \varepsilon_4\ \varepsilon_5 - d_1]^\tau\,, \qquad \psi := [\beta_1\ \beta_2\ \beta_3\ \beta_4\ \alpha_1\ \alpha_2\ \alpha_3\ \alpha_4\ ]^\tau\,,$$

and

$\mathbf{E} =$

$$\begin{vmatrix} c_{1234} & c_{123} & c_{12} & c_1 & s_{1234} & s_{123} & s_{12} & s_1 \\ s_{1234} & s_{123} & s_{12} & s_1 & -c_{1234} & -c_{123} & -c_{12} & -c_1 \\ -c_{234} & -c_{34} & -c_4 & -1 & s_{234} & s_{34} & s_4 & 0 \\ s_{234} & s_{34} & s_4 & 0 & c_{234} & c_{34} & c_4 & 1 \\ -a_1 - a_2c_2 - a_3c_{23} & -a_2 - a_3c_3 & -a_3 & 0 & a_2s_2 + a_3s_{23} & a_3\,s_3 & 0 & 0 \end{vmatrix}$$

Observe that $\mathbf{E}$ only depends upon the joint angles θ_i and the link lengths a_i.

3.3 Solving for the ARID Kinematic Parameters

Let ${}^0\mathbf{M}_4$ be a measurement of the ARID end-frame pose expressed in the base frame. The calibration problem is to solve for the unknown kinematic parameters in ${}^0\mathbf{T}_4$ of (3-10), given one or more measurements: ${}^0\mathbf{M}_4 = {}^0\mathbf{T}_4$. At this juncture one must determine which kinematic parameters are known. For example, if d_1, the link lengths a_i , and the joint angles θ_i are known with a high degree of precision, one need only solve for ψ in (3-12). Since ψ contains eight unknowns, the system is under-determined for one measurement and over-determined with two measurements, assuming of course, that the β_i and α_i do not change significantly for the two robot configurations in which the measurements are made.

If all the kinematic parameters are unknown, the problem becomes non-linear. One can use the inverse kinematics solutions to express the *sines* and *cosines* of the revolute joint angles in terms of rational polynomials in the link lengths. The last column in ${}^0\mathbf{M}_4 = {}^0\mathbf{T}_4$ will then provide two equations in the three unknowns,

a_1, a_2, and a_3. Two measurements will yield four equations in the three link lengths. A least-squares solution can be employed to solve for them. With the link lengths determined, the joint angles for the two measurements may be calculated. Finally, one may compute ψ , given that d_1 has been calibrated separately. This procedure requires that the kinematic parameters do not vary significantly for the two measurement configurations of the robot.

The rest of this paper deals with how to generate the measurement poses ${}^0\mathbf{M}_4$.

4. Calibration Measurement Technique

The approach proposed here is to mount a digital camera and four sonic sensors onto the end-effector flange of the ARID robot with approximately the same total mass as the Lockheed end-effector. Refer to Figure 6.1 for a stylized side view of this calibration end-effector.

The camera pose with respect to the flange must be known. The camera will view a calibrated strip (Fig. 5.2) of four-inch squares with appropriate fiducial markings (Fig. 5.1). The calibration strip will run along the Orbiter *y-axis* on a partial, bay-door mock-up (Fig. 5.3). The strip permits a visual calibration measurement every four inches for a total of 28 measurements along the bay door. For high curvature areas of the bay-door, calibration might be required every one or two inches, particularly near the hinges. The author does not expect more than two or three such one-inch squares will be needed. Most calibration squares will be 4 inch squares. The number of calibration strips required will have to be determined by experiment.

A frame-grabber will be needed to capture the image and simple vision software to compute the gray level centroid for each fiducial mark. From these centroids the camera *x-y* position and orientation with respect to the image can be computed.

The four sonar sensors, arranged in an + pattern about the camera, compute the pitch and yaw of the camera frame and range data provides the distance from the camera center to the image center.

The sonar and vision measurements yield a total of six parameters and uniquely determines the pose of the camera, hence, the end-effector flange frame.

5. Vision Measurement

5.1 Details of the Calibration Square

Figure 5.1 illustrates one proposed calibration square. Each square contains five, solid fiducial squares $\frac{1}{4}" \times \frac{1}{4}"$ and a center fiducial $\frac{1}{2}" \times \frac{1}{4}"$. The centroids of these fiducial marks constitutes the critical information proffered by the calibration square. The fiducial in the upper left-hand-corner of the calibration square uniquely identifies quadrant two. Unless the robot end-effector pose deviates more than several inches, this fiducial mark will provide redundant information.

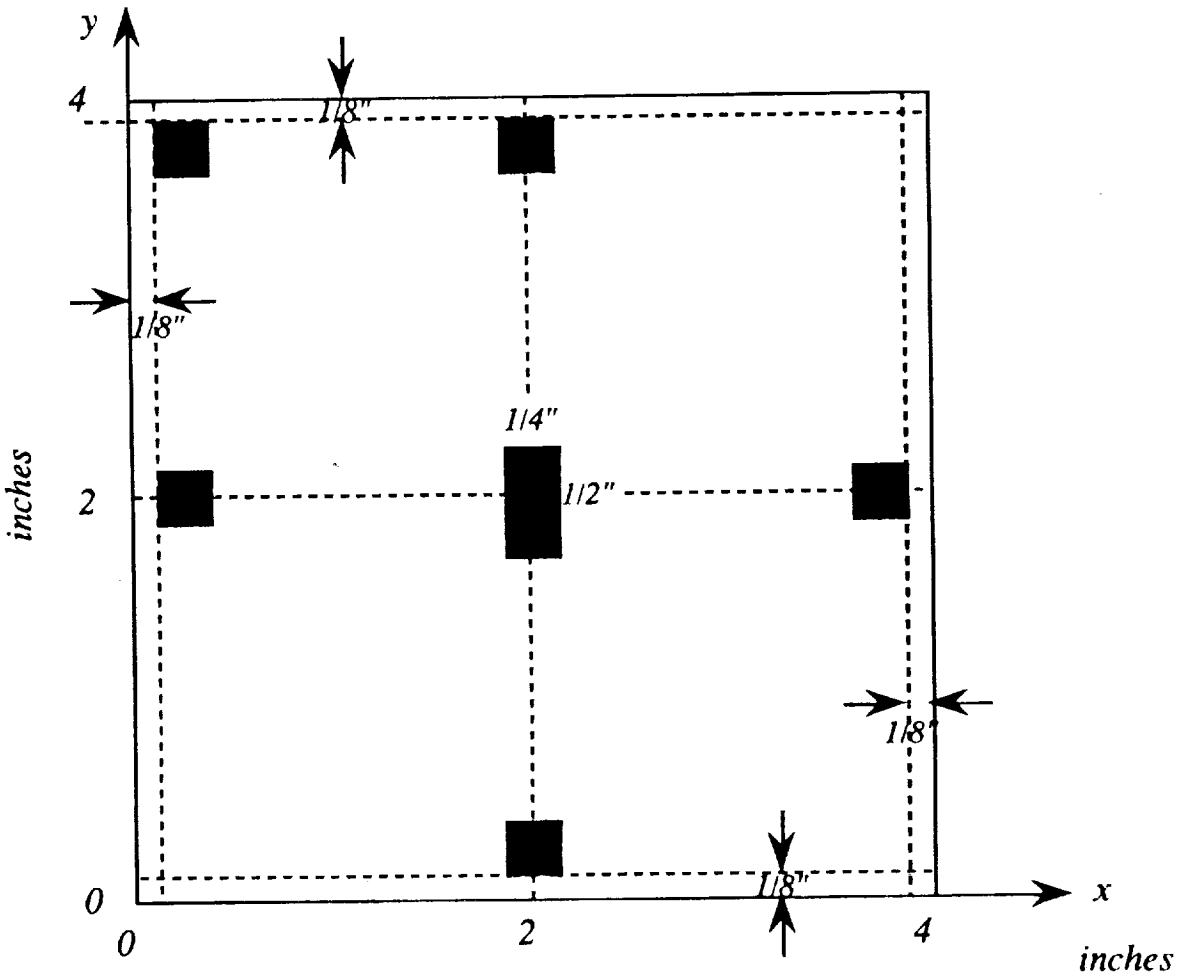

Figure 5.1 Typical visual calibration square.

The centroids of the remaining four perimeter fiducials determine the orientation and center of the calibration square with respect to the camera image. The upper-

center and lower-center fiducial centroids determine the vertical axis of the calibration square while the left-center and right-center fiducial centroids determine the horizontal axis of the calibration square. The centroid of the center fiducial marks the center of the calibration square and should be at the intersection of the vertical and horizontal axes determined by the other four just mentioned. The *y-axis* parallels the long side of the center fiducial and the *x-axis* parallels the short side.

The center fiducial, having twice the area of the other fiducials will be easy to identify in a camera image. From the center fiducial one can easily identify the others. In theory, the central fiducial yields all the information about the position and orientation of the calibration square. The redundant fiducials provided on the calibration square increase the the accuracy of the measurement.

Since the measurement of a fiducial centroid depends upon an area measurement, the computation will be robust to noise. Isolated white pixels in a black fiducial square will not significantly affect the computation of the fiducial's centroid.

For a 512×512 pixel camera, if the calibration frame fills the field of view, each pixel will correspond to a displacement of $\frac{4 \text{ inches}}{512} = \frac{1}{128}$ inch ≈ 0.0078 inches.

5.2 The Calibration Strip

A calibration strip consists of a sequence of concatenated calibration squares drawn on vellum or some other durable, thin, compliant material (Fig. 5.2). This strip, placed upon a mock-up segment of the bay door surface (Fig. 5.3) will permit visual calibration of the ARID robot at prescribed intervals. For instance, the ~112" width of the orbiter bay door divides into 28 four inch intervals. A calibration strip would consist of 28, four-inch squares. At the hinge-end of the bay door the sharp curvature over four inches may require adjustments to the sonar range measurement. This will be discussed in the section on sonar measurements.

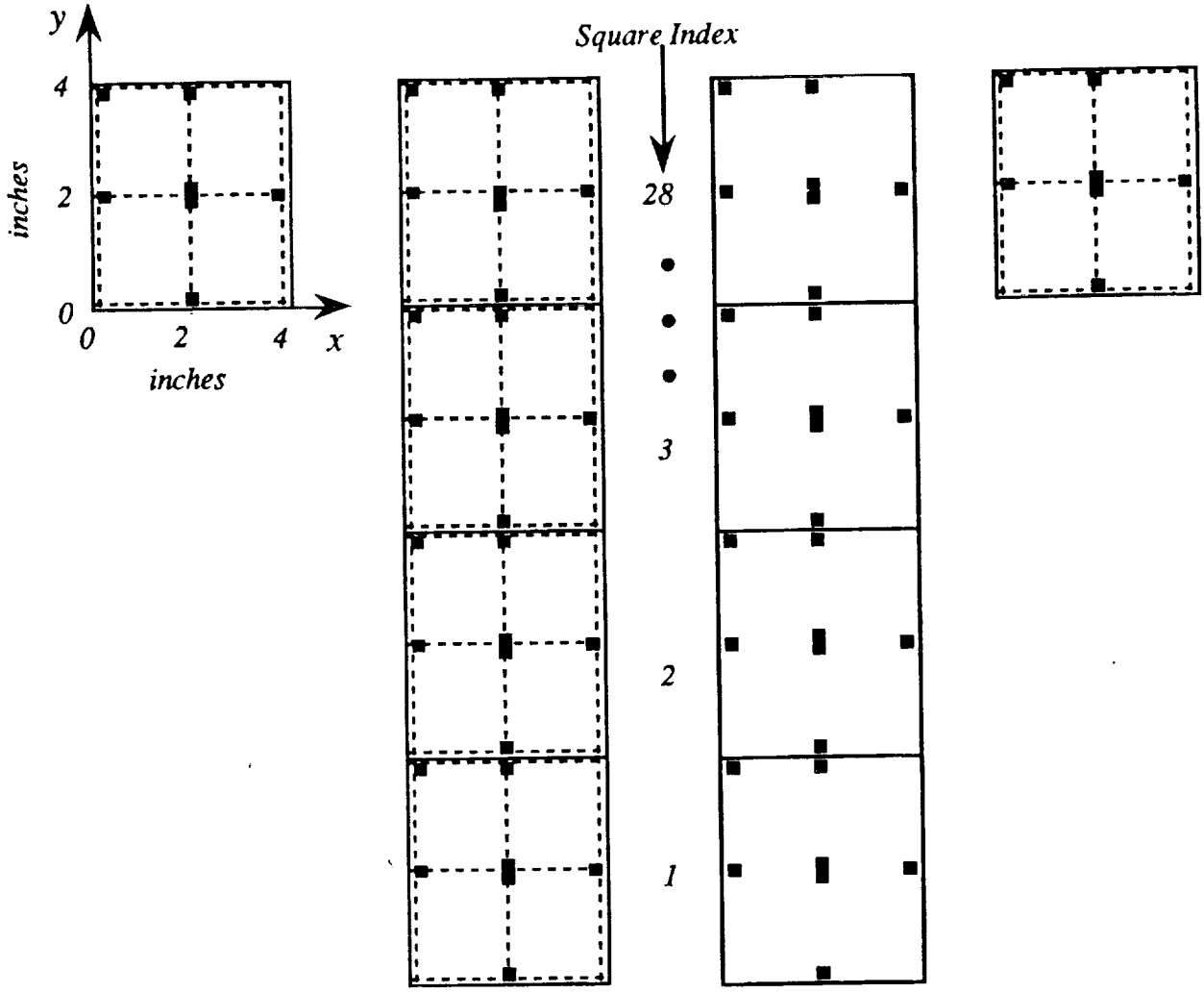

Figure 5.2 Visual calibration strip for the ARID robot.

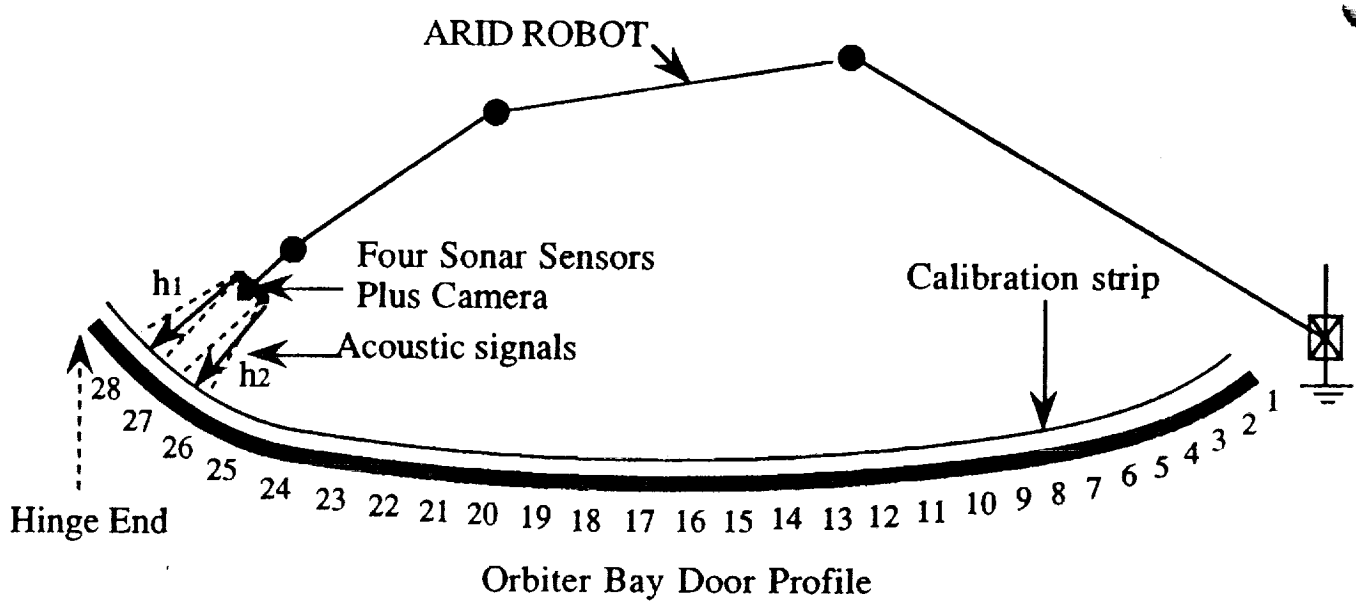

Figure 5.3 Layout of the four inch wide calibration strip. Indexes mark four inch intervals on the bay door.

5.3 Image Measurements

Figure 5.4 depicts the image frame x'-y'-z', the camera frame x-y-z, and the calibration frame x_c-y_c-z_c. The camera coordinates of an object point $\mathbf{p} = [x \;\; y \;\; z]^\tau$ on the calibration strip and its image point $\mathbf{p}' = [x' \;\; y' \;\; f\,]^\tau$ satisfy the projection equations

$$\frac{x'}{f} = \frac{x}{z} \qquad \text{and} \qquad \frac{y'}{f} = \frac{y}{z}.$$

The vision system yields the image coordinates x' and y' and the focal length f of the camera. The camera z-coordinate of the object point can be determined a number of ways. Section 7.4 derives an expression for x,y,z based upon the image data and the acoustic measurements performed by.the four sonar sensors.

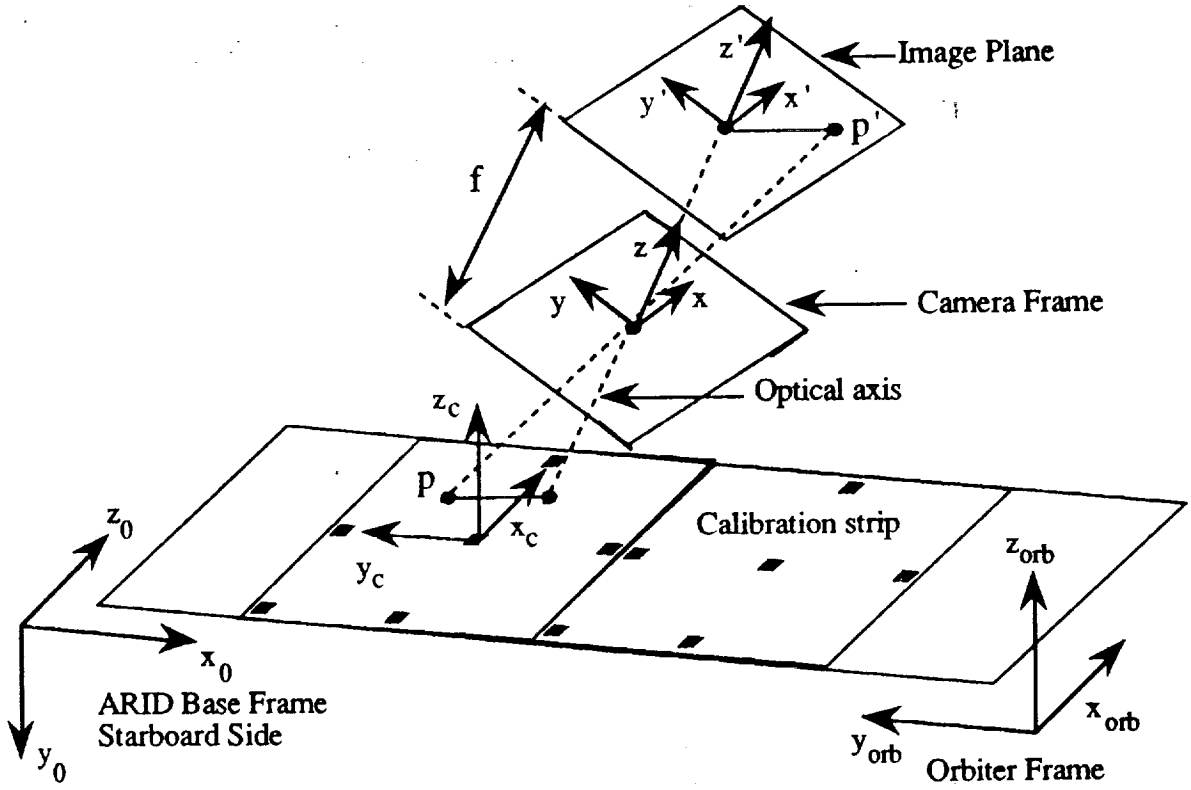

Figure 5.4 Depiction of the image, camera, calibration, ARID and Orbiter frames.

In Fig. 5.5 the camera visual field includes fiducial points p_3, p_4, p_6 of one calibration square and points p_1 and p_2 of another. The image coordinates $\mathbf{p}_i'$ of these fiducial points, along with range information from the sonars, allow us to compute their camera-coordinates $\mathbf{p}_i$ (Section 7.4). The camera field-of-view must be large enough to include at least three non-collinear fiducials in order to determine the rigid-body transformation between the camera frame and the calibration frame. For example, in Fig. 5.5 the coordinates of $\mathbf{p}_3$, $\mathbf{p}_4$ and $\mathbf{p}_6$ yield sufficient information to do that. The vectors

$$\boldsymbol{a} := [a_x \;\; a_y]^\tau = \mathbf{p}_4 - \mathbf{p}_6 \quad \text{and} \quad \boldsymbol{b} := [b_x \;\; b_y]^\tau = \mathbf{p}_4 - \mathbf{p}_3$$

define the coordinate frame axes vectors $x_c = \frac{\mathbf{a}}{|\mathbf{a}|}$ and $y_c = \frac{\mathbf{b}}{|\mathbf{b}|}$ of the calibration square with respect to the camera frame. The third axis equals the cross-product of the other two: $z_c = x_c \times y_c$ The vectors x_c, y_c, z_c should be orthogonal. Measurement error may cause $x_c^\tau y_c \neq 0$, hence, the matrix

$$^{camera}R_{calibration} = [x_c \quad y_c \quad z_c],$$

Figure 5.5 Camera image of a calibration square.

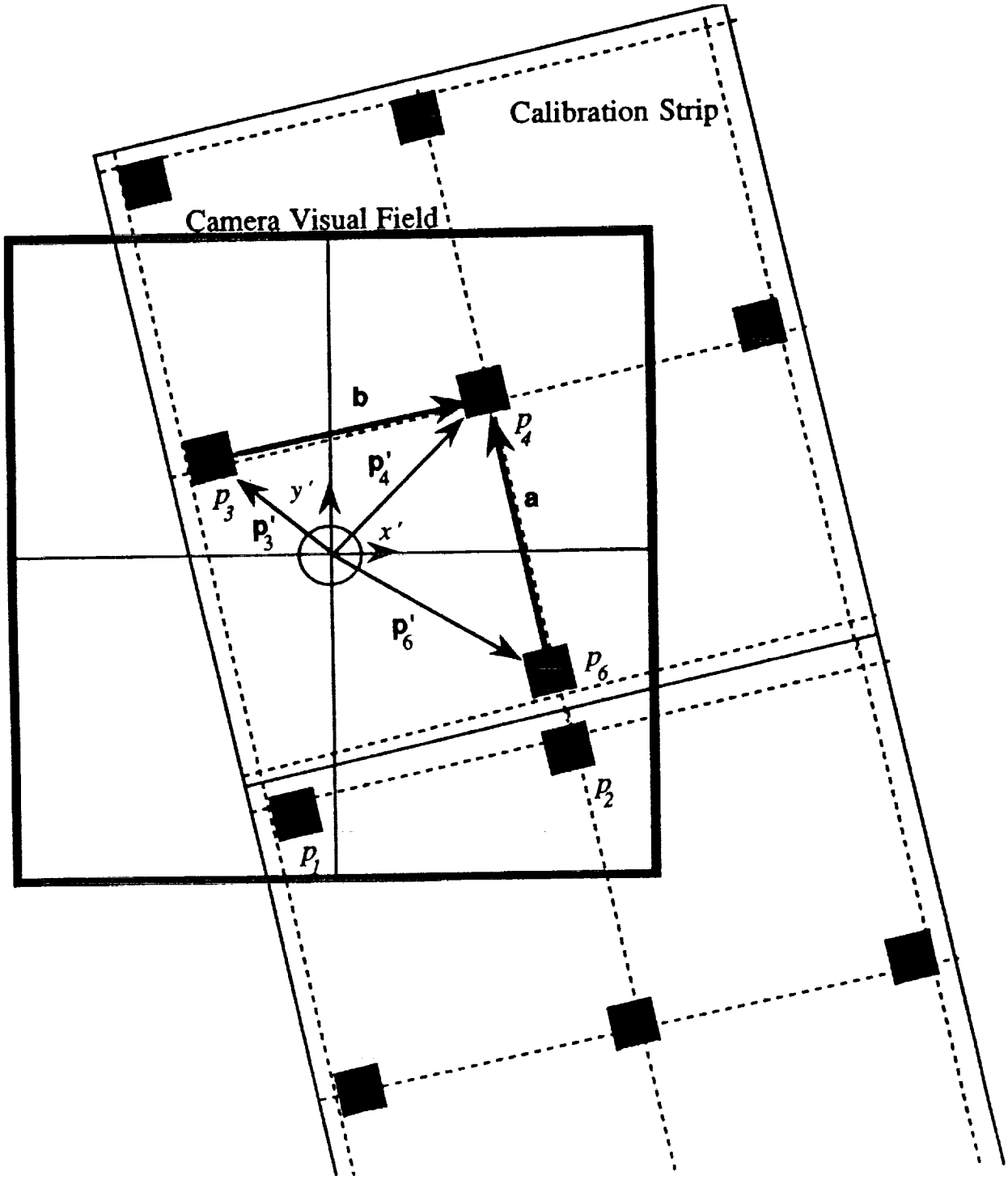

which transforms calibration-coordinates into camera-coordinates, may not be a true rotation as it would be with exact measurements. In any case, the measured rigid-body transformation which converts calibration-coordinates to camera-coordinates equals

$$ {}^{\text{camera}}\mathbf{M}_{\text{calibration}} = \begin{bmatrix} {}^{\text{camera}}\mathbf{R}_{\text{calibration}} & \mathbf{p}_4 \\ 0\ 0\ 0 & 1 \end{bmatrix}. $$

With ${}^{0}\mathbf{T}_4$ equal to the forward transform of the ARID and ${}^{4}\mathbf{T}_{\text{camera}}$ equal to the fixed, rigid-body transformation relating the camera-frame to the ARID end-effector frame, we have the identity,

$$ {}^{0}\mathbf{M}_{\text{calibration}} = {}^{0}\mathbf{T}_4\ {}^{4}\mathbf{T}_{\text{camera}}\ {}^{\text{camera}}\mathbf{M}_{\text{calibration}} $$

where ${}^{0}\mathbf{M}_{\text{calibration}}$ relates the ARID base-frame to the coordinate system of the calibration square under view. The above relationship yields one set of equations in the unknown parameters for each calibration pose measured. Section 8.0 will elaborate the procedure.

5.4 Fiducial Identification Algorithm

The above computation hinges on the assumption that the fiducial marks can be identified. Refer to Figure 5.6 in following the logic of the **FID** algorithm below. The assumption is that a center fiducial always appears in the camera field-of-view. Assume there are n pixels per inch.

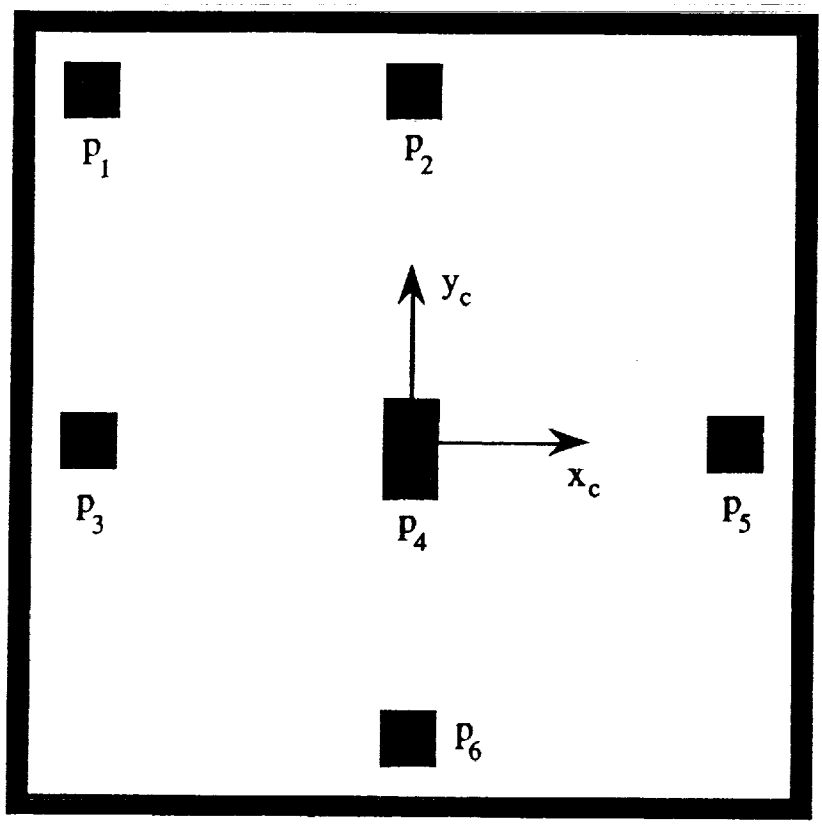

Figure 5.6 A typical calibration square with fiducial centroids indicated by p_i .

FID Algorithm

1. Scan image left-to-right, top-to-bottom, starting at the upper left-hand-corner until a blob is encountered with area: $\frac{n^2}{8}$. The centroid of that blob equals the center point $\mathbf{p}_4$. The longest side of the center blob determines the *y-axis*. The direction of the *y-axis* will usually be towards increasing *y'* of the image frame. For this not to be the case the ARID would have to be in error by 180°.

2. Determine the centroid and the midpoint of two adjacent edges of the center blob. The lines from the centroid to the two edges provide a rough estimate of the *x-* and *y-axes* of the calibration-frame in which the fiducial is located.

3. From the center fiducial search for the perimeter fiducials approximately *1.75 n* pixels along the four directions found in Step 2. Find the centroid of any blob with area equal to $\frac{n^2}{16}$ and compute the longest vector along each axis to increase the accuracy of the axes measurements.

6. ACOUSTIC MEASUREMENTS

The acoustic sensor measures four perpendicular distances h_i , $i = 1,2,3,4$, to the calibration strip (Fig. 6.1, also refer to Fig. 7.1). Section 7.0 illustrates how the acoustic measurements determine the plane of a calibration square, assuming, of course, that the bay door is locally flat. The curvature along the Orbiter's *y-axis* requires the sonar separation to be small compared to the curvature. Since we desire to calibrate the ARID every four inches, and four inches is small compared to the bay door curvature (except near the hinges), one solution would be to make the sonar separation d along the *y-axis* equal to four inches, if this is possible. The Orbiter is quite flat along the *x-axis*, so the separation of the sonar sensors can be further apart along that axis. In the ensuing discussion the distance between the two *x-axis* sonars will be assumed equal to the distance between the two *y-axis* sonars. This distance will be denoted by d.

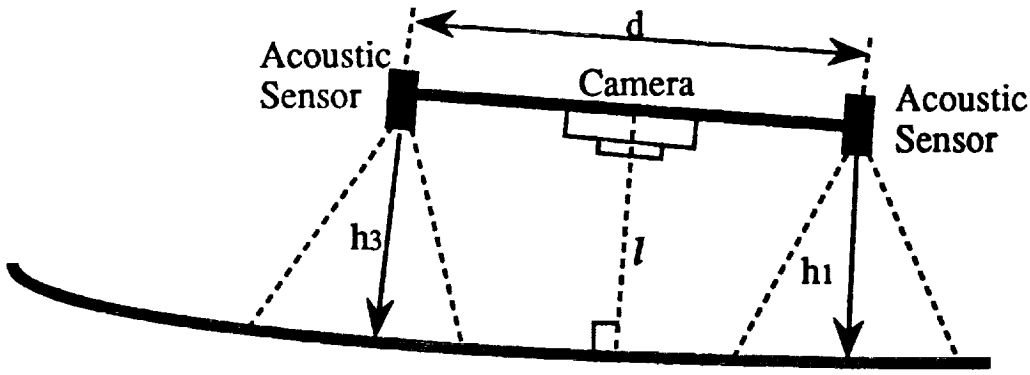

Orbiter Bay Door Profile

Figure 6.1 Side view of the calibration end-effector showing the camera and two of the four acoustic sensors.

We emphasize that the sonar sensors must scan a locally flat surface. Should this not be possible on an Orbiter bay door mock-up, the calibration strip can be placed on a flat surface and the ARID calibrated on that surface. From preliminary experiments with the ARID, such a calibration procedure might actually work better than using an Orbiter bay door mock-up section.

The integration of the sonar measurements with the vision imaging to locate the calibration square fiducial points in camera-frame coordinates will be described next.

7. CAMERA COORDINATES OF CALIBRATION POINTS

The goal of this section is to compute the camera-frame coordinates of the point $p = p(x,y,z)$ on the calibration strip, given

1. The absolute distance between pixels,
2. The focal length f of the camera,
2 The distance between the sonar sensors 2 γ,
3. Sonar measurements h_i , $i = 1,2,3,4$, and
4. The camera-frame coordinates of its image point $p' = p(x',y',f)$.

Figure 7.1 depicts the calibration end-effector taking a measurement. The sonar sensors measure the heights h_i , $i = 1,2,3,4$, and the camera takes an image of the calibration strip. The camera has focal length f . The distance between the sonar sensors d = 2 γ. The camera-frame origin coincides with the lens center and the optical axis coincides with the the frame's *z-axis*.

Since the fiducial points on the calibration strip have known positions, the computed coordinates of a fiducial point p can be compared to its known value, provided one can identify that fiducial. We treated the problem of identifying a specific fiducial in Section 5.4.

Measurement of the position of any three, non-collinear, fiducial points completely determines the plane of the calibration strip, the *calibration-plane*, with respect to the camera-frame and, therefore, provides a complete calibration measurement.

The acoustic measurements yield the positions of the points p_i , $i = 1,2,3,4$, on the calibration-plane. Four points over-determine the plane. Since the orbiter bay doors are not exactly flat and the acoustic measurements may not, in any case, precisely place the four points on a common plane, one may wish to find a plane that "best-fits" the four points. In this case, one may wish to employ the Moore-Penrose inverse to compute the unique plane that fits the data in a least-squares sense.

From Fig. 7.1 one can determine the camera-frame coordinates of the point p_i, $i = 1,2,3,4$, in terms of the acoustically measured heights h_i , $i = 1,2,3,4$, and the between-sensor distance d = $\sqrt{2}$ γ.

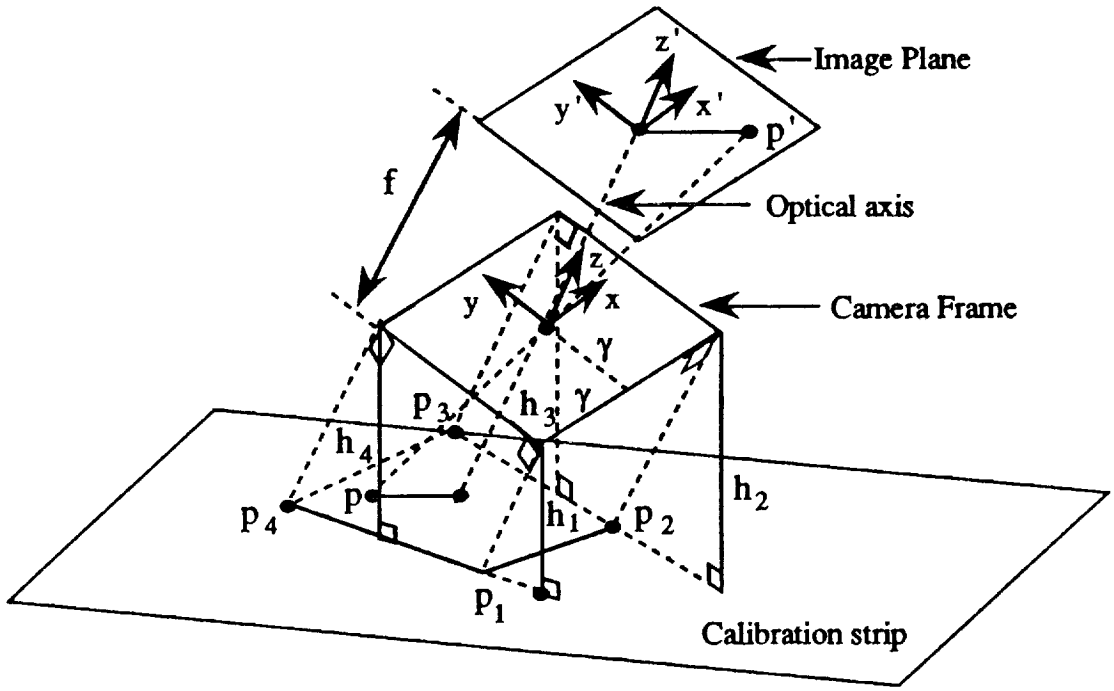

Figure 7.1 Acoustic and visual measurement parameters

Consider the detail of the plane determined by the parallel lines h_1 and h_4 in Fig. 7.2. One expects the acoustic sensor to measure the perpendicular distance to the calibration plane since the reflection along the perpendicular travels the shortest path. Experimental observation appears to verify this expectation.

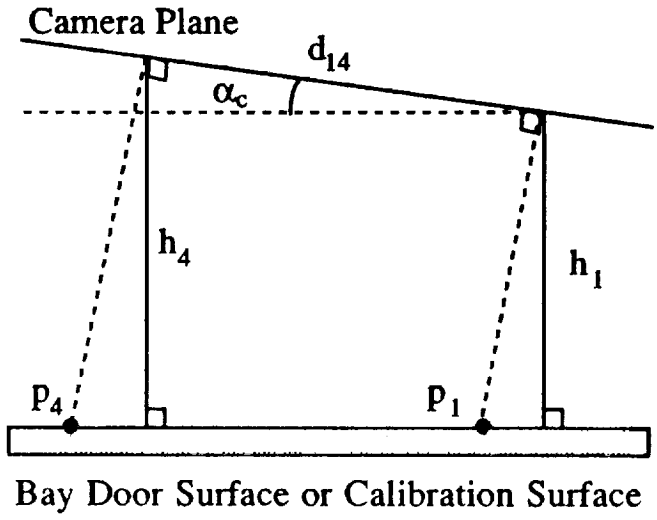

Figure 7.2 Acoustic and visual measurement parameters

The acoustic measurements h_1 and h_4 allow us to compute the camera coordinate *z-components* of the points p_1 and p_4. In Fig. 7.2, the distance $d_{14} = d\sqrt{2}$, hence,

$$\sin(\alpha_c) = \frac{h_4 - h_1}{d\sqrt{2}}. \tag{7-1}$$

The camera z-coordinates of the points p_1 and p_4 compute to

$$z_1 = \frac{-h_1}{\cos(\alpha_c)} \quad \text{and} \quad z_4 = \frac{-h_4}{\cos(\alpha_c)}, \tag{7-2}$$

hence, the camera coordinates of these two points equal, respectively,

$$\mathbf{p}_1 = \begin{bmatrix} -\gamma \\ -\gamma \\ \dfrac{-h_1}{\cos(\alpha_c)} \end{bmatrix}, \quad \mathbf{p}_4 = \begin{bmatrix} -\gamma \\ \gamma \\ \dfrac{-h_4}{\cos(\alpha_c)} \end{bmatrix}. \tag{7-3}$$

A similar consideration of the plane determined by the parallel lines h_2 and h_3 permits expressing the camera coordinates of points p_2 and p_3,

$$\mathbf{p}_2 = \begin{bmatrix} \gamma \\ -\gamma \\ \dfrac{-h_2}{\cos(\beta_c)} \end{bmatrix}, \quad \mathbf{p}_3 = \begin{bmatrix} \gamma \\ \gamma \\ \dfrac{-h_3}{\cos(\beta_c)} \end{bmatrix}. \tag{7-4}$$

In this case, the angle β_c is determined by

$$\sin(\beta_c) = \frac{h_3 - h_2}{d\sqrt{2}}. \tag{7-5}$$

These values assumes the sonar measurements determine the perpendicular distance to the calibration strip.

7.1 Computing the Calibration-Plane Equation

From the coordinates of any three of the four points p_i , $i = 1,2,3,4$, one can compute the coefficients $\{\eta_x , \eta_y , \eta_z , \xi\}$ in the calibration-plane equation,

$$\eta_x x + \eta_y y + \eta_z z + \xi = 0, \tag{7-6}$$

or, equivalently,

$$\frac{\eta_x}{\xi} x + \frac{\eta_y}{\xi} y + \frac{\eta_z}{\xi} z = -1. \tag{7-7}$$

Substituting the coordinates of p_i , $i = 1,2,3$, into the above equation leads to the linear system in the unknown coefficients,

$$A \nu = -\begin{bmatrix} 1 \\ 1 \\ 1 \end{bmatrix}, \tag{7-8}$$

where

$$A = \begin{bmatrix} -\gamma & -\gamma & \dfrac{-h_1}{\cos(\alpha_c)} \\ \gamma & -\gamma & \dfrac{-h_2}{\cos(\beta_c)} \\ \gamma & \gamma & \dfrac{-h_3}{\cos(\beta_c)} \end{bmatrix}, \quad \nu = \begin{bmatrix} \nu_x \\ \nu_y \\ \nu_z \end{bmatrix} = \frac{1}{\xi} \begin{bmatrix} \eta_x \\ \eta_y \\ \eta_z \end{bmatrix}. \tag{7-9}$$

As long as p_i , $i = 1,2,3$, are not collinear, A is invertible and

$$\nu = -A^{-1} \begin{bmatrix} 1 \\ 1 \\ 1 \end{bmatrix}, \tag{7-10}$$

determines the coefficients for the plane equation.

This method can be applied to all four points as well, except that **A** becomes $\mathbf{A} = [\mathbf{p}_1 \ \mathbf{p}_2 \ \mathbf{p}_3 \ \mathbf{p}_4]^\tau$, and is no longer invertible. The Moore-Penrose inverse (pseudo-inverse) $\mathbf{A}^+$, however, can be used to find a plane that fits the data in a least-squares sense. The resultant solution ν_s computes to

$$\nu_s = -\mathbf{A}^+ \begin{bmatrix} 1 \\ 1 \\ 1 \end{bmatrix}. \tag{7-11}$$

If three of the four points are not colinear, **A** has full-column rank and

$$\mathbf{A}^+ = (\mathbf{A}^\tau \mathbf{A})^{-1} \mathbf{A}^\tau . \tag{7-12}$$

The solution obtained with the Moore-Penrose inverse yields a plane equation that fits the data with least-squared-error ε,

$$\varepsilon := \left| -\begin{bmatrix} 1 \\ 1 \\ 1 \end{bmatrix} - \mathbf{A}\,\nu_s \right|^2 \leq \left| -\begin{bmatrix} 1 \\ 1 \\ 1 \end{bmatrix} - \mathbf{A}\,\nu \right|^2 \quad \text{for all } \nu. \tag{7-13}$$

In other words, no other plane will produce a smaller ε than the plane determined by the coefficients ν_s.

7.2 Alternative Computation of the Calibration-Plane Equation

The computation of the coefficients of the calibration-plane equation in the previous discussion required the inversion of the matrix **A**. The computational requirements are significantly reduced and symbolic solutions obtained by taking advantage of the properties of a plane.

From the coordinates of three, non-collinear points p_i , $i = 1,2,3$, compute the coefficients in the calibration-plane equation,

$$\eta_x x + \eta_y y + \eta_z z + \xi = 0, \tag{7-14}$$

by computing the coefficients of x,y, and z in

$$[x \ \ y \ \ z\,] \cdot (\mathbf{p}_2 - \mathbf{p}_1) \times (\mathbf{p}_3 - \mathbf{p}_1) + \xi = 0. \tag{7-15}$$

and the constant term from

$$\xi = -\mathbf{p}_1^{\tau}(\mathbf{p}_2-\mathbf{p}_1)\times(\mathbf{p}_3-\mathbf{p}_1)\,. \tag{7-16}$$

The first term in the above equation is the vector box product, hence, the coefficients may also be computed in terms of determinants. For the situation depicted in Fig. 7.1, for example,

$$[x \quad y \quad z]\cdot(\mathbf{p}_2-\mathbf{p}_1)\times(\mathbf{p}_3-\mathbf{p}_1) = \begin{vmatrix} x & y & z \\ 2\gamma & 0 & \frac{h_1}{\cos(\alpha_c)} - \frac{h_2}{\cos(\beta_c)} \\ 2\gamma & 2\gamma & \frac{h_1}{\cos(\alpha_c)} - \frac{h_3}{\cos(\beta_c)} \end{vmatrix}. \tag{7-17}$$

The coefficients of x,y,z in the resulting express for the above determinant equal

$$\eta_x = 2\gamma\left(\frac{h_2}{\cos(\beta_c)} - \frac{h_1}{\cos(\alpha_c)}\right), \quad \eta_y = 2\gamma\frac{h_3-h_2}{\cos(\beta_c)}, \quad \eta_z = 4\gamma^2. \tag{7-18}$$

To calculate the constant ξ evaluate

$$\xi = -\begin{vmatrix} -\gamma & -\gamma & \frac{-h_1}{\cos(\alpha_c)} \\ 2\gamma & 0 & \frac{h_1}{\cos(\alpha_c)} - \frac{h_2}{\cos(\beta_c)} \\ 2\gamma & 2\gamma & \frac{h_1}{\cos(\alpha_c)} - \frac{h_3}{\cos(\beta_c)} \end{vmatrix} = -\begin{vmatrix} -\gamma & -\gamma & \frac{-h_1}{\cos(\alpha_c)} \\ 2\gamma & 0 & \frac{h_1}{\cos(\alpha_c)} - \frac{h_2}{\cos(\beta_c)} \\ 0 & 0 & \frac{-h_1}{\cos(\alpha_c)} - \frac{h_3}{\cos(\beta_c)} \end{vmatrix} \tag{7-19}$$

to obtain

$$\xi = 2\gamma^2\left(\frac{h_1}{\cos(\alpha_c)} + \frac{h_3}{\cos(\beta_c)}\right). \tag{7-20}$$

Collecting these results together yields,

$$\nu_1 = \frac{1}{\gamma\left(\frac{h_1}{\cos(\alpha_c)} + \frac{h_3}{\cos(\beta_c)}\right)} \begin{bmatrix} \left(\frac{h_2}{\cos(\beta_c)} - \frac{h_1}{\cos(\alpha_c)}\right) \\ \frac{h_3 - h_2}{\cos(\beta_c)} \\ 2\gamma \end{bmatrix}. \qquad (7\text{-}21)$$

If the three points p_i , $i = 1,2,4,$ had been selected to determine the plane, then

$$\nu_2 = \frac{1}{\gamma\left(\frac{h_2}{\cos(\beta_c)} + \frac{h_4}{\cos(\alpha_c)}\right)} \begin{bmatrix} \frac{h_2}{\cos(\beta_c)} - \frac{h_1}{\cos(\alpha_c)} \\ \frac{h_4 - h_1}{\cos(\alpha_c)} \\ 2\gamma \end{bmatrix} \qquad (7\text{-}22)$$

and $$\xi = 2\gamma^2\left(\frac{h_2}{\cos(\beta_c)} + \frac{h_4}{\cos(\alpha_c)}\right). \qquad (7\text{-}23)$$

A necessary and sufficient condition for the two sets of plane coefficients to be the same, $\nu_1 = \nu_2$, is that

$$\frac{h_1}{\cos(\alpha_c)} + \frac{h_3}{\cos(\beta_c)} = \frac{h_2}{\cos(\beta_c)} + \frac{h_4}{\cos(\alpha_c)}. \qquad (7\text{-}24)$$

If the measured heights satisfy this condition, then all four points must be on the same plane. Of course, with measurements, one cannot guarantee this condition will hold and the more complex, least-squared solution may be preferred.

Now that we have the equation for the calibration-plane, we can use the visual data to compute the camera-coordinates of any point p on the calibration-plane from the coordinates of its image point p' on the image plane.

7.3 Camera-Coordinates of a Point on the Calibration Strip

From geometric optics and the coordinate frame definitions depicted in Fig. 7.1, the coordinates of $\mathbf{p} = [x \quad y \quad z]^\tau$ and its image point $\mathbf{p}' = [x' \quad y' \quad f\,]^\tau$ satisfy the projection equations

$$\frac{x'}{f} = \frac{x}{z} \quad \text{and} \quad \frac{y'}{f} = \frac{y}{z}. \qquad (7\text{-}25)$$

In Fig. 7.1 the *z-axis* component of the object must always be negative.

Since every point p on the calibration-plane must satisfy

$$\nu^{\tau} \mathbf{p} = -1, \tag{7-26}$$

one can compute the range of the object in terms of its x and y coordinates,

$$z = \frac{\nu_x x + \nu_y y + 1}{-\nu_z}. \tag{7-27}$$

Substitute into (7-27) the values for x and y given in (7-25) and solve for z to obtain

$$z = \frac{-f}{\nu_x x' + \nu_y y' + \nu_z f}. \tag{7-28}$$

Computing x and y with this value of z yields

$$\begin{bmatrix} x \\ y \end{bmatrix} = \frac{-1}{\nu_x x' + \nu_y y' + \nu_z f} \begin{bmatrix} x' \\ y' \end{bmatrix}. \tag{7-29}$$

From ν_1 computed earlier (7-21) and the definitions

$$\eta_1 := \frac{h_1}{\cos(\alpha_c)}, \quad \eta_2 := \frac{h_2}{\cos(\beta_c)}, \quad \eta_3 := \frac{h_3}{\cos(\beta_c)}, \quad \eta_4 := \frac{h_4}{\cos(\alpha_c)}, \tag{7-30}$$

$$\cos(\alpha_c) = \sqrt{1 - \left(\frac{h_4 - h_1}{d\sqrt{2}}\right)^2},$$

and

$$\cos(\beta_c) = \sqrt{1 - \left(\frac{h_3 - h_2}{d\sqrt{2}}\right)^2},$$

we obtain the camera coordinates x, y of any point in the object plane in terms of the acoustic measurements h_i, the visual measurements x', y', and the distance d between the sonar sensors,

$$\begin{bmatrix} x \\ y \end{bmatrix} = \frac{-\gamma(\eta_1 + \eta_3)}{(\eta_2 - \eta_1) x' + (\eta_3 - \eta_2) y' + 2\gamma f} \begin{bmatrix} x' \\ y' \end{bmatrix} \tag{7-31}$$

and

$$z = \frac{-\gamma f (\eta_1 + \eta_3)}{(\eta_2 - \eta_1)\, x' + (\eta_3 - \eta_2)\, y' + 2\, \gamma\, f}. \qquad (7\text{-}32)$$

In the next section the camera coordinates of the fiducial points will be used to determine the rigid-body transformation between the camera and calibration square under view.

7.4 The Camera-to-Calibration-Frame Transformation

Assume the fiducial centroids p_i , i = *1,2,3,4,5,* on a calibration square have been identified (Fig. 7.3) by the ***FID*** algorithm. In Section 7.3 we indicated how the camera coordinates x_i ,y_i , z_i of each fiducial centroid p_i can be calculated from acoustic measurements and the camera image-coordinates x_i', y_i' of its image point p_i'. Therefore, the camera-frame coordinates of the calibration-frame of the square under view equal

$$\mathbf{x}_c = \frac{\mathbf{p}_5 - \mathbf{p}_3}{|\mathbf{p}_5 - \mathbf{p}_3|}, \quad \mathbf{y}_c = \frac{\mathbf{p}_2 - \mathbf{p}_6}{|\mathbf{p}_2 - \mathbf{p}_6|}, \quad \mathbf{z}_c = \mathbf{x}_c \times \mathbf{y}_c . \qquad (7\text{-}33)$$

These vectors should be orthogonal. Measurement error may cause $\mathbf{x}_c^{\tau}\, \mathbf{y}_c \neq 0$, hence, the matrix

$$^{\text{camera}}\mathbf{R}_{\text{calibration}} = [\mathbf{x}_c \quad \mathbf{y}_c \quad \mathbf{z}_c\,], \qquad (7\text{-}34)$$

which transforms calibration-coordinates into camera-coordinates may not be a true rotation as it would be with exact measurements. In any case, the measured rigid-body transformation which converts calibration-coordinates to camera-coordinates equals

$$^{\text{camera}}\mathbf{M}_{\text{calibration}} := \begin{bmatrix} ^{\text{camera}}\mathbf{R}_{\text{calibration}} & \mathbf{p}_4 \\ 0\ 0\ 0 & 1 \end{bmatrix}. \qquad (7\text{-}35)$$

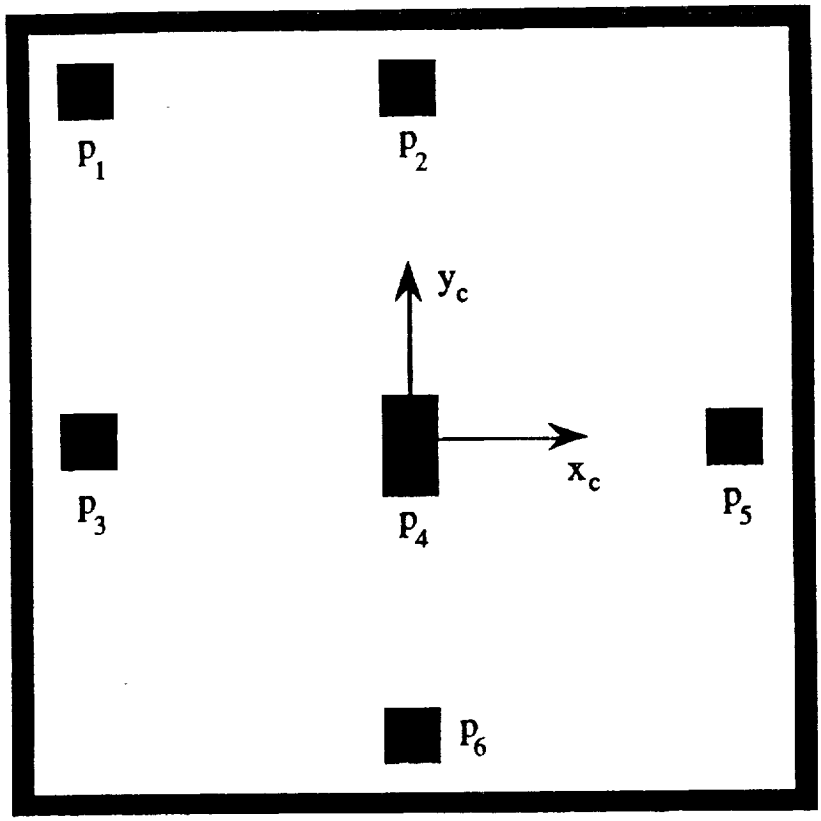

Figure 7.3 A typical calibration square with fiducial centroids indicated by p_i.

Knowledge of the ARID forward kinematics, the relationship of the camera-frame to the ARID end-frame and, now, the camera-coordinates of the fiducial points, one can compute the fiducial point coordinates with respect to the ARID base frame. Assuming the calibration strip has been accurately positioned with respect to the ARID base frame, one can consequently calibrate the ARID at each calibration square by comparing the calibrated, fiducial-point, base-frame coordinates with the measured fiducial-point, base-frame coordinates. In the next section, these ideas will be developed further.

8. CALIBRATION OF THE ARID

Let ${}^{0rb}\mathbf{M}_{calibration}$ be a precisely measured rigid-body transformation from the Orbiter frame to a calibration square of interest. Define ${}^{0rb}\mathbf{M}_0$ to be a precisely measured rigid-body transformation from the Orbiter frame to the ARID base-frame. The rigid-body transformation ${}^{4}\mathbf{M}_{camera}$, relating the camera frame to the ARID end-frame is fixed and assumed known. If this is not the case, a tool-frame calibration-model must be appended to the existing ARID model and additional

kinematic parameters will need to be determined along with the ARID parameters. To simplify the development here, ${}^{4}\mathbf{M}_{camera}$ is assumed known. The rigid-body transformation ${}^{camera}\mathbf{M}_{calibration}$ (7-35) is calculated from the acoustic and visual measurements.

The rigid-body transformation from the Orbiter frame to the calibration-frame must equal

$$ {}^{0rb}\mathbf{M}_{calibration} = {}^{0rb}\mathbf{M}_{0}\ {}^{0}\mathbf{T}_{4}\ {}^{4}\mathbf{M}_{camera}\ {}^{camera}\mathbf{M}_{calibration} \qquad (7\text{-}35) $$

Solving for ${}^{0}\mathbf{T}_{4}$ yields

$$ {}^{0}\mathbf{T}_{4} = {}^{0}\mathbf{M}_{0rb}\ {}^{0rb}\mathbf{M}_{calibration}\ {}^{calibration}\mathbf{M}_{camera}\ {}^{camera}\mathbf{M}_{4} \qquad (7\text{-}35) $$

All the transformations on the left-side of (7-35) are known. If we assume the joint displacements are accurately known then one can solve for the unknown kinematic parameters in ${}^{0}\mathbf{T}_{4}$ (3-10), namely, a_i, $i = 1,2,3$, and the eight angle parameters in ψ (3-12). Since (7-35) only provides 7 equations, two independent measurements will be required.

From the two measurements eight equations and eight unknowns derive from (3-11a,b,c,d). If the resulting 8×8 matrix is well conditioned, then it may be inverted to compute ψ, independently of the linear parameters a_i. In this approach (3-11e) could serve as a partial check of the solution.

For the ARID, the three linear parameters a_i can be solved by a set of equations based on the first two entries of the last column of ${}^{0}\mathbf{T}_{4}$. These equations, interestingly, do not depend upon the angle parameters in ψ to first order.

9. CONCLUSIONS

A kinematics error-model and an experimental procedure has been proposed for calibrating the ARID robot. A camera and sonar end-effector measures the pose of the ARID end-frame for different calibration poses. A minimum of two measurements determine the kinematics calibration-model of the ARID for a particular calibration-square, assuming the joint displacements are accurately measured, the calibration surface is planar, and the kinematic parameters do not vary rapidly in the region above a particular four inch calibration square. Preliminary experiments suggest this is the case.

Recommendations

The theoretical developments presented in this paper and the experimental results expressed in a companion paper [1], suggest that the ARID manipulator will admit of effective calibration. On this basis the author encourages the Robotics Section to vigorously pursue implementation of the calibration technique described herein.

REFERENCES

[1] Doty, K.L., 1992, "Arid Relative Calibration Experimental Data and Analysis", NASA Faculty Fellow Report, Kennedy Space Center.

[2] Horn, B.K.P., 1986, *Robot Vision*, MIT Press, Cambridge Mass.

1992 NASA/ASEE SUMMER FACULTY FELLOWSHIP PROGRAM

JOHN F. KENNEDY SPACE CENTER
UNIVERSITY OF CENTRAL FLORIDA

ARID RELATIVE CALIBRATION EXPERIMENTAL DATA AND ANALYSIS

PREPARED BY:	Dr. Keith L. Doty
ACADEMIC RANK:	Professor
UNIVERSITY AND DEPARTMENT:	University of Florida Department of Electrical Engineering
NASA/KSC	
DIVISION:	Mechanical Engineering Directorate
BRANCH:	Special Projects (RADL)
NASA COLLEAGUE:	Willis Crumpler Bill Jones Eduardo Lopez
DATE:	August 7, 1992
CONTRACT NUMBER:	University of Central Florida NASA-NGT-60002 Supplement: 8

ACKNOWLEDGEMENTS

The author gratefully acknowledges the support of the University of Central Florida faculty and staff along with the Boeing and NASA staffs whose diligence and kindness make the NASA Faculty Fellowship program at the Kennedy Space Center so efficient and productive. Particular thanks to Willis Crumpler, Bill Jones, Eduardo Lopez, Gabor Tamasi, Todd Graham and Carol Valdez of NASA; Ron Remus, Joe Looney, Jose Lago and Brian Yamauchi of Boeing and Loren Anderson and Kari Stiles of the University of Central Florida. A special thanks to my office mate, Carl Latino of Oklahoma State University, for stimulating discussions and all-around good fellowship.

ABSTRACT

Several experiments measure the orientation error of the ARID end-frame as well as linear displacements in the Orbiter's *y-* and *z-axes*. In each experiment the position of the ARID on the trolley is fixed and the manipulator extends and retracts along the Orbiter's *y-axis*. A sensor platform consisting of four sonars arranged in a "+" pattern measures the platform pitch about the Orbiter's *y-axis* (angle β) and yaw about the Orbiter's *x-axis* (angle α). Corroborating measurements of the yaw error were performed using a carpenter's level to keep the platform perpendicular to the gravity vector at each ARID pose being measured.

SUMMARY AND CONCLUSIONS

The preliminary experimental work performed here suggests that the ARID manipulator will admit efficient, reliable calibration. The pitch β of the tool-frame averages around 0.6 ± 0.02 degrees while the error in yaw α is as large as 4.65 ± 0.04 degrees when the ARID is stretched out to 4.45 ± 0.04 degrees when the ARID end-frame is close to the trolley. A commanded translation in four inch increments along the Orbiter's *y-axis* produced a consistent $3\ 15/16 \pm 1/32$ inch motion, with the exception of two points. The two anomalous points could be due to experimental error or to a bug in the ARID software. Less likely, in the author's judgement, the anomalies might be due to some ARID structural problem. The measurements also demonstrated that the ARID sags about one-half inch over its range of reach. The further the arm extends, the greater the sag.

TABLE OF CONTENTS

1. INTRODUCTION

Figure 1 depicts the experimental setup for relative calibration of the ARID manipulator. We measured the deviation in the sensor platform from level as the ARID extended and retracted at a fixed location on the trolley. The four sonars measured the height of the sensor platform from the table at four points. The angle $\alpha = \theta_1 + \theta_2 + \theta_3 + \theta_4$ equals the total angle change about the *x-Orbiter* axis induced by the revolute joints and the fixed angle θ_1. The deviation of the angle α from 90° can be computed from the sonar values h_1 (Top Sonar) and h_3 (Bottom Sonar). The angle β, which the ARID cannot actively compensate for, is the angle about the *y-Orbiter* axis and can be computed from the sonar values h_4 (Right Sonar) and h_2 (Left Sonar).

The idea behind these experiments is to determine whether calibration of the ARID robot will require elaborate procedures or not. For example, will calibration adjustments to α significantly depend upon how far the arm is extended?

After a brief discussion of the experiments, the actual data and experimental procedures are presented for each experiment. Several graphs of the data help to visualize the behavior and sources of kinematic error in the ARID.

2. DISCUSSION OF THE EXPERIMENTS

In *Experiments 1,2 and 3* we recorded the manipulator joint angles, the tool-center-point Orbiter-cartesian-coordinates, the angle α, and the four sonar readings. In *Experiments 2 and 3*, the arm is first extended and then retracted while keeping the sensor platform perpendicular to the gravity vector. The table, which was approximately leveled, appeared to be flat enough to make meaningful deductions from the sonar data. The experimental data seem to justify this claim.

If the table were perfectly flat, the sensor platform perfectly parallel and the sonar sensors perfectly accurate, the four sonars would have identical readings. Of course these perfect conditions cannot be met. All four sonars gave different readings. However, each sonar consistently measured the distance to the table, and so, maintained a fairly consistent relationship to the others, a desirable feature which will permit further calibration of the sonars. At a nominal 24 inches, the sonar readings consistently provided 3 digits accuracy with an uncertainty in the fourth digit not exceeding 0.060 inch.

In *Experiment 3* the sensor platform was commanded to be at $\alpha = 90°$, which, as seen in the earlier experiments, corresponds to about $\alpha = 94.6°$. This means the sensor platform was not parallel to the table during *Experiment 3*. The idea here

was to test the total angular error in α from the Top and Bottom Sonar readings only and compare with the error in α measured in *Experiments 1 and 2.*

Experiment 4 attempted to quantify linear moves of the ARID. As the arm extends in 4 inch increments along *y-Orbiter* at constant elevation and trolley position, a plum bob hanging from the center of the sensor platform translates. The position of the bob tip is recorded on computer paper placed on the table surface.

3. CONCLUSIONS

While time has not permitted a thorough analysis of the data collected, it is hoped the data given in this paper will be of further use and analysis. Without absolute calibration, one is not able to quantify the ARID correction factors at this time. However, general comments about the ARID can be made from these preliminary experiments:

1. Effective calibration of the ARID should not pose any insurmountable difficulties. All errors appear to be correctable to produce the position tolerances required of the tool-center-point.

2. Separate calibration of the ARID revolute joints and the trolley should work quite well. This will reduce the number of data points.

3. A further reduction in calibration appears feasible using a calibration-model. This has yet to be shown however.

In sum, the experimental results obtained here are quite encouraging. The ARID position and orientation errors do not appear to be as large or as unpredictable as once thought.

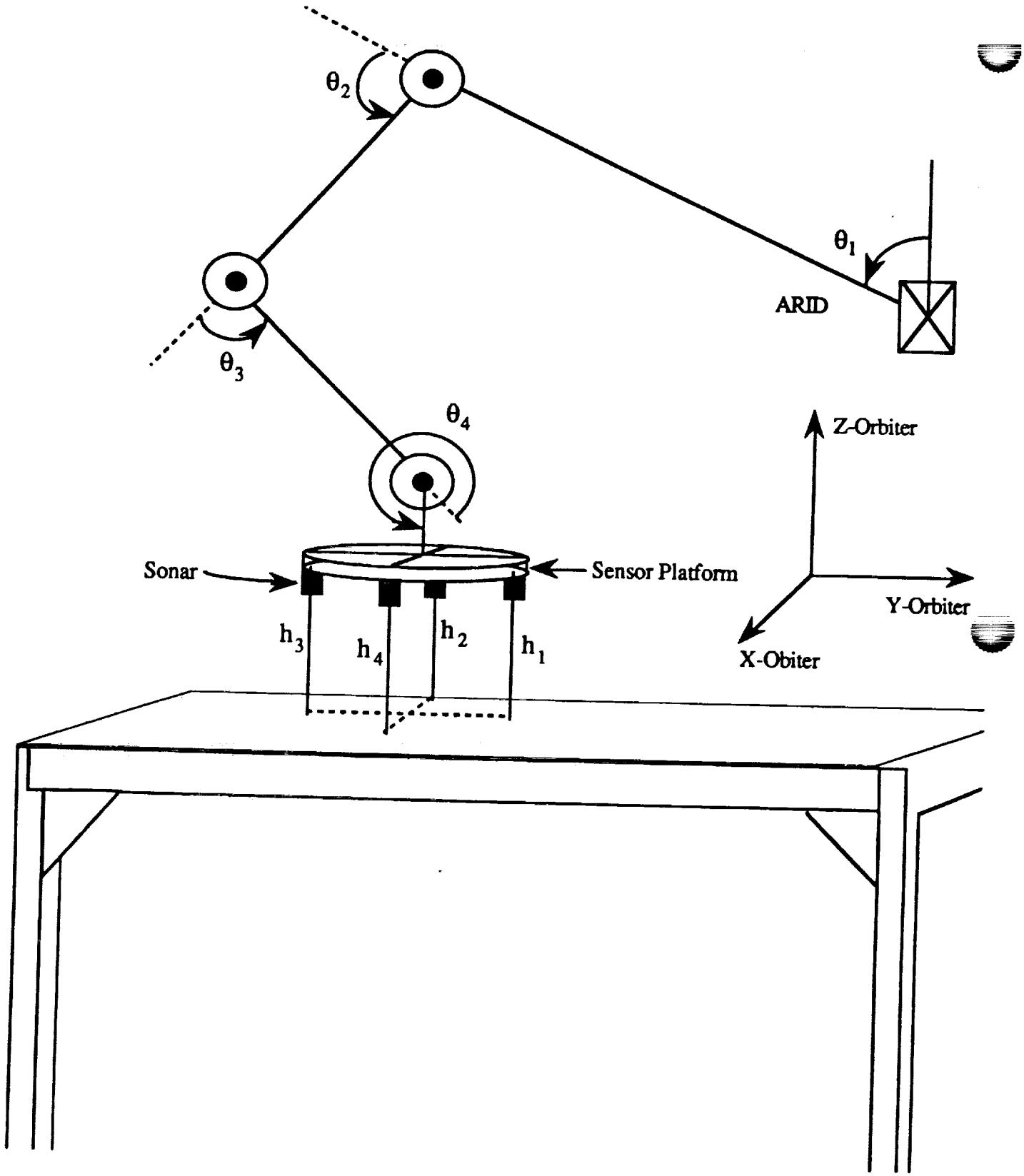

Figure 1 Experimental setup for the relative calibration experiments.

A1. EXPERIMENT 1: ANGLE ERRORS WHILE DECREASING Y

DATA FILE: EXP4.XCL

The sensor platform is kept parallel to X-Y plane of Orbiter. For each pose, the angle $\alpha = \theta_1 + \theta_2 + \theta_3 + \theta_4$ was adjusted to maintain the sensor platform orthogonal to the gravitational gradient. A carpenter's level resting on the platform indicated when the sensor platform was level. The repeatability of these measurements were within ± 0.04 degrees.The value of x-Orbiter and z-Orbiter were fixed at $x = 1018$ inches and $z = 366$ inches during the experiment.

Sonar measurements were taken in 4 inch increments for decreasing y-Orbiter, starting at $y = 220$ inches and ending at $y = 156$ inches (*Graph 1*, Graphs start on page 17.). A flat workbench beneath the sensor platform extended from $y = 204$ inches down to $y = 160$ inches. Thus, the sonars measured the distance from the sensor platform to the workbench and provided the necessary information for calculating the delta error in angle $\delta\alpha$ (Delta Alpha in the tables) and the total error in β (Beta in the tables). Since the greater part of the error in α is accounted for by keeping the sensor platform level, the Delta Alpha term corresponds to an additional angular error according to the sonar sensor readings. *Graph 4* plots $\delta\alpha$ and β.

EXPERIMENT 1: MANIPULATOR CONFIGURATION DATA

Joint 1 inches	Joint 2 degrees	Joint 3 degrees	Joint 4 degrees	X-Obiter inches	Y-Orbiter inches	Z-Orbiter inches
1022	66.0354	74.6549	-20.025	1018	156	366
1022	67.6619	78.7086	-25.6452	1018	160	366
1022	69.7574	82.1524	-31.1845	1018	164	366
1022	72.2576	84.9751	-36.4773	1018	168	366
1022	75.1458	87.2103	-41.5808	1018	172	366
1022	78.3716	88.8606	-46.417	1018	176	366
1022	81.9323	89.936	-51.053	1018	180	366
1022	85.7404	90.4319	-55.3171	1018	184	366
1022	89.7997	90.3483	-59.2827	1018	188	366
1022	94.0593	89.682	-62.8761	1018	192	366
1022	98.4625	88.4402	-66.0174	1018	196	366
1022	103.0012	86.6138	-68.7197	1018	200	366
1022	107.6145	84.2222	-70.8914	1018	204	366
1022	112.3593	81.2103	-72.6243	1018	208	366
1022	117.1814	77.5925	-73.8086	1018	212	366
1022	122.0921	73.3373	-74.4241	1018	216	366
1022	127.1358	68.3678	-74.4583	1018	220	366

EXPERIMENT 1: ALPHA ANGLE AND SONAR DATA

Alpha degrees	Top Sonar inches	Bottom Sonar inches	Left Sonar inches	Right Sonar inches
85.46	23.2902	58.637	23.1988	23.3611
85.52	23.4018	23.299	23.2974	23.4689
85.52	23.4577	23.3739	23.363	23.5387
85.55	23.5412	23.4499	23.4446	23.6143
85.57	23.6018	23.5133	23.4985	23.6682
85.61	23.6762	23.5882	23.5807	23.7458
85.61	23.7165	23.6265	23.62	23.7922
85.65	23.7693	23.6896	23.6701	23.8492
85.66	23.8224	23.7344	23.7138	23.8888
85.66	23.8579	23.7632	23.7446	23.9227
85.68	23.885	23.794	23.775	23.9529
85.69	23.91	23.83	23.8102	23.981
85.74	23.9087	23.831	23.8072	23.9759
85.74	*59.0233	23.8245	23.8035	23.9593
85.76	*59.007	23.8435	23.8163	23.9678
85.8	*58.9945	23.8551	24.5672	25.0558
85.84	*58.9569	23.8378	*58.9563	59.1856

* These sonar measurements cannot be used since the associated sonar sensor is no longer above the table surface.

A2. EXPERIMENT 2: ANGLE ERRORS WHILE INCREASING Y
DATA FILE: EXP4.XCL

Experiment 2 possesses the same setup as *Experiment 1*. The only difference between the experiments is the direction of motion of the manipulator. The manipulator is moved from $y = 156$ inches to $y = 220$ inches in 4 inch increments during this experiment. *Graph 2* indicates the sonar readings for this experiment and *Graph 3* the difference in the respective sonar readings of *Experiments 1 and 2*. Ideally, the readings should be the same. The plots indicate the errors tend to be about ±0.010 inches about an average.

EXPERIMENT 2: MANIPULATOR CONFIGURATION DATA

Joint 1 inches	Joint 2 degrees	Joint 3 degrees	Joint 4 degrees	X-Obiter inches	Y-Orbiter inches	Z-Orbiter inches
1022	66.0354	74.6549	-20.025	1018	156	366
1022	67.683	78.7373	-25.7551	1018	160	366
1022	69.7824	82.1754	-31.2924	1018	164	366
1022	72.2909	84.9954	-36.601	1018	168	366
1022	75.1775	87.2224	-41.6846	1018	172	366
1022	78.4293	88.8717	-46.5857	1018	176	366
1022	81.9818	89.9376	-51.1841	1018	180	366
1022	85.7928	90.4264	-55.4439	1018	184	366
1022	89.8476	90.3372	-59.3895	1018	188	366
1022	94.0948	89.6695	-62.949	1018	192	366
1022	98.5061	88.4198	-66.1006	1018	196	366
1022	103.0303	86.5969	-68.7718	1018	200	366
1022	107.6522	84.1963	-70.9532	1018	204	366
1022	112.367	81.2041	-72.6358	1018	208	366
1022	117.1736	77.5997	-73.798	1018	212	366
1022	122.0921	73.3373	-74.4241	1018	216	366
1022	127.1358	68.3678	-74.4583	1018	220	366

EXPERIMENT 2: ALPHA AND SONAR DATA

Alpha degrees	Top Sonar inches	Bottom Sonar inches	Left Sonar inches	Right Sonar inches
85.46	23.2902	58.637	23.1988	23.3611
85.46	23.3839	23.301	23.2906	23.4533
85.46	23.4408	23.3644	23.3485	23.5184
85.48	23.5196	23.4451	23.4284	23.6014
85.51	23.5903	23.5204	23.5015	23.6672
85.51	23.6522	23.5784	23.5614	23.7275
85.53	23.6925	23.617	23.6058	23.7736
85.57	23.753	23.6842	23.661	23.8326
85.59	23.7997	23.7262	23.6995	23.8726
85.61	23.8383	23.7638	23.7388	23.9136
85.62	23.867	23.7896	23.7679	23.9417
85.65	23.8955	23.8218	23.8001	23.9698
85.69	23.9103	23.8486	23.8157	23.9837
85.73	*59.0375	23.8503	23.8184	23.9817
85.77	*58.9915	23.832	23.8038	23.9637
85.8	*58.9952	23.8618	24.5747	24.9497
85.84	*58.9569	23.8378	*58.9563	59.1856

* These sonar measurements cannot be used since the associated sonar sensor is no longer above the table surface.

A3. EXPERIMENTS 1 & 2: ALPHA AND BETA ANGLE ERRORS

The errors $\delta\alpha$ and β are computed from

Delta Alpha = atan[Bottom_Sonar - Top_Sonar)/16],

Beta = atan[Left_Sonar - Right_Sonar)/16],

respectively. *Graph 4* plots the $\delta\alpha$ and β angle errors together and *Graph 5* plots the total angle error $\varepsilon_\alpha := 90° - \alpha$ for *Experiment 1 and 2* combined.

EXPERIMENT 1

Alpha Error =90 -Alpha degrees	Delta Alpha degrees	Beta degrees
4.54	*65.645750	-0.5811741
4.48	-0.3681203	-0.6141156
4.48	-0.3000839	-0.629154
4.45	-0.3269405	-0.6076706
4.43	-0.316914	-0.6076706
4.39	-0.3151236	-0.5911998
4.39	-0.3222854	-0.616622
4.35	-0.2854022	-0.6413278
4.34	-0.3151236	-0.6266476
4.34	-0.3391154	-0.6377473
4.32	-0.3258662	-0.6370312
4.31	-0.2864765	-0.6116092
4.26	-0.2782404	-0.60409
4.26	*-65.55531	-0.5579
4.24	*-65.53364	-0.5425032
4.2	*-65.51883	-1.7491263
4.16	*-65.50634	*-0.821064

EXPERIMENT 2

Alpha Error =90 -Alpha degrees	Delta Alpha degrees	Beta degrees
4.54	*65.645750	-0.5811741
4.54	-0.2968611	-0.5826064
4.54	-0.2735853	-0.6083867
4.52	-0.2667815	-0.6194865
4.49	-0.2503093	-0.59334[illegible]
4.49	-0.2642749	-0.5947804
4.47	-0.2703625	-0.6008675
4.43	-0.2463703	-0.6144737
4.41	-0.2632006	-0.6198445
4.39	-0.2667815	-0.6259315
4.38	-0.2771662	-0.6223509
4.35	-0.2639168	-0.6076706
4.31	-0.2209458	-0.6015836
4.27	*-65.54819	-0.5847547
4.23	*-65.53119	-0.5725806
4.2	*-65.51514	-1.342624
4.16	*-65.50634	*-0.821064

* These computations cannot be used since the associated sonar sensor is no longer above the table surface.

Some statistics computed for these angles, in degrees, are given below. Subscript 1 refers to *Experiment 1* and subscript 2 to *Experiment 2*.

Angle $\delta\alpha$: $\delta\alpha_{1av} = -0.3149743$, $\delta\alpha_{2av} = -0.2633797$

Angle α: $\alpha_{1av} = 4.34941176$, $\alpha_{2av} = 4.39529412$

Standard Deviation angle α: $\sigma_1 = 0.10579878$, $\sigma_2 = 0.1248558$

Angle β: $\beta_{1av} = -0.6187405$, $\beta_{2av} = -0.6076109$

A4. ARID SAG

As the ARID arm extends the sensor platform came closer to the flat table surface, even though the z- coordinate was supposedly fixed at *366* inches. This effect, called *sag* , appears to follow a quadratic curve, although this has not been verified. The total sag from $y = 204$ inches to $y = 160$ inches as measured by the different sonars at $x = 1018$ inches is tabulated below. Over the 44 inch span involved in the experiments, the tool-center-point drops a little over one-half an inch.

SAG COMPUTATIONS

	Top Sonar	Bottom Sonar	Left Sonar	Right Sonar
Sag Exp1	0.5069	0.532	0.5098	0.507
Sag Exp2	0.5264	0.5476	0.5251	0.5304

A5. EXPERIMENT 3: SONAR MEASUREMENT OF ALPHA ERROR

DATA FILE: EXP5.XCL

The total angle $\alpha = \theta_2 + \theta_3 + \theta_4$ was set equal to 90° through the ARID user interface. The actual angle α is less than the set-point established by the ARID control program, as *Experiments 1 and 2* demonstrated. Consequently, the sensor platform was not parallel to X-Y plane of the Orbiter during *Experiment 3*. The value of x-Orbiter and z-Orbiter were fixed at x= *1018* inches and z = *366* inches during the experiment.

Sonar measurements were taken in 4 inch increments for decreasing y-Orbiter, starting at y = *220* inches and ending at y = *156* inches. A flat workbench beneath the sensor platform extended from y = *204* inches down to y = *160* inches. Thus, the sonars measured the distance from the sensor platform to the workbench and provided the necessary information for calculating the errors in angle α (Alpha in the tables) and β (Beta in the tables).

EXPERIMENT 3: MANIPULATOR CONFIGURATION DATA

Joint 1 degrees	Joint 2 degrees	Joint 3 degrees	Joint 4 degrees	X Orbiter inches	Y Orbiter inches	Z Orbiter inches	Alpha degrees
1022	66.328	76.1573	-17.2802	1018	160	366	89.9999
1022	68.1183	80.0433	-22.9564	1018	164	366	89.9999
1022	70.3506	83.2977	-28.4431	1018	168	366	89.9999
1022	72.9923	85.9472	-33.7343	1018	172	366	89.9999
1022	76.01	88.0057	-38.8105	1018	176	366	89.9999
1022	79.3677	89.4797	-43.6421	1018	180	366	89.9999
1022	83.0268	90.3711	-48.1927	1018	184	366	89.9999
1022	86.9466	90.6805	-52.4219	1018	188	366	89.9999
1022	91.0865	90.4079	-56.2892	1018	192	366	89.9999
1022	95.4076	89.5532	-59.7556	1018	196	366	89.9999
1022	99.8757	88.1161	-62.7866	1018	200	366	89.9999
1022	104.463	86.0946	-65.3524	1018	204	366	89.9999
1022	109.1504	83.4827	-67.4279	1018	208	366	89.9999
1022	113.9287	80.2671	-68.9906	1018	212	366	89.9999
1022	118.8012	76.4221	-70.0181	1018	216	366	89.9999
1022	123.7853	71.9024	-70.4825	1018	220	366	89.9999

EXPERIMENT 3: SONAR DATA

Top Sonar inches	Bottom Sonar inches	Left Sonar inches	Right Sonar inches
24.1232	22.9023	23.4291	23.5767
24.203	22.901	23.4934	23.6577
24.2652	22.9769	23.5756	23.7319
24.315	23.0169	23.6264	23.7827
24.383	23.0881	23.6857	23.8387
24.4236	23.1417	23.7392	23.8973
24.4676	23.1936	23.7845	23.9431
24.5159	23.2444	23.8299	23.9864
24.5505	23.2892	23.861	24.0244
24.5691	23.3105	23.8854	24.0512
24.5917	23.3282	23.9125	24.0681
24.608	23.3638	23.9308	24.0841
25.378	23.379	23.9369	24.0922
59.752	23.378	23.9426	24.0918
59.7324	23.3916	24.3526	24.5982
59.7094	23.3885	59.1076	59.3513

A6. EXPERIMENT 3: ALPHA AND BETA ANGLE ERRORS

The angle error in α and β were compute from

Alpha Error= atan[Bottom_Sonar - Top_Sonar)/16]

Beta Error= atan[Left_Sonar - Right_Sonar)/16] .

The results of these computations are tabulated below and appear in *Graphs 6 and 7*, respectively. According to this experiment the error in α decreases with increasing *y-Orbiter* just as in *Experiments 1 and 2* (*Graph 5*). The numerical values correspond within 3% to 6% of each other. *Graph 8* compares the value of β measured in *Experiments 1,2 and 3*. The values of β differ by no more than 0.1 degree. While 0.1 degree corresponds to about an 17% error, the absolute magnitude of the error will not cause the too-center-point to deviate more than *displacement* $\approx 24" \times 0.1\ \pi\ /180° < 0.020$ inch. Thus, using the average value of β for all manipulator configurations will probably be sufficient.

EXPERIMENT 3: ANGLE ERROR FROM SONAR READINGS

Alpha Error	Beta Error
-4.36357	-0.5285386
-4.6521934	-0.5883354
-4.6034532	-0.5596903
-4.6383191	-0.5596903
-4.6269347	-0.5478742
-4.5806818	-0.5661355
-4.5525713	-0.5679258
-4.5436752	-0.5604065
-4.5073765	-0.5851128
-4.4977674	-0.5937063
-4.5152059	-0.5571839
-4.4465148	-0.5489484
*-7.1214904	-0.5561097
*-66.256524	-0.5342677
*-66.237234	*-0.879421
*-66.225658	*-0.872619

* These computations cannot be used since the associated sonar sensor is no longer above the table surface.

A7. EXPERIMENT 4: LINEAR DISPLACEMENT ALONG Y
DATA FILE: EXP4.XCL

The user commands the ARID robot to go to poses $P = (x_0, y, z_0, \alpha)$. The value of y was commanded to range from 180 inches to 220 inches in 4 inch increments while $x_0 = 1018$ inches and $z_0 = 366$ inches. For each pose, the angle $\alpha = \theta_2 + \theta_3 + \theta_4$ was adjusted so that the sensor platform remained perpendicular to the gravity vector. A plum bob hanging from the sensor platform was used to mark off the linear moves on a piece of computer paper placed on a flat table underneath the sensor platform. The accuracy of the technique was estimated to be $\pm \frac{1}{32}$ inch. *Graph 9* depicts the data tabulated below.

EXPERIMENT 4: DATA

Y-Orbiter inches	Y Increment inches
180	3.9375
184	3.9375
188	3.9375
192	3.9375
196	3.875
200	3.9375
204	3.9375
208	3.96875
212	3.9375
216	3.984375
220	-------
Total Increment Y-Orbiter	39.390625
Tape Measure	39.4375
Commanded	40

A8. GRAPHS OF ARID EXPERIMENTS

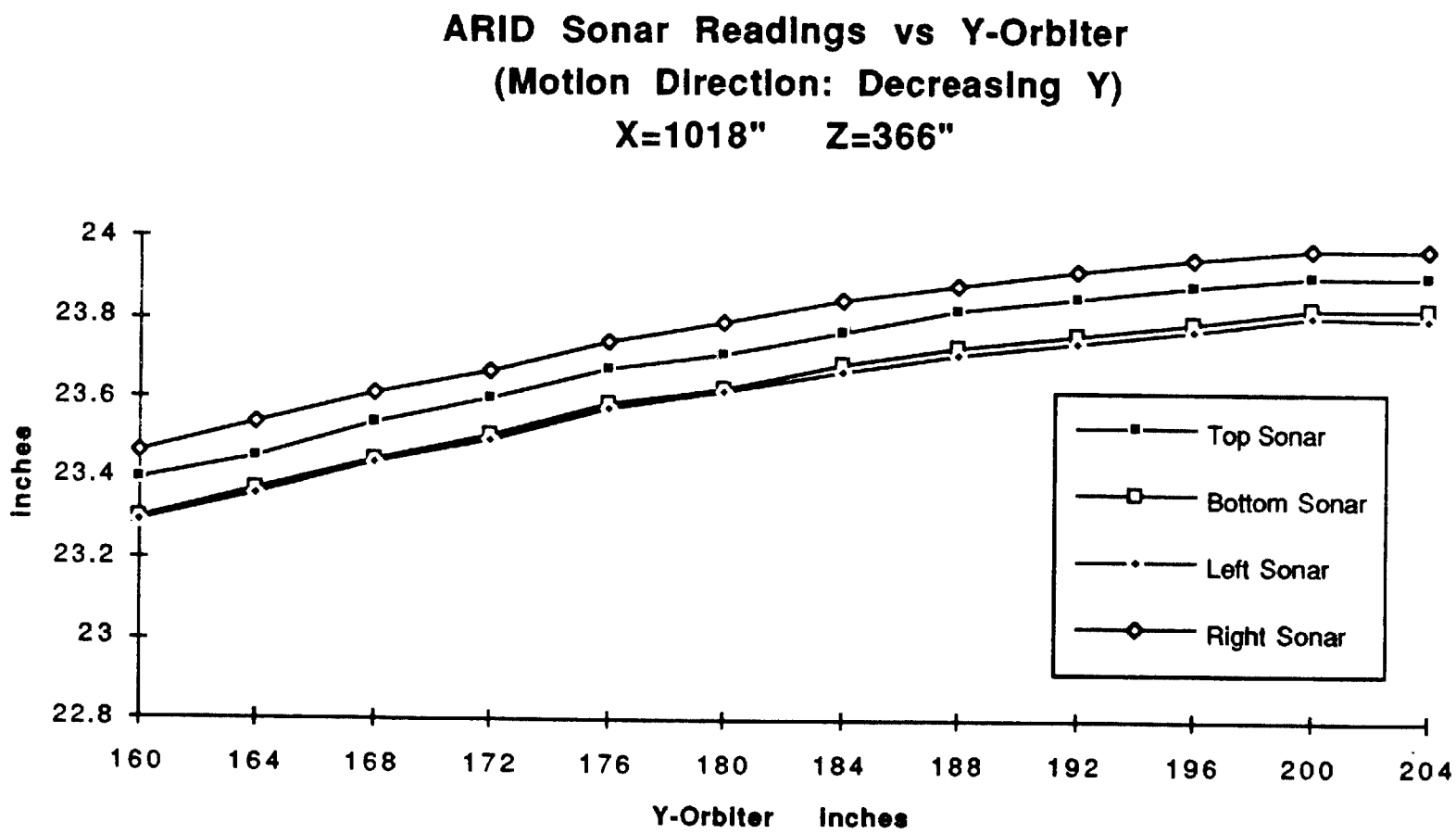

Graph 1 Sonar Readings, Experiment 1.

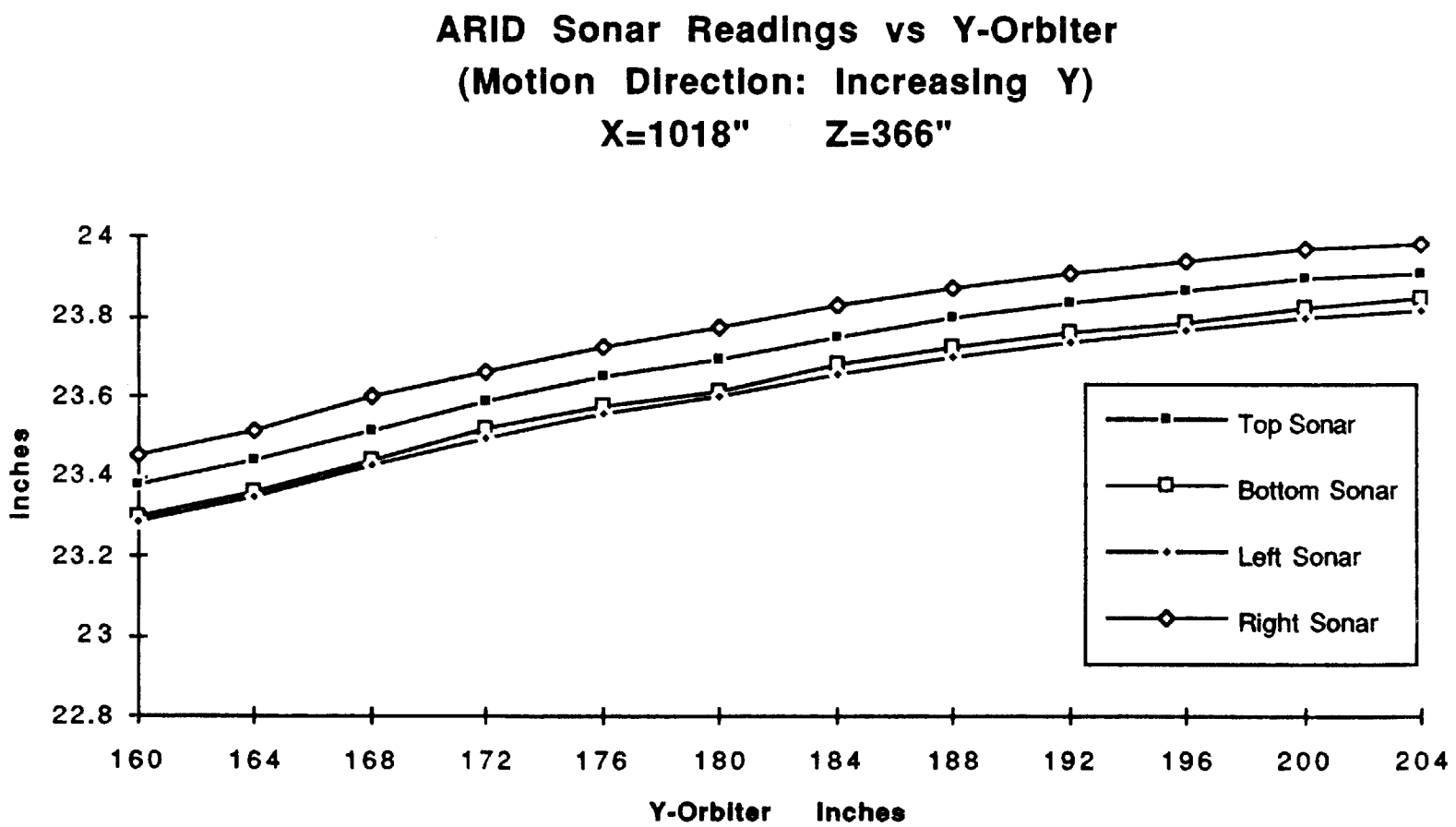

Graph 2 Sonar Readings, Experiment 2.

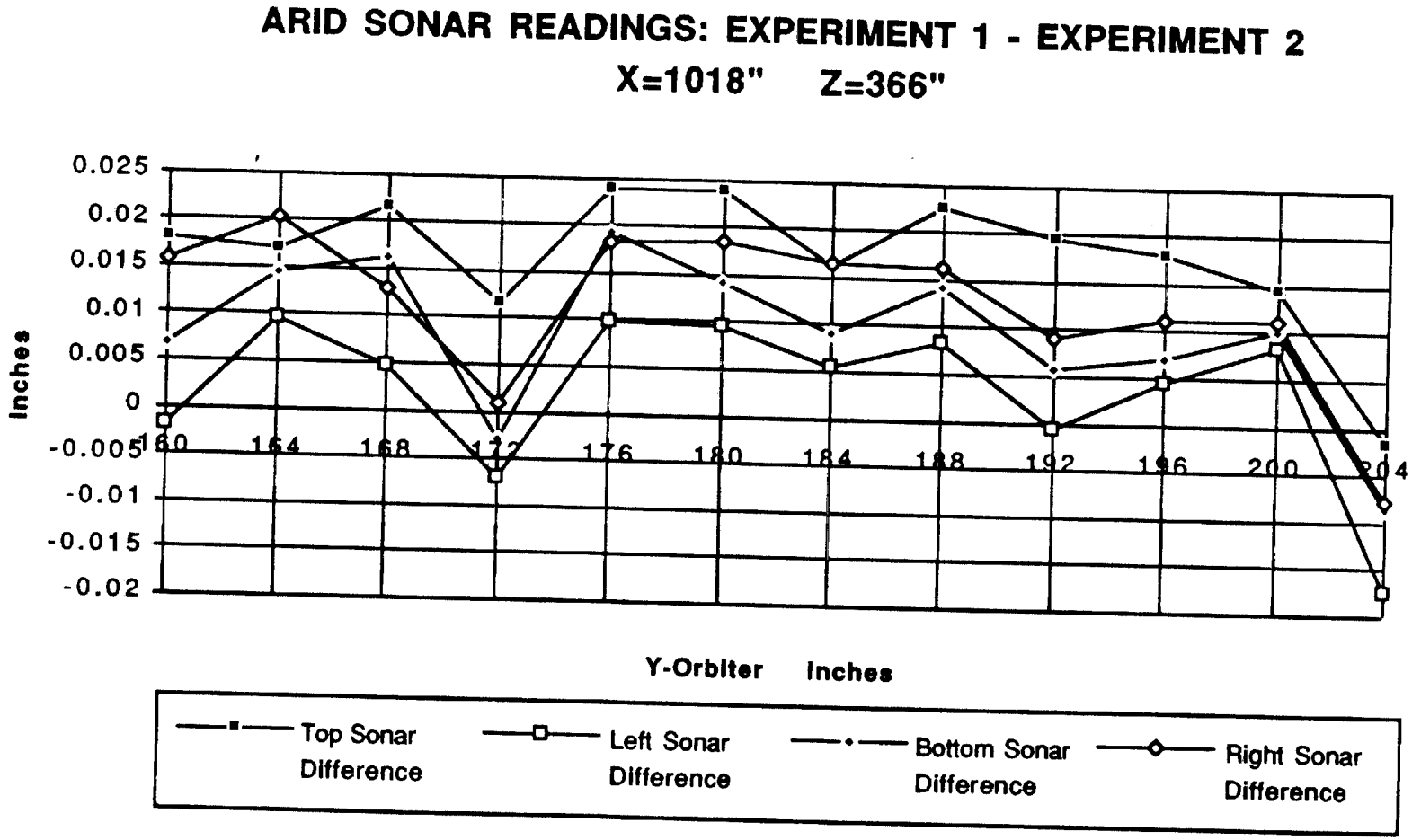

Graph 3 Difference in Sonar Readings, Experiments 1 and 2.

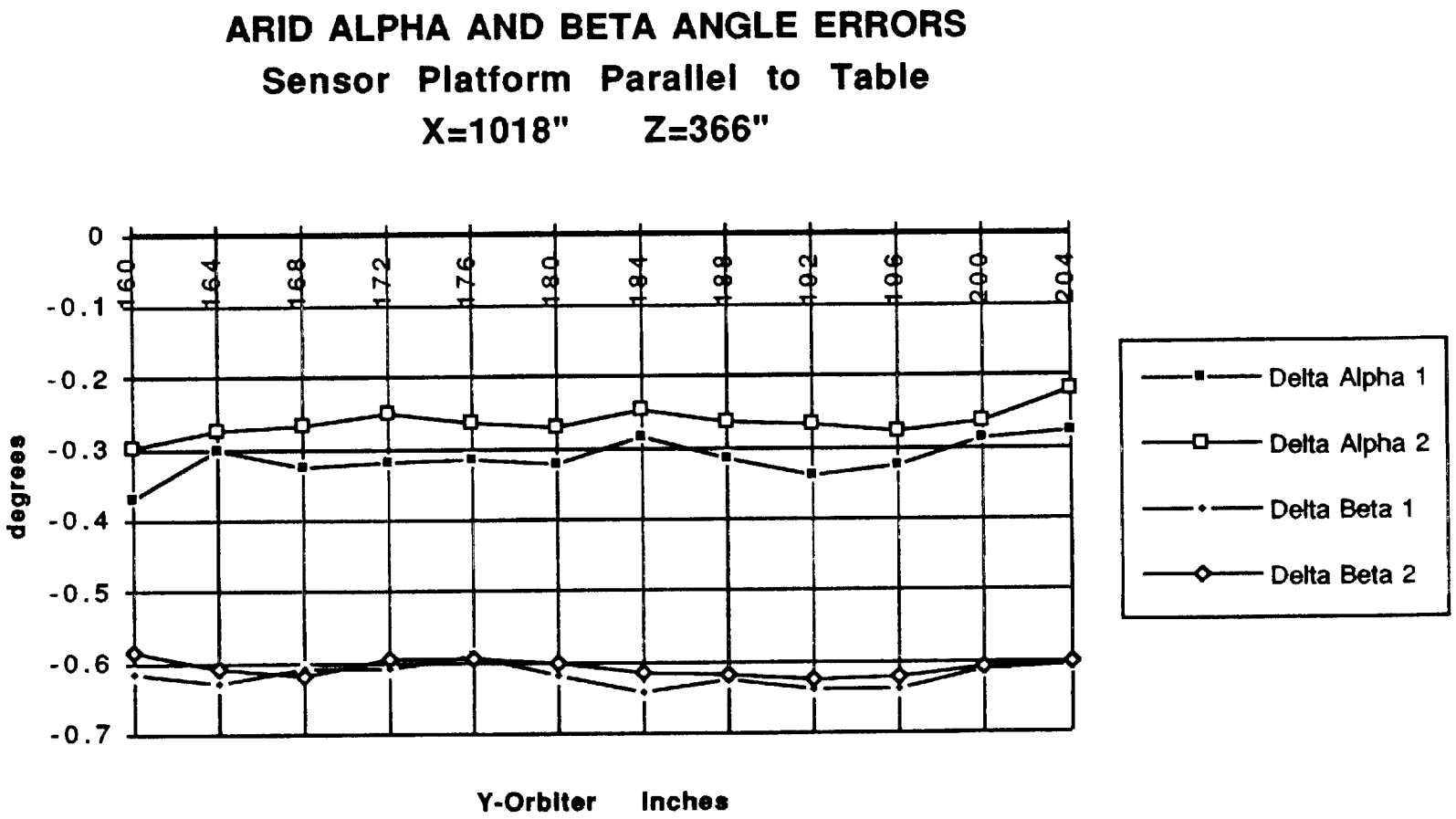

Graph 4 Delta error in α and total error in β based upon sonar readings, Experiments 1 and 2.

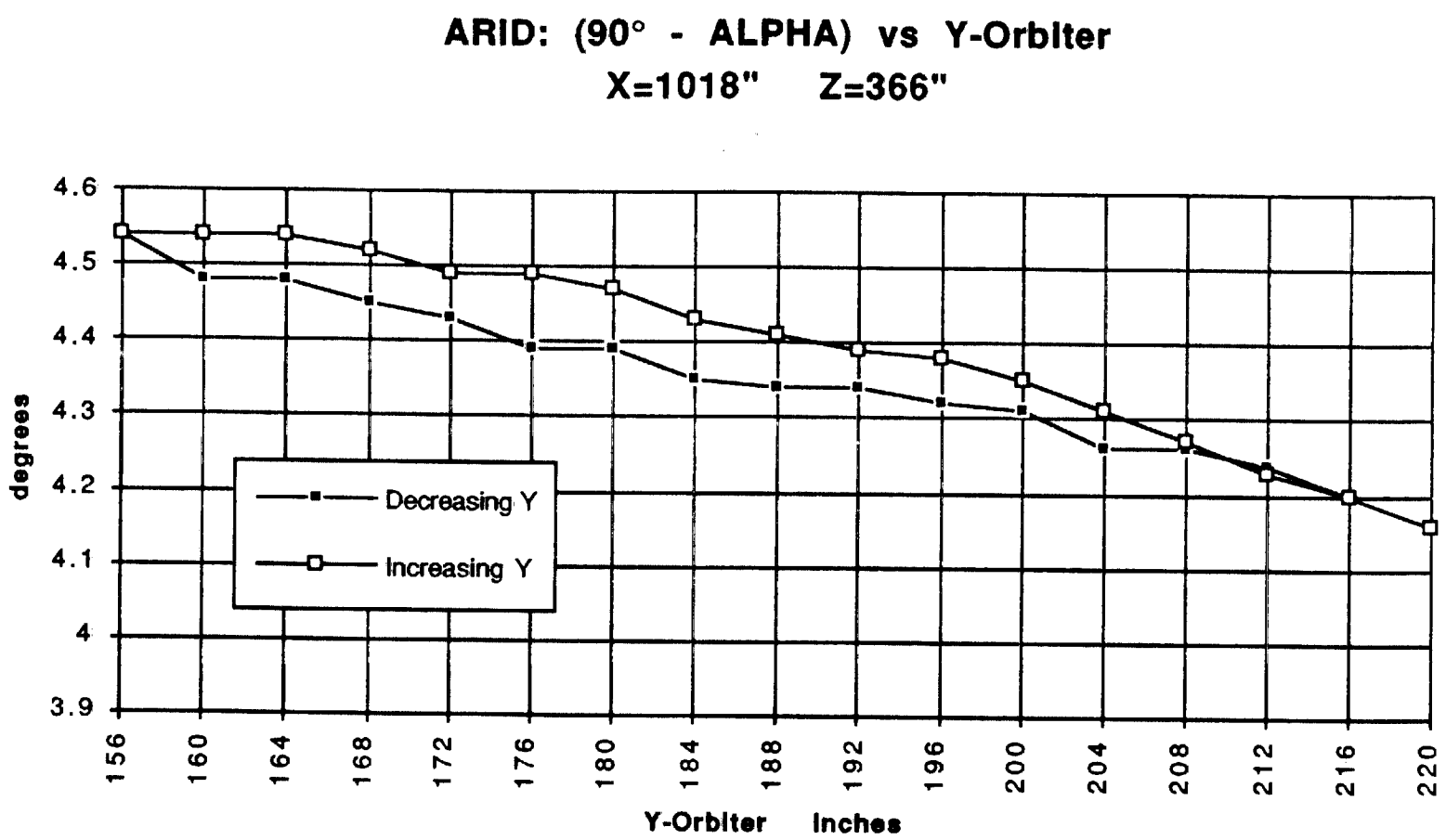

Graph 5 Total error in α, Experiments 1 and 2.

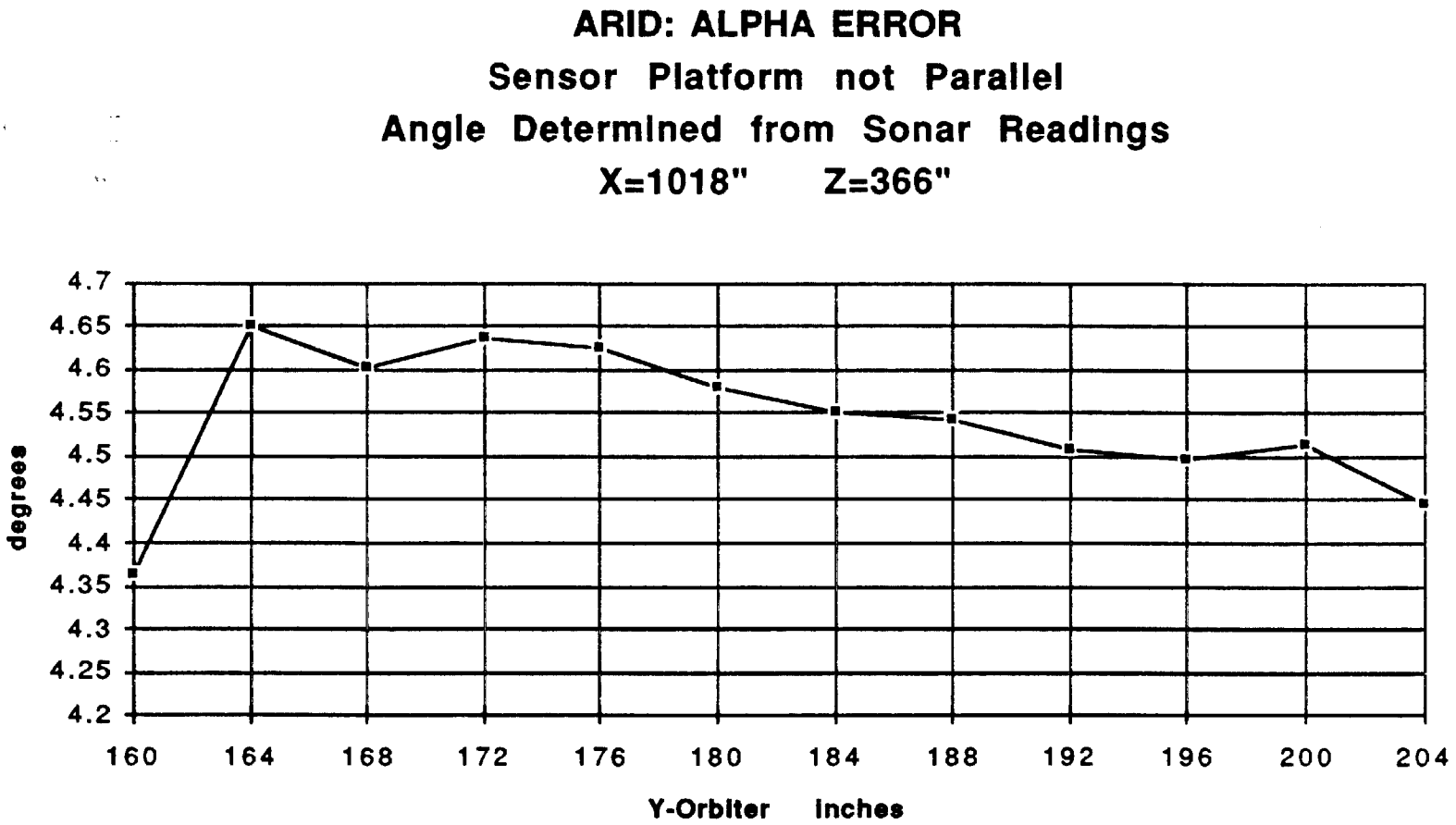

Graph 6 Total error in α based upon sonar readings, Experiment 3.

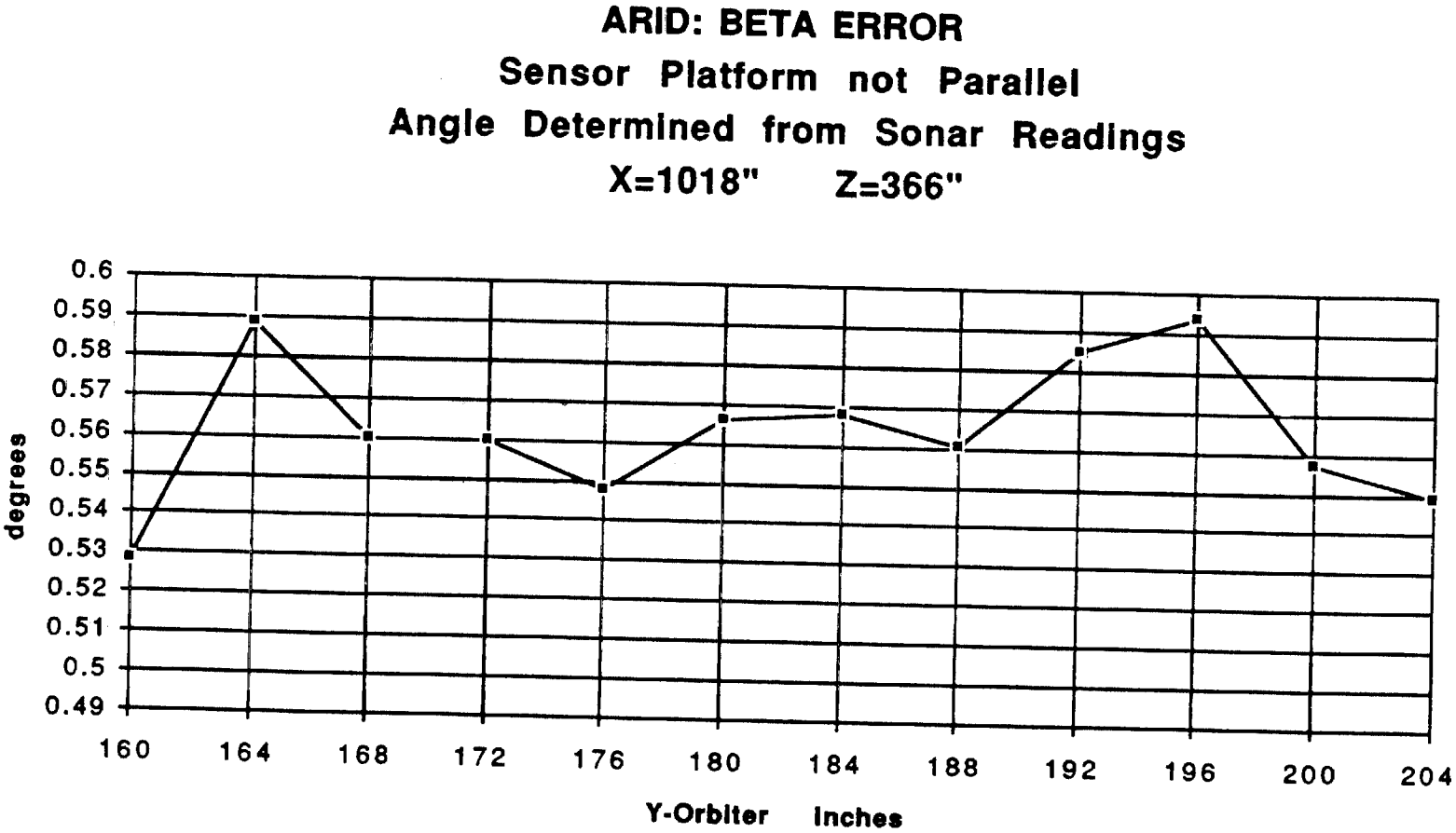

Graph 7 Total error in β based on sonar readings, Experiment 3.

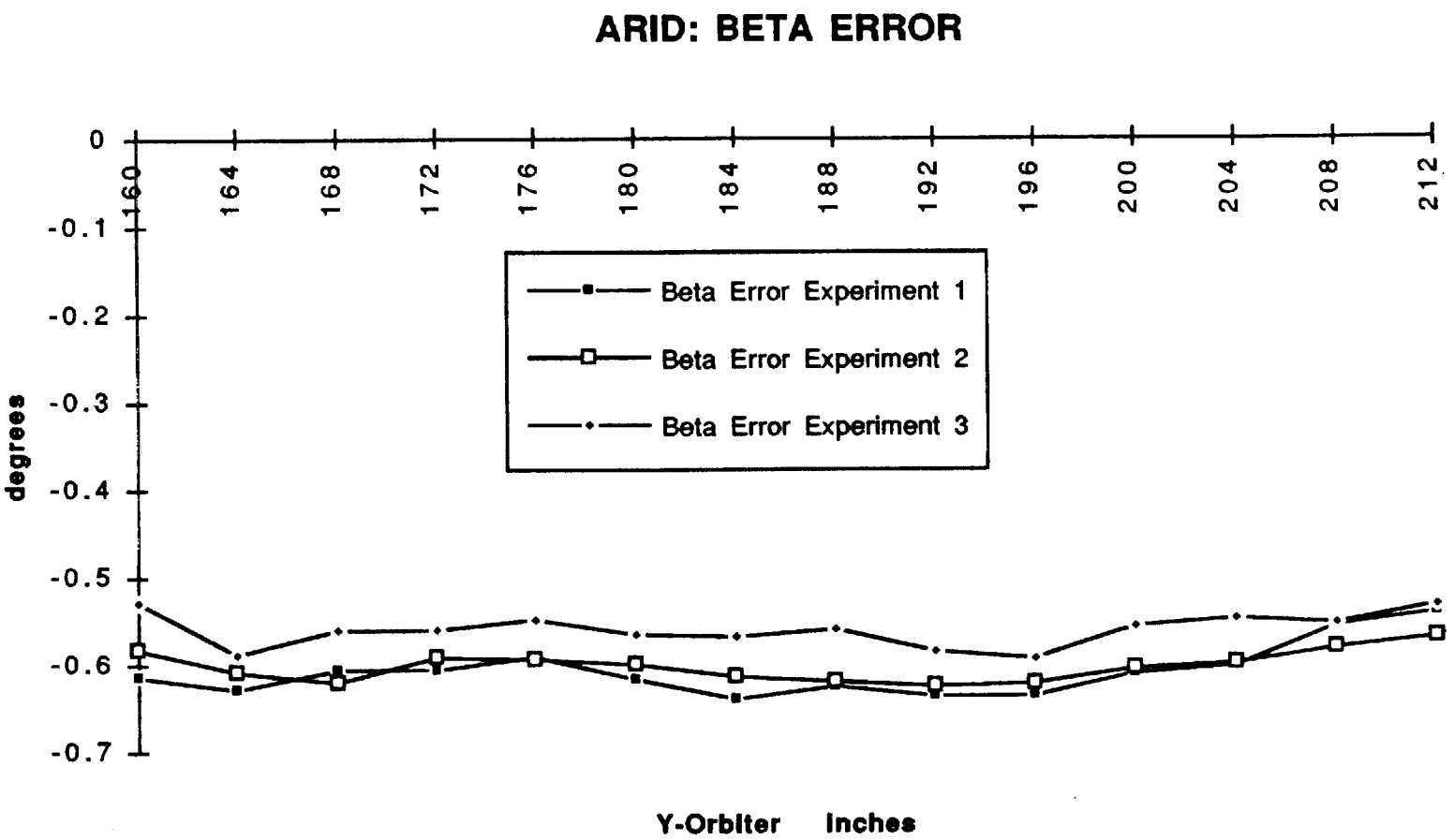

Graph 8 Total error in β, Experiments 1, 2 and 3.

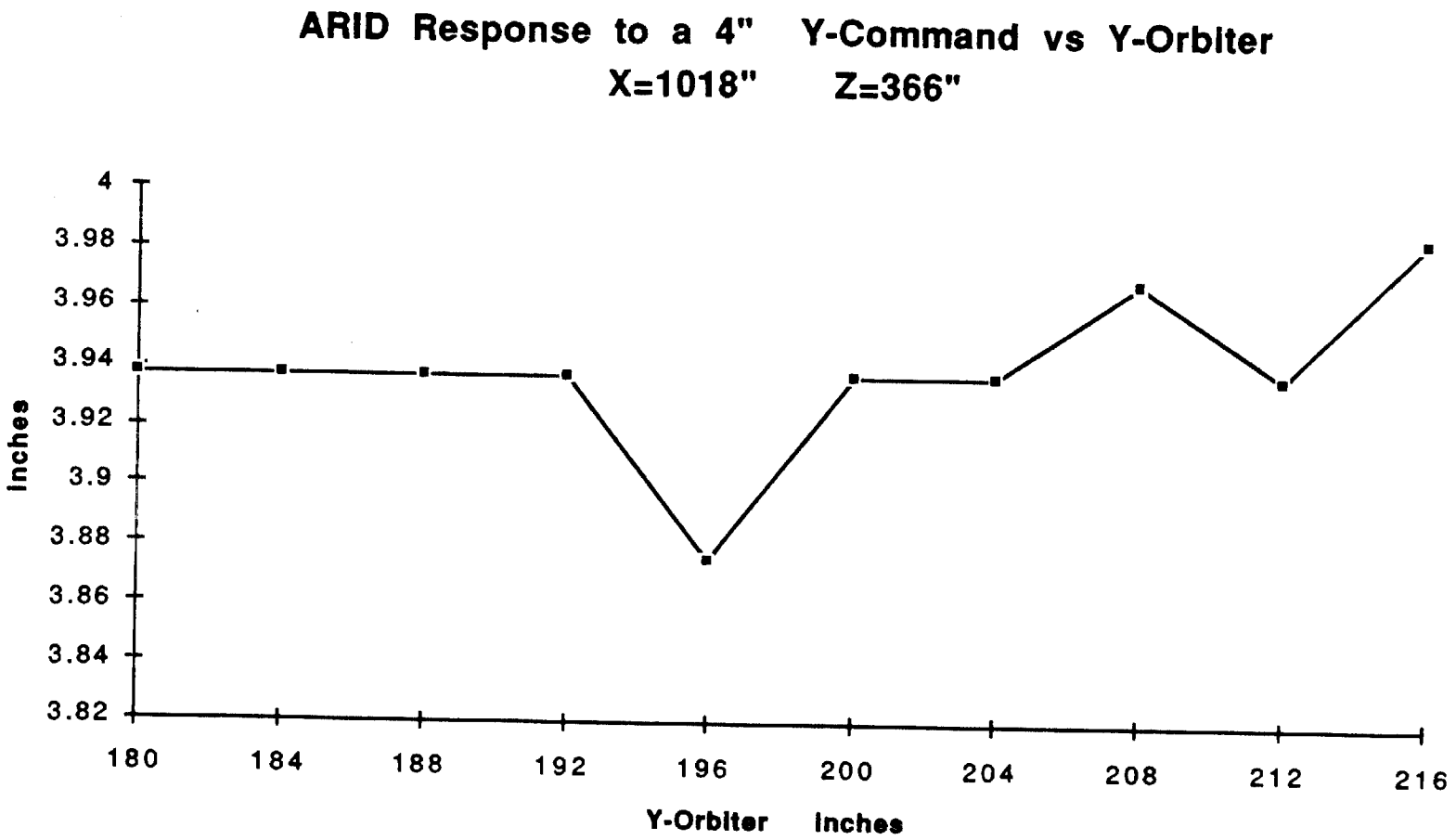

Graph 9 ARID response to successive 4 inch moves along *y-Orbiter*, Experiment 4.

1992 NASA/ASEE SUMMER FACULTY FELLOWSHIP PROGRAM

JOHN F. KENNEDY SPACE CENTER
UNIVERSITY OF CENTRAL FLORIDA

WATER QUALITY MODELING USING GEOGRAPHIC INFORMATION SYSTEM (GIS) DATA

PREPARED BY:	Dr. Bernard A. Engel
ACADEMIC RANK:	Associate Professor
UNIVERSITY AND DEPARTMENT:	Purdue University Agricultural Engineering Department
NASA/KSC	
DIVISION:	Biomedical Operations and Research
BRANCH:	Biological Research and Life Support
NASA COLLEAGUE:	John Sager
DATE:	August 10, 1992
CONTRACT NUMBER:	University of Central Florida NASA-NGT-60002 Supplement: 8

Abstract

Protection of the environment and natural resources at the Kennedy Space Center (KSC) is of great concern. The potential for surface and ground water quality problems resulting from non-point sources of pollution was examined using models. Since spatial variation of parameters required was important, geographic information systems (GIS) and their data were used. The potential for groundwater contamination was examined using the SEEPAGE (System for Early Evaluation of the Pollution Potential of Agricultural Groundwater Environments) model. A watershed near the VAB was selected to examine potential for surface water pollution and erosion using the AGNPS (AGricultural Non-Point Source Pollution) model.

Summary

Protection of the environment and natural resources at the Kennedy Space Center (KSC) is of great concern. The potential for surface and ground water quality problems resulting from non-point sources of pollution was examined using models. Since spatial variation of parameters required was important, geographic information systems (GIS) and their data were used. Soil property data were unavailable, so GIS layers of soil properties were derived from the Soils 5 database. The potential for groundwater contamination was examined using the SEEPAGE (System for Early Evaluation of the Pollution Potential of Agricultural Groundwater Environments) model. The SEEPAGE model indicated that from a hydrologic factors standpoint nearly all of KSC has a high potential for groundwater contamination. A watershed near the VAB was selected to examine potential for surface water pollution and erosion. The watershed was simulated for a series of rainfall events using the AGNPS (AGricultural Non-Point Source Pollution) model. Based on the simulation results, the watershed did not have significant erosion problems and only small amounts of nutrients and sediment were transported from the watershed into surface waters.

TABLE OF CONTENTS

LIST OF ILLUSTRATIONS

LIST OF TABLES

INTRODUCTION

The Kennedy Space Center (KSC) is not only important because of the NASA activities but is also home to 22 wildlife species listed as Endangered or Threatened on either the Federal or State lists. When NASA purchased land for the development of KSC in the early 1960's, not all of the land was needed for the space program. As a result, the U.S. Fish and Wildlife Service in cooperation with NASA established the Merritt Island National Wildlife Refuge in 1963. Thus, the effects of NASA activities on the environment and natural resources are of great concern.

A variety of monitoring and research activities are conducted by scientists at KSC to protect the KSC environment and natural resources and to better understand the relationships between these systems and NASA operations. These activities include: water quantity and quality monitoring and modeling (Dwornik, 1984; Heaney et al., 1984; Bennett, 1989; Dierberg and Jones, 1989), soil resources inventory development (Schmalzer and Hinkle, 1990a and 1991), climate monitoring (Madsen et al., 1989; Dreschel et al., 1990; Mailander, 1990), wildlife monitoring (Breininger and Schmalzer, 1990; Dreschel et al., 1991), and vegetation monitoring (Breininger, 1990; Schmalzer and Hinkle, 1990b; Provancha and Hall, 1991).

Computer based tools play an important role in the monitoring and research activities listed above (Hinkle et al., 1988). An extensive GIS database has been developed for KSC by the KSC GIS (Geographic Information Systems) and Remote Sensing Laboratory. The data in the GIS has many potential uses for studies such as those described above. For example, Breininger et al. (1991) interpreted remotely sensed data using the computer to obtain vegetation maps for use in the GIS. The vegetation map layer and other map layer data within the GIS were used to map scrub jay habitat.

The objective of this project was to begin development of a prototype computer-based spatial decision support system to address environmental and natural resources issues for the Kennedy Space Center. Water resources concerns were selected as the first component to be examined. The decision support system was expected to utilize GIS, simulations, and expert system techniques.

PROCEDURES

2.1 Identification of Environmental and Natural Resource Concerns

The first step in the project was to identify environmental and natural resource concerns for the Kennedy Space Center that have an important spatial component. Previous and current projects were reviewed to gain an understanding of KSC concerns in these areas. Publications describing environmental and natural resource work conducted at KSC were reviewed. Some of the publications reviewed were referenced in the INTRODUCTION section of this document. Scientists working for Bionetics that are responsible for environmental and natural resource monitoring and research at KSC were asked to describe their current projects and possibilities for future projects.

Based on these discussions and the literature review, the following concerns having a significant spatial component were identified:

1. Surface and ground water quality and quantity
   Water quality and quantity are concerns for several reasons. Large volumes of water are used for KSC operations. In the future it may be necessary to obtain some of the water required from on-site sources, likely groundwater. The groundwater is also closely linked to surface water since the water table is very shallow. Thus, degradation of groundwater quality will affect surface water quality. Water is also important to much of the wildlife and vegetation at KSC. Numerous wetlands and water impoundments are located on KSC that provide homes for a variety of vegetation and wildlife.

2. Wildlife protection
   Because of the number of Threatened or Endangered species and the wide variety of species that make their homes at KSC for all or part of the year, protection of wildlife is of great concern. A better understanding of the wildlife and the systems in which they live is needed so that NASA activities can be designed to minimize effects on wildlife.

3. Vegetation protection
   Vegetation is important to the wildlife that reside at KSC. In addition, numerous Threatened or Endangered vegetation types are located at KSC.

4. Climatic conditions
   A variety of climatic conditions are of interest. Climatic parameters are important for many reasons including the understanding of vegetation and wildlife systems, understanding the effects of NASA activities as opposed to climate changes, and planning NASA activities.

2.2 Water Resources Problem

Water resources problems were selected for further investigation in this project. The problems to be explored were the potential for groundwater contamination at KSC and potential for runoff, soil erosion, and contamination of surface water. These problems have spatial components that can best be solved using GIS data and techniques. Groundwater contamination potential for all of KSC was to be explored. A watershed near the VAB (the area surrounding the VAB and to its north and east) was selected to examine runoff, erosion and chemical movement with runoff and sediments. This watershed was selected since mitigation of the wetland into which it drains is being considered.

The models selected for use in this project were SEEPAGE (System for Early Evaluation of the Pollution Potential of Agricultural Groundwater Environments) (Carpenter, 1992) and AGNPS (AGricultural Non-Point Source Pollution) (Young et al., 1989). SEEPAGE is used to evaluate the potential for groundwater contamination from both point and non-point sources considering hydrologic factors. AGNPS is used to analyze runoff, erosion and non-point source pollution of surface waters in watersheds. These models were selected since both use a distributed parameter approach, thus providing the capability to consider spatial variation of the processes modeled. Additional model details are provided in the sections that follow.

2.3 SEEPAGE Model

SEEPAGE (Carpenter, 1992) is used to evaluate the potential for groundwater contamination from both point and non-point sources from a hydrologic factor standpoint. SEEPAGE considers hydrologic factors to locate areas with low, moderate, high, and very high potential for groundwater pollution using GIS data. SEEPAGE considers the following factors:

1. Soil slope
2. Depth to water table
3. Vadose zone material
4. Aquifer material
5. Soil depth
6. Attenuation potential

The attenuation potential factor further considers the following factors:

1. Soil surface texture
2. Subsoil texture
3. Surface layer pH
4. Organic matter content of surface
5. Soil drainage class
6. Soil permeability

These factors are combined using a weighting scheme described in detail by Carpenter (1992). This approach is similar to that used in the DRASTIC model (Aller et al., 1987). For each factor considered, weights are assigned to possible values of the factor. For example, the soil slope factor has the possible values shown in Table 2.1 and associated point source and non-point source weights.

Table 2.1 SEEPAGE Soil Slope Factor Weights

Percent Slope	Point Source	Non-Point Source
0-2	10	30
2-6	9	27
6-9	5	15
9-12	3	9
>12	1	3

2.4 AGNPS Model

Distributed parameter watershed models such as AGNPS are able to incorporate the influences of the spatially variable controlling parameters (e.g., topography, soils, land use, etc.) in a manner internal to computational algorithms. The primary advantage of a distributed parameter model is its potential for providing a more accurate simulation of the system being modeled. For watershed models, a second advantage of this approach is its ability to simultaneously simulate conditions at all points within the watershed. This allows simulation of processes that change both spatially and temporally throughout the watershed such as erosion.

AGNPS has been developed to analyze non-point source pollution in watersheds. It uses a distributed parameter approach to quantify a watershed by dividing the area into a grid of square cells as shown in Figure 2.1. Within this framework, runoff characteristics and transport processes of sediments and nutrients are simulated for each cell and routed to its outlet. This permits the runoff, erosion, and chemical movement at any point in the watershed to be examined. Thus, it is capable of identifying upland sources contributing to a potential problem and prioritizing those locations where remedial measures could be initiated to improve water quality. Runoff in AGNPS is predicted by applying the Soil Conservation Service (SCS) curve number runoff method to each cell. Erosion in AGNPS is predicted by a modified version of the USLE (Young et al., 1989) applied to each cell. Sediment routing is performed for five particle size classes: clay, silt, small aggregates, sand and large aggregates. Sediment is routed through the watershed as described by Young et al. (1989). The nutrient movement components of AGNPS are adapted from CREAMS (Frere et al., 1980). Chemical transport calculations are divided into soluble- and sediment-adsorbed phases. Runoff, erosion, and nutrient movement within cells are routed to the watershed outlet.

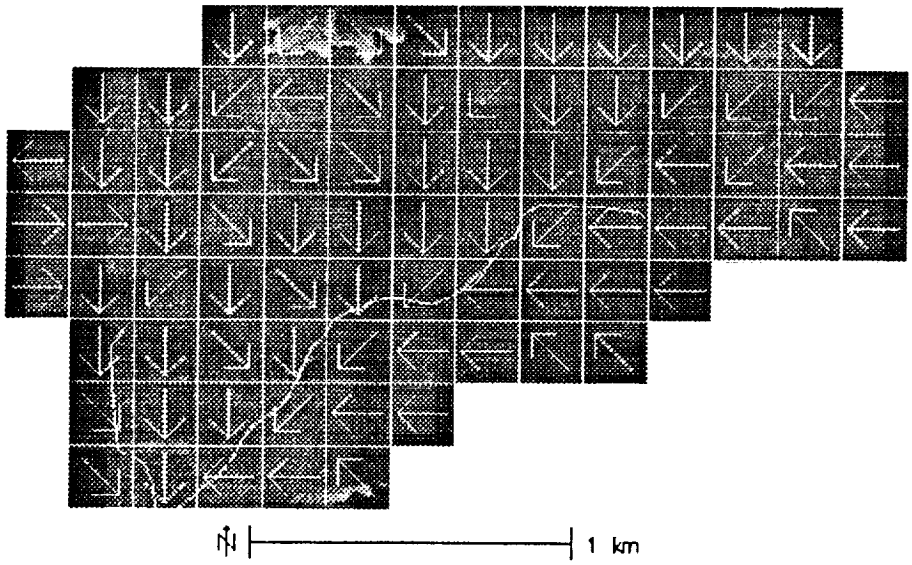

Figure 2.1 Grid Cell and Flow Direction Representation of a Watershed

When modeling with AGNPS, a watershed is divided into square grids (cells) usually ranging in size from 1 to 40 acres. In general, large cell sizes have been used because of the time required to collect model input requirements. The AGNPS inputs required for each cell are shown in Table 2.2, and outputs by cell are shown in Table 2.3.

Table 2.2 AGNPS Cell Input Requirements

Cell number	Cell into which it drains	SCS curve number
Average slope (%)	Slope shape factor	Average slope length
Average channel slope	Mannings *n* for channel	USLE K factor
USLE C factor	USLE P factor	Surface condition constant
Overland flow direction	Soil texture	Nutrient level
Fertilizer incorporation	Point source indicator	Gully source level
Chemical oxygen demand factor	Impoundment factor	Channel indicator
Channel side slope		

Table 2.3 AGNPS Cell Output

Runoff volume	Delivery ratios by particle size
Peak runoff rate	Sediment associated phosphorus mass
Sediment yield	Soluble phosphorus mass
Upland erosion	Soluble phosphorus concentration
Deposition	Fraction of runoff generated
Sediment generated	Enrichment ratios by particle size
Chemical oxygen demand concentration	Chemical oxygen demand mass
Sediment concentration	Sediment particle size distribution
Soluble nitrogen mass	Soluble nitrogen concentration
Sediment associated nitrogen mass	

The problems with models such as AGNPS include the time, expertise, and cost of acquiring the model data, running the model, and interpreting model results. To help overcome these problems, AGNPS was integrated with a raster-based GIS tool called GRASS (Engel et al., 1992). GRASS (Geographical Resource Analysis Support System) (U.S. Army, 1991) is a widely used GIS tool for natural resource applications. The integrated system assists with development of AGNPS input from GIS layers, running the model, and interpretation of the spatially varying results. It can significantly reduce the time required to generate and manage data for AGNPS, to evaluate non-point source pollution problem areas, and to identify potential solutions for these problem areas.

2.5 GIS Data

The next step was to identify GIS databases available or under development for KSC and those that would be required for AGNPS and SEEPAGE. Numerous GIS datasets were available from the KSC GIS and Remote Sensing Laboratory. These datasets were in either the ERDAS or ARC/INFO data formats. ERDAS is a GIS and remote sensing classification tool, and ARC/INFO is a GIS tool. To facilitate the use of the AGNPS/GRASS system and SEEPAGE, ERDAS and ARC/INFO datasets were moved to GRASS. GRASS also provides several other benefits including cost (it is public domain), source code availability, expert system development tools are available within GRASS, and it is well suited for modeling. A listing of the datasets moved to GRASS is provided in Appendix A.

Numerous soil properties were required for SEEPAGE and AGNPS but were unavailable in the existing KSC GIS data. However, a soil series layer was available for which the required soil property layers were derived from the Soils 5 database using the GRASS r.soils5 command. Additional soil property layers that were of interest to scientists conducting ecological studies at KSC were derived using this process. The soil property layers derived and their brief descriptions are listed in Appendix B. Other soil property data that is available in Soils 5 could be easily extracted to build GIS data sets if desired using the r.soils5 command in GRASS. GRASS data layers can also be moved to either ERDAS or ARC/INFO using the procedure described in Appendix C.

Additional GIS layers required by SEEPAGE and AGNPS were obtained by reclassifying existing data layers. Several elevation derived layers (slope steepness, slope length, overland flow direction or aspect) were required for AGNPS, however, elevation data were not available in GIS form. Elevation contours for the VAB watershed area were obtained from the USGS 1:24,000 topographic maps for the area. An elevation surface was fit to the area using surface fitting tools in GRASS. Once an elevation surface was obtained, elevation derived layers were obtained using the GRASS r.watershed command (U.S. Army, 1991). SCS CN values required by AGNPS and other spatial inputs were derived from GRASS data using techniques described in Engel et al. (1992), Rewerts and Engel (1991), Srinivasan and Engel (1991a), and Srinivasan and Engel (1991b).

Several GIS data layers should be developed for KSC in the future. These include: elevation (including layers that can be derived from elevation), drainage, and locations and types of potential contaminants. These data layers would have many potential uses.

RESULTS AND DISCUSSION

3.1 Groundwater Quality

GIS layers were developed for each of the factors considered in SEEPAGE using tables such as Table 2.1 above. For the example in Table 2.1, the GIS slope layer was assigned the weights in the table using the GRASS r.reclass command. GIS data layers for the other factors considered were assigned weights in a similar manner. Once all layers had been assigned weights, the weighted layers were added together using the GRASS r.mapclac command to produce new GIS layers: point source pollution potential and non-point source pollution potential. These layers were then reclassified using the GRASS r.reclass command to obtain qualitative pollution potential categories from the numerical weights based on the SEEPAGE table for doing so (Carpenter, 1992).

As expected, the model predicted that from a hydrologic standpoint most of KSC has a high potential for groundwater contamination for both point and non-point sources as shown in Table 3.1.

Table 3.1 Hydrologic Potential for Groundwater Contamination at KSC

Contaminant Source	Low (acres)	Moderate (acres)	High (acres)	Very High (acres)
Non-Point Source	0	671	54,733	0
Point Source	0	691	54,714	0

Tables 3.2 and 3.3 provide information on the areas of SEEPAGE contamination potential by aquifer recharge zone. These values were obtained by overlaying the SEEPAGE layers with the aquifer recharge layer. Areas that have high potential for contamination and are located in primary and secondary aquifer recharge areas are of the greatest concern. These areas are shown for point source contaminants as the dark areas within the KSC boundaries in Figure 3.1. The areas are nearly identical for non-point source contaminants.

Table 3.2 NPS Contamination Potential by Aquifer Recharge Zone

Recharge Potential	Moderate (acres)	High (acres)
Primary recharge	0	4,934
Secondary recharge	3	13,962
Tertiary recharge	669	35,301

Table 3.3 Point Source Contamination Potential by Aquifer Recharge Zone

Recharge Potential	Moderate (acres)	High (acres)
Primary recharge	0	4,934
Secondary recharge	3	13,962
Tertiary recharge	688	35,281

Figure 3.1 Areas with High Potential for Point Source Groundwater Contamination and Primary or Secondary Aquifer Recharge

One should keep in mind that the SEEPAGE results are based only on hydrologic factors and do not consider groundwater recharge locations, distances to water uses, aquifer water use volume, land uses, contaminant locations, contaminant characteristics, or potential for introduction of potential contaminants to the soil. One should also note that SEEPAGE does not provide information about potential for surface water contamination. However, based on SEEPAGE results, care should be taken when working with potential contaminants at KSC, especially in the areas with a high potential for contamination based on hydrologic factors that are located in primary or secondary aquifer recharge areas as shown in Figure 3.1.

3.2 Erosion and Surface Water Quality

The watershed near the VAB was delineated using watershed boundary information from an ERDAS GIS layer as a starting point. Watershed boundaries were refined using the elevation data and watershed delineation functions within GRASS. Based on these items of information and visits to the watershed site, the watershed to be simulated was delineated. A better estimate of the watershed boundaries would require a detailed elevation survey. A cell size of 148 feet (0.5 acres in area) was selected for the simulation. This cell size was selected due to the variability in soils and vegetation within the watershed. Simulations for a cell size of 296 feet (2.0 acres in area) were also run for comparison purposes.

Once all of the spatial inputs were derived for AGNPS, a series of weather events was selected for simulation. AGNPS requires a rainfall amount and a rainfall erosivity (energy-intensity EI value) to describe a rainfall event. The rainfall events that were selected for simulation are listed in Table 3.4. These events are representative of the range of storms experienced at KSC that are likely to cause erosion and surface water quality concerns.

Table 3.4 Simulation Rainfall Events Used With AGNPS

Rainfall Event	Rainfall Depth (inches)	Rainfall Erosivity (EI)
1	1.0	10
2	1.0	25
3	2.0	10
4	2.0	25
5	2.0	50
6	2.0	75
7	3.0	25
8	3.0	50
9	3.0	75
10	4.0	25
11	4.0	50
12	4.0	75
13	5.0	25
14	5.0	50
15	5.0	75
16	6.0	50
17	6.0	75
18	7.5	75

Using tools developed by Engel et al. (1992), the study watershed was simulated for the above rainfall events using an antecedent moisture condition of II (AMC II) when estimating the SCS curve numbers needed by AGNPS. In addition, some of the rainfall events were simulated using other AMC conditions (I or III corresponding to dryer and wetter conditions, respectively).

Results of the model runs were returned to the GRASS GIS using tools developed by Engel et al. (1992) for interpretation and analysis of AGNPS results. The results for the parameters of interest are summarized in Table 3.5 for events shown in Table 3.4. The runoff depth is the average depth of runoff from the 1127 acre watershed. Volume of runoff can be obtained by multiplying the watershed area by the runoff depth. The peak runoff is the peak rate at which water leaves the watershed for an event. Upland erosion is the amount of soil eroded as a result of interrill and splash erosion. Channel erosion is the amount of soil moved as a result of concentrated flow processes including those in channels. The sediment delivered column is the amount of soil that leaves the watershed. One should note that this value is much less than erosion since much of the soil that is eroded is deposited within the watershed. The nitrogen, phosphorus, and COD columns indicate the total masses of nitrogen, phosphorus, and chemical oxygen demand that leave the watershed. For nitrogen and phosphorus, these masses are the total for the runoff and sediment phases. Total masses of nitrogen, phosphorus, and COD leaving the watershed can be obtained by multiplying the values in the columns by the watershed area (1127 acres).

Table 3.5 VAB Watershed Simulation Results for a Grid Cell Size of 0.5 Acres and AMC II

Rainfall Event (Table 3.4)	Runoff Depth (inches)	Peak Flow (cfs)	Upland Erosion (tons/acre)	Channel Erosion (tons/acre)	Sediment Delivered (tons)	Nitrogen (lbs/acre)	Phosphorus (lbs/acre)	COD (lbs/acre)
1	0.0	16	0.00	0.63	49.4	0.23	0.13	0.97
2	0.0	16	0.01	0.63	49.7	0.23	0.13	0.97
3	0.3	86	0.00	1.48	118.3	0.52	0.25	5.58
4	0.3	86	0.01	1.48	119.3	0.52	0.25	5.58
5	0.3	86	0.02	1.48	120.8	0.52	0.26	5.58
6	0.3	86	0.03	1.48	122.4	0.54	0.26	5.58
7	0.6	199	0.01	2.28	190.5	0.79	0.37	13.16
8	0.6	199	0.02	2.28	192.5	0.80	0.37	13.16
9	0.6	199	0.03	2.27	194.5	0.81	0.38	13.16
10	1.1	340	0.01	3.04	269.9	1.08	0.49	22.72
11	1.1	340	0.02	3.04	272.1	1.08	0.50	22.72
12	1.1	340	0.03	3.04	274.3	1.08	0.50	22.72
13	1.7	498	0.01	3.75	346.6	1.35	0.60	33.60
14	1.7	498	0.02	3.75	348.9	1.36	0.60	33.60
15	1.7	498	0.03	3.75	351.3	1.37	0.60	33.60
16	2.3	667	0.02	4.41	421.9	1.62	0.70	45.40
17	2.3	667	0.03	4.41	421.9	1.62	0.70	45.40
18	3.4	936	0.03	4.90	526.7	1.99	0.85	64.45

A limited number of watershed simulations were run for other moisture conditions as indicated above. A portion of these results are shown in Tables 3.6 and 3.7 for AMC I and AMC III, respectively. Results for the watershed simulation using a cell size of 2.0 acres for a limited number of rainfall events with AMC II are shown in Table 3.8.

Table 3.6 VAB Watershed Simulation Results for a Grid Cell Size of 0.5 Acres and AMC I

Rainfall Event (Table 3.4)	Runoff Depth (inches)	Peak Flow (cfs)	Upland Erosion (tons/acre)	Channel Erosion (tons/acre)	Sediment Delivered (tons)	Nitrogen (lbs/acre)	Phosphorus (lbs/acre)	COD (lbs/acre)
7	0.2	65	0.01	1.33	102.5	0.41	0.22	4.29
8	0.2	65	0.02	1.33	102.8	0.42	0.22	4.29
9	0.2	65	0.03	1.32	103.6	0.42	0.22	4.29

Table 3.7 VAB Watershed Simulation Results for a Grid Cell Size of 0.5 Acres and AMC III

Rainfall Event (Table 3.4)	Runoff Depth (inches)	Peak Flow (cfs)	Upland Erosion (tons/acre)	Channel Erosion (tons/acre)	Sediment Delivered (tons)	Nitrogen (lbs/acre)	Phosphorus (lbs/acre)	COD (lbs/acre)
7	1.3	393	0.01	3.18	296.0	1.42	0.58	25.42
8	1.3	393	0.02	3.17	297.5	1.42	0.59	25.42
9	1.3	393	0.03	3.17	299.1	1.43	0.59	25.42

Table 3.8 VAB Watershed Simulation Results for a Grid Cell Size of 2.0 Acres and Rainfall of 3.0 Inches with Rainfall Erosivity (EI) of 50

Antecedent Moisture AMC	Runoff Depth (inches)	Peak Flow (cfs)	Upland Erosion (tons/acre)	Channel Erosion (tons/acre)	Sediment Delivered (tons)	Nitrogen (lbs/acre)	Phosphorus (lbs/acre)	COD (lbs/acre)
I	0.2	126	0.02	0.57	41.3	0.27	0.12	4.63
II	0.7	382	0.02	1.01	83.8	0.53	0.21	13.96
III	1.4	740	0.02	1.36	129.3	1.27	0.39	26.45

Based on the AGNPS simulation results presented in Tables 3.5 to 3.8, the VAB watershed does not have an erosion problem. This is expected since the terrain is flat, the vegetation provides good cover, and the soils are resistant to erosion (low USLE K factors). Upland erosion rates are extremely small. Most of the erosion that occurred was a result of concentrated flow and channel processes, and these values are well within acceptable ranges. To minimize erosion from this watershed, efforts should be focused on maintaining the channels. Good vegetation in the channels will minimize erosion. Very little of the soil eroded actually leaves the watershed. The sediment delivered column shows the masses of soil that leave the watershed. Most of the soil that is eroded is deposited within the watershed. Since this watershed is similar to much of KSC, erosion in other areas of KSC is expected to be similar and thus is not likely a problem.

The nitrogen, phosphorus, and COD columns of Tables 3.5 to 3.8 indicate that movement of nutrients and chemical oxygen demand from the watershed are relatively small. The values for nitrogen and

phosphorus include the amounts moved with both the runoff and sediment. The simulated masses of nitrogen and phosphorus moved from the watershed are likely higher than actual values since the minimum levels of soil nitrogen and phosphorus allowed by AGNPS are likely higher than those encountered for the soils and land uses within the study watershed. The masses of nitrogen, phosphorus, and COD moved from the watershed should not create problems in the waters into which they are moved. Since this watershed is similar to much of the rest of KSC, movement of nutrients into surface water is not expected to be a significant problem for other areas of KSC. The masses of nutrients moved into surface waters near citrus production may be higher but are not likely to present significant problems.

The simulated runoff volumes and peak rates of runoff shown in Tables 3.5 to 3.8 are within expected ranges and should not create problems in receiving waters. The soils, highly vegetated areas, and flat terrain result in relatively low volumes of runoff and peak rates of flow from the watershed.

SUMMARY AND CONCLUSIONS

The environment, wildlife, and natural resources are important considerations in KSC operations. Research and monitoring concerns within these areas with significant spatial components were examined to determine the role that geographic information systems (GIS) can and should play. Water quality, both ground and surface, was identified as an important concern. The SEEPAGE model was selected to examine the hydrologic potential for contamination of groundwater from both point and nonpoint source pollutants. To explore potential surface water quality issues, the AGNPS non-point source pollution model was selected. This model has been integrated with a GIS system that greatly simplifies its operation and interpretation of its results.

To facilitate the use of these models, existing GIS data was moved from the ERDAS and ARC/INFO GIS tools to the GRASS GIS tool. The AGNPS model had already been integrated with GRASS and numerous hydrologic modeling tools are available within GRASS to assist in preparing spatial data inputs for AGNPS and other models. The SEEPAGE model was easily implemented using using functions within GRASS. Several GIS data layers were unavailable for KSC including soil properties required for AGNPS and SEEPAGE. Using tools within the GRASS GIS, the Soils 5 database, and the soil series GIS layer, the required soil property GIS layers were developed. Additional soil property data layers that were useful for research and monitoring studies at KSC were also derived.

Once the required spatial inputs had been obtained, the SEEPAGE model was implemented within the GRASS GIS for both point and non-point sources of contamination. GIS layers were produced showing potential for groundwater contamination for KSC. The resulting layers indicated that nearly 99 percent of the KSC area has a high potential for groundwater contamination from both point and non-point sources from a hydrologic conditions perspective. The remaining area (approximately 1 percent) has a moderate potential for groundwater contamination. The groundwater contamination potential layers were overlain with the aquifer recharge layer to determine the areas that are of the most concern. Approximately 9% of the KSC land area has a high potential for groundwater contamination from a hydrologic factor standpoint and is a primary aquifer recharge area. Approximately 25% of the KSC land area has a high potential for groundwater contamination from a hydrologic factor standpoint and is a secondary aquifer recharge area. Keep in mind however, that contaminant locations, contaminant properties and numerous other factors that would be important in determining the true potential for groundwater contamination were not considered.

The AGNPS model was run for an approximately 1127 acre watershed located near the VAB, largely to the north and east. A series of rainfall depth and erosivity (related to intensity) events were used to study the effects of rainfall event characteristics. A watershed grid cell size of 0.5 acres was used for most of the simulations, although a cell size of 2.0 acres was used to explore potential differences in simulation results due to cell size. Smaller rainfall events, similar to those that occur on many afternoons during the summer months, caused very little nutrient movement as a result of non-point sources and resulted in very little soil erosion. The erosion that did occur was largely the result of concentrated flows. Most soil that was eroded did not leave the watershed but was deposited in concentrated flow areas within the watershed.

A series of larger rainfall events that would be expected approximately once every 10 years was also simulated using AGNPS. As with the smaller storms, erosion and nutrient movement are not significant problems. Most of the erosion that occurs is the result of concentrated flows, such as water in ditches. With good vegetation in these areas, erosion and soil leaving the watershed can be minimized. The

amount of nitrogen and phosphorus leaving the watershed should not create problems and are likely larger than actual values because of the conservative minimum nutrient availability assumption within AGNPS.

The watershed simulated with AGNPS is similar to most other areas of KSC. Thus, erosion and non-point source pollution are not likely to be problems within KSC. Potential pollutants from the developed areas (parking lots, building rooftops, etc.) were not considered by the simulation and may contribute pollutant loads that are of concern to some surface water bodies.

RECOMMENDATIONS FOR CONTINUED WORK

Suggestions for continued work on this project are presented in this section.

Development of a decision support system to assist with environmental and natural resource issues at KSC that uses GIS, simulations, expert systems, and other computer-based tools should continue. This project demonstrated the potential for using a portion of these tools to quickly identify environmental and natural resource problems.

The potential for movement of contaminants from parking lots and areas with buildings into surface and ground water should be explored.

Additional GIS data layers are needed for projects such as this and other applications. One of the more important layers is elevation. Elevation can be used to derive other data layers including slope and aspect (flow direction). Drainage and locations and types of potential contaminants are among other layers that should be developed.

Existing KSC GIS and remotely sensed data should be fully documented. Documentation should include history of GIS data layers, scale of map from which they were developed, description of content, definitions of categories, persons who developed layer, and other information that would be useful to those interested in using the data.

Existing KSC databases that would be useful to research and monitoring programs concerned with the environment and natural resources should be fully documented.

APPENDIX A DATA IMPORTED TO GRASS

Raster Data Imported to GRASS

GRASS Raster Name	Content
sorecotm	Original soil series data from ERDAS
farfldep	Far field deposition from ERDAS
fedlantm	Vegetation on federal land from ERDAS
habitsj	Scrub Jay habitat from ERDAS
ignition	Burned areas from ERDAS
impoundm	Impoundment areas from ERDAS
kscensaf	
kschydro	KSC hydrology from ERDAS
kscjuwet	KSC wetlands from ERDAS
kscmask	KSC boundaries from ERDAS
kscrectm	KSC vegetation from ERDAS
poparea	Scrub Jay population areas from ERDAS
rechartm	Aquifer recharge areas from ERDAS
savrectm	Scrub area vegetation and density from ERDAS
soils	Soil series from ERDAS
vegclass	Vegetation map from ERDAS
watersheds	Watershed boundaries from ERDAS

Vector Data Imported to GRASS

GRASS Vector Name	Content
builds	KSC buildings from ARC/INFO
flood	Flood plain from ARC/INFO
ksc.contours	USGS 1:24000 contour lines for KSC from ARC/INFO
lcafar	Launch pad A farfield deposition from ARC/INFO
preserves	from ARC/INFO
roads	Roads in Brevard County from ARC/INFO
roadscl	KSC roads from ARC/INFO
upwrcl	KSC underground power lines from ARC/INFO
usewercl	KSC underground sewer lines from ARC/INFO
ustmdmcl	KSC underground storm drains from ARC/INFO
uwatercl	KSC underground water lines from ARC/INFO

Point (Sites) Data Imported to GRASS

GRASS Sites Name	Content
biosites	Biomass monitoring sites from ARC/INFO
boat	from ARC/INFO
fh20inpu	from ARC/INFO
manatee	Manatee sites from ARC/INFO
miscvege	from ARC/INFO
savbiomas	from ARC/INFO
savtransect	Monitoring transects from ARC/INFO
testfish	from ARC/INFO
waterlevel	from ARC/INFO
waterquality	Water quality testing sites from ARC/INFO

APPENDIX B SOIL PROPERTY GIS LAYERS DEVELOPED

Soil Property Data Layers Developed in GRASS Using Soils 5

GRASS Raster Name	Content
sorecotm	Original soil series data from ERDAS
soils.short	Reclassified soil series from sorecotm; used to obtain soil properties from Soils 5
aashto	AASHTO from Soils 5
avail.water	Available soil water in soil layer 1 (in/in) from Soils 5
avail.water2	Available soil water in soil layer 2 (in/in) from Soils 5
avail.water3	Available soil water in soil layer 3 (in/in) from Soils 5
avail.water4	Available soil water in soil layer 4 (in/in) from Soils 5
avail.water5	Available soil water in soil layer 5 (in/in) from Soils 5
avail.water6	Available soil water in soil layer 6 (in/in) from Soils 5
bedrock.depth	Depth of bedrock (inches) from Soils 5
bedrock.hard	Bedrock hardness from Soils 5
bulk.density	Bulk density of soil layer 1 (g/cm3) from Soils 5
caco3	CaCO3 content of soil layer 1 (%) from Soils 5
cec	CEC of soil layer 1 (mg/100g) from Soils 5
cemented.pan.depth	Depth of cemented pan (inches) from Soils 5
class.expand	Expanded soil class from Soils 5
clay	Clay content (%) of soil layer 1 from Soils 5
corrosivity.concrete	Corrosivity of soil layer 1 to concrete from Soils 5
corrosivity.steel	Corrosivity of soil layer 1 to steel from Soils 5
drainage	Soil drainage class from Soils 5
flood.dur	Flooding duration from Soils 5
flood.freq	Flooding frequency from Soils 5
frac10	Fraction of soil particles in layer 1 greater than 10 inches from Soils 5
frac3-10	Fraction of soil particles in layer 1 between 3 and 10 inches from Soils 5
great.grp	Soil great group from Soils 5
gypsum	Gypsum content of soil layer 1 from Soils 5
hydgrp.project	Hydrologic soil groups from Soils 5; Highest group used if ranges were given
hydgrp.project2	Hydrologic soil groups from Soils 5; Lowest group used if ranges were given
k.usle	USLE K (soil erodibility) value from Soils 5
layer1.depth	Depth of soil layer 1 from Soils5
layer2.depth	Depth of soil layer 2 from Soils5
layer3.depth	Depth of soil layer 3 from Soils5
layer4.depth	Depth of soil layer 4 from Soils5
layer5.depth	Depth of soil layer 5 from Soils5
layer6.depth	Depth of soil layer 6 from Soils5
liq.limit	Liquid limit of the soil from Soils 5
minerology	Soil minerology from Soils 5

GRASS Raster Name	Content
organic.matter	Organic matter content of soil layer 1 from Soils 5
pan.hardness	Hardness of cemented pan from Soils 5
permeability	Permeability of soil layer 1 from Soils 5
permeability.2	Permeability of soil layer 2 from Soils 5
permeability.3	Permeability of soil layer 3 from Soils 5
permeability.4	Permeability of soil layer 4 from Soils 5
permeability.5	Permeability of soil layer 5 from Soils 5
permeability.6	Permeability of soil layer 6 from Soils 5
ph	Soil pH of soil layer 1 from Soil 5
plasticity.index	Plasticity index from Soils 5
salinity	Salinity of soil layer 1 from Soils 5
sand	Sand content of soil layer 1 (%) from Soils 5
sar	Sodium Adsorption Ratio from Soils 5
shrink.swell	Soil shrink-swell potential from Soils 5
silt	Estimated silt content of soil layer 1
slope.low	Lowest slope expected from Soils 5
slope.up	Highest slope expected from Soils 5
soil.class.exp	Expanded soil classes from Soils 5
soil.class.reaction	Reaction of soil class from Soils 5
soil.descrip	Soil description from Soils 5
soil.other	from Soils 5
soil.part.size	Soil particle size from Soils 5
soil.prop.note	Soil property note from Soils 5
soils	Soil series from ERDAS
soils.hydg	Hydrologic soil groups from Soils 5
soils.mlra	Soil mlra from Soils 5
soils.short	Soil series names; Reclassed from soils
sub.grp.mod	Sub-group modifier from Soils 5
subsidence.init	Initial subsidence from Soils 5
subsidence.total	Total subsidence from Soils 5
t.usle	USLE T factor from Soils 5
texture.layer2	Soil texture of layer 2 from Soils 5
texture.reclass	Soil texture of layer 1 from Soils 5
unified	unified from Soils 5
wattbl.depth	Water table depth from Soils 5
wattbl.depth.lower	Lower water table depth from Soils 5
wattbl.depth.upper	Upper water table depth from Soils 5
wind.erosion	Wind erosion expected from Soils 5
wind.ifact	Wind erosion equation i factor from Soils 5

APPENDIX C EXPORTING DATA FROM GRASS

C.1 Exporting GIS Layers from GRASS to ERDAS

The most efficient way to export GRASS raster data layers to the ERDAS GIS format is using ARC on a SUN workstation. Before starting ARC, the GISDBASE variable should be set to the location of the GRASS data. For example:

setenv GISDBASE /export/local/apps2/grass4/data

Next start ARC. From the ARC prompt, use the convertimage command to convert a GRASS raster file into the ERDAS format. The convertimage command requires the following arguments in the order given:

1. GRASS raster file name in the format LOCATION:MAPSET:raster file
2. ERDAS GIS file to be created
3. ERDAS (this indicates that an ERDAS format file is to be created

An example use of the command is:

convertimage ksc:PERMANENT:ph ph ERDAS

This command would convert the GRASS raster file ph into an ERDAS GIS format file also called ph.

Before using the file in ERDAS, the ERDAS fixhed command should be run to edit the categories, cell size, and coordinates.

C.2 Exporting GRASS GIS Layers to ARC/INFO

The following describes the process to export GRASS vector files into the ARC/INFO format and then import into ARC/INFO. GRASS contains the v.out.arc command for exporting vector data into an ARC/INFO format. Its arguments are the coverage type (polygon or line), the GRASS vector file name, and the name of the ARC file that will be created. Additional details of the v.out.arc command are provided in its GRASS man page. Once the new ARC file is created, the ARC generate command is used. The following sequence of commands are used in ARC.

generate
input arc_line_file_name
LINES

In the above sequence, arc_line_file_name is the file name that is created by the GRASS v.out.arc command.

REFERENCES

Aller, L., T. Bennett, J.H. Lehr, and R.J. Petty. 1987. DRASTIC: A Standardized System for Evaluating Groundwater Pollution Potential Using Hydrogeologic Settings. U.S. Environmental Protection Agency, EPA 600/2-87/035, 455p.

Bennett, D.B. 1989. Water Resources Analysis of a Multiobjective Drainage Network in the Indian River Lagoon Basin. Water Resources Research Center Publication No. 108. University of Florida, Gainesville, FL. 154p.

Breininger, D.R. 1990. Avifauna of hammocks and swamps on John F. Kennedy Space Center. Florida Field Naturalist 18:21-44.

Breininger, D.R. and P.A. Schmalzer. 1990. Effects of fire and disturbance on plants and birds in a Florida oak/palmetto scrub community. American Midland Naturalist 123:64-74.

Breininger, D.R., M.J. Provancha, and R.B. Smith. 1991. Mapping Florida scrub jay habitat for purposes of land use management. Photogrammetric Engineering and Remote Sensing. 57:1467-1474.

Carpenter, S.G. 1992. SEEPAGE: A system for early evaluation of the pollution potential of agricultural groundwater environments. USDA, Soil Conservation Service, Morgantown, WV, 23p.

Dierberg, F.E. and K.L. Jones. 1989. Assessment of stormwater runoff for recycle in cooling towers at KSC, Florida. Water Resources Bulletin 25(1):43-47.

Dreschel, T.W., B.C. Madsen, L.A. Maull, C.R. Hinkle, and W.M. Knott, III. 1990. Precipitation chemistry: Atmospheric loading to the surface waters of the Indian River Lagoon basin by rainfall. Florida Scientist 53(3):184-188.

Dreschel, T.W., R.B. Smith, and D.R. Breininger. 1991. Florida scrub jay mortality on roadsides. Florida Field Naturalist 18:82-83.

Dwornik, D.S. 1984. A Stormwater Collection and Reuse System for the Kennedy Space Center, Florida. Water Resources Research Center Publication No. 83. University of Florida, Gainesville, FL. 197p.

Engel, B.A., R. Srinivasan, and C. Rewerts. 1992. Runoff, Erosion and Chemical Movement Simulation Using GIS. In: Integrating Environmental Modeling and GIS, NCGIA, Santa Barbara, CA (In Press).

Frere, M.H., J.D. Ross, and L.J. Lane. 1980. The nutrient submodel. In: CREAMS, A Field Scale Model for Chemicals, Runoff, and Erosion from Agricultural Management Systems. U.S. Department of Agriculture, Conservation Research Report 26. pp. 65-85.

Heaney, J.P., B. Koopman, D.S. Dwornik, and D.R. Saliwanchik. 1984. Water Resources of the Kennedy Space Center. Water Resources Research Center Publication No. 82. University of Florida, Gainesville, FL. 259p.

Hinkle, C.R., C.R. Hall, M.J. Provancha, P.A. Schmalzer, A.M. Koller, Jr., and W.M. Knott, III. 1988. The use of remotely sensed environmental data and geographic referenced data management for environmental impact assessments. Chemical Propulsion Information Agency (CPIA) Publication 485.

Madsen, B.C., T.W. Dreschel, and C.R. Hinkle. 1989. Characterization and evaluation of acid rain in Central Florida from 1978 to 1987 - Ten year summary report. NASA Technical Memorandum TM 102149. Kennedy Space Center, FL.

Mailander, J.L. 1990. Climate of the Kennedy Space Center and vicinity. NASA Technical Memorandum 103498. Kennedy Space Center, FL. 62p.

Provancha, J.A. and C.R. Hall. 1991. Observations of associations of sea grass beds and manatees in East Central Florida. Florida Scientist 54:87-98.

Rewerts, C.C. and B.A. Engel. 1991. ANSWERS on GRASS: Integrating a watershed simulation with a GIS. ASAE Paper 91-2621, American Society of Agricultural Engineers, St. Joseph, MI. 8 pp.

Schmalzer, P.A. and C.R. Hinkle. 1990a. Geology, geohydrology and soils of Kennedy Space Center: A review. NASA Technical Memorandum 103813. Kennedy Space Center, FL. 46p.

Schmalzer, P.A. and C.R. Hinkle. 1990b. Flora and threatened and endangered plants of John F. Kennedy Space Center, Florida. NASA Technical Memorandum 102791. Kennedy Space Center, FL. 68p.

Schmalzer, P.A. and C.R. Hinkle. 1991. Dynamics of vegetation and soils of oak/saw palmetto scrub after fire: Observation from permanent transects. NASA Technical Memorandum 103817. Kennedy Space Center, FL. 149p.

Srinivasan, R. and B.A. Engel. 1991a. A knowledge based approach to extract input data from GIS. ASAE Paper No. 91-7045, American Society of Agricultural Engineers, St. Joseph, MI.

Srinivasan, R. and B.A. Engel. 1991b. GIS estimation of runoff using the CN technique. ASAE Paper No. 91-7044, American Society of Agricultural Engineers, St. Joseph, MI.

U.S. Army. 1991. GRASS-GIS software and reference manual. U.S. Army Corps of Engineers, Construction Engineering Research Laboratory, Champaign, IL.

Young, R.A., C.A. Onstad, D.D. Bosch, and W.P. Anderson. 1989. AGNPS: A nonpoint-source pollution model for evaluating agricultural watersheds. Journal of Soil and Water Conservation. 44(2):168-173.

N93-19397

1992 NASA/ASEE SUMMER FACULTY FELLOWSHIP PROGRAM

JOHN F. KENNEDY SPACE CENTER
UNIVERSITY OF CENTRAL FLORIDA

NETWORK PROBLEM THRESHOLD

PREPARED BY:	Dr. Raghvendra R. Gejji
ACADEMIC RANK:	Assistant Professor
UNIVERSITY AND DEPARTMENT:	Western Michigan University Department of Electrical Engineering
NASA/KSC	
DIVISION:	Electronic Systems
BRANCH:	Communication
NASA COLLEAGUE:	John Schnitzius
DATE:	August 14, 1992
CONTRACT NUMBER:	University of Central Florida NASA-NGT-60002 Supplement: 8

ACKNOWLEDGMENT

For organizing and supporting my activities at KSC under NASA-ASEE-SFRFP, I thank:

Loren Anderson, *Program Director*
Carol Valdes, *Program Director*
Jerry Barnes, *Section Chief*
Perry Rogers, *Branch Chief*

For numerous technical suggestions and encouragement, I thank:

John Schnitzius, *NASA Colleague*
Don Philp

For discussions, information and equipment, I thank:

Bryan Boatright
Kelly Furlong
Victor Gonzalez
Keith Ledig
Jeff Leitner
Ray Pecaut
Al Purrinos
Felix Soto Toro
Kari Stiles
Dave Sweigert
Jerry Talley

ABSTRACT

Network transmission errors such as collisions,CRC errors, misalignment, etc. are statistical in nature. Although errors can vary randomly, a high level of errors does indicate specific network problems, e.g. equipment failure. In this project, we have studied the random nature of collsions theoretically as well as by gathering statistics, and established a numerical threshold above which a network problem is indicated with high probability.

SUMMARY

In this report, we are concerned with the use of observed performance data on a CSMA/CD network, such as gathered by routine network monitoring equipment, for network fault detection. For this we need to understand the random nature of variations in network performance. Arrival of messages in a network is governed by random fluctuations in user demand. So network performance is statistical in nature, and network error levels can vary randomly. The goal of this project is to establish a threshold above which network error rates can be considered as indicative of unexpected network problems, such as equipment failure.

The approach we will take is described by three components of the project. One, we will study a theoretical probabilistic model for network collision rates. Two, we will gather statistics from channel 3/P of KSC's BCDS network. Three, we will correlate theory with actual data. Finally we will use the theoretical model to establish a usable network problem threshold.

In Sec. 2.2, a simple model for probabilities for success, collision and idle is developed for lightly loaded networks. For this the collision window is seen to be fundamental. The success probability can be written as the product of network traffic and collision window. The probability of collision per slot, increases as the square of the product of traffic and collision window, while the probability of collision per packet increases linearly with the same product. This model is extended for network utilization in Sec. 2.4. In Sec. 2.3, the theoretical model is adapted to relate its parameters to those observed from a network manager device, such as percentage of colliding transmissions.

Because of the importance of the collision window, an apparatus and method was developed to measure the network delay (Fig. 3-1). For the KSC network, the measured collision window was 80 μs . In Sec. 3.7, actual data taken from the network manager is analyzed. When we study individual data points corresponding to the default 10 s updates from the network manager, the collision rates vary from 0 to 10 percent over a traffic range of 30-250 pkts/s (Fig. 3-4). No obvious conclusion emerges. But, when points corresponding to nearly the same traffic are grouped, and we study average percentage of colliding transmissions versus network traffic, a linear relationship is observed, confirming the theoretical analysis.(Fig. 3-5)

In Sec. IV, we study the distribution of data on percentage of colliding transmissions for conditions of nearly constant network traffic. Based on the properties of exponential probability density function, a threshold level and an implementation rule is developed. The implementation rule states that if the observed collision percentage over a 10 s interval exceeds 0.037 times the network traffic in packets/s, then there is a 99% probability that an unusual condition such as equipment failure is indicated.

TABLE OF CONTENTS

LIST OF ILLUSTRATIONS

LIST OF ABBREVIATIONS AND ACRONYMS

BCDS	--	Broadband Communication Distribution System
CIF	--	Central Instrumentation Facility
CRC	--	Cyclic Redundancy Check
CSMA/CD	--	Carrier Sense Multiple Access with Collision Detection
EDL	--	Engineering Development Laboratory
HER	--	Head End Remodulator
HQ	--	Headquarters Building
KSC	--	Kennedy Space Center
LAN	--	Local Area Network
NMC	--	Network Monitor Console
NRM	--	Network Resource Monitor
RCV	--	Receive
RX	--	Receive
TX	--	Transmit
XMT	--	Transmit

I. INTRODUCTION

In this report, we are concerned with the use of observed performance data on a CSMA/CD network, such as gathered by routine network monitoring equipment, for network fault detection. For this we need to understand the random nature of variations in network performance. Arrival of messages in a network is governed by random fluctuations in user demand. As a result, network performance is statistical in nature, and network error levels can vary randomly.

How can error levels be used for diagnostics? From experience, we know that a "too-high" error level will indicate a network problem e.g. equipment failure. But how high is "too-high"?

Some of the types of data collected by network monitoring equipment are: collisions, CRC errors, and misalignments. Collisions occur when two users randomly happen to transmit at the same time. CRC errors are caused when part of the transmission is corrupted. This error is detected by the CRC code. Misalignment means that the length of the message did not follow standard rules. In this project we will focus on understanding and using collision performance data. This is not to say that collisions are undesirable *per se*. Collisions are unavoidable and generally not considered bad, because the network corrects for them. However, we are considering reported collision levels as indicators of other types of trouble with the network. For this, we ask what level of collisions are reasonable, and when we could conclude that an unreasonably high collsion rate is indicative of a network problem.

There is extensive prior literature on the theoretical performance analysis of CSMA/CD networks [1,2,3,4]. But the study of collision rates is generally not considered important in the literature for reasons given above. Rather, theoretical studies are more concerned with the maximum possible throughput and corresponding delay performance. So most theoretical analyses are concerned with modeling heavily loaded networks to understand their throughput delay characteristics. These analyses result in very general but quite complex models involving Markov queueing theory and matrix algebra. In practice, operational networks tend to be fairly lightly loaded and a complex model is not necessary. In this report, we show how a simple model for collision performance on a lightly loaded network can be used for network management purposes.

The approach we will take is described by three components of the project. One, we will study a theoretical probabilistic model for network collision rates. Two, we will gather statistics from channel 3/P of KSC's BCDS network. Three, we will correlate theory with actual data. Finally we will use the theoretical model to establish a usable network problem threshold.

II. THEORETICAL MODEL

2.1 COLLISION WINDOW

Central to the theoretical development is the concept of collision window. This is the time it takes on a CSMA/CD network from the instant of one station deciding to start a transmission, to the instant that *all* stations have "heard" the transmission, and decided to defer their own transmissions till the current transmission completes. This is the fundamental unit of time in developing the probabilistic event model in our work, and hence also referred to as a single slot.

Elements of the total delay and estimates are given below in Table 2-1. Precise knowledge is lacking due to lack of technical documentation availability from the manufacturer. These data are taken from IEEE STD 802.3 (supplement)[5]. The various delays are stated in terms of allowable bit periods. These have been converted to time units using 0.2 μs/bit corresponding to the BCDS 5 Mb/s transmission speed.

TABLE 2-1 Collision Window Elements

	BITS		μs
TX DATA to RF energy =	24	=	4.8
Propagation delay 1800m x 3.8ns/m =			6.8
H.E.R. RF to DATA =	75	=	15.0
H.E.R. DATA to RF =	24	=	4.8
Propagation delay 1800m x 3.8ns/m		=	6.8
RCV RF to RX DATA =	75	=	15.0
	Total	=	53.2

We will use a round figure of **60 μs** as our theoretical estimate to make allowances for taps, drop cables, amplifiers, etc. Later, in Sec. III, we will describe how the actual network delay was measured.

2.2 SUCCESS, IDLE AND COLLISIONS PER SLOT

Let us introduce the following notation:

- λ -- Average packet arrival rate at any one station
- T -- Collision window
- n -- Number of stations
- p -- For any one station, the probability of initiating a transmission within a slot.
- P_S -- For a given slot of time T, the probability of initiating a successful transmission
- P_I -- For a given slot, the probability of idle
- P_C -- For a given slot, the probability of a collision
- P_{CP} -- For a given packet, the probability of a collision. (Note that this is different from P_C)
- OP_{CP} -- Observed probability of collision per packet

R -- Total network traffic in packets/s
D -- Average packet duration in sec
m -- Average packet length in units of T

The random nature of arrivals at a single station is governed by the Poisson distribution:

$$p_k = \frac{(\lambda T)^k e^{-\lambda T}}{k!}$$

where, p_k = Probability of k arrivals, k = 0,1,2,...

We will assume in our theoretical development that all stations are equally loaded, which is reasonable for the BCDS system, because each station is a bridge, which forwards traffic from a baseband ethernet LAN.

Then total traffic

$$R = n\lambda \text{ packets/s},$$

$$p = \lambda T,$$

and P_S = Pr(Exactly 1 packet at only 1 of n stations)
$= np(1-p)^{n-1} \approx np = n\lambda T$.

Interestingly, P_S can be written as the product of network traffic and collsion window

$$P_S = RT. \qquad (2\text{-}1)$$

Next,

P_I = Pr(0 packets at all of n stations)
$= (1-p)^n$.

Hence,

$$P_C = 1 - P_S - P_I = 1 - (1-p)^{n-1}[np + 1 - p]. \qquad (2\text{-}2)$$

2.3 RELATE TO NRM DATA

Actual observations on the network are taken with a device called the NRM. The NRM reports the absolute number of collisions, from which it is easy to determine the proportion of transmitted packets that experience a collision. So we need to theoretically develop an equation for the proportion of packets that collide.

$$P_{CP} = \frac{\text{\# of collisions}}{\text{\# of xmt packets}} = \frac{\text{Pr(collision/slot)}}{\text{Pr(xmt success/slot)}}$$

$$= \quad P_C/P_S$$

For low traffic, p is small, and $P_I \approx 1$, so the above method of (2-2) is not accurate. For example, if

$n = 33$,
$\lambda = 3$ frames/s/station ,
$T = 25$ μs,

then, $p = 75E\text{-}6 = 0.000075$. Notice that $p << 1$. Next,

$P_S = 25E\text{-}4 = 0.0025$,
$P_I = (1\text{-}.000075)^{32} = 0.997602787$ (Notice, ≈ 1),

and

$P_C = 1 - P_S - P_I = -1.028E\text{-}4$,

which is impossible, since probability can never be negative.

A better way is to approximate $(1-p)^{n-1}$ as $(1-(n-1)p)$, since p is small, and write:

$$P_C = 1 - (1-(n-1)p)(np + 1 - p)$$
$$= [(n-1)p]^2.$$

Then

$$P_{CP} = P_C/P_S = [(n-1)^2/n]p \approx (n-1)p \text{ for } n >> 1 .$$

Comparing with $P_S = np$, we see that P_{CP} will increase linearly with traffic R. As for P_S in (2-1), P_{CP} can also be approximated as the product of network traffic and collsion window

$$P_{CP} = RT. \qquad (2\text{-}3)$$

It is interesting that the probability of collision per slot, P_C, increases as the square of the product RT, while the probability of collision per packet P_{CP} increases linearly with RT.

2.4 NETWORK UTILIZATION

Although not the primary concern of this work, the model developed above can be used to develop an equation for network utilization.

For this we introduce:

m = Average packet size in units of T = D / T

For example, if the average packet is 150 bytes long, it will take 150 x 8 x 0.2 = 240 μs at the BCDS transmission rate of 5 Mb/s. Now if T = 80 μs, then m = 240/80 = 3.

Considering the possible events during one slot, we see that the network will be idle for 1 slot with probability P_I, it will lead to a successful transmission, occupying on the average m slots, with probability P_S, and with probability P_C, it will lead to a collision. A collision will consume on the average, a certain number of time slots to resolve, which will depend on the backoff algorithm. But the resolution will require at least one additional slot, so we will optimistically assume a collision will consume on an average, 2 slots, one for the collision, one for the minimum backoff. We will see soon that this assumption is not very significant for lightly loaded networks. Then we can write the average network utilization as:

$$\rho = \frac{mP_s}{mP_s + P_I + 2P_C}.$$

Since $P_C << 1$ and $P_I \approx 1$, we can write approximately,

$$\rho \approx mP_s / (1 + mP_s). \tag{2-4}$$

When $mP_s << 1$, we can simply approximate (2-4) as mP_s. Notice that from (2-1), $mP_s = mTR$, and hence,

$$\rho = mP_s = D\,R \tag{2-5}$$

= Average Packet Duration X Network Traffic in pkts/s.

For example, if the network traffic is 150 pkts/s and the average duration is 240 μs, then ρ = 0.036 or 3.6% average. The peak utilization can be much higher.

2.5 SIMPLER DERIVATION

A mathematically simpler derivation for the proportion of colliding packets is obtained by changing our argument approach slightly. Once a given packet starts transmitting, collision will occur if one of the remaining stations attempt to transmit within the collision window, and so

$$\begin{aligned} P_{CP} &= \Pr(\text{ one or more of (n-1) stations will transmit}) \\ &= 1 - \Pr(\text{none of n-1 stations will transmit}) \\ &= 1 - (1-p)^{n-1} \\ &\approx 1 - [1-(n-1)p] \\ &= (n-1)p, \end{aligned}$$

which is the same as (2-3).

Since $p = \lambda T$ as seen in (2-1), we need to know the packet arrival rate and collision window to predict percent of colliding packets. In the next section we will discuss practical measurement of these quantities for the KSC BCDS network and relate them to observed collision rates.

III. TEST RESULTS

3.1 COLLISION WINDOW MEASUREMENT

Fig. 3-1 shows the test setup used to measure the collision window. Note that the Head-end Remodulator is really part of the network equipment, and not part of the test equipment. The following equipment was used:

1 - Tektronix type 7904 Oscilloscope
2 - Tektronix 7A22 Differential Amplifier Vertical Modules
1 - Tektronix 7B92A Dual Time Base
1 - Network General SNIFFER Network Analyzer
2 - Ungermann-Bass Buffered Repeaters
2 - Black-Box (TM) Ethernet 4-port Direct Connects (Fan-out Boxes)

The test equipment is set up in the EDL building which is at the end of the BCDS cable. The HER is located in the CIF building, about 1800m distant. The SNIFFER is set up to generate a stream of 64-bit wide packets at 30 ms interval. Each packet must travel through the first fan-out box toward the cable. As it does so, a voltage signal appears on the RCV terminals of the first fan-out box. Then the packet travels through the buffered repeater and propagates along the cable to the HER. The 4/Q channel, which is a test channel, was used for the experiment to avoid interference with other users. At the HER, the packet is demodulated and remodulated on a different frequency and propagates back down the cable. It is then recieved by the second buffered repeater and sent to the second fanout box, causing a signal to appear on the RCV terminals of the second fanout box. The RCV terminals (pins 5 and 12) [6] of the two fanout boxes are connected to the left and right vertical channels of the scope respectively. By observing both signals simultaneously, we detected the relative delay between them. We note that the measured delay includes not only the network delay, but also the delay introduced by the two buffered repeaters.

3.2 EFFECT OF BUFFERED REPEATER PACKET PROCESSING LATENCY

The ethernet baseband speed = 10 Mb/s and the BCDS broadband speed = 5 Mb/s. Due to the speed difference, the buffered repeaters must store the packet and then forward it [7]. This introduces a delay which is equal to the packet duration. In going from baseband to broadband, the delay is 0.1 μs/bit, and from broadband to baseband it is 0.2 μs/bit. This gives a total delay of 0.3 μs/bit or 2.4 μs/byte. To account for the buffered repeater processing latency, total delay was measured for different packet sizes. The results are shown in Table 3-1.

TABLE 3-1 Effect of Buffered Repeater Latency

Packet Size (Bytes) (x)	Total Delay (μs) (y)
64	230
96	310
128	390
160	470

Now let y represent the measured delay, and x represent the packet size in bytes. Fit a linear equation $y = mx + c$. Then m represents the processing delay per byte introduced by the buffered repeaters, and c is the fixed network delay that is independent of packet size.

Result: m = 2.4 μs/byte, c = 80 μs

The measured network delay **80 μs** is close to theoretical estimate of 60 μs. We will use the 80 μs figure as the best available value for the collision window.

3.3 PRACTICAL PREDICTION OF PERCENT COLLIDING TRANSMISSIONS

Using the theoretical model, we can predict the expected proportion of transmitted packets that will collide. Because we have identified a linear relation between P_{CP} and R in (2-3), the application of our theoretical model is extremely simple.

Let us use:

Network Traffic = 125 packets/s
Collision Window = 80 μs

Proportion of Colliding Transmissions = $125 \times 80 \times 10^{-6}$
= 0.01

or 1%

RULE OF THUMB : Theory predicts a collision rate of 1% for a traffic level of about 125 pkts/s. This will change proportionally with traffic.

3.4 MEASUREMENT OF NETWORK PERFORMANCE

Two types of equipment were considered :

SNIFFER (TM) : Made by Network General Corp.
NMC (TM) : Made by Ungermann-Bass.

The NMC (Network Monitor Console) was selected for the project since it provides more suitable data than the SNIFFER. The SNIFFER attaches to the BCDS network through a device called a BUFFERED REPEATER. As part of its function, the Buffered Repeater discards transmitted packet fragments that normally result from a collision. Hence these packets are not passed to the SNIFFER. As a result the data analysis presented by SNIFFER is incomplete regarding information on BCDS collision rates.

Fig. 3-2 shows an example of a screen from the NRM, which is a functional part of the NMC. The A side of the screen refers to the BCDS and is of interest to us. The NRM was used to monitor channel 3/P of th e KSC BCDS system.

3.5 NETWORK PACKET ARRIVAL RATE AND COLLISION RATE FROM NRM DATA

In section II we saw that the network traffic R was a key parameter in determining collision performance. The total network packet arrival rate can be easily obtained from NRM data.

As seen in Fig. 3-2, each bridge keeps a running count of total XMT and RCV packets, which are then reported by the NRM. In Fig. 3-2, for example, we are observing the bridge located on the 2nd floor of the HQ building. The screen is updated every 10 second. Because cumulative counts are reported, two observations are necessary to get a picture of current activity.

For example:
Observation 1: XMTPKT = 209 ; RCVPKT = 25180 ;
After 10 s : XMTPKT = 235 ; RCVPKT = 27101 .

Then, total Network Traffic in 10 s = 26 + 1921 = 1,947 ,

And, Network Packet Arrival Rate = 195 pkts/s .

Observations indicate that the network packet arrival rate can vary from 50 to 500 pkts/s on BCDS 3/P channel.

A similar approach is needed to calculate the actual proportion of colliding packets.

For example:
Observation 1: XMTPKT = 629 ; COLLISN = 8 ;
After 10 s : XMTPKT = 846 ; COLLISN = 11 .

Therefore there were 217 packets successfully transmitted by this bridge in the last 10 seconds. In addition, 3 transmission attempts resulted in collisions. Therefore the total number of attempts is 220 and the collsion rate over the last 10 s is

$$OP_{CP} = 3/220 = 0.0136 \text{ or about } 1.4\% .$$

3.6 DATA COLLECTION

Because it would be very difficult to analyze large quantities of data one screen at a time, we can use a log file to make the task simpler. An example log file is shown in Fig. 3-3. Each line in this file represents data from one 10 second update of the NRM screen. NMC data has been collected by taking 1,080 readings over a one day period. This represents 20 minutes worth of data, i.e. 120 points, every hour for 9 hours. The resulting log files can be analyzed using a spreadsheet program.

3.7 DATA ANALYSIS

Fig. 3-4 shows a sample data analysis of a log file. The method of Sec. 3.5 was applied to each line of a log file taken on June 17, 1992. The network traffic in packets/s and percentage of colliding transmissions was calculated for each 10 s update interval. The results are plotted in Fig. 3-4. As we can see, the raw data is somewhat confusing, with the collision percentage scattered anywhere from 0 to 10%, and traffic ranging from 30 to 250 pkts/s. There are two reasons for this confusion. One, the network traffic ranges over one order of magnitude, and from (2-3), so will P_{CP}, the collision probability per packet. Two, the theoretical development of Sec. II and (2-3) give us the expected or average value for the percentage of colliding transmissions. The actual data value will be a random value which is a sample taken from a certain probability distribution with the mean given by (2-3). So if we take many observations corresponding to a given traffic level, the average should tend toward the theoretical average of (2-3). With many data points for a given value of network traffic, we can study the shape of the probability distribution function by plotting occurrences of actual percent colliding transmission values.

Although we have many data points in Fig. 3-4, they do not all correspond to the same traffic level. Next, we group the data points into bins of approximately equal traffic. Thus all data points corresponding to network traffic of 25-50 packets/s are grouped together. Similarly, other groups are formed corresponding to traffic ranges of: 50-75, 75-100, 100-125 etc. packets/s. It is important to note that each group will have a different number of data points in it. We cannot control this, rather it is controlled by random fluctuations in the network traffic based on user demand. Then, for each group, we calculate the average traffic and average percentage of colliding packets. The average percent colliding packets versus average traffic is plotted in Fig. 3-5. Each point in Fig. 3-5 represents a group of data points of approximately equal traffic from Fig. 3-4, as described above. The points in Fig. 3-5 exhibit the expected linear trend. If we fit a straight line through these points, while forcing it through the origin, we obtain a slope of 0.0095. The regression equation then becomes:

$$OP_{CP}\ (\%) = 0.0095\ R\ . \qquad (3\text{-}1)$$

To compare with the results of Sec. 3.2, we note that substituting R = 125 in (3-1) leads to OP_{CP} = 1.2%. This agrees closely with the 1% collision level predicted by theory based on our measurement of the network collision window.

IV. THRESHOLD CALCULATION

4.1 PROBABILITY DENSITY FUNCTION FOR OCCURRENCES OF COLLISION PERCENTAGES

Let us focus on the data points belonging to just one of the bins mentioned in Sec. 3.7
We will study the data points corresponding to a traffic range of 75-100 pkts/s. We note from Fig. 3-4, that a large number of data points correspond to no collision or 0% collision rate. For higher collision rate values, the number of times they occur becomes progressively less. Fig. 4-1 plots the number of occurrences in the range 0-0.5, 0.5-1, etc. %, versus the lower limit of each range. Also shown is the shape of an exponential curve. Based on empirical observations, we will conjecture that the probability density function follows an exponential shape. A theoretical proof of the shape of the density function is still a question for further research.

4.2 95% AND 99% CONFIDENCE LIMITS FOR EXPONENTIAL DISTRIBUTION FUNCTION

The distribution function for an exponential density function with mean a^{-1} is

$$F_X(x) = Pr(X \leq x) = 1 - e^{-ax} . \qquad (4\text{-}1)$$

For the 95% confidence level we solve (4-1) for x such that

$$F_X(x) = 0.95 ,$$

which yields

$$x = (-1/a)\ \ln(0.05) = 3\ a^{-1}.$$

That is, at 95% confidence level, the sample value x is less than 3 times the mean. This is shown in graphical form in Fig. 4-2.

Similarly solving (4-1) for $F_X(x) = 0.99$ yields

$$x = 4.6\ a^{-1}.$$

4.3 THRESHOLD DETERMINATION

From Sec. 3.3, we know that the expected or mean collision rate in % is

$$P_{CP}(\%) = 100*80*10^{-6}*R = 0.008\ R \qquad (4\text{-}2)$$

Combining this with the results of Sec. 4.2, we get the following thresholds:

At 95% confidence level

$$T_{h1} = 3x0.008xR = 0.024\ R . \qquad (4\text{-}3)$$

At 99% confidence level

$$T_{h2} = 4.6 \text{ x}0.008\text{xR} = 0.037 \text{ R} . \quad (4\text{-}4)$$

4.4 RECOMMENDED IMPLEMENTATION

Procedure

1. Use NRM data to calculate traffic using the method described in Sec. 3.5, i.e.

$$R = \Delta(\text{XMTPKTS+RCVPKTS}) / \Delta T .$$

2. Calculate observed proportion of colliding packets using the method of Sec. 3.5, i.e.

$$OP_{CP} \ (\%) = \ 100 * \Delta(\text{COLLISNS}) / \Delta(\text{XMTPKTS} + \text{COLLISNS}).$$

3. Calculate thresholds T_{h1} and T_{h2} using formulas (4-3) and (4-4) given above.

4. If threshold T_{h1} is exceeded, there is >95% probability of a network hardware problem.
   If threshold T_{h2} is exceeded, there is >99% probability of a network hardware problem.

4.5 GRAPHICAL EXAMPLE

In Fig. 4-3, we see a spreadsheet analysis similar to Fig. 3-4, based on data taken on July 15. We can see that the data indicates higher levels of traffic as well as collision rates than Fig. 3-4. Application of the procedure of Sec. 4.4 shows that there are a considerable number of data points above the threshold. So we would conclude that this data indicates an unusually high collision rate, that would lead us to suspect some type of equipment problem.

V. CONCLUSIONS

We have presented an analysis of the collision probability in a CSMA/CD network with the idea of using our theoretical understanding in combination with observed collision performance data to draw conclusions about network problems. A simple theoretical model for this purpose has been developed which can be easily related to observed network data. From this model, we see that the percentage of colliding transmissions will increase in proportion to network load. The collision window was seen to be an important network property. An apparatus and methodology was developed to measure the network delay for KSC. The results of the theoretical model were in good agreement with actual collision performance data taken from the network during routine operation. A formula for the threshold and a recommended procedure for implementing it have been developed. The implementation rule states that if observed network collision rates exceed the threshold, a network problem is indicated with high probability.

VI. REFERENCES

[1] Keiser, Gerd E., *Local Area Networks*, McGraw-Hill : New York, 1989, pp. 234-236.

[2] Schwartz, Mischa, *Telecommunication Networks, Protocols, Modeling and Analysis*, Addison Wesley : Reading, MA, 1987, pp. 444-446.

[3] Lam, Simon S., "A carrier sense multiple access protocol for local networks," *Computer Networks*, vol. 4, no.1, Jan. 1980, pp. 21-32.

[4] Tobagi, Fouad A., and Hunt, V. Bruce, "Performance analysis of carrier sense multiple access with collision detection," *Computer Networks*, v.4, 1980, pp. 245-259.

[5] ANSI/IEEE Standard 802.3b,c,d and e, *Supplements to carrier sense multiple access with collsion detection*, 1989, p. 97.

[6] ANSI/IEEE Standard 802.3, *Carrier sense multiple access with collision detection*, 1986, p. 95.

[7] Ungermann-Bass, *Product Specification Guide*, Santa Clara, CA, Spring 1992, p. 5-3.

DELAY MEASUREMENT

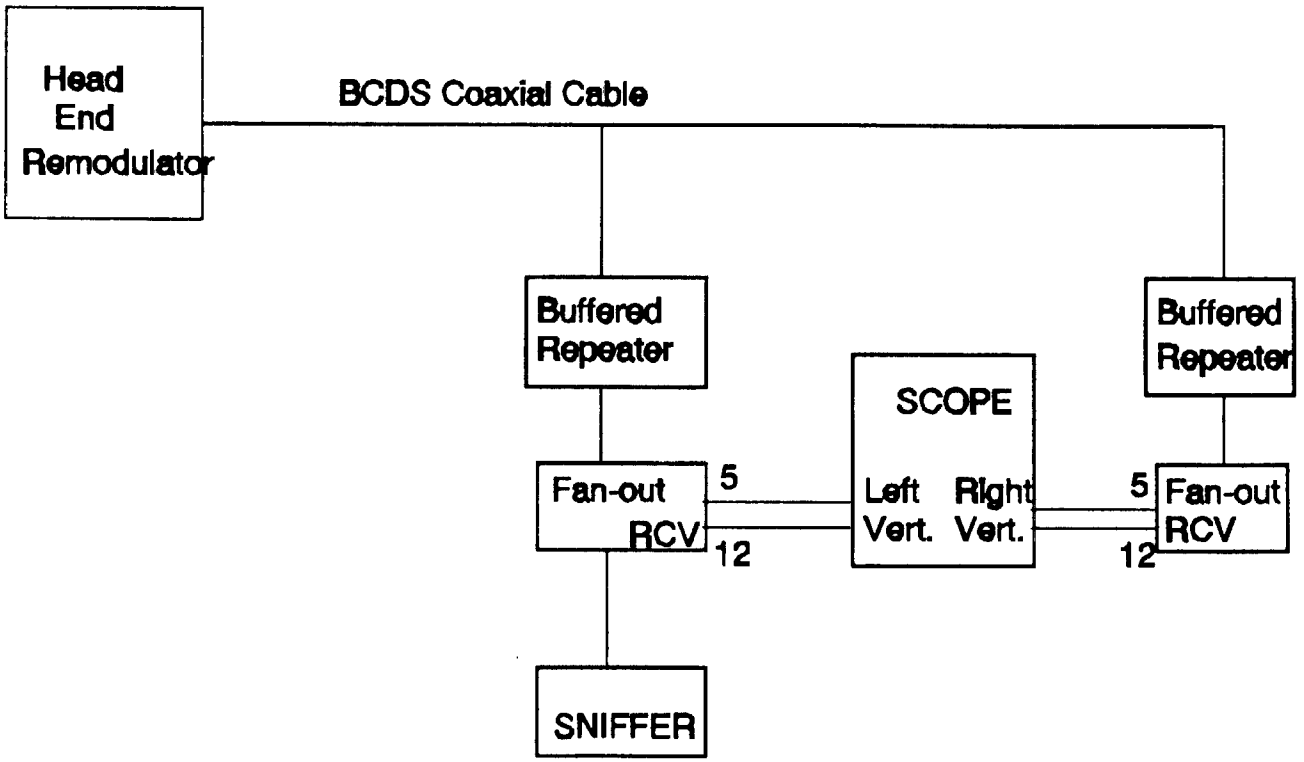

Figure 3-1 Test Setup

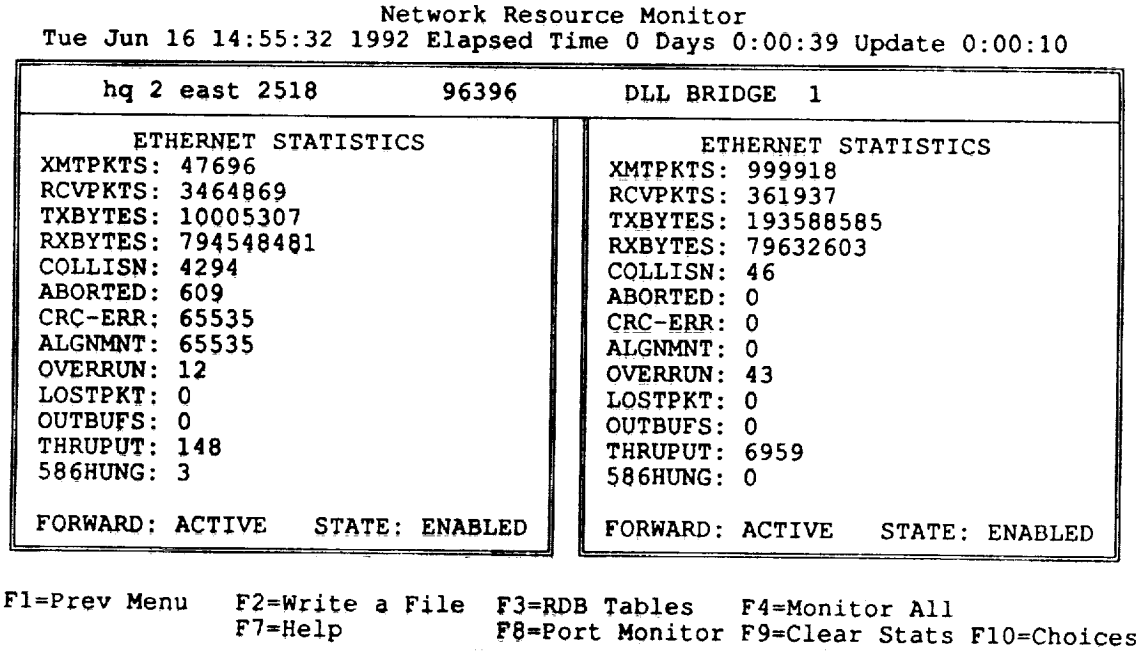

Figure 3-2. Example NRM screen.

```
Name: hq 2 east 2518        Address: 96396
Type: DLL BRIDGE            NetID: 1
Wed Jun 17 08:27:39 19  Update 0:00:10
Time      XMTPKTS A  RCVPKTS A  TXBYTES A  RXBYTES A  COLLISN A  CRC-ERR A
08:28:58  4          7268       1700       1166270    0          1
08:29:08  5          8397       2152       1336310    0          1
08:29:18  6          9387       2604       1556375    0          1
08:29:28  7          10368      3056       1760815    0          1
08:29:38  8          10967      3508       1864166    0          1
08:29:48  10         11830      4358       1973602    0          1
08:29:58  11         12361      4810       2067351    0          1
08:30:08  54         13194      8370       2182999    0          2
08:30:18  97         14153      11930      2314550    0          2
08:30:28  168        14984      17562      2428938    0          2
08:30:38  169        15991      18014      2573177    0          3
08:30:48  171        16988      18864      2782542    0          3
08:30:58  179        18489      19834      2999141    0          3
08:31:08  215        19314      22876      3111832    0          3
08:31:18  272        20088      27472      3219796    0          3
08:31:28  399        20958      37248      3335106    1          3
08:31:38  414        21745      38736      3469666    1          3
08:31:48  416        22565      39586      3636555    1          3
08:31:58  417        23299      40038      3755670    1          5
08:32:08  418        25022      40490      4029934    1          5
08:32:18  419        26079      40942      4218496    1          5
08:32:28  434        27742      42430      4502791    3          5
08:32:38  435        28954      42882      4714739    3          5
```

Figure 3-3. Example Log file from NRM.

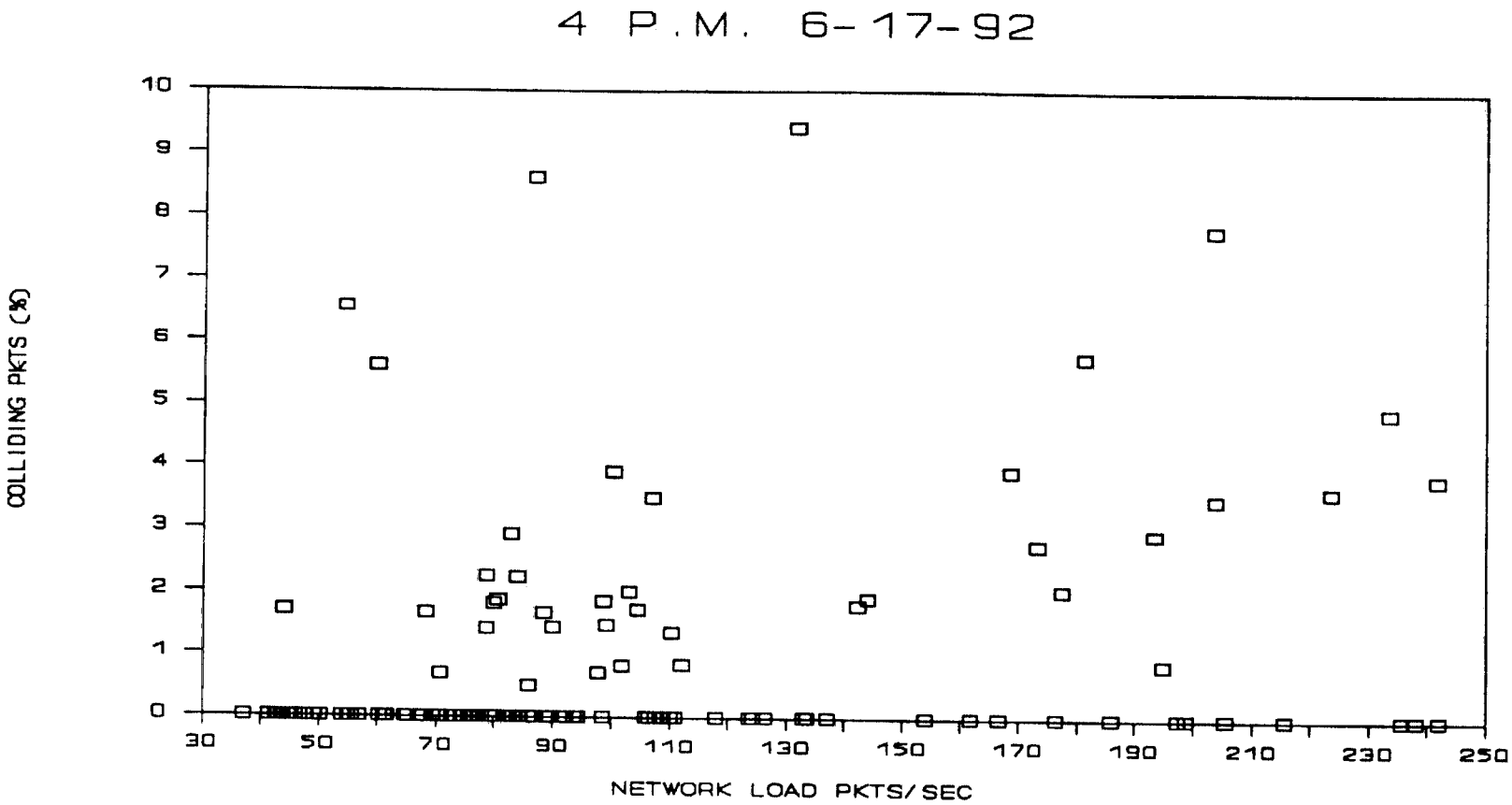

Figure 3-4 Analysis of 10 second update data points.

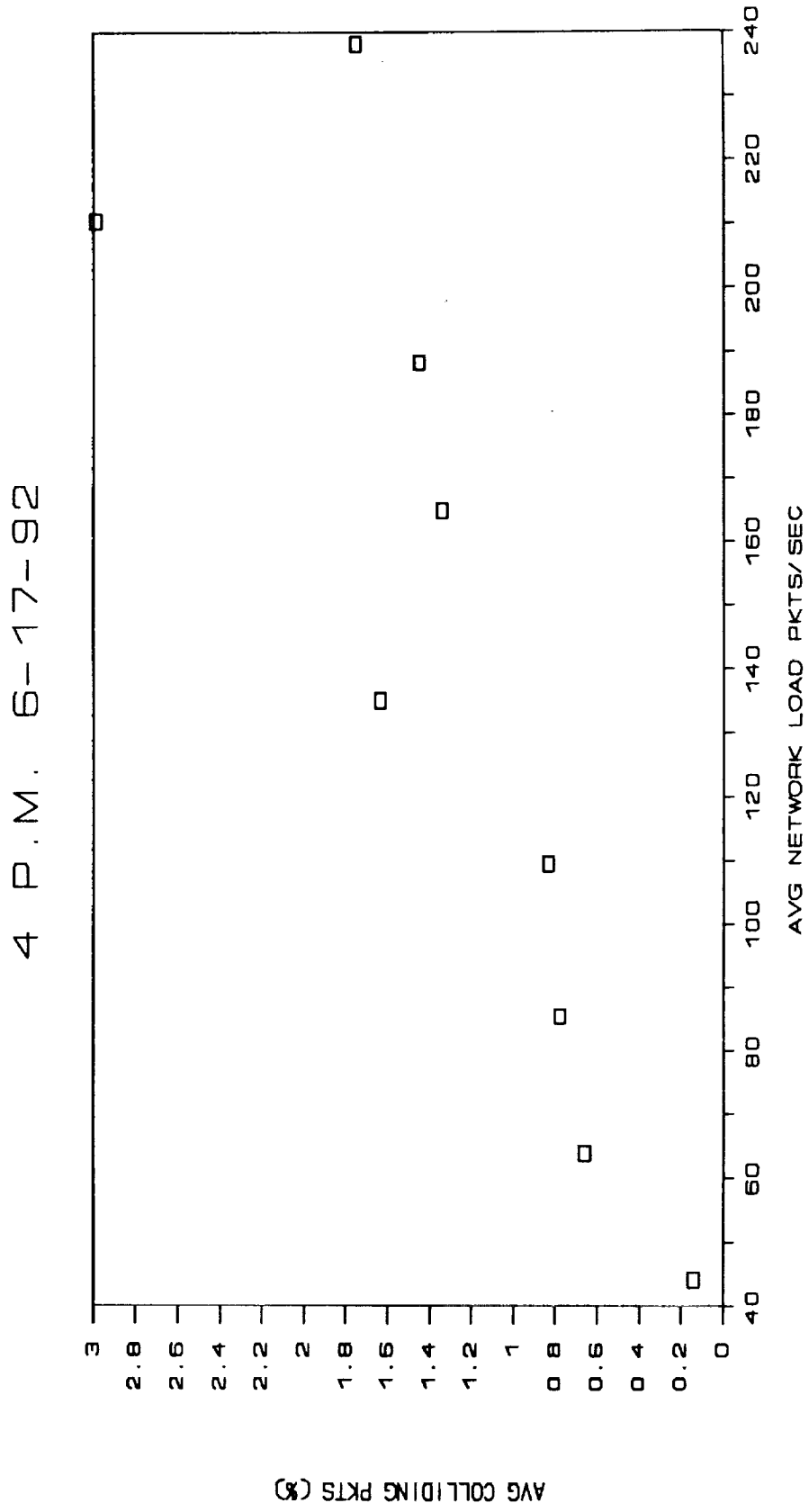

Figure 3-5. Analysis after grouping data points by traffic.

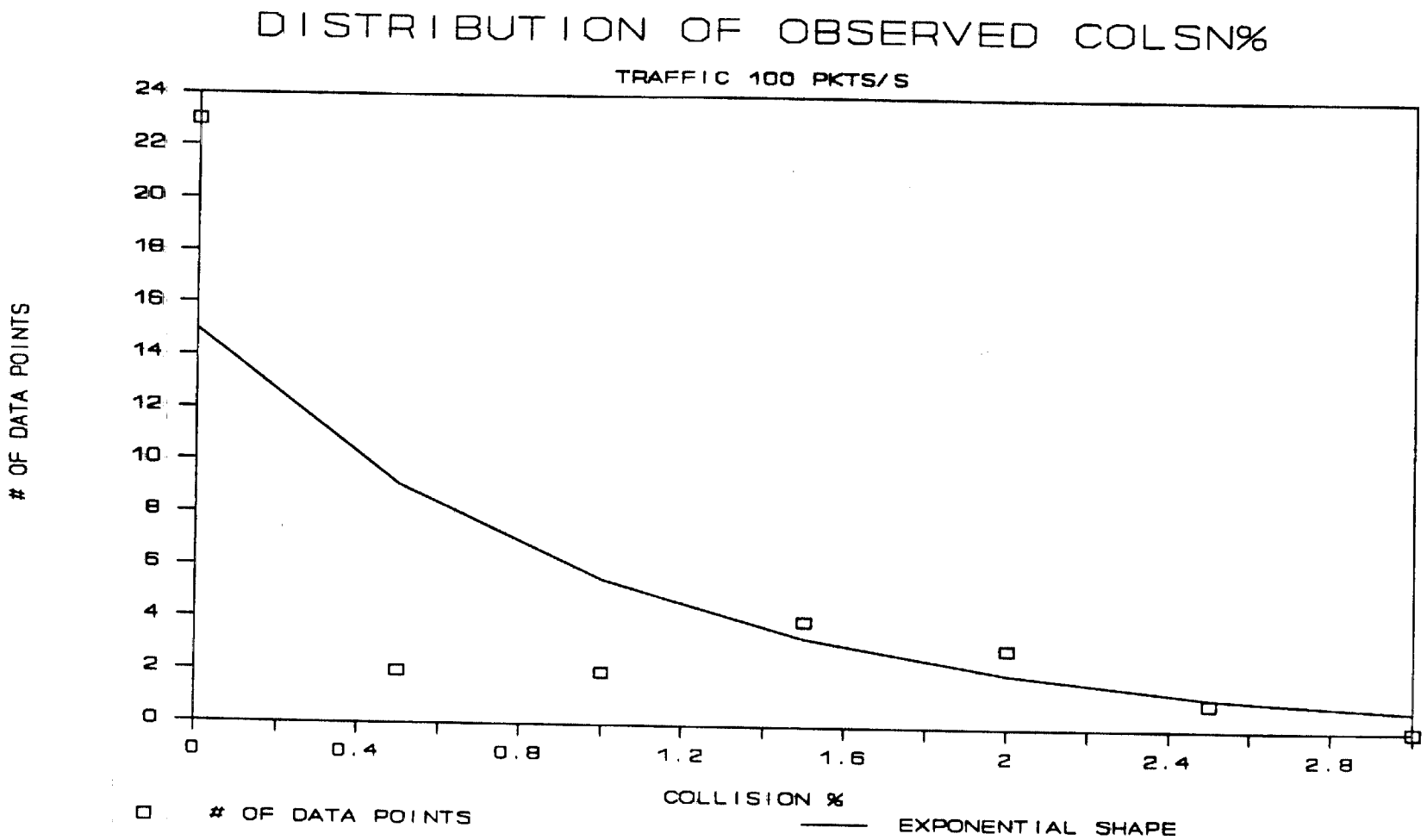

Figure 4-1. Number of occurrences vs percentage colliding packets, for fixed traffic.

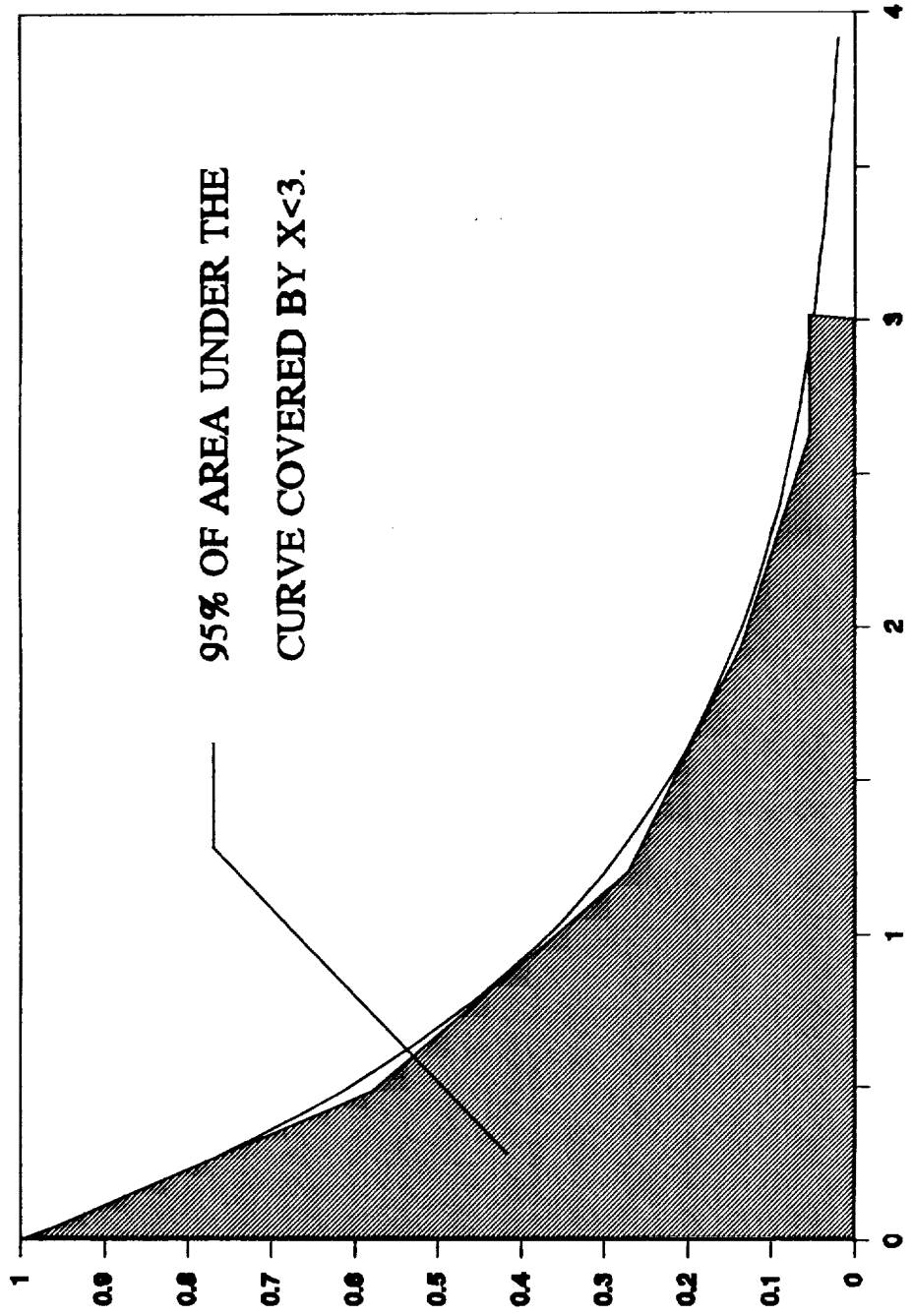

Figure 4-2. 95% confidence limit from exponential density function.

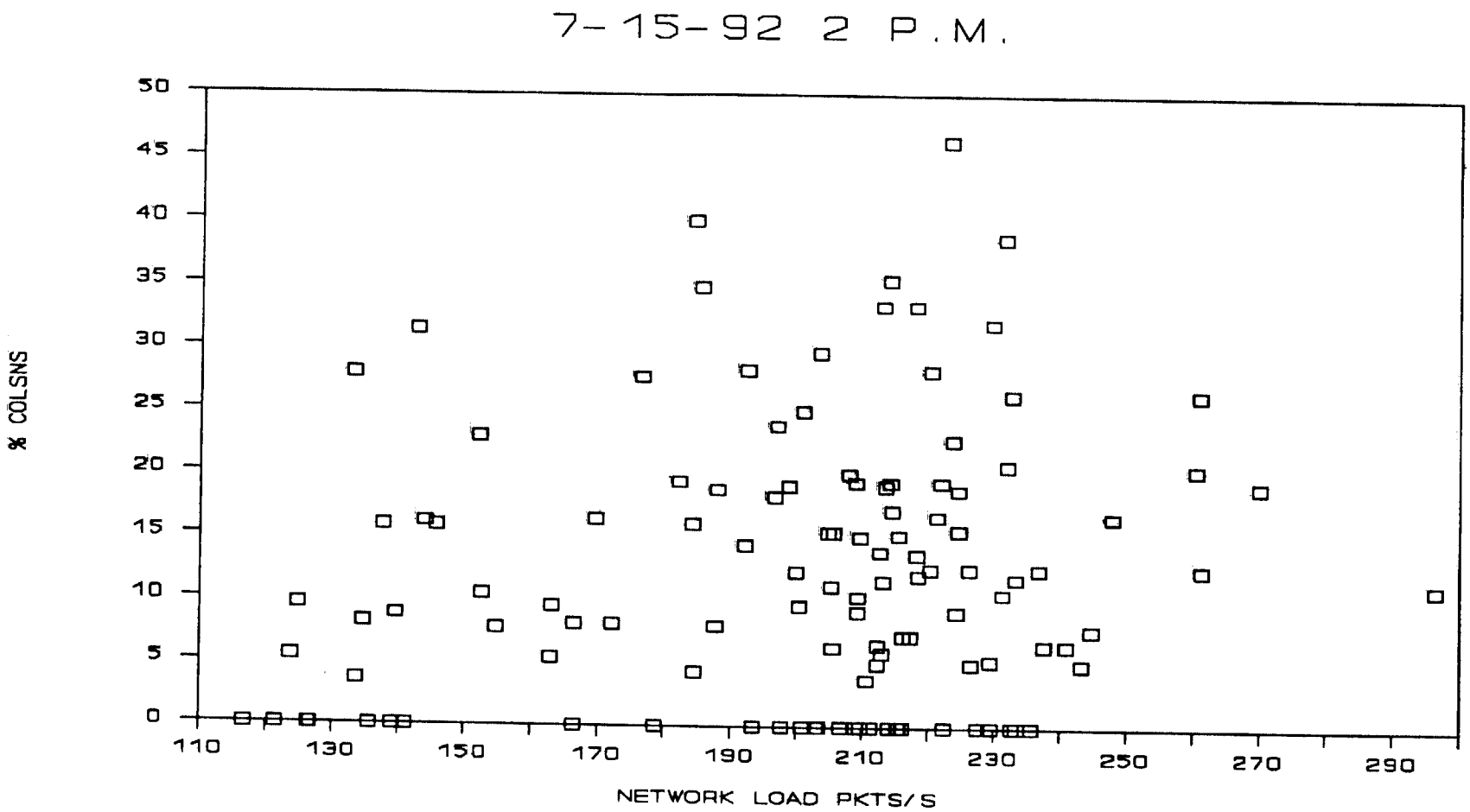

Figure 4-3. Example of data with collision percent exceeding threshold.

N93-19398

1992 NASA/ASEE SUMMER FACULTY FELLOWSHIP PROGRAM

JOHN F. KENNEDY SPACE CENTER
UNIVERSITY OF CENTRAL FLORIDA

REDUNDANT DRIVE CURRENT IMBALANCE PROBLEM OF THE AUTOMATIC RADIATOR INSPECTION DEVICE (ARID)

PREPARED BY:	Dr. Carl D. Latino
ACADEMIC RANK:	Associate Professor
UNIVERSITY AND DEPARTMENT:	The Oklahoma State University Department of Electrical and Computer Engineering
NASA/KSC	
DIVISION:	Mechanical Engineering Directorate
BRANCH:	Special Projects (RADL)
NASA COLLEAGUE:	Willis Crumpler Bill Jones Eduardo Lopez
DATE:	August 7, 1992
CONTRACT NUMBER:	University of Central Florida NASA-NGT-60002 Supplement: 8

ACKNOWLEDGMENTS

I very much wish to thank my KSC colleagues Mr. Eduardo Lopez, Bill Jones and Willis Crumpler for the opportunity of working on the ARID Current Imbalance Problem and for all the support they provided. Their effort in order to help solve this interesting problem was greatly appreciated. I also wish to thank the many NASA and Boeing employees who provided help and information necessary to better understand the problem . A special thanks goes to Carol Valdez who was a most enjoyable person to interface with. Her excitement and desire to please made us wish the summer had been longer. On the University of Central Florida side, I wish to thank Dr. Loren Anderson and Kari Stiles. With their friendly demeanor and high degree of professionalism, they helped make the summer a most enjoyable and educational experience. These individuals have provided me with valuable experiences which I have taken back with me. I hope that in return I have provided some useful information both in the findings outlined in this report and in my problem solving techniques.

ABSTRACT

The Automatic Radiator Inspection Device (ARID), is a 4 Degree Of Freedom(DOF) robot with redundant drive motors at each joint. The device is intended to automate the labor intensive task of space shuttle radiator inspection. For safety and redundancy, each joint is driven by two independent motor systems. Motors driving the same joint, however, draw vastly different currents. The concern was that the robot joints could be subjected to undue stress. It was the objective of this summer's project to determine the cause of this current imbalance. In addition it was to determine, in a quantitative manner, what was the cause, how serious the problem was in terms of damage or undue wear to the robot and find solutions if possible. It was concluded that most problems could be resolved with a better motor control design. This document discusses problems encountered and possible solutions.

SUMMARY

The four degree of freedom ARID robot, with its unique double motor drive system at each joint exhibits some unique problems. Each of ARID's joints is actuated by two identical motors which are driven by independent drive systems. The two motors are controlled by separate computers in order to impart maximum redundancy to ARID. This is an application requiring very accurate and careful control for proper operation. During testing it was discovered that the motors at each joint were not being equally loaded. It might be expected that two motors driving any given joint would encounter approximately equal torque loads. This turned out not to be the case. Unequal currents, often differing by seven or more amperes, were measured for the motors at Joint #2 (the most heavily loaded of the revolute joints). The question was, whether this was a problem. If so, was it caused by damaged equipment or was it inherent in the system design. The current differences, besides being excessive, were also unpredictable and non repeatable. Tests were run to help quantify and identify the problem. Whether this was a small annoyance or a potential hazard to the reliability or longevity of ARID was the question. Were the motors the correct kind and if not could they be made to work properly?. Tests were run to better understand the problem and to better understand the ARID system. It was concluded that the current imbalance problem was a symptom of inadequate motor control. A design is outlined in this report that if implemented will improve motor control and system performance as well as greatly reduce costs.

TABLE OF CONTENTS

1 INTRODUCTION

The Automated Radiator Inspection Device (ARID) is a four degree of freedom robot whose intended use is the inspection of the space shuttle radiator panels. The purpose of ARID is to navigate a camera over the panels at a precise distance of 24 inches so that computer images can be made and compared with previous ones taken. To maintain maximum safety margins it was decided to provide each of the four joints with redundant motor drives controlled by separate computers. During testing it was discovered that the two motors driving the same joint were not being loaded equally. In other words, although the joint motors were given the same commands, they saw different loads. In addition, the loading was not consistent in that the motor that was more heavily loaded at one time was loaded less at a different time during normal operations. Ideally, the two motors are to operate in concert and carry approximately the same load. If they do not, they could in fact be fighting one another causing continual undue stresses to the joint. This loading problem is similar to that of two drivers moving a heavy load half on one truck and half on the other. The two are told how fast to go and where to stop but they must do it while looking only at their own instrument panel. If each driver is instructed where to go and how fast to move but is given no information about how the other driver is moving, chances are good that the load will be dropped. The current ARID system is operated in a similar fashion. The joint motors are given the same commands and told to go. Neither motor has knowledge of what the other is doing. The system, once commanded to move, then ignores other commands until the motion is complete. It is this very lack of control that is a major part of the problem. In moving the load, if each driver is asked to move one inch and stop and no new command is issued until both have achieved the objectives successful transfer of the load is possible. Repeating the process of taking small steps until the final objective is met is a way of solving this problem. The ARID motor control system is, however not designed to permit small motion without introducing other problems. In the ARID it was found that the current disparity was unreasonably large. Graphs of actual experiments illustrate this situation. During some tests, the load was unevenly distributed but maintained its relationship, such as the case of one truck carrying most of the load. Others showed the load change back and forth between motors. Measurements taken showed that while at some time one joint motor operated at 5 amperes, the other used 12. This seven ampere differential meant that a large torque was being absorbed by the joint. Whether this was a mere inconvenience or reason for concern was the main objective of this undertaking. The ARID robot is constructed with one prismatic and three revolute joints. Joint #1, at the trolley, is the prismatic joint. The joint demonstrating the greatest current

imbalance was Joint #2, the first revolute joint (one closest to the trolley). The main objective of this effort was, therefore, to solve the problem for Joint #2. In solving this problem, the lesser problem of joints #3 and #4 should also be solved.

2 THE ARID SYSTEM

The ARID system consists of the motor control, the arm and the software. Figure 1 illustrates two views of the ARID robot arm .

2.1 THE COMPUMOTOR DRIVE SYSTEM

The Compumotor motor is a precision stepper motor which in conjunction with the Motor Driver, Resolver and Indexer make up the ARID drive system. A block diagram of the Compumotor system is given in Figure 2. For a more detailed description refer to the Compumotor literature. The Indexer is a card which is installed in a slot in the Personal Computer (PC). The PC acts as the host for the system. One PC drives the master while the other the slave. The Indexer communicates with the PC in parallel and in turn calculates and sends pulses and direction information to the Motor Driver. Communications to and from the motor driver is othrwise serial via an RS 232 port. The Motor driver is part of a closed loop system which includes the motor and Resolver. The Motor Driver is microprocessor controlled and provides the voltages and signals necessary to move the motor. The processor allows the user to define the PID (Proportional, Integral and Differential) feedback constants which it uses to define the total system response. The Resolver which is directly connected to the motor shaft provides motor position information which is fed back to the motor drive. It is a very critical and sensitive part of the system. In order to operate properly it must see a precisely calibrated resistor. The company tunes the cable to the resolver before shipment and cables are not to be swapped. This is not a reliable way of monitoring shaft position. The motor system was purchased as an off-the-shelf item and not intended to be operated in a trajectory tracking mode. ARID is in fact attempting to operate in trajectory tracking since master and slave must track one another.

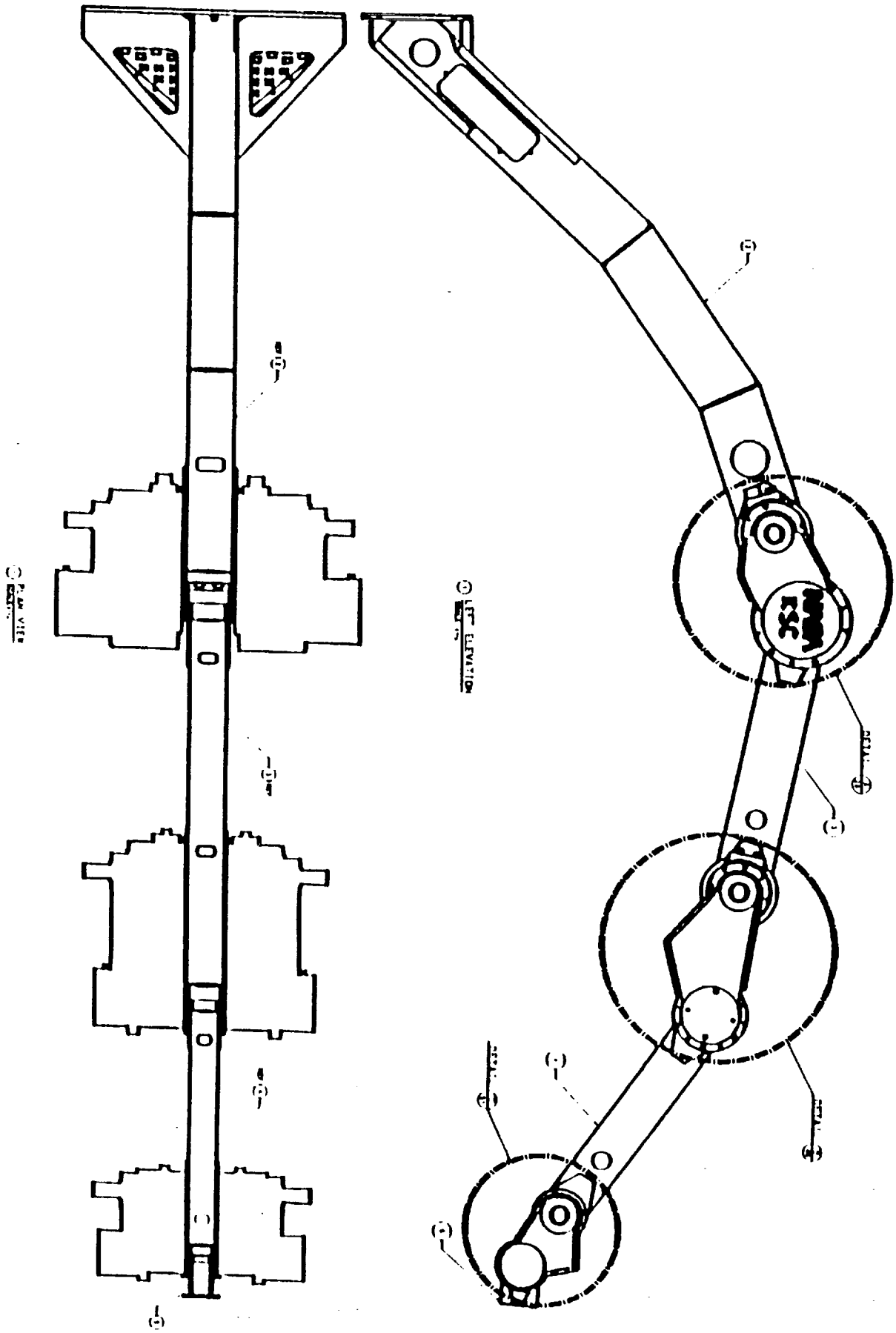

Figure 1. ARID Robot Arm

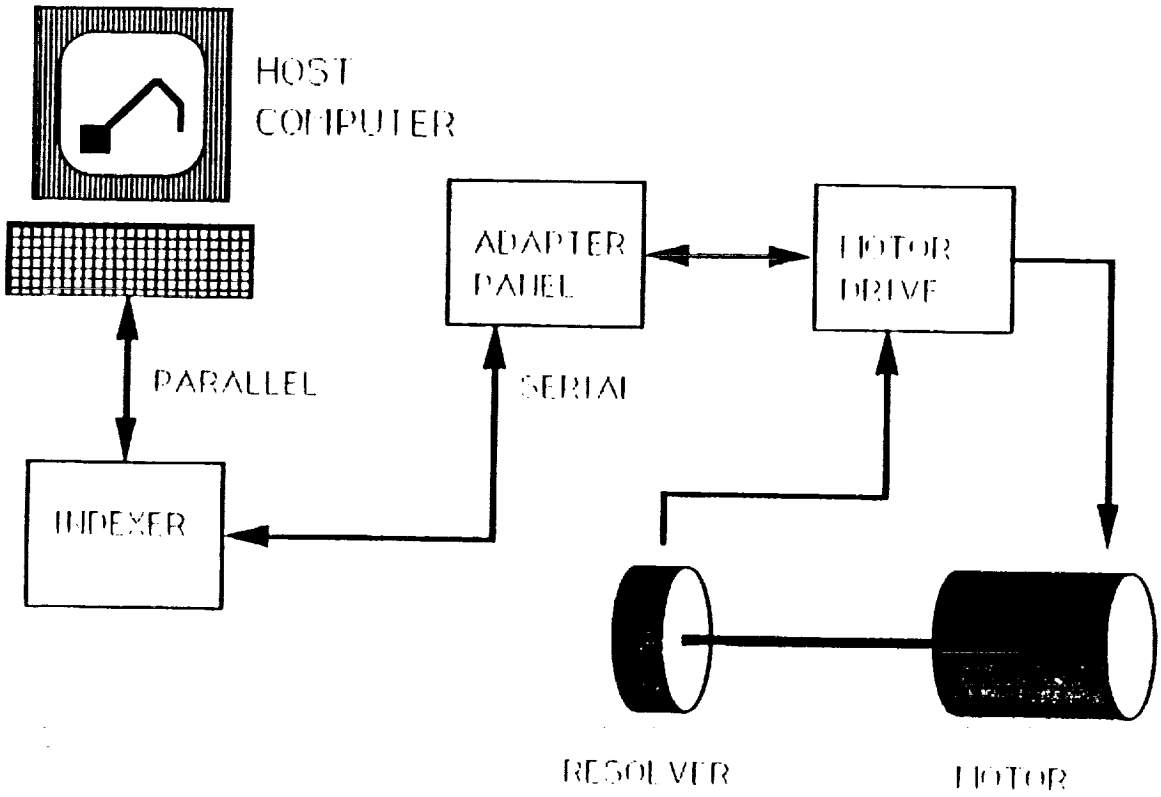

MOTOR DRIVE SYSTEM

Figure 2. Compumotor Control System

This is in effect a closed loop system operated in open loop. In order to drive the motor, the host computer must write a program to the Indexer. This program describes the velocity profile that the motor is to follow. This profile describes a move from one point to another. To move the motor, from rest, is accelerated to a velocity, which it maintains for some computed time then is decelerated so that it stops after having moved a prescribed distance or number of steps. Since the motors do not operate identically when operated clockwise and counterclockwise, this introduces a possible source of error. The velocity of the motor is directly proportional to the rate at which pulses are sent to the motor driver from the indexer. Acceleration is accomplished by increasing the rate of pulses sent. Constant velocity is accomplished by sending pulses at a fixed rate. If no pulses are sent, this implies a stop command. These pulses in effect modify the desired position of the motor as presented to the motor driver. The motor driver is part of a closed loop which controls the motor in a servo loop. The loop is controlled by three constants which are Proportional, Integral and Differential. These constants are most useful when describing a system with constant loading. ARID, however, provides a varying load to the motors therefore the selected values must be a compromise and cannot be optimal. To minimize the timing skew between issuance of drive commands to the two motors, a synchronizing scheme is adopted to hold off the GO to one until both motor systems are commanded to go. This is accomplished by a hardware AND function. The AND gates are mounted on the Adapter box. The Adapter box has little hardware and will not be discussed here. How much timing skew this method actually introduces in the system is not known. Motor control from a positional standpoint is theoretically very accurate. Each motor rotation is controlled by issuing pulses and direction information. Each complete motor rotation requires 5000 pulses therefore extremely accurate positioning should be possible unless pulses are somehow lost. In addition to this great accuracy, the high gear ratio of the drive system, would make the loss of a few counts negligible. This seems not to be the case since the motor disparity is noticeable. This necessitates a more thorough testing of both the Compumotor system and the drive software that was developed to drive ARID. The one unresolvable problem inherent in the system is the serial nature of the system operation slowing down the command flow and motor position monitoring. Although pulses issued by the Indexer arrive at the motor unimpeded, motor position information can only be obtained via serial link.

Once commanded to GO, the Indexer will continue with its operation of sending pulses and direction information and will not accept further commands. This makes it impossible to break into the control loop. An alternative which would eliminate this problem is to design a motor control system without the serial interface bottleneck. To this end the Compumotor motor drive system would

need to be redesigned. Although the Compumotor motors appear to be of very high quality, lower cost dc motors can be used instead. The only real requirements are that the motor have the proper torque and the shaft position be known i.e. with a shaft encoder, which is more reliable than a resolver. This proposed motor system would be interfaced to the host computer via a custom microcomputer control system. In this way system cost could be greatly reduced while at the same time system performance increased. To limit the redesign effort it might be advantageous to maintain the motor and motor drive manufactured by Compumotor. To operate this proposed system, the host issues a stream of motor positions. The motor goes to the most recently issued position. During motor move operations each motor drive system performs self checks and allows the host to read motor position real time. It should be stressed that if another motor system is considered, rigorous system testing should be done to verify system performance before installation on ARID. It seems apparent that the motor control system is the weak link of the ARID robot. The resolver is an analog device whose output must be digitized before it is used as a feedback signal.

2.1.1 MOTORS

The motors used in ARID are Compumotor KH 230 for Joint #1, KH 710 for Joint #2, KH 230 for Joint #3 and KS 210 for Joint #4. They are all high precision stepper motors. For more information refer to the appropriate Compumotor manuals. Motor control is accomplished via IBM Personal Computer (PC). The PC sends ASCII Commands to a Compumotor PC23 Indexer card which is installed on the computer backplane. The PC23 in turn communicates with the motor driver via the Adapter Box. These motors, in conjuction with the Compumotor system, were designed for accurate positioning. These motors are expensive and not ideally suited to the ARID applicaiton. With enhanced software or a more suitably designed control system these motors should be made to work more effectively.

2.1.2 HOW A MOTOR IS COMMANDED TO MOVE

The motor may be commanded to move in a variety of ways (refer to Compumotor manuals for more detailed description). The motors are instructed to move to desired positions or at desired velocities. The commands are sent from the host to the Indexer card as a series of ASCII characters. These are

decoded into pulses, pulse rates and direction information. This information is sent to a control system to actually move the motors. The motors, being of very high precision, if commanded and loaded equally should track one another very closely. If two motors are driven equally and do not respond the same, one or both may be losing or gaining counts. This must be verified by more thorough testing and positions and velocity information collected by external means. This is needed to verify if the configuration as designed is feasible. The present ARID system is restricted to operating point to point. This is a limitation imposed by the current Compumotor system. Each of the two motors on the same joint are commanded to move independently of the other. If there is some preload on the linkage between the two motors one motor will see a greater load than the other because of the torsional spring inherent in the system. There is no way in the current system application that this imbalance is being monitored or compensated. Some changes could be made to the initialization software which might alleviate the severity of this problem. Since software is the most flexible part of the design, including some software changes is the easiest and first thing that should be attempted to try to reduce the preload problem.

2.2 THE ARID JOINTS

2.2.1 THE ARID PRISMATIC JOINT

Joint #1 is the least compliant of the ARID joints because the trolley is driven by motors through a rigid gear drive system Figure 3 is a schematic model of joint 1. This joint, although different, demonstrated a similar type of current imbalance problem as the other joints. During normal operations there were unusual sounds emanating from Joint #1 that at times seemed to indicate that the motors were either slipping or the trolley was binding. The stiffness in the spring between the motors of Joint #1 is greater than that of the revolute joints because the motor is connected to the pinion via a 45:1 planetary gear system. The danger of causing severe damage to the hardware seems very real here if the motors are not properly controlled. More testing is needed to quantify the actual stressing. Estimates can be made by knowing the motor characteristics, current imbalance and gear ratios. The two pinions engage the same steel rack. This configuration has very little compliance. In an effort to introduce some compliance at this joint, the PID controller constants to the motors driving this

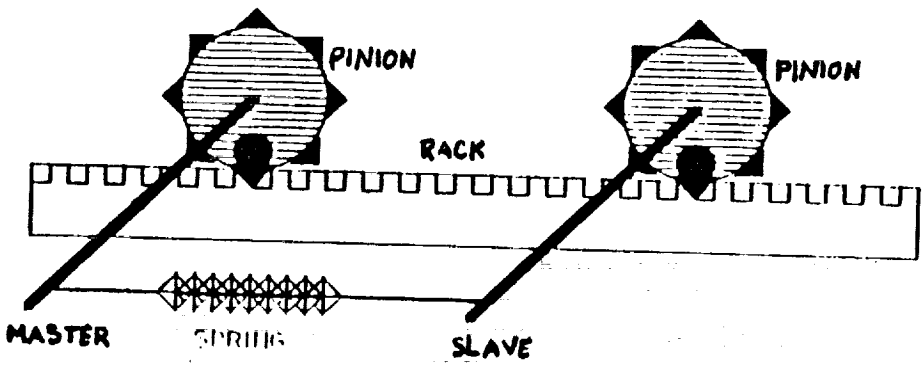

ARID PRISMATIC JOINT

Figure 3. ARID Prismatic Joint

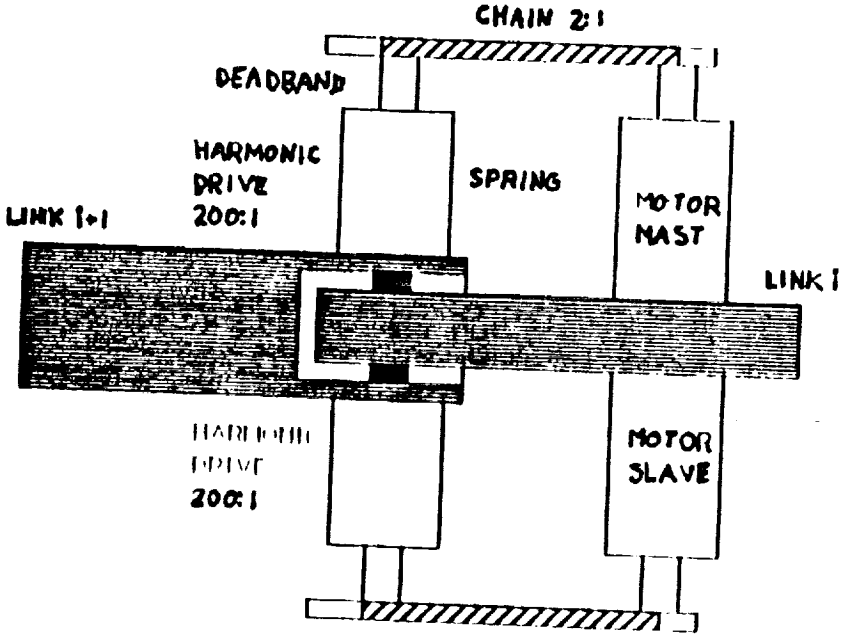

Figure 4. ARID Revolute Joint

joint were made to be different so that one motor would have some give relative to the other.

2.2.2 THE ARID REVOLUTE JOINT

The three ARID revolute joints are all very similar. Figure 4 is a diagram of the revolute joints. Each is articulated by two Compumotor precision stepper motors. Each motor drives the joint via a 2:1 chain drive and a 200:1 harmonic drive for Joints #2 and #3, while Joint #4 uses 160:1 harmonic drive . This gear reduction between the motor angle and link angle in addition to the great accuracy of the motors, makes it theoretically possible to control the joint positions with great accuracy. Although Joint #4 is slightly different than #2 and #3 in that a less powerful motor and smaller gear ratio is used the effective operation is very similar. There are two identical drives allocated to each joint. When the master rotates clockwise its slave theoretically moves in an identical fashion counterclockwise and vice versa.

The motors are commanded to move a precise number of steps each following a velocity profile. Since the motor control is so accurate and the gear ratios so large, the motors should always end up at the correct place at the end of a commanded move and so should the corresponding joints. This is, however, not the case as evidenced by measurements taken and observations made this summer. Since the master and slave computers do not communicate directly with the host computer or with one another, it is possible that they do not drive the motors precisely the same way or at precisely the same time. A mechanical model of the joint is given in Fig. 5. The deadband and friction are nonlinear effects that make the motor loading hard to predict.

2.3 OVERVIEW OF SYSTEM OPERATION

Assuming the system begins at rest, and it is desired to move one of the ARID joints. The motor must be moved from some starting point to an ending point. The master computer sends a series of commands in the form of ASCII characters to the Compumotor PC 23 Indexer. These commands are a program which are used to tell the motor at what rate it should accelerate to what velocity to move then the deceleration rate. It is the function of the Indexer to decode these commands into pulse and direction information which it sends to the motor driver.The motor control loop then drives the motor to the desired position and

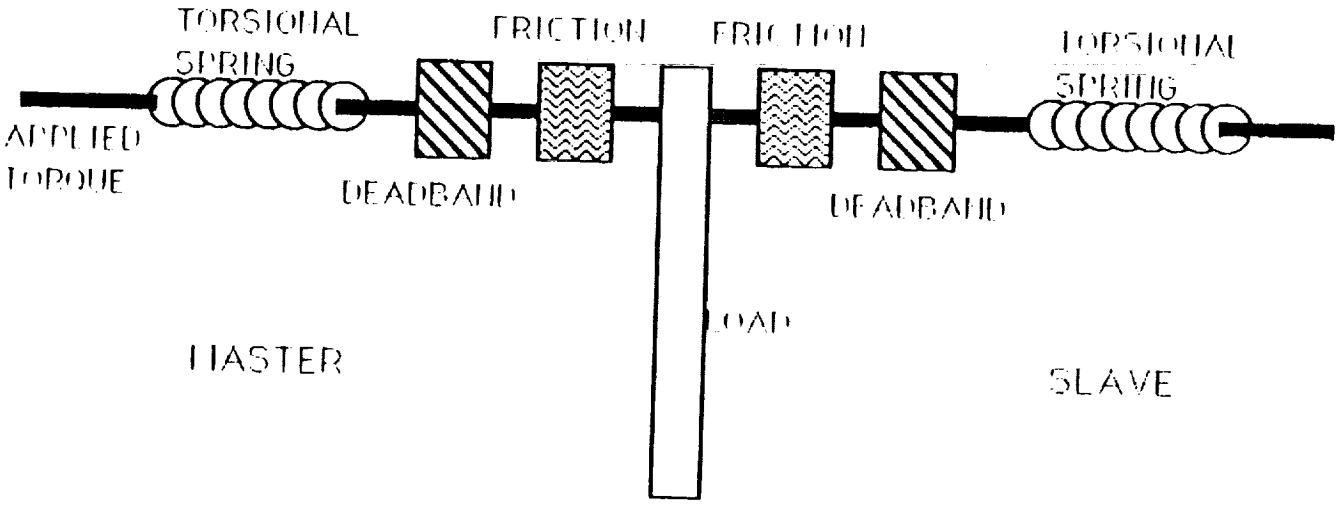

MECHANICAL MODEL OF JOINT

Figure 5. ARID Joint Model

stops. Only at this time can the next comand be received. A major drawback of this operating scheme is its point to point operating mode. Another is the difficulty in receiving real time motor position data. These are bottlenecks in the existing ARID system.

2.3.1 OBSERVATIONS

In order to become more familiar with the operation and anomalies of the system, the robot was run in a normal manner and its operation closely observed. Some unpredictable sounds were heard emanating from the various joints. There was also unexpectedly large amount of vibration. These symptoms seemed to indicate that somehow the two motors were not cooperating in their transit from point to point, there was something binding or a combination of the two. The sounds and vibrations were not consistent nor limited to any one specific joint. On some occasions one of the revolute joints would actually ratchet the harmonic drive. This loses positional relationship between master and slave as well as cause potential damage to the transmission. Since there is no feedback between master and slave, the system might continue to operate instead of emergency stopping. This is not only an inconvenience and unreliable in operation but could result in permanent damage to the system. If a joint actually ratchets, the computer has lost position information about the joint angle. If this condition is not detected quickly, and corrective measures taken, severe damage to the robot could result. Consider for example that a joint is commanded to make a long move. If near the beginning of the move, ratcheting occurs, there is the possibility that continuing the operation could go undetected and damage the joint. Tests were performed to monitor motor currents on joint #2 while the ARID end effector was loaded and unloaded. Loaded with 75 pounds, the revolute joints ratcheted. Had both sides been carrying about the same load this should not have happened since this is within the ARID load carrying specifications. This test was not repeated. When moving the prismatic joint, the trolley, on occasion would bounce as if there was a bump on the track. This could have an effect on the robot calibration especially over a period of time. Upon closer inspection, no bump was found on the track. It was suspected to be the result of the motors being driven unevenly or caused by a frictional problem. This brings up the possibility that one or both motors were gaining or losing counts relative to one another. This error did not correct for itself and appeared to be cumulative. After one of these bumps the system appeared to function "normally" for a period of time before the symptom would be observed again. It was discovered upon investigation that the two motor drives were assigned different

Proportional, Integral and Differential values. This fact causes the two motors to respond differently which in effect introduces a sort of software compliance. This compliance was introduced to reduce the more serious problems experienced when both motors were driven with the same PID values. The jumping phenomenon was reported to have occurred even when one of the motors was totally disengaged from driving the trolley. This indicates a possible static friction problem with the track. Tests should be conducted to isolate and correct this problem.

3 THE CURRENT IMBALANCE PROBLEM

Ideally, when two motors are driven at the same time in the same way and are both driving the same load, i.e. see the same torque, they should draw the same current. Tests performed on ARID, however, showed that currents varied in excess of seven amperes between the two motors driving Joint #2. This seemed to indicate that the two motors may not have been at the same angular position and or velocity or that some preloading of the harmonic drive or other mechanical component existed. To further complicate matters, the currents seemed at times to fluctuate where first the master was doing most of the work then the slave would do more. While one was seeing an increasing load, the other experienced a decreasing load. To better see the problem, tests were run to collect current and position data for both the master and slave. Data collection was quite cumbersome for the Compumotor system since the link is serial. This is another reason why the Compumotor system is not optimally suited to the ARID application. It was found that not only did the currents vary, but that sometimes the master did the driving while the slave coasted and at other times the reverse was true. When motor position was monitored, a deadband in the joint between the motors was discovered. One motor would respond to a seemingly increasing load while the other to a decreasing load, at the same time. Other tests running under identical situations showed that although one motor carried the majority of the load, both currents were increasing and decreasing at the same time. Motor position differences seemed to remain relatively constant until the motors reversed direction. With motor direction reversal the motor position difference changed sign but maintained the same relative position difference. This seemed to indicate the existence of a deadband or loose torsional spring in the connection between the motors. Joints #2 and #3 showed differences of +10000 or -10000. This is still a puzzle as to what number is

actually being read. From data collected, the position storage is done by 16 bit devices . This means that 10000/65536 = 0.15258.. rotations or about 9 degrees between the two motors. Joint #4 displayed difference of about +4000 to -4000. These number seems too large and needed verifying what this actually means.

3.1 TESTING

To identify the cause of the problem, a series of tests were run to help locate the problem area. Early tests were run to observe the current imbalance phenomonon.

Plot #1a is current versus time of the master and slave motors on joint #2. Joint #2 was moved from 125 degrees up to 25 degrees and back to 125. It can be seen that on the way up (from 125 to 25) both master and slave currents are increasing. This seems reasonable since as the arm raises it presents a greater torque load at the joint. The currents although not equal, were increasing together. This indicated that they were both trying to do the same thing. This much was predictable. When the motors changed direction and began to move downward, the slave current dropped to below that of the master. This can be explained by preload at the joint. That is the slave saw the greater load at the start because the slave motor was ready to move the joint while the master still had slack. When the direction changed, it was the master that bore the brunt of the load. Since the joint was lowering, the currents decreased as expected. The slave current, however, bottomed out and the master current increases again. This did not seem right since the slave has in effect let go and the master had to do the work of lowering the arm. When the joint reached bottom (125 degrees) the master "let go" and it was the slave that did all the lifting. This time the current disparity was even greater than it was on the first transition from 125 to 25 degrees. A torque preload at the joint is not sufficent to explain this behavior as evidenced by Plot #1b which is anothe test run the same way as that for Plot #1a. In Plot #1b, both master and slave started out equally loaded, but after a change in direction their behavior becomes very erratic and unpredictable. Other tests run gave equally unpredictable results. The system seemed to operate in a chaotic fashion. The only consistency was the system's inconsistncy. If the system in fact exhibits chaotic behavior, then proper operation is only possible with feedback. Attempting to solve the problem with torque control should prove unsuccessful because normal system loading is unpredictable. That is to say that even under normal operation, the load can vary within tolerable limits without cause for alarm. The two motors could be seeing different loads due to

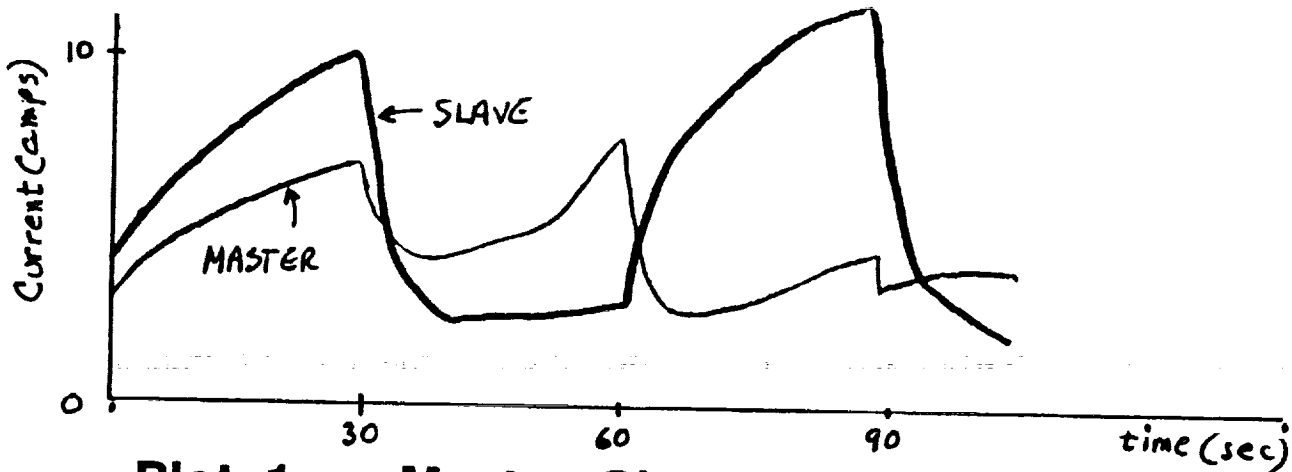

Plot 1a. Master Slave Currents Joint#2

Plot 1b. Master Slave Currents Joint#2

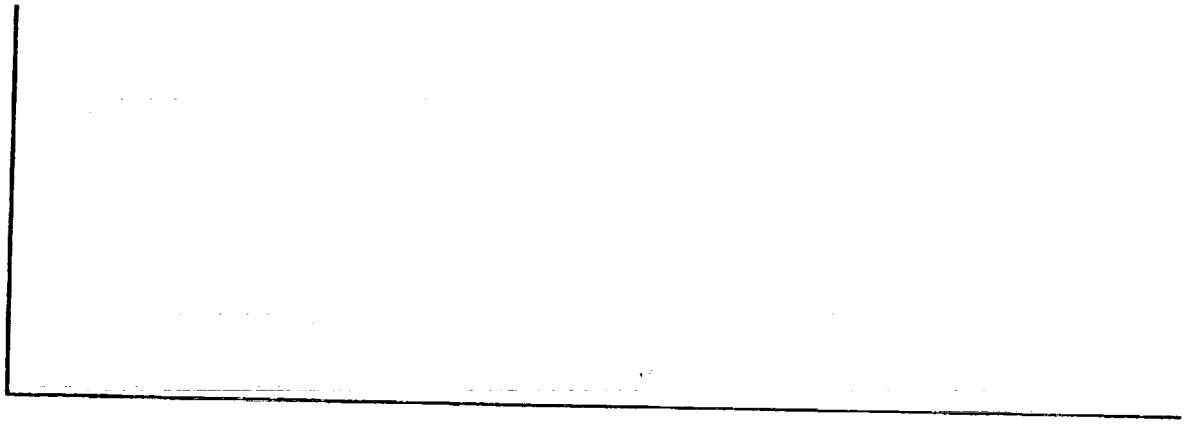

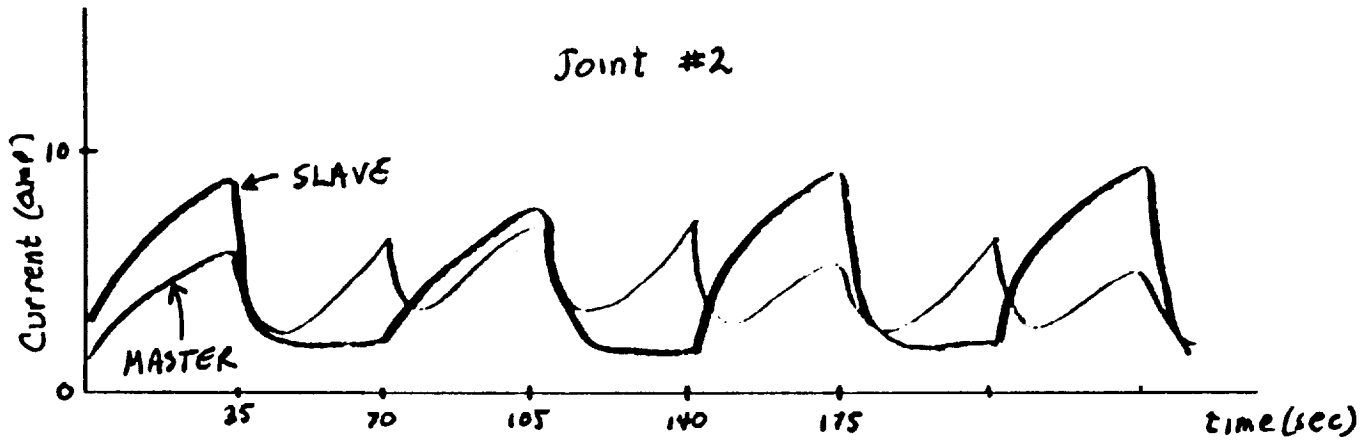

Plot 2a Master Slave Currents Joint#2

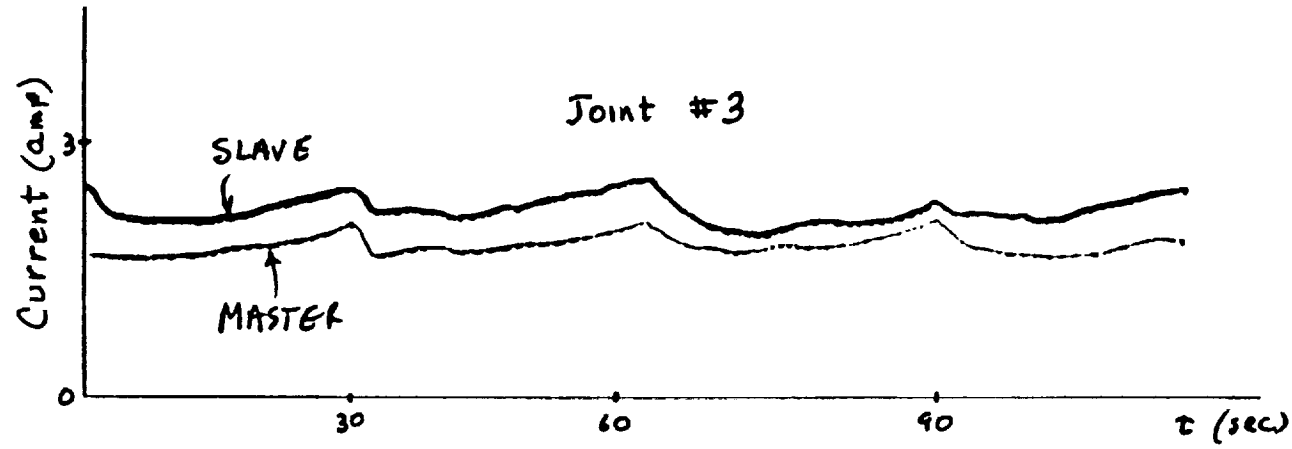

Plot 2b Master Slave Currents Joint#3

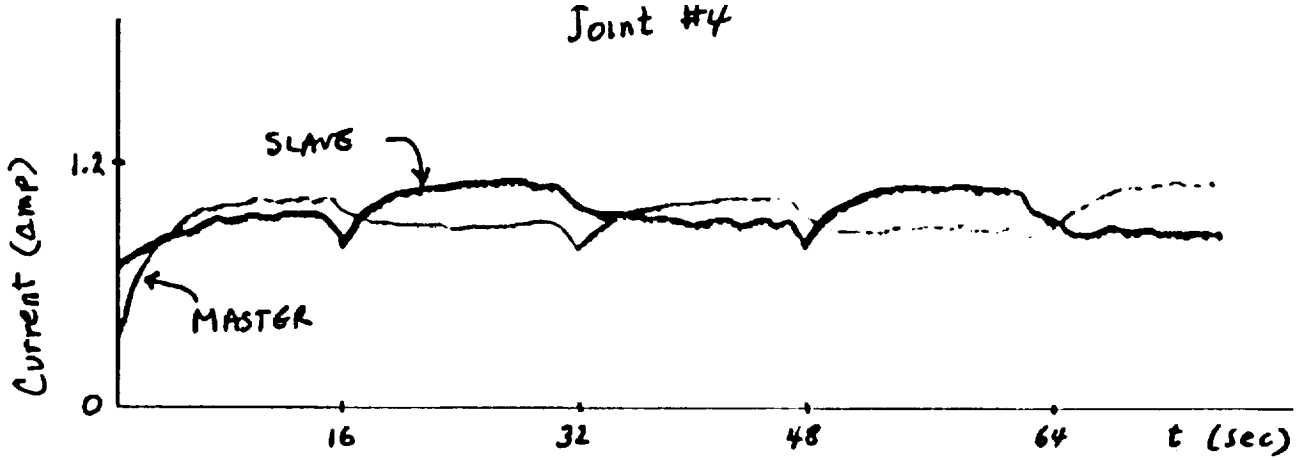

Plot 2c. Master Slave Currents Joint#4

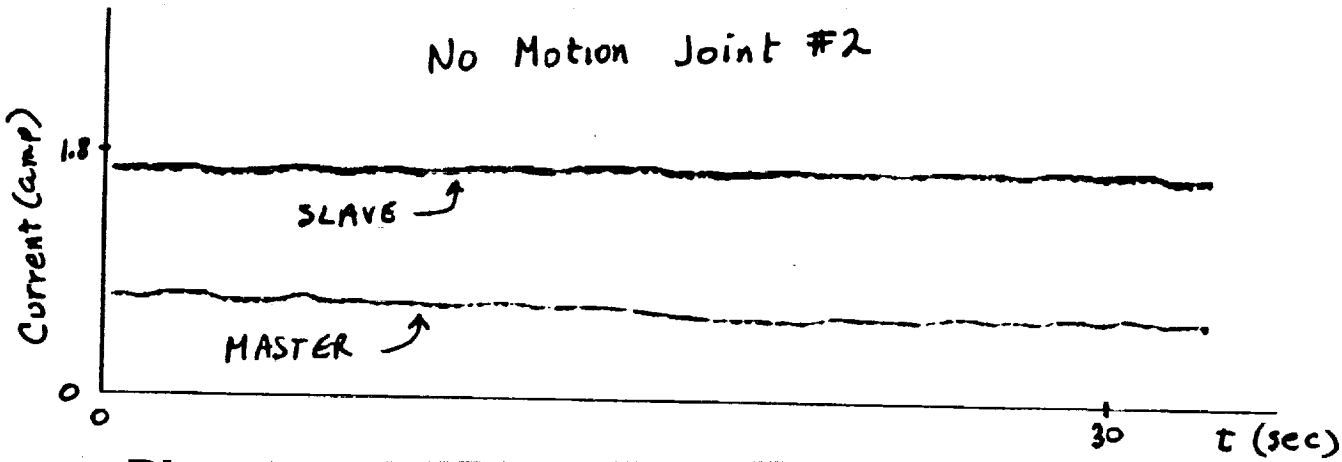

Plot 3a. Master Slave Currents Joint#2

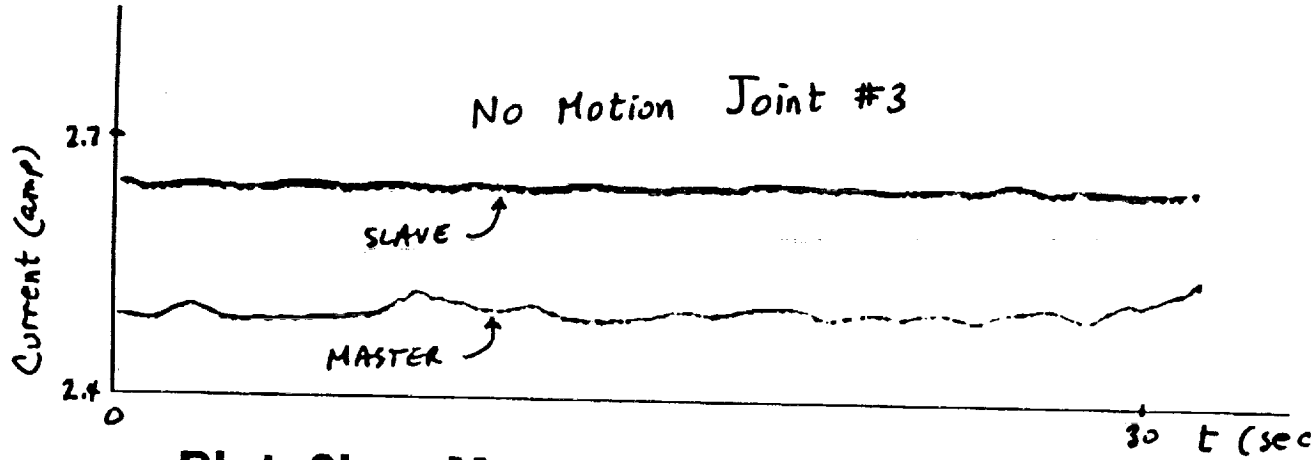

Plot 3b. Master Slave Currents Joint#3

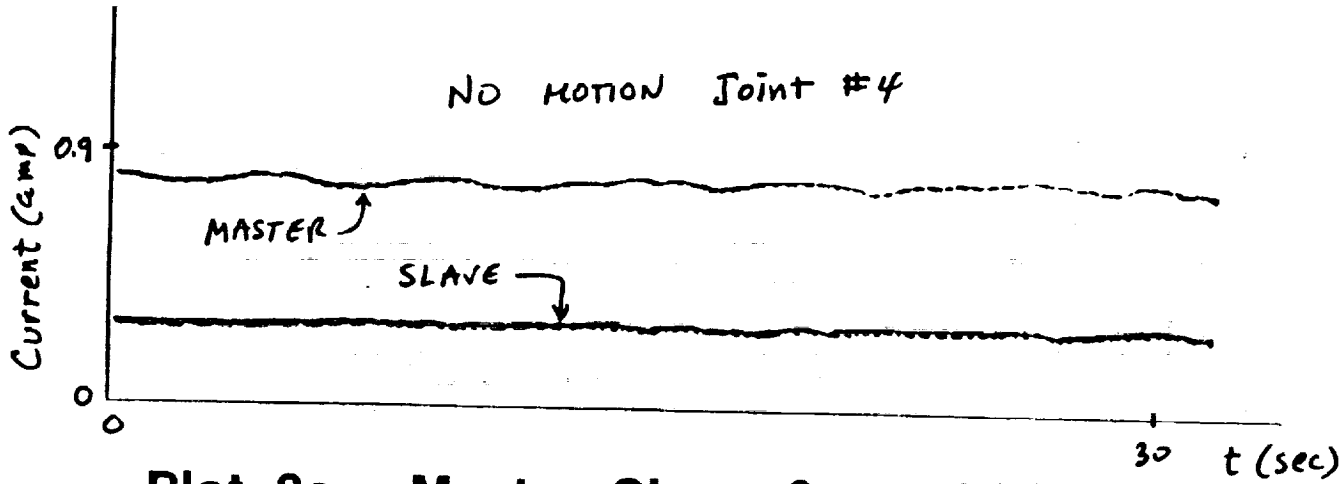

Plot 3c. Master Slave Currents Joint#4

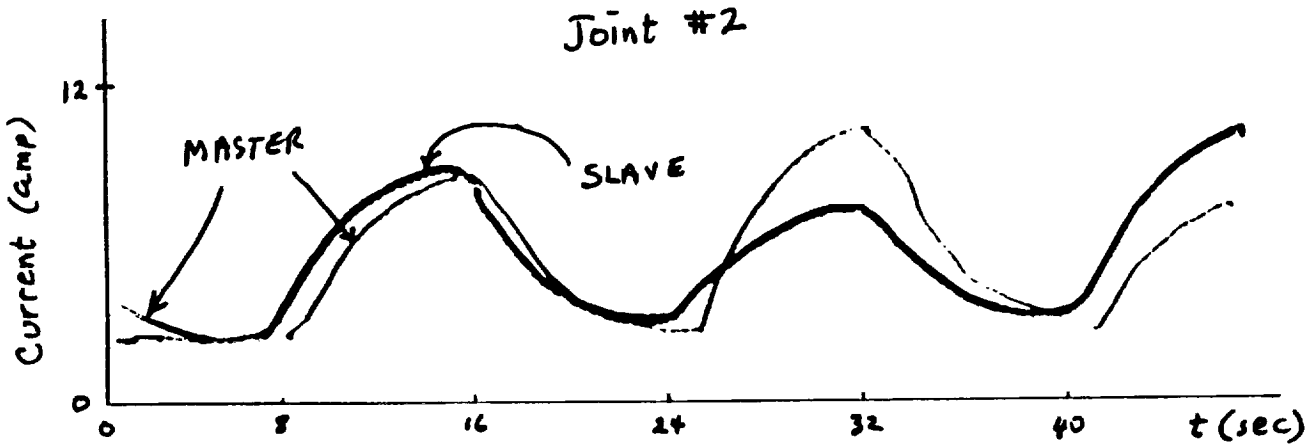

Plot 4a. Joint #2 Test

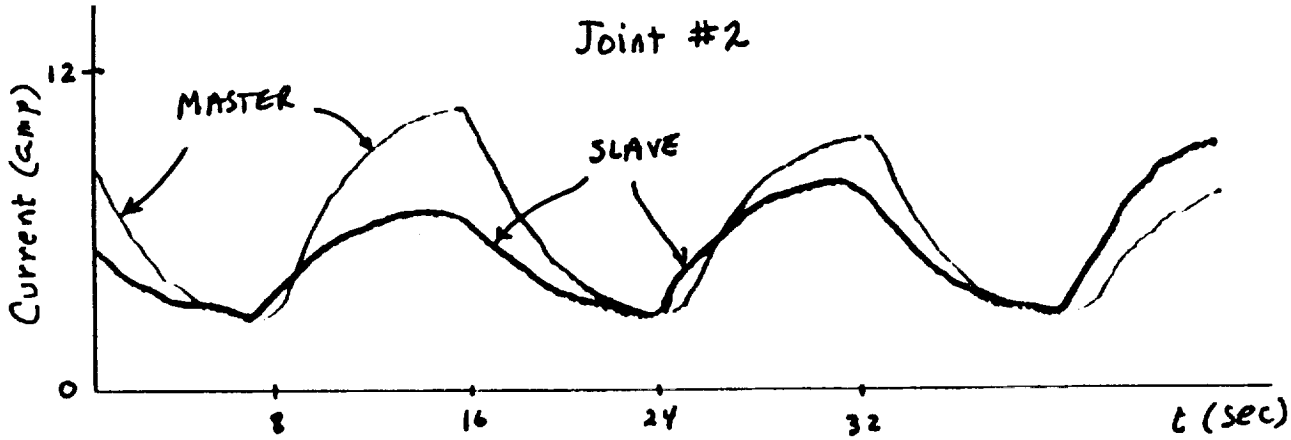

Plot 4b. Joint #2 Test

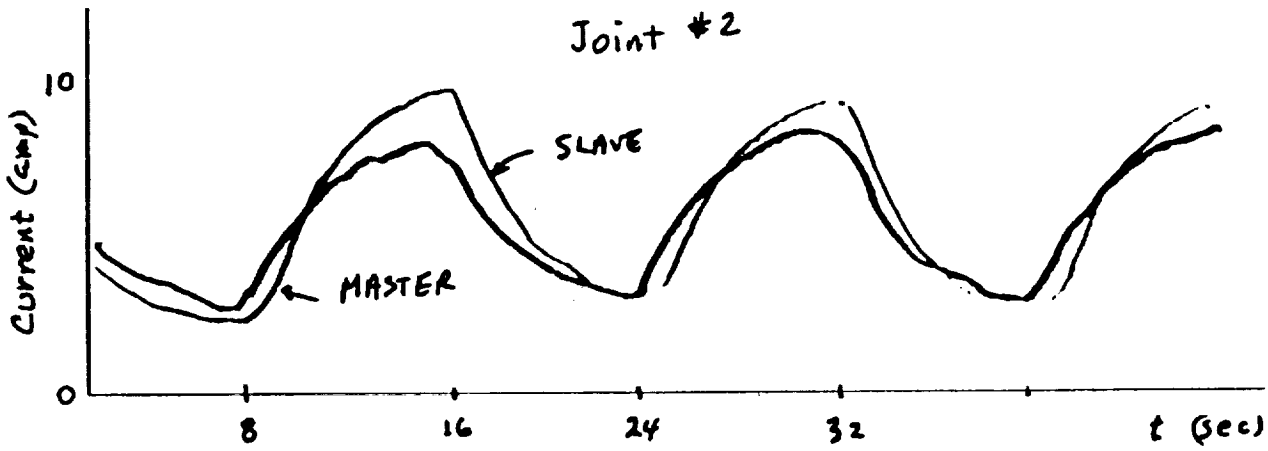

Plot 4c. Joint #2 Test

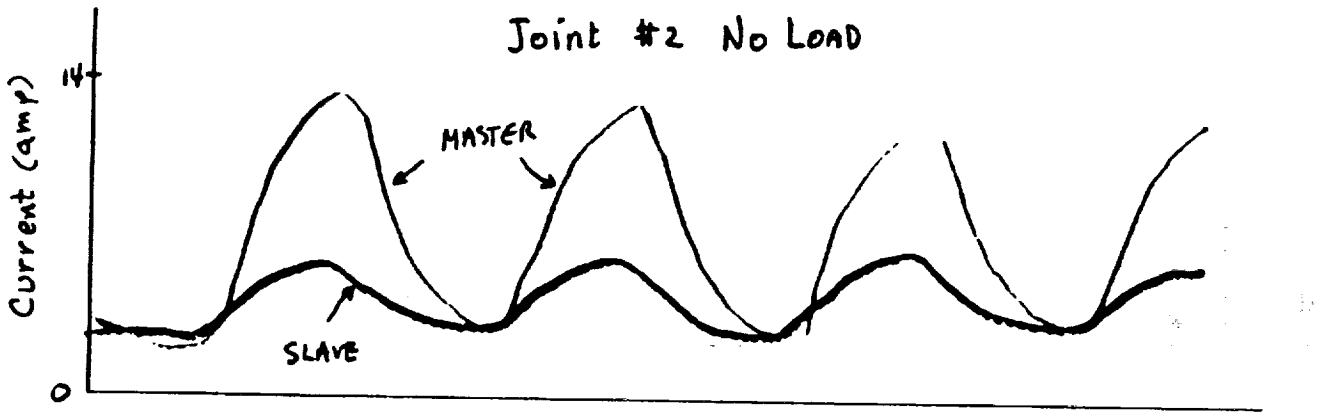

Plot 5a. Joint #2 No Load

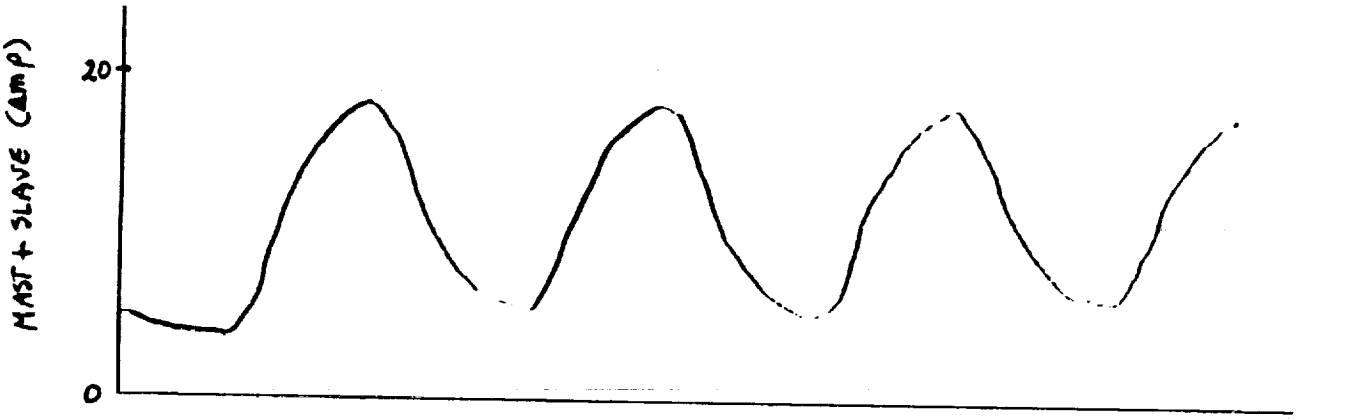

Plot 5b. Master + Slave Currents

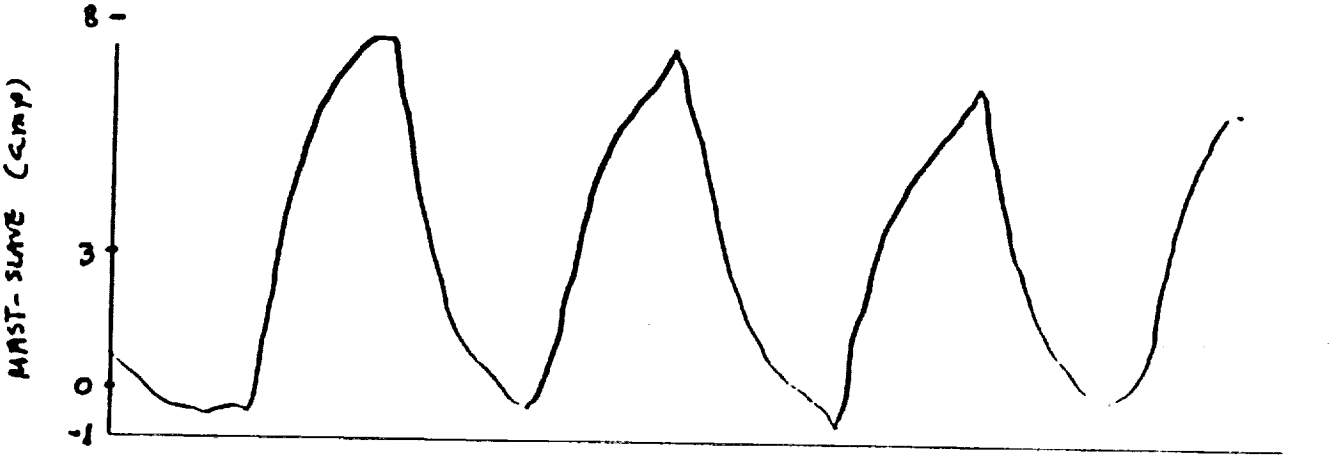

Plot 5c. Master - Slave Currents

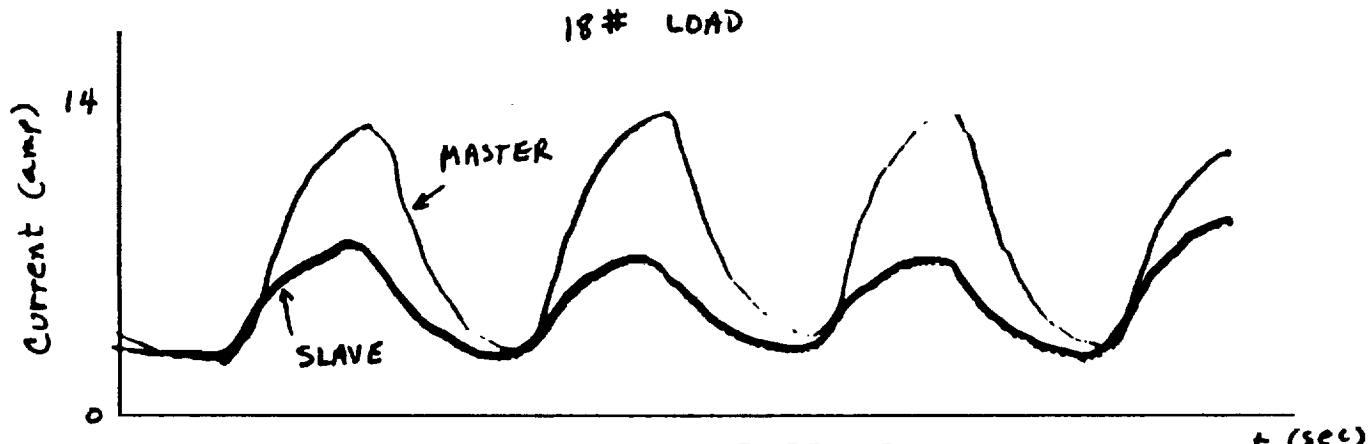

Plot 6a. Joint #2 No Load

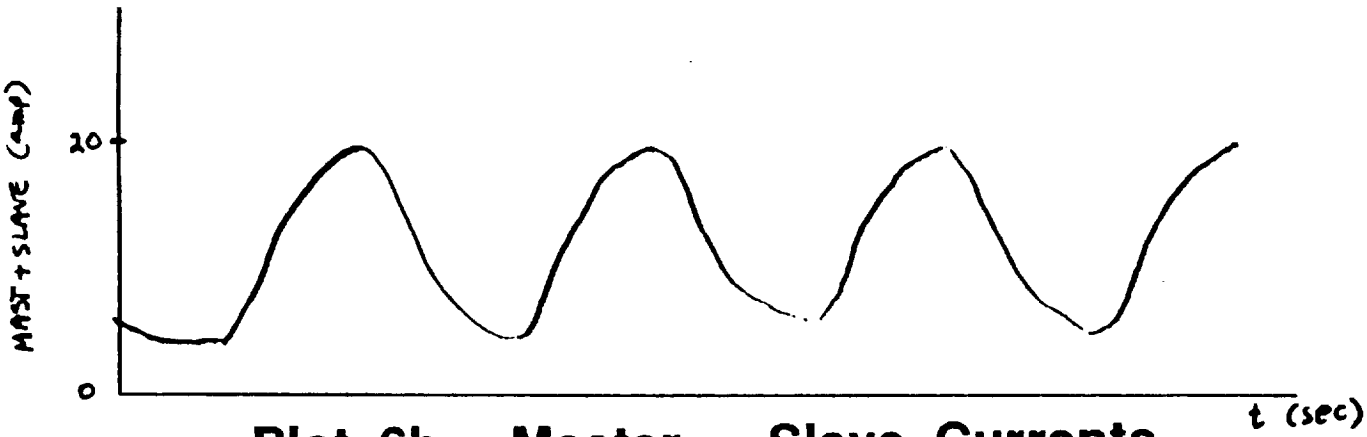

Plot 6b. Master + Slave Currents

Plot 6c. Master - Slave Currents

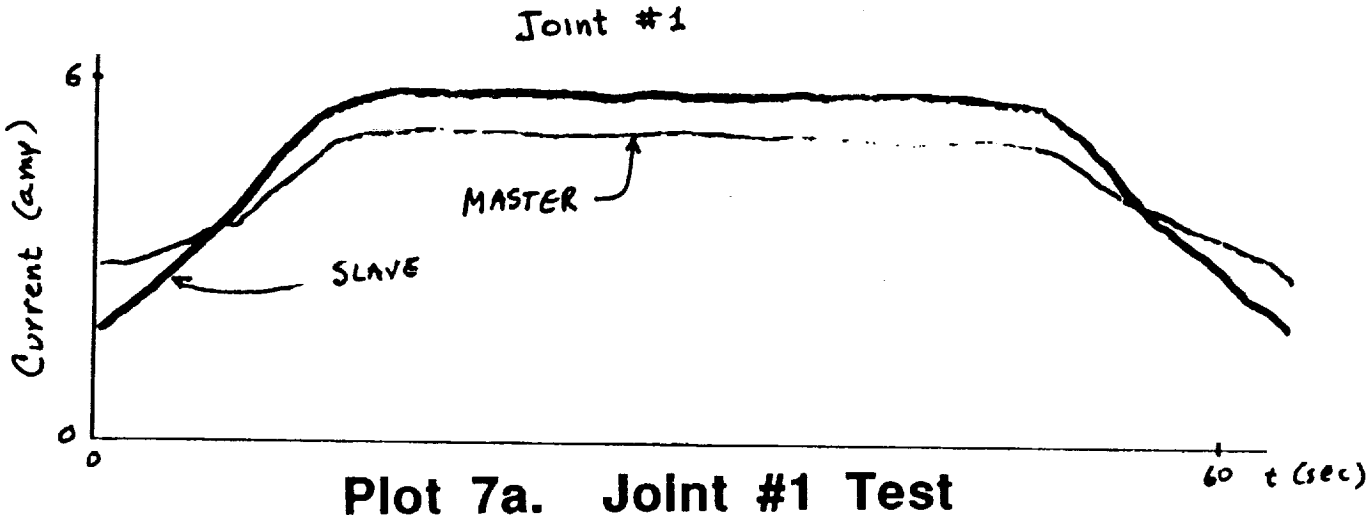

Plot 7a. Joint #1 Test

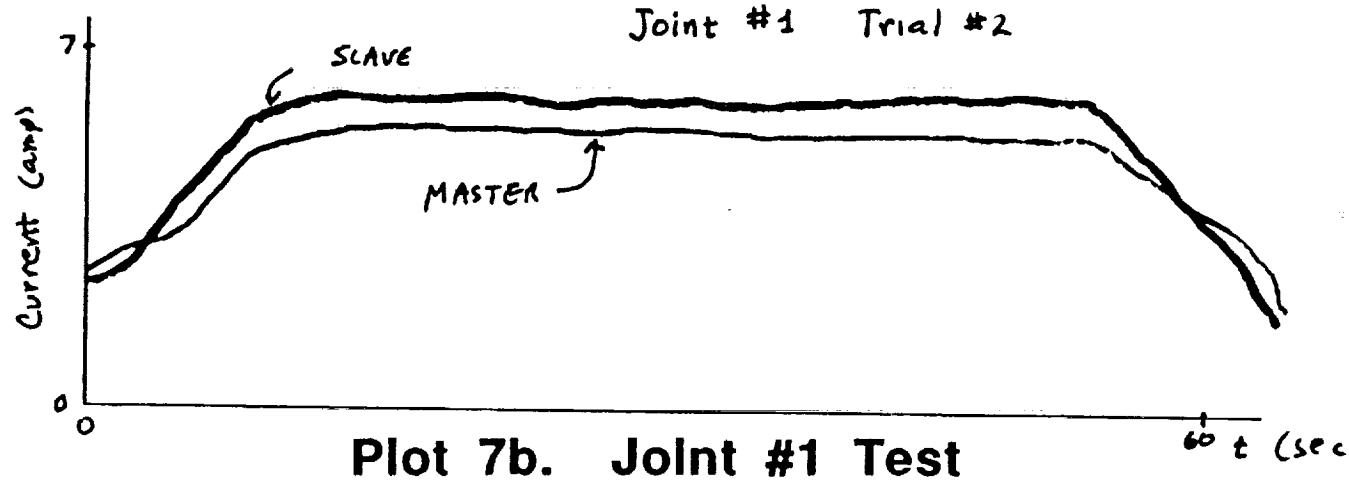

Plot 7b. Joint #1 Test

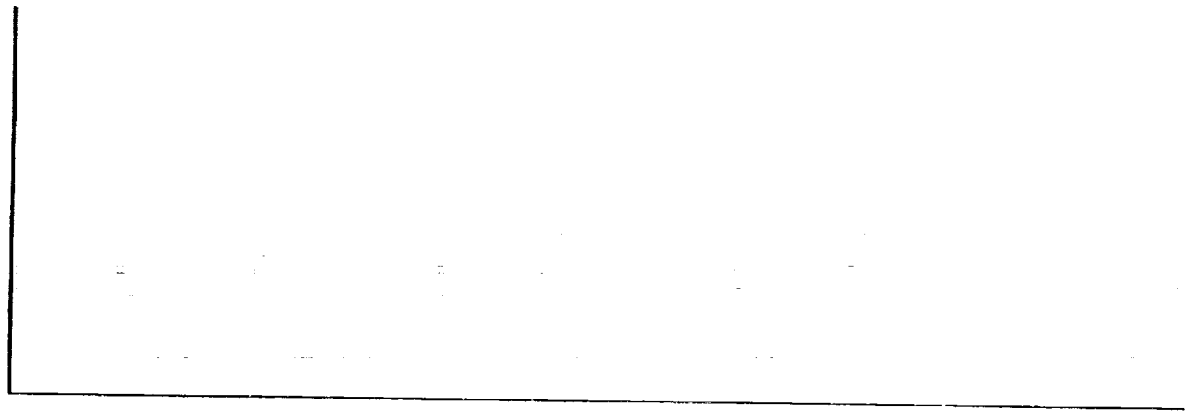

ordinary frictional forces inherent in the system. Various tests were run without consistent results further indicating that some nonlinear force is at play. The following are plots of tests actually run. Plot 2a shows current load on Joint #2 while the joint was articulated. Plots 2b and 2c are similar tests for joints #2 and #3. Plot 3a, 3b and 3c where a no motion current test. The one amp difference at joint #2 seems acceptable, Joint #3 showed a mere 0.2 amps but Joint #4, the smallest joint had a 0.5 amp differential. Plots 4a 4b and 4c were tests run consecutively with varying results. Worst case for these tests was about 5 amps. Plots 5a, 5b and 5c illustrate a case of great imbalance. During this test currents varied by nearly 8 amps. Plot 6a, 6b and 6c show the effect of adding an 18# load at the end effector. It seemed that the additional load was taken up for the most part by the relatively unloaded slave. Current differences dropped slightly to below 7 amps. Plot 7a and 7b is data taken at joint #1. Current imbalance is small but notice the reduced rate of acceleration and deceleration of the master. This is most certainly an effect of the different PID values.

It was suspected that torque preload was the main problem. To prove or disprove that torque preload was in fact the culprit, it was decided to remove the drive chain from the master motor on Joint #2. In so doing, the slave was left to drive the link by itself. The test was to move Joint #2 in 2 degree steps from 90 degrees to 118 and back to 90 then repeat the cycle. In addition to the link, the harmonic drive of the master link was being back driven. Back driving a harmonic drive is an undesirable operating mode if not carefully performed. Since the input of the harmonic drive was not loaded, this operation was not dangerous to perform. Testing of the loading effects of the back driven harmonic drive should help shed some light on the current imbalance problem. It seemed that the back driven harmonic drive should present a constant load, it did not. The variable loading effects can, however, be explained by a static friction model.

To explain this in simple terms consider the application of a torque on the input of the harmonic drive. When this torque is small the output doesn't move, compliance in the joint takes up the torque and acts as a torsional spring, therefore the load increases with applied torque. As torque is increased, the output shaft, which was free to rotate, but did not because of friction, begins to rotate thereby relieving some of the load on the torsional spring. This reduced load is felt at the input (the actual driving force) and loading effects on the driving motor are reduced. This continues until the driving torque is less than the frictional forces experienced and the output shaft stops rotating and the harmonic drive again begins performing like a torsional spring. This "slip and stick" action is similar to the pushing of a piece of chalk across a blackboard.

The unpleasant sound heard is because of this slip and stick. This nonlinearity increases the difficulty of load prediction and makes the feasability and reliability of ARID questionable in its present configuration. Proper lubrication and track adjustments might reduce the slip and stick problem. The surprising thing about this test was that when the current at the unloaded motor was observed it was not constant as expected. The currents instead varied from less than 0.5 to over 2.5 amperes. This current phenomenon repeated for the unloaded motor. Another thing to note is that if one motor is disconnected while the other is not, there is a backdriving of the harmonic drive of the undriven side. This backdriving is actually taking place to some extent even while both sides are being driven simultaneously. This may not be a problem but if it is, it may not be resolvable unless some greater interaction between the master and slave sides is introduced in the ARID system. One modification which might alleviate some of the problems requires a closer control of the motors by a more direct interaction between the ARID software and the Compumotor drives. This should be accomplished by the redesign of the Compumotor drive system. this can be accomplished by replacing the current Indexer with a custom system and somehow tapping into the Driver. Software can be properly written to maintain a very high degree of redundancy and safety while accomplishing this feat.

There is no independent way of measuring actual joint angle. Plans are under way to put shaft encoders at the joints for this purpose. Some way of monitoring this discrepancy is highly recommended for reliable system operation. This is especially true in case of some system failure.

3.2 GENERAL IMPROVEMENTS

Since the torque produced by a motor is proportional to the current, the torque imbalance can easily be estimated for each joint. This imbalance stresses the joint and could fatigue and ultimately lead to structural failure. This problem may not be so severe at the revolute joints because the harmonic drives have some compliance. This compliance allows the two motors to operate differently while still within acceptable limits. One of the problems which was observed was largely due to the fact that the motors did not start at the same point. When the system is first turned on there is no provision made to check if there is any stress on the joint. This is a synchronizing problem which should be tops on the list of things to be corrected.

When the robot is synchronized a ramp and microswitch arrangement is used. Since this ramp and microswitch is located at the joint, a deformation of the switch resulting in a link error angle results in a motor error 400 times as great. A similar switch placed at the motor or the use of a shaft encoder at the joint can easily rectify this problem. Probably related to this problem, the two motors synchronizing to different positions may cause enough angular displacement to result in a current imbalance. This imbalance could be minimized if a small routine is added to the ARID software which adjusts one motor relative to the other so as to minimize the current imbalance. The software can be written so this adjustment can be done manually or automatically. If the problem is related to the initial synchronization, this addition may greatly reduce the symptom of current imbalance. If this does not solve the problem, there may be some drift in the motor positions. This may be due to the Compumotor system, or due to the way the motors are commanded to operate. A method for attempting to synchronizing the two motor drives already exists in the ARID drive software. The accuracy of this method must be verified. It seems that even under best circumstances there will be a time skew between when the two motors begin to move. In addition, the profile of the motor motions must match very closely or the motors may fight one another. It was found that there seemed to be a deadband or backlash between the two motors, this was observed when the motors were told to change direction. Data sampling is at a slow rate, in the order of one sample per 1.2 seconds. This is inherent in the Compumotor system design and makes system monitoring difficult. For a better view of what is really happening, more extensive testing must be performed by collecting data at higher rates. For proper operation the motors must track one another both positionally and in velocity. Motor position and velocity must be monitored independently to verify that the motors in fact start together and no slipping of the motors occurs. If the motors are monitored sufficiently fast for position alone, the velocities will automatically be very close. During actual ARID operation some feedback between the master and slave should be included, to ensure proper tracking, taking care not to defeat the purpose of the redundancy. With proper motor control, which seems difficult in the current system, the current imbalance problem should be eliminated or at least greatly reduced. There will always be some imbalance due to the unpredictable nature of the system friction and some residual preloading but this should be well within acceptable limits if proper monitoring is included in the system design.

For increased system reliability it seems essential to reduce loop delays and enable more direct control on the system. The Indexer interface between the computer and the drive motors should be eliminated or replaced with something enabling a closer direct interaction with the motor. The reliability of the motor

control or lack thereof is the most critical single item needed for a reliable ARID system.

3.3 CUSTOM MOTOR CONTROL SYSTEM

For more reliable operation, ARID requires a closed loop motor control system capable of quickly responding to continually changing commands. Such a system requires direct interface with the control loop as well as feedback between master and slave. Motor control is the heart of the ARID system and must function with a high degree of reliability. The motor control should be flexible since the loads seen by the motors vary unpredictably. Control is the most important single factor of the proposed system. The system receives trajectory data and information of the other motor as its inputs. The data can be monitored at a high rate allowing rapid and accurate response. Each motor is driven by a microprocessor controller which also maintains a history of the motor operation. There should be one such system per motor. Each system is interfaced with the host computer in a memory mapped fashion in order to permit maximum system operating speed and accuracy. With such a system the host issues position information and is able to read motor status real time. A simplified block diagram of such a system is shown in Figure 6. The above described system can be designed and built with lower cost motors than the current system. If it is desired to keep the existing motors on ARID then a cost effective approach which is recommended here is to replace the Indexer with a custom microcomputer based interface. This method should enable the motors to be integrated into the control loop as well as enable the ARID system to operate in a trajectory tracking mode. In general, the motor system should be controllable and observable. The motor system proposed here will be useful in ARID as well as future robot applications.

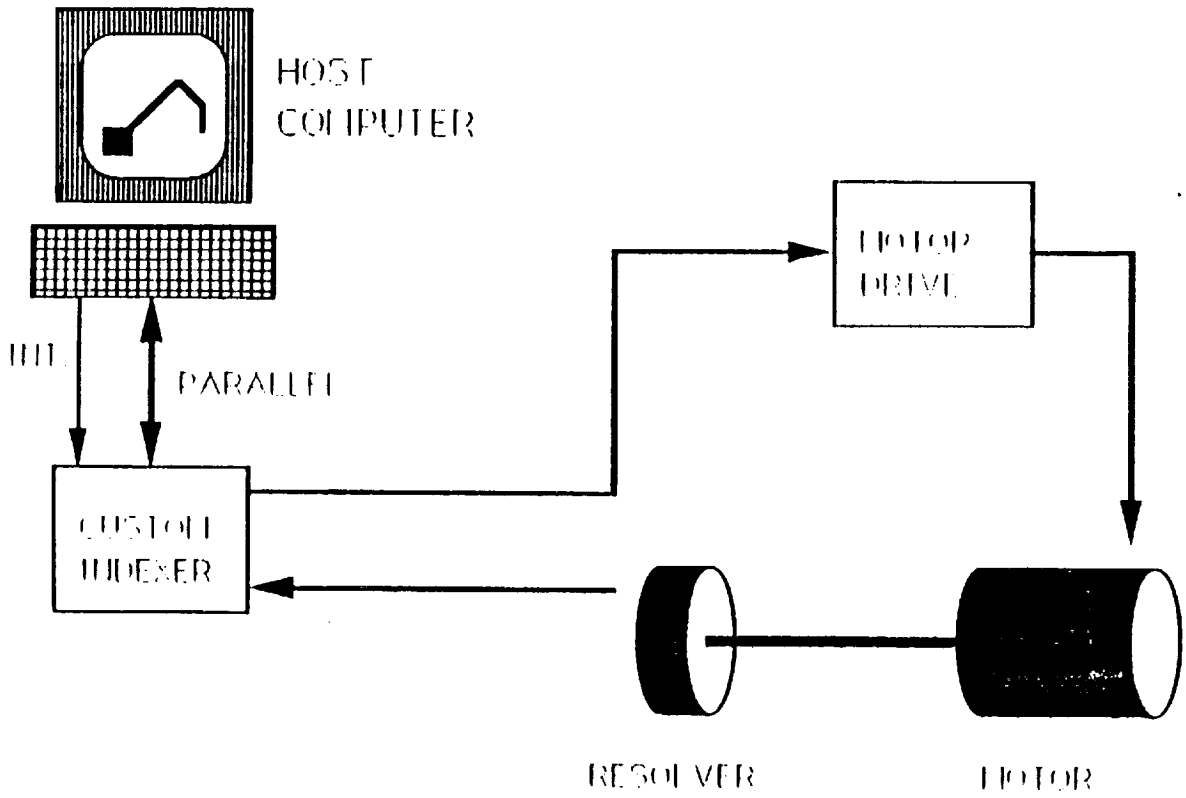

MOTOR DRIVE SYSTEM

Figure 6. Preferred Motor Control System

4 CONCLUSIONS

The current imbalance problem was found to be a symptom of a system design problem. The existing system seems to have inadequate control over the motors. The problem may be alleviated with software by synchronizing the motors to a more accurate level than how they are currently done. The Compumotor system uses a rather cumbersome way of operating the motors especially for this application. Although the starting and ending points are known, the actual path taken by the motor is unknown. This is especially true in Joint #1 where the PID values are set to different values. This alleviates the symptom, not the problem. The resolver is another question mark. It introduces an unnecessary complication to the system in that the cable resistance becomes part of the circuit. This does not seem like a good way to go. A digital shaft encoder is a much more reliable and robust way of closing the loop. The motor operation should, in any event, be verified independently of the Compumotor system.

The use of ramps and microswitches for synchronizing the joints is too inaccurate a method to meet the rigid ARID operating requirements. Joint information should be independently available. In addition, a scheme for relieving the torque on any of the joints by individually controlling the motors is needed. Once the motors are synchronized and torsional stresses removed the system should operate more accurately until some anomaly occurs. An anomaly, if it actually occurs, cannot be easily corrected for in the present system. Tests conducted showed that even with proper synchronizing of the joint, motor current loading could not be predicted. This means that attempting force control as a primary feedback is not a total solution. A more suitable motor control system should be designed to replace the existing one. By proper distribution of the software load, the proposed system would make effective use of the multiple processor power. In addition to close monitoring of the motors for control purposes, safety and other procedures can be handled by the additional processing power available. Providing some memory at each joint would also allow for the monitoring and later plotting of the motor performance during real time operation. The point to point nature of the existing ARID system operation is one of the major drawbacks of the existing system. The proposed motor control system redesign removes this problem. With proper motor control and system feedbacks, the current imbalance problem and associated problems can be minimized.

1992 NASA/ASEE SUMMER FACULTY FELLOWSHIP PROGRAM

JOHN F. KENNEDY SPACE CENTER
UNIVERSITY OF CENTRAL FLORIDA

CHEMICAL CHARACTERIZATION OF SOME AQUEOUS LEACHATES FROM CROP RESIDUES IN "CELSS"

PREPARED BY: Dr. Brooks C. Madsen

ACADEMIC RANK: Professor

UNIVERSITY AND DEPARTMENT: University of Central Florida
Chemistry Department

NASA/KSC

DIVISION: Biomedical Operations and Research

BRANCH: Biological Research and Life Support

NASA COLLEAGUE: John C. Sager

DATE: July 17, 1992

CONTRACT NUMBER: University of Central Florida
NASA-NGT-60002 Supplement: 8

ACKNOWLEDGEMENTS

Interaction with several NASA and Bionetics Corporation personnel who are part of the Biological Research and Life Sciences Office was vital to successes achieved during the ten week period. John Sager, Bill Knott and Ross Hinkle were very supportive at the administrative level and made it possible for me to spend a rewarding and refreshing summer. Conversations and discussions with Jay Garland, Dick Strayer and Ray Wheeler were useful from a technical standpoint. A progress seminar that I presented at the request of John Sager and Jay Garland during week five of my stay provided an early opportunity for focusing the project and positive comments that I received served to strengthen my sense of accomplishment.

Special thanks are given to Barbara Peterson who willingly relinquished a corner of the Analytical Laboratory to me and the patience that she showed when my mess encroached on her side of the sink is much appreciated. Barb's enthusiasm and persistent smile made each day enjoyable even when a malfunctioning instrument caused frustration. The summer was too short which suggests that I stayed busy in a productive and enjoyable manner and that frequent interactions with very special people were part of the daily routine.

ABSTRACT

Aqueous leachate samples prepared from crop residues that are produced as a component of the Controlled Ecological Life Support System program designed to support long duration space missions have been compared and general chemical characterization has been accomplished. Solid phase extraction and high performance liquid chromatography were used to accomplish comparisons based on chromatographic and ultraviolet absorption properties of the components that are present. Specific compounds were not identified, however, general composition related to the presence of phenol-like compounds was explored.

SUMMARY

Aqueous leachate samples prepared from potato, soybean and wheat crop residues that are produced as a component of the Controlled Ecological Life Support System program designed to support long duration space missions have been compared and general chemical characterization has been accomplished. Solid phase extraction and high performance liquid chromatography were used to accomplish comparisons based on chromatographic and ultraviolet absorption properties of the components that are present. Specific compounds were not identified, however, several compounds known to be present in these plant residues were used for comparison purposes. General composition related to the presence of phenol-like compounds was explored. The leachates are highly colored and an aqueous fraction of the leachates exhibited chromatographic properties similar to tannin-like materials. Microbial treatment of leachate samples removes or converts most of the tannin-like and phenol-like constituents. An exhaustive characterization is not a feasible undertaking because of the complexity associated with leachate composition.

TABLE OF CONTENTS

LIST OF ILLUSTRATIONS

LIST OF TABLES

I. Introduction

The Controlled Ecological Life Support Systems(CELSS) program has as a main objective the construction of a life support system that will provide food, water and oxygen for long duration space missions and will allow for recycling of some of the wastes produced(1-4). An ongoing project involves growing plants under hydroponic conditions. The plants of current focus include wheat, soybeans, lettuce and potatoes. It is desirable to recycle non-edible portions of the plants to minimize waste product buildup and to minimize the need for additional materials to support the plant growth cycle.

One current problem involves the characterization of crop residues, specifically the root, stem and chaff portions of these plants. The water soluble leachate of these dried residues contain both inorganic and organic constituents. The inorganic constituents have been characterized and can be recycles as fertilizer in the growth chambers(5). The aqueous leachate can be treated microbially to decrease the organic matter content (Richard Strayer, private communication), however, a brown color persists to some extent and increases in intensity as the leachate is used to replenish the hydroponic solution. Preliminary investigations have shown that the organic composition of the leachate can be subdivided into broad categories with complex chemical makeup. It is not unusual for a natural product material to contain in excess of 100 different chemical species. Specific fractions might include carbohydrates, organic acids, polyphenols, tannins and humic materials. A variety of analytical techniques are typically employed to derive solutions to complex chemical problems of this nature.

This report describes attempts to obtain a basic understanding of the chemical makeup of the organic composition of water leachate solutions derived from crop residues with specific emphasis on compounds that have exhibited phytotoxicity. Potentially useful techniques include liquid chromatography, spectrophotometry, gas chromatography and mass spectrometry. The presence and persistence of phytotoxic substances in a variety of crop residues has been recognized for some time (6). Many of these substances exhibit significant water solubility and have been shown to inhibit seed germination and growth of various crops. The separation and identification of specific compounds from soils and crop residues suspected to be phytotoxic have been attempted using a variety of techniques. These include combinations of column, paper and thin-layer chromatography and more recently gas chromatography and high-performance liquid chromatography (HPLC) (7). For example the presence of vanillic, p-hydroxybenzoic, protocatechuic, p-coumaric, syringic and ferulic acids (8, 9) were reported as phytotoxic compounds in

weeds and subtilled soils. These compounds and others of similar structure can readily be detected using ultraviolet spectroscopy. The utility of HPLC in the chemical characterization of plant products can be demonstrated by studies such as reported by Lee, et al (10) where separation, identification and quantification of sugars, non-volatile acids, flavones, flavone glycosides, carotenoids and anthocyanidins were reported. A photodiode array detector was used to characterize spectral properties of each class of compounds. Other examples of studies that relate to measurement of specific compounds in plant crops include the determination of phenolic acids in potato tubers (11, 12), non-volatile constituents including gallic acid in tea (13), and phenolic constituents in rhubarb (14). New methods of analysis for tannins has been the subject of a recent review (15). The chemical makeup of tannins is extremely complex. Broad groups of water soluble compounds include hexahydroxydiphenic acids, gallic acid esters with molecular weights less than 3000, proanthocyanidins with molecular weights less than 20,000 and additional compounds with molecular weights near 200 are also present.

The yellow-brown color associated with aqueous systems that contain dissolved organic matter is typically associated with the presence of tannic and humic acids. Color can also be associated with the presence of flavonoid compounds. Anthocyanins, flavonols and flavones constitute this flavonoid group of compounds. The basic structure of each group is shown below (16):

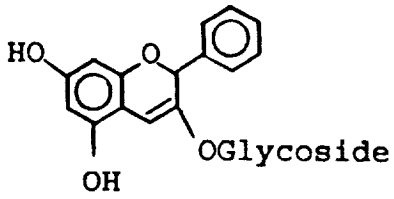

Anthocyanins

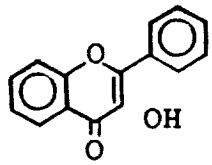

Flavonols

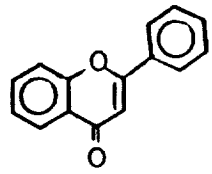

Flavones

Various sugars may be attached to the ring system, typically at the phenyl ring which increases the water solubility of these compounds. The anthocyanins are intensely colored and account for the brilliant colors associated with many flowers. Substituted flavones and flavonols tend to exhibit yellow-brown colors that deepen as concentration increases.

This study has progressed from an initial investigation where leachate fractions and subfractions from potato, soybean and wheat were compared by HPLC to determine if major similarities or differences exist. Each fraction represents a very complex combination of chemical compounds. Progress made to provide general and specific makeup of these fractions is reported below.

II. Experimental

2.1 CHEMICALS

Acid and phenol derivative samples were purchased from Aldrich Chemicals except that Naringin and Morin were from J. T. Baker and Quercetin was from Eastman Chemicals. Methanol used to prepare samples and as HPLC eluent were HPLC grade purchased from Fisher or J. T. Baker. Water was obtained from a Hydrodyne Ultrapure/Picopure purification system which provided 18 megohm water filtered through a 0.45μ filter. All HPLC mobile phase solvents were filtered through Nylon 66 0.45μ filters prior to use. All aqueous based mobile phases were prepared fresh at three to four day intervals. Standard solutions of the various analytes were prepared in methanol at concentrations of 200-1500 ppm. All analyte solutions at these concentrations were stable during the last eight weeks of the study when stored in clear glass vials at room temperature.

2.2 INSTRUMENTATION

Routine HPLC was performed using a Perkin-Elmer HPLC that included a PE Series 4 LC Microprocessor Controlled Solvent Delivery System, Rheodyne 7125-075 rotary injection valve with 50 μl sample loop, reverse phase columns and LC 85B Variable Wavelength Spectrophotometric Detector. Chromatograms were obtained using a LCI-100 Laboratory Computing Integrator. Typical injection volumes of 10-20 μl were used in most applications and were delivered to the injector using a 100 μl syringe. Full scale absorbance of 5.0 units (5.0 AUFS) was provided from the LC 85B. An attenuation of 1024 on the Computing Integrator is required to display the entire 5.0 unit absorbance scale on the integrator printout. A typical attenuation setting of 16(0.078 AUFS) was determined to be acceptable for the display of most chromatograms in this study.

Several different mobile phase compositions and two different columns available in the Life Support Laboratory Analytical Laboratory were used in this investigation. Descriptions of the mobile phase compositions and columns are included in Table 2 as part of the presentation of results.

A PC controlled Varian Instruments HPLC located in the University of Central Florida Chemistry Department was used to partially characterize selected leachate fractions. This system consists of a Model 9010 Pump Module, rotary injection valve equipped with a 25 μl injection valve, 225 x 4.6 mm Brownlee ODS column with ODS guard column and Model 9065 Photodiode Array Spectrophotometer Detector.

Ultraviolet absorption spectra were obtained using either a Perkin-Elmer 552 UV-Visible spectrophotometer with Hitachi Model 52 X-Y recorder for output or a Beckmann Model DU-64 microprocessor controlled UV-Visible spectrophotometer. Samples were diluted in 40:60 methanol:water that contained 0.13% phosphoric acid.

2.3 LEACHATES

Preliminary studies were performed on samples of untreated plant leachates labelled LS-2, LP-3 and LW obtained from Dr. Jay Garland as were all subsequent leachate samples. Fresh portion of leachate were prepared on June 16, 1992 by mixing 5g of several different dry leachate samples with 100 ml of deionized water. After standing for approximately 2 hr. the solutions were filters under suction through Whatmann No. 1 filter paper. A second filtration of each sample was performed using 0.45 μ Nylon 66 filters. Small portions of samples identified as LP-1, LP-2, LS-1, LS-2 and LS-3 were frozen until subsequent use. A sample identified as MS-T was also obtained. This sample represents a mixed soybean leachate that had been microbially treated to reduce organic matter content. An additional sample identified as LWHS represented treated wheat leachate that had been periodically added to a growth chamber hydroponic solution over a 60 day period.

2.4 SOLID PHASE EXTRACTION (SPE)

Most leachate sample were partitioned into fractions prior to HPLC investigation. Partitioning was accomplished using Sep-Pak Bond-Elute-CH cartridges from Analytichem International. Cartridges were conditioned prior to use by washing with 5-0.8 ml aliquots of methanol and 5-0.8 ml aliquots of water. Flow was controlled at less than 1.0 ml/min by vacuum applied to the cartridge. Accurately measured aliquots of leachate sample and eluent were used to selectively partition components and elute leachate fractions from the Sep-Pak. Leachate not subjected to SPE were filtered through 0.45μ Nylon 66 filters before injection. Eluents from the SPE process were not filtered prior to injection. Treatment of samples by SPE resulted in several eluent fractions depending on the specific scheme employed. Table 1 summarizes the general fraction labelling scheme that was used. It was possible to increase the amount of leachates subjected to SPE by increasing the amount of cartridge packing material. When necessary this was accomplished by removal of packing material from up to six cartridges and dry packing into a single cartridge.

Table 1. Solid Phase Extraction Elution Scheme and Fraction Identification Scheme

SepPak-CH Conditioning	
4 x 0.8 ml Methanol	
4 x 0.8 ml Water	
Leachate Application	
1 or 2 x 0.8 ml Sample*	Fraction 1
Fraction Elution	
1 x 0.8 ml Water	Fraction 2A
1 x 0.8 ml Water	Fraction 2B
etc.	
1 x 0.8 ml 25% Methanol/Water	Fraction 3A1
1 x 0.8 ml 25% Methanol/Water	Fraction 3A2
etc.	Fraction 3A3
1 x 0.8 ml 60% Methanol/Water	Fraction 3B1
1 x 0.8 ml 60% Methanol/Water	Fraction 3B2
etc.	Fraction 3b3
1 x 0.8 ml Methanol	Fraction 4
etc.	
1 x 0.8 ml 0.1% HCL/Methanol	Fraction 5

* The contents of multiple SPE cartridges were combined to increase sample capacity in selected experiments.

2.5 SAMPLE STORAGE

All leachate samples were stored frozen at -4 °C. Fractions obtained from SPE were also stored at -4 °C. Samples were warmed to room temperature prior to use in any experiment.

III. RESULTS AND DISCUSSION

3.1 REPRESENTATIVE COMPOUNDS

Several compounds have been studied in the past in relation to phytotoxic effects that they exhibit on plant growth. Preliminary experimentation in this study focused on the HPLC and SPE behavior of several compounds that were easily obtainable. These compounds are presented in Figure 1 along with their respective chemical structures. Included are several benzoic acid derivatives, cinnamic acid derivatives and flavonoid compounds. Chromatograms that demonstrate the separation possible for mixtures of related compounds are presented in Figure 2. HPLC retention times obtained for several of these compounds under various chromatographic conditions are presented in Table 2. These observations suggest that the separation of fairly complex mixtures of these types of compounds is feasible and practical.

The SPE behavior of six different compounds is summarized in Table 3. The partitioning behavior of compounds with quite similar structure is drastically different. For example salicylic acid demonstrates a relatively large water solubility by predominant elution in f1/2 while ferulic acid which has methoxy groups in the 3 and 5 positions instead of hydroxy groups shows no affinity for the aqueous eluent.

3.2 LEACHATE SOLID PHASE EXTRACTION AND CHROMATOGRAPHY

The results of HPLC on four leachate samples are presented in Figure 3. An indication of the complexity of the problem is illustrated by the chromatograms obtained directly from potato, soybean and wheat leachates. An abbreviation scheme as described in the experimental section of this report was employed to identify leachate samples. There are similarities in the measured chromatograms but substantially different specific details are present. Each has a region corresponding to elution times of less than 10 minutes where components with significant water solubility elute. These could be tannin type compounds. In the region corresponding to 10 to 40 minute elution times for compounds with greater organic-like character compared to the earlier eluting components are observed. The general broad band elution pattern with superimposed peaks suggests complex sample makeup.

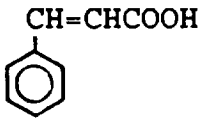

Cinnamic Acid(FW 148.16)

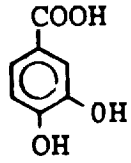

Protocatechuic Acid(FW 154.12)

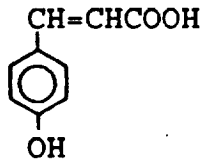

Coumaric Acid(FW 164.16)

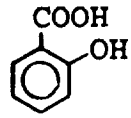

Salicylic Acid(FW 138.12)

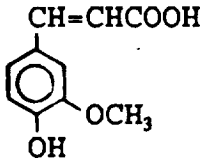

Ferulic Acid(FW 194.19)

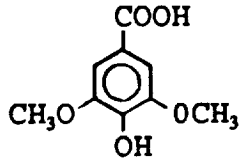

Syringic Acid(FW 198.17)

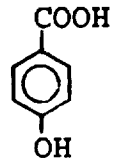

p-Hydroxy-Benzoic Acid(FW 138.12)

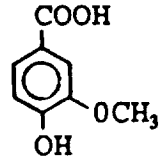

Vanillic Acid(FW 168.14)

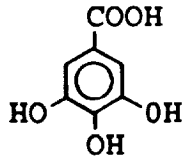

Gallic Acid(FW 170.12)

Figure 1. Chemical Structures of Representative Compounds.

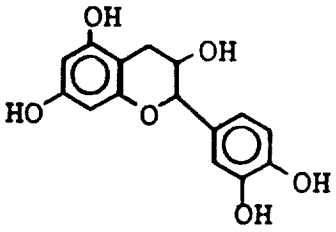

Catechin Hydrate(FW 290.28)

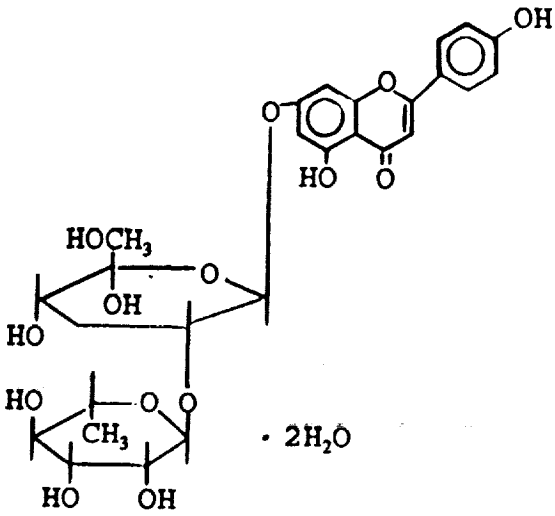

Naringin(FW 616.58)

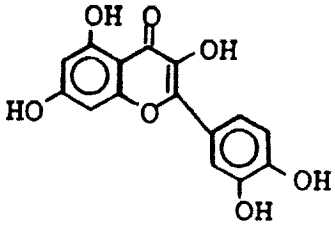

Quercetin(FW 302.24)

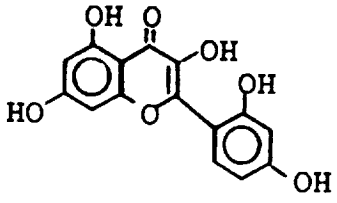

Morin(FW 302.24)

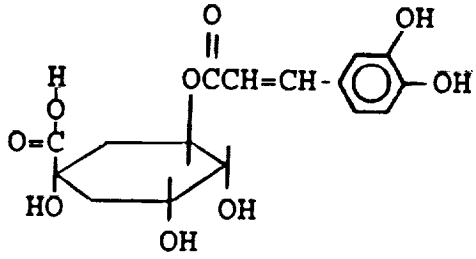

Chlorogenic Acid(FW 354.81)

Figure 1. (Continued)

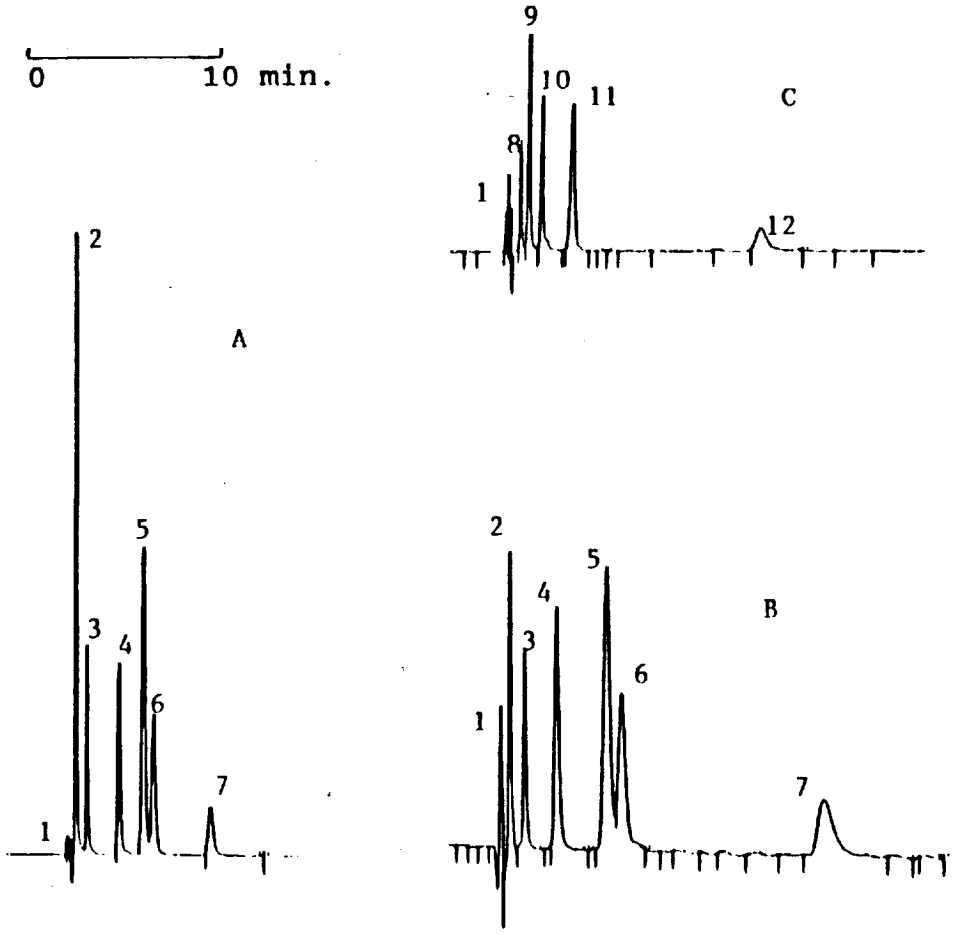

Figure 2. Chromatograms of Some Representative Compounds Measured at 280 nm. Compounds: 1 - V_o, 2 - gallic acid, 3 - protocatechuic acid, 4 - syringic acid, 5 - coumaric acid, 6 - ferulic acid, 7 - salicylic acid, 8 - catechin, 9 - chlorogenic acid, 10 - p-hydroxybenzoic acid, 11 - naringin, 12 - quercetin. A: Column A, mobile phase MP1; B: Column A, mobile phase MP1; C: Column C, mobile phase MP2.

Table 2. Chromatographic Retention Behavior for Representative Compounds

Column	A		B	C				
Mobile Phase Composition								
% Methanol	40	35	40	40	35	30	20	20
0.22% H_3PO_4:H_2O	60	65	60	60	60	70	60	65
% Acetonitrile							20	15
Mobile Phase Designation	MP1							MP2
	Retention Times, minutes**							
Gallic Acid	3.4	3.6	2.4	3.3	3.6	3.9	3.2	3.0
Protocatechuic Acid	4.0	4.4	3.0	4.4	5.0	6.1	4.0	3.6
Syringic Acid	5.8	6.6	4.6	7.0	9.3	13.2	5.7	4.5
Coumaric Acid	7.2	9.1	6.9	11.0	15.4	23.3	8.3	5.9
Ferulic Acid	7.6	10.2	7.5	11.9	17.4	27.8	9.1	6.3
Salicylic Acid	10.8	13.6				35.7	19.8	13.0
Cinnamic Acid	25.4							30.5
Naringin	9.0				27.6			9.1
Quercetin	29.5							
Catechin	4.0				4.8			3.9
Chlorogenic Acid	4.8				6.1			3.9
p-HydroxyBenzoic Acid	5.7							5.5

(A) Zorbax C8, 250 x 4.6 mm, 1.0 ml/min, V_o = 2.7 ml
(B) Brownlee C18, 225 x 4.6 mm, 1.0 ml/min, V_o = 2.2 ml
(C) Altex Econosil C18, 250 x 4.6 mm, 1.0 ml/min, V_o = 2.2 ml

** Reported retention times are approximate and will vary by 10% due to variation in flow rates, temperature, etc.

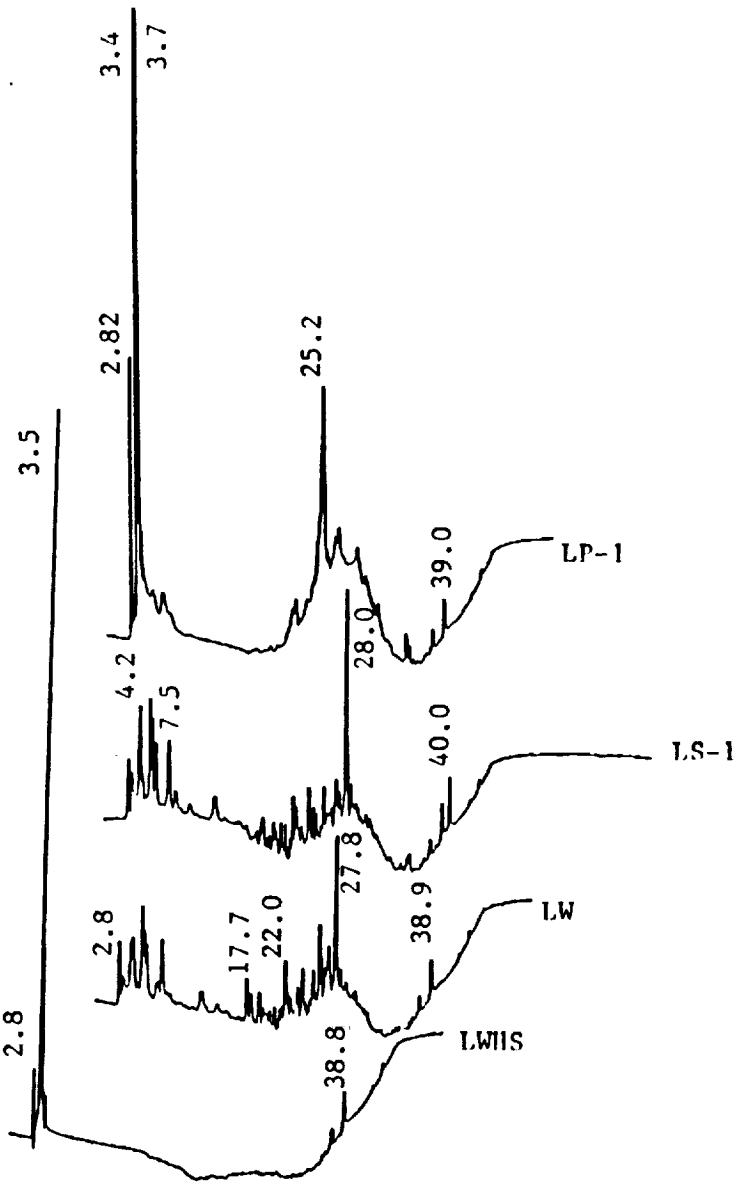

Figure 3. Chromatograms for Potato, Soybean and Wheat Leachates Measured at 280 nm using Mobile Phase Gradient Elution. Column A, mobile phase: 0-10 min. 0.22% aqueous phosphoric acid; 10-40 min. linear ramp 0% to 100% methanol:0.22% aqueous phosphoric acid; 40 min. and longer 100% methanol.

Table 3. Partitioning Behavior for Some Representative Compounds During Solid Phase Extraction.

	Fraction Number		
Components	1/2	3a	3b
Gallic Acid	93%	6%	1%
Protocatechuic Acid	77%	23%	
Syringic Acid		83%	17%
Coumaric Acid		100%	
Ferulic Acid		100%	
Salicylic Acid	87%	13%	

One sample of microbially treated wheat leachate was also chromatographed and the result for this sample is displayed at the bottom of Figure 3. The microbial treatment has substantially reduced the numbers and concentrations of components previously observed to be present in the untreated wheat leachate. It is possible that the chromatograms displayed in Figure 3 do not detail the entire water soluble composition. Only components that exhibit an ultraviolet absorption at 280 nm and that elute from the column during the 1 hr. run will be detected. For example sugars and carbohydrates do not absorb radiation at 280 nm and their presence will not be detected.

Because leachate composition is very complex attempts were made to obtain simpler fractions of the various leachates by SPE. The use of the available SPE-CH cartridge allows for fractionation by removal of nonpolar or moderately polar components from the aqueous sample upon passage through the cartridge. Removal is based on preferential solubility of each considered component in water or the nonpolar cyclohexyl(-CH) chemical moiety. The SPE-SAX cartridge will interact to remove negatively charged ionic species from aqueous solution based upon ion exchange interaction. The chromatograms shown in Figure 4 are obtained from potato leachate after passage through the identified SPE cartridge. Chromatogram A represents eluent from the -SAX and represents non-ionic water soluble constituents. Chromatogram B represents eluent from the -CH and will include anions and highly polar components that will not be retained by the -CH. Chromatogram C represents eluent that is devoid of ionic, moderately polar and non-polar constituents. Each fraction includes a broad band that elutes in less than 6 minutes and each probably consists of a mixture of compounds with similar chemical properties.

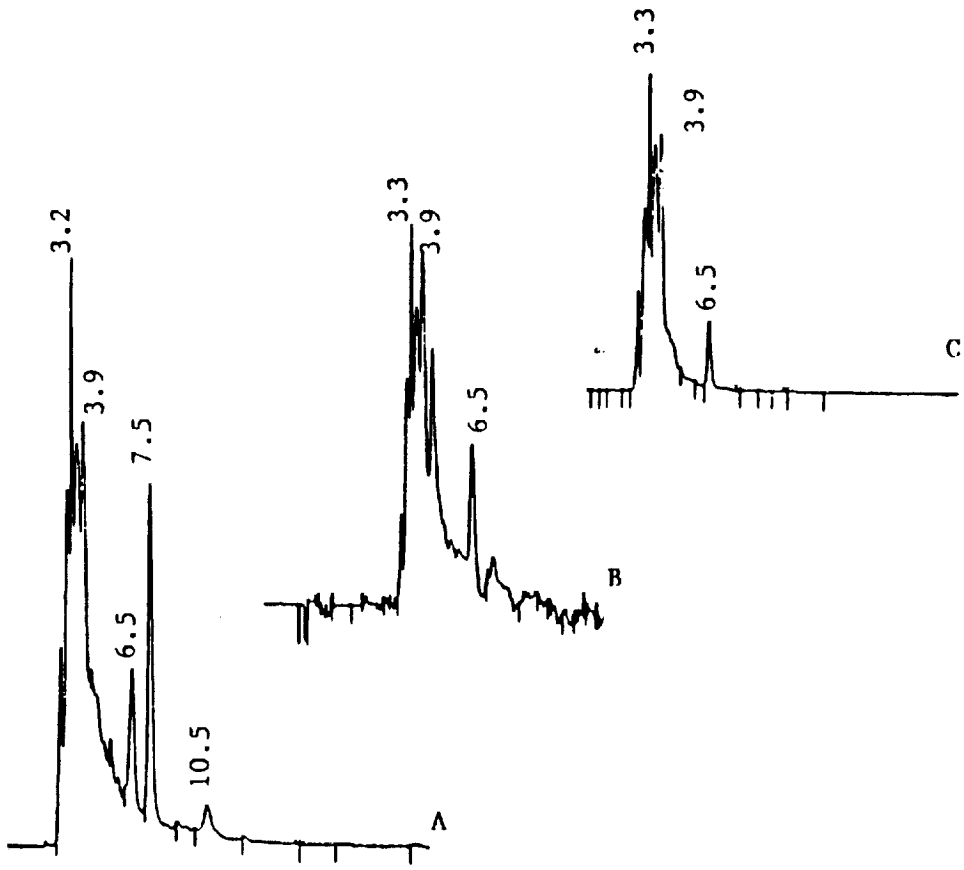

Figure 4. Comparison of Chromatogram Fractions(f1/2) from SPE -CH and -SAX Treatment of Potato Leachate(LP-1) at 280 nm. A: eluent from -SAX; B: eluent from -CH; C: eluent from -CH and -SAX in series. Column A, mobile phase MP1.

Some representative chromatograms for potato and soybean leachate fractions are presented in Figure 5. The two different potato leachates yield nearly identical chromatograms for each fraction but different than those for the one soybean sample shown in Figure 5. Each potato fraction yields one major peak and considerable band background indicative of a complex mixture of compounds which are probable of related structure or similar relative solubility between water and a non-polar organic solvent. The fractions identified as f3a and f3b that correspond to the soybean sample each yield one major peak.

The ability of organic molecules to absorb UV radiation is a function of chemical structure and bonding considerations. Each compound will absorb over a somewhat characteristic range of wavelengths. Chromatogram appearance can therefore be influenced by selection of monitoring wavelength. Chromatograms displayed in Figure 6 demonstrate this effect. Potato leachate fractions were chromatographed and monitored at three different wavelengths. The changing amplitude of the peaks appearing at approximately 6.0 minutes in f1/2, at approximately 6.3 minutes in f3A and the peak at approximately 5.2 minutes in f3B demonstrate how selection of wavelength can influence chromatogram appearance. At the same time it can be possible to derive some information about compound identity from peak amplitude changes that are observed. For example, the peak at 4.5 minutes in f3A corresponds closely to that of protocatechuic acid and protocatechuic acid absorbs more strongly at 254 nm than at 280 nm and does not absorb at 320 nm. The UV absorption spectrum for this compound and other compounds is presented in Figure 7. Chlorogenic acid also has a retention time of approximately 4.5 minutes, however, it absorbs very strongly at 320 nm. Chlorogenic acid can be ruled out as a possible candidate for this peak based on UV absorption properties. Protocatechuic acid while exhibiting UV absorption consistent with that seen in the chromatograms is primarily partitioned into f1/2 and should not be seen in chromatograms of f3A.

The UV spectra presented in Figure 7 were obtained in methanol-0.13% aqueous phosphoric acid to approximate mobile phase composition used for most HPLC separations. Spectra represent various classes of compounds. For example, spectra A-E are from benzoic acid derivatives, Spectra L and M are from cinnamic acid derivatives, spectra N and P are tannic acid and gallic acid, respectively and spectra G and H are for pentahydroxyflavones. Additional reference to these spectra will be presented later in this report.

The use of UV spectral properties for identification is limited in a positive sense because these spectra are devoid of spectral fine-structure that is present in other techniques such as infrared and nuclear magnetic resonance spectroscopy and mass

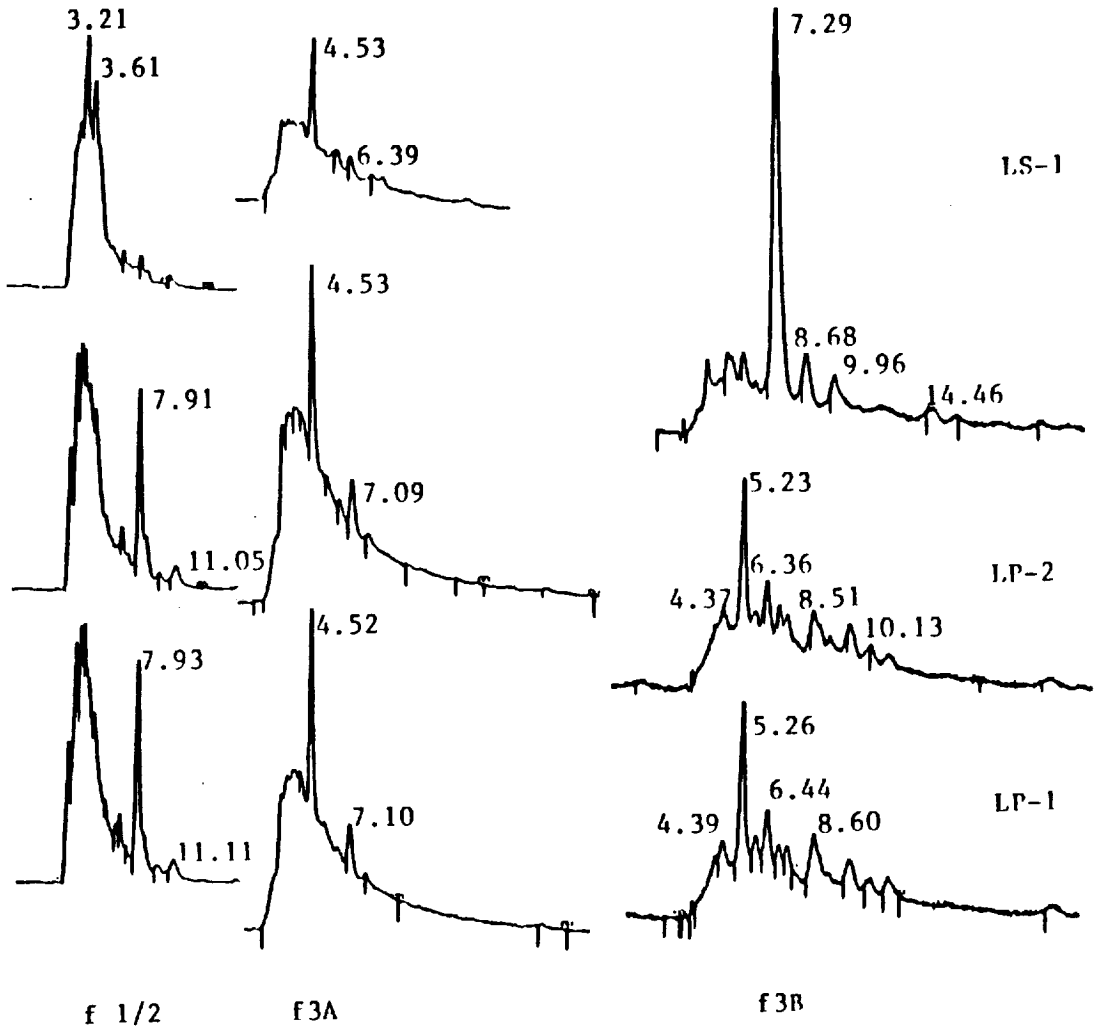

Figure 5. Chromatograms for Aqueous and Aqueous-Methanol SPE Fractions of Leachates Measured at 280 nm. Column A, mobile phase MP1.

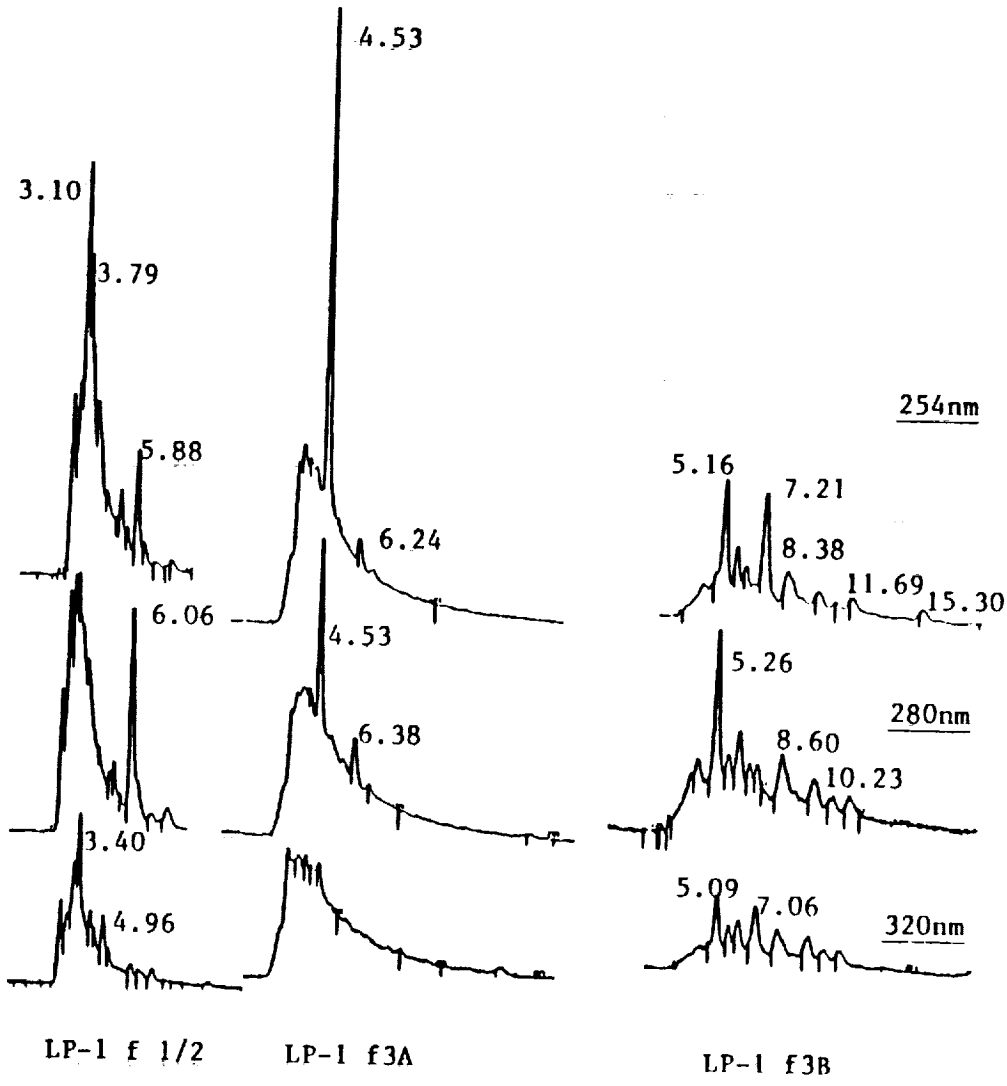

Figure 6. Chromatograms for Potato Leachate SPE Fractions Obtained at Different Wavelengths. Column A, mobile phase MP1.

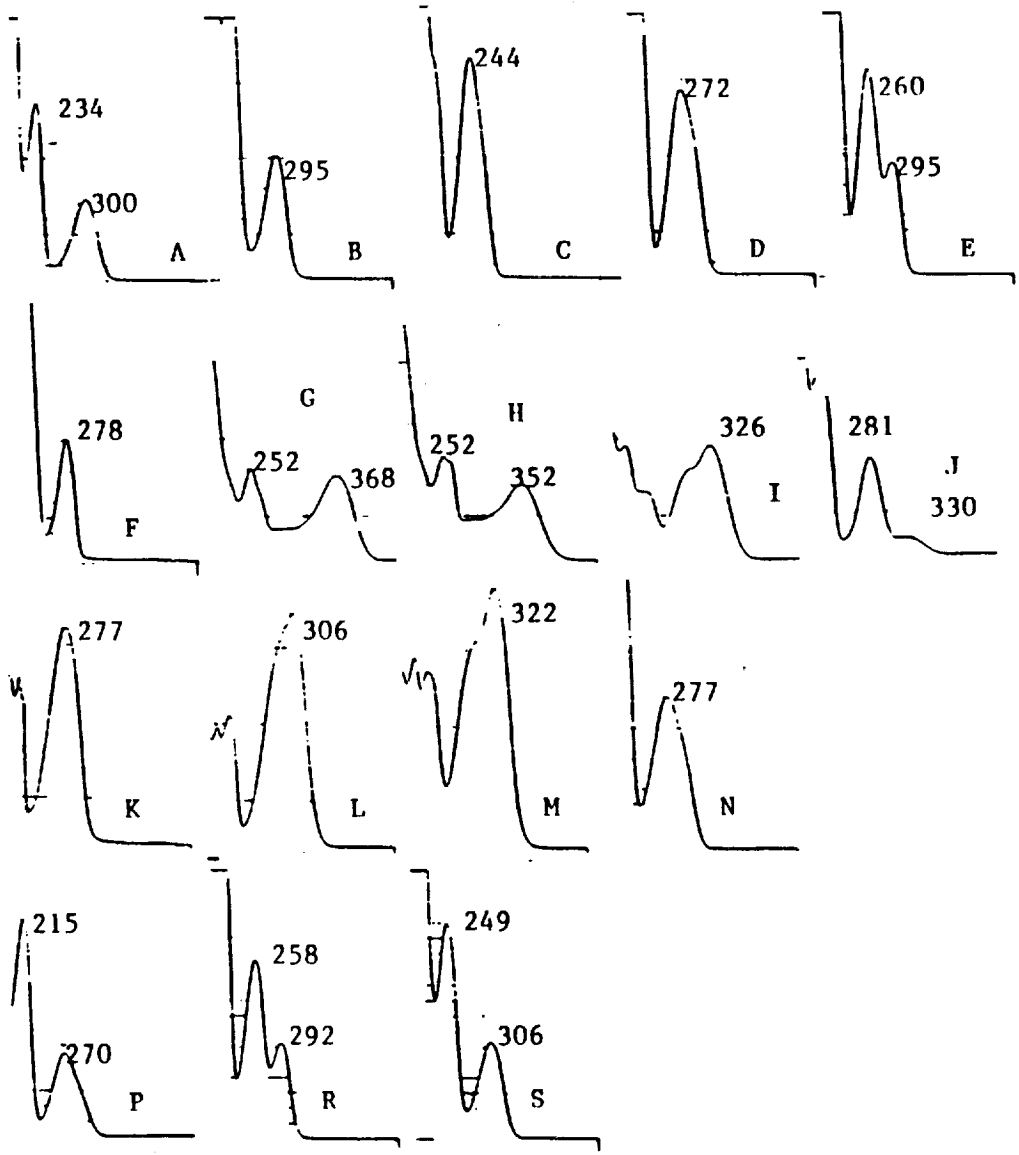

	Compound	µg/ml		Compound	µg/ml
A	Salicylic Acid	9.5	J	Naringin	10.4
B	m-Hydroxybenzoic Acid	20.4	K	t-Cinnamic Acid	5.4
C	p-Hydroxybenzoic Acid	6.6	L	Coumaric Acid	5.9
D	Syringic Acid	11.8	M	Ferulic Acid	10.5
E	Vanillic Acid	19.2	N	Tannic Acid	10.5
F	Catechin Hydrate	29.1	P	Gallic Acid	5.2
G	Quercetin	4.5	R	Protocatechuic Acid	7.7
H	Morin	4.2	S	3,5-Dihydroxy-Benzoic Acid	19.2
I	Chlorogenic Acid	2.7			

X-axis represents 200nm-450nm. Y-axis represents 1.0 AUFS.

Figure 7. Ultraviolet Absorption Spectra for Selected Representative Compounds.

spectrometry. It is an ideal choice as a detection technique for HPLC because instrumentation is relative simple and inexpensive and it allows detection to take place at very low concentration levels. Co-chromatography is a technique that can be successfully applied to aid in identification of unknowns in chromatographic separations. Figure 8 shows chromatograms of a soybean leachate fraction without and with addition of two known compounds. Comparison of the two chromatograms clearly show that the peak that is observed at 4.5 minutes is not due to either catechin or chlorogenic acid. The peak at 7.29 minutes in LS-1, f3B(see Figure 5) coincides identically with that of ferulic acid. Co-chromatography of that sample with a second portion of the sample to which ferulic acid had been added resulted in no additional peak. However the peak width had increased slightly. Further chromatography using different mobile phases ultimately resulted in separation of the single peak into two peaks which showed that the sample peak was not due to the presence of ferulic acid. The use of retention time comparisons, co-chromatography and evaluation of UV spectral properties has eliminated any of the compounds identified in Figure 2 as candidates for being present in the leachate samples that were used in this study.

Before leachate is used in a plant growth chamber it is treated microbially to reduce the total carbon content. This is accomplished by conversion of carbohydrates and sugars to carbon dioxide which is removed from the system. This treatment changes the organic content of the leachate. A sample of treated soybean leachate was fractionated by SPE and chromatograms of the fractions were obtained. These chromatograms are shown in Figure 9. Relatively clean chromatograms are obtained at 280 nm which demonstrates the effectiveness of the treatment in modifying composition. Chromatograms obtained at 230 nm also show the relative absence of components in f3A and F3B. The chromatogram of fraction f1/2 shows the presence of compounds that absorb at this lower wavelength. These compounds are not likely to be significantly aromatic or unconjugated in nature because aromatic and extensively conjugated systems will absorb consistent with spectra presented in Figure 7.

In an attempt to gain some insight into the chemical makeup of the leachate fractions, chromatograms were obtained from a small number of SPE fractions of LS-2 using a diode-array detector equipped LC. The results of this endeavor are displayed in Figure 10. It is possible to obtain the UV absorption spectrum for components responsible for major peaks in the chromatograms. Several chromatographic peaks are identified and cross referenced to the UV spectrum obtained from each peak. Peaks numbered 2, 3, 6, 7 and 8 provided spectra of reasonable definition. Spectrum 6 is of a shape similar to that of vanillic acid(see Figure 7) and the other four spectra with broad absorption bands in the 350-380

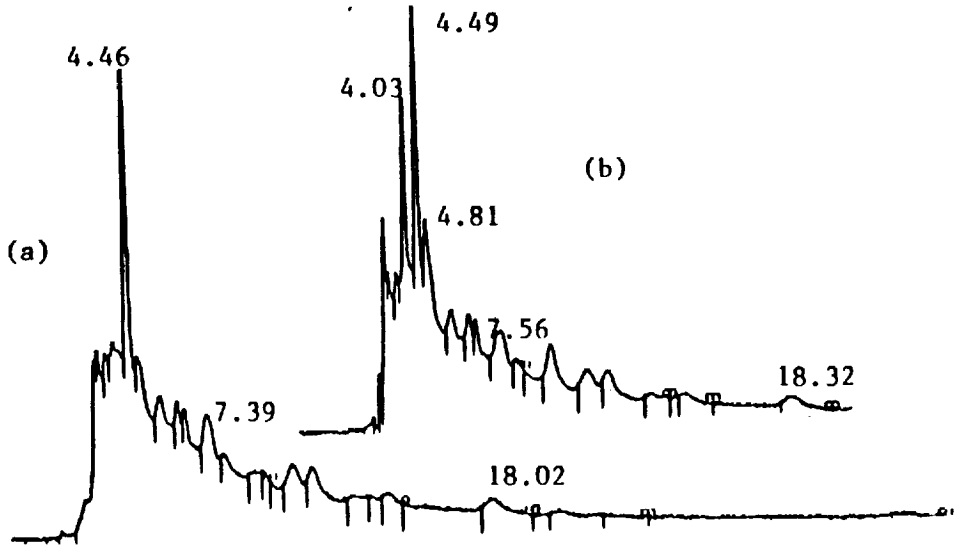

Figure 8. Cochromatography of Catechin and Chlorogenic Acid with the SPE Aqueous Fraction From Soybean Leachate. A: LS-1, 2:3 sample:methanol. B: same as A plus 2.0 ppm catechin(T_r 4.03 min.) and 0.4 ppm chlorogenic acid(T_r 4.81 min.). Column A, mobile phase MP1.

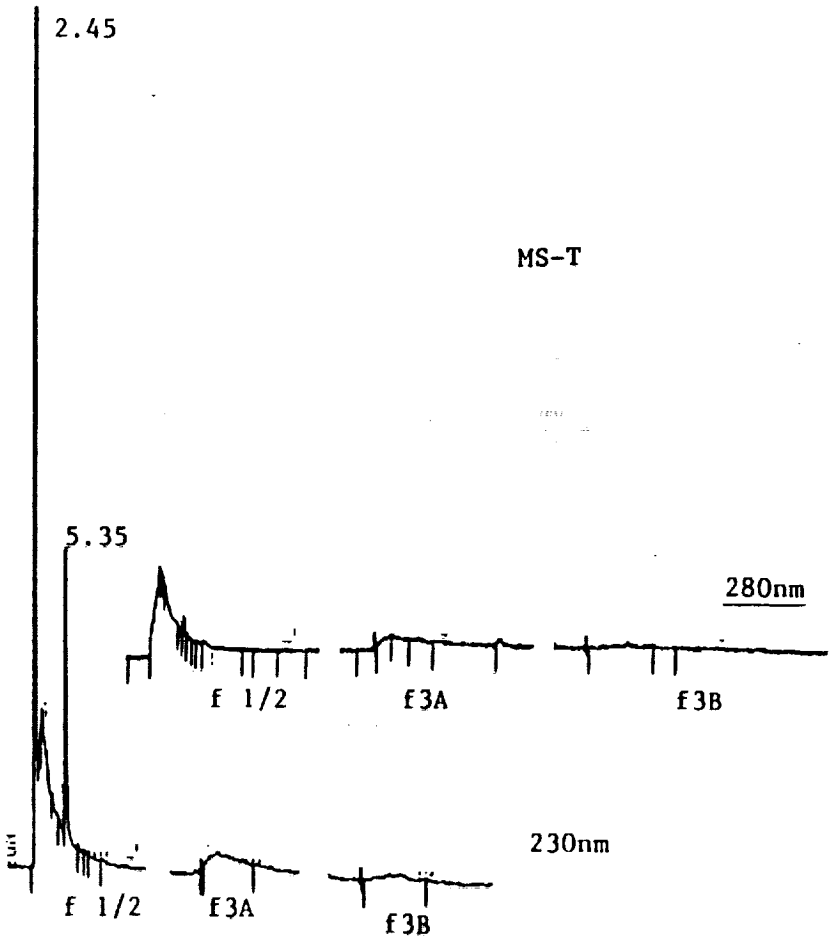

Figure 9. Chromatograms of Microbially Treated Soybean Leachate SPE Fractions. Column A, mobile phase MP1.

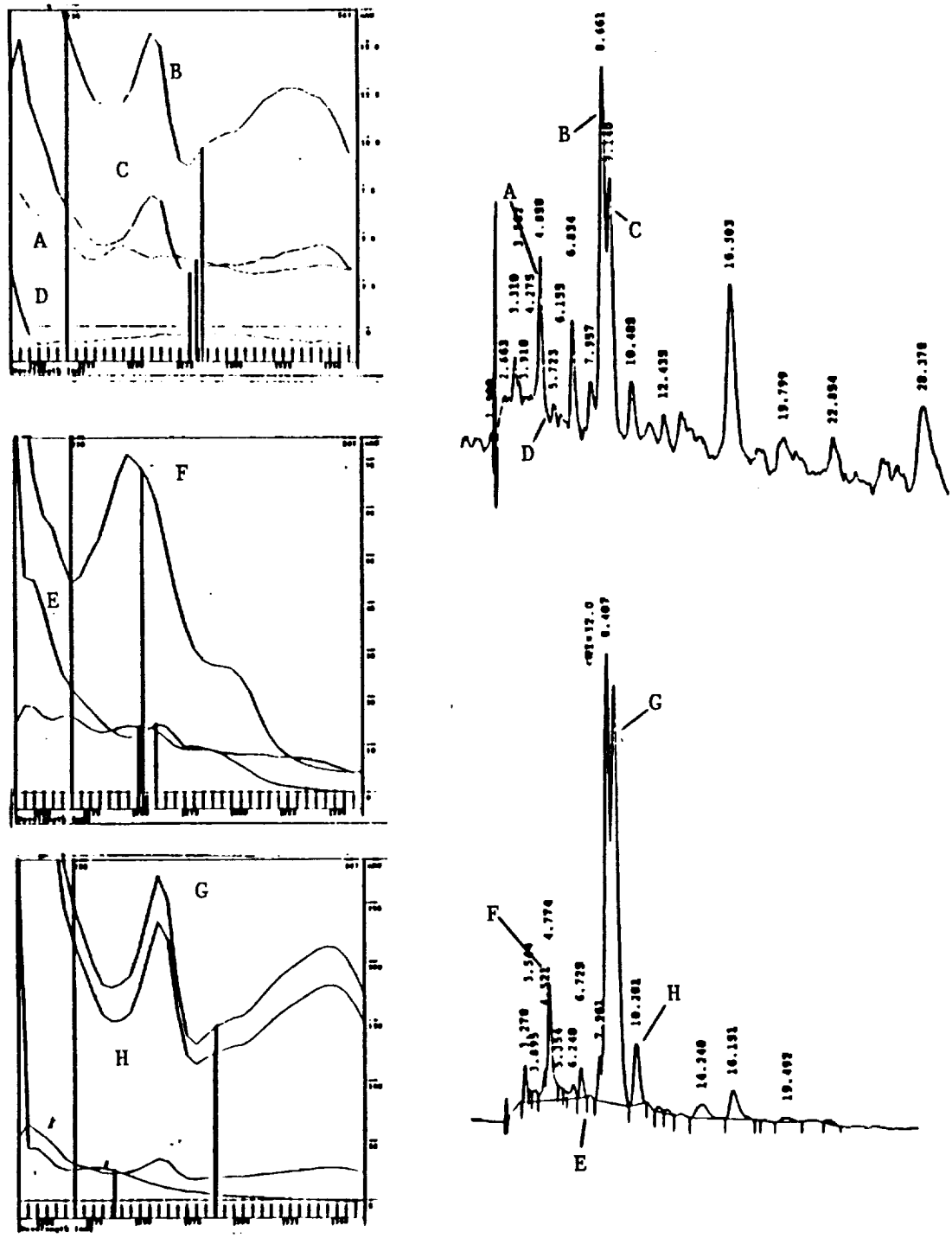

Figure 10. Ultraviolet Absorption Spectra from Selected Chromatogram Peaks Obtained with a Diode Array Detector. Column B; mobile phase MP1; sample LS-2, top chromatogram (f3b4 from 8 ml sample fractionation on -CH bed consisting of the contents from 7 cartridges), bottom chromatogram (f3b1 from 1.6 ml sample fractioned on single -CH bed). Spectra numbering coincides with chromatogram peak numbering. X-axis 190-375 nm.

nm range are similar to those of quercetin and morin(see Figure 7). This spectral evidence suggests that some of the components contained in SPE f3 may by flavonoid compounds. Further study in this direction would seem to be appropriate.

IV. SUMMARY COMMENTS

The use of solid phase extraction and high performance liquid chromatography for characterization of general similarities and differences in the chemical composition of aqueous leachates from crop residues in the Controlled Ecological Life Support System program has been accomplished. The composition is complex and potato, soybean and wheat leachates exhibit general similarities in composition due to the presence of highly colored anionic materials, as well as other colored compounds that can be fractioned from the samples by solid phase extraction. High performance liquid chromatography using ultraviolet absorption as the detection tool was used to further characterize composition. It is apparent that a modest number of individual compounds of unique structure and other groups of compounds with similar structure constitute the organic composition of the leachates. No specific compounds were identified, however, it is possible to determine the presence of tannin-like and phenolic-like classes of compounds in untreated leachate and in microbially treated leachate. It has been demonstrated that several specific phenolic-like compounds that are produced by many crop plants are not present in measurable quantities in the leachate samples that were available. However, it is possible that related compounds are responsible for the chromatographic behavior observed. An extension of this work should include the identification of some of these compounds. Once identified controlled experiments that relate to persistence and accumulation of these compounds in the treated leachate enriched hydroponic solutions used in the growth chambers will be possible. An exhaustive characterization is not possible because of the complexity associated with the leachate composition. In fact it is probably not necessary to fully characterize the composition as long as a general understanding of the type of compounds that are present is documented and studies undertaken to understand the role played by these compounds in the hydroponic solutions.

V. REFERENCES

1. Knott, W. M. The Breadboard Project: A Functioning CELSS Plant Growth System. Adv. Space Res. Vol. 12. No. 5. 1992. pp. 45-52.

2. Koller, A. M. CELSS Breadboard Facility Project Plan. Biomedical Operations and Research Office. National Aeronautics and Space Administration, Kennedy Space Center. March 1986.

3 Mackowiak, C. L., L. P. Owens-Hall, C. R. Hinkle, and R. P. Prince. Continuous Hydroponic Wheat Production Using a Recirculating System. NASA Tech. Memorandum TM 102784 September 1990.

4. Prince, R. P., and W. M. Knott. CELSS Breadboard Project at the Kennedy Space Center. In: D. W. Ming and D. L. Henninger (eds.), Lunar Base Agriculture: Soils for Plant Growth. Amer. Soc. Agron., Madison, WI 1989.

5. Garland, J. L., and C. L. Mackowiak. Utilization of the Water Soluble Fraction of Wheat Straw as a Plant Nutrient Source. NASA Tech. Memorandum TM 103497 June 1990.

6. Guenzi, W. D., T. M. McCalla and F. A. Norstadt. Presence and Persistence of Phytotoxic Substances in Wheat, Oat, Corn, and Sorghum Residues. Agronomy Journal. Vol. 59. March-April 1967. pp. 163-165.

7. Shilling, D. G., L. A. Jones, A. D. Worsham, C. E. Parker, and R. F. Wilson. Isolation and Identification of Some Phytotoxic Compounds from Aqueous Extracts of Rye(Secale Cereale L.). J. Agric. Food. Chem. Vol. 34. 1986. pp. 633-638.

8. Guenzi, W. D., T. M. McCalla, and F. A. Worstadt. Agron. J. Vol. 59. 1967. pp. 163-168.

9. Chow, G. H., and Z. A. Patrick. J. Chem. Ecol. Vol. 2. 1976. pp. 369-373.

10. Lee, H. S., R. D. Carter, S. M. Barros, D. J. Dezman, and W. S. Castle. J. food Composition and Analysis. Vol. 3. 1990. pp. 9-19.

11. Ramamurthy, M. S., B. Maiti, P. Thomas, and P M. Nair. High-Performance Liquid Chromatography Determination of Phenolic Acids in Potato Tubers during Wound Healing. J. Agric. Food Chem. Vol. 40. 1992. pp. 569-592.

12. Malmberg, A. G., and Olof Theander. Determination of Chlorogenic Acid in Potato Tubers. J. Agric. Food. Chem. Vol. 33. 1985. pp. 549-551.

13. Hoefler, A. C., and Philip Coggon. Reversed-Phase High-Performance Liquid Chromatography of Tea Constituents. J. Chromatog. Vol. 129. 1976. pp. 460-463.

14. Kashiwada, Y., G. Nonake, and I. Nishioka. Studies on Rhubarb. XV. Simultaneous Determination of Phenolic Constituents by High-Performance Liquid Chromatography. Chem. Pharm. Bull. Vol 37(4). 1989. pp. 999-1004.

15. Okuda, Takuo, T. Yoshida, and T. Hatano. New Methods of Analyzing Tannins. J. Natural Products. Vol. 52(1). 1989. pp. 1-31.

16. Salisbury, F. B., and C. W. Ross. Plant Physiology. 2nd Ed. Wadsworth Publishing Co., Inc. Belmont, CA 1978. pp. 216-221.

N93-19400

1992 NASA/ASEE SUMMER FACULTY FELLOWSHIP PROGRAM

JOHN F. KENNEDY SPACE CENTER
UNIVERSITY OF CENTRAL FLORIDA

EVALUATION OF ULTRASONIC CAVITATION OF METALLIC AND NON-METALLIC SURFACES

PREPARED BY:	Dr. Narinder K. Mehta
ACADEMIC RANK:	Investigator
UNIVERSITY AND DEPARTMENT:	University of Puerto Rico - Mayaguez Department of Chemical Engineering College of Engineering
NASA/KSC	
DIVISION:	Material Science
BRANCH:	Microchemical Analysis
NASA COLLEAGUE:	Gale Allen
DATE:	August 2, 1992
CONTRACT NUMBER:	University of Central Florida NASA-NGT-60002 Supplement: 8

DEDICATION

This project is dedicated to my wife, Luz Maria, and to my precious flowers, Jyoti Marie, Tahnee Yngrid and Narinder Jr., who are always there when I need them.

ACKNOWLEDGMENT

I would like to thank NASA/ASEE Summer Faculty Fellowship Program, to Dr. Loren Anderson of the University of Central Florida, to Mr. Charles (Charlie) Hoppesch and Mr. William (Irby) Moore, Mr. Dennis Armstrong and Mrs. Carol Valdes of the Kennedy Space Center (KSC) for providing me with the opportunity to work at KSC for another summer. Thanks to Mrs. Kari Stiles for her willingness to help in all the administrative matters.

Special thanks are extended to Ms. Gale Allen, KSC project coordinator and Mr. Charlie Hoppesch for suggesting the project, and for their guidance and encouragement in all phases of the project.

There are many other professionals who assisted me during the course of this project. My sincere appreciation goes to Mr. Stan Young, Mr. Lee Underhill, Dr. Orlando Melendez, Mr. Mitch Buckley, Mr. Scott Johnson and Ms. Dionne Broxton for their assistance and advice throughout the project.

Special friendly thanks are extended to other professionals and summer participants working in the Microchemical analysis Laboratories who made me feel welcome, and for the pleasant interactions we all had while working in the laboratories.

The support of Dr. Felix Santiago, Dr. A. Rodriguez and Dr. Rafael Munoz of my home institute, the University of Puerto Rico is gratefully acknowledged.

ABSTRACT

The purpose of this summer project was to evaluate the ultrasonic cavitational effect on metallic and non-metallic surfaces, using commercially available ultrasonic baths operating at low frequencies and higher generator power output. Experimental data on the material loss, microphotographic and optical microscopic evaluation of the nozzle area for the three metal alloy specimens, and the hardness data for the non-metallic polymer disks were obtained to assess the applicability of the proposed replacement method of ultrasonic cavitation of the parts with water for the validation process. The results indicate that the proposed method can be utilized for validating cleaned small parts made of stainless steel, brass and non-metal based polymer disks. The method is equally applicable to anodized aluminum parts using moderate piezoelectric ultrasonic baths.

SUMMARY

1,1,2 trichloro-1,2,2 trifluoro ethane (CFC-113) commercially known as Freon-113 is the primary test solvent used for validating the cleaned hardware at the Kennedy Space Center (KSC). Due to the ozone depletion problem, the current United States policy calls for the phase out of Freons by 1995. NASAs chlorofluorocarbon (CFC) replacement group at KSC has opted to use water as a replacement fluid for the validation process since water is non-toxic, inexpensive, and is environmentally friendly. The replacement validation method calls for the ultrasonification of the small parts with water at 52 degrees Celcius for a cycle or two of 10-minute duration each using commercial ultrasonic baths. In this project, experimental data was obtained to assess the applicability of the proposed validation method for any damage of the metallic and non-metallic surfaces resulting from ultrasonic cavitation.

Commercially available ultrasonic baths operating at low frequencies and higher output power do not cause any surface cavitation of the stainless steel and the brass metal parts, and also to the non-metallic polymer disks commercially known as Nylon 6/6 and Vespel-21. Surface area of the anodized aluminum parts is found to be greatly affected by the ultrasonic cavitational effect of the powerful magnetostrictive type Branson and Blue Wave ultrasonic baths.

The experimental data obtained demonstrates that the CFCs proposed method can be utilized for validating cleaned small parts made of stainless steel, brass and the non-metallic polymer disks. The method is equally applicable to small parts made of anodized aluminum using moderate piezoelctric ultrasonic water baths.

TABLE OF CONTENTS

LIST OF ILLUSTRATION

EVALUATION OF ULTRASONIC CAVITATION OF METALLIC AND NON-METALLIC SURFACES

I-INTRODUCTION

1.1 OBJECTIVE:

To evaluate that ultrasonic validation of the cleaned metallic and non-metallic specimens with water as a replacement fluid for Freon-113 does not cause surface erosion of the cleaned surfaces.

1.2 BACKGROUND:

Small precision parts made of metallic and non-metallic materials in quantities are routinely used at the Kennedy Space Center (KSC). For a safe space shuttle launch, it is of utmost importance that they be verified clean of organic materials before use in an oxygen rich environment as that of the Orbiter.

Presently, 1,1,2 trichloro-1,2,2 trifluoro ethane (CFC-113) known as Freon-113 is the primary test solvent used for validating the cleaned hardware at KSC.

Freons including CFC-113 are known to remain in the atmosphere long enough to migrate to altitudes due to their high volatility, and are known to be a threat to the earth's protective ozone layer. The current United States Government policy calls for ending the production of these compounds, and phase out by 1995.

Due to the ozone depletion problem, KSCs chlorofluorocarbon (CFC) replacement group at the Material Science Laboratory is working to find a replacement for CFC-113 for the validation process of the cleaned parts.

Among the options, the CFC group decided to use water as the replacement fluid since water is non-toxic, non-flammable, environmentally friendly, inexpensive, and is compatible with other materials.

CFCs proposed replacement method for the validation calls for the ultrasonification of the small parts with water at 52 degrees Celcius for a cycle or two of a 10-minute duration each, and analyze the resulting water for its Total Organic Carbon Content (TOC). This analytical procedure has demonstrated encouraging results for the removal of the non-volatile residue (NVR) material from small metal parts for the validation process.

Switching to a new methodology for the validation process requires that not only the proposed approach should meet KSCs strict NVR requirement of less than 5 mg/ft^2 but also should not affect the hardware adversely under any circumstances. Ultrasonification may take out the NVR material from the cleaned parts for the validation process but may cause surface etching of the parts. This research project is focussed basically to address the following:

1. Will the proposed ultrasonic validation test method utilizing water and commercial ultrasonic baths operating at low frequencies and higher generator output power may result in the surface cavitation of the nozzle area of the commonly used fittings made of stainless steel, brass and anodized aluminum?

2. How the polymer-based Vespel SP-21 and Nylon 6/6 disks will perform to the proposed ultrasonic validation method i.e., will there be a variation in their performance specifications?

II-MATERIALS AND METHODS

2.1 Metal and Non-metal Specimens:

Small standard commercial metal fittings (Swagelok type), abundantly used at KSC and made of stainless steel (SS-400-6-4AN), brass (B-400-6-AN) and anodized aluminum (A-400-6-AN) were used to monitor the effect of the proposed ultrasonic validation method for surface erosion or activity of the parts. Especially, the precision nozzle area of these metal fittings were monitored for any ultrasonic cavitational effect during the course of this investigation since any resulting surface activity to this area will render them useless for non-compliance with the strict KSC specifications.

Most of the metal fittings were newly purchased for this study except for some previously used specimens made of stainless steel and brass. These used samples were supplied by the CFC group and were tested only in the ultrasonic water bath (blackstone) operating at 24-26 KHz frequency for this study.

The non-metallic polymer disc components commercially known as Nylon 6/6 and graphite reinforced Vespel SP-21 were studied for hardness resulting from the ultrasonic test runs, and were supplied by the failure analysis group of the Material Science Laboratory.

2.2 Ultrasonic Baths:

Two types of technologies are currently used to stimulate cavitation in an aqueous medium. They are Piezoelectric and Magnetostrictive.

Piezoelectric type ultrasonic baths operating at 24-26 KHz frequency having 600 watts of generator output power (Blackstone), and 27 KHz frequency with 1000 watts of output power (Sonic Systems) were used for the experimental studies. The basic difference in their performance is the output power since the higher generator output power normally increases the number of bubbles in the ultrasonic water tank for a higher cleaning efficiency.

Magnetostrictive type sonic water baths (MagnaPak by Branson) and (Blue Wave by Swen) operating on 20 KHz and 30 KHz respectively, and both having 1000 watts of generator output power were also used for this study. These baths operating at low frequencies and generating a larger size of the vacuum bubbles, result in a higher ultrasonic effect of cleaning and erosion.

2.3 Ultrasonic Bath Water Quality:

Water quality is an important factor for the commercially available ultrasonic baths. Pure water is difficult to cavitate while tap water cavitates easily. Tap water having some detergent to improve mixing was used in the ultrasonic baths. Before the ultrasonic runs, the water was degassed to increase the formation of cavitation bubbles.

2.4 Specimen Holder Trays:

Stainless trays having approximately 2 liters of pure heated deionized water maintained at 52 degrees Celcius were used for the ultrasonic test runs. These trays were placed into the ultrasonic bath insuring that the water level in the ultrasonic bath and the sample tray was nearly at the same level.

2.5 Sample Handling:

2.5.1 Rotary System for Metal Specimens:

Single frequency generators normally used in commercial ultrasonic baths, may result in an intense cleaning in some areas and not enough in the other areas of the tank due to the formation of the hot spots. To avoid this localized effect during an experimental run, a slow moving rotary device (carousel type moving system) using a laboratory stirrer and a disc of plexiglass having twelve holes was fabricated in the laboratory. The metal specimens, tied with nylon cords were suspended into the test stainless steel tray having deionized water, and were kept in a constant slow motion all the time to avoid the localized effects of hot spots.

2.5.2 Polymer Discs Specimens:

Polymer discs specimens were placed in separate compartments of a perforated plastic tray. The tray was suspended into the test stainless steel tray having deionized water for providing a uniform action of the ultrasonic waves during a test run.

2.6 Scanning Electron Microscope:

The instrument used for recording the microphotographs was a Cambridge S 200 Scanning Electron Microscope. The methodology used for recording the microphotographs is the standard procedure used in the SEM laboratory for doing this type of work.

2.7 Test Procedure:

2.7.1 Metal Specimens:

Small standard metal fittings of random sizes were cleaned with Freon-113, dried in an oven, air cooled and weighed. Scanning Electron Microphotographs (SEMs) of a pre-identified nozzle area of the selected specimens for a particular test run, were taken before subjecting all the specimens to ultrasonic cavitation for varying intervals. All the ultrasonic test runs were preceded by an initial 10-minute cycle for obtaining uniform water test bath conditions. For certain test runs, a specimen (blank) was taken out of the stainless tray at the beginning of the experiment after the initial 10-minute period. After the required ultrasonic test cycle(s), a part was taken out, dried in an oven, air cooled, weighed, and saved for the SEM photograph.

SEM of the nozzle area of a particular specimen photographed initially was also taken after the ultrasonic test run. In some test runs, water of a complete test cycle of 120 minutes was filtered through a 0.45 micron filter paper for the microscopic evaluation of the residue for the presence of micron-sized eroded metal pieces. A total of twelve 10-minute cycle test runs were made during a complete test of the standard fittings. CFCs proposed validation method recommends a maximum of two 10-minute ultrasonic cycles for validation purposes. Since the parts are reusable, it was decided to test run them for a maximum of twelve 10-

minute cycles. The percent material loss for each specimen was calculated after each cycle.

2.7.2 Polymer Specimens:

Polymer specimens were cleaned with Freon-113, air dried and weighed in batches of four disks each. The specimens were tested in ultrasonic water baths for 4-, 8- and 12 cycles. After the test runs, the samples were placed on a paper towel to remove the excess water, air dried (overnight), weighed and saved for the hardness test. Water absorption for each batch, and for the individual disk was calculated after the ultrasonic test runs. Hardness of the polymer specimens was measured with a Durometer Type D (ASTM D2240) Shore Hardness Tester provided by the Failure Analysis Group of the Material Science Laboratory. Microscopic evaluation was done using a common laboratory optical microscope.

III-RESULTS AND DISCUSSIONS

3.1 Metal Specimens:

The material loss in mass units (mg) due to ultrasonic cavitation for all the tested specimens was found to be on a microscopic level, and is expressed in terms of the percent mass loss. The percent mass loss plotted as a function of the total ultrasonification time in minutes was found to be non-linear, and is presented in Figures 3-1 to 3-3 for the ultrasonic water baths used in this project. In the case of the anodized aluminum and the brass specimens, the small material loss in the early cycles reflects the probable occurrence of an incubation period followed by a rapid surface erosion which levels out to a final steady-state erosion of the material. This trend is highly noticeable with more efficient magnetostrictive ultrasonic water baths.

The material loss in the initial cycles may also be attributed to the presence of statistically weak spots in the solid surface due to the grain size and inhomogeneities of the structure of the material. The stainless steel specimens did not demonstrate this trend up to a maximum of two hours of ultrasonic test run. The data obtained for the specimens utilizing different ultrasonic water baths are described below.

3.1.1 Blackstone Ultrasonic Bath (24-26 KHz, 600 watts):

3.1.1.1 Material Loss:

An anodized aluminum specimen (Figure 3-1) demonstrated the maximum percent mass loss of 11×10^{-3} for a 20-minute ultrasonic test cycle compared to a maximum of 5.4×10^{-3} for a 60-minute test run for a brass specimen (Figure 3-2), and 4.2×10^{-3} for a 20-minute test run for a stainless steel specimen (Figure 3-3). The data obtained on the anodized aluminum specimens reflect a random distribution of the percent mass loss ranging from 10.5×10^{-3} for a 10-minute cycle specimen to a 5.9×10^{-3} for a specimen tested for two hours. The brass specimens demonstrated a similar pattern of random fluctuation in the percent mass loss ranging from 1.1×10^{-3} for a 20-minute test run to 2.7×10^{-3} for a specimen tested for two hours. The mass loss pattern observed for the stainless steel specimens was similar to the brass and the

aluminum specimens with the percent mass loss ranging from 1.6×10^{-3} for a 10-minute cycle to 2.5×10^{-3} for two hours of ultrasonic test run. The data obtained for brass and stainless steel are of the used specimens supplied by the CFC laboratory. Some of the material loss may be attributed to the dirty and the greasy material adhered to the specimens, and which were cleaned up during the test runs.

3.1.1.2 Microscopic Evaluation:

SEMs of the nozzle area of the anodized aluminum specimens subjected to ultrasonic cavitation from 40- to 120 minutes revealed surface activity resulting from ultrasonic cavitation on a microscopic level to all the specimens. Figures 3-4 and 3-5 are the microphotographs of four and twelve cycles test run specimens. A slight preferential erosion of the grain boundaries was observed in the 101x magnified microphotograph (Figure 3-5) obtained for a 12-cycle test specimen. An optical microscopic evaluation of the same specimen also revealed an area under the threads where the base aluminum metal was slightly exposed. This may be due to a weaker anodized coating near the thread area of the specimen. No surface activity of the nozzle area was observed under an optical microscope demonstrating that the surface integrity of the specimen was maintained even after 120 minutes of the test run. A specimen tested for a 20-minute cycle did not reveal any surface activity arising from the ultrasonic cavitation of the specimen.

SEMs of the used brass specimens tested for 4- and 8 cycles are presented in Figures 3-6 and 3-7 respectively. An unusual pattern on the nozzle area of the specimens prompted a concern that there may be a surface erosion activity resulting from the ultrasonic cavitational effect. In order to verify this concern, newly purchased specimens were cleaned with a moderate 10% Ferric Chloride acidic solution before subjecting them to ultrasonic cavitation for 4-, 8- and 12 cycles. SEMs (Figures 3-8a to 3-9b) of the cleaned and the raw specimens were obtained before and after the ultrasonic cavitation test runs. A careful evaluation of these SEMs did not reveal the same pattern as was observed earlier with the used parts supplied by the CFC group. The pattern observed previously on the nozzle area of the used samples must be the result of a poor machine finish or heavily used parts which resulted in a pronounced effect (pattern) on the SEM photographs. The microphotograph (Figure 3-10) of a test run brass specimen (new) tested for 12 cycles

did not reveal any surface activity or erosion due to ultrasonic cavitation.

Figures 3-11a and 3-11b are the SEMs of a used stainless steel specimen subjected to ultrasonic cavitation for 120 minutes. These microphotographs demonstrate a highly effective cleaning action of the ultrasonic water bath without any cavitational damage to the specimen; Figure 3-11b, a magnified microphotograph especially reflect this effectiveness.

3.1.2 SONIC Systems Ultrasonic Bath (27 KHz, 1000 watts):

3.1.2.1 Material Loss:

The anodized aluminum specimens revealed a higher ultrasonic cavitational effect of the Sonic Systems ultrasonic water bath as demonstrated by the data obtained on the material loss due to the ultrasonic test runs. The maximum percent mass loss for an anodized aluminum specimen (Figure 3-1) was 50×10^{-3} for a 120-minute test run compared to 8.3×10^{-3} for a 80-minute test run for a brass specimen (Figure 3-2), and 4.3×10^{-3} for a 40-minute test run for a stainless steel (Figure 3-3) specimen. The material loss from the anodized aluminum specimens seems to stabilize after a 40-minute test run with the percent mass loss of 43×10^{-3} for a specimen reaching to a maximum of 50×10^{-3} for 120 minutes of test run for another specimen.

The brass specimens demonstrated a random fluctuation in their percent mass loss ranging from 3.8×10^{-3} for a 20-minute test run to 4.6×10^{-3} for two hours of test run. The stainless steel specimens also demonstrated a similar pattern of random loss with the percent mass loss of 1.1×10^{-3} for a 20-minute test run specimen compared to 2.3×10^{-3} for a 120-minute of test run for another specimen.

3.1.2.2 Microscopic Evaluation:

SEMs of the nozzle area of the anodized aluminum specimens tested for 2-, 4-, 8- and 12 cycles in the Sonic Systems ultrasonic water bath demonstrated the impact of ultrasonic cavitation on a microscopic level to all the specimens. Figures 3-12 and 3-13 of a 20- and 120-minute test run specimens revealed a slight surface activity (erosion) of the grain boundaries. The residue obtained after filtering the water sample of the complete test run was subjected to an

optical microscopic evaluation. The identification of the metal fragments in the residue (Figure 3-14) prompted to reveal the presence of weak spots or boundaries in the solid surface of the anodized aluminum specimens. The metal fragments from these weak spots on the solid metal surface loosened during the incubation period, and this surface activity of the specimens was reflected in the magnified SEMs of the specimens described before.

The evaluation of the SEMs of the nozzle area of the brass and the stainless steel specimens tested for 4-, 8- and 12 cycles did not reveal any unusual surface activity due to ultrasonic cavitation. However, eroded metal fragments were also identified in the water residue of a complete test cycle for brass specimens. Figures 3-15 and 3-16 are the microphotographs of a complete 120-minute test run for a brass and a stainless steel specimen respectively. The microphotographs clearly demonstrate the ultrasonic cleaning action without any observable cavitational effect to the nozzle area of the specimens.

3.1.3 Branson Ultrasonic Bath (20 KHz, 1000 watts):

3.1.3.1 Material Loss:

The ultrasonic cavitational test runs in this magnetostrictive ultrasonic water bath resulted in a unique trend of material loss compared to the Sonic Systems Peizoelectric ultrasonic water bath of the same generator output power. The material loss in terms of the percent mass loss reached a maxima during the 120 minutes of the test run for all the three metal alloy specimens tested in this project. It reached a maximum value of 61×10^{-3} for the anodized aluminum (Figure 3-1) specimen compared to 10×10^{-3} and 1.9×10^{-3} for the brass (Figure 3-2) and the stainless steel (Figure 3-3) specimen respectively. Ultrasonic cavitational effect to the anodized aluminum specimen was found to be higher with the percent mass loss rising from 12×10^{-3} for a 10-minute test run to 61×10^{-3} for a 120-minute test run for another anodized aluminum specimen; a five fold increase. A brass specimen demonstrated the percent mass loss from 3.3×10^{-3} for a 10-minute test run to 10×10^{-3} for another specimen for a two hour test run; a three fold increase. Figures 3-1 and 3-2 reflect a definite steady erosion rate for the anodized aluminum and brass specimens during the ultrasonic test runs using Branson ultrasonic water bath. Again, the stainless steel specimens (Figure 3-3) resulted in

a minimum ultrasonic cavitational effect with the percent mass loss distributed randomly from 0.9×10^{-3} for a 20-minute test run rising to 1.9×10^{-3} for two hours of the test run.

3.1.3.2 Microscopic Evaluation:

The evaluation of the SEMs of the nozzle area of the anodized aluminum specimens tested from four to twelve cycles reflected a pronounced effect of surface erosion using the Branson ultrasonic water bath. The microphotographs (Figures 3-17 to 3-19a) clearly demonstrate the presence of random pits and damage to the nozzle area of the specimens subjected to ultrasonic cavitation from four to twelve cycles. Figure 3-19b is a 919x magnified microphotograph of the nozzle area of a 12-cycle anodized aluminum specimen. It revealed an extensive worked surface with widened pits due to ultrasonic cavitation. The damage was not found to be so profound for a 2-cycle specimen (Figure 3-20). A careful optical microscopic evaluation of all the tested anodized aluminum specimens, revealed the absence of the anodized coating from the nozzle as well as from the under-thread areas of the specimens; the erosion of the coating was very much pronounced for a 12-cycle specimen while the 2-cycle specimen revealed the absence of the metal coating to the under-thread area of the specimen (Figure 3-21).

The evaluation of the SEMs obtained for the brass and stainless steel specimens tested from two to twelve cycles did not reveal any unusual surface activity as a result of ultrasonic cavitation. The SEMs of the nozzle area of a 12-cycle test run specimens of brass (Figures 3-22a and 3-22b) and stainless steel (Figures 3-23a and 3-23b) clearly demonstrate the effectiveness of ultrasonic cleaning without causing any surface erosion or damage to the specimens.

3.1.4 Blue Wave (Swen) Ultrasonic Bath (30 KHz, 1000 watts):

3.1.4.1 Material Loss for Anodized Aluminum:

The anodized aluminum specimens tested in this magnetostrictive ultrasonic bath demonstrated a similar trend of material loss as compared to Sonic Systems and Branson ultrasonic Baths. The percent material loss was found to be 14.5×10^{-3} for a specimen tested for 20 minutes as compared to 63.7×10^{-3} for another specimen tested for 120 minutes.

3.1.4.2 Microscopic Evaluation:

The evaluation of the SEMs of the nozzle area of the anodized aluminum specimens (Figures 3-24 and 3-25) tested from two to twelve cycles revealed an extensive etching of the grain boundaries of the specimens; the etching is highly pronounced for 8- and 12 cycles specimens as compared to 2- and 4 cycles specimens. Figure 3-25 demonstrate a highly worked surface area of these specimens due to ultrasonic cavitation. The surface etching to the anodized aluminum surface by this magnetostrictive ultrasonic bath followed a similar pattern of cavitational damage as was observed previously in the case of the more powerful magnetostrictive Bronson ultrasonic bath i.e., surface damage has a linear relationship with the ultrasonification time.

3.2 Polymer Specimens:

3.2.1 Water Absorption:

Nylon 6/6 and graphite reinforced Vespel-21 polymer disks tested in the Sonic Systems and Branson ultrasonic water baths resulted in water absorption by the specimens. The amount of water absorbed by the Nylon 6/6 disks in the Sonic Systems ultrasonic water bath was slightly lower than in the Branson ultrasonic water bath (Figure 3-26). It ranged from 0.027 percent for a 4-cycle test run to 0.112 percent for a 12-cycle run for the Sonic Systems water bath compared to 0.077 percent for a 4-cycle run to 0.27 percent for a 12-cycle run for the Branson ultrasonic bath. For the graphite reinforced Vespel-21 disks, the percent water absorption was on a microscopic level; it varied from 0.002 for a 4-cycle test run to 0.012 for a 12-cycle run using Sonic Systems ultrasonic water bath compared to 0.005 for a 4-cycle test run to 0.032 for a 12-cycle run for the Branson ultrasonic water bath.

3.2.2 Hardness Test:

Nylon 6/6 and Vespel-21 specimens before and after subjecting to ultrasonic cavitation in the Sonic Systems and Branson ultrasonic water baths for 4-, 8- and 12 cycles were tested for hardness. The purpose of this test was to evaluate any variation in their hardness performance specification resulting from the ultrasonic cavitation. The data obtained on Durometer Type D hardness scale varied from 81 to 83 for

all the Nylon 6/6 specimens (4 disks/cycle) as compared to 85 to 86 for all the Vespel-21 specimens before and after the test run. For the comparison purposes, a typical laboratory polyethylene bottle cap gave a value of 70 on the Durometer scale. The variation in the hardness data before and after the ultrasonic cavitation of the specimens demonstrate that the polymer disks are very resistant to ultrasonic cavitation.

3.2.3 Microscopic Study:

The specimens (batches of Nylon 6/6 and Vespel-21) before and after the ultrasonic cavitation test of 4-, 8- and 12 cycles for the two ultrasonic baths (Sonic Systems and Branson) were subjected to optical microscopic evaluation. The evaluation did not reveal any unusual surface activity due to ultrasonic cavitation of the specimens.

IV-CONCLUSIONS

1. Ultrasonic cavitation of the stainless steel and brass specimens with water in the three commercially available ultrasonic baths (Blackstone, Sonic Systems and Branson) operating at low frequencies (20-27 KHz) and higher power output (600-1000 watts) did not result in surface cavitation of the nozzle area of the tested parts.

2. The anodized aluminum fittings are found to be slightly affected (microscopic level) in the Blackstone (24-26 KHz, 600 watts) and the Sonic Systems (27 KHz, 1000 watts) ultrasonic baths. The surface integrity of the nozzle area of the specimens are maintained even after two hours of ultrasonic cavitation in these baths.

3. The nozzle surface of the anodized aluminum fittings is found to be greatly affected by the ultrasonic cavitational action of the more powerful magnetostrictive commercial Branson (20 KHz, 1000 watts) and Blue Wave (30 KHz, 1000 watts) ultrasonic baths.

4. On the basis of the material loss, it can be concluded that the anodized aluminum specimens pass through an incubation period of approximately 20 minutes followed by a rapid material loss which levels off to a final steady-state erosion of the material in the ultrasonic baths operating with output power of 1000 watts.

5. The material loss of the specimens subjected to ultrasonic cavitation in different ultrasonic water baths for two hours is found to be on a microscopic level of percent mass loss, and is as follows:

   - About 32 times higher for an anodized aluminum specimen and about 5 times higher for a brass specimen as compared to a stainless steel fitting using Branson ultrasonic bath.

   - About 22 times higher for an anodized aluminum specimen and 2 times higher for a brass specimen as compared to a stainless steel specimen using Sonic Systems ultrasonic bath.

   - About 2 times higher for anodized aluminum specimen

as compared to a stainless steel and a brass specimen using Blackstone ultrasonic bath.

6. On the basis of the hardness test, Nylon 6/6 and graphite reinforced Vespel-21 polymer disks are not found to be affected by the ultrasonic cavitational action of up to two hours using Branson and Sonic Systems ultrasonic water baths.

7. The results have demonstrated that the proposed replacement ultrasonic test method of the CFC group can be used for validating cleaned small parts made of stainless steel and brass using commercial ultrasonic baths operating at low frequencies and higher power output. For the validation of the anodized aluminum parts, more moderate piezoelectric ultrasonic baths are found to be effective without causing adverse surface damage to the specimens.

V-RECOMMENDATIONS

Even if ultrasonic cavitation does affect the nozzle surface area of the anodized aluminum specimens adversely, it is suggested that physical testing of the cavitated parts should be carried out to evaluate the variation in their performance specification due to ultrasonic cavitation.

For the removal of the non-volatile residue (NVR) material for the clean validation process, it is recommended to explore the possibility of using water at or near the supercritical water (SCW) conditions (high temperature and pressure), since at SCW conditions, water has properties as of a fluid and a gas thus increasing its solvation power*. Experimental runs should be carried out to optimize the temperature and pressure conditions for the maximum removal of the NVR materials.

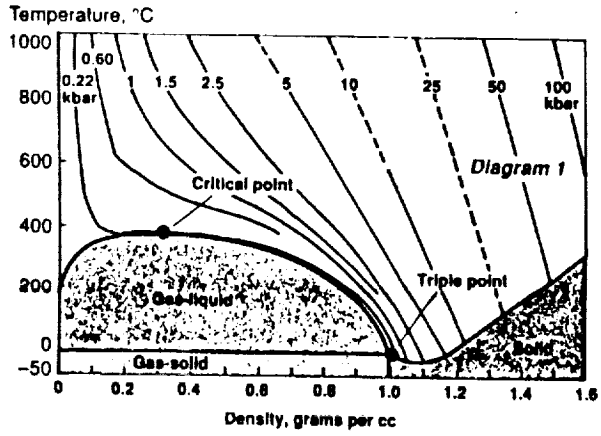

* Shaw, R. W. et al., "Supercritical Water, a Medium for Chemistry", Chem. & Engg. News 1991, 69(51), 26.

APPENDIX

WHAT IS ULTRASONIC CAVITATION ?

Ultrasonic cleaners use transducers which change electric energy into mechanical vibrations. These vibrations produce pressure waves travelling through water at the speed of sound (1450 m/s). High pressure side of the wave causes water to expand to form vapors and during compression, the vapor condenses into unstable and short-lived micron-sized cavitation bubbles (areas of vacuum). These bubbles are alternately expanded and compressed by the applied pressure waves passing through water. The bubbles continue to grow until they collapse when the pressure around them becomes positive. This is like THUNDERCLAPS on a microscopic scale. Minute areas of high pressure are created by these thunderclaps.

Before the bubble implosion, the bubble size is affected by the ultrasonic frequency applied by the transducer. The size of a bubble is inversely proportional to the frequency of the ultrasonic bath. So it is important to increase input power for maintaining a higher number of bubbles per unit volume with higher ultrasonic frequencies. Also, the number of bubbles present in the tank water is increased by increasing electrical input power.

During bubble implosion, the temperature and pressure of the gas within the bubble can reach 5500 degrees Celcius and 70,000 Lb/sq. inch (500 atmospheres) respectively. The liquid surrounding the bubble can reach 2,100 degrees Celcius. When the bubble is next to a surface to be cleaned, the implosion pressure may propel a jet of water towards that surface at about 250 MPH. The formation of millions and millions of cavitation bubbles and their collapse clean the objects literally inside and out but may also cause pitting and erosion of the solid surface.

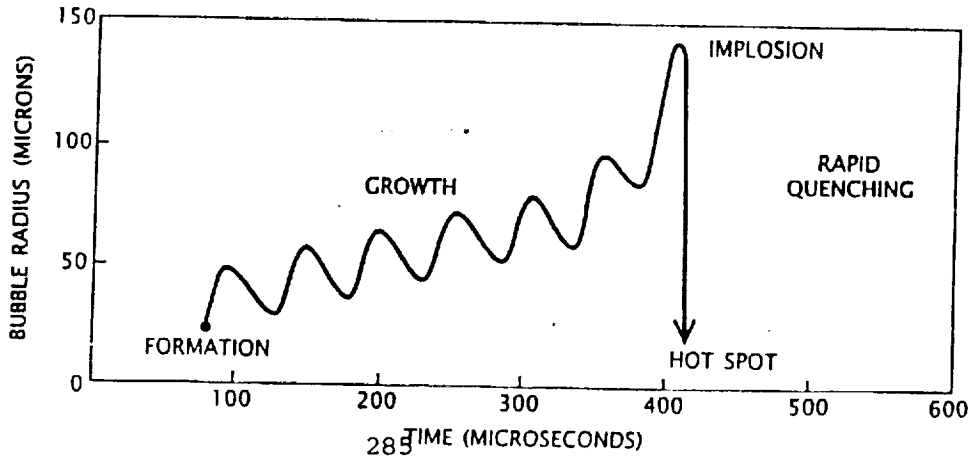

Figure 3-1

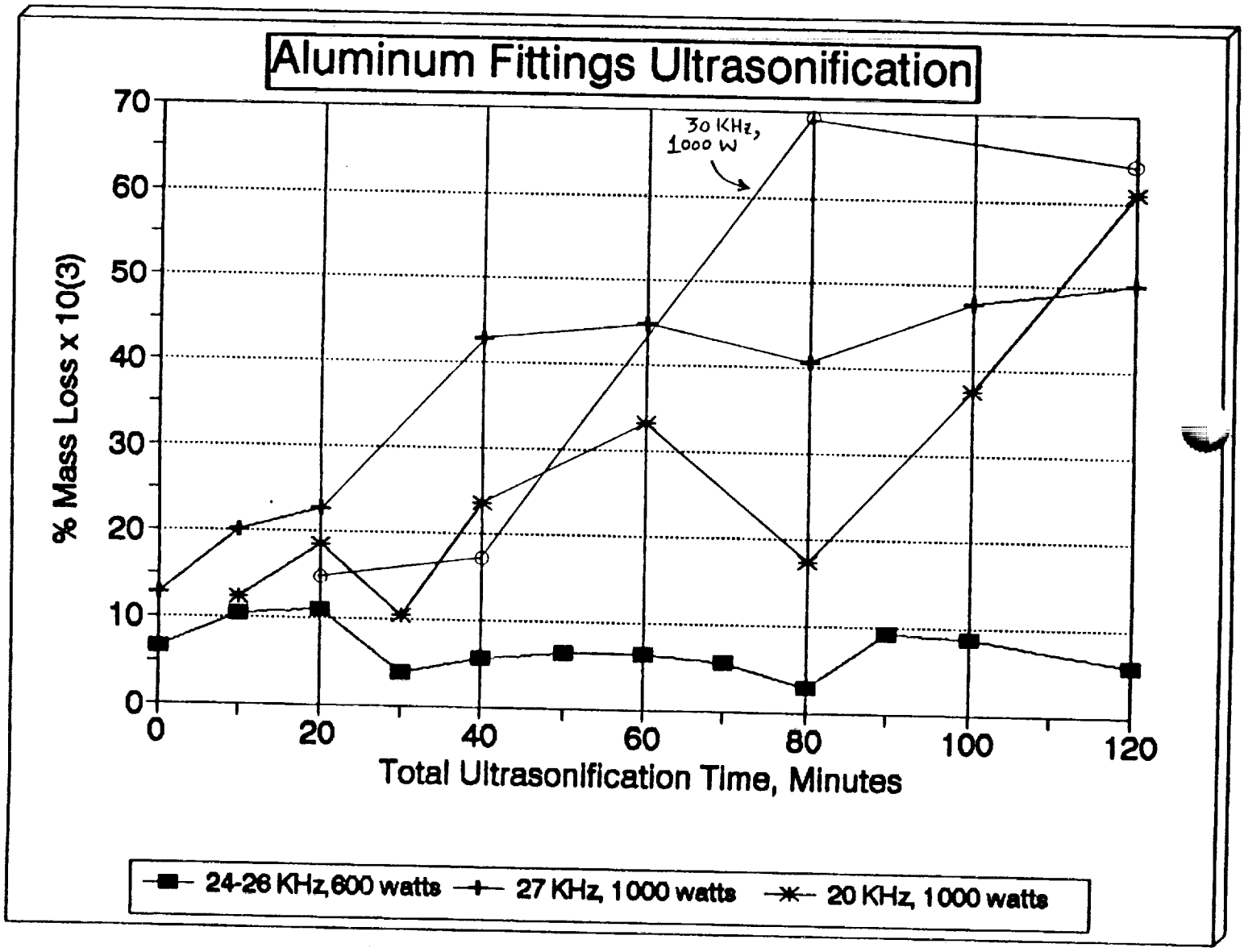
Aluminum Fittings Ultrasonification
30 KHz, 1000 W
% Mass Loss x 10(3)
70
60
50
40
30
20
10
0
0
20
40
60
80
100
120
Total Ultrasonification Time, Minutes
24-26 KHz, 600 watts
27 KHz, 1000 watts
20 KHz, 1000 watts

Figure 3-2

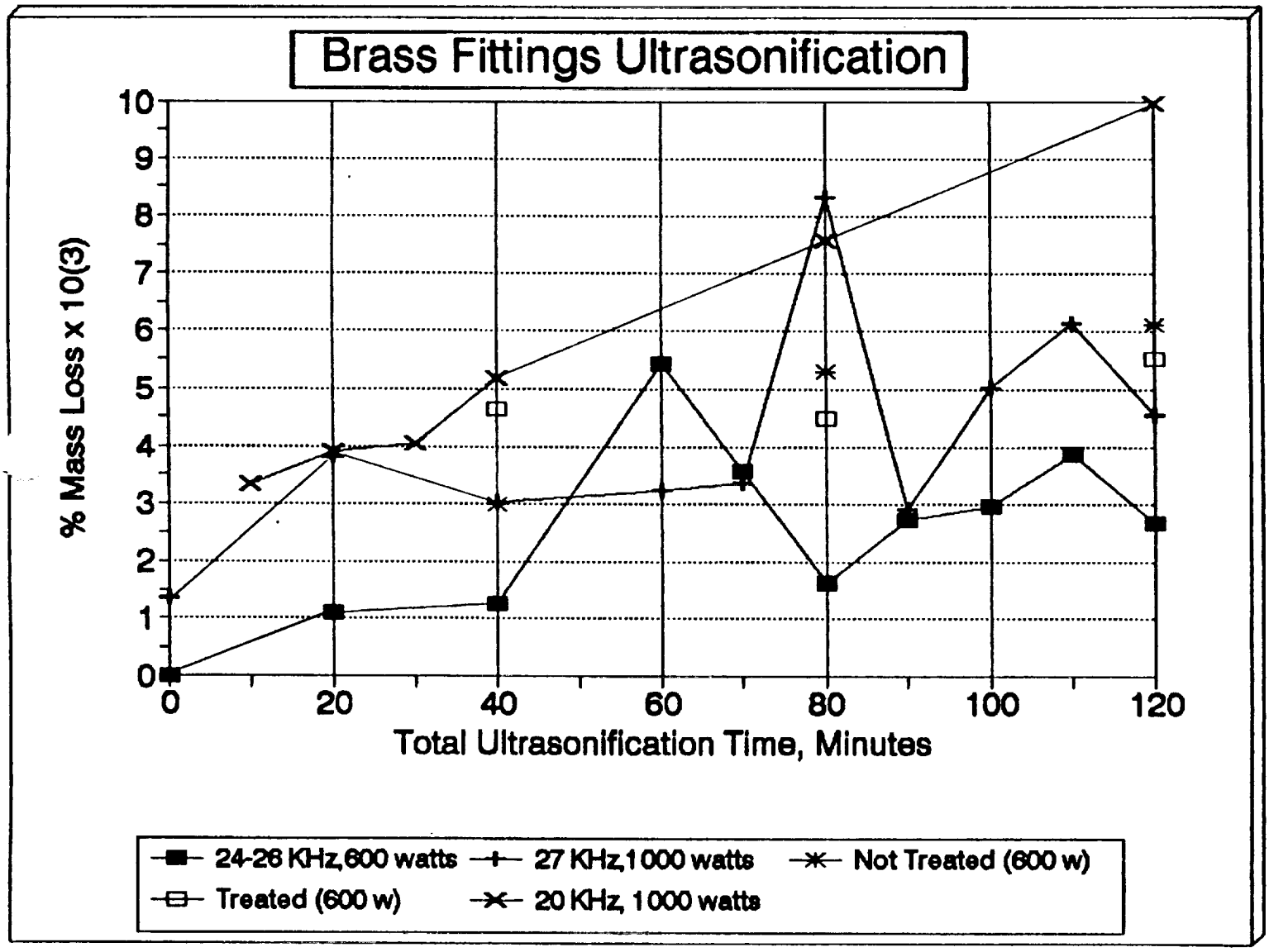
Brass Fittings Ultrasonification
% Mass Loss x 10(3)
0
1
2
3
4
5
6
7
8
9
10
0
20
40
60
80
100
120
Total Ultrasonification Time, Minutes
24-26 KHz,600 watts
27 KHz,1000 watts
Not Treated (600 w)
Treated (600 w)
20 KHz, 1000 watts

Figure 3-3

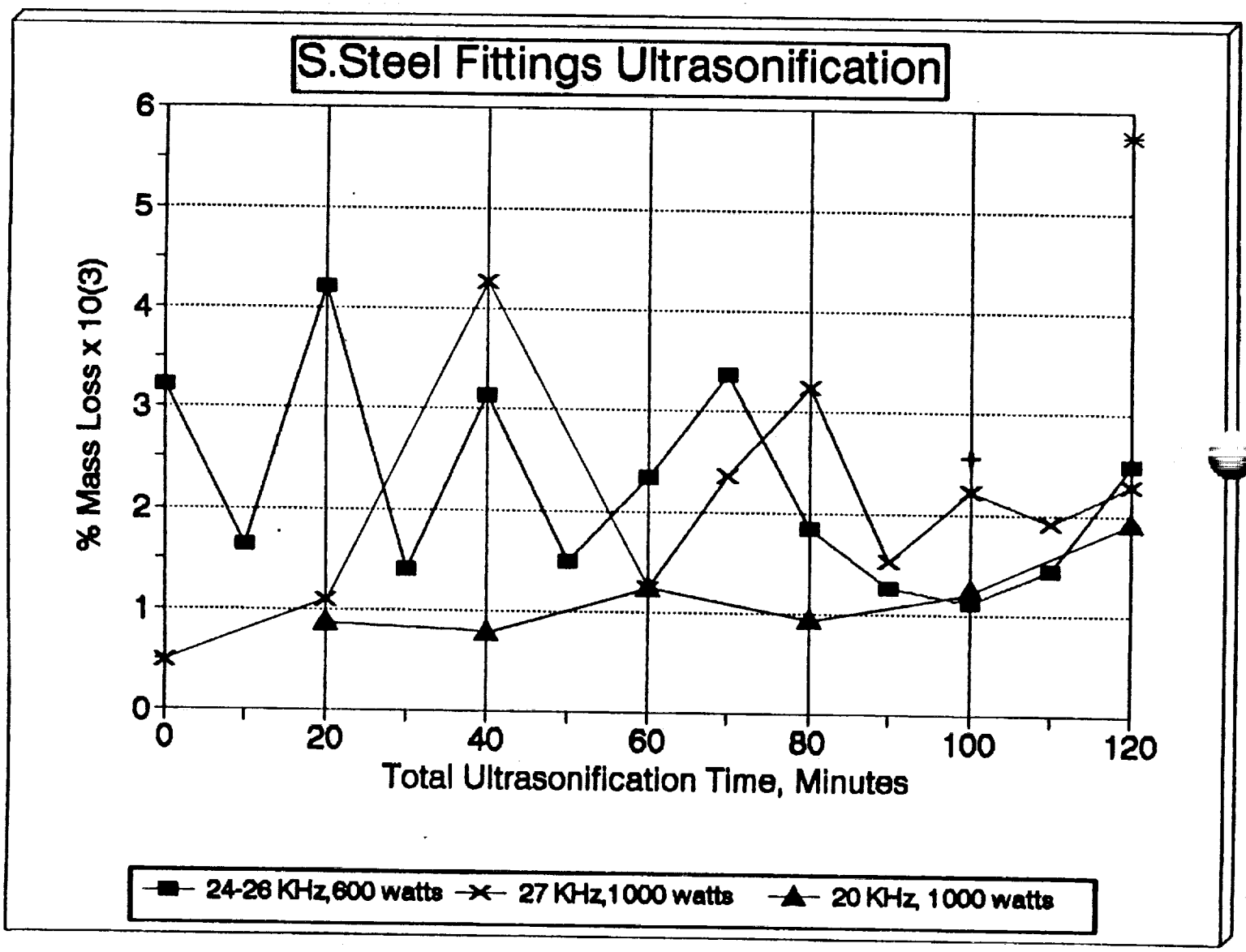
S.Steel Fittings Ultrasonification
% Mass Loss x 10(3)
0
1
2
3
4
5
6
0
20
40
60
80
100
120
Total Ultrasonification Time, Minutes
24-26 KHz,600 watts
27 KHz,1000 watts
20 KHz, 1000 watts

Figure 3-4

SEM/Anodized Aluminum/4 cycles/Blackstone

Anodized
Aluminum
T = 0

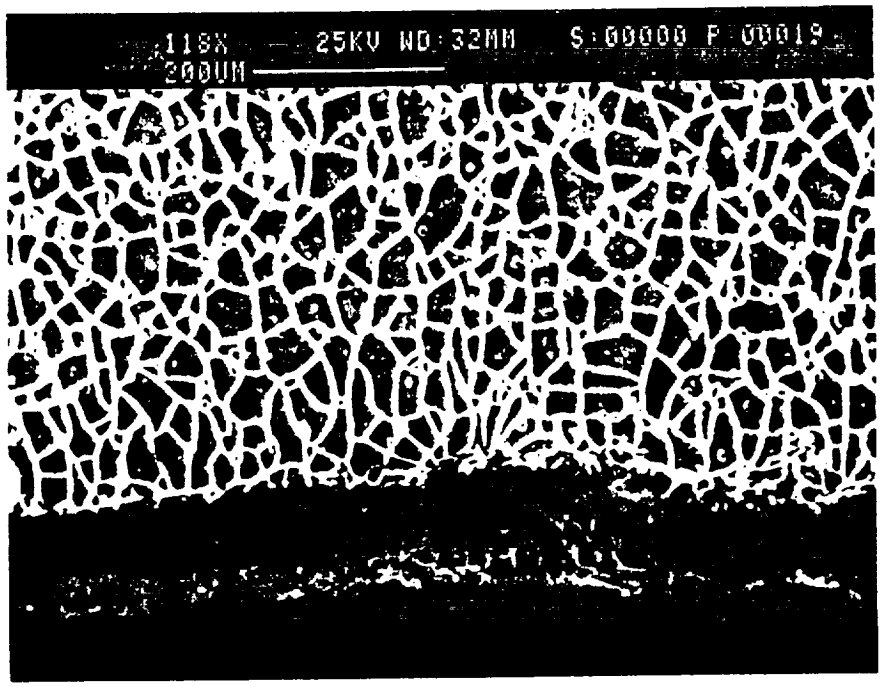

Anodized
Aluminum
T = 40 minutes

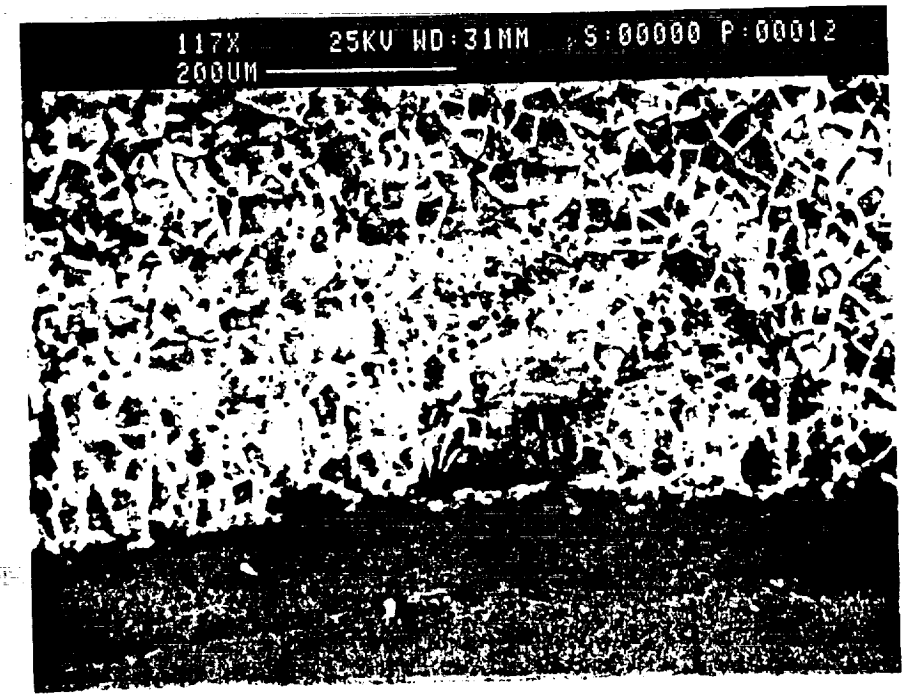

Figure 3-5

SEM/Anodized Aluminum/12 cycles/Blackstone

Anodized
Aluminum
T = 0 minutes

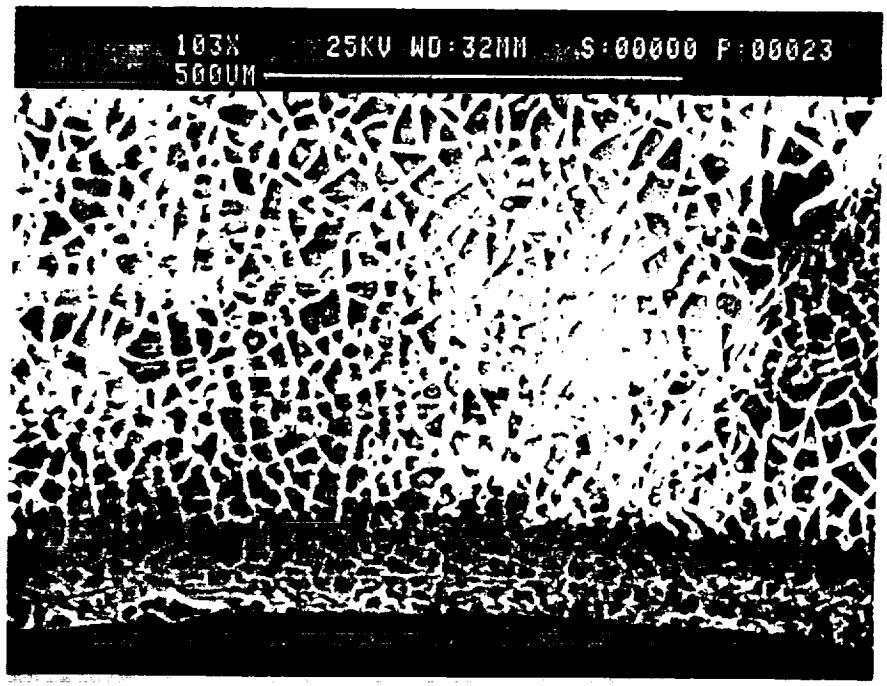

Anodized
Aluminum
T = 120 minutes

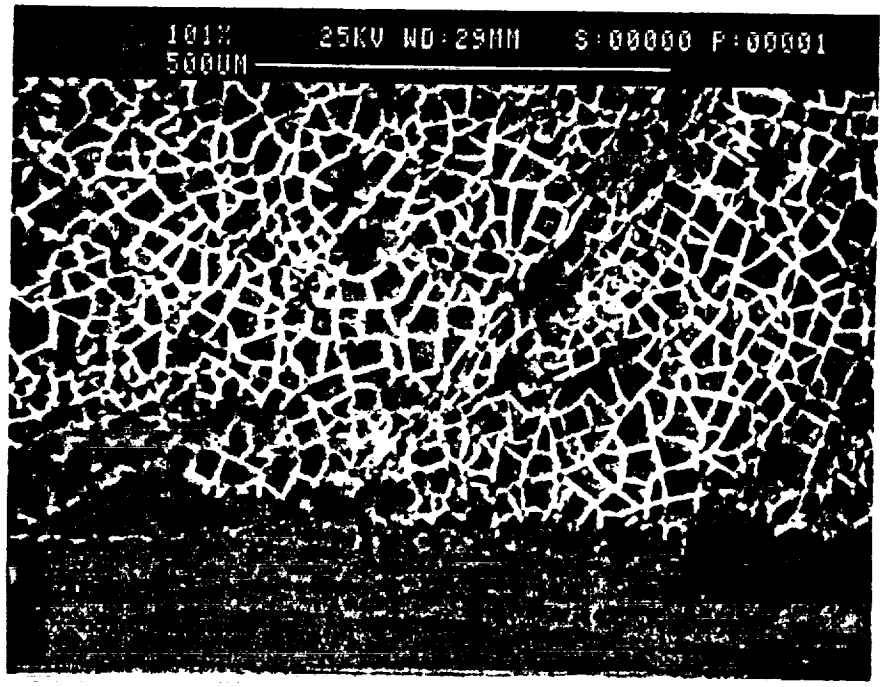

Figure 3-6

SEM/Brass/4 cycles/Blackstone

Brass
T = 0

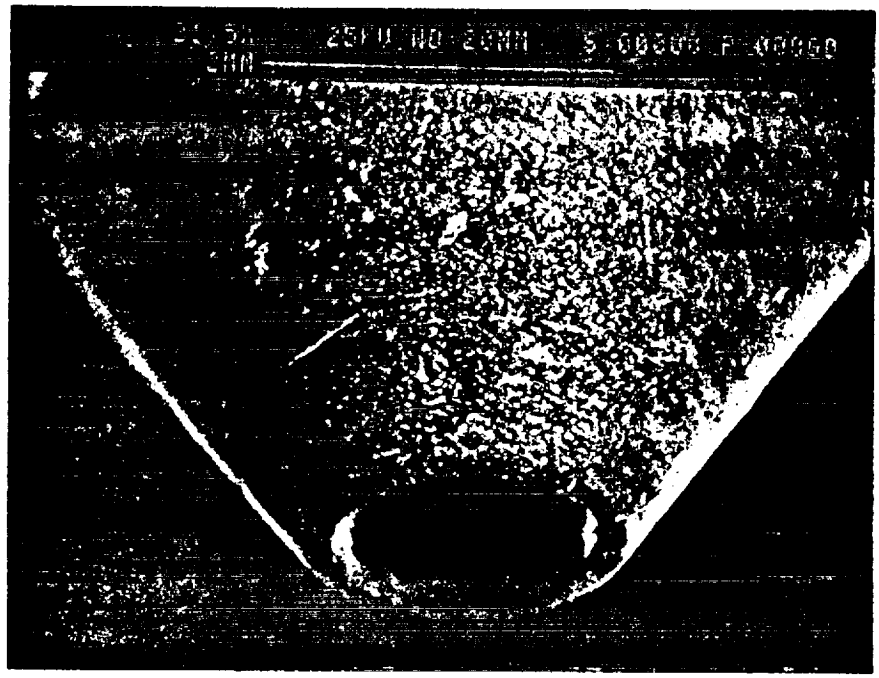

JUNE
0 cycl

#- 3 BRASS

Brass
T = 40 minutes

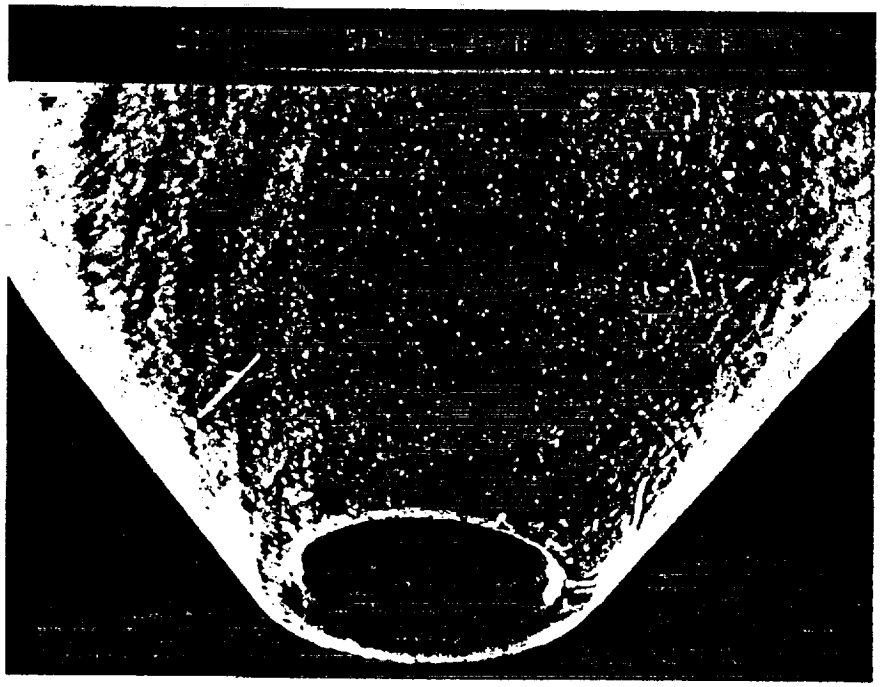

BRASS
4 cycles

June 11

#3

Figure 3-7

SEM/Brass/8 cycles/Blackstone

Brass
T = 0

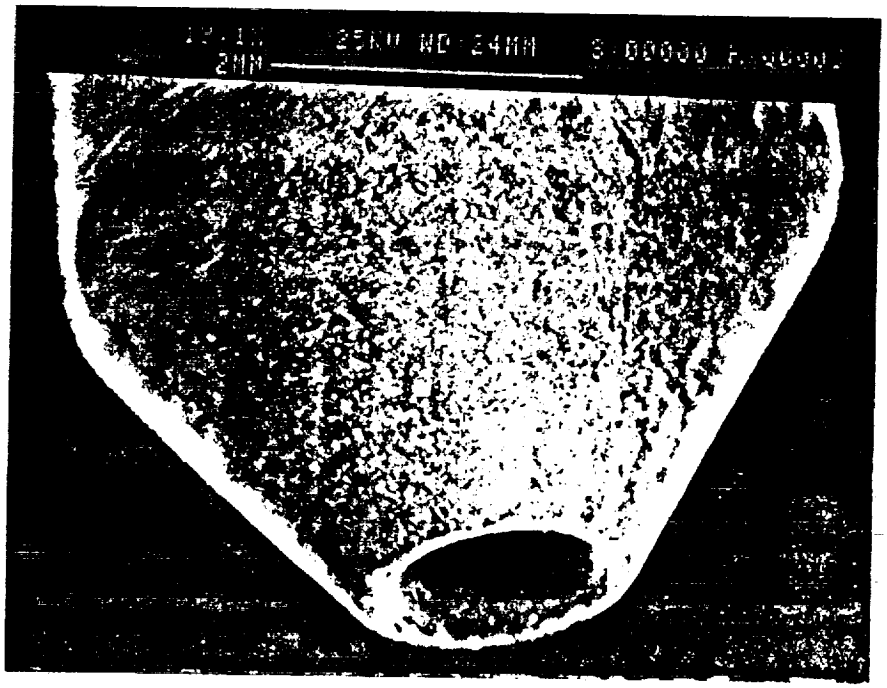

Brass
T = 80 minutes

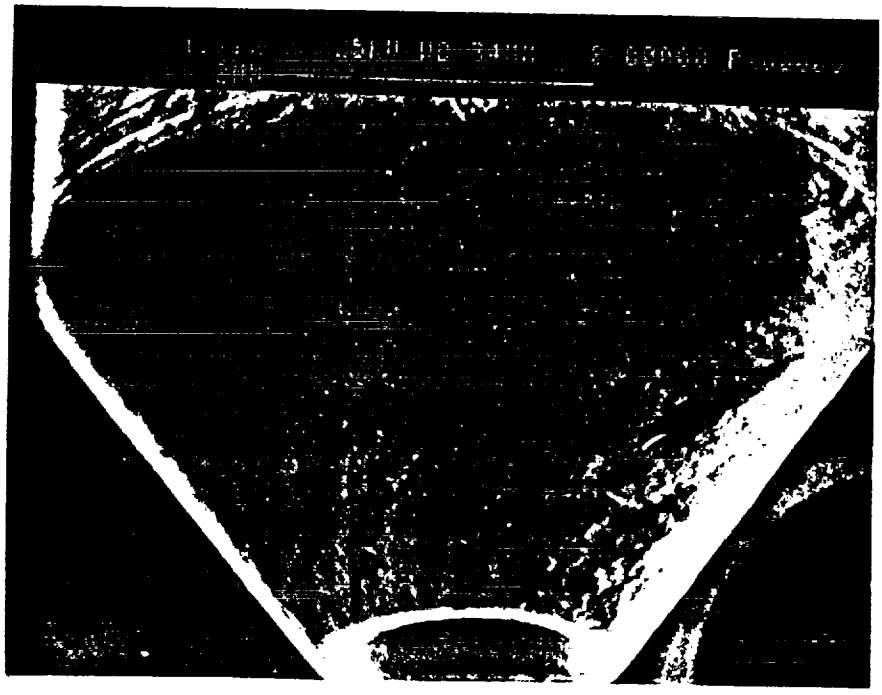

Figure 3-8a

SEM/Brass Treated with ferric chloride/4 cycles/Blackstone

Brass
T = 0

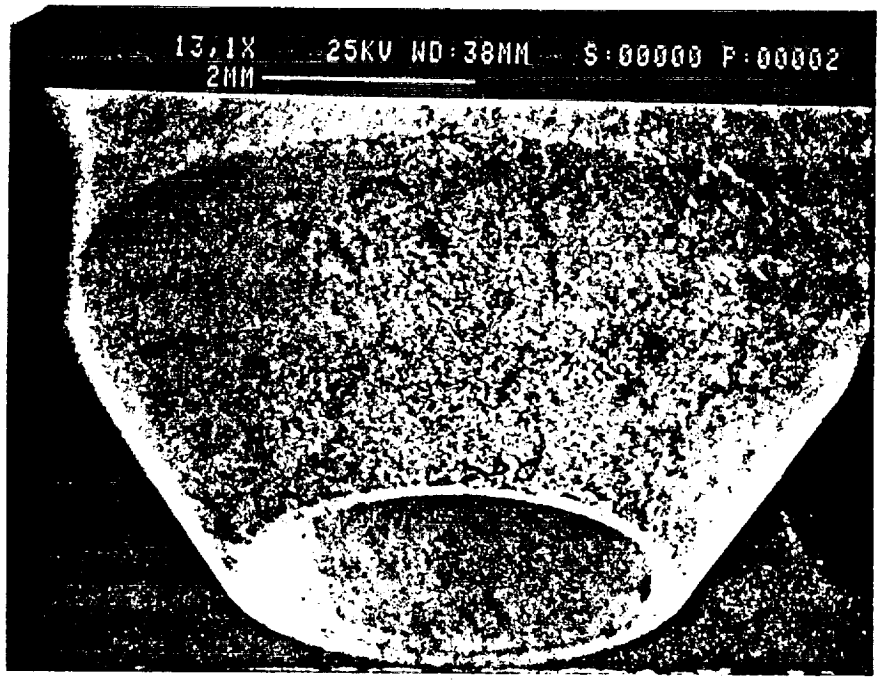

Brass
T = 40 minutes

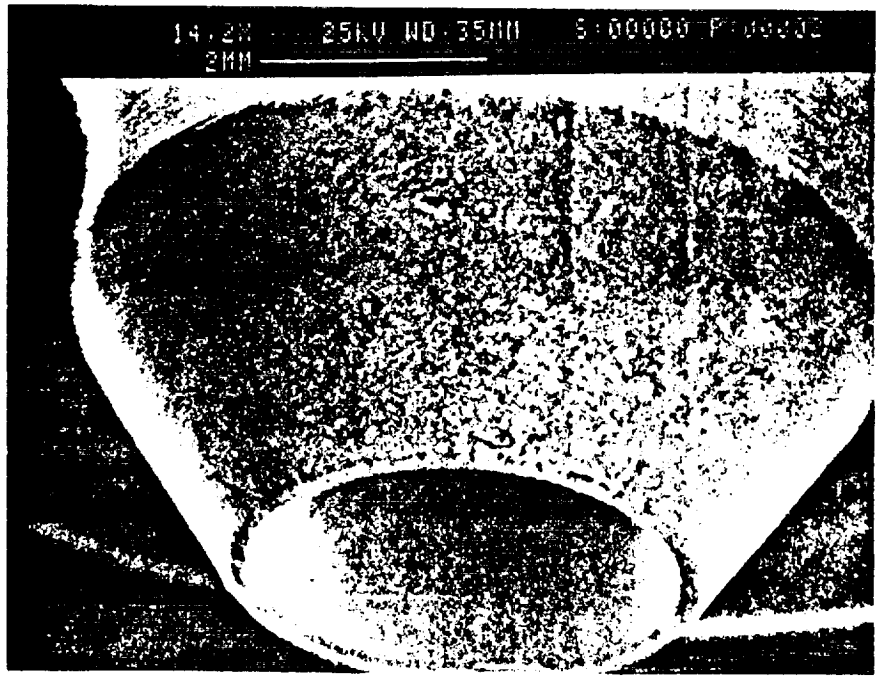

Figure 3-8b

SEM/Brass Not Treated/4 cycles/Blackstone

Brass
T = 0

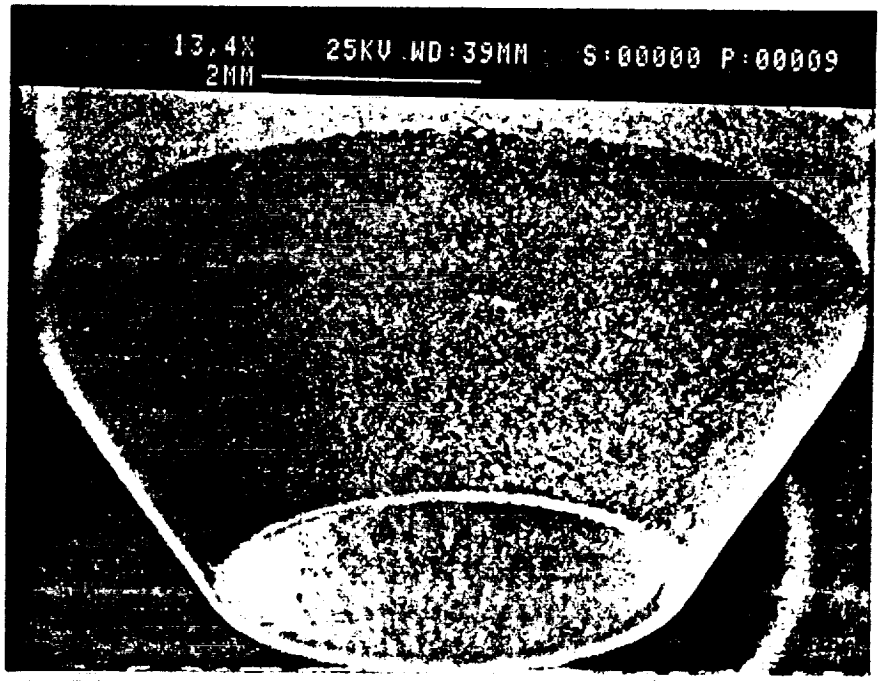

Brass
T = 40 minutes

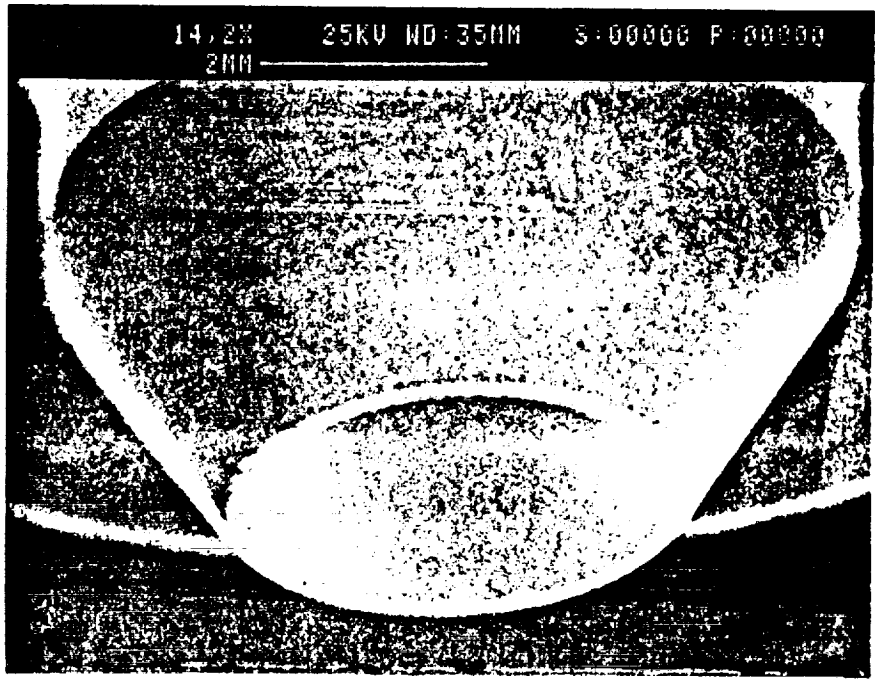

Figure 3-9a

SEM/Brass Treated with Ferric Chloride/8 cycles/Blackstone

Brass
T = 0

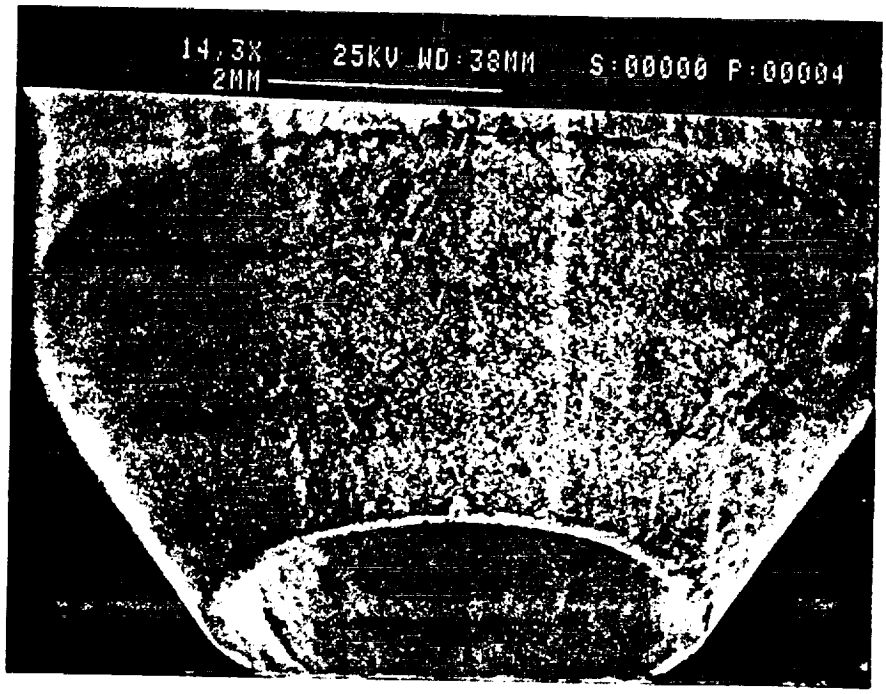

Brass
T = 80 minutes

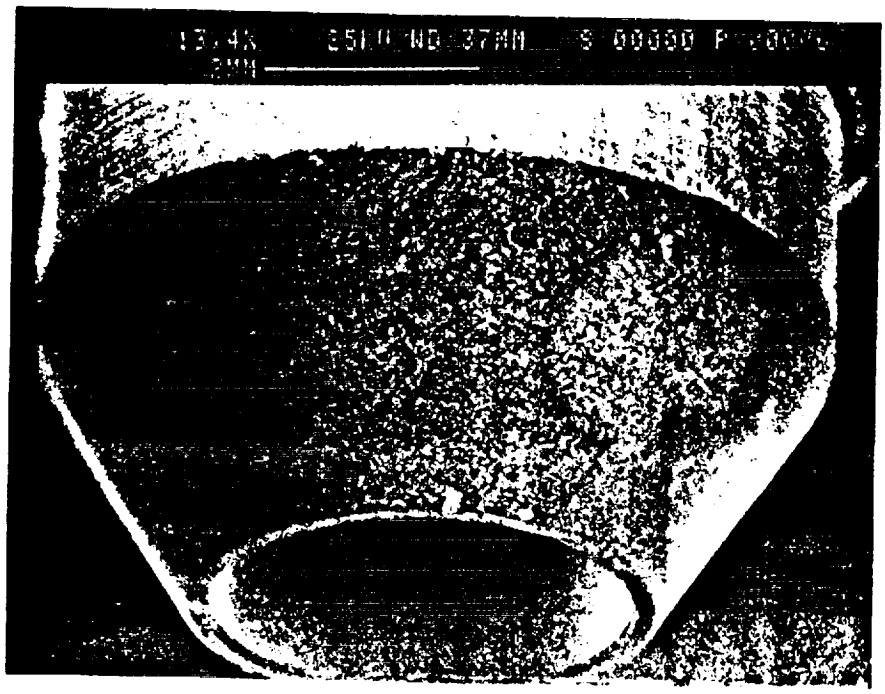

Figure 3-9b

SEM/Brass Not Treated/8 cycles/Blackstone

Brass
T = 0

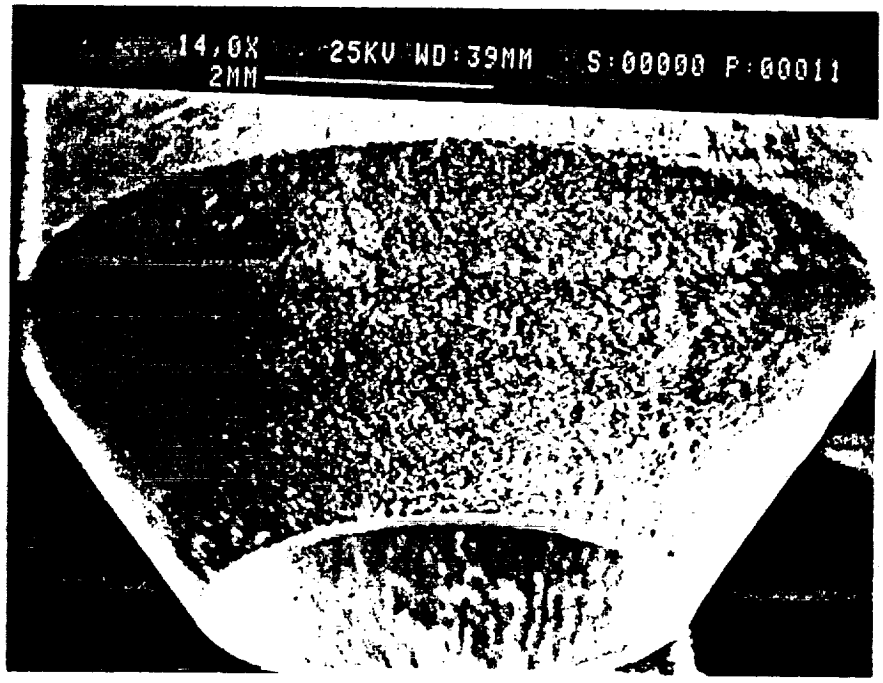

Brass
T = 80 minutes

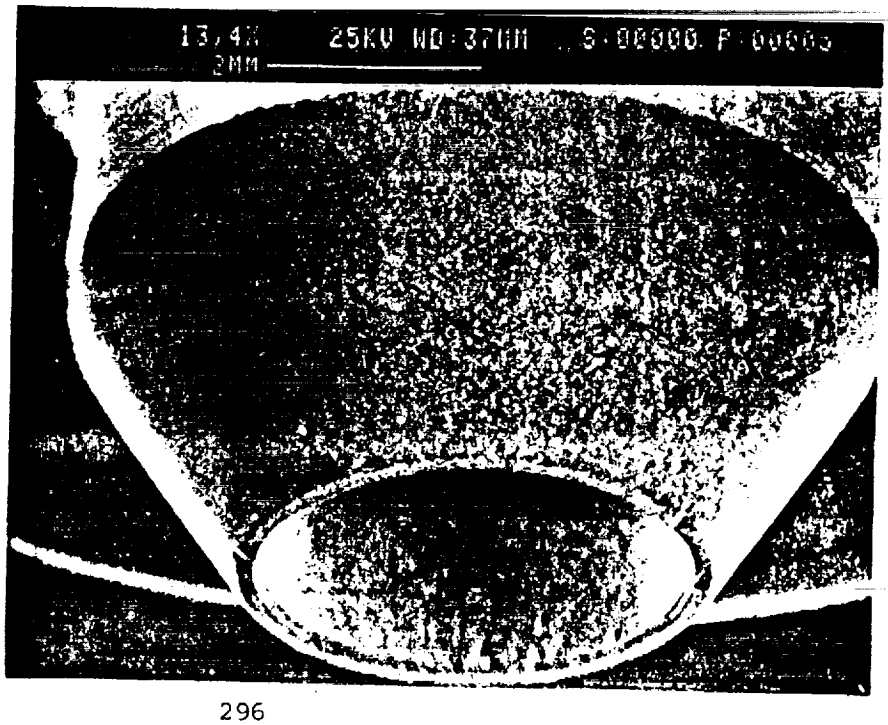

Figure 3-10

SEM/Brass/12 cycles/Blackstone

Brass
T = 0

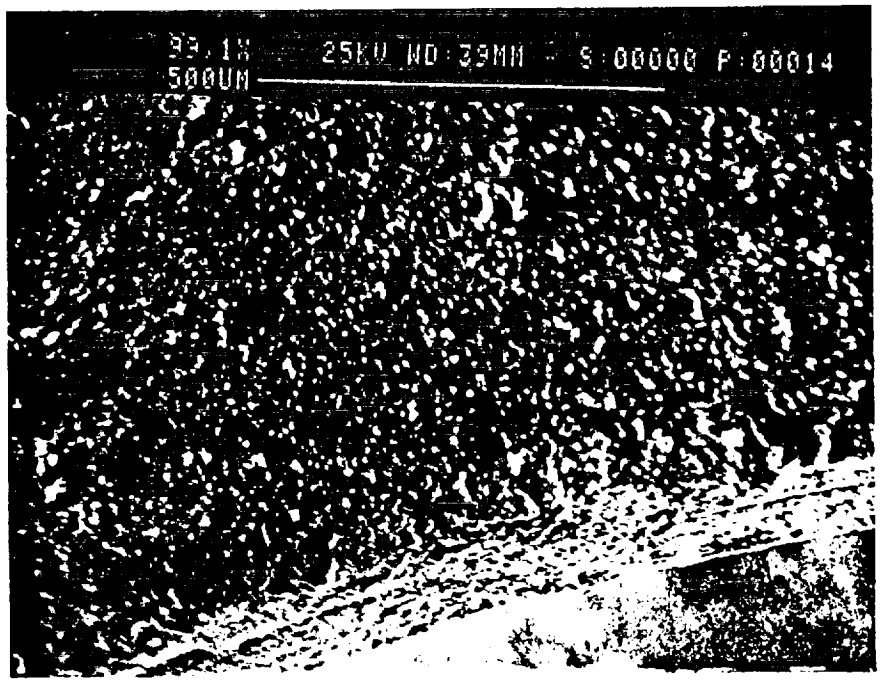

T=0

BRASS #34

Brass
T = 120 minutes

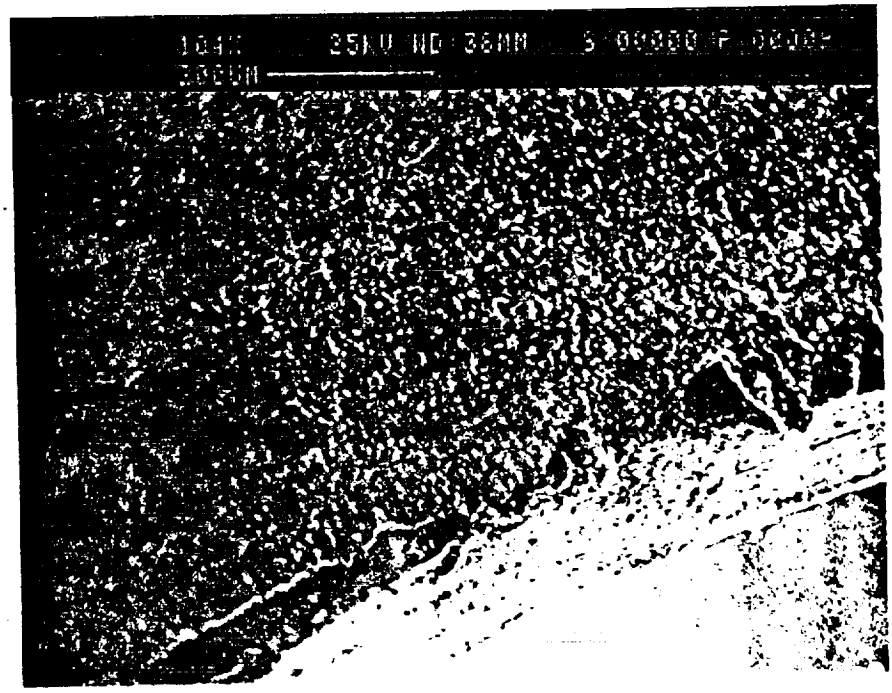

Figure 3-11a

SEM/Stainless Steel/12 cycles/Blackstone

Stainless Steel
T = 0

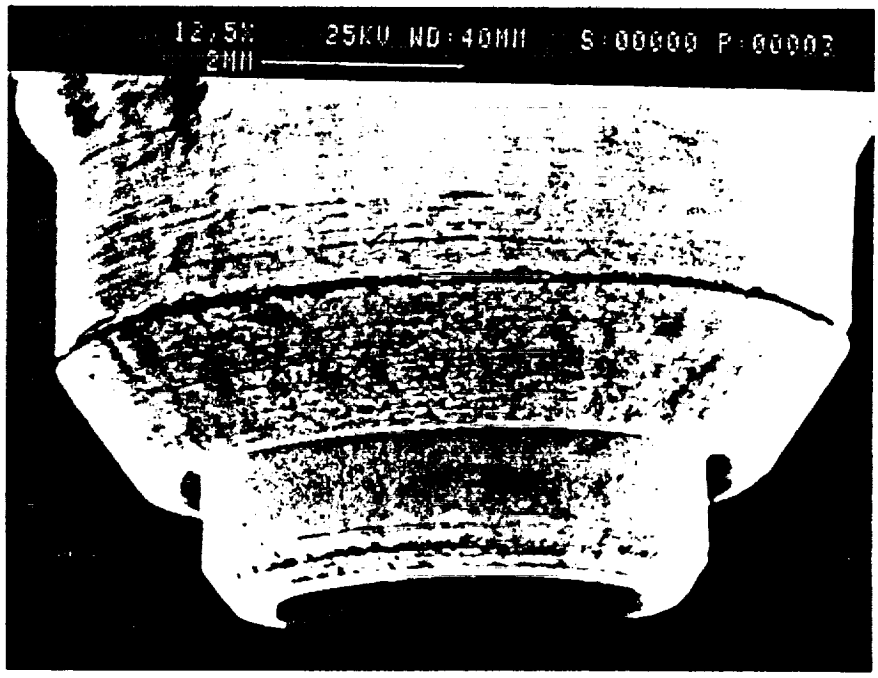

SS. Samp #1 Jun. orig Samp

Stainless Steel
T = 120 minutes

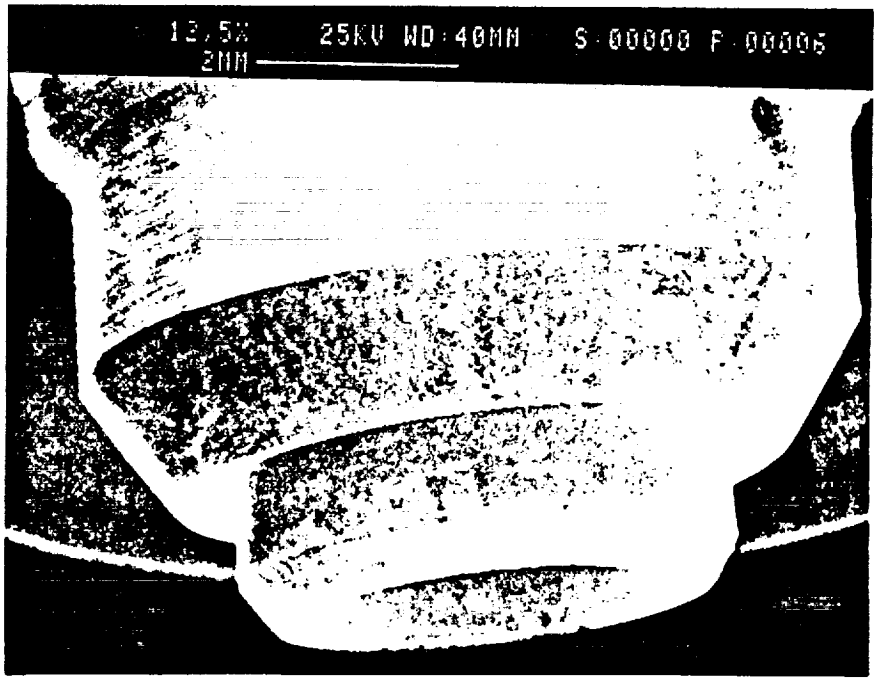

SS. Sample #1 June 8 after 12 cycle

Figure 3-11b

SEM/Stainless Steel/12 cycles/Blackstone

Stainless Steel
T = 0

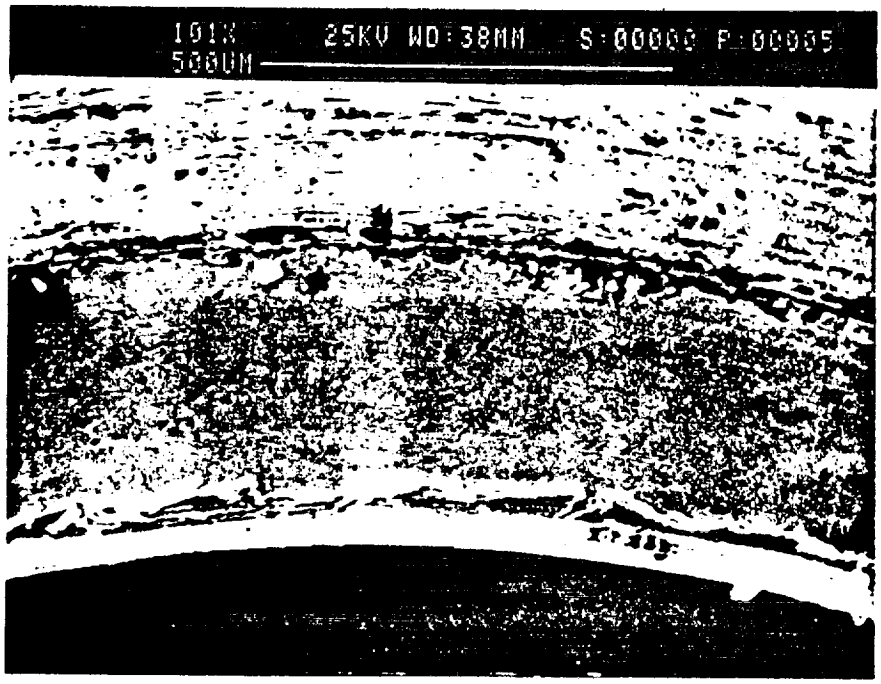

S.S. Sample #1 run 4 orig Surf

Stainless Steel
T = 120 minutes

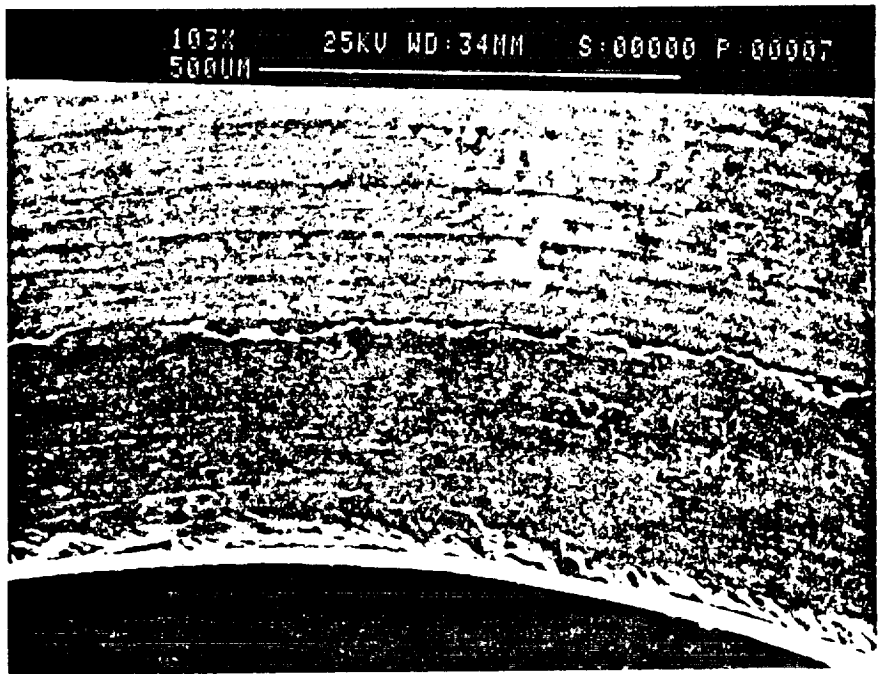

SS. Sample #1 SEM after 12 cycle

Figure 3-12

SEM/Anodized Aluminum/2 cycles/Sonic Systems

Anodized
Aluminum
T = 0

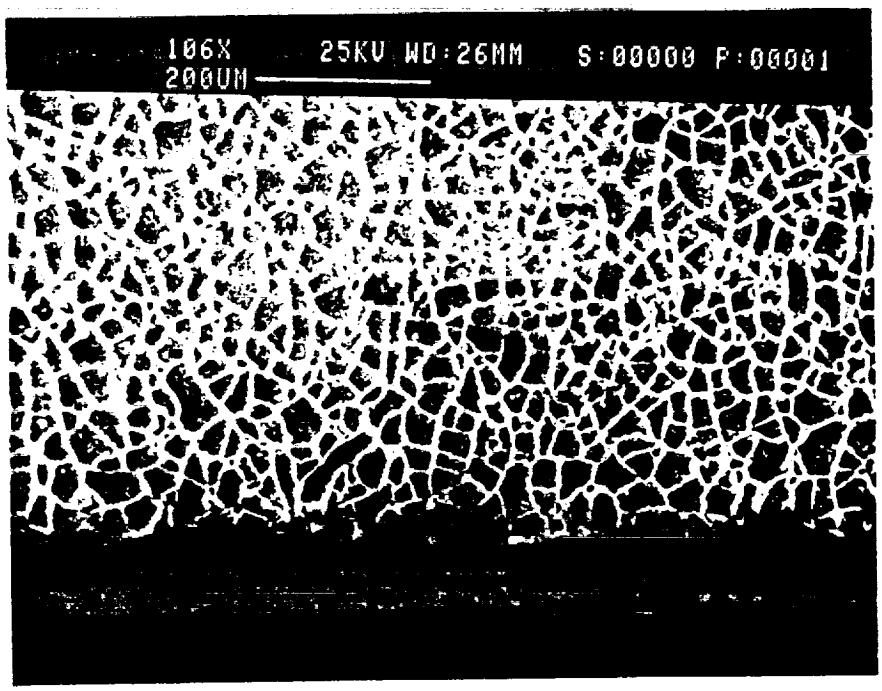

Anodized
Aluminum
T = 20 minutes

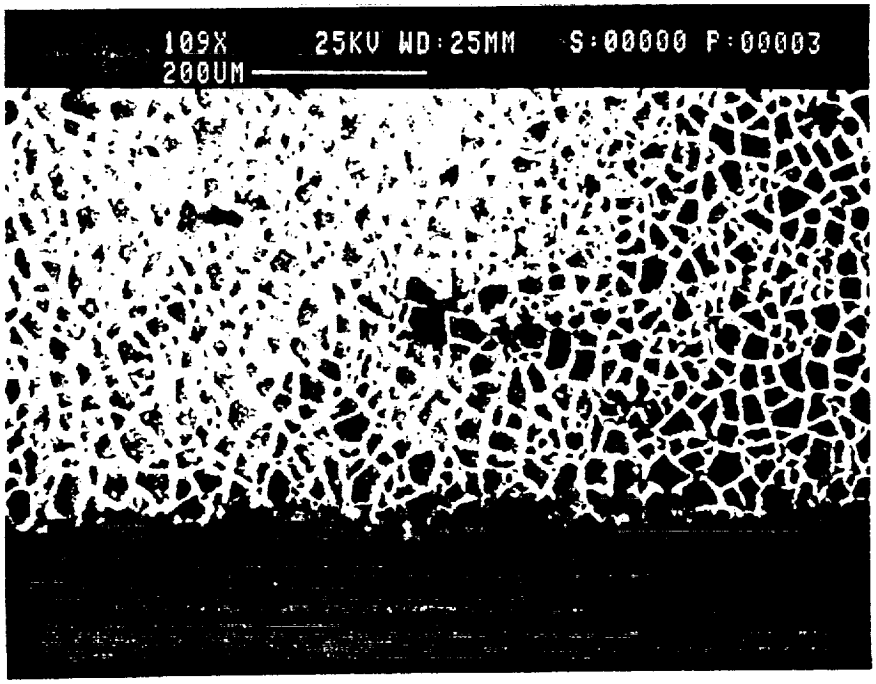

Figure 3-13

SEM/Anodized Aluminum/12 cycles/Sonic Systems

Anodized
Aluminum
T = 0

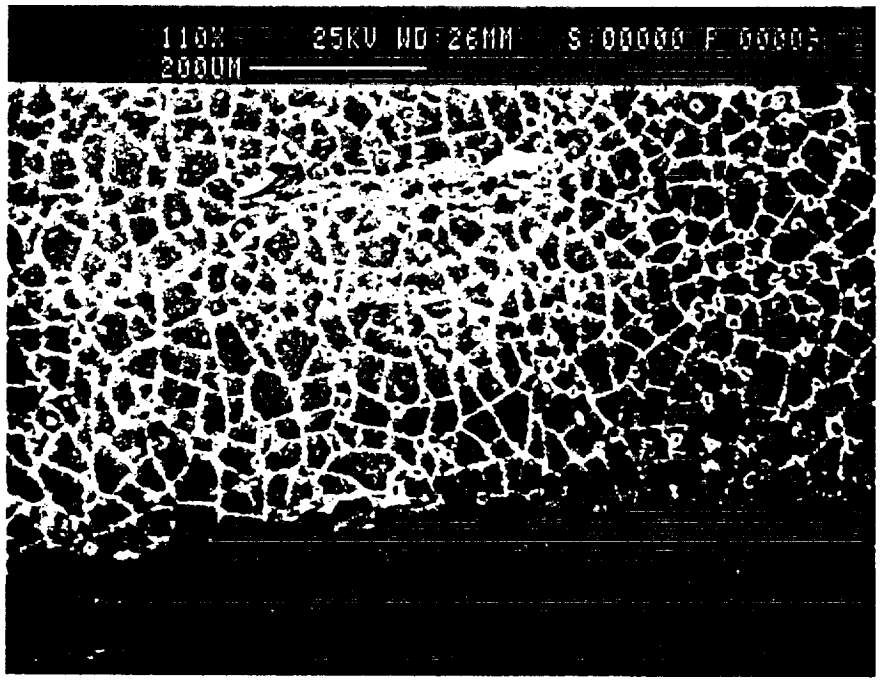

Anodized
Aluminum
T =120 minutes

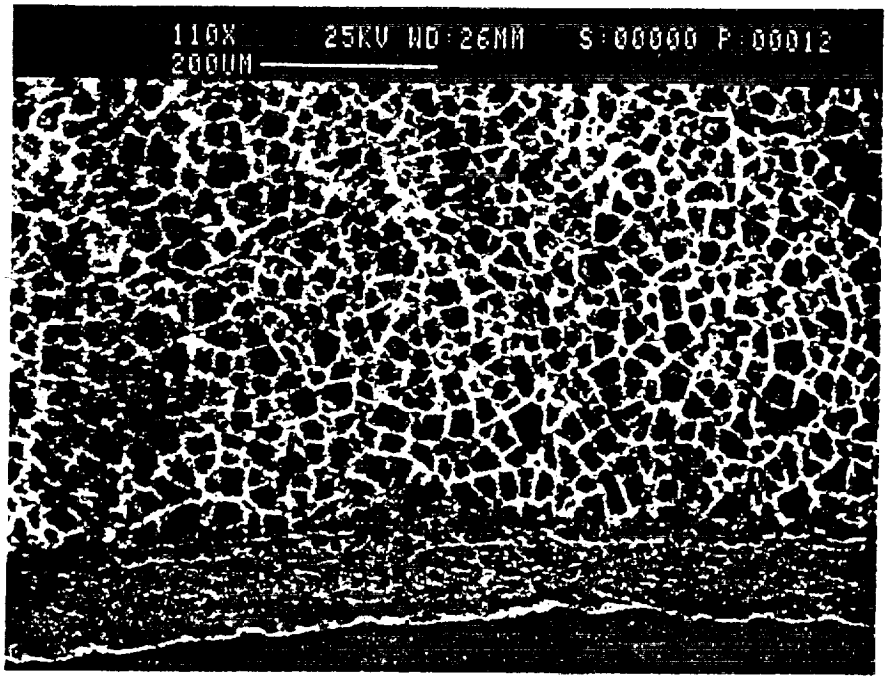

Figure 3-14

Optical Photograph of Water Residue (Anodized Aluminum Run)

Figure 3-15

SEM/Brass/12 cycles/Sonic Systems

Brass
T = 0

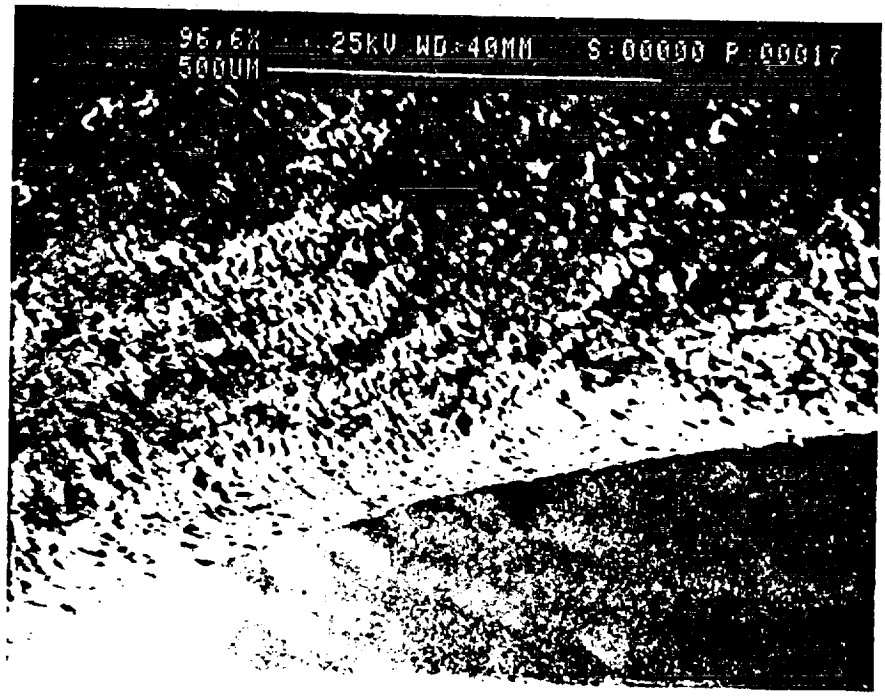

Brass
T = 120 minutes

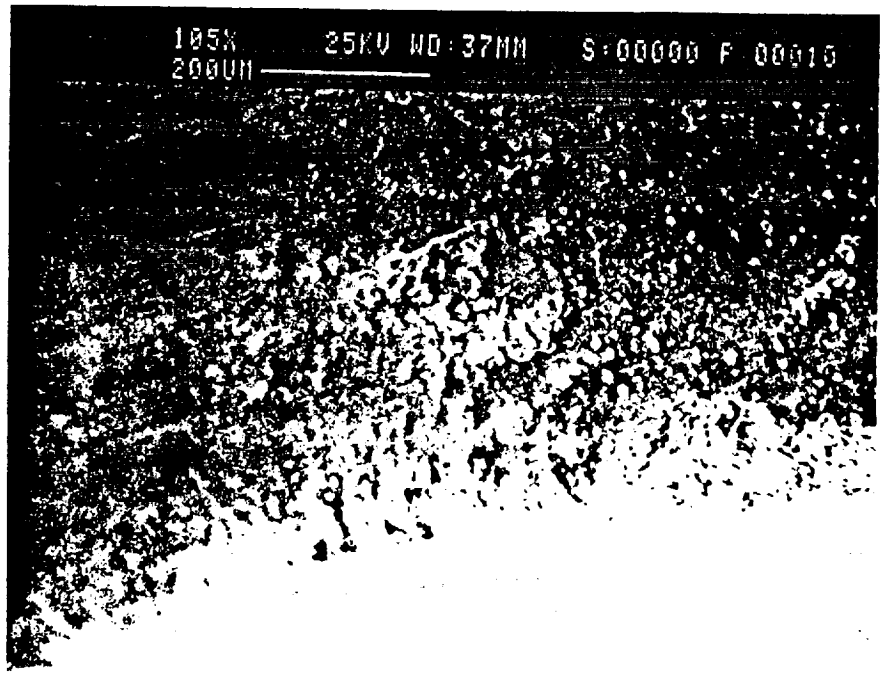

Figure 3-16

SEM/Stainless Steel/12 cycles/Sonic Systems

Stainless Steel
T = 0

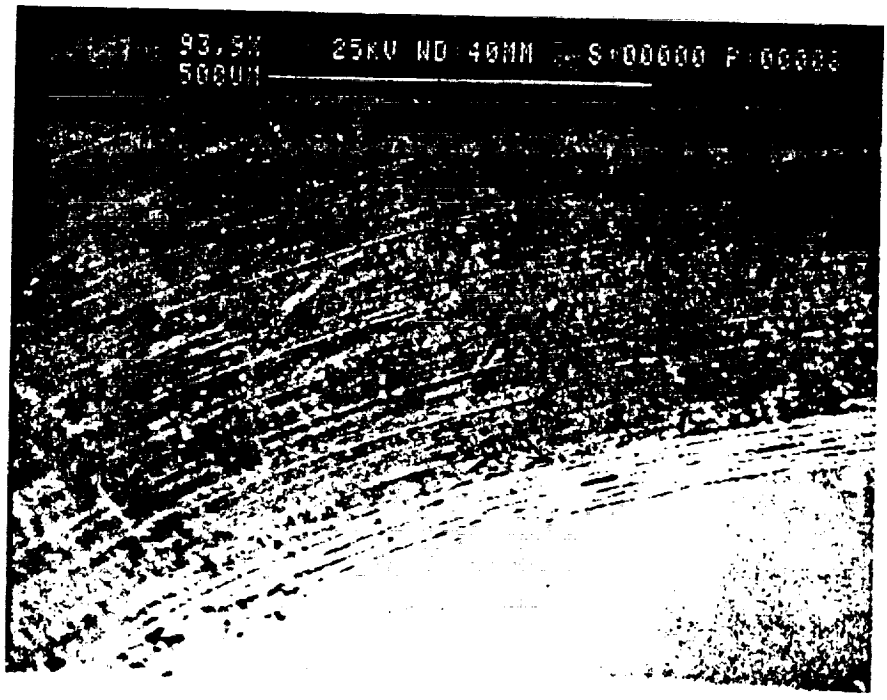

Stainless Steel
T = 120 minutes

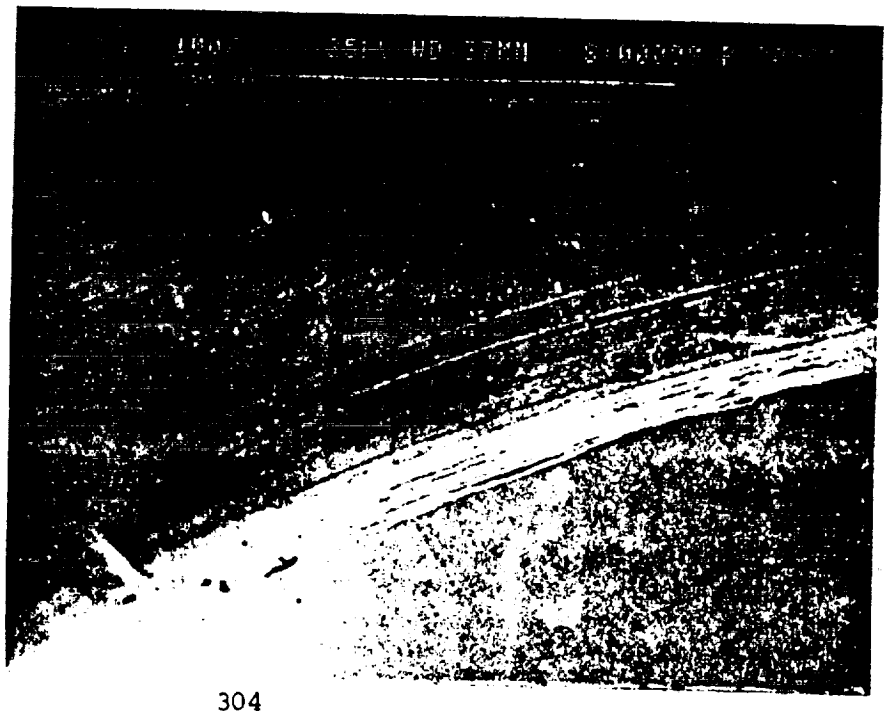

Figure 3-17

SEM/Anodized Aluminum/4 cycles/Branson

Anodized
Aluminum
T = 0

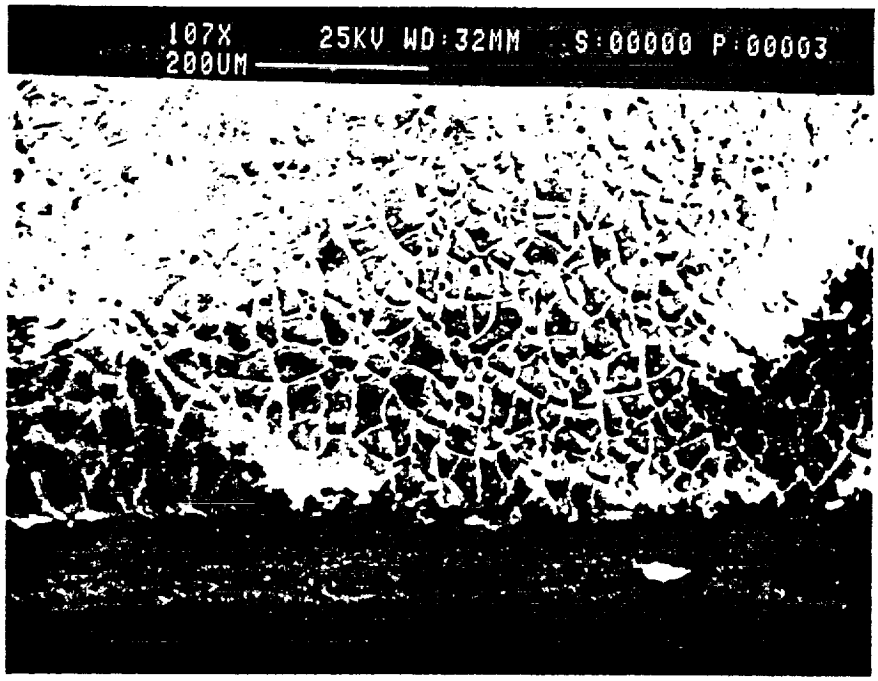

Anodized
Aluminum
T = 40 minutes

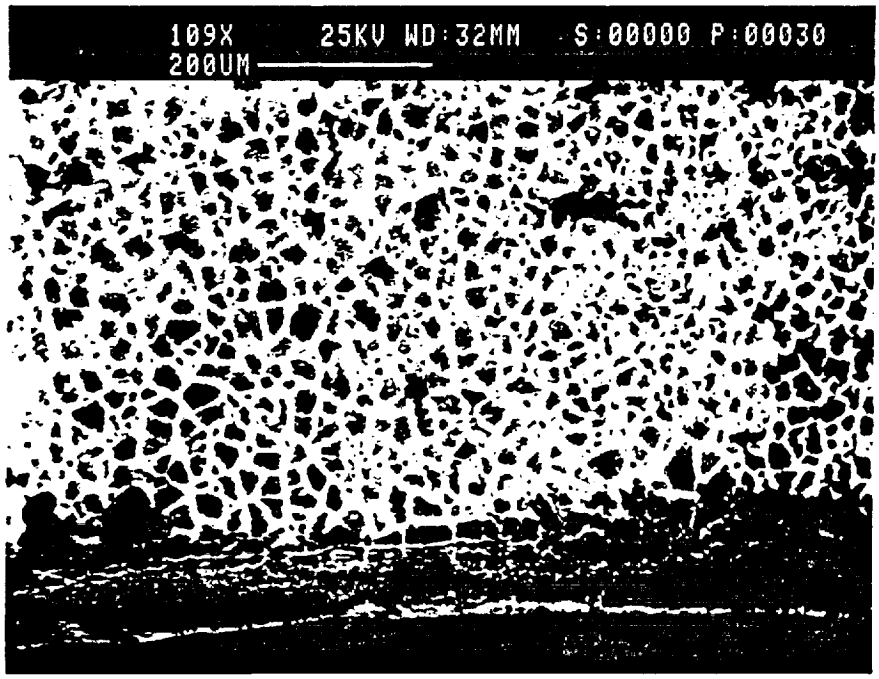

Figure 3-18

SEM/Anodized Aluminum/8 cycles/Branson

Anodized
Aluminum
T = 0

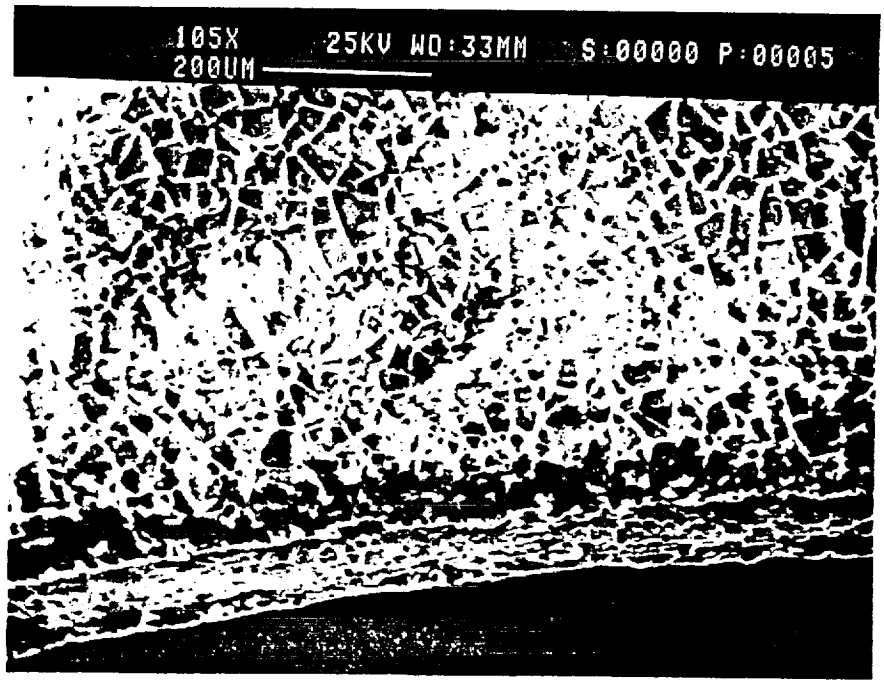

Anodized
Aluminum
T = 80 minutes

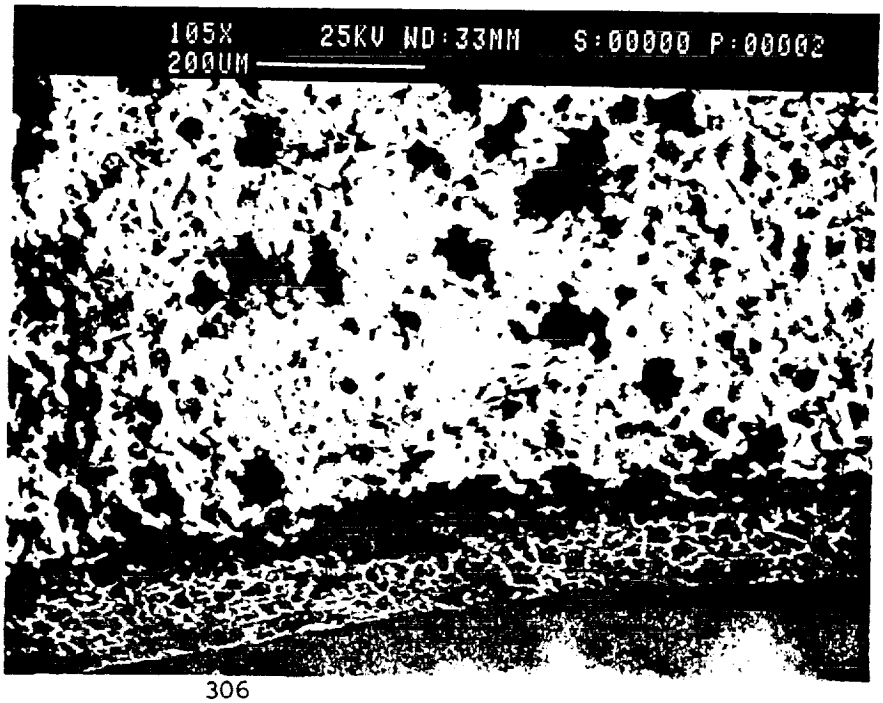

Figure 3-19a

SEM/Anodized Aluminum/12 cycles/Branson

Anodized
Aluminum
T = 0

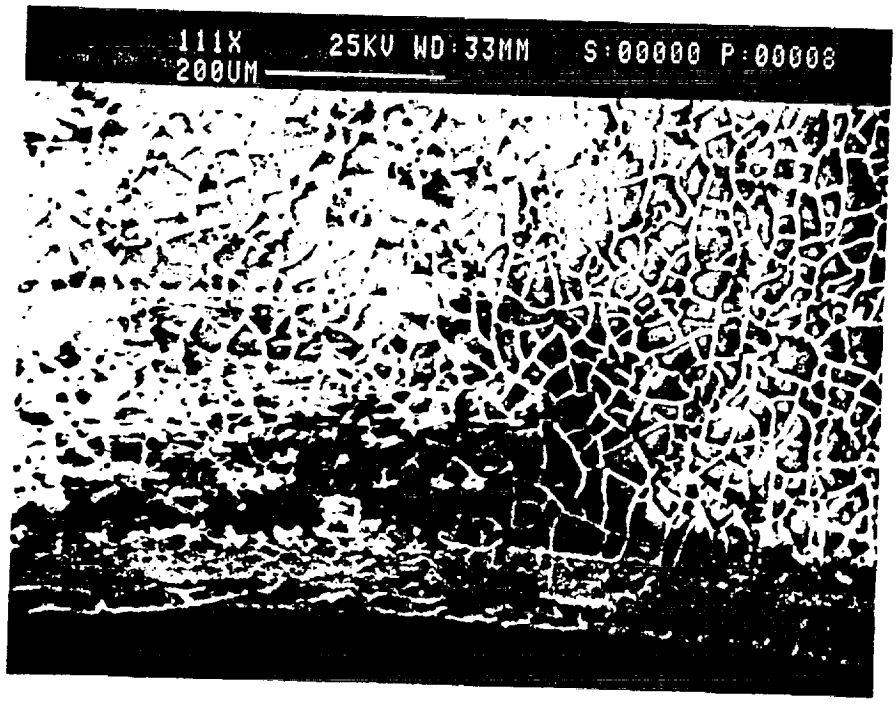

Al #308 T=0

Anodized
Aluminum
T = 120 minutes

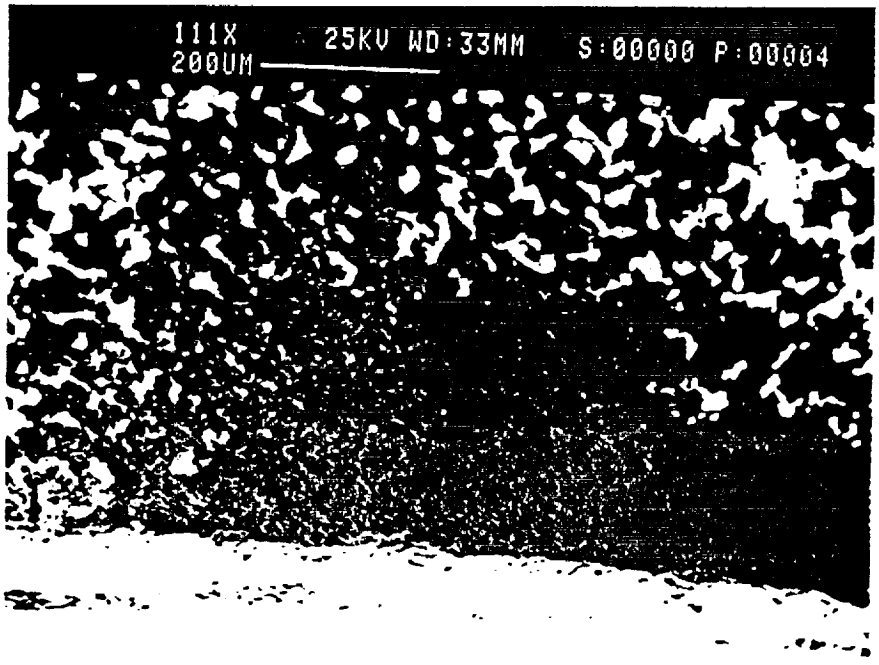

Al #305 120 cycles

Figure 3-19b

SEM/Anodized Aluminum/12 cycles/Branson

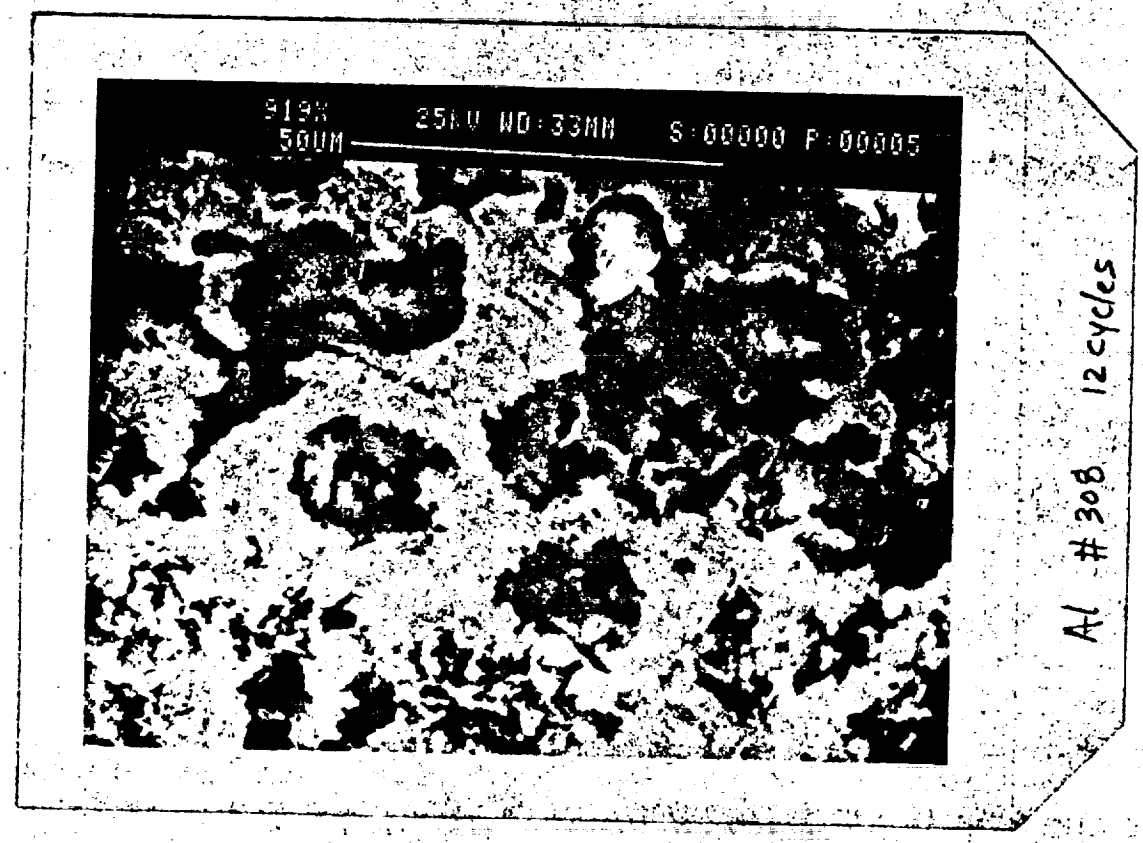

Anodized
Aluminum
T = 120 minutes

Figure 3-20

SEM/Anodized Aluminum/2 cycles/Branson

Anodized Aluminum T = 0 minutes

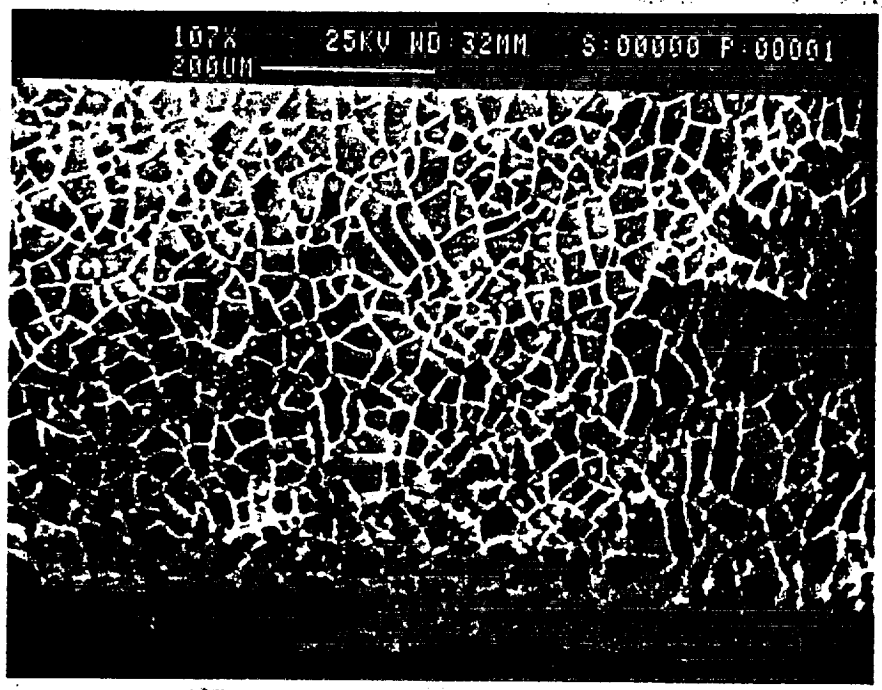

Al #303 T=0

Anodized Aluminum T = 20 minutes

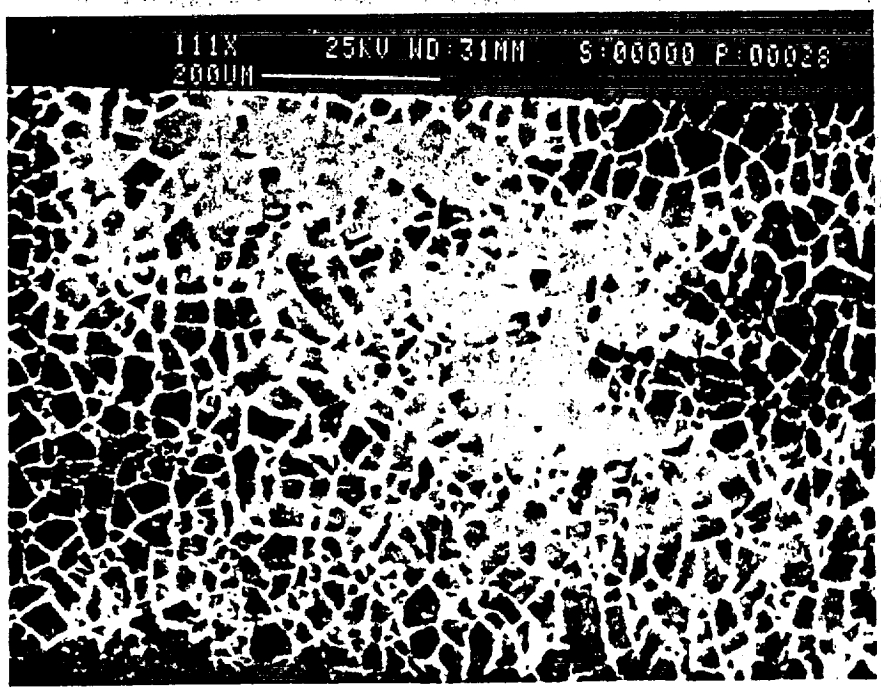

Al 303 2cycles

Figure 3-21

Optical Photograph/Anodized Aluminum/2- and 12 cycles/Branson

Anodized
Aluminum
T = 20 minutes

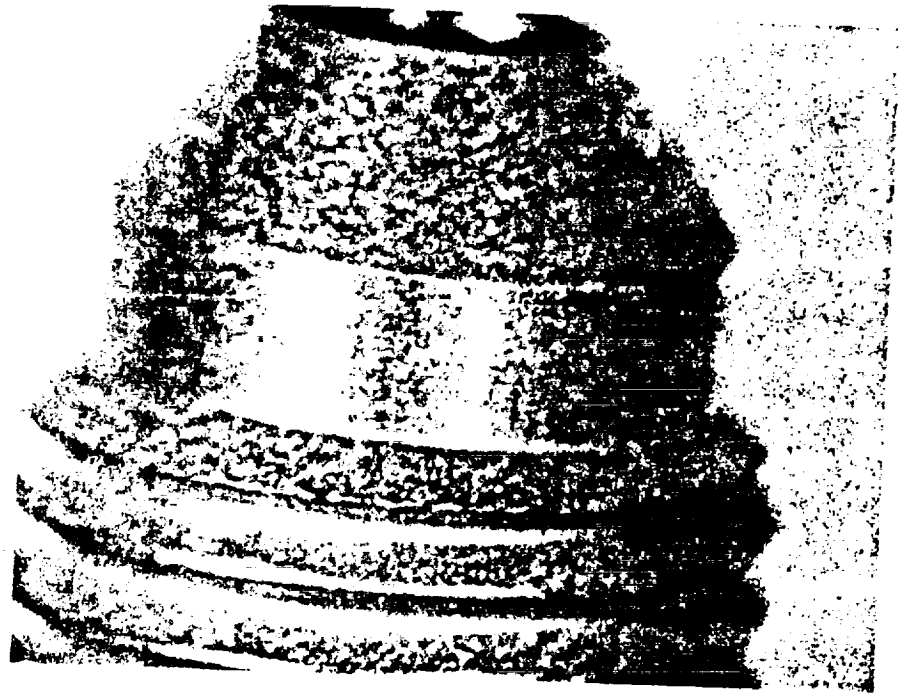

Anodized
Aluminum
T = 120 minutes

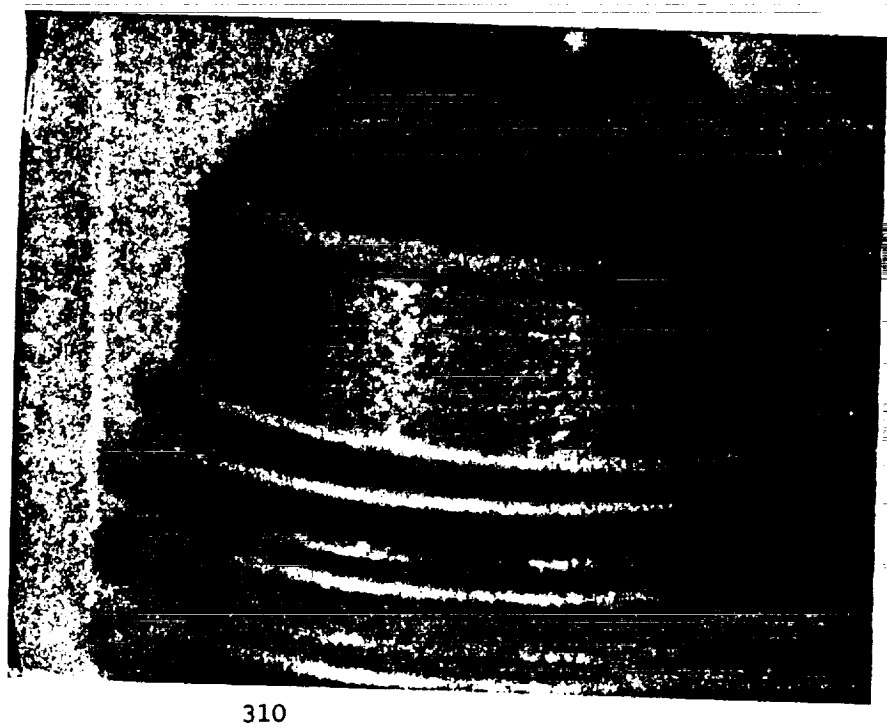

Figure 3-22a

SEM/Brass/12 cycles/Branson

Brass
T = 0 minutes

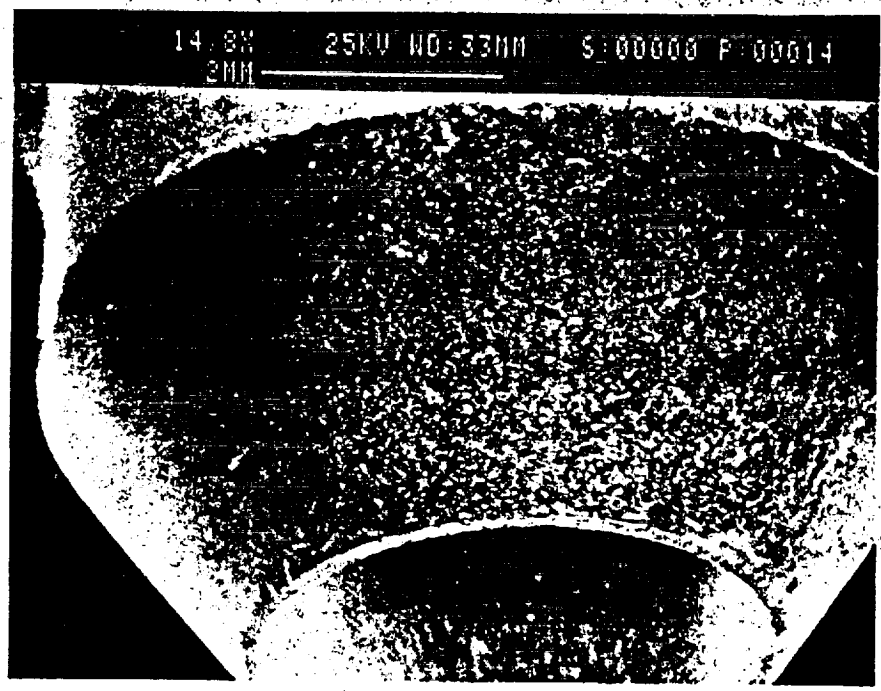

Brass #205 T=0

Brass
T = 120 minutes

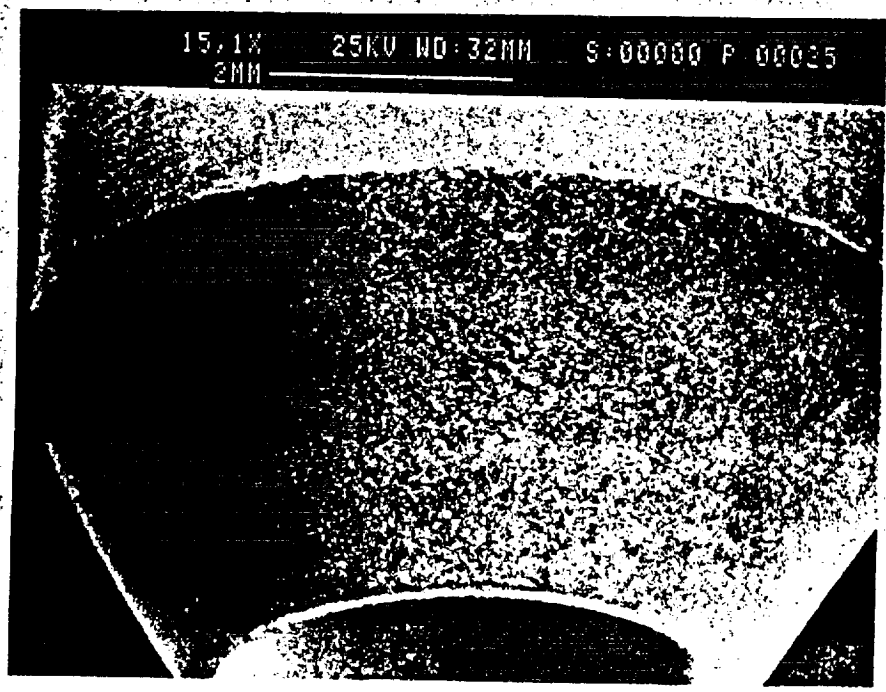

Brass #205 12 cycles

Figure 3-22b

SEM/Brass/12 cycles/Branson

Brass
T = 0 minutes

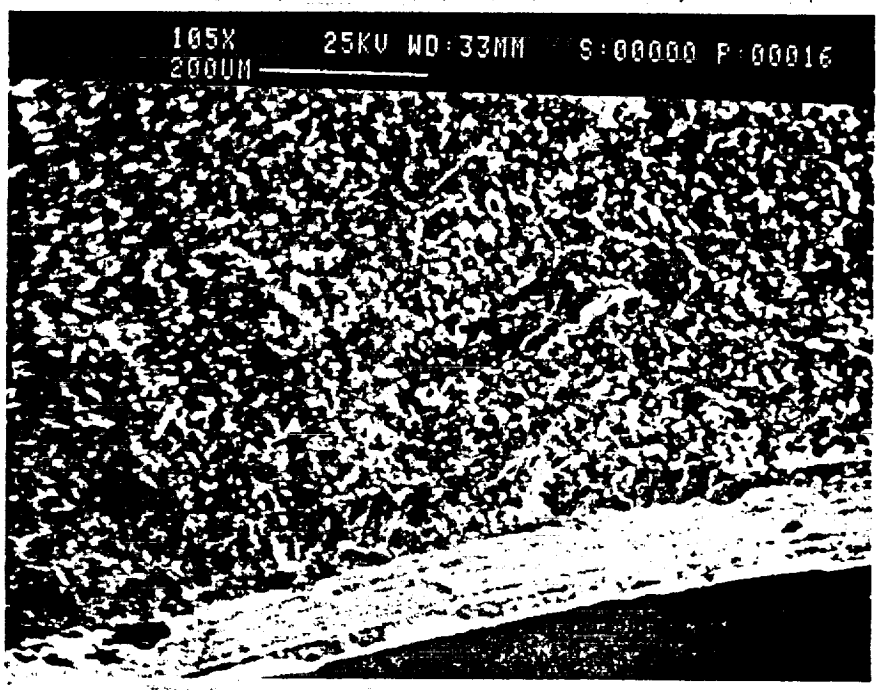

Brass # 208 T-0

Brass
T = 120 minutes

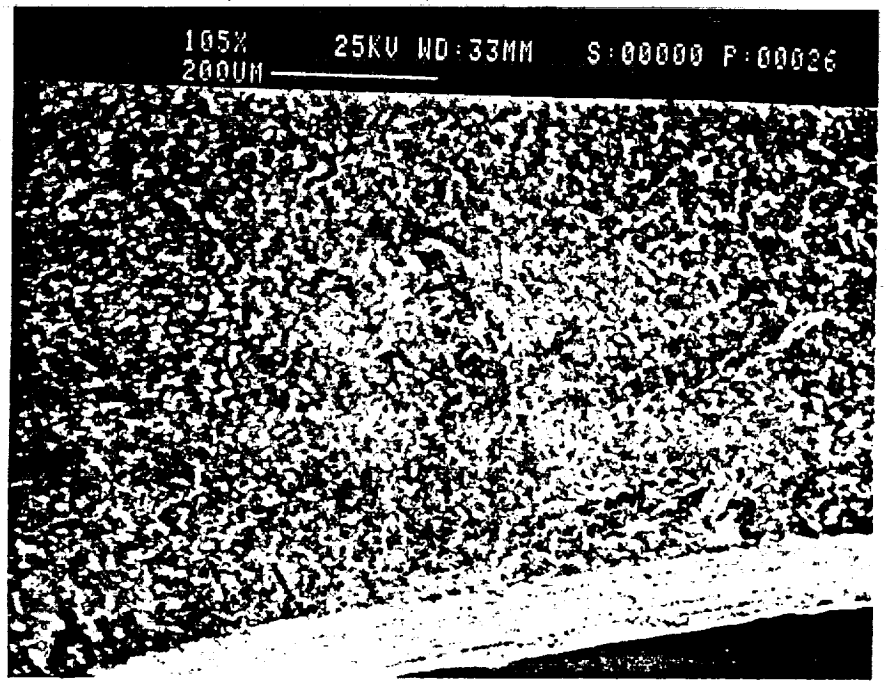

Brass # 205 12 cycles

Figure 3-23a

SEM/Stainless Steel/12 cycles/Branson

Stainless Steel
T = 0 minutes

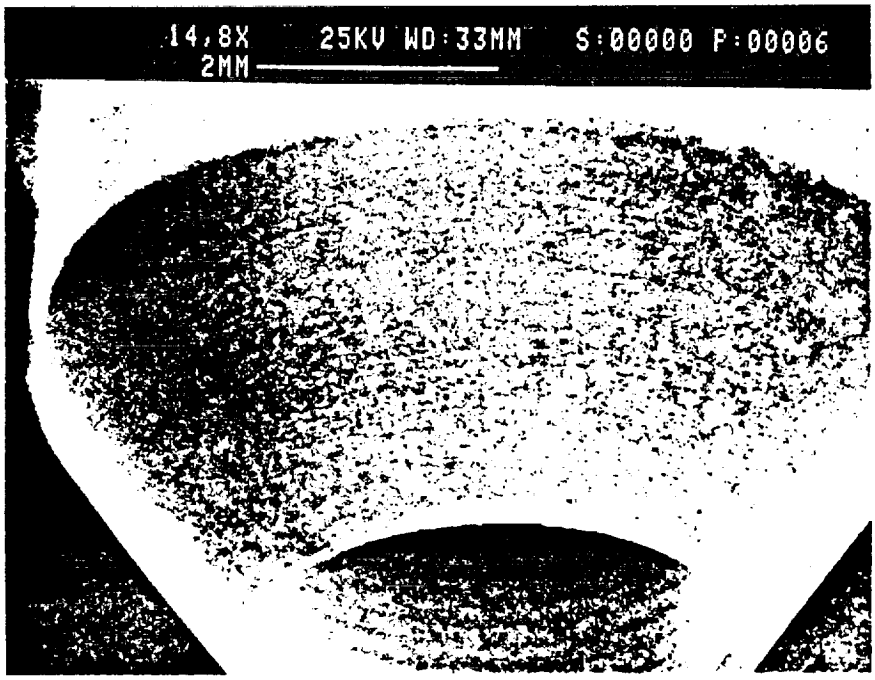

RS

SS #254 T=0

Stainless Steel
T = 120 minutes

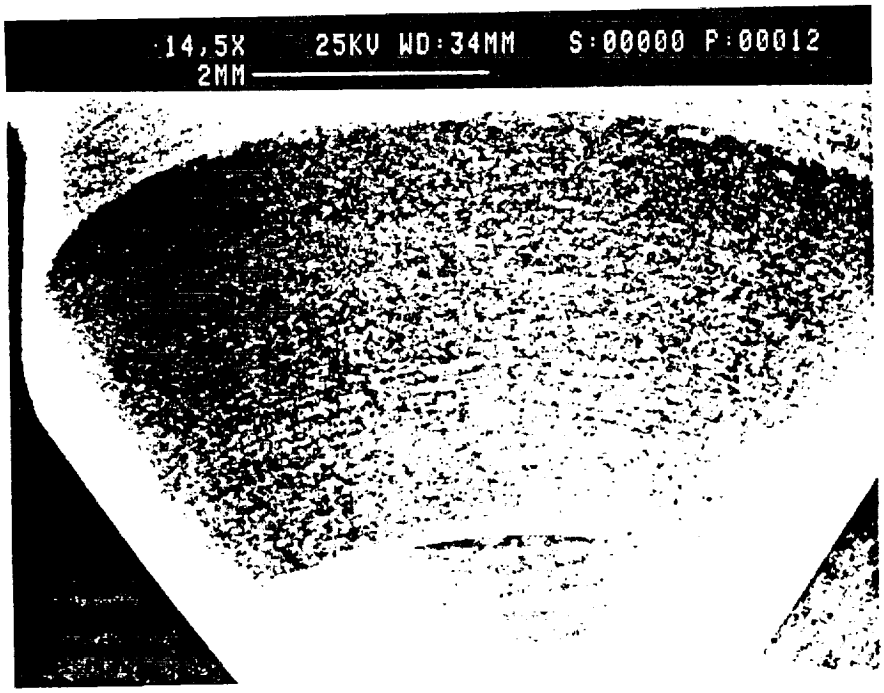

SS #254 12 cycles of Low Setting cycles

Figure 3-23b

SEM/Stainless Steel/12 cycles/Branson

Stainless Steel
T = 0 minutes

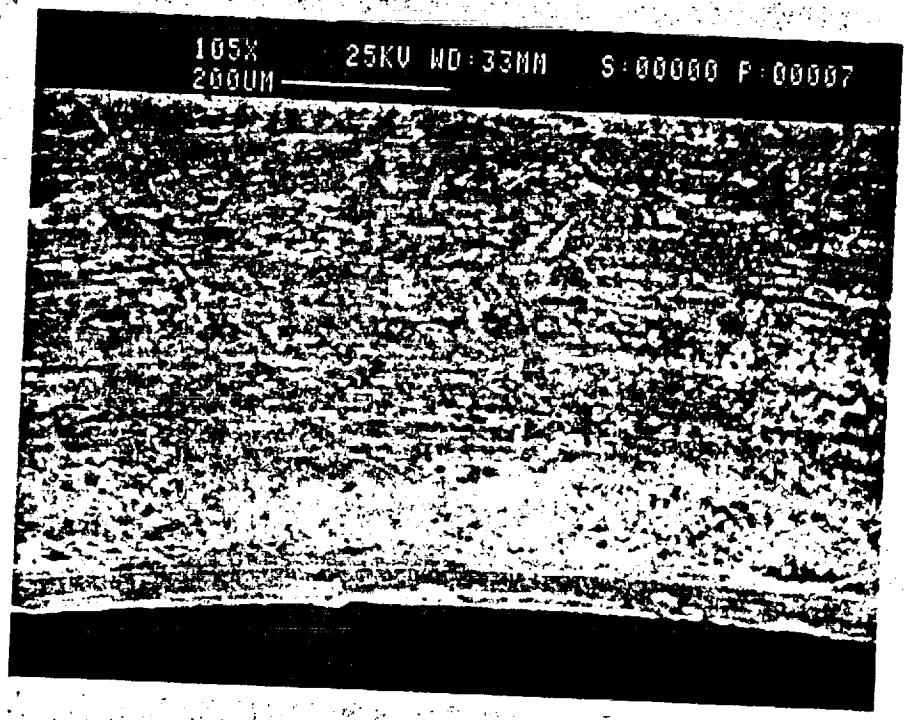

Stainless Steel
T = 120 minutes

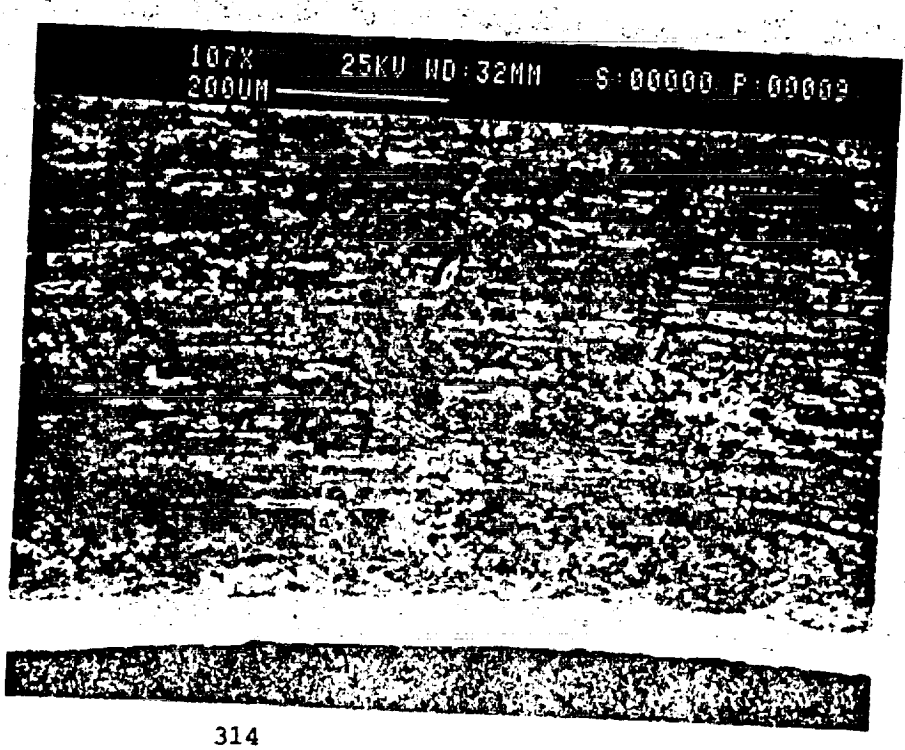

SS #256 12 cycles

Figure 3-24

SEM/Anodized Aluminum/Blue Wave

Anodized
Aluminum
T = 20 minutes

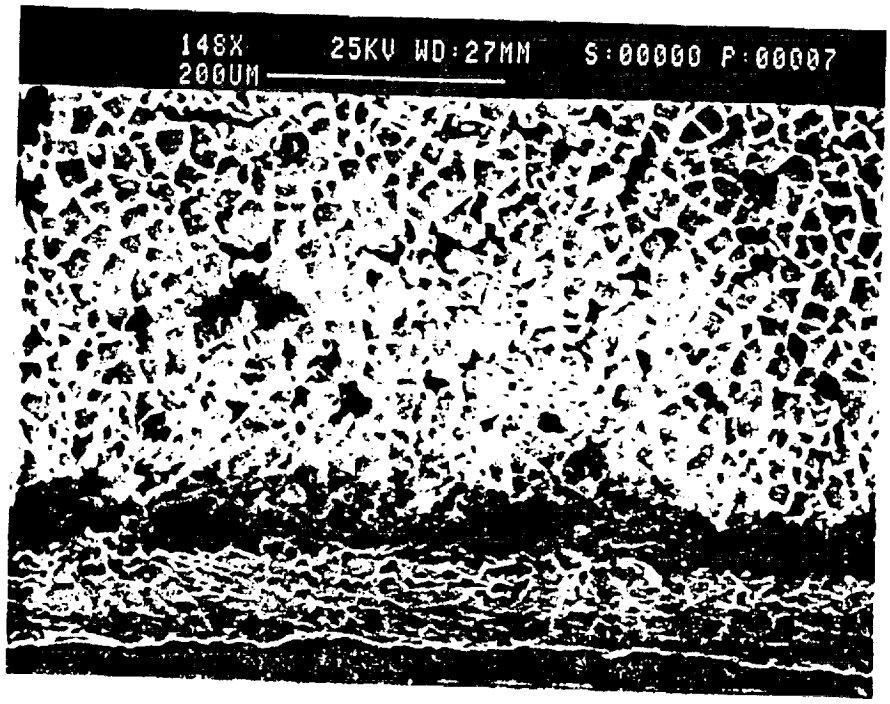

Anodized
Aluminum
T = 40 minutes

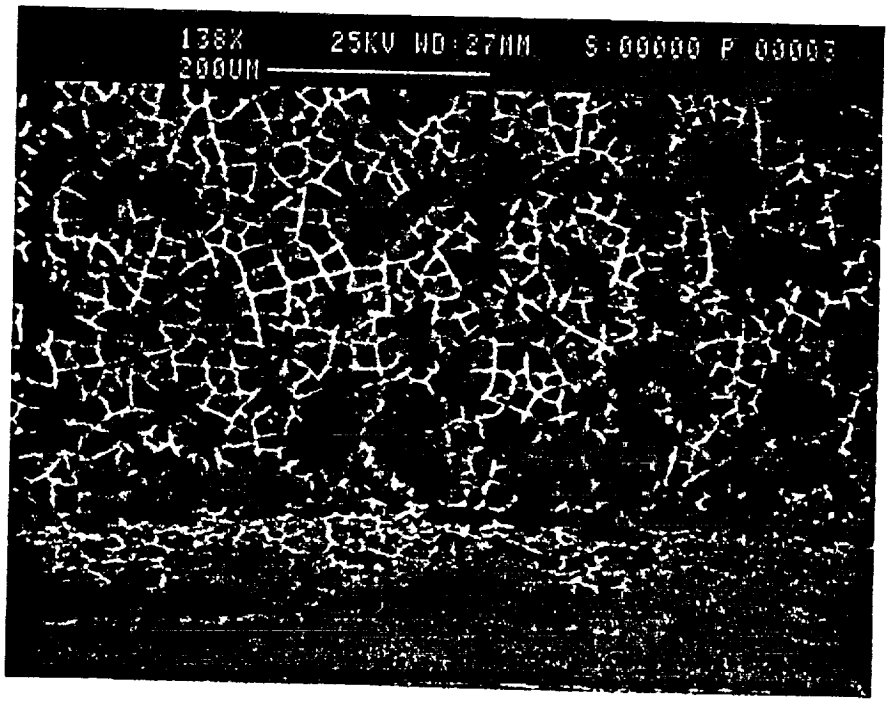

Figure 3-25

SEM/Anodized Aluminum/Blue Wave

Anodized
Aluminum
T = 80 minutes

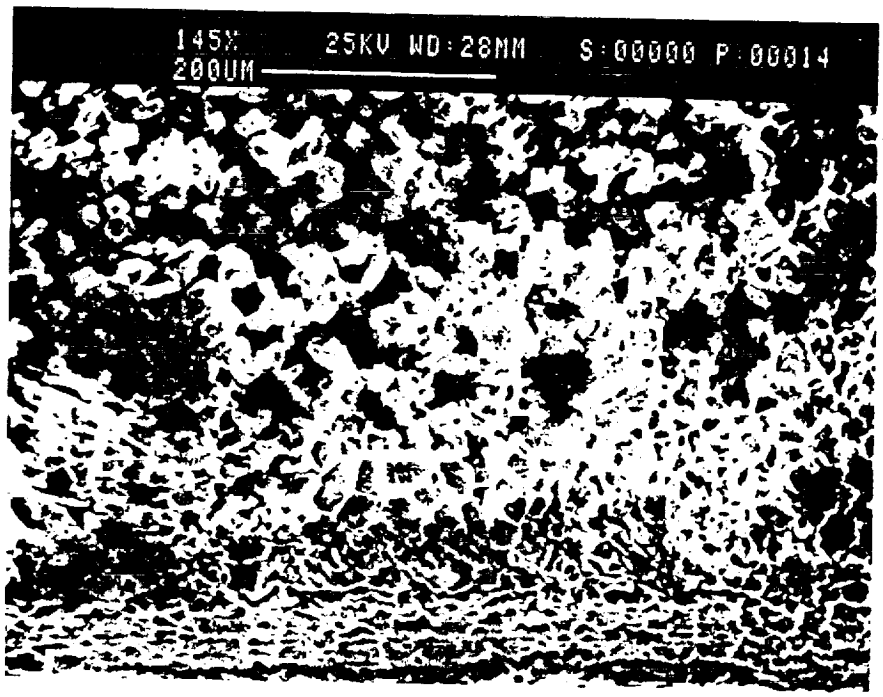

Anodized
Aluminum
T = 120 minutes

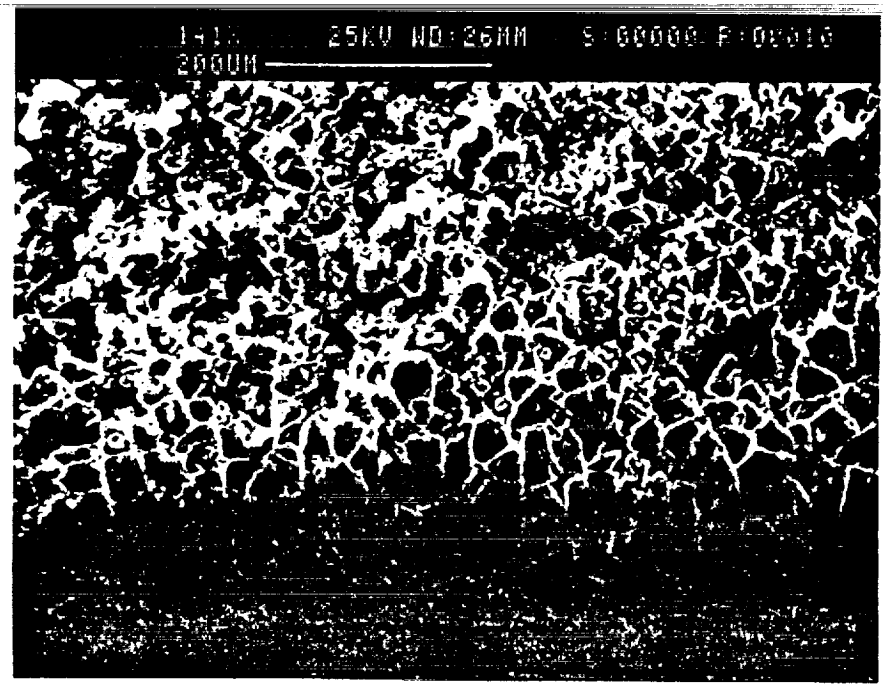

Figure 26

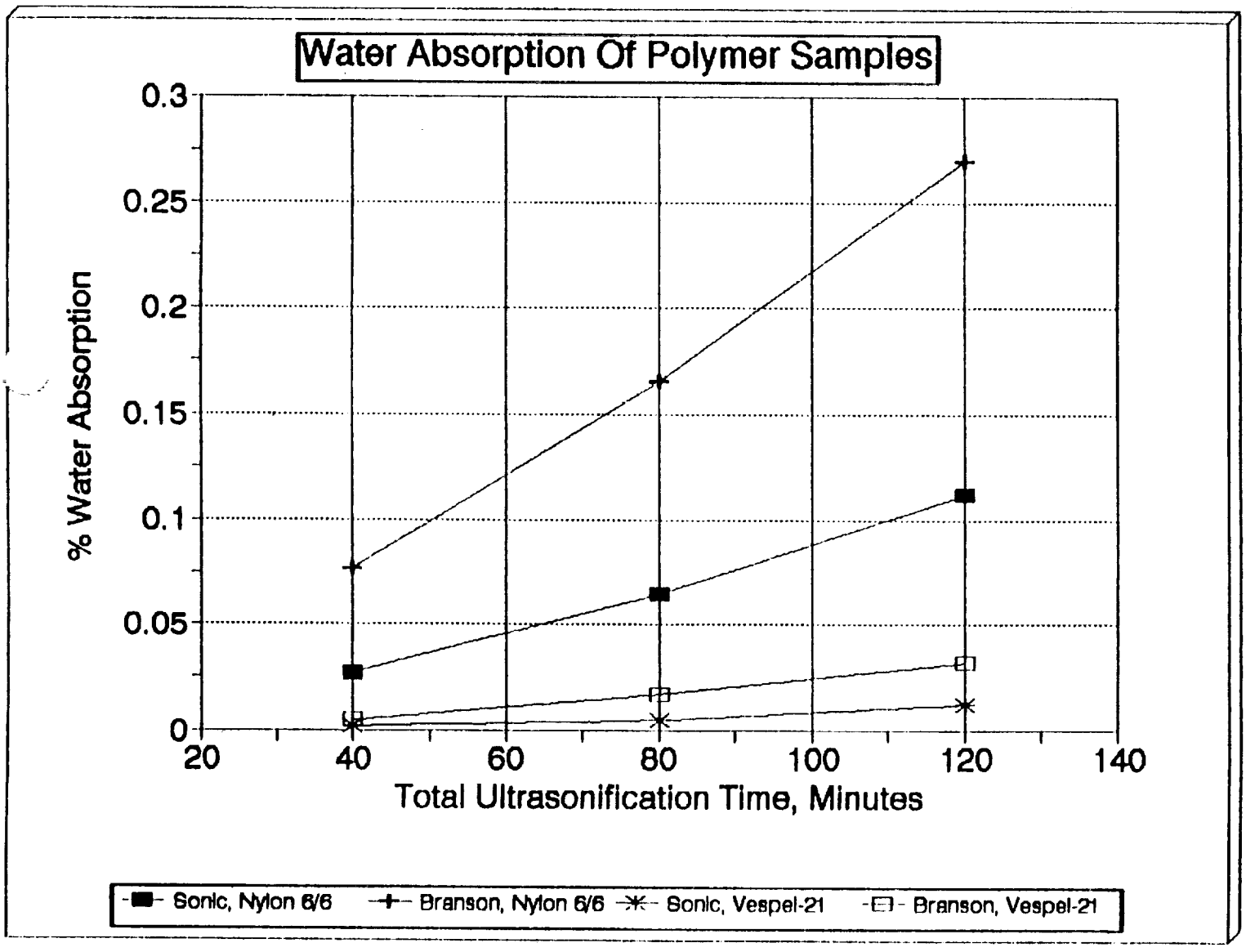
Water Absorption Of Polymer Samples
% Water Absorption
0.3
0.25
0.2
0.15
0.1
0.05
0
20
40
60
80
100
120
140
Total Ultrasonification Time, Minutes
Sonic, Nylon 6/6
Branson, Nylon 6/6
Sonic, Vespel-21
Branson, Vespel-21

1992 NASA/ASEE SUMMER FACULTY FELLOWSHIP PROGRAM

JOHN F. KENNEDY SPACE CENTER
UNIVERSITY OF CENTRAL FLORIDA

AUTOMATICALLY CALIBRATING ADMITTANCES IN KATE'S AUTONOMOUS LAUNCH OPERATIONS MODEL

PREPARED BY: Dr. Steve Morgan

ACADEMIC RANK: Associate Professor

UNIVERSITY AND DEPARTMENT: Baylor University
Department of Engineering
and Computer Science

NASA/KSC

DIVISION: Engineering Development

BRANCH: Artificial Intelligence

NASA COLLEAGUE: Carrie Parrish
Peter Engrand

DATE: August 7, 1992

CONTRACT NUMBER: University of Central Florida
NASA-NGT-60002 Supplement: 8

Acknowledgements

Thank you, Bob Merchant, for all the technical guidance this summer. Your knowledge of today's and tomorrow's KATE models made the automatic admittance calibrator the practical tool that it is today. Thank you, collaborators Carrie Parrish and Peter Engrand, for helping chart my course and clear the way this summer administratively. Thank you especially, Carol Valdez, Kari Stiles, and Loren Anderson, for operating the NASA/ASEE Summer Faculty Fellowship Program so flawlessly. I can't remember when I've enjoyed working more.

Abstract

This report documents a 1000-line Symbolics LISP program that automatically calibrates all 15 fluid admittances in KATE's Autonomous Launch Operations (ALO) model. (KATE is Kennedy Space Center's Knowledge-based Autonomous Test Engineer, a diagnosis and repair expert system created for use on the space shuttle's various fluid flow systems.) As a new KATE application, the calibrator described here breaks new ground for KSC's Artificial Intelligence Lab by allowing KATE to both *control and measure* the hardware she supervises. By automating a formerly manual process, the calibrator: 1) saves the ALO model builder untold amounts of labor, 2) enables quick repairs after workmen accidently adjust ALO's hand valves, and 3) frees the modeler to pursue new KATE applications that previously were too complicated. Also reported are suggestions for enhancing the program: 1) to calibrate ALO's TV cameras, pumps, and sensor tolerances, and 2) to calibrate devices in other KATE models, such as the shuttle's LOX and Environment Control System (ECS).

Summary

Last summer, this author gather several of KATE's model builders' tools into a Model Verification Toolkit. Coding the design of one of those tools, an automatic admittance calibrator for KATE's Autonomous Launch Operations (ALO) model, became the topic of this summer's project. A two-week survey of ALO's knowledge bases revealed the 15 admittances to be calibrated. During the next two weeks, the calibrator's designer manually adjusted valves and pump speeds of the ALO model, recorded its pressures with a pencil, and solved admittance equations off-line, until he discovered the best procedure for measuring every admittance. The ensuing four-week coding and testing effort produced the automated admittance calibrator program attached as Appendix A. Its typical output appears as Appendix B. This report is its documentation. The KATE modeler who first proposed this summer project claims he is pleased to have it.

Table Of Contents

LIST OF ILLUSTRATIONS

LIST OF TABLES

I
BACKGROUND

1.1 KATE

Kennedy Space Center's Knowledge-based Autonomous Test Engineer (KATE) is an artificially-intelligent diagnosis and repair expert system. KATE oversees the operation of fluid flow systems like that pictured in Figure 1-1. Guided by knowledge of admittances in the system hardware, KATE predicts flows from actual pressure measurements, and vice versa. When her predictions differ significantly from actual measurements, she uses something like fault tree analysis to isolate the error to a single failed device. KATE's Autonomous Launch Operations (ALO) model even swaps out the failed component for a redundant one to keep a simulated launch on schedule. Others of KATE's models include LOX, a very detailed model of the shuttle's liquid oxygen tanking operations, and the Environmental Control System (ECS), a model of the shuttle crew's breathing air processing.

1.2 KATE's ALO-H2O Model

A photograph of KATE's ALO-H2O hardware model appears in Figure 1-1. A hardware scale model of the shuttle's oxygen tanking operations, it substitutes cryogenic liquid oxygen with water and pressurized nitrogen gas for greater safety. A computer-aided design rendering of this hardware (see Figure 1-2) serves as KATE's ALO knowledge base. It shows connections of all significant devices along with their current operating conditions. Unfortunately, the fluid flow components' 15 admittances are hidden from view inside the model's software, since these do not correspond one-to-one to the 79 individual illustrated devices. Meaningless details such as pipe dimensions and tees are omitted entirely from the model for simplicity.

1.3 Building KATE's Models

KATE's model builders are busy people. Creating a KATE model like ALO is first an exercise in computer-aided design (CAD). But CAD models seldom include the functional detail that KATE requires for error diagnosis. Furthermore, KATE is written in LISP, and CAD information must be painstakingly reformatted as knowledge-base frames. These frames amount to upwards of 15,000 lines of LISP code even for the simple ALO model shown in Figure 1-2. Obscure interactions among knowledge base elements consume considerable debugging time during the never-ending development of ever more complicated expert systems.

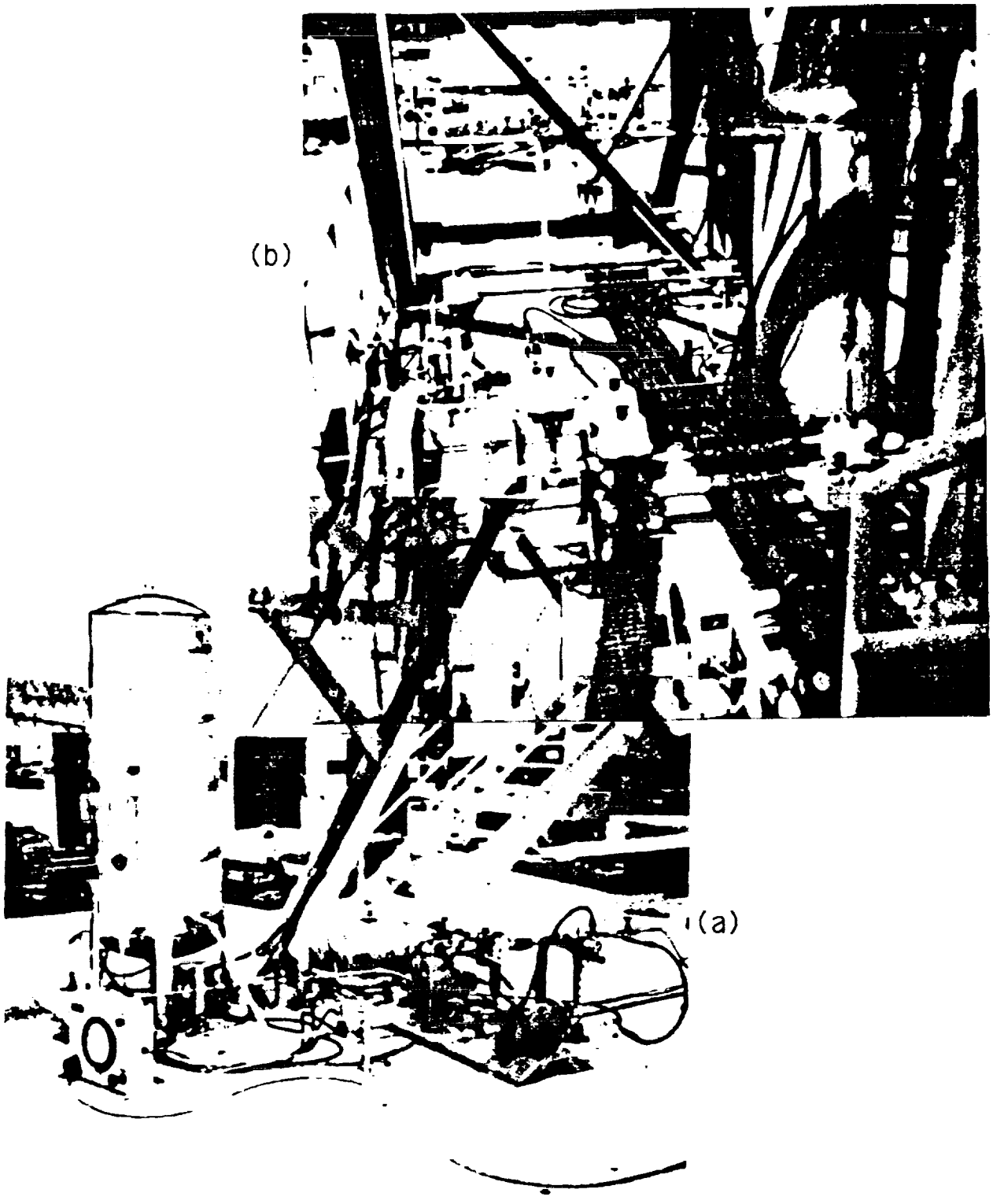

Figure 1-1. KATE's ALO-H2O Model Hardware: a) ground level pump circuit, b) vehicle tank circuit 20-feet up.

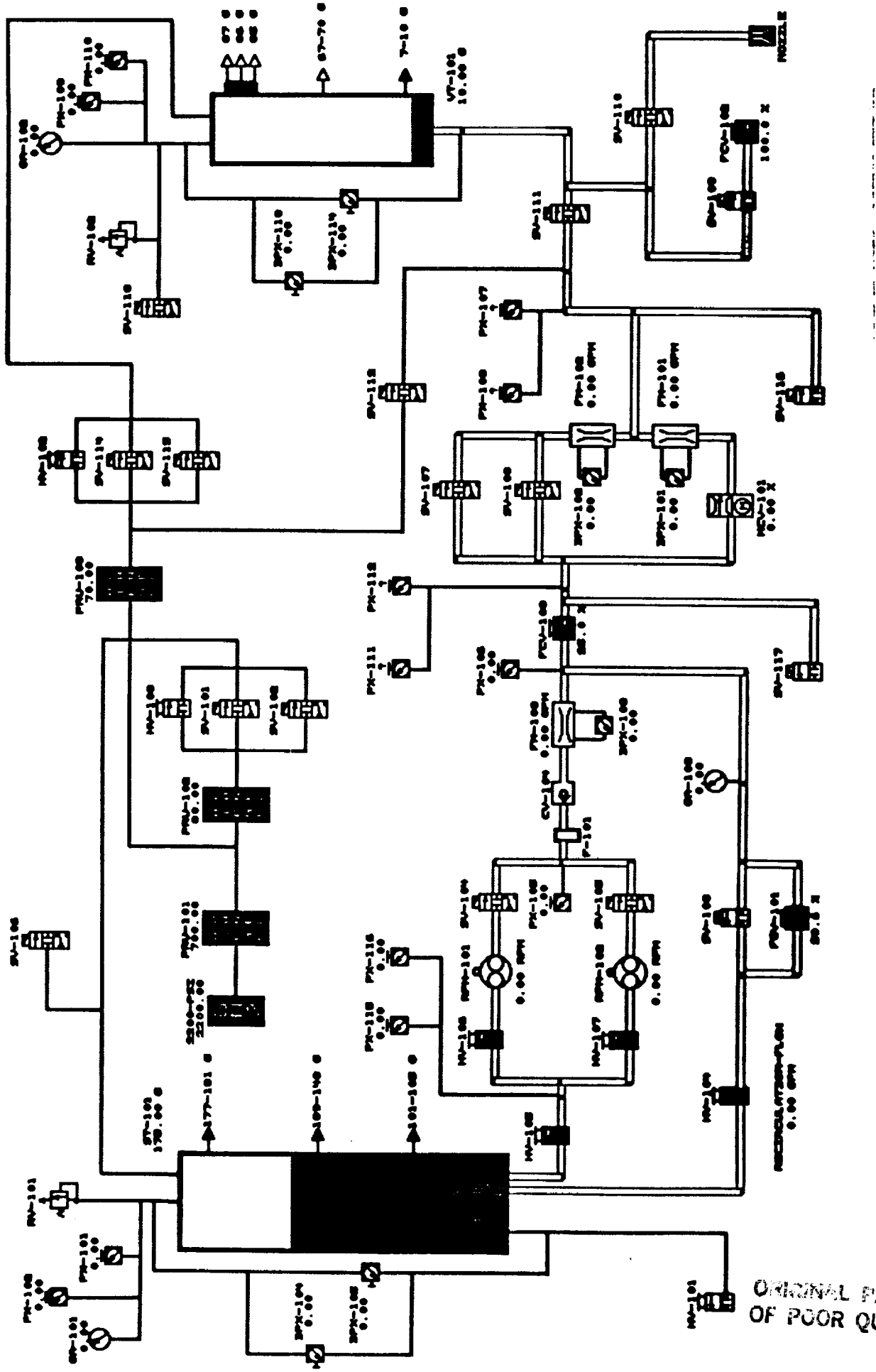

Figure 1-2. ALO User's Terminal Overview Screen

1.4 KATE's Model Verification Tools

KATE's modelers frequently create little blocks of LISP code just to assist them in their efforts. In the summer of 1991, this author gathered several of these into a Model Verification Toolkit [1]. A linear regression algorithm, which fits straight lines to random model measurements in a least-squares sense, was one of the first model verification tools. Recently Boeing personnel have added a Knowledge Base Editor, which makes encoding CAD device data into KATE's frames much easier. Additional tools were proposed, including a program to automatically calibrate the ALO model's 15 admittances. That program became this summer's project. The toolkit is already saving modelers precious time and enabling them to apply KATE to more complicated and more powerful systems.

II
METHODS

2.1 KATE's Fluid-Flow Admittance Equation

KATE's admittance equation evolves from the law of energy conservation, which equates the potential energy of a pressure head across a pipe to the kinetic energy lost by fluid flowing against pipe friction. (See Figure 2-1 below.)

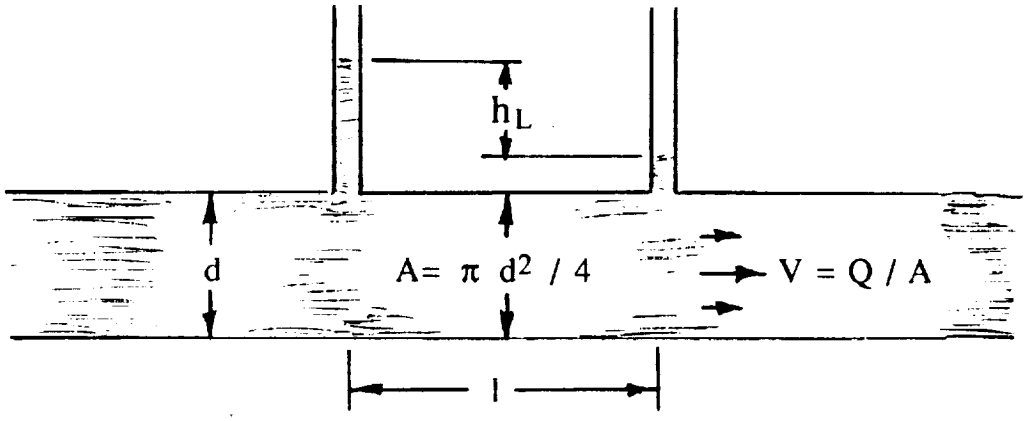

Figure 2-1. Energy Conserved By Fluid Flowing In A Pipe [2]

Darcy's equation [2] restates this basic law in terms of pipe dimensions:

$$h_L = f\, l\, V^2 / 2\, d\, g,$$

where h_L is pressure head in feet,
f is the dimensionless pipe friction factor,
l and d are pipe length and diameter in feet,
V is mean fluid velocity in feet/second,
and the gravitation constant, g, is 32.2 feet/sec^2.

Knowing that the specific weight of water is 62.37 pounds/foot^3 at 60°F, we can convert the head, h_L, to a pressure drop, ΔP, in psig:

$$h_L = \Delta P\ (144\ in^2/ft^2)\ /\ (62.37\ pounds/foot^3) = 2.309\ \Delta P.$$

Recognizing that fluid flow rate, Q, is the product of mean velocity, V, and pipe area, $\pi\ d^2\ /\ 4$, we can rewrite Darcy's formula as the ratio of flow rate and the square root of pressure drop:

$$V\ /\ \sqrt{h_L} = \sqrt{2\ g\ d\ /\ f\ l} = Q\ (4\ /\ \pi\ d^2)\ /\ \sqrt{2.309\ \Delta P.}$$

KATE lumps all of these pipe constants into one and calls them "admittance,"

$$A_i = (\pi\ d^2\ /\ 4)\ \sqrt{2\ g\ d\ 2.309\ /\ f\ l}$$
$$= Q\ /\ \sqrt{\Delta P}. \qquad (2.1)$$

The dimensions of admittance are ft^3-inches/minute-$\sqrt{pound}$. Instead of obtaining the admittance of a complicated pipe circuit from many length and diameter measurements, KATE finds it more convenient to measure flow rate and pressure drop and to solve equation 2.1 above.

2.2 Statistical Averaging

Actually, pressures and flows are measured at many pump speeds, and the several admittances are statistically averaged to reduce measurement noise. The average value (i.e., mean) of a sampled population is their sum divided by the number of samples taken. A small standard deviation (i.e., the root-mean-square of the samples' distances from their mean) may be regarded as a figure of merit on the random sampling process. When sampling from a normal, Gaussian population, the user can be assured that 95% of his samples will fall within ± 1 standard deviation (s.d.) of the mean. An excessive admittance s.d. (say 20% larger than the mean or more) warns of unreliable pressure or flow measurements. In such cases, the calibration should be done over.

2.3 ALO's "Readily Apparent" Admittances

Bob Merchant's April 1, 1992 Memo [3] details the proposal for ALO's automatic admittance calibrator. Only those "readily apparent" admittances carrying measurable flows and bracketed by measurable pressures are to be calibrated. Other admittances may be neglected, since they are of no use to KATE in predicting pressures and flows during failure diagnoses. The 15 admittances that meet this "readily apparent" definition are illustrated in an electronic analog of ALO in Figure 2-2. Those who are unfamiliar with the ALO model can easily locate traditional admittance values in ALO's knowledge base by refering to the right-hand two columns of Table 2-1.

2.4 Tank Pressurization

When the ALO model pressurizes (or depressurizes) the storage and vehicle water tanks, gas flow rate is not measured. But flow can be inferred from measured pressures of the tanks and their gas supplies (or vents) [3]. Tank pressures rise exponentially toward the supply pressure (or fall toward atmospheric pressure) asymptotically with time. According to the Gas Law, the amount of gas in a tank varies in proportion to its pressure. Thus, the time dependent amount of gas in either of ALO's tanks (in cubic feet) is:

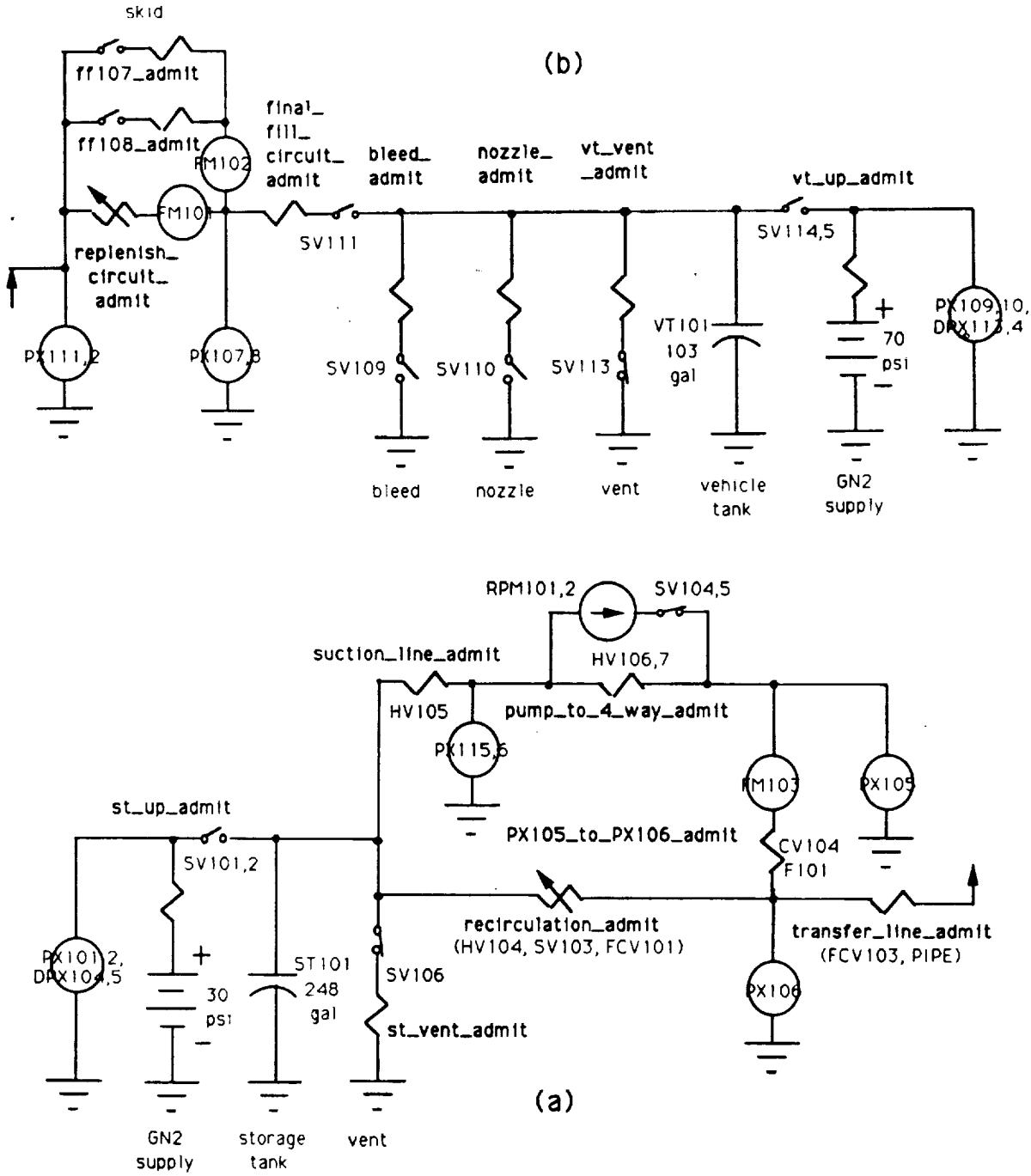

Figure 2-2. ALO's "Readily Apparent" Fluid Flow Admittances: a) ground level pump circuit, b) vehicle tank circuit 20-feet up.

Table 2-1
ALO's "Readily Apparent" Admittances

Admittance	Bracketing Pressures	Flow Meas.	Reference (page-line)	Trad'l Value
1. Tank Pressurization (Nitrogen Gas) Circuits....				
st-up-admit	30psig supply to storage tank	Fcn	8-16[4]	23.
vt-up-admit	70psig supply to vehicle tank	of	8-6[4]	18.5
st-vent-admit	Storage tank to atm via SV106	tank	9-14[4]	25.5
vt-vent-admit	Vehicle tank to atm via SV113	pres.	9-6[4]	53.
2. Pump Circuits....				
suction-line-admit	From storage tank to PX115	FM103	2-67[5]	15.5
pump-to-4-way-admit	From PX115 to PX105	FM103	1-39[6]	10.58
px105-to-px106-admit	From PX105 to PX106	FM103	new	4.65
pump-circuit-admit	Three admits above in series	-	2-38[5]	4.1*
recirculation-admit	PX106 to storage tank, SV103 closed	FM103	3-71[5]	1.64
	Ditto, but with SV103 open	FM103	3-71[5]	7
3. Vehicle Tank Circuits....				
ff107-admit	PX111 to PX107, only SV107 open	FM102	6-38[5]	6.47
ff108-admit	PX111 to PX107, only SV108 open	FM102	6-40[5]	6.47
fast-fill-circuit-admit	Two admits above in parallel	-	6-38[5]	6.47*
replenish-circuit-admit	MCV101 xfer function (e.g., 33%)	FM103	8-61[5]	0.02786x -0.7013
skid-admit	Two admits above in parallel	-	9-24[5]	6.69*
final-fill-circuit-admit	From PX107 to vehicle tank	FM102	1-16[5]	7.3
upper-fill-circuit-admit	Two admits above in series	-	12-26[5]	4.93*
transfer-line-admit	From PX106 (up 20 ft) to PX111	FM102	5-25[5]	2.36
tank-fill-admit	Two admits above in series	-	13-27[5]	2.13*
4. Vehicle Tank Drain Circuits....				
nozzle-admit	Vehicle tank to atm via SV110	FM102	14-21[5]	0.55
bleed-admit	Vehicle tank to atm via SV109	$-flow_{vt}$	14-9[5]	0.34

* Derived admittances are *functions* of measured ones (not constants) and they vary with valve positions.

$$N_i = P_i N_0 / P_0 , \qquad (2.2)$$

in which N_0 is the capacity of the empty tank,
P_0 is absolute atmospheric pressure, and
P_i is the measured tank pressure time function.

The ratio N_0 / P_0 must be measured when the tanks are empty, the only time ALO can accurately assess their ullage air-space volume.

2.5 Infering Gas Flow Rate

Given the amount of gas in the tank as a function of time, it is a simple matter to compute gas flow rate as a function of time:

$$Q_i = (N_i - N_{i-1}) / T_S \qquad (2.3)$$

in which Ts is the sampling time interval in minutes. KATE's 4-second (i.e., 1/15 minute) "heart beat" interval is a convenient sampling time interval. The pressure drop across the tank pressurization (or depressurization) circuit is the difference in the tank pressure and the source (or vent) pressure, $P_i - P_S$. Therefore, the circuit admittance time function is

$$\begin{aligned} A_i &= Q_i / \sqrt{P_i - P_S} \\ &= (N_0/P_0)\,(P_i - P_{i-1}) / (T_S \sqrt{P_i - P_S}). \end{aligned} \qquad (2.4)$$

For a given tank ullage, the ratio N_0/P_0T_S is constant. That is,

$$N_0/P_0T_S = 32.75 \text{ cuft/psi-min}$$

for the 32.75 cuft ullage of ALO's empty storage tank, and

$$N_0/P_0T_S = 13.77 \text{ cuft/psi-min}$$

for the 13.77 cuft ullage of ALO's empty vehicle tank. Thus,

$A_i = 32.75\,(P_i - P_{i-1}) / \sqrt{P_i - 30\text{psi}}$, for pressurizing the storage tank,
$A_i = 32.75\,(P_i - P_{i-1}) / \sqrt{P_i}$, for depressurizing the storage tank,
$A_i = 13.77\,(P_i - P_{i-1}) / \sqrt{P_i - 70\text{psi}}$, for pressurizing the vehicle tank, and
$A_i = 13.77\,(P_i - P_{i-1}) / \sqrt{P_i}$, for depressurizing the vehicle tank.

As before, averaging the calculated admittances, A_i, reduces measurement noise.

2.6 Motor Control Valve Transfer Function

KATE can set ALO's skid replenish valve MCV-101 to any desired position from fully closed to 100% open. Its variable admittance is characterized by the transfer function:

$$\text{Admittance} = \%\text{open} * \text{slope} + \text{admit}_0,\ r = \_\_\_\_\ \%. \tag{2.5}$$

In this function, the slope, admittance intercept, and correlation coefficient, r, are defined by the least-squared-error linear regression equations [7]:

$$\text{slope} = \frac{n \Sigma xy - \Sigma x \Sigma y}{n \Sigma x^2 - (\Sigma x)^2}, \tag{2.6}$$

$$\text{admit}_0 = \frac{\Sigma y - \text{slope}\ \Sigma x}{n}, \text{ and} \tag{2.7}$$

$$\text{correlation, } r = \frac{n \Sigma xy - Sx\ Sy}{\sqrt{\{[n \Sigma x^2 - (\Sigma x)^2][n \Sigma y^2 - (\Sigma y)^2]\}}}, \tag{2.8}$$

in which x and y represent the %open variable (typical range: 0.30 to 0.40) and the valve's admittances at those %open valve settings respectively. The correlation coefficient, r, tells the modeler the linearity (a figure of merit) of the transfer function. Correlations of 99.9% are common for this valve. Correlations less than 95% should prompt the modeler to take a new set of measurements.

2.7 Coding The Admittance Calibrator

Pressures must be sampled from the ALO model before the equations above can yield the 15 desired admittances. These pressures arise from plausible flows induced in some fluid circuit by one of ALO's two pumps. Collecting pressure samples is a simple matter of calling the LISP function, GET-CURRENT-VALUE, every four seconds with a pressure transducer's CAD reference designator as the function argument [8]. For example,

```
(L (SETQ x (GET-CURRENT-VALUE 'PX-115)))
```

evaluates actual pump head pressure when called by a control procedure. The pumps respond to motor speed commands, such as:

```
(C  RPM-101  (3600  rpm)  "pump rapidly"),
```

and ALO's valves respond to control procedure calls like these:

(C SV-103 OPEN "quicken recirculation flow")

(C SV-111 CLOSED "prevent fluid loss during tank pressurization")

(C MCV-101 (0.40 %) "replenish vehicle tank boil off").

Table 2-2 shows the best valve and pump settings, as well as flows and pressures to be measured for every ALO admittance. This table and the equations above constitute the automated admittance calibrator's software design. Its LISP code [9] and data output [10] are attached as Appendices A and B. Its operating instructions are:

1. Select CONTROL PROCEDURES on KATE's overview menu.
2. Left-click on DO-IT-ALL.

Table 2-2
ALO's Admittance Measurement Environments

Admittance	Valves Open/Closed* SV-1xx 01 03 04 06 07 08 09 10 11 13 14	MCV -101	Pump Speed	Flow FM10x	Pressure Meas. upstr-dnstr+Δelev
Tank Pressurization and Depressurization Procedures....					
st-up-admit	O C C C C C C C C C O	.0	0	N_i-N_{i-1}	30psig-PX101+0"
vt-up-admit	O C C C C C C C C C O	.0	0	divided	70psig-PX109+0"
st-vent-admit	C C C O C C C C C O C	.0	0	by	PX101-0psig+0"
vt-vent-admit	C C C O C C C C C O C	.0	0	Ts	PX109-0psig+0"
FastFlow Procedure....					
suction-line-admit	C C O O O C C C O O C	.0	2500-3500	3	PX101+DPX104-PX115-5"
pump-to-4-way-admit	C C O O O C C C O O C	.0	2500-3500	3	PX105-PX115+19"
PX105-to-PX106-admit	C C O O O C C C O O C	.0	2500-3500	3	PX105-PX106+24"
transfer-line-admit	C C O O O C C C O O C	.0	2500-3500	2	PX106-PX111-236"
ff-107-admit	C C O O O C C C O O C	.0	2500-3500	2	PX111-PX107-1"
final-fill-circuit-admit	C C O O O C C C O O C	.0	2500-3500	2	PX107-DPX113-PX109-3"
FF108 and MCV101 Procedures....					
ff-108-admit	C C O O C O C C O O C	.0	3500-2500	2	PX111-PX107-1"
replenish-circuit-admit	C O O O C C C C O O C	.3-.4	3500	1	PX111-PX107-1"
Nozzle and Bleed Procedures....					
nozzle-admit	C C O O O C C O O O C	.0	3500-2500	2-vtin	PX109+DPX113-0psig-0"
bleed-admit	C C O O O C O C O O C	.0	2500-3500	2-vtin	PX109+DPX113-0psig-0"
Recirc Procedure....					
recirculation-admit	C O/C O O C C C C C O C	.0	3500-2500	3	PX106-PX101-DPX104

* KATE initially *closes* all solenoid and motor control valves.

III
RESULTS

3.1 ALO's Traditional (Standard) Vs. Automatically Calibrated Admittances

The first and last pages of the automatic admittance calibrator's 25-page output file [10] appear here as Appendix B. Table 3-1 compares these 15 automatically calibrated admittances with the traditional ones, taken as standard values. The right-hand column (see "Meas. Error") is the automatically calibrated admittance minus the traditional one, all divided by the traditional one. Significant measurement errors are discussed below.

3.2 Tank Pressurization And Depressurization Admittances

ALO calculates the storage and vehicle tank ullage pressure and vent admittances afresh every time they are used, because their equations include tank ullage-space variables. (Section 2.4 suggests that a better policy might be calibrating these constant admittances once and for all with both tanks empty.) Table 3-1 shows traditional (standard) values of 23, 18.5, 25.5, and 53 for these four admittances. Their automatically calibrated counterparts are about 1/10th of these amounts. Close inspection of ALO's knowledge base equations [4] reveals assumed ullage spaces for both tanks that are about 10 times actual size. Though this knowledge base error has been in place since ALO's beginning, it probably has not affected ALO's performance much. Gas flow has little effect upon ALO's (more important) modeled fluid flow. Standard deviations (sd's) of all tank pressurization admittances are 29% of their means. These excessive sd's probably result from the fact that only three samples were taken in calibrating each admittance.

3.3 Pump Circuit Admittances

Some large errors among ALO's five pump circuit admittances demand explanation. Most striking is the -72% error in pump-to-4-way-admit. ALO's knowledge base [6] traditionally defines this admittance as extending from the pump inlet, where there is no pressure transducer, to transducer PX-105. Consistent with the "readily apparent" principle advanced in section 2.2 above, its automated counterpart extends from pressure transducer PX-115 to PX-105. Hand valve HV-106 is excluded from the standard admittance but included in the automated one. Explaining that ALO is "still under development," ALO's modeler claims that he prefers the automated value over the traditional standard. Soon ALO's knowledge base will change to reflect pump-to-4-way-admit's new "readily apparent" definition instead. The greater accuracy of the composite pump-circuit-admit suggests that the other three component admittances in the pump circuit also may contradict our new "readily apparent"

III
RESULTS

3.1 ALO's Traditional (Standard) Vs. Automatically Calibrated Admittances

The first and last pages of the automatic admittance calibrator's 25-page output file [10] appear here as Appendix B. Table 3-1 compares these 15 automatically calibrated admittances with the traditional ones, taken as standard values. The right-hand column (see "Meas. Error") is the automatically calibrated admittance minus the traditional one, all divided by the traditional one. Significant measurement errors are discussed below.

3.2 Tank Pressurization And Depressurization Admittances

ALO calculates the storage and vehicle tank ullage pressure and vent admittances afresh every time they are used, because their equations include tank ullage-space variables. (Section 2.4 suggests that a better policy might be calibrating these constant admittances once and for all with both tanks empty.) Table 3-1 shows traditional (standard) values of 23, 18.5, 25.5, and 53 for these four admittances. Their automatically calibrated counterparts are about 1/10th of these amounts. Close inspection of ALO's knowledge base equations [4] reveals assumed ullage spaces for both tanks that are about 10 times actual size. Though this knowledge base error has been in place since ALO's beginning, it probably has not affected ALO's performance much. Gas flow has little effect upon ALO's (more important) modeled fluid flow. Standard deviations (sd's) of all four tank pressurization admittances are 29% of their means. These excessive sd's probably result from the fact that only three samples were taken in calibrating each admittance.

3.3 Pump Circuit Admittances

Some large errors among ALO's five pump circuit admittances demand explanation. Most striking is the -72% error in pump-to-4-way-admit. ALO's knowledge base [6] traditionally defines this admittance as extending from the pump inlet, where there is no pressure transducer, to transducer PX-105. Consistent with the "readily apparent" principle advanced in section 2.2 above, its automated counterpart extends from pressure transducer PX-115 to PX-105. Hand valve HV-106 is excluded from the standard admittance but included in the automated one. Explaining that ALO is "still under development," ALO's modeler claims that he prefers the automated value over the traditional standard. Soon ALO's knowledge base will change to reflect pump-to-4-way-admit's new "readily apparent" definition instead. The greater accuracy of the composite pump-circuit-admit suggests that the other three component admittances in the pump circuit also may contradict our new "readily apparent"

Table 3-1
The Answers

Admittance	Traditional Admittance	Auto Cal Admit (mean +/- sd)	Meas. Error
1. Tank Pressurization (Nitrogen Gas) Circuits....			
st-up-admit	23	2.280±.6677	10.1x
vt-up-admit	18.5	1.842±.5394	10.0x
st-vent-admit	25.5	2.485±.7279	10.3x
vt-vent-admit	53	5.077±1.487	10.4x
2. Pump Circuits....			
suction-line-admit	15.5	14.62±6.179	-6%
pump-to-4-way-admit	10.58	2.922±1.235	-72%
px105-to-px106-admit	4.65	5.701±2.409	+23%
pump-circuit-admit	4.1*	2.560*	-38%
recirculation-admit, SV103 closed	1.64	1.696±.7166	+3%
ditto but with SV103 open	7	6.213±2.595	-11%
3. Vehicle Tank Circuits....			
ff107-admit	6.47	6.066±2.564	-6%
ff108-admit	6.47	6.353±2.685	-2%
fast-fill-circuit-admit	6.47*	6.066*	-6%
replenish-circuit-admit (a transfer function)	0.02786x -0.7013	0.02781x-0.7, r=1.	0% @33%open
skid-admit	6.69*	5.375*	-20%
final-fill-circuit-admit	7.3	6.977±2.949	-4%
upper-fill-circuit-admit	4.93*	4.258*	-14%
transfer-line-admit	2.36	2.360±.9975	0%
tank-fill-admit	2.13*	2.064*	-3%
4. Vehicle Tank Drain Circuits....			
nozzle-admit	0.55	0.02286±.02158	-96%
bleed-admit	0.34	0.06923±.02797	-80%

* Derived admittances are *functions* of measured ones (not constants), and they vary with valve positions.

principle. Sd's of the pump circuit admittances range from 42 to 44% of their means.

3.4 Vehicle Tank Circuits

Component admittances in the vehicle tank circuit show smaller errors. A dead-level perfect overall tank circuit admittance (i.e., tank-fill-admit) suggests minor changes in admittance definitions again, as ALO's modeler embraces the "readily apparent" concept. He dismisses these errors (all $\leq$ 20%) as "insignificant." One might argue that automated admittances reported here should agree *exactly* with traditional ones. All pressures and flows the calibrator measured were *modeled* values, arising from traditional admittances in ALO's knowledge base. Actually, ALO adds a "realistic" offset [11] to every modeled pressure before displaying it on the user's overview screen and before delivering it to the user's program via GET-CURRENT-VALUE. In the range -0.72 to +0.34 psi, these small offsets add a fixed measurement error that the admittance calibrator's statistical averaging cannot eliminate. A -0.72 psi offset on a 2.4 psi pressure measurement could account for a +20% error in admittance. Sd's of all four constant vehicle tank admittances are 42% of their means.

3.5 Nozzle And Bleed Admittances

Automatic calibration of nozzle and bleed valve admittances presents some interesting design problems. The space shuttle's engine nozzle valve never opens during oxygen tanking, and the bleed valve only opens occasionally, when the tank has been overfilled. One might logically wonder why ALO models these valve admittances at all, since it is preoccupied with device failures during tanking. Evidently, these admittances lie at the edge of ALO's knowledge domain -- bizarre errors lie waiting there for the unwary. For example, 10.13 gallons of water typically flows from the storage tank to the vehicle tank every minute during the fast-fill oxygen tanking procedure. When the nozzle valve opens, and an unmeasured portion (this path has no flowmeter) of that 10.13 gpm flows out the nozzle, the vehicle tank's inlet flow *rises* to 10.30 gpm! Final-fill-admit, nozzle-admit, and bleed-admit all have solenoid valve SV-111 in common, so combining two or more of these admittances is meaningless. As the vehicle tank approaches half-full with the bleed valve open, its inlet flow typically approaches zero and then reverses, augmenting the bleed path's pumped flow. The paradoxical negative admittances that arise at these times suggest confusion in the knowledge base. In the light of this discussion, maybe a 96% error is not so bad. Sd's of the nozzle and bleed admittances are 94 and 40% of their means.

3.6 Error Summary

Causes of calibrator errors range from ALO "realistically" offsetting modeled pressures to variant admittance definitions to errors in ALO's evolving

knowledge base equations. ALO's modeler claims to be better satisfied with the automatically calibrated admittances than with the traditional ones. And customer satisfaction is the ultimate test of any automated productivity aid. Statistics (sd's) of all admittances will improve when procedure compiler enhancements (currently underway) permit looping a dozen times on a variable pumping speed.

IV
CONCLUSIONS

4.1 Enhanced Modeler Productivity

Perhaps it is stretching a point to compare the automated admittance calibrator's 8-minute run time with those 6 to 8 months ALO's modeler spent filling his 63-page notebook [13] with manual admittance calculations. (He also developed other parts of the model in that same time interval.) But there is no denying that automated admittance calibration does save ALO's modeler considerable time and effort. He is pleased to have it. It deserves to be included among the other modeler productivity aids in KATE's Model Verification Toolkit. Creating it has been an illuminating experience. This author has a deeper understanding of the problems KATE's modelers encounter and how to help them.

4.2 Clarified ALO Model

In the process of opening their minds to students, teachers often discover ways of improving their own reasoning processes. ALO's traditional admittances came from painstaking manual measurements of pumps, valves, pipes, tees, and elbows (and complicated combinations of these) on the space shuttle launch pad. ALO's modeler came up with the "readily apparent" admittance definition specifically to guide this newcomer in developing the automatic admittance calibrator. These 15 easily measured admittances (i.e., flow rates divided by square roots of pressure drops), plus a scant few of their series and parallel combinations, could replace the dozens of arbitrarily defined admittances that now litter ALO's knowledge base. His fresh look at ALO has clarified the model builder's task.

4.3 KATE's Philosophical Advancement

In the automated admittance calibrator, we have an novel application of KATE in which she changes hardware systems and then measures the effects of those changes. Two years ago, ALO's modeler broke new ground by enabling KATE to control environments she formerly observed passively. Now we have gone a step further toward making KATE a master of hardware environments. As her ALO model knowledge base measures its own admittances, KATE shows considerably more introspection than the average computer program. Could we speculate that KATE has achieved artificially intelligent "self-awareness"?

V
RECOMMENDATIONS

5.1 ALO's Future

ALO's automatic admittance calibrator has proved itself in a *modeled* environment. (Simulated by ALO's software, the pressures and flows the calibrator measured did not come from real hardware.) Now it is ready to be attached to the real hardware model (see Figure 1-1) in KSC's Large Equipment Test Facility (LETF). If a repeated Chapter 3 error analysis on real hardware is successful, ALO's modeler should arrange for the calibrator to stuff its 15 admittances directly into the knowledge base. If automatically calibrating ALO's admittances improves both model quality and modeler productivity, could calibrating other items be beneficial? Yes, indeed. ALO's TV cameras, pumps, and sensor tolerances should be calibrated next, as described below. Later this portable tool can be installed in KATE's LOX and ECS models to reap more productivity gains.

5.2 Automatically Calibrating ALO's Cameras

Occasionally ALO's two television cameras get bumped, and then they don't aim at failed devices as they should. A user-interactive calibration procedure is needed to trim camera pan, tilt, and focus upon demand. The procedure is summarized in the software design of Table 5-1. Because it relies heavily upon hardware, this procedure should be coded and tested after ALO is reinstalled in KSC's LETF area.

Table 5-1
TV Camera Calibration Procedure

1. Notice which device icon the mouse is pointing at.
2. Slew the camera to the coordinates already given in the device frame's *cam-coord* slot.
3. Pause while the user bumps the camera servo joy stick to manually trim its direction and focus.
4. Automatically read the camera's actual position from its servo hardware.
5. Write these new camera coordinates into the device frame's slot.

5.3 Automatically Calibrating ALO's Pumps

KATE needs to know how much head pressure to expect from ALO's pumps for any given rpm command. Pumps age, so automating calibration of the pumps' rpm-to-pressure transfer function can be expected to improve both

model performance and modeler productivity by permitting more frequent, and less time consuming updates. Table 5-2 summarizes a procedure for calibrating ALO's pumps. A coded but untested control procedure for pump calibration appears in Appendix A (see ".pump-data"). This procedure illustrates some experimental code that the calibrator's other procedures do not have. To improve portability to other KATE models, a disk file carries raw pressure measurements from a data-taking control procedure to a separate LISP analysis function. To simplify procedure coding, an improved looping macro (see "REPEAT") allows a *variable* to control pump speed. Control procedure compiler enhancements that are underway now will make these calibrator improvements workable.

Table 5-2
Pump Calibration Procedure

1. Configure ALO's valves the same as "pump-to-4-way" in Table 2-2.
2. Run pump from 1800 to 3600 rpm in 100 rpm steps.
3. Measure pump head pressure (PX105 minus PX115) in every step.
4. Use linear regression to obtain a straight line transfer function that relates commanded rpm values to measured pump head pressure.
5. If the linear regression algorithm reports a correlation poorer than 95%, check the pump and do it again.
6. Stuff the transfer function into the pump's knowledge base frame.

5.4 Calibrating Sensor Tolerances

ALO's modeler needs a sensor tolerance calibrator to tell him when tolerances get too sloppy. Device failures trigger KATE's diagnoser when actual measurements differ from their modeled values by more than a prescribed tolerance. KATE's modelers typically respond to false alarms (i.e., diagnoses triggered by out-of-tolerance sensors, not device failures) by arbitrarily widening sensor tolerances. Tolerances have been known to grow so large that device failure does not trigger the diagnoser. (Such growth admittedly is rare, because the catastrophic device failures that KATE is capable of diagnosing affect measurements dramatically.) The sensor tolerance calibration procedure in Table 5-3 below was inspired by conversation with Steve Beltz [13].

Table 5-3
Sensor Tolerance Calibration Procedure

1. Collect a complete set of measured-modeled differences for all sensors every 4-seconds (i.e., every KATE "heart beat").
2. After collecting 100Kbytes or more of these, alarm the user every time a measured-modeled difference exceeds $\pm$99 percentile.
3. After collecting 1Mbytes of these, display their histograms.

4. If the user approves, stuff each of the 99-percentile limits into its sensor tolerance slot in the model knowledge base.
5. Stop collecting measured-modeled differences:
    a. Anytime the user wants to.
    b. For 7 seconds after any abrupt control procedure change.
    c. While a sensor is "nuked" (i.e., the knowledge base's way of telling the diagnoser to ignore a temporarily dubious measurement).
6. Display histograms and flush the accumulated measured-modeled differences prematurely, if the user demands.

APPENDIX A

AUTOMATED ADMITTANCE CALIBRATOR PROGRAM LISTING

```
;;; -*- Mode: LISP; Syntax: Common-lisp; Package: KATE; Base: 10 -*-


(SETF *ADMIT-FILE* "G:>MORGAN>ANSWERS.LISP")

;;; KATE-ALO's Initial State:
;;;   Hand valves, HV-104, -105, -106, -107, CV-104 all open.
;;;   Flow-control hand valves, FCV-101 = 30%, FCV-103 = 25%, FCV-102 = 100%.
;;;   All solenoid and motor control valves closed.
;;;   ST-101 = 175gal, VT-101 = 10gal.

(defun format2 (arg)
  (zwei:with-editor-stream (admit-stream :buffer-name *ADMIT-FILE*)
    (format admit-stream "~A~%" arg))
  arg)

;(defun format2 (arg)   ;;;  replace PRINTs with format2 to redirect output to the ANSWERS file
;  (format *rprt* "~A~%" arg))

;(defun format2 (arg)
;  (print arg))

(defvar *.ST-ULLAGE* nil "volume of storage tank air space: 0.0 to 245.8/7.481 cu.ft.")
(defvar *.VT-ULLAGE* nil "volume of vehicle tank air space: 0.0 to 100.0/7.481 cu.ft.")
(defvar *.rpm*  nil "current pump speed command: 1800 - 3600 rpm")
(defvar *.opencmd*  nil "current control valve position command: 0.0 to 1.0")
(defvar *.valve*  nil "current control valve of interest: MCV-101 or FCV-101")
(defvar *.st-up-admit*  nil "storage tank ullage pressurizing admittance")
(defvar *.vt-up-admit*  nil "vehicle tank ullage pressurizing admittance")
(defvar *.st-vent-admit*  nil "storage tank ullage venting admittance")
(defvar *.vt-vent-admit*  nil "vehicle tank ullage venting admittance")
(defvar *.suction-line-admit*  nil "storage tank to pump circuit admittance")
(defvar *.pump-to-4-way-admit*  nil "pump to PX-105 admittance")
(defvar *.PX105-to-PX106-admit*  nil "PX-105 to PX-106 admittance")
(defvar *.transfer-line-admit*  nil "PX-106 to skid admittance")
(defvar *.ff-107-admit*  nil "fast fill valve SV-107 admittance")
(defvar *.ff-108-admit*  nil "fast fill valve SV-108 admittance")
(defvar *.final-fill-circuit-admit*  nil "PX-107 to vehicle tank admittance")
(defvar *.replenish-circuit-admit*  nil "skid's slow fill admittance")
(defvar *.nozzle-admit*  nil "vehicle tank to nozzle admittance")
(defvar *.bleed-admit*  nil "vehicle tank to bleed outlet admittance")
(defvar *.recirculation-admit*  nil "PX-106 to storage tank backflow admittance")
(defvar *.pump-circuit-admit* nil "series pump-to-4-way-admit,suction-line-admit,PX105-to-PX106-admit")
(defvar *.fast-fill-circuit-admit*  nil "ff-107-admit and ff-108-admit in parallel")
(defvar *.skid-admit*  nil "replenish-circuit-admit and fast-fill-circuit-admit in parallel")
(defvar *.upper-fill-circuit-admit*  nil "skid-admit and final-fill-circuit-admit in series")
(defvar *.tank-fill-admit*  nil "upper-fill-circuit-admit and transfer-line-admit in series")
(defvar *.FM-103* nil "list of 30 FM-103 samples taken in 2 minutes")
(defvar *.FM-103sloflo* nil "list of 3 FM-103 samples taken with SV-103 closed")
(defvar *.FM-103fasflo* nil "list of 3 FM-103 samples taken with SV-103 open")
(defvar *.FM-102* nil "list of 30 FM-102 samples taken in 2 minutes")
(defvar *.FM-101* nil "list of 30 FM-101 samples taken in 2 minutes")
(defvar *.%open* nil "list of 10 control valve %open samples taken in 2 minutes")
(defvar *.PX-101* nil "list of 30 PX-101 samples taken in 2 minutes")
(defvar *.PX-109* nil "list of 30 PX-109 samples taken in 2 minutes")
(defvar *.DPX-104* nil "list of 30 DPX-104 samples taken in 2 minutes")
(defvar *.PX-115* nil "list of 30 PX-115 samples taken in 2 minutes")
(defvar *.PX-105* nil "list of 30 PX-105 samples taken in 2 minutes")
(defvar *.PX-106* nil "list of 30 PX-106 samples taken in 2 minutes")
(defvar *.PX-106sloflo* nil "list of 3 PX-106 samples taken with SV-103 closed")
(defvar *.PX-106fasflo* nil "list of 3 PX-106 samples taken with SV-103 open")
(defvar *.PX-111* nil "list of 30 PX-111 samples taken in 2 minutes")
(defvar *.PX-107* nil "list of 30 PX-107 samples taken in 2 minutes")
(defvar *.DPX-113* nil "list of 30 DPX-113 samples taken in 2 minutes")
(defvar *.a1* nil "temp space in FastFlow")
(defvar *.a2* nil "temp space in FastFlow")
(defvar *.a3* nil "temp space in FastFlow")
(defvar *.b1* nil "temp space in FastFlow")
(defvar *.b2* nil "temp space in FastFlow")
(defvar *.b3* nil "temp space in FastFlow")
(defvar *.c1* nil "temp space in FastFlow")
(defvar *.c2* nil "temp space in FastFlow")
(defvar *.c3* nil "temp space in FastFlow")
(defvar *.d1* nil "temp space in FastFlow")
(defvar *.d2* nil "temp space in FastFlow")
(defvar *.d3* nil "temp space in FastFlow")
```

```
(defvar *.e1* nil "temp space in FastFlow")
(defvar *.e2* nil "temp space in FastFlow")
(defvar *.e3* nil "temp space in FastFlow")
(defvar *.f1* nil "temp space in FastFlow")
(defvar *.f2* nil "temp space in FastFlow")
(defvar *.f3* nil "temp space in FastFlow")
(defvar *.g1* nil "temp space in FastFlow")
(defvar *.g2* nil "temp space in FastFlow")
(defvar *.g3* nil "temp space in FastFlow")
(defvar *.h1* nil "temp space in FastFlow")
(defvar *.h2* nil "temp space in FastFlow")
(defvar *.h3* nil "temp space in FastFlow")
(defvar *.i1* nil "temp space in FastFlow")
(defvar *.i2* nil "temp space in FastFlow")
(defvar *.i3* nil "temp space in FastFlow")
(defvar *.j1* nil "temp space in FastFlow")
(defvar *.j2* nil "temp space in FastFlow")
(defvar *.j3* nil "temp space in FastFlow")
(defvar *.k1* nil "temp space in FastFlow")
(defvar *.k2* nil "temp space in FastFlow")
(defvar *.k3* nil "temp space in FastFlow")
(defvar *.slow-recirc* nil "recirculation line admittance with SV-103 closed")
(defvar *.fast-recirc* nil "recirculation line admittance with SV-103 open")
(defvar *.pump-speed* nil "current pump speed during calibration")
(defvar *.pmp-spd-list* nil "all 19 pump speeds during calibration")
(defvar *.pump-xfer-fcn* nil "calibrated transfer function of RPM-101")
(defvar *.FM103admit* 3.75  "admittance of FM103 flow meter venturi")
(defvar *.FM102admit* 3.63  "admittance of FM102 flow meter venturi")
(defvar *.FM101admit* 0.667 "admittance of FM101 flow meter venturi")
(defvar *.in-to-psi*  27.7   "divide by this to convert inches of H2O to psi")
(defvar *.gal-to-cuft* 7.481 "divide by this to convert gallons to cubic feet")
(defvar *.ST-cap* 245.8 "storage tank capacity in gallons")
(defvar *.VT-cap* 103.0 "vehicle tank capacity in gallons")
(defvar *.ST-supl* 30 "storage tank's GN2 supply pressure")
(defvar *.VT-supl* 70 "vehicle tank's GN2 supply pressure")
(defvar *.atm* 0 "atmospheric pressure in psig")

;;;  Look for these on KATE's mouseable Control Procedures menu....
(setf *SYSTEM-PROCEDURES* '(.pressurize .depressurize .fastflow .ff108 .mcv101 .nozzle .bleed .recirc .de
rived .done .do-it-all bob))

;;;   Bob's ALO-KB Caller....
(defun GET-TANK-ULLAGE (tank-capacity amt)
  "Input is tank-capacity (in gal) and amt of fluid in tank (in gal),
   output is ullage space in ft3"
  (/ (- tank-capacity amt) 7.481))

;;;   ************************************************************************************************

;;;   **********************   Scott's Regression Line Drawing Package      ****************************

;;;   ************************************************************************************************

(defflavor graph-pane (mxx mnx mxy mny scale)
           (tv::window)
  :settable-instance-variables
  :readable-instance-variables)

(defvar *graph-pane* nil)

(setq *graph-pane*
      (tv::make-window 'graph-pane
                       :size '(500 500)
                       :blinker-p nil
                       :save-bits t
                       :label nil))

(defmethod (scale graph-pane)(xl yl)
  (setq mxx (apply #'max xl)
        mnx (apply #'min xl)
        mxy (apply #'max yl)
        mny (apply #'min yl))
  (cond ((> (- mxx mnx)(- mxy mny))
         (setq scale (/ 450 (- mxx mnx))))
        (t (setq scale (/ 450 (- mxy mny))))))
```

```
(defmethod (plot graph-pane) (xl yl)
  (do* ((xw xl (cdr xw))
        (yw yl (cdr yw))
        (x (car xw) (car xw))
        (y (car yw) (car yw)))
       ((null x))
    (graphics::draw-circle (+ 25 (round (* (- x mnx) scale)))
                           (- 475 (round (* (- y mny) scale)))
                           4
                           :stream self)))

(defmethod (draw-fit graph-pane) (xl yl)
  (let* ((a-b (CDR (.regres xl yl)))
         (a (car a-b))
         (b (cadr a-b))
         (pt1-y (+ a (* b mnx)))
         (pt2-y (+ a (* b mxx))))
    (graphics::draw-line (+ 25)
                         (- 475 (round (* (- pt1-y mny) scale)))
                         (+ 25 (round (* (- mxx mnx) scale)))
                         (- 475 (round (* (- pt2-y mny) scale)))
                         :thickness 2
                         :stream self)))

(defun test-fit (x y)
  (send *graph-pane* :expose)
  (send *graph-pane* :clear-window)
  (scale *graph-pane* x y)
  (plot *graph-pane* x y)
  (draw-fit *graph-pane* x y))

;;;     ************************************************************************************************

;;;     ************************     ALO-H2O Admittance Calibration Equation Verifier     ****************

;;;     ************************************************************************************************

;;;   The pressure and flow rate data below were manually recorded by Steve Morgan in July 1992 for use
;;;   in testing candidate admittance equations during the automatic admittance calibrator design phase.

(defun .test-press ()       ;;;    empty the tank !!!
  (SETQ *.PX-101* '(1.76 3.04 4.29)
        *.ST-ULLAGE* (format2 (/ (- *.ST-cap* 175) *.gal-to-cuft*))                ; =9.5 cuft
        *.st-up-admit* (.tankadmit *.ST-ULLAGE* *.PX-101* 30)                ; =2.27
        *.PX-109* '(1.06 2.29 3.51)
        *.VT-ULLAGE* (format2 (/ (- *.VT-cap* 10) *.gal-to-cuft*))                    ; =12 cuft
        *.vt-up-admit* (.tankadmit *.VT-ULLAGE* *.PX-109* 70)))              ; =1.78

(defun .test-depress ()      ;;;   Empty the tank!!!
  (SETQ *.ST-ULLAGE* (format2 (/ (- *.ST-cap* 175) *.gal-to-cuft*))                ; =9.5 cuft
        *.PX-101* '(12.2 11.3 10.4)
        *.st-vent-admit* (.tankadmit *.ST-ULLAGE* *.PX-101* 0)               ; =2.51
        *.VT-ULLAGE* (format2 (/ (- *.VT-cap* 10) *.gal-to-cuft*))                 ; =12 cuft
        *.PX-109* '(15.1 13.4 11.9)
        *.vt-vent-admit* (.tankadmit *.VT-ULLAGE* *.PX-109* 0)))             ; =5.09

(defun .test-Fast-Flow ()
  (SETQ *.fm-103*  '(10.3 13. 15.6)
        *.fm-102*  '(10.3 13. 15.6)
        *.px-101*  '(0. 0. 0.)
        *.dpx-104* '(2.39 2.22 2.07)
        *.px-115*  '(1. .2 0.)
        *.px-105*  '(23.4 32.8 44.)
        *.px-106*  '(20.6 28. 36.8)
        *.px-111*  '(5.7 9.1 13.1)
        *.px-107*  '(2.5 4.2 6.2)
        *.dpx-113* '(.49 .76 1.1)
        *.px-109*  '(0. .1 .2)
        *.suction-line-admit* (CAR (.stat (.admittances                    ;  =10.1
              *.fm-103* (.ad (/ -5 *.in-to-psi*) (mapcar #'- (mapcar #'+ *.px-101* *.dpx-104*) *.px-115*
)))))
        *.pump-to-4-way-admit* (CAR (.stat (.admittances
              *.fm-103* (.ad (/ 19 *.in-to-psi*)   (mapcar #'- *.px-105* *.px-115*)))))  ;  =2.2
        *.PX105-to-PX106-admit* (CAR (.stat (.admittances
              *.fm-103* (.ad (/ 24 *.in-to-psi*)   (mapcar #'- *.px-105* *.px-106*)))))  ;  =5.4
        *.transfer-line-admit* (CAR (.stat (.admittances
```

```
            *.fm-102* (.ad (/ -236 *.in-to-psi*) (mapcar #'- *.px-106* *.px-111*)))))  ;  =4.0
        *.ff-107-admit* (CAR (.stat (.admittances
            *.fm-102* (.ad (/ -1 *.in-to-psi*)   (mapcar #'- *.px-111* *.px-107*)))))  ;  =5.9
        *.final-fill-circuit-admit* (CAR (.stat (.admittances                          ;  =7.3
            *.fm-102* (.ad (/ -3 *.in-to-psi*) (mapcar #'- (mapcar #'- *.px-107* *.dpx-113*) *.px-109*
)))))))

(defun .test-ff108 ()
  (SETQ *.FM-102* '(10.3 13. 15.6)                                                  ;  =6.3
        *.px-111* '(6. 9.1 12.8)
        *.px-107* '(3.3 4.8 6.5)
        *.ff-108-admit* (CAR (.stat (.admittances
                                    *.FM-102* (.ad (/ -1 *.in-to-psi*) (mapcar #'- *.px-111* *.px-107*)
))))))

(defun .test-mcv101 ()
  (SETQ *.%open* '(.30 .40 .50 .60 .70 .80 .90 1.00)   ; = 2.7 * %open - 0.65 & r = 99.98%
        *.FM-101* '(.9 2.6 4.3 5.9 7.3 8.5 9.6 10.6)
        *.px-111* '(42.5 41.8 40.4 38.8 36.6 34.6 32.5 30.6)
        *.px-107* '(.6 .5 .8 1.1 1.4 2. 2.2 2.5)
        *.replenish-circuit-admit* (.regres *.%open* (.admittances
            *.FM-101* (.ad (/ -1 *.in-to-psi*) (mapcar #'- *.px-111* *.px-107*))))))

(defun .test-nozzle ()
  (SETQ *.px-107*  '(3.4 4.8 6.5)                                                   ; =-1.
        *.FM-102*  '(9.6 12.7 15.6)
        *.px-109*  '(0. 0. .1)
        *.dpx-113* '(1.54 1.4 1.2)
        *.nozzle-admit* (CAR (.stat (.admittances (mapcar #'- *.FM-102* (.mul *.final-fill-circuit-admit*

          (mapcar #'sqrt (.ad (/ -3 *.in-to-psi*) (mapcar #'- *.px-107*
                                                    (mapcar #'+ *.px-109* *.dpx-113*)))))) ; vt-inl
et-flow
                                                  (mapcar #'+ *.px-109* *.dpx-113*)))))) ; vt-inlet-pres

(defun .test-bleed ()
  (SETQ *.px-107*  '(3.5 5.1 7.1)                                                   ;  =-0.75
        *.FM-102*  '(9.6 12.7 15.5)
        *.px-109*  '(0. 0. .1)
        *.dpx-113* '(1.71 1.83 1.92)
        *.bleed-admit* (CAR (.stat (.admittances (mapcar #'- *.FM-102* (.mul *.final-fill-circuit-admit*
          (mapcar #'sqrt (.ad (/ -3 *.in-to-psi*) (mapcar #'- *.px-107*
                                                    (mapcar #'+ *.px-109* *.dpx-113*)))))) ; vt-inl
et-flow
                                                  (mapcar #'+ *.px-109* *.dpx-113*)))))) ; vt-inlet-pres

(defun .test-recirc ()
  (SETQ *.%open*          '(.0   1.00)
        *.px-106sloflo*   '(23.8 32.1 43.2)     ;  SV-103 closed
        *.FM-103sloflo*   '(7.6  9.1  10.6)
        *.px-101*         '(0.   0.   0.)
        *.dpx-104*        '(2.04 2.04 2.04)
        *.px-106fasflo*   '(9.2  12.6 16.6)     ;  SV-103 open
        *.FM-103fasflo*   '(19.5 23.4 27.3)
        *.recirculation-admit* (.regres *.%open*    ;;;   admit = 5.6 * %open + 1.6 (r=99%)
         (LIST (CAR (.stat (.admittances
               *.FM-103sloflo* (mapcar #'- (mapcar #'- *.px-106sloflo* *.px-101*) *.dpx-104*))))
               (CAR (.stat (.admittances
               *.FM-103fasflo* (mapcar #'- (mapcar #'- *.px-106fasflo* *.px-101*) *.dpx-104*)))))))))

;;;     ************************************************************************************************

;;;     ************************     ALO-H2O Admittance Calibration Test Procedures     ******************

;;;     ************************************************************************************************

;;;   1.  Measure admittances of tank pressurization and depressurization lines with both tanks EMPTY.

(defprocedure .pressurize
  :pretty-name "Calibrating st- & vt-up-admit...."
  :actions
  ((L (format2 '(Calibrating st- & vt-up-admit....)))
   (L (SETQ *.ST-ULLAGE* (/ (- *.ST-cap* (GET-MODEL-VALUE 'ST-101 'level-out)) *.gal-to-cuft*)
            *.VT-ULLAGE* (/ (- *.VT-cap* (GET-MODEL-VALUE 'VT-101 'level-out)) *.gal-to-cuft*)))
;;;   Closed final-fill line (SV-111) prevents water loss.
   (C SV-101 OPEN    "Open storage tank's 30psi GN2 supply valve.")
```

```
    (C SV-114 OPEN    "Open vehicle tank's 70psi GN2 supply valve.")
    (WT 4)
    (L (SETQ *.a1* (GET-CURRENT-VALUE 'PX-101-M)
             *.b1* (GET-CURRENT-VALUE 'PX-109-M)))
    (WT 4)
    (L (SETQ *.a2* (GET-CURRENT-VALUE 'PX-101-M)
             *.b2* (GET-CURRENT-VALUE 'PX-109-M)))
    (WT 4)
    (L (setf *.a3* (GET-CURRENT-VALUE 'PX-101-M)
             *.b3* (GET-CURRENT-VALUE 'PX-109-M)))
    (L (SETQ *.st-up-admit* (.tankadmit *.ST-ULLAGE* (LIST *.a1* *.a2* *.a3*) *.ST-supl*)

             *.vt-up-admit* (.tankadmit *.VT-ULLAGE* (LIST *.b1* *.b2* *.b3*) *.VT-supl*)
             *.dummy* 1))  ;;;  Humor the balky "L" function
    (C SV-101 CLOSED  "Reinitialize.")
    (C SV-114 CLOSED  "Reinitialize.")))

(defprocedure .depressurize                    ;;;   Warning:  PX-101,2 not accurate above 25 psig !
  :pretty-name "Calibrating st- & vt-vent-admit...."
  :actions
  ((L (format2 '(Calibrating st- & vt-vent-admit....)))
   (L (SETQ *.ST-ULLAGE* (/ (- *.ST-cap* (GET-MODEL-VALUE 'ST-101 'level-out)) *.gal-to-cuft*)
            *.VT-ULLAGE* (/ (- *.VT-cap* (GET-MODEL-VALUE 'VT-101 'level-out)) *.gal-to-cuft*)))
;;;   Closed final-fill line (SV-111) prevents water loss.
    (C SV-106 OPEN    "Open storage tank vent.")
    (C SV-113 OPEN    "Open vehicle tank vent.")
    (WT 4)
    (L (SETQ *.a1* (GET-CURRENT-VALUE 'PX-101-M)
             *.b1* (GET-CURRENT-VALUE 'PX-109-M)))
    (WT 4)
    (L (SETQ *.a2* (GET-CURRENT-VALUE 'PX-101-M)
             *.b2* (GET-CURRENT-VALUE 'PX-109-M)))
    (WT 4)
    (L (setf *.a3* (GET-CURRENT-VALUE 'PX-101-M)
             *.b3* (GET-CURRENT-VALUE 'PX-109-M)))
;    (REPEAT 30 (WT 4)   ;;;   sample tank pressures every 4 seconds for 2 minutes
;           (L (setf *.PX-101* (CONS (GET-CURRENT-VALUE 'PX-101-M) *.PX-101*)
;                    *.PX-109* (CONS (GET-CURRENT-VALUE 'PX-109-M) *.PX-109*)))) ;;; "L" won't do this yet
    (L (SETQ *.st-vent-admit* (.tankadmit *.ST-ULLAGE* (LIST *.a1* *.a2* *.a3*) *.atm*)

             *.vt-vent-admit* (.tankadmit *.VT-ULLAGE* (LIST *.b1* *.b2* *.b3*) *.atm*)
             *.dummy* 1))
    (C SV-101 CLOSED  "Reinitialize.")
    (C SV-114 CLOSED  "Reinitialize.")))

;;;   Return the mean of all admittances, Ai, and print both their mean and standard deviation.
;;;   Bulk of gas in tank, Ni = N0 * Pi / P0, where N0 and P0 are initial ullage in cuft and absolute
;;;   pressure in psi.  Gas flow rate, Qi = (Ni - Ni-1) / Ts, where Ts is interval between pressure
;;;   samples in minutes.  Admittance, Ai = Qi / SQRT(Pi - Ps), where Ps is gas source pressure while
;;;   pressurizing or atm while depressurizing.  In other words,...
;;;                N0      Pi - Pi-1
;;;        Ai = ----- , ------------- , and P0 and Ts usually cancel out.
;;;             P0 Ts   SQRT(Pi - Ps)
(defun .tankadmit (ullage p Psource)
  (CAR (.stat (.admittances (.mul ullage (mapcar #'abs (.del (format2 p))))  ;  flows
                            (mapcar #'abs (.drop p Psource))))))             ;  dP

;;;   Replace any zero pressures with 1 micro-psi to humor the divide function.
(defun .humor (p)
  (mapcar #'(lambda (x) (max x 1.e-6)) p))

;;;   Subtract source pressure from every pressure sample.
(defun .drop (p Psource)
  (mapcar #'(lambda (x) (- x Psource)) p))

;;;   Find differences in consecutive pressure sample pairs.
(defun .del (p)
  (mapcar #'- p (cdr p)))

;;;   Get list of admittances = flows / SQRT (pressure drops).
(defun .admittances (flows pressures)
  (mapcar #'/ (format2 flows) (.humor (mapcar #'sqrt (format2 pressures)))))

;;;   2.  Calibrate Admittances Along the Fast Flow Path....

(defprocedure .FastFlow
```

```
    :pretty-name "Calibrating 6 fast-fill path admits...."
    :actions
    ((L (format2 '(Calibrating 6 fast-fill path admits....)))
     (C SV-106  OPEN       "Open storage tank vent.")
     (C SV-113  OPEN       "Open vehicle tank vent.")
     (C SV-104  OPEN       "Open pump circuit.")
     (C SV-107  OPEN       "Open main skid valve.")
     (C SV-111  OPEN       "Open final fill circuit.")
     (C RPM-101 (2500 rpm) "Pump slowly.")
     (WT 12)
     (L (SETQ *.a1* (GET-CURRENT-VALUE 'DPX-102-M) *.b1* (GET-CURRENT-VALUE 'PX-101-M)
              *.c1* (GET-CURRENT-VALUE 'DPX-104-M) *.d1* (GET-CURRENT-VALUE 'PX-115-M)
              *.e1* (GET-CURRENT-VALUE 'PX-105-M)  *.f1* (GET-CURRENT-VALUE 'PX-106-M)
              *.g1* (GET-CURRENT-VALUE 'PX-111-M)  *.h1* (GET-CURRENT-VALUE 'PX-107-M)
              *.i1* (GET-CURRENT-VALUE 'DPX-113-M) *.j1* (GET-CURRENT-VALUE 'PX-109-M)
              *.k1* (GET-CURRENT-VALUE 'DPX-103-M)))
     (C RPM-101 (3000 rpm) "Pump moderately.")
     (WT 4)
     (L (SETQ *.a2* (GET-CURRENT-VALUE 'DPX-102-M) *.b2* (GET-CURRENT-VALUE 'PX-101-M)
              *.c2* (GET-CURRENT-VALUE 'DPX-104-M) *.d2* (GET-CURRENT-VALUE 'PX-115-M)
              *.e2* (GET-CURRENT-VALUE 'PX-105-M)  *.f2* (GET-CURRENT-VALUE 'PX-106-M)
              *.g2* (GET-CURRENT-VALUE 'PX-111-M)  *.h2* (GET-CURRENT-VALUE 'PX-107-M)
              *.i2* (GET-CURRENT-VALUE 'DPX-113-M) *.j2* (GET-CURRENT-VALUE 'PX-109-M)
              *.k2* (GET-CURRENT-VALUE 'DPX-103-M)))
     (C RPM-101 (3500 rpm) "Pump rapidly.")
     (WT 4)
     (L (SETQ *.a3* (GET-CURRENT-VALUE 'DPX-102-M) *.b3* (GET-CURRENT-VALUE 'PX-101-M)
              *.c3* (GET-CURRENT-VALUE 'DPX-104-M) *.d3* (GET-CURRENT-VALUE 'PX-115-M)
              *.e3* (GET-CURRENT-VALUE 'PX-105-M)  *.f3* (GET-CURRENT-VALUE 'PX-106-M)
              *.g3* (GET-CURRENT-VALUE 'PX-111-M)  *.h3* (GET-CURRENT-VALUE 'PX-107-M)
              *.i3* (GET-CURRENT-VALUE 'DPX-113-M) *.j3* (GET-CURRENT-VALUE 'PX-109-M)
              *.k3* (GET-CURRENT-VALUE 'DPX-103-M)))
;;;   suction-line-admit's pressure drop = PX101 + DPX104 - PX115 - 5"
    (L (SETQ *.suction-line-admit*  (CAR (.stat (.admittances
                    (.mul *.FM103admit* (mapcar #'sqrt (LIST *.k1* *.k2* *.k3*)))     ; FM-103 flows
                    (.ad (/ -5 *.in-to-psi*) (mapcar #'- (mapcar #'+ (LIST *.b1* *.b2* *.b3*) (LIST *.c1*
*.c2* *.c3*))
                                                (LIST *.d1* *.d2* *.d3*))))))   ; PX101 + DPX104 - 5"
             *.pump-to-4-way-admit* (CAR (.stat (.admittances
                    (.mul *.FM103admit* (mapcar #'sqrt (LIST *.k1* *.k2* *.k3*)))     ; FM-103 flows
                    (.ad (/ 19 *.in-to-psi*) (mapcar #'- (LIST *.e1* *.e2* *.e3*)
                                                (LIST *.d1* *.d2* *.d3*))))))   ; PX105 - PX115 + 19"
             *.PX105-to-PX106-admit* (CAR (.stat (.admittances
                    (.mul *.FM103admit* (mapcar #'sqrt (LIST *.k1* *.k2* *.k3*)))     ; FM-103 flows
                    (.ad (/ 24 *.in-to-psi*) (mapcar #'- (LIST *.e1* *.e2* *.e3*)
                                                (LIST *.f1* *.f2* *.f3*))))))   ; PX105 - PX106 + 24"
             *.transfer-line-admit* (CAR (.stat (.admittances
                    (.mul *.FM102admit* (mapcar #'sqrt (LIST *.a1* *.a2* *.a3*)))     ; FM-102 flows
                    (.ad (/ -236 *.in-to-psi*) (mapcar #'- (LIST *.f1* *.f2* *.f3*)
                                                (LIST *.g1* *.g2* *.g3*))))))  ; PX106 - PX111 - 236"
             *.ff-107-admit* (CAR (.stat (.admittances
                    (.mul *.FM102admit* (mapcar #'sqrt (LIST *.a1* *.a2* *.a3*)))     ; FM-102 flows
                    (.ad (/ -1 *.in-to-psi*) (mapcar #'- (LIST *.g1* *.g2* *.g3*)
                                                (LIST *.h1* *.h2* *.h3*))))))   ; PX111 - PX107 - 1"
             *.final-fill-circuit-admit* (CAR (.stat (.admittances
                    (.mul *.FM102admit* (mapcar #'sqrt (LIST *.a1* *.a2* *.a3*)))     ; FM-102 flows
                    (.ad (/ -3 *.in-to-psi*) (mapcar #'- (mapcar #'- (LIST *.h1* *.h2* *.h3*) (LIST *.i1*
*.i2* *.i3*))
                                                (LIST *.j1* *.j2* *.j3*))))))   ; PX107 - DPX113 - PX109 - 3"
             *.dummy* 1))  ;  fake out the L-function
    (C RPM-101 (0 rpm) "Stop pumping.")
    (C SV-106  CLOSED  "Reinitialize.")
    (C SV-113  CLOSED  "Reinitialize.")
    (C SV-104  CLOSED  "Reinitialize.")
    (C SV-107  CLOSED  "Reinitialize.")
    (C SV-111  CLOSED  "Reinitialize.")))

;;;   3.  Redirect skid flow and calibrate the other two skid admittances.
(defprocedure .ff108
  :pretty-name "Calibrating SV-108's admittance...."
  :actions
  ((L (format2 '(Calibrating SV-108's admittance....)))
   (C SV-106  OPEN       "Open storage tank vent.")
   (C SV-113  OPEN       "Open vehicle tank vent.")
   (C SV-104  OPEN       "Open pump circuit.")
   (C SV-108  OPEN       "Open other skid valve.")
```

```
   (C SV-111  OPEN       "Open final fill circuit.")
   (C RPM-101 (3500 rpm) "Pump rapidly.")
   (WT 12)
   (L (SETQ *.a1* (GET-CURRENT-VALUE 'DPX-102-M)
            *.g1* (GET-CURRENT-VALUE 'PX-111-M)  *.h1* (GET-CURRENT-VALUE 'PX-107-M)))
   (C RPM-101 (3000 rpm) "Pump moderately.")
   (WT 4)
   (L (SETQ *.a2* (GET-CURRENT-VALUE 'DPX-102-M)
            *.g2* (GET-CURRENT-VALUE 'PX-111-M)  *.h2* (GET-CURRENT-VALUE 'PX-107-M)))
   (C RPM-101 (2500 rpm) "Pump slowly.")
   (WT 4)
   (L (SETQ *.a3* (GET-CURRENT-VALUE 'DPX-102-M)
            *.g3* (GET-CURRENT-VALUE 'PX-111-M)  *.h3* (GET-CURRENT-VALUE 'PX-107-M)))
   (L (SETQ *.ff-108-admit* (CAR (.stat (.admittances (.mul *.FM102admit* (mapcar #'sqrt (LIST *.a1* *.a2
* *.a3*))) ; FM-102 flow
          (.ad (/ -1 *.in-to-psi*) (mapcar #'- (LIST *.g1* *.g2* *.g3*) (LIST *.h1* *.h2* *.h3*)))))))))  ;
 PX111 - PX107 - 1"
   (C RPM-101 (0 rpm) "Stop pumping.")
   (C SV-106  CLOSED  "Reinitialize.")
   (C SV-113  CLOSED  "Reinitialize.")
   (C SV-104  CLOSED  "Reinitialize.")
   (C SV-108  CLOSED  "Reinitialize.")
   (C SV-111  CLOSED  "Reinitialize.")))

(defprocedure .mcv101
  :pretty-name "Calibrating MCV-101's admittance transfer function...."
  :actions
  ((L (format2 '(Calibrating MCV-101's admittance transfer function....)))
   (C SV-106  OPEN       "Open storage tank vent.")
   (C SV-113  OPEN       "Open vehicle tank vent.")
   (C SV-104  OPEN       "Open pump circuit.")
   (C SV-103  OPEN       "Speed up recirculation.")
   (C MCV-101 (.30 %)    "Open replenish valve to 30%")
   (C SV-111  OPEN       "Open final fill circuit.")
   (C RPM-101 (3500 rpm) "Pump rapidly.")
   (WT 25)
   (L (SETQ *.a1* (GET-CURRENT-VALUE 'DPX-101-M)
            *.g1* (GET-CURRENT-VALUE 'PX-111-M) *.h1* (GET-CURRENT-VALUE 'PX-107-M)))
   (C MCV-101 (.35 %)   "Open replenish valve to 35%")
   (WT 25)
   (L (SETQ *.a2* (GET-CURRENT-VALUE 'DPX-101-M)
            *.g2* (GET-CURRENT-VALUE 'PX-111-M) *.h2* (GET-CURRENT-VALUE 'PX-107-M)))
   (C MCV-101 (.40 %)   "Open replenish valve to 40%")
   (WT 25)
   (L (SETQ *.a3* (GET-CURRENT-VALUE 'DPX-101-M)
            *.g3* (GET-CURRENT-VALUE 'PX-111-M) *.h3* (GET-CURRENT-VALUE 'PX-107-M)))
   (L (setf admit (.admittances (.mul *.FM101admit* (mapcar #'sqrt (LIST *.a1* *.a2* *.a3*)))
                                (.ad (/ -1 *.in-to-psi*) (mapcar #'- (LIST *.g1* *.g2* *.g3*) (LIST *.h1*
 *.h2* *.h3*))))
            *.replenish-circuit-admit* (.regres '(30. 35. 40.) admit)))
   (C RPM-101 (0. rpm) "Stop pumping.")
   (C SV-106  CLOSED  "Reinitialize.")
   (C SV-113  CLOSED  "Reinitialize.")
   (C SV-104  CLOSED  "Reinitialize.")
   (C SV-103  CLOSED  "Reinitialize.")
   (C SV-111  CLOSED  "Reinitialize.")
   (C MCV-101 (.0 %)  "Reinitialize.")))

;;;   4.  Calibrate nozzle and bleed valves.
(defprocedure .nozzle
  :pretty-name "Calibrating nozzle admittance...."
  :actions
  ((L (format2 '(Calibrating nozzle admittance....)))
   (C SV-106  OPEN       "Open storage tank vent.")
   (C SV-113  OPEN       "Open vehicle tank vent.")
   (C SV-104  OPEN       "Open pump circuit.")
   (C SV-107  OPEN       "Open main skid valve.")
   (C SV-111  OPEN       "Open final fill circuit.")
   (C SV-110  OPEN       "Open nozzle valve.")
   (C RPM-101 (3500 rpm) "Pump rapidly.")
   (WT 12)
   (L (SETQ *.a1* (GET-CURRENT-VALUE 'DPX-102-M) *.h1* (GET-CURRENT-VALUE 'PX-107-M)
            *.i1* (GET-CURRENT-VALUE 'DPX-113-M) *.j1* (GET-CURRENT-VALUE 'PX-109-M)))
   (C RPM-101 (3000 rpm) "Pump moderately.")
   (WT 4)
   (L (SETQ *.a2* (GET-CURRENT-VALUE 'DPX-102-M) *.h2* (GET-CURRENT-VALUE 'PX-107-M)
```

```
            *.i2* (GET-CURRENT-VALUE 'DPX-113-M) *.j2* (GET-CURRENT-VALUE 'PX-109-M)))
    (C RPM-101 (2500 rpm) "Pump slowly.")
    (WT 4)
    (L (SETQ *.a3* (GET-CURRENT-VALUE 'DPX-102-M) *.h3* (GET-CURRENT-VALUE 'PX-107-M)
            *.i3* (GET-CURRENT-VALUE 'DPX-113-M) *.j3* (GET-CURRENT-VALUE 'PX-109-M)))
;;;   Nozzle flow = FM102 - vt_inlet_flow, and
;;;   nozzle pressure drop = vt_inlet_pressure (i.e., the nozzle vents to the atmosphere).
    (L (SETQ *.nozzle-admit* (CAR (.stat (.admittances
      (mapcar #'- (.mul *.FM102admit* (mapcar #'sqrt (format2 (LIST *.a1* *.a2* *.a3*)))) (.vt-inlet-flow)
)   ;  flow
      (.vt-inlet-pressure))))))                                                    ; dP
    (C RPM-101 (0 rpm) "Stop pumping.")
    (C SV-106  CLOSED  "Reinitialize SV106.")
    (C SV-113  CLOSED  "Reinitialize SV113.")
    (C SV-104  CLOSED  "Reinitialize SV104.")
    (C SV-107  CLOSED  "Reinitialize SV107.")
    (C SV-111  CLOSED  "Reinitialize SV111.")
    (C SV-110  CLOSED  "Reinitialize SV110.")))

;;;   Vt_inlet_pressure = PX109 + DPX113.
(defun .vt-inlet-pressure ()
  (mapcar #'+ (LIST *.j1* *.j2* *.j3*) (LIST *.i1* *.i2* *.i3*)))

;;;   Vt_inlet_flow = final_fill_circuit_admit * SQRT (PX107 - 3" - vt_inlet_pressure).
(defun .vt-inlet-flow ()
  (.mul *.final-fill-circuit-admit*
        (mapcar #'sqrt (.ad (/ -3 *.in-to-psi*) (mapcar #'- (LIST *.h1* *.h2* *.h3*) (.vt-inlet-pressure)
)))))

;;;   Multiply every element of a list by a scalar.
(defun .mul (multiplier x)
  (mapcar #'(lambda (x) (* x multiplier)) x))

;;;   Add a scalar to every element of a list.
(defun .ad (augend x)
  (mapcar #'(lambda (x) (+ x augend)) x))

(defprocedure .bleed
  :pretty-name "Calibrating bleed admittance...."
  :actions
  ((L (format2 '(Calibrating bleed admittance....)))
   (C SV-106  OPEN       "Open storage tank vent.")
   (C SV-113  OPEN       "Open vehicle tank vent.")
   (C SV-104  OPEN       "Open pump circuit.")
   (C SV-107  OPEN       "Open main skid valve.")
   (C SV-111  OPEN       "Open final fill circuit.")
   (C SV-109  OPEN       "Open bleed valve.")
   (C RPM-101 (3500 rpm) "Pump rapidly.")
   (WT 12)
   (L (SETQ *.a1* (GET-CURRENT-VALUE 'DPX-102-M) *.h1* (GET-CURRENT-VALUE 'PX-107-M)
            *.i1* (GET-CURRENT-VALUE 'DPX-113-M) *.j1* (GET-CURRENT-VALUE 'PX-109-M)))
   (C RPM-101 (3000 rpm) "Pump moderately.")
   (WT 4)
   (L (SETQ *.a2* (GET-CURRENT-VALUE 'DPX-102-M) *.h2* (GET-CURRENT-VALUE 'PX-107-M)
            *.i2* (GET-CURRENT-VALUE 'DPX-113-M) *.j2* (GET-CURRENT-VALUE 'PX-109-M)))
   (C RPM-101 (2500 rpm) "Pump slowly.")
   (WT 4)
   (L (SETQ *.a3* (GET-CURRENT-VALUE 'DPX-102-M) *.h3* (GET-CURRENT-VALUE 'PX-107-M)
            *.i3* (GET-CURRENT-VALUE 'DPX-113-M) *.j3* (GET-CURRENT-VALUE 'PX-109-M)))
;;;   Bleed flow = FM102 - vt_inlet_flow, and
;;;   bleed pressure drop = vt_inlet_pressure (i.e., the bleed valve vents to the atmosphere).
   (L (SETQ *.bleed-admit* (CAR (.stat (.admittances
     (mapcar #'- (.mul *.FM102admit* (mapcar #'sqrt (format2 (LIST *.a1* *.a2* *.a3*)))) (.vt-inlet-flow)
) ; flow
     (.vt-inlet-pressure))))))                                                    ; dP
   (C RPM-101 (0 rpm) "Stop pumping.")
   (C SV-106  CLOSED  "Reinitialize SV106.")
   (C SV-113  CLOSED  "Reinitialize SV113.")
   (C SV-104  CLOSED  "Reinitialize SV104.")
   (C SV-107  CLOSED  "Reinitialize SV107.")
   (C SV-111  CLOSED  "Reinitialize SV111.")
   (C SV-109  CLOSED  "Reinitialize SV109.")))

;;;   5.  Redirect pump flow, and calculate recirculation-admit.
(defprocedure .recirc
  :pretty-name "Calibrating recirculation path admittance...."
```

```
  :actions
  ((L (format2 '(Calibrating recirculation path admittance....)))
   (C SV-106  OPEN       "Open storage tank vent.")
   (C SV-113  OPEN       "Open vehicle tank vent.")
   (C SV-104  OPEN       "Open pump circuit.")
   (C SV-103  OPEN       "Speed up recirculation.")
   (C RPM-101 (3500 rpm) "Pump rapidly.")
   (WT 12)
   (L (SETQ *.a1* (GET-CURRENT-VALUE 'DPX-103-M) *.b1* (GET-CURRENT-VALUE 'PX-101-M)
            *.c1* (GET-CURRENT-VALUE 'DPX-104-M) *.f1* (GET-CURRENT-VALUE 'PX-106-M)))
   (C RPM-101 (3000 rpm) "Pump moderately.")
   (WT 4)
   (L (SETQ *.a2* (GET-CURRENT-VALUE 'DPX-103-M) *.b2* (GET-CURRENT-VALUE 'PX-101-M)
            *.c2* (GET-CURRENT-VALUE 'DPX-104-M) *.f2* (GET-CURRENT-VALUE 'PX-106-M)))
   (C RPM-101 (2500 rpm) "Pump slowly.")
   (WT 4)
   (L (SETQ *.a3* (GET-CURRENT-VALUE 'DPX-103-M) *.b3* (GET-CURRENT-VALUE 'PX-101-M)
            *.c3* (GET-CURRENT-VALUE 'DPX-104-M) *.f3* (GET-CURRENT-VALUE 'PX-106-M)))
   (L (SETQ *.fast-recirc* (CAR (.stat (.admittances
                               (.mul *.FM103admit* (mapcar #'sqrt (format2 (LIST *.a1* *.a2* *.a3*)))) ; F
M-103 flow
                               (mapcar #'- (mapcar #'- (LIST *.f1* *.f2* *.f3*) (LIST *.b1* *.b2* *.b3*))
                                       (LIST *.c1* *.c2* *.c3*)))))))            ; PX106 - PX101 - DPX104
   (C SV-103  CLOSED     "Slow down recirculation.")
   (L (SETQ *.a1* (GET-CURRENT-VALUE 'DPX-103-M) *.b1* (GET-CURRENT-VALUE 'PX-101-M)
            *.c1* (GET-CURRENT-VALUE 'DPX-104-M) *.f1* (GET-CURRENT-VALUE 'PX-106-M)))
   (C RPM-101 (3000 rpm) "Pump moderately.")
   (WT 4)
   (L (SETQ *.a2* (GET-CURRENT-VALUE 'DPX-103-M) *.b2* (GET-CURRENT-VALUE 'PX-101-M)
            *.c2* (GET-CURRENT-VALUE 'DPX-104-M) *.f2* (GET-CURRENT-VALUE 'PX-106-M)))
   (C RPM-101 (3500 rpm) "Pump rapidly.")
   (WT 4)
   (L (SETQ *.a3* (GET-CURRENT-VALUE 'DPX-103-M) *.b3* (GET-CURRENT-VALUE 'PX-101-M)
            *.c3* (GET-CURRENT-VALUE 'DPX-104-M) *.f3* (GET-CURRENT-VALUE 'PX-106-M)))
   (L (SETQ *.slow-recirc* (CAR (.stat (.admittances
                               (.mul *.FM103admit* (mapcar #'sqrt (format2 (LIST *.a1* *.a2* *.a3*)))) ; F
M-103 flow
                               (mapcar #'- (mapcar #'- (LIST *.f1* *.f2* *.f3*) (LIST *.b1* *.b2* *.b3*))
                                       (LIST *.c1* *.c2* *.c3*)))))))            ; PX106 - PX101 - DPX104
;;;   *.recirculation-admit* is a transfer function, mx+b, where m = 1 with SV103 open or 0 when closed:
   (L (SETQ *.recirculation-admit* (.regres '(0. 1.00)
                                            (LIST *.slow-recirc* *.fast-recirc*))))
   (C RPM-101 (0 rpm) "Stop pumping.")
   (C SV-106  CLOSED  "Reinitialize SV-106.")
   (C SV-113  CLOSED  "Reinitialize SV-113.")
   (C SV-104  CLOSED  "Reinitialize SV-104.")
   (C SV-103  CLOSED  "Reinitialize SV-103.")))

;;;    6.  Calibrate all derived admittances.

(defun .inseries (x y)
  (format2 (/ 1.0 (sqrt (+ (/ 1.0 (* x x)) (/ 1.0 (* y y)))))))

(defun .inparallel (x y)
  (format2 (+ x y)))

(defun .xferfcn (equation percent)                ;;;  equation of the form (y=__*x+__&r=__)
  (+ (* percent (CAR equation)) (CADR equation))) ;;;  percent ranges from 0. to 1.00

(defprocedure .derived
  :PRETTY-NAME "Calculating 5 derived admittances."
  :ACTIONS
  ((L (format2 '(Calibrating 5 derived admittances....)))
   (L (SETQ *.pump-circuit-admit* (.inseries *.pump-to-4-way-admit*
                                             (.inseries *.suction-line-admit* *.PX105-to-PX106-admit*))
            *.fast-fill-circuit-admit* *.ff-107-admit*  ;; only primary fast-fill valve is open usually
            *.skid-admit* (.inparallel *.fast-fill-circuit-admit* (.xferfcn *.replenish-circuit-admit* 0.3
3))
            *.upper-fill-circuit-admit* (.inseries *.skid-admit* *.final-fill-circuit-admit*)
            *.tank-fill-admit*          (.inseries *.upper-fill-circuit-admit* *.transfer-line-admit*)))))

;;; 7.  Print out all 14 admittances....

(defun .prtem ()
  (PROGn
    (format2 (LIST 'st-up-admit=              *.st-up-admit*))
```

```
    (format2 (LIST 'vt-up-admit=              *.vt-up-admit*))
    (format2 (LIST 'st-vent-admit=            *.st-vent-admit*))
    (format2 (LIST 'vt-vent-admit=            *.vt-vent-admit*))
    (format2 (LIST 'suction-line-admit=       *.suction-line-admit*))
    (format2 (LIST 'pump-to-4-way-admit=      *.pump-to-4-way-admit*))
    (format2 (LIST 'PX105-to-PX106-admit=     *.PX105-to-PX106-admit*))
    (format2 (LIST 'transfer-line-admit=      *.transfer-line-admit*))
    (format2 (LIST 'ff-107-admit=             *.ff-107-admit*))
    (format2 (LIST 'ff-108-admit=             *.ff-108-admit*))
    (format2 (LIST 'final-fill-circuit-admit= *.final-fill-circuit-admit*))
    (format2 (LIST 'replenish-circuit-admit=  *.replenish-circuit-admit*))
    (format2 (LIST 'nozzle-admit=             *.nozzle-admit*))
    (format2 (LIST 'bleed-admit=              *.bleed-admit*))
    (format2 (LIST 'recirculation-admit=      *.recirculation-admit*))
    (format2 (LIST 'pump-circuit-admit=       *.pump-circuit-admit*))
    (format2 (LIST 'fast-fill-circuit-admit=  *.fast-fill-circuit-admit*))
    (format2 (LIST 'skid-admit=               *.skid-admit*))
    (format2 (LIST 'upper-fill-circuit-admit= *.upper-fill-circuit-admit*))
    (format2 (LIST 'tank-fill-admit=          *.tank-fill-admit*))
    (format2 (LIST 'pump-xfr-fcn=             *.pump-xfer-fcn*))))

(defun .see-press ()
  (PROGn
    (format2 (LIST '*.a*= *.a1* *.a2* *.a3*))
    (format2 (LIST '*.b*= *.b1* *.b2* *.b3*))
    (format2 (LIST '*.c*= *.c1* *.c2* *.c3*))
    (format2 (LIST '*.d*= *.d1* *.d2* *.d3*))
    (format2 (LIST '*.e*= *.e1* *.e2* *.e3*))
    (format2 (LIST '*.f*= *.f1* *.f2* *.f3*))
    (format2 (LIST '*.g*= *.g1* *.g2* *.g3*))
    (format2 (LIST '*.h*= *.h1* *.h2* *.h3*))
    (format2 (LIST '*.i*= *.i1* *.i2* *.i3*))
    (format2 (LIST '*.j*= *.j1* *.j2* *.j3*))
    (format2 (LIST '*.k*= *.k1* *.k2* *.k3*))))

(defprocedure bob
              :actions
   ((L (setf aaaaa nil))
    (REPEAT 5
            (L (scl:beep))
            (WT 2)
            (L (setf aaaaa (cons 'ff aaaaa))))))

;;;  8.  Calibrate pump transfer function....

(defprocedure .pump-data
  :PRETTY-NAME "Calibrate pump transfer function."
  :ACTIONS
  ((L (format2 "Calibrating pump transfer function...."))
   (C SV-106  OPEN       "Open storage tank vent.")
   (C SV-113  OPEN       "Open vehicle tank vent.")
   (C SV-104  OPEN       "Open pump circuit.")
   (C SV-107  OPEN       "Open main skid valve.")
   (L (SETQ *.PX-105* nil *.pump-speed* 1800 *.PX-115* nil *.pmp-spd-list* nil))
   (C SV-111  OPEN       "Open final fill circuit.")
   (REPEAT 19
           (C RPM-101 *.pump-speed* "Ramp it up.")  ;; can't vary speed in a REPEAT yet.
           (WT 4)                                   ;; Steve Morgan, 15 July 1992
           (L (SETQ *.PX-105*       (CONS (GET-CURRENT-VALUE 'PX-105-M) *.PX-105*)
                    *.PX-115*       (CONS (GET-CURRENT-VALUE 'PX-115-M) *.PX-115*)
                    *.pmp-spd-list* (CONS *.pump-speed* *.pmp-spd-list*)
                    *.pump-speed*   (+ 100 *.pump-speed*)
                    *.dummy* 0)))
;  Add file access functions to save *.PX-115*, *.PX-115*, and *.pmp-spd-list* later.
   (C RPM-101 (0 rpm) "Stop pumping.")
   (C SV-106  CLOSED  "Close storage tank vent.")
   (C SV-113  CLOSED  "Close vehicle tank vent.")
   (C SV-104  CLOSED  "Shut down pump circuit.")
   (C SV-107  CLOSED  "Close main skid valve.")
   (C SV-111  CLOSED  "Close final fill circuit.")))

(defun .pump-analysis ()
;  Add file access functions to obtain *.PX-115*, *.PX-115*, and *.pmp-spd-list* later.
   (SETQ *.pump-xfer-fcn* (.regres *.pmp-spd-list* (.ad (/ 19 *.in-to-psi*) (mapcar #'- *.PX-105* *.PX-11
5*)))))
;    (test-fit (format2 *.pmp-spd-list*) (format2 (.ad (/ 19 *.in-to-psi*) (mapcar #'- *.PX-105* *.PX-115*
```

```
))))))) ;; see it

(defprocedure .done
  :PRETTY-NAME "All done, thanks."
  :ACTIONS
  ((L (.prtem))))

(defun .test-it-all ()
  (PROGn
    (test-fit '(1 2.5 3) '(2 3 4))
    (.test-press)
    (.test-depress)
    (.test-Fast-Flow)
    (.test-ff108)
    (.test-mcv101)
    (.test-nozzle)
    (.test-bleed)
    (.test-recirc)))

(defprocedure .do-it-all
  :actions
    ((proc .pressurize)
;     (L    (.see-press))
     (proc .depressurize)
;     (L    (.see-press))
     (proc .fastflow)
;     (L    (.see-press))
     (proc .ff108)
;     (L    (.see-press))
     (proc .mcv101)
;     (L    (.see-press))
     (proc .nozzle)
;     (L    (.see-press))
     (proc .bleed)
;     (L    (.see-press))
     (proc .recirc)
;     (L    (.see-press))
     (proc .derived)
;     (L    (.see-press))
     (proc .done)))

;;;  ************************************************************************************************************

;;;  *************************  S T E V E ' S  S T A T I S T I C S  L I B R A R Y  ****************

;;;  ************************************************************************************************************

;;;  Optionally change to log (base e) or log-log graph...
(defun .logem (x)
  (mapcar 'log x))

;;;  Regression line: y = a + b x, r = ___...
(defun .regres (x y)
  (format2 (list (.slope (length x) (.sum x) (.sum y) (.sumsqr x) (.sumxy x y))
                 (.y-intcpt (length x) (.sum x) (.sum y) (.slope (length x) (.sum x) (.sum y) (.sumsqr x)
 (.sumxy x y)))
                 (.correl (length x) (.sum x) (.sum y) (.sumsqr x) (.sumsqr y) (.sumxy x y))
                 '(Y=__*X+__&R=__))))

;;;  Slope, b = (n * sumxy - sumx * sumy) / (n * sumxsqr - sumx * sumx)...
(defun .slope (n sx sy sx2 sxy)
  (/ (- (* n sxy) (* sx sy))
     (- (* n sx2) (* sx sx))))

;;;  Y-intercept, a = (sumy - b * sumx) / n...
(defun .y-intcpt (n sx sy b)
  (/ (- sy (* b sx))
     n))

;;;  Correlation, r = (n * sumxy - sumx * sumy) / sqrt[(n  * sumxsqr - sumx * sumx) ( n * sumysqr - sumy
* sumy)]...
(defun .correl (n sx sy sx2 sy2 sxy)
  (/ (- (* n sxy) (* sx sy))
     (sqrt (* (- (* n sx2) (* sx sx))
              (- (* n sy2) (* sy sy)))))) /
```

```
;;;  Mean * n...
(defun .sum (x)
  (cond ((null x) 0.0)
        ((atom x) x)
        (t (apply '+ (mapcar '.sum x)))))

;;;  Variance * n...
(defun .sumsqr (x)
  (cond ((null x) 0.0)
        ((atom x) (* x x))
        (t (apply '+ (mapcar '.sumsqr x)))))

;;;  Covariance...
(defun .sumxy (x y)
  (cond ((null x) 0.0)
        ((atom x) (* x y))
        (t (apply '+ (mapcar '.sumxy x y)))))

;;;   True Mean...
(defun .mean (x)
  (/ (.sum x) (length x)))

;;;   Standard Deviation...
(defun .sd (x)
  (- (/ (sqrt (.sumsqr x)) (length x)) (.mean x)))

;;;   Print elementary statistics....
(defun .stat (x)
  (format2 (list (.mean x)
                 (.sd   x)
                 '(mean=__ & s.d.=__))))

;;;  Reference:  JE Freund & RE Walpole: Mathematical Statistics, 3rd Ed., P-H, 1972.
```

APPENDIX B

CALIBRATOR OUTPUT LISTING

```
(CALIBRATING ST- & VT-UP-ADMIT....)
(CALIBRATING ST- & VT-UP-ADMIT....)
(CALIBRATING ST- & VT-UP-ADMIT....)
(CALIBRATING ST- & VT-UP-ADMIT....)
(1.3197069 2.6098394 3.8703947)
(12.209784 11.929865)
(28.680294 27.39016 26.129604)
(2.2796974 -0.6677079 (MEAN=__ & S.D.=__))
(1.2394838 2.4679117 3.6852846)
(15.271193 15.133762)
(68.76051 67.53209 66.31471)
(1.8416097 -0.539395 (MEAN=__ & S.D.=__))
(1.3197069 2.6098394 3.8703947)
(12.209784 11.929865)
(28.680294 27.39016 26.129604)
(2.2796974 -0.6677079 (MEAN=__ & S.D.=__))
(1.2394838 2.4679117 3.6852846)
(15.271193 15.133762)
(68.76051 67.53209 66.31471)
(1.8416097 -0.539395 (MEAN=__ & S.D.=__))
(CALIBRATING ST- & VT-VENT-ADMIT....)
(CALIBRATING ST- & VT-VENT-ADMIT....)
(CALIBRATING ST- & VT-VENT-ADMIT....)
(CALIBRATING ST- & VT-VENT-ADMIT....)
(3.7532854 3.2441072 2.771594)
(4.81885 4.4718537)
(3.7532854 3.2441072 2.771594)
(2.4850721 -0.7278601 (MEAN=__ & S.D.=__))
(3.6191034 2.8400812 2.153575)
(9.684409 8.534298)
(3.6191034 2.8400812 2.153575)
(5.0773726 -1.4871159 (MEAN=__ & S.D.=__))
(3.7532854 3.2441072 2.771594)
(4.81885 4.4718537)
(3.7532854 3.2441072 2.771594)
(2.4850721 -0.7278601 (MEAN=__ & S.D.=__))
(3.6191034 2.8400812 2.153575)
(9.684409 8.534298)
(3.6191034 2.8400812 2.153575)
(5.0773726 -1.4871159 (MEAN=__ & S.D.=__))
(CALIBRATING 6 FAST-FILL PATH ADMITS....)
(CALIBRATING 6 FAST-FILL PATH ADMITS....)
(CALIBRATING 6 FAST-FILL PATH ADMITS....)
(CALIBRATING 6 FAST-FILL PATH ADMITS....)
(13.699469 16.86502 19.976784)
(0.91344094 1.2903118 1.8511173)
(14.62123 -6.178755 (MEAN=__ & S.D.=__))
(13.699469 16.86502 19.976784)
(23.071518 33.07944 44.906635)
(2.9218197 -1.2346271 (MEAN=__ & S.D.=__))
(13.699469 16.86502 19.976784)
(5.7749076 8.752077 12.279726)
(5.7007403 -2.4094164 (MEAN=__ & S.D.=__))
(6.6288023 8.447623 10.216957)
(7.8893814 12.8127365 18.742004)
(2.3600085 -0.9974568 (MEAN=__ & S.D.=__))
(6.6288023 8.447623 10.216957)
(1.1949272 1.9406204 2.8330002)
(6.066092 -2.5638316 (MEAN=__ & S.D.=__))
(6.6288023 8.447623 10.216957)
(0.88412863 1.4795318 2.1698658)
(6.976916 -2.9486809 (MEAN=__ & S.D.=__))
(13.699469 16.86502 19.976784)
(0.91344094 1.2903118 1.8511173)
(14.62123 -6.178755 (MEAN=__ & S.D.=__))
(13.699469 16.86502 19.976784)
(23.071518 33.07944 44.906635)
(2.9218197 -1.2346271 (MEAN=__ & S.D.=__))
(13.699469 16.86502 19.976784)
(5.7749076 8.752077 12.279726)
(5.7007403 -2.4094164 (MEAN=__ & S.D.=__))
(6.6288023 8.447623 10.216957)
(7.8893814 12.8127365 18.742004)
(2.3600085 -0.9974568 (MEAN=__ & S.D.=__))
(6.6288023 8.447623 10.216957)
(1.1949272 1.9406204 2.8330002)
```

tank pressure
flow
dP

ditto
:

flow
dP

ditto
:

```
(6.066092 -2.5638316 (MEAN=__ & S.D.=__))
(6.6288023 8.447623 10.216957)
(0.88412863 1.4795318 2.1698658)
(6.976916 -2.9486809 (MEAN=__ & S.D.=__))
(CALIBRATING SV-108 'S ADMITTANCE....)
(CALIBRATING SV-108 'S ADMITTANCE....)
(CALIBRATING SV-108 'S ADMITTANCE....)
(CALIBRATING SV-108 'S ADMITTANCE....)
(10.22679 8.358611 6.4019327)
(2.5856705 1.735714 1.0150461)
(6.3529034 -2.685051 (MEAN=__ & S.D.=__))
(10.22679 8.358611 6.4019327)
(2.5856705 1.735714 1.0150461)
(6.3529034 -2.685051 (MEAN=__ & S.D.=__))
(CALIBRATING MCV-101 'S ADMITTANCE TRANSFER FUNCTION....)
(CALIBRATING MCV-101 'S ADMITTANCE TRANSFER FUNCTION....)
(CALIBRATING MCV-101 'S ADMITTANCE TRANSFER FUNCTION....)
(CALIBRATING MCV-101 'S ADMITTANCE TRANSFER FUNCTION....)
(0.37875423 0.7495712 1.1039773)
(7.905173 7.5464616 7.149731)
(0.027816162 -0.7000845 0.99999374 (Y=__*X+__&R=__))
(0.37875423 0.7495712 1.1039773)
(7.905173 7.5464616 7.149731)
(0.027816162 -0.7000845 0.99999374 (Y=__*X+__&R=__))
(0.37875423 0.7495712 1.1039773)
(7.905173 7.5464616 7.149731)
(0.027816162 -0.7000845 0.99999374 (Y=__*X+__&R=__))
(0.37875423 0.7495712 1.1039773)
(7.905173 7.5464616 7.149731)
(0.027816162 -0.7000845 0.99999374 (Y=__*X+__&R=__))
(CALIBRATING NOZZLE ADMITTANCE....)
(CALIBRATING NOZZLE ADMITTANCE....)
(CALIBRATING NOZZLE ADMITTANCE....)
(CALIBRATING NOZZLE ADMITTANCE....)
(7.8357015 5.238446 3.0496871)
(-0.0586195 0.065597534 0.042866707)
(0.5412985 0.5452448 0.52057886)
(0.02285788 0.021576738 (MEAN=__ & S.D.=__))
(7.8357015 5.238446 3.0496871)
(-0.0586195 0.065597534 0.042866707)
(0.5412985 0.5452448 0.52057886)
(0.02285788 0.021576738 (MEAN=__ & S.D.=__))
(CALIBRATING BLEED ADMITTANCE....)
(CALIBRATING BLEED ADMITTANCE....)
(CALIBRATING BLEED ADMITTANCE....)
(CALIBRATING BLEED ADMITTANCE....)
(7.8169947 5.2061214 3.0175722)
(0.055433273 0.071427345 0.036339283)
(0.62161875 0.6242012 0.59833926)
(0.0692315 -0.027968463 (MEAN=__ & S.D.=__))
(7.8169947 5.2061214 3.0175722)
(0.055433273 0.071427345 0.036339283)
(0.62161875 0.6242012 0.59833926)
(0.0692315 -0.027968463 (MEAN=__ & S.D.=__))
(CALIBRATING RECIRCULATION PATH ADMITTANCE....)
(CALIBRATING RECIRCULATION PATH ADMITTANCE....)
(CALIBRATING RECIRCULATION PATH ADMITTANCE....)
(CALIBRATING RECIRCULATION PATH ADMITTANCE....)
(30.0 30.0 28.974215)
(20.539597 20.539597 20.185389)
(15.253061 11.207141 7.769389)
(6.2120996 -2.5950906 (MEAN=__ & S.D.=__))
(30.0 30.0 28.974215)
(20.539597 20.539597 20.185389)
(15.253061 11.207141 7.769389)
(6.2120996 -2.5950906 (MEAN=__ & S.D.=__))
(4.361521 6.2761393 8.543359)
(7.8315954 9.394584 10.960884)
(21.331217 30.704245 41.794704)
(1.695516 -0.71660936 (MEAN=__ & S.D.=__))
(4.361521 6.2761393 8.543359)
(7.8315954 9.394584 10.960884)
(21.331217 30.704245 41.794704)
(1.695516 -0.71660936 (MEAN=__ & S.D.=__))
(4.5165834 1.6955161 1.0 (Y=__*X+__&R=__))
(4.5165834 1.6955161 1.0 (Y=__*X+__&R=__))
```

```
(4.5165834 1.6955161 1.0 (Y=__*X+__&R=__))
(4.5165834 1.6955161 1.0 (Y=__*X+__&R=__))
(CALIBRATING 5 DERIVED ADMITTANCES....)
(CALIBRATING 5 DERIVED ADMITTANCES....)
(CALIBRATING 5 DERIVED ADMITTANCES....)
(CALIBRATING 5 DERIVED ADMITTANCES....)
5.31131
2.5600228
5.375187
4.2580447
2.0641644
5.31131
2.5600228
5.375187
4.2580447
2.0641644
(ST-UP-ADMIT= 2.2796974)
(VT-UP-ADMIT= 1.8416097)
(ST-VENT-ADMIT= 2.4850721)
(VT-VENT-ADMIT= 5.0773726)
(SUCTION-LINE-ADMIT= 14.62123)
(PUMP-TO-4-WAY-ADMIT= 2.9218197)
(PX105-TO-PX106-ADMIT= 5.7007403)
(TRANSFER-LINE-ADMIT= 2.3600085)
(FF-107-ADMIT= 6.066092)
(FF-108-ADMIT= 6.3529034)
(FINAL-FILL-CIRCUIT-ADMIT= 6.976916)
(REPLENISH-CIRCUIT-ADMIT= (0.027816162 -0.7000845 0.99999374 (Y=__*X+__&R=__)))
(NOZZLE-ADMIT= 0.02285788)
(BLEED-ADMIT= 0.0692315)
(RECIRCULATION-ADMIT= (4.5165834 1.6955161 1.0 (Y=__*X+__&R=__)))
(PUMP-CIRCUIT-ADMIT= 2.5600228)
(FAST-FILL-CIRCUIT-ADMIT= 6.066092)
(SKID-ADMIT= 5.375187)
(UPPER-FILL-CIRCUIT-ADMIT= 4.2580447)
(TANK-FILL-ADMIT= 2.0641644)
(PUMP-XFR-FCN= NIL)        not implemented
(ST-UP-ADMIT= 2.2796974)
(VT-UP-ADMIT= 1.8416097)
(ST-VENT-ADMIT= 2.4850721)
(VT-VENT-ADMIT= 5.0773726)
(SUCTION-LINE-ADMIT= 14.62123)
(PUMP-TO-4-WAY-ADMIT= 2.9218197)
(PX105-TO-PX106-ADMIT= 5.7007403)
(TRANSFER-LINE-ADMIT= 2.3600085)
(FF-107-ADMIT= 6.066092)
(FF-108-ADMIT= 6.3529034)
(FINAL-FILL-CIRCUIT-ADMIT= 6.976916)
(REPLENISH-CIRCUIT-ADMIT= (0.027816162 -0.7000845 0.99999374 (Y=__*X+__&R=__)))
(NOZZLE-ADMIT= 0.02285788)
(BLEED-ADMIT= 0.0692315)
(RECIRCULATION-ADMIT= (4.5165834 1.6955161 1.0 (Y=__*X+__&R=__)))
(PUMP-CIRCUIT-ADMIT= 2.5600228)
(FAST-FILL-CIRCUIT-ADMIT= 6.066092)
(SKID-ADMIT= 5.375187)
(UPPER-FILL-CIRCUIT-ADMIT= 4.2580447)
(TANK-FILL-ADMIT= 2.0641644)
(PUMP-XFR-FCN= NIL)
(ST-UP-ADMIT= 2.2796974)
(VT-UP-ADMIT= 1.8416097)
(ST-VENT-ADMIT= 2.4850721)
(VT-VENT-ADMIT= 5.0773726)
(SUCTION-LINE-ADMIT= 14.62123)
(PUMP-TO-4-WAY-ADMIT= 2.9218197)
(PX105-TO-PX106-ADMIT= 5.7007403)
(TRANSFER-LINE-ADMIT= 2.3600085)
(FF-107-ADMIT= 6.066092)
(FF-108-ADMIT= 6.3529034)
(FINAL-FILL-CIRCUIT-ADMIT= 6.976916)
(REPLENISH-CIRCUIT-ADMIT= (0.027816162 -0.7000845 0.99999374 (Y=__*X+__&R=__)))
(NOZZLE-ADMIT= 0.02285788)
(BLEED-ADMIT= 0.0692315)
(RECIRCULATION-ADMIT= (4.5165834 1.6955161 1.0 (Y=__*X+__&R=__)))
(PUMP-CIRCUIT-ADMIT= 2.5600228)
(FAST-FILL-CIRCUIT-ADMIT= 6.066092)
(SKID-ADMIT= 5.375187)
```

```
(UPPER-FILL-CIRCUIT-ADMIT= 4.2580447)
(TANK-FILL-ADMIT= 2.0641644)
(PUMP-XFR-FCN= NIL)
(ST-UP-ADMIT= 2.2796974)
(VT-UP-ADMIT= 1.8416097)
(ST-VENT-ADMIT= 2.4850721)
(VT-VENT-ADMIT= 5.0773726)
(SUCTION-LINE-ADMIT= 14.62123)
(PUMP-TO-4-WAY-ADMIT= 2.9218197)
(PX105-TO-PX106-ADMIT= 5.7007403)
(TRANSFER-LINE-ADMIT= 2.3600085)
(FF-107-ADMIT= 6.066092)
(FF-108-ADMIT= 6.3529034)
(FINAL-FILL-CIRCUIT-ADMIT= 6.976916)
(REPLENISH-CIRCUIT-ADMIT= (0.027816162 -0.7000845 0.99999374 (Y=__*X+__&R=__)))
(NOZZLE-ADMIT= 0.02285788)
(BLEED-ADMIT= 0.0692315)
(RECIRCULATION-ADMIT= (4.5165834 1.6955161 1.0 (Y=__*X+__&R=__)))
(PUMP-CIRCUIT-ADMIT= 2.5600228)
(FAST-FILL-CIRCUIT-ADMIT= 6.066092)
(SKID-ADMIT= 5.375187)
(UPPER-FILL-CIRCUIT-ADMIT= 4.2580447)
(TANK-FILL-ADMIT= 2.0641644)
(PUMP-XFR-FCN= NIL)
```

REFERENCES

[1] Steve Morgan: *KATE's Model Verification Tools.* University of Central Florida's 1992 NASA/ASEE Summer Faculty Fellowship Program, Contractor Report No. NASA-NGT-60002, Supplement 6, August 9, 1992.

[2] John K. Vennard: *Elementary Fluid Mechanics.* 4th Ed., New York, Wiley, 1963, p.280.

[3] Bob Merchant: "The initial phase of the admittance calculator." In G:>KATE>DOC>ALO>ADMITTANCE-CALCULATOR.LISP.9, April 5, 1992.

[4] Bob Merchant's ALO Knowledge Base File G:>KATE>ALO-KB>FLUIDS-PRESSURES.LISP.18, March 4, 1992.

[5] Bob Merchant's ALO Knowledge Base File G:>KATE>ALO-KB>ADMITTANCES .LISP.23, June 4, 1992.

[6] Bob Merchant's ALO Knowledge Base File G:>KATE>ALO-KB>FLOW-RATES-PRESSURES.LISP.15, January 20, 1992.

[7] JE Freund & RE Walpole: "Mathematical Statistics," 3rd Ed., Prentice-Hall, 1972.

[8] Bob Merchant's ALO Control Procedures File: G:>KATE>ALO-KB>CONTROL-PROCEDURES .LISP.41, March 6, 1992.

[9] Steve Morgan's Automatic Admittance Calibrator Program Listing: G:>MORGAN>LAST.LISP.7, August 6, 1992.

[10] Steve Morgan's Calibrator Output Listing: G:>MORGAN>ANSWERS.LISP.6, August 6, 1992.

[11] Bob Merchant's ALO Knowledge Base File G:>KATE>ALO-KB>ALO-H2O.LISP.37, May 8, 1992.

[12] Bob Merchant: "ALO Admittance Plots And Calculations Notebook," 63pp., January 1, 1992.

[13] Steve Beltz' Personal Communication on "Sensor Tolerances." July 15, 1992.

1992 NASA/ASEE SUMMER FACULTY FELLOWSHIP PROGRAM

JOHN F. KENNEDY SPACE CENTER
UNIVERSITY OF CENTRAL FLORIDA

MATERIAL SELECTION AND EVALUATION OF NEW ENCAPSULATION COMPOUNDS FOR ELECTRIC CABLES FOR LAUNCH SUPPORT SYSTEM

PREPARED BY:	Dr. Asit K. Ray
ACADEMIC RANK:	Associate Professor
UNIVERSITY AND DEPARTMENT:	Christian Brothers University Department of Chemical Engineering
NASA/KSC	
DIVISION:	Materials Science Laboratory
BRANCH:	Failure Analysis and Materials Evaluation
NASA COLLEAGUE:	Coleman Bryan
DATE:	August 7, 1992
CONTRACT NUMBER:	University of Central Florida NASA-NGT-60002 Supplement: 8

ACKNOWLEDGEMENT

I am grateful to the NASA/ASEE Summer Faculty Program, Dr. Loren A. Anderson of the University of Central Florida, and Ms. Carol Valdes of the John F. Kennedy Space Center (KSC) for providing me the opportunity of spending an enjoyable, productive, and rewarding summer. Many thanks to Dr. Anderson for his kind and efficient overseeing of the Fellows and to Ms. Kari Stiles for her administrative help. Thanks are due to Mr. Charles Hoppesch and Mr. Irby Moore of the Materials Science Laboratory for their help and cooperation.

Special thanks are extended to my KSC colleague, Mr. Coleman Bryan, for suggesting the projects and for his guidance and encouragement in all phases of these projects. Thanks are also due to all of the professionals working in the Failure Analysis and Materials Evaluation Branch who made me feel welcome and for the help and pleasant interactions while working in the different laboratories.

Finally, special thanks are due to Robert Frankfort for conducting the flammability test and coordinating the hypergolic compatibility test and to Steve Sojourner of Boeing Aerospace Operations for providing technical data and making the samples for the hydrolytic stability and flammability tests.

ABSTRACT

Eight urethane compounds were evaluated as possible replacement for the existing encapsulating compounds for electrical cables for the Launch Support System at Kennedy Space Center (KSC). The existing encapsulating compound, PR-1535, contains the curative MOCA 4-4'-Methylene-BIS (2-chloroaniline), which is a suspect carcinogen and hence may be the subject of further restrictions of its use by the Occupational Safety and Health Administration (OSHA). The samples made in the configuration of cable joints and in the form of disks were evaluated for flammability and hypergolic compatibility. These also underwent accelerated weatherability tests that measured the residual hardness of the exposed samples. Three candidates and the existing compound passed the hardness test. Of these, only one candidate and the existing compound passed the flammability test. The thermal and hydrolytic stability (weatherability) of these samples was studied using thermogravimetric analysis (TGA), thermomechanical analysis (TMA), and differential scanning calorimetric (DSC) techniques. The TMA and DSC data correlated with the residual hardness data; whereas, the TGA data showed no correlation.

A hypergolic compatibility test will be conducted on the compound V-356-HE80, which passed both the flammability and accelerated weatherability tests.

TABLE OF CONTENTS

LIST OF ILLUSTRATIONS

1.0 INTRODUCTION

1.1 Background Information

The connectors used in the Launch Support electrical cables are encapsulated with a polyurethane potting compound to ensure protection against tropical temperature and humidity. One component of the current encapsulation compound PR-1535, made by Product Research and Chemical, Inc., contains the curative MOCA [4-4'-Methylene-BIS (2-chloroaniline)], which is a suspect carcinogen and may be subject to OSHA restrictions of its use (1). A direct substitute of this material would be very desirable if not necessary.

1.2 Overall Scope of the Project [Boeing Aerospace Operations (BAO) and KSC]

The following procedures are used for Qualification Test Requirements for encapsulation compounds for electrical cables for Launch Support.

a. Boeing Aerospace Operations encapsulated electrical cable components using the appropriate molding process for each compound (seven candidates and the current material).

b. Boeing Aerospace Operations evaluated electrical properties and processibility (molding).

c. The Materials Science Laboratory (MSL) evaluated chemical and physical properties.

d. KSC will generate an Approved Product List (APL) for electrical cable insulating compounds and revise molding procedures due to change of potting materials.

1.3 Scope of This Project (Materials Science Laboratory)

The scope includes the evaluation of the thermal and hypergolic stability, weatherability, and flammability of the seven candidates and current electrical cable insulating compounds.

2.0 MATERIALS AND METHODS

2.1 Encapsulating Chemical Compounds

Eight chemical compounds were chosen from the Qualified Products List of products qualified under Military Specification QPL.24041-16 and the current encapsulating compound:

a. PR-1535: A polyether polyol polymer with totuene diisocyanate (TDI) with MOCA is used as a curing agent.

b. PR-1574: Same as PR-1535, except 2-hydroxypropyl aniline is used as a curing agent.

c. PR-1592: Same as PR-1535, except an aromatic diamine is used as a curing agent.

d. PR-1590: Same as PR-1535, with slight modification of the chemical composition of the curative.

e. PS-799: Same as PR-1535, except with polyamine used as a curing agent.

Note: All the above compounds are manufactured by Product Research and Chemical Corporation.

f. Conathan EN-9 (CONAP Inc.): Poly (oxy-1,4-butane diyl)-hydro-hydroxy trimethylol pentane with TDI and (methyl thio) toluene diamine used as a curing agent.

g. Conathan EN-1556 (CONAP Inc.): Ethohexadiol with TDI and 2-propanol-1, 1' phenyl aminobis diamine used as a curing agent.

h. V-356-HE80 (BP Chemicals): Polytetramethylene glycols with isophorone diisocyanate and a polyol curative (non-TDI, non-MOCA polyurethane) used as a curing agent.

The preparation of urethane polymers is a two-step reaction. The first step is the formation of prepolymer by the reaction of a diol and diisocyanate. The second step is the chain extension by reacting with a curing agent, which is typically an amine.

2.2 Encapsulation of Electrical Cable Joints (Boeing)

The electrical cable components were encapsulated in special molds by applying the potting polyurethane compounds using an air pressurized injection gun fitted with a cartridge and allowing the encapsulated parts to cure according to specifications provided by the manufacturers and procedures used by Boeing at KSC (MIL-M-24041, KSC-SPEC-E-0029, and KSC-STD-132).

These components yielded as-used configuration samples. Special samples in the form of disks were made using special molds that were used for the evaluation of accelerated weatherability.

2.3 Thermal and Hydrolytic Stability (Weatherability)

The high temperature-humidity conditioning was done inside a desiccator containing a saturated solution of potassium sulfate in a forced convection oven with the precision of ±0.5 degree Centigrade (°C). The conditioning of 28 days at 100 °C and 95 percent relative humidity (RH) is intended to simulate about ten years of service at 35 °C and 95 percent RH (2). This is a reasonable simulation used for many of the military applications.

The samples, in the form of disks (2.8 millimeters in diameter and 1 millimeter in thickness), were taken out of the desiccator/oven every seventh day, air cooled, cleaned with tap water and deionized water, and subjected to hardness measurements. The samples were cut, removed for thermal analyses, and then put back in the desiccator/oven.

2.4 Hardness Measurement

The hardnesses of the samples were measured using Shore Durometer (Type A). The data reported are averages of three samples, five measurements per sample.

2.5 Flammability Test

The flammability test was done using the Upward Flame Propagation Test (NASA Handbook 8060.1C, Test 1), which is a slight modification of ASTM D568 with the requirement that the specimen be "self-extinguishing." The samples in user-configuration form (cable joints) were held at 45 degrees to the flame and supported by a needle rather than a clamp to reduce heatsink size. In order to pass,

the sample had to survive a direct current (dc) of 55 amperes through 16 American wire gauge (AWG) (MIL-W-5086, polyvinyl chloride insulated) for a period of 30 seconds versus 2.5 minutes for ASTM D568, without ignition and charring.

2.6 Hypergolic Compatibility Test

The hypergolic compatibility tests on the samples were conducted by Wiltech Corporation (a KSC contractor) that followed the procedures described in KSC Report 91-5331. This test is conducted by placing 0.5 millimeter (ml) of the appropriate fluid [hydrazine (N_2H_4), monomethylhydrazine (MMH), and nitrogen tetroxide (N_2O_4)] on the top of the sample and monitoring the temperature for 10 minutes. A temperature increase of 2.8 °C constitutes failure.

2.7 Thermal Analysis

Dynamically programmed thermogravimetric analyses of the samples were carried out using a Dupont TGA 951 module, controller, and Dupont 2100 Thermal Analyst data analyzer in a nitrogen atmosphere. The Thermal Analyst 2100 controlled and tracked the progress of the experiment, collected data, and printed or plotted the results of the experiments.

A Dupont Thermomechanical Analyzer 943 was used to study the depth of penetration of a probe on the surface of the samples as a function of temperature. A weight of 10 grams (g) was used on the weighing pan attached to the end of the probe. TMA analyses were carried out using Dupont TMA module, controller, and Thermal Analyst 2100.

Differential Scanning Calorimetric analyses were carried out with a Dupont DSC 2910 module, controller, and Thermal Analyst 2100. A nitrogen purge flow rate of 50 milliliters per minute was used. Samples for the DSC runs were cooled to near 0 °C using a special cooling accessory with crushed ice as the coolant.

A heating rate of 10 °C per minute was used in all the TGA, TMA, and DSC runs.

3.0 RESULTS AND DISCUSSIONS

3.1 Hydrolytic and Flammability Studies

The results of the hydrolytic stability and flammability tests are summarized in table 1. Of the eight candidates and the existing encapsulation compounds, only the existing encapsulation compounds and one of the candidate compounds (V-356HE80) passed the flammability test.

Figure 1 represents the results of weatherability in the form of residual hardness versus time of exposure for the eight compounds. The compounds EN-9 and PR-1574 exhibited very little loss of hardness with exposure in 100 °C, 95 percent RH for a period of four weeks. The compound PR-1535 (current product) showed appreciable loss of hardness with exposure time and barely passed the minimum Shore A hardness of 40 requirement. The compounds PS-799 and EN-1556 exhibited a drastic decrease in hardness with values approaching zero after three weeks of exposure. The compound V-356-HE80 demonstrated good hydrolytic stability with little loss of hardness after the first week of exposure. This agrees with the vendor data (figure 2) which shows loss of hardness for the first week but very little loss of hardness at exposure time beyond that. The starting hardness of this compound could not be determined properly, probably because the curing process had not been completed at the time of hardness measurements. The hardness of ~50 is much lower than the hardness value of 80 specified by the vendor. Improper formulation and/or molding could be the cause of this low hardness. Previous hydrolytic stability tests conducted on this material started with the Shore A hardness of 82 and had final Shore A hardness of 64.

The sample PR-1590 did not survive one week of exposure as the hardness reduced to zero at that point.

3.2 Thermal Analysis

3.2.1 Thermogravimetric Analysis

Thermal and hydrolytic degradation (accelerated weatherability) of samples would be expected to lead to scission of the polymer chains, decreased crosslinked density, and molecular weight changes affecting mechanical and thermal

Table 1. Hydrolytic Stability and Flammability of Polyurethane Compounds

Sample	Flammability	Shore Durometer, Type A				
		Week 0 (Zero)	Week 1	Week 2	Week 3	Week 4
PR-1535	Passed	85	70	58	44	38
V-356-HE80	Passed	--	49	48	44	44
PR-1574	Failed	92	90	84	80	83
PR-1592	Failed	92	70	53	33	23
EN-9	Failed	93	89	83	82	82
PS-799	Failed	84	57	26	0	--
EN-1556	Failed	82	39	19	0	--
PR-1590	Failed	66	0	--	--	--

properties. TGA measures weight loss as a function of temperature.

Figures 3, 4, 5, and 6 show the TGA data of the current compound, PR-1535, and the candidate, V-356-HE80, the two compounds which successfully passed the flammability and the hydrolytic stability tests. The weight loss started about 300 °C for the zero, one, two, three, and four weeks of exposed samples of PR-1535 (figure 4). These temperatures did not correlate to the trend in the hardness versus exposed time data; that is, the incipient temperature of weight loss should decrease with a decrease in hardness due to polymer degradation. Since the TGA monitors only volatilization and weight loss, this does not exclude the possibility that other thermal degradation reactions not producing volatile products,are involved in the failure process.

C-5

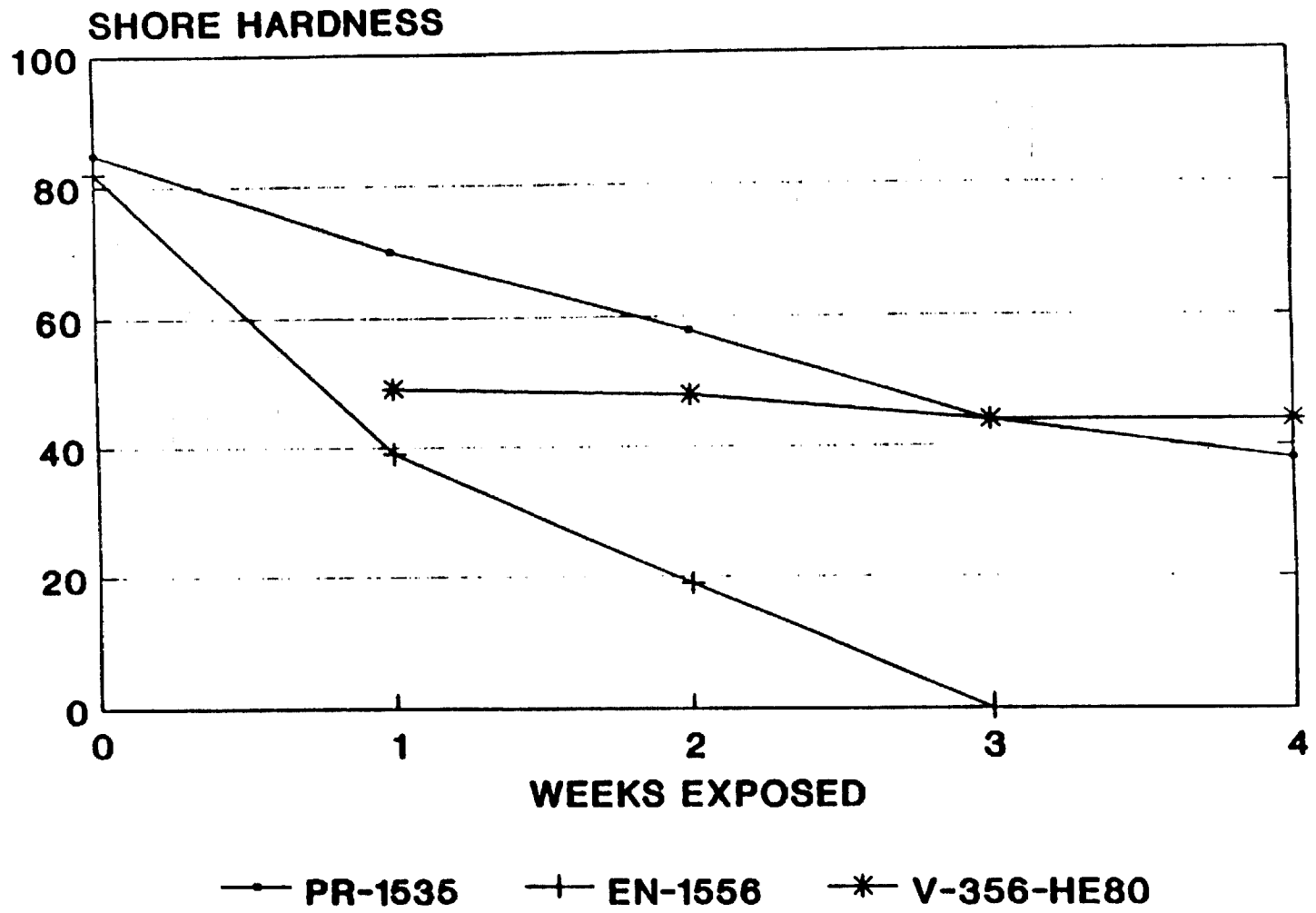

Figure 1. Residual Hardness of Polyurethane Samples (Sheet 1 of 2)

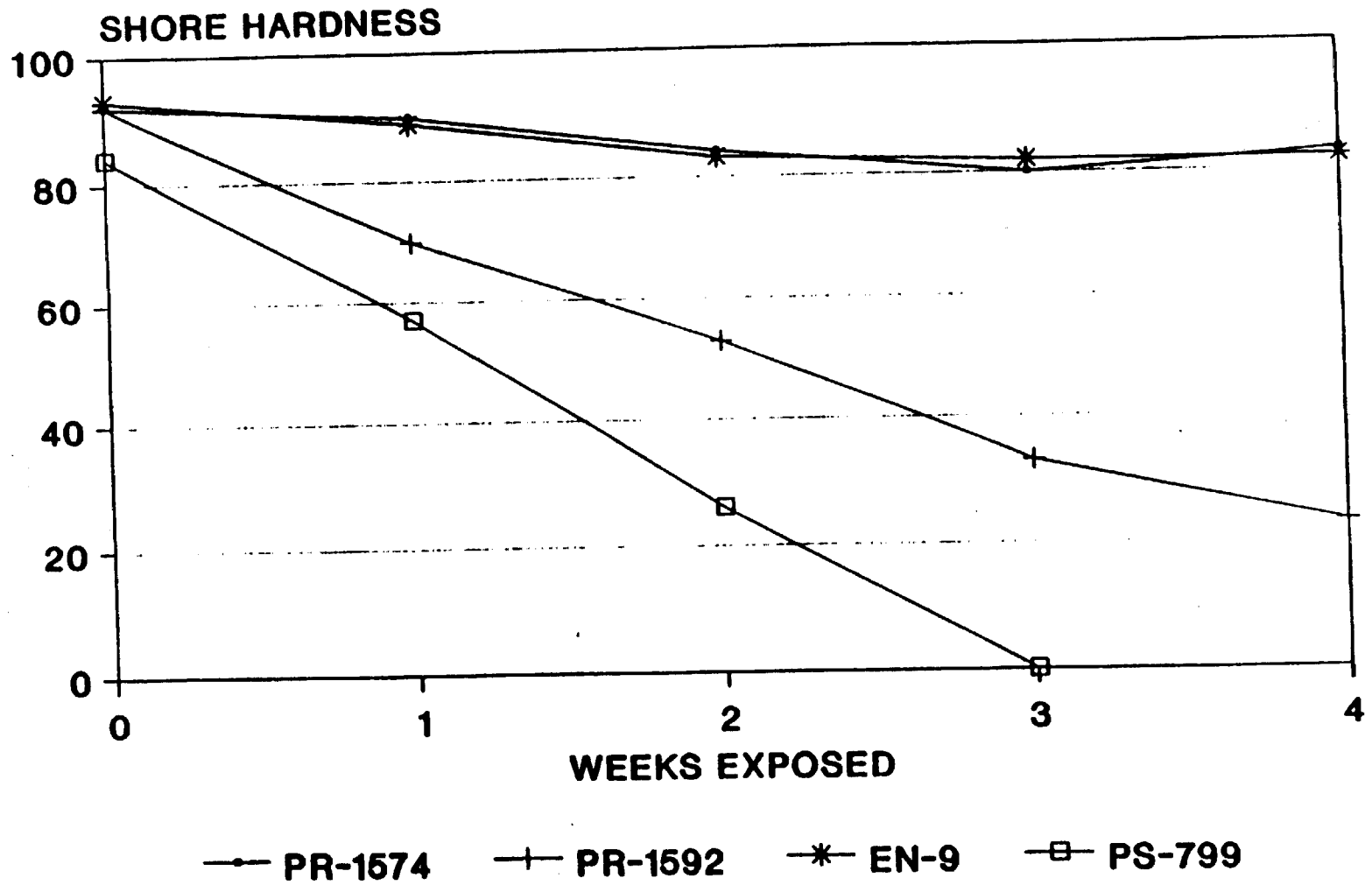

Figure 1. Residual Hardness of Polyurethane Samples (Sheet 2 of 2)

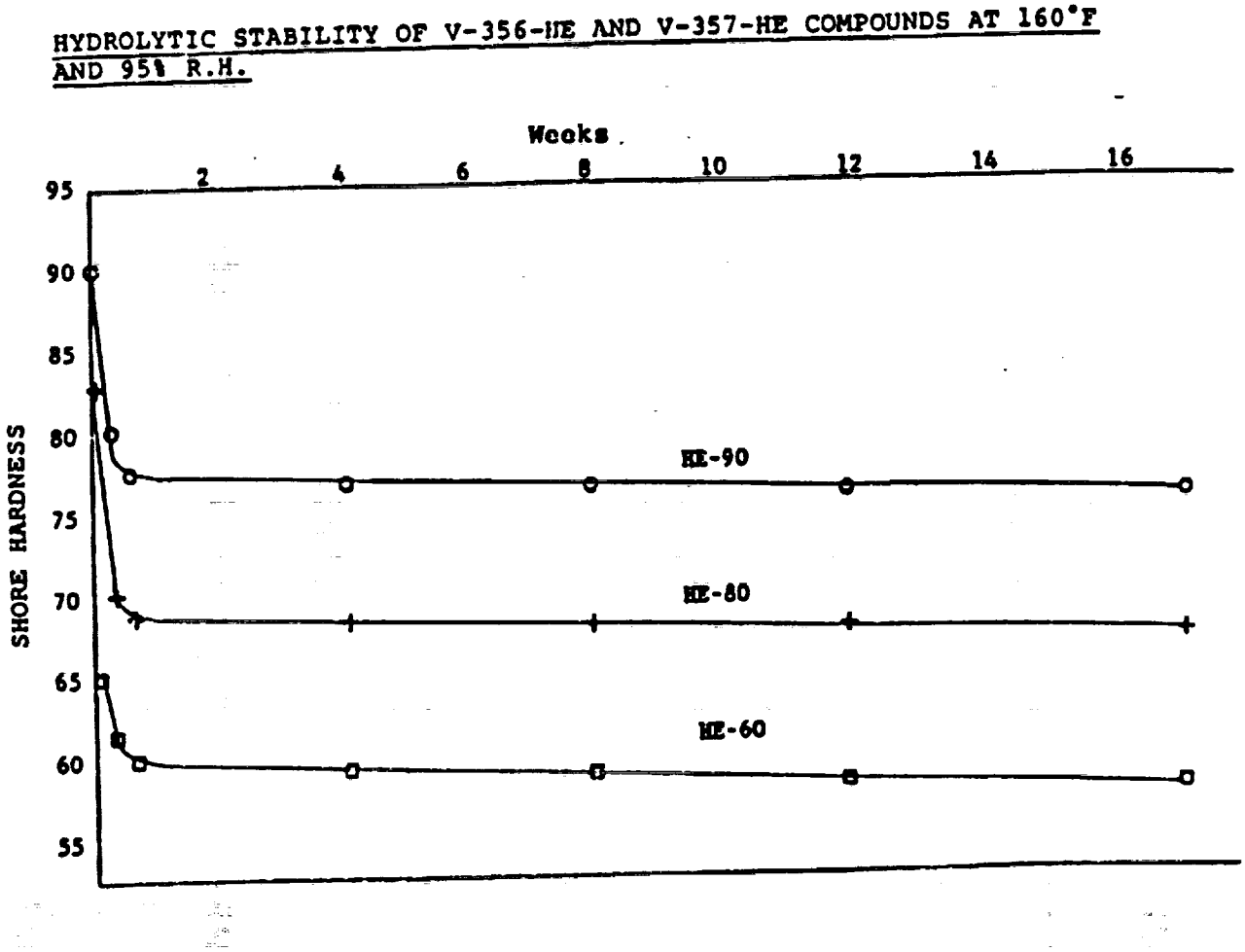

Figure 2. Residual Hardness of Polyurethane V-356-HE80 (Vendor Data)

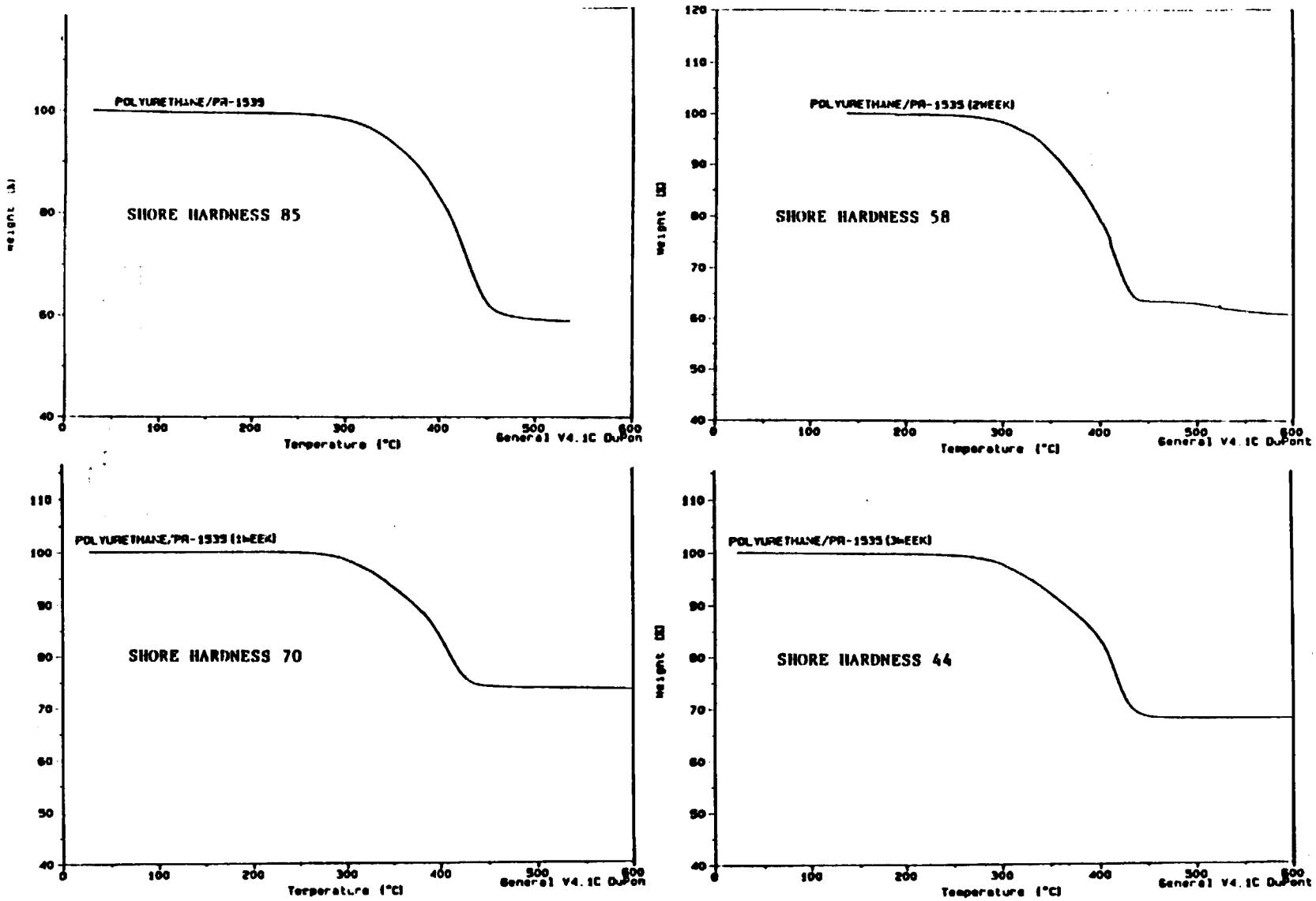

Figure 3. Thermogravimetric Curves of Polyurethane PR-1535

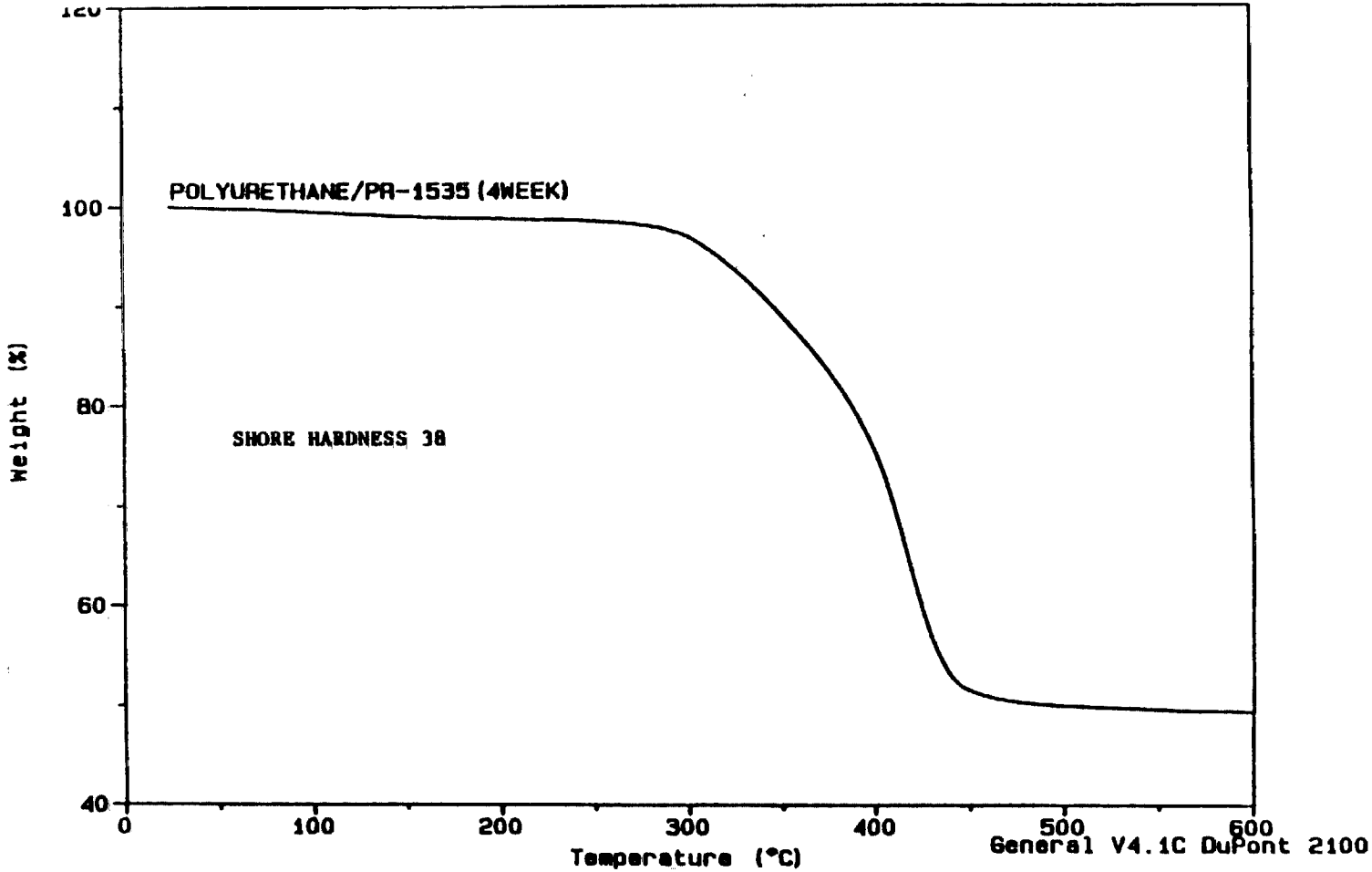

Figure 4. Thermogravimetric Curve For Polyurethane PR-1535 (Week 4)

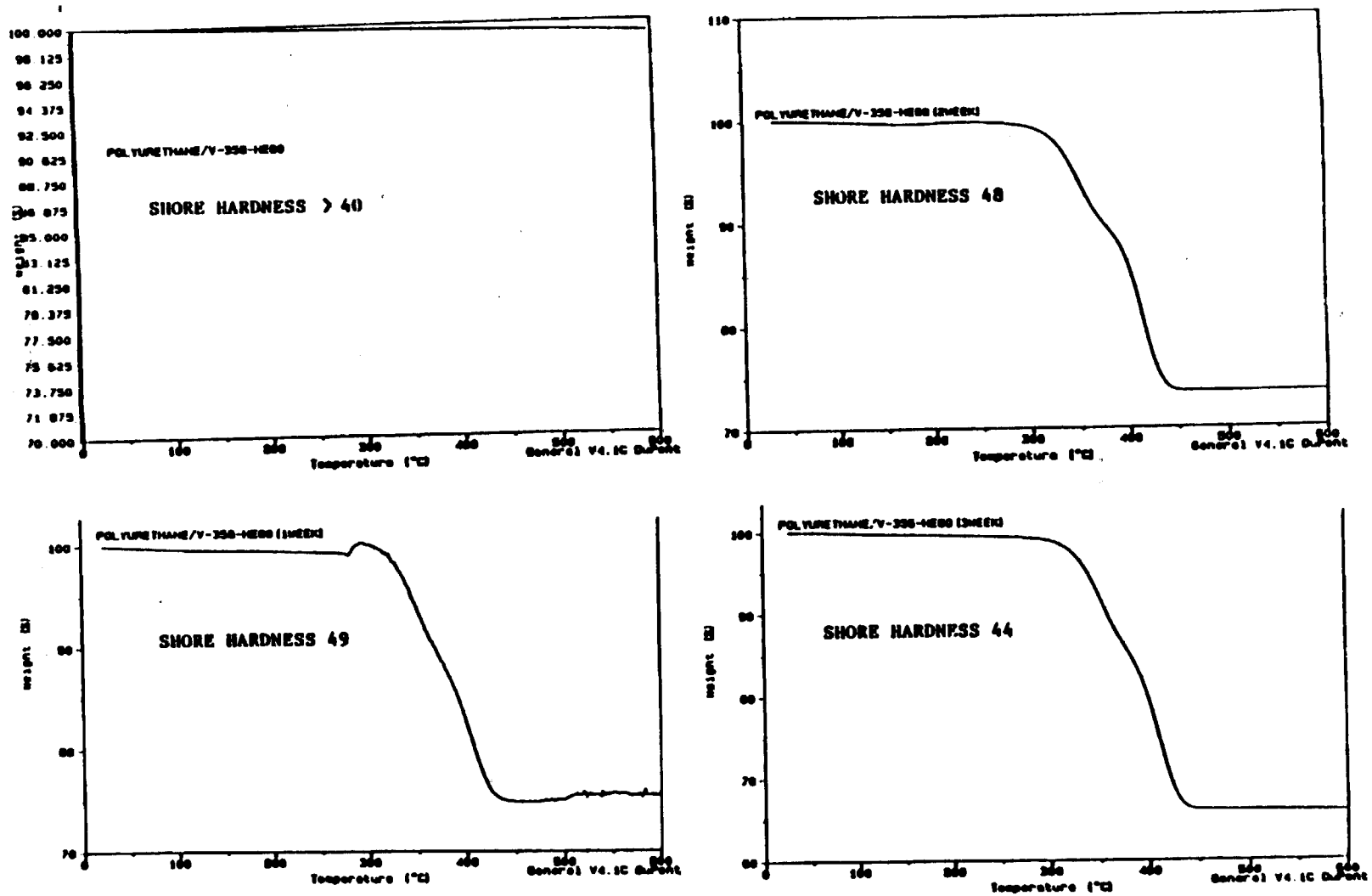

Figure 5. Thermogravimetric Curves of Polyurethane V-356-HE80

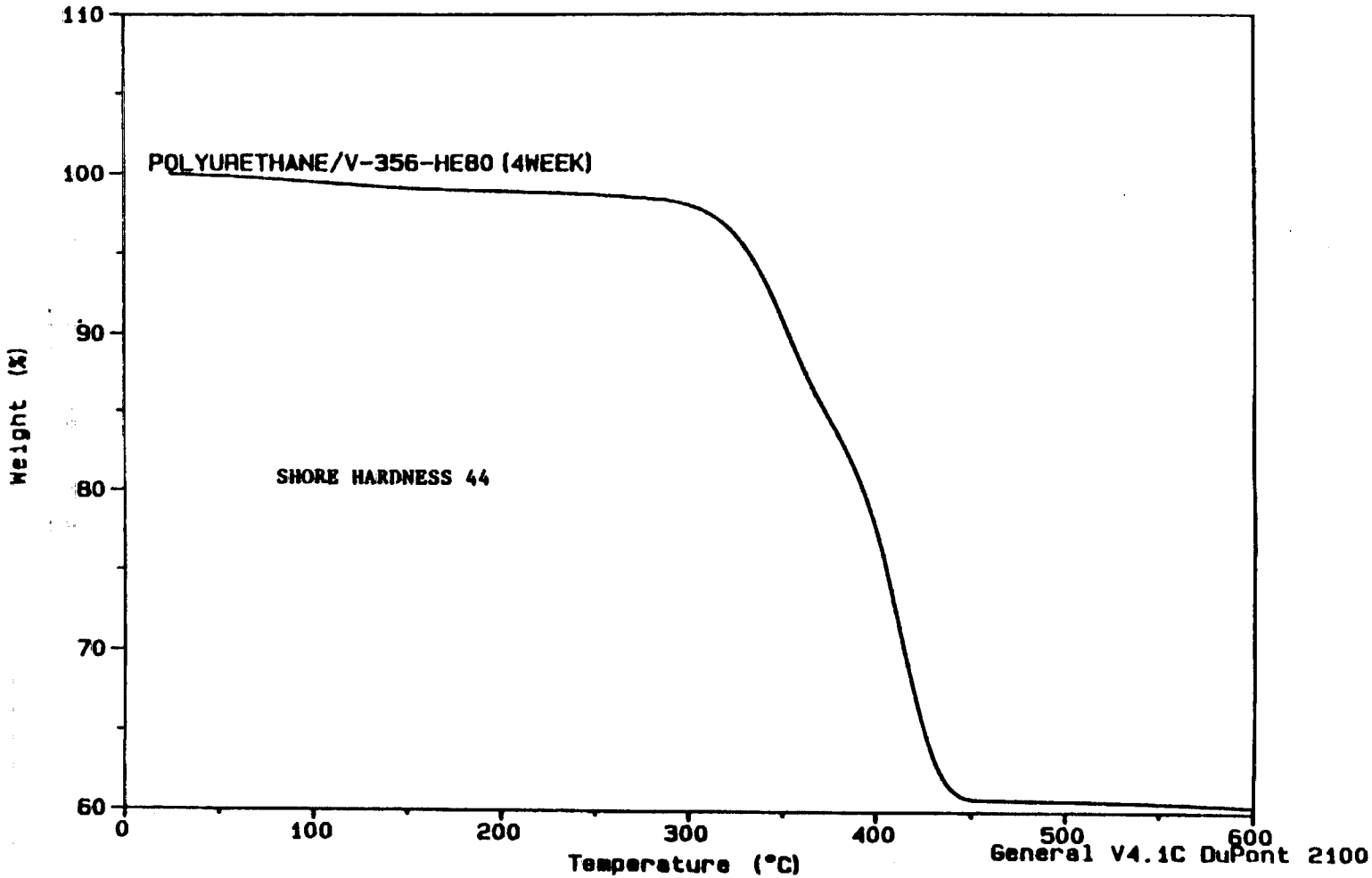

Figure 6. Thermogravimetric Curve For Polyurethane V-356-HE80 (Week 4)

The TGA data for the compound V-356-HE80 (figure 5) is consistent with the hardness versus time exposed data; that is, the incipient temperature of weight loss is practically independent of the weeks of exposure, except the first week when most of the degradation seemed to occur. This is supported by vendor data (figure 2) which shows hydrolytic degradation to occur within the first week (3). The thermal environment used by the vendor was some 30 °C lower than that used in this study, with relative humidity being the same at 95 percent.

3.2.2 Thermomechanical Analysis

Since the TGA study did not show meaningful correlation between the hardness and incipient temperature of weight loss, the TMA study was conducted. The depth of penetration of a quartz probe on the surface of the samples was measured as a function of temperature. Figures 7 and 8 show the results of this study. The sharp decrease in dimension indicates the softening of the sample as it is subjected to programmed temperature increase. This softening temperature decreased for the sample PR-1535 as the exposure time increased (figure 6) signifying polymer degradation. The data for the unexposed (zero week) sample are inconclusive because of the slippage of the probe on the small sample at about 150 °C. This trend correlates with the loss of hardness with an increase of exposure time. The data for the sample V-356-HE80 are shown in figure 8. The softening temperature decreased by about only 10 °C for the entire hydrolytic exposure of four weeks. The data for the first, second, and third weeks were inconclusive because of the slippage of the probe caused by the smallness of the samples available. Because of the limitation of samples provided, samples of adequate shape and size for the TMA study were not always available. The softening temperatures were measured using the double-tangent-intersection method.

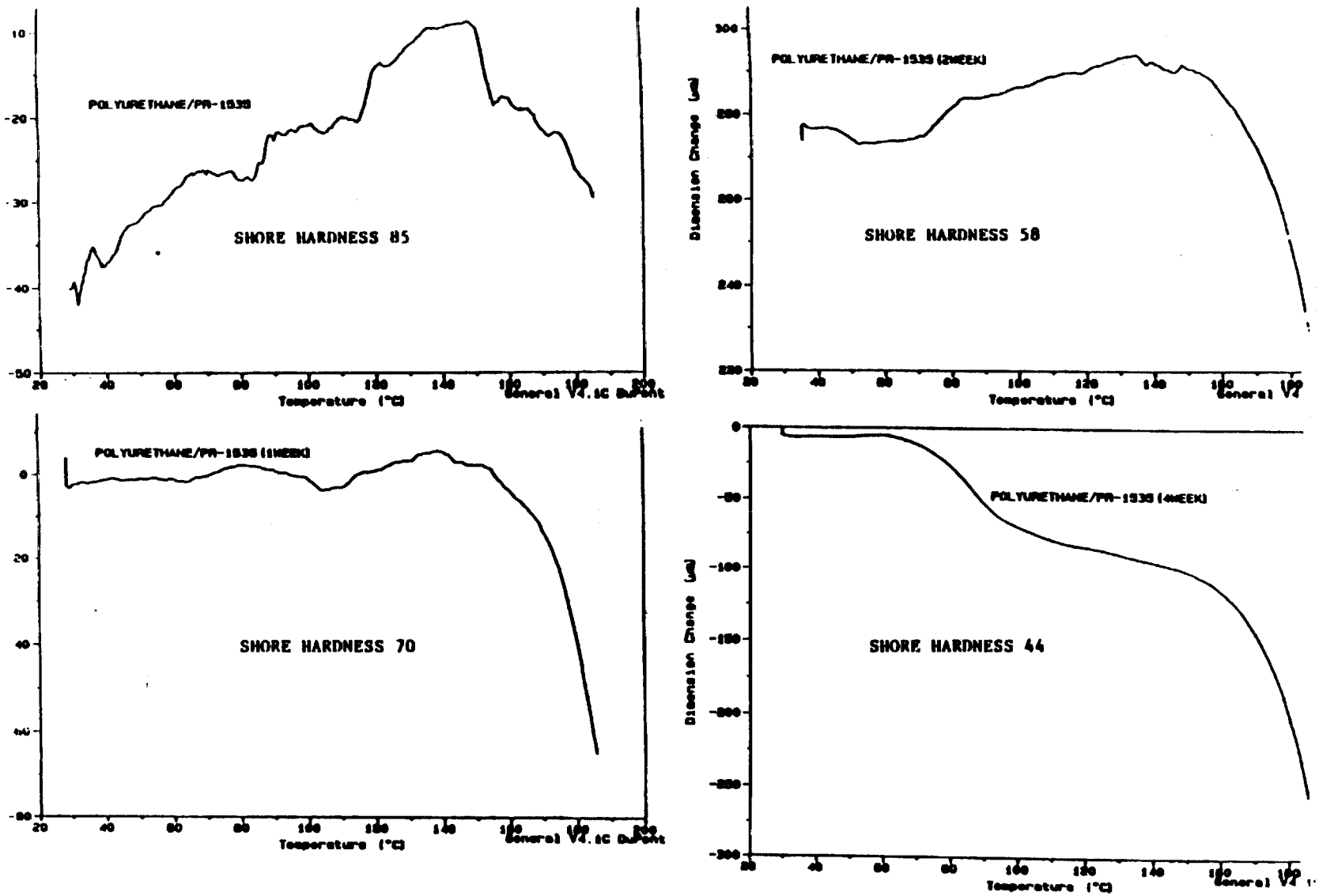

Figure 7. Thermomechanical Curves For Polyurethane PR-1535

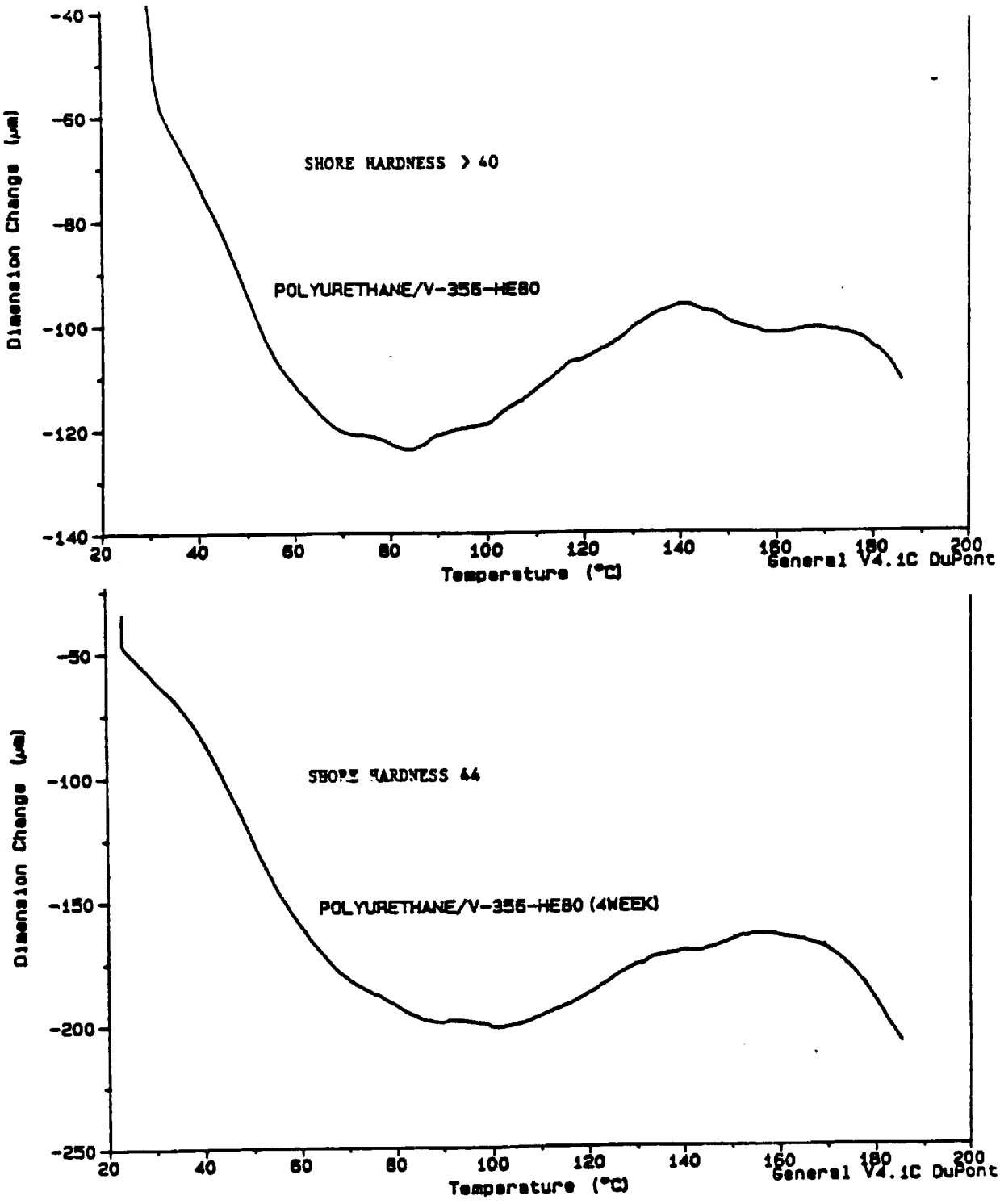

Figure 8. Thermomechanical Curves For Polyurethane V-356-HE80

3.2.3 Differential Scanning Calorimetry Analysis

Figures 9, 10, 11, and 12 show the thermograms of the compounds PR-1535 and V-356-HE80. The sample PR-1535 gave two small endotherms at 240 °C and 220 °C at zero and two weeks of exposure respectively (figures 9 and 10). Similar transitions, but less pronounced, were evident for the one, three, and four weeks of exposed samples. As the exposed time increased, the thermograms showed increased exotherm between 50 to 220 °C. These exotherms are most probably due to the curing effect.

J. Mead, et al, reported similar high temperature transitions for the polyether polyurethane system prepared from an aromatic glycol and TDI with a diamine curative (4).

The thermograms for the compound V-356-HE80 show practically no difference between the unexposed, one, two, and three weeks of exposed samples.

The four-week exposed sample shows a transition at about 70 °C. This change does not correlate to the hardness data. Further work is needed to resolve this anomaly.

4.0 CONCLUSIONS

Of the eight polyurethane compounds [current product (PR-1535) and seven candidates], only four compounds (PR-1535, PR-1574, EN-9, and V-356-HE80) passed the hydrolytic stability (weatherability) test. Of these four compounds, only two (PR-1535 and V-356-HE80) passed the NASA flammability test.

TMA gave softening points of the unexposed and exposed samples, which correlated with residual hardness data. DSC data showed some correlation with residual hardness data and increased curing effect with weeks exposed. TGA data showed practically no correlation with the residual hardness data.

5.0 RECOMMENDATIONS

Based on the accelerated hydrolytic stability and flammability tests, the compound V-356-HE80 is recommended to replace the current product PR-1535 which contains MOCA, provided it passes the hypergolic compatibility test.

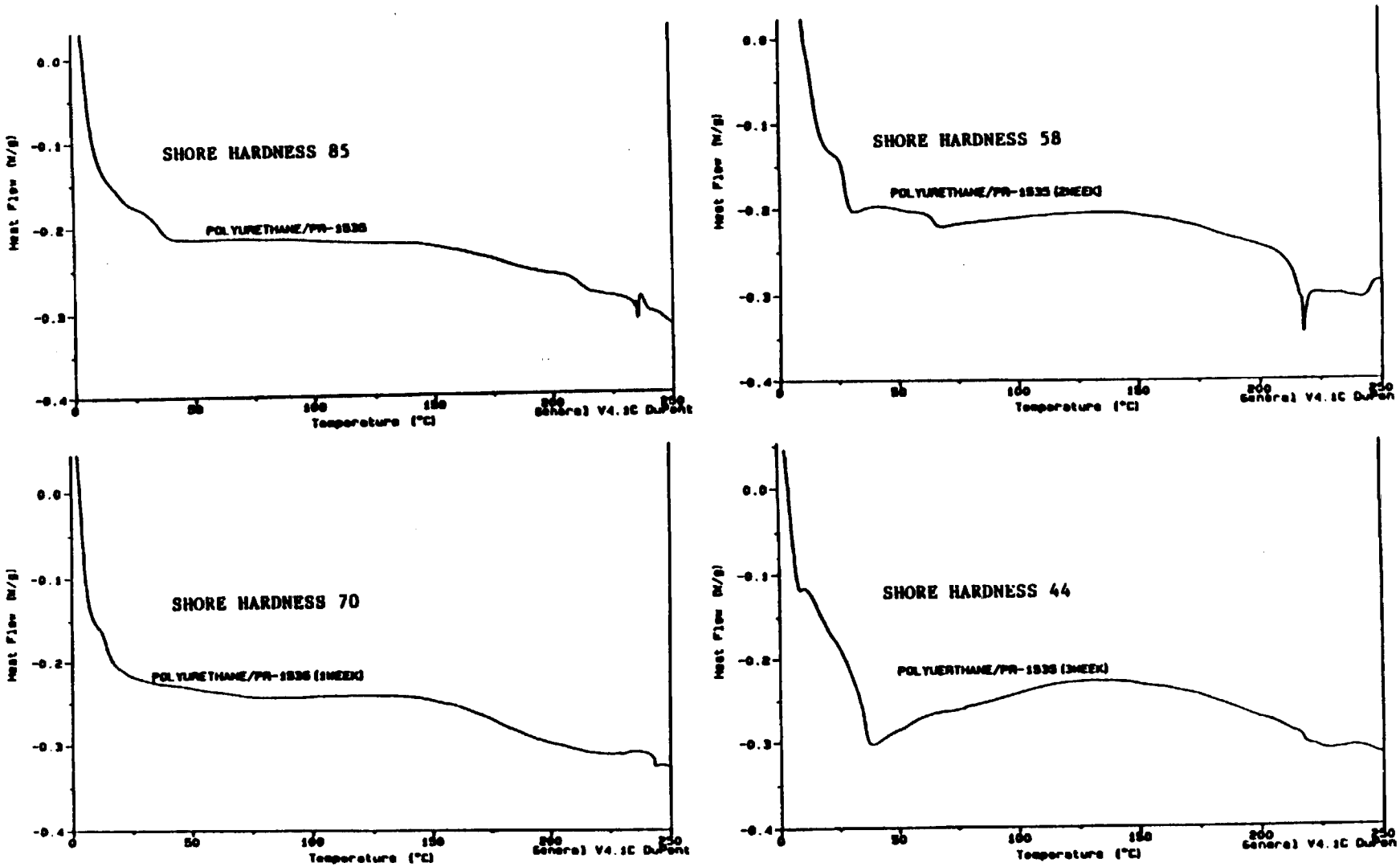

Figure 9. Differential Scanning Calorimeter Curves For Polyurethane PR-1535

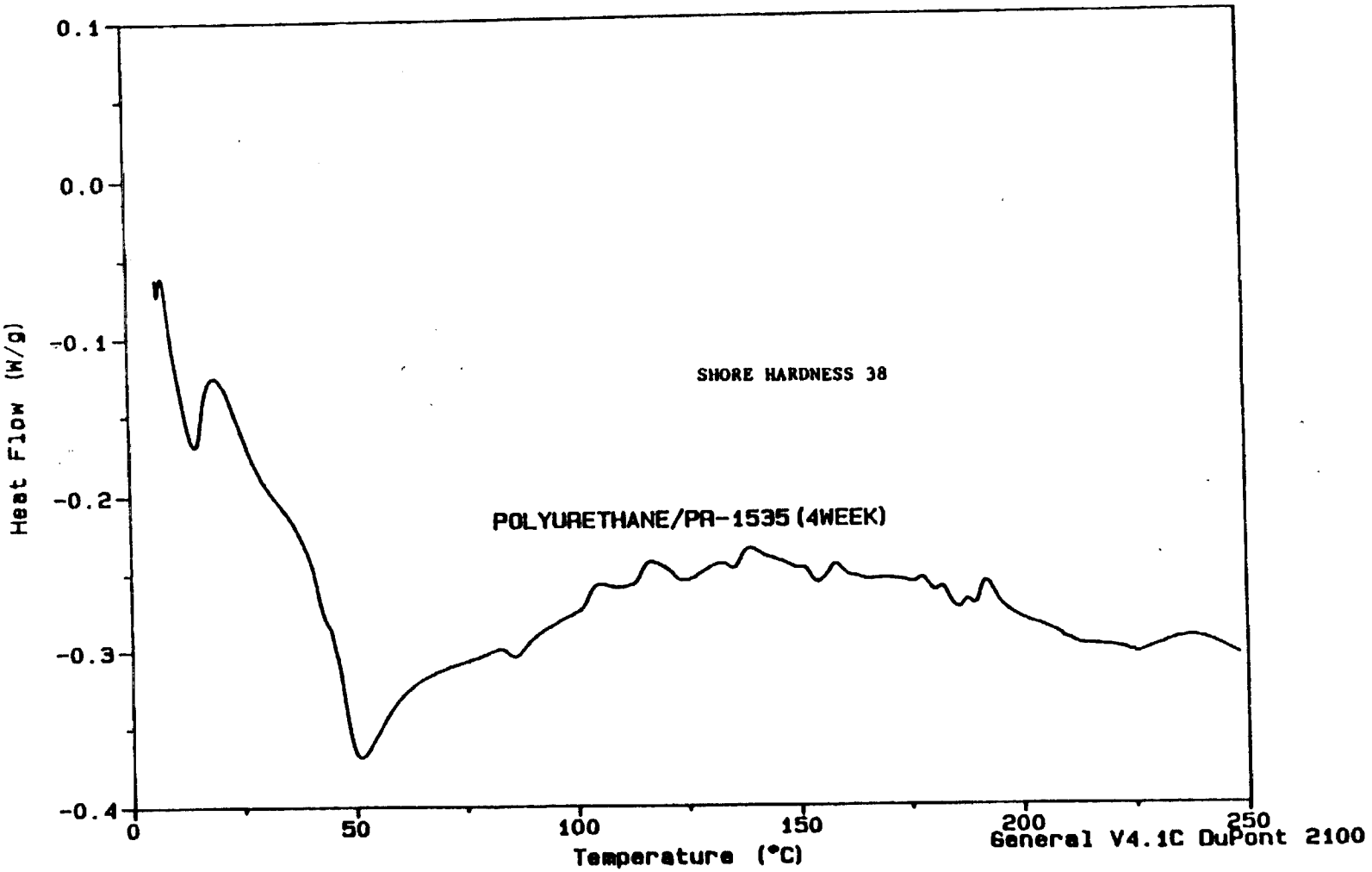

Figure 10. Differential Scanning Calorimeter Curves For Polyurethane PR-1535 (Week 4)

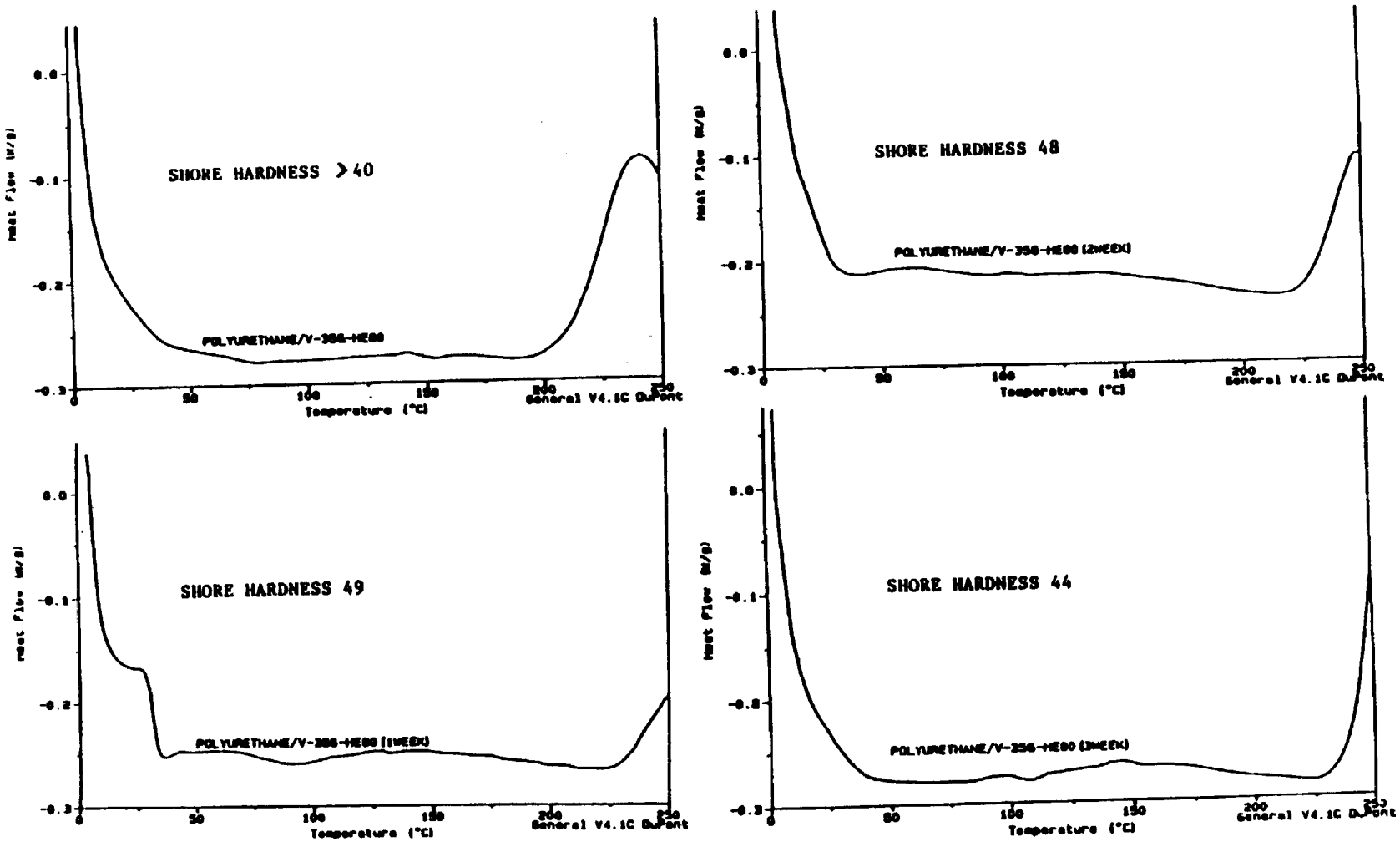

Figure 11. Differential Scanning Calorimeter Curves For Polyurethane V-356-HE80

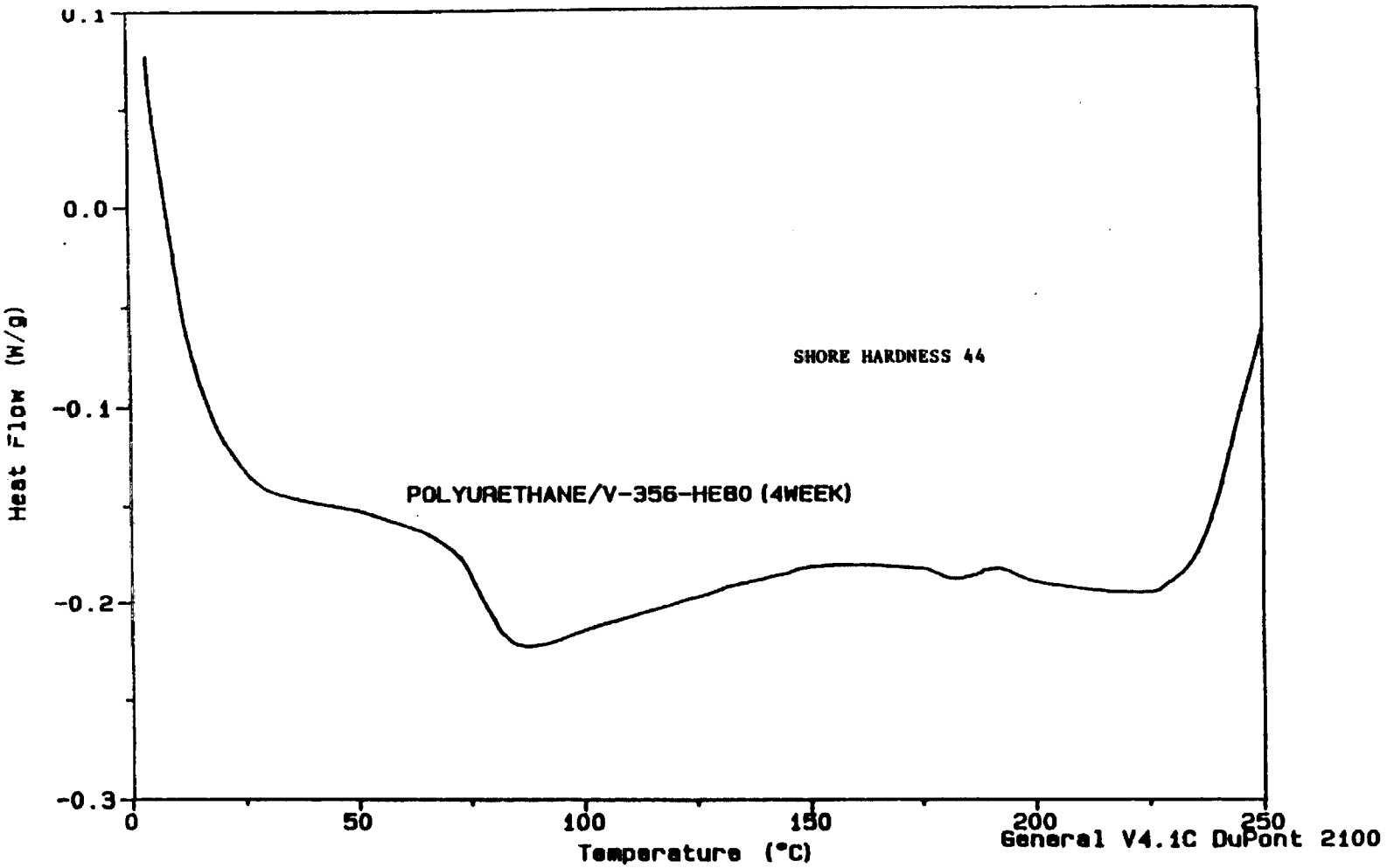

Figure 12. Differential Scanning Calorimeter Curves For Polyurethane V-356-HE80 (Week 4)

6.0 REFERENCES

1. Fred H. Gahimer, TR-2039, Naval Avionics Facility, Indianapolis, IN.

2. Fred H. Gahimer and Frederick W. Nieske, TR-1530, Naval Avionics Facility, Indianapolis, IN.

3. Personal communication from Dr. Babayan of BP Chemicals, Fibers and Materials, Santa Ana, CA.

4. Joey Mead, Sachchide Singh and David Roylance Polymer Engineering and Science, Jan 1987, Vol. 27, #2, P-134.

N93-19403

1992 NASA/ASEE SUMMER FACULTY FELLOWSHIP PROGRAM

JOHN F. KENNEDY SPACE CENTER
UNIVERSITY OF CENTRAL FLORIDA

DETERMINATION AND REPRESENTATION OF ELECTRIC CHARGE DISTRIBUTIONS ASSOCIATED WITH ADVERSE WEATHER CONDITIONS

PREPARED BY:	Dr. John T. Rompala
ACADEMIC RANK:	Associate Professor
UNIVERSITY AND DEPARTMENT:	University of Wisconsin - Stout Physics Department
NASA/KSC	
DIVISION:	Electronic Systems
BRANCH:	Atmospheric Science
NASA COLLEAGUE:	Launa Maier
DATE:	August 7, 1992
CONTRACT NUMBER:	University of Central Florida NASA-NGT-60002 Supplement: 8

TABLE OF CONTENTS

ACKNOWLEDGEMENTS

This participant in the NASA/ASEE Summer Faculty Fellowship Program extends thanks to all those associated with the program for this opportunity for creativity and education. Special thanks are offered to NASA representative Ms. Carol Valdes for helping us all gain a complete picture of operations at KSC and for assisting us fulfill our individual objectives. Special thanks to University of Central Florida representatives, Dr. Loren Anderson and Ms. Kari Stiles for their assistance in making participation in the program a unincumbered experience.

The support, advice, direction and encouragement given to the participant by his colleague, Ms. Launa Maier, is greatly appreciated.

Much is owed to many others for their contribution to this summer's effort. The support given by Mr. Nicholus Schultz and his colleagues was of special value. Thanks to all my fellow participants in the program for their camaraderie. Their support will be long remembered.

Support in preparation for this summer's investigation was given to the participant by his home institution, the University of Wisconsin-Stout. That support comes in the form of a Faculty Research Initiative Grant. The success of the current investigation is due in good measure to the preliminary work carried out under that grant. That support is greatly appreciated.

JTR

ABSTRACT

Algorithms are presented for determining the size and location of electric charges which model storm systems and lightning strikes. The analysis utilizes readings from a grid of ground level field mills and geometric constraints on parameters to arrive at a representative set of charges. This set is used to generate Three dimensional graphical depictions of the set as well as contour maps of the ground level electrical environment over the grid. The composite, analytic and graphic, package is demonstrated and evaluated using controlled input data and archived data from a storm system. The results demonstrate the packages utility as: an operational tool in appraising adverse weather conditions; a research tool in studies of topics such as storm structure, storm dynamics, and lightning; and a tool in designing and evaluating grid systems.

INTRODUCTION

1.1 ELECTRIC FIELD MILL

An electric field mill is a device used to determine the size of an electric field component. The device consists of two metallic coaxial disks of the same radius separated by a fixed distance. The axis of these disks is pointed in the direction of the field component to be investigated. The lower disk is radially segmented and fixed in position. The upper disk has similarly segmented but has alternate segments removed. This upper disk is rotated. As that disk rotates the electric field flux to the lower segments undergoes continual change. This changing flux between the disks induces a voltage between the plates. Knowledge of this voltage and the distance between the disks permits the determination of the electric field component (reference 1).

1.1.1 KSC/CCAFS GRID OF ELECTRIC FIELD MILLS. The Kennedy Space Center and the Cape Canaveral Air Force Station are spanned by a grid of more than thirty vertically directed ground level field mills. With the earth acting as a nearly perfect conductor of electricity, these mills monitor the full ambient field. The current study deals with data obtained through that system and the interpretation of that data for operational uses at the station and center and the potential use by investigators.

1.1.2 OPERATIONAL USE OF FIELD MILL DATA. Information from these mills is gathered and recorded. The real-time data is used to appraise the potential for a lightning strike. If conditions warrant, a warning is issued and precautions in the threatened area are taken to minimize any damage or injury which might occur due to a strike.

1.1.3 SCIENTIFIC USE OF MILL DATA. The data generated by these mills is also archived. This stored information represents an invaluable data base for investigating the storms which frequent this area. Real-time data has also been used to monitor the region's electric field during experimentation.

1.2 FORMATS FOR INTERPRETATION OF FIELD MILL DATA

Two formats for presenting field mill data are currently employed. contour maps and strip charts. Each format emphasizes a different aspect of the available data. Each represents a different tool used by observers in appraising the situation and ezch impacts the decision making process.

1.2.1 STRIP CHART. The data stream from the field mills is continuous and finds its most immediate represention in strip charts. This presentation emphasizes

the time development of the electric field but, of necessity, is focused to the output of a small number of mills. The investigator's attention is directed toward the behavior of the electric field over a limited region of the grid.

1.2.2 CONTOUR MAP. The information from the entire working grid can be digitalized and the representative readings from the various mills over a particular time interval can be accumulated. This time interval can be made short enough so as to represent nearly instantaneous data. With knowledge of the field level at the various grid mill sites, algorithms can be employed to determine the approximate field values at other locals within the grid. Lines can be constructed connecting those locals which, according to the algorithm, experience the same field strength. Contours constructed in this way give a quick overview of the regional electric field at a particular time. Continual updating is needed to provide an investigator with an impression of the time development of the field over the region.

1.3 CHARGE DISTRIBUTION FORMAT

Presently, contours are generated by a linear approach which generates a highly reliable surface contour map. That approach is not well suited to investigation of other physical aspects of a storm system. It makes no attempt to mimic the physical charge distribution. A model which is based on a presumed system which is closer to the physical system would yield much more information regarding the system. A successful model would still be able to generate surface contours. In addition, it would be able to show the relative size, polarity and position of representative charges. This information could be used in developing approximations for the total energy of the system. Monitoring of the time development of this distribution would give information on the mechanism involved in storm dynamics. Information on storm development and activity would become tractable. Combined with other meteorological information, the role of surface charge and wind convergence on storm activity and lightning strikes could be studied.

1.3.1 THE RELATION OF ELECTRIC FIELD TO ELECTRIC CHARGE. Each electric charge can be considered as having its own electrical environment. It is through this electric field that it interacts with other charges within its environment. The size and direction of that environment at any point about a charge is given by Coulomb's law (ref 2,3). An accumulation of charges produces a more complex environment, but the composite is still a vector sum of the effect of the contribution of individual charges. Given a charge distribution it is possible, though perhaps tedious, to determine its unique electrical environment at all locations.

1.3.2 THE UTILITY OF A CHARGE DISTRIBUTION REPRESENTATION. In order to gain as much information from a data set as is possible it is reasonable to

construct a mathematical model which resembles the physical system as closely as possible. In the field of electrodynamics the formalism for such an undertaking is complete and well tested. The potential for interpretation and applications of a functional model are extensive. The depiction of a storm system by a charge distribution would be progress in that direction.

1.3.3 THE LIMITATION IN DETERMINING THE REPRESENTATION. The traditional problem in electrodynamics involves the study of a given charge distribution in a setting of conductors and dielectrics. It is commonly agreed that the field for such systems is unique and can be determined using the most expedient mathematical approach available, of which there are many. The analysis of a storm system considers the opposite approach. A field over a limited region is known and the charge responsible for that field is to be determined. Due to this limited knowledge the charge distribution determined is not unique. Many charge distributions can have the same environment over a limited region. It has been this shortcoming which is primarily responsible for the lack of effort to formulate algorithms for finding any charge distribution to fit the data.

1.4 BASIC PREMISE

The current investigation attempts to initiate a search for a charge distributions which corresponds to distributions found in storm systems and involved in lightning strikes. The initial candidate distribution is determined by field mill readings only. It is presumed that confirmation of the results can gained by including limiting information apart for field. This other information would include restrictions on the physical systems probable dimensions. It would also include information based on insight gained through other means such the general models for charge distributions which are considered viable. The level and distribution of the energy in the system would also result in a strong restrictions on form of possible candidate distributions.

1.5 PRELIMINARY ALGORITHMS TO GENERATE REPRESENTATIVE CHARGE DISTRIBUTIONS

This investigator began such developments during work in the summer of '91 as a NASA/ASEE Summer Faculty Fellow. . These efforts consisted of an analysis of past modeling techiques and the introduction of innovations (ref. 4).

1.5.1 MODEL_A. This investigator reformulated the algorithm used by operations to construct field contours. It was found that the model used in that original process transforms the relationship between the electric field and the charges producing the field to a linear one. This is achieved through a dramatic reduction in the degrees of freedom in the problem. The assumed charge system is

taken as an array of charges agreeing in number to the number of operable field mills. The location of these charges is fixed. A single charge is taken as located at a given height above any particular mill. The size of the charges are the only variables to be determined. Since the number of unknowns agrees with the number of independent mill values, a linear set of equations results and the charges determined. In turn these charges are used to determine the field over a grid covering the region and generate contour maps.

1.5.2 MODEL_B. As an alternate approach, this investigator introduced a mathematical formalism for data analysis. The description of a single charge includes four variables, three for the location of the charge and a fourth for its type and size. Thus the field value of four mills is sufficient to characterize a charge. Coulomb's law provides a set of four coupled, but none linear, equations for the determination of the four charge parameters. This model was developed to verify that the technique used in obtaining a solution is correct and functional. A hypothetical test charge was considered and the field values generated by that charge determined. The model correctly located the hypothetical single charge based on the four field values.

1.5.3 MODEL_C. With the mathematical technique thus established, limited time was spent that summer constructing a model consisting of two charges. By determining a single charge and subtracting its effect from the overall field a second charge producing this residual field could be determined. An iteration process balanced the contribution of the two charges. Results were encouraging and work was continued on the mathematical process by which the mill values are to be used in the analysis. This continued effort was conducted independently and under a Faculty Research Initiative Grant awarded by the University of Wisconsin-Stout. By the time the current investigation resumed here KSC, this model was nearly fully functional.

1.6 COMPONENTS OF AN APPLICATION PACKAGE

The intent of continued investigation is to design a new tool for the analysis of field mill readings for operational and scientific purposes. This application package will also include compatibility with traditional approaches, offer new approaches and provide for future modification.

1.6.1 DATA ACQUISITION. Data formats for projected models should include the input of archived information and for real-time input. The models presented have been formulated using a recorded set of data. Mr. Llyod Albright and Mr. Richard Neely of EG&G Florida, DPS have already introduced variations in the computer code developed for Model_A so that it gives real-time contours, and in another version, includes graphical information on wind velocity over the region.

1.6.2 DEVELOPMENT OF ALGORITHMS FOR DATA ANALYSIS. The computer programs written by the investigator are in FORTRAN. This language was chosen due to the principle investigator's familarity with the language and because it is a widely know and used in the scientific community (ref. 5-7). This will facilitate the use of the programs as a basis for modifications and innovations

1.6.3 PRESENTATION OF RESULTING REPRESENTATIVE CHARGE DISTRIBUTION. An essential feature of the models presented is the graphical representation of the resulting analysis. A graphical format facilitates the analysis of large data set, such as field mill data. This is carried out in an interactive framework.

1.6.4 INTEGRATION OF RESULTING PRESENTATIONS WITH TRADITIONAL FORMATS. The experience and insight gained from traditional presentations is a valuable asset in appraising the data. The models presented include the contour format of presentation.

1.6.5 INTRODUCTION OF TECHNIQUES FOR APPRAISING THE APPROPRIATENESS OF THE ALGORITHMS. Along with the introduction of analytical techniques the models presented were tested using controlled and specially formulated data sets. The development of computer programs to produce this data are part of the data handling system. They serve as a mechanism for appraising a model's utility. They can also be used to judge the effectiveness of the mill grid system.

THE APPLICATION PACKAGE: ANALYTICAL COMPONENT

2.1 THE PHYSICAL SYSTEM MODELED

The models presented are intended to represent an adverse storm system. Such systems contain continuous but variable distributions of positive and negative charge. One of the more popular depictions of a common system places a large positive charge at a high altitude, a counterpart large negative charge near the zero degree Centigrade level and a small positive charge at a lower level (ref. 8). The models forwarded do not attempt, at this stage of development, to suggest the structure of these continuous distributions. They take the initial step similar toward working models currently considered viable. In these models, large regions of a system are considered to have a single polarity and represented as a single point charge.

2.2 THE STRUCTURE OF MODEL_D AND MODEL_E

Model_C attempted to describe the charge system using two charges. This is a strong restriction an the model. The model did serve as a mechanism for fostering the analytical techniques use in the current effort. This summer's work has been devoted to the development of models which search out several charges.

2.2.1 CHARGE CHARACTERISTICS. Ten charges was taken as the working number but the programs are easily modified to permit variations in this number. The ten charges are assumed to be point charges. No restrictions are placed on their polarity or size. The only restriction placed on charges is that they be below the eighteen kilometers in altitude. No restrictions are placed on their horizontal location.

2.2.2 DETERMINATION OF A DOMINATE CHARGE'S SIZE AND LOCATION. The model ranks all the field mill readings in terms of intensity and selects the dominate polarity. The mill showing the largest reading in that set is selected as the central mill. Three other mills with high ranking readings in the vicinity of the central mill are chosen to complete the quartet needed to locate the charge. Once four such readings are obtained the locating algorithm developed with earlier models is employed to determine the charge size and location.

2.2.3 DETERMINATION OF A DOMINATE CHARGE'S INFLUENCE ON THE SYSTEM. With a charge so determined, its electric field environment contribution of that charge is calculated. In particular, the electric field contribution at the location of each field mill is determined and subtracted from the total field value to produce a residual electric field.

2.2.4 ITERATION PROCESSES APPLIED TO THE RESIDUAL ELECTRIC FIELD. The residual electric field is now used as the principal field and the augmented field mill values are re-ranked and the dominate influence in the residual field is determined. Four field mill values are selected using the process described above to determine the charge most likely responsible for this influence. The contribution to the field from this charge is then calculated. The role of the first charge and this second charge are reversed and the two re-evaluated in order to obtain a balanced combination. With these charges determined there combined environment is calculated and subtracted from the total field. This new residual field is used to determine a third charge and its electric field contribution. The process continues until ten charges are determined. Model_E employs an extended iteration process The balancing of charges is itself iterated several times in order to obtain a more representative distribution between the charges.

2.3 TECHNIQUES FOR SELECTING THE FIELD MILL VALUES USED IN THE ANALYSIS

The selection of the four field mills to be used in the determination of the four parameters associated with a charge, location and signed size, is a critical step in the analysis. Since all mills are under the environmental effect of many charges it is difficult to chose four mills which are dominated by the influence of a single charge. The process used in the formalism presented relies on guidelines based on the geometric considerations.

2.3.1 LIMITATIONS ON FIELD MILL RANGE. The first physical restriction placed on the model is based on distance from the central mill. It is presumed that the mill registering the largest absolute reading has a charge near its zenith. Using this field mill location as a hub, a radial range is established. Mills within that range are then investigated. Mills with the same polarity as the hub mill and which are high ranked in value are considered as candidates for the calculation process. Since the grid of field mills is irregular in orientation and span this process may not yield successful candidates. If this occurs the restriction on range is relaxed until four successful candidates are located.

2.3.2 LIMITATION ON CHARGE ALTITUDE. One of consequences of placing a restriction on range is that mills which are 'close' to the hub are also nearly below the charge to be located. As a result errors in determining the charge's altitude are increased. The error tends in the direction of large altitudes. If a calculation results in a charge altitude which is unreasonably large, the search for four other mills within the existing range is initiated. If after repeated searches, no physically reasonable results are achieved, the restrictions on range are relaxed until four successful candidates are determined.

2.3.3 INOPERATIVE FIELD MILLS. All values from active mills are included in the analysis. In ordinary operational situations not all mills will be functioning. In order to accommodate for this contingency the program provides for a flag to be assigned to inoperative mill. Flagged mills are withdrawn from the analysis. This is achieved by giving an inoperative field mill a value of absolute zero to the precision of the computer use. Once the grid of active field mills is determined care is taken so that active mills are not inadvertently eliminated if, at some time in the analysis, the residual value of the mill becomes zero.

2.3.4 SINGULARITIES. The calculations of the charge parameters takes several different paths should any combination of the four field values be identical. If a pair of values are equal, singularities in the calculation will result since division by the difference in field values is required at several points in the straight forward analysis. The programs presented consider all possible paths for the various combinations of identical values among the four-mills and provides alternate paths for each possibility. Each leads to a determination of the charge parameters. The possibility of mills having a common value is to be expected, especially since mills within a fixed range are sought out.

2.4 SUPPLEMENTAL FEATURES

Addition components have been added to the basic analytical framework of the analytical component to enhance its utility and facilitate its application. These features also serve as an illustration of how other innovations can be introduced into the program. This frame has been applied to two fundamental models, Model_D and Model_E. The resulting programs are labeled ANALYSIS_D and ANALYSIS_E.

2.4.1 COMPARISON OF ACTUAL AND MODEL FIELDS. With a distribution of representative charges so determined, a check on the reliability of that distribution can be applied to the results. The programs presented carry out such a calculation and incorporate the results in the output data file. The total field due to the entire set of charges is determined. In particular, the field at each field mill location is determined and compared to the input value for that mill. This variation is then compared to the inherent error for a mill according to a process suggested by Jacobson and Krider (ref. 9) and refered to here as Variation C.

2.4.2 INTERACTIVE FEATURES. In order to allow for applications to operation formats, the analysis programs also permits the user to direct the analysis to particular field mill reading files of interest. The user also labels the destination file. Since the input data usually includes a sequence of data sets, either real-time or archived, the program is structured to carry out an analysis of that sequence and store the results as directed by the user.

THE APPLICATION PACKAGE: GRAPHICAL COMPONENT

3.1 UTILITY OF GRAPHICAL REPRESENTATIONS

The output data of the analytic component is stored in files as labeled by the user. These files contain the designator for the data set, the four parameters associated with each of the ten charges and the results of the Variation C test for that data set. These files can be viewed directly, produced as hard copies or used in further analysis. In the current application this data presented graphically as a contour map or as a 3D distribution.

3.1.1 APPRAISAL OF DATA FOR USE IN OPERATIONS. The combined information from strip-charts, contours, and charge distributions should give an experienced observer a cleared picture of the electrical environment in the area. It is presumed that as experience with observed charge distributions increases and as the reliability of those models improves, observers will develop expertise in appraising the potential of cloud to ground, cloud to cloud, and triggered strikes (ref. 10,11).

3.1.2 ANALYSIS OF DATA IN RESEARCH. Expertise in appraising distributions is gained through direct comparisons on situations, events, and graphical representations. The archive data available here at KSC on a variety of meteorological parameters is extensive. The suggested analysis package can be applied to that data in a full scale research program to determine the storm development and activity is reflected in patterns depicted in charge distributions representations.

3.2 GRAPHICAL REPRESENTATION OF DATA

Two types of data representation have been developed to illustrate the utility and potential for further types of representations. The first of these is the familiar two dimensional contour of the electric field at ground level. This is done to establish a link with existing expertise and as means of comparing the results of the suggested models to those generated by the traditional Model_A. This representation also served as a guide in the development of more complex representations. The second type of representation is that of the three dimensional charge distribution. These modes illustrate the flexibility of the analysis package.

3.2.1 TWO DIMENSIONAL CONTOUR. The formalism for this depiction was developed by this investigator last summer and was incorporated into the present packages. That development include the generation of a map of the geographic area. The map shows major land features and the location of the field mills in the grid. The time required to produce the analysis was greatly reduced by a modification introduced to Model_A by Mr. Richard Neely of EG&G of Florida, DPS.

3.2.2 THREE DIMENSIONAL CHARGE DISTRIBUTION. This representation gives a picture of the relative scale and scope of the system being observed. It also depicts the relative local and strength of various components of that system as interpreted by the model used.

3.2.2.1 Depiction of the Local The map used in the contour illustration is again used for the three dimensional display. It is placed on the x-y plane of a right handed system. The map is given the usual orientation for quick referencing by the observer.

3.2.2.2 Depiction of Charge Location. The representative charges are shown as closed circles positioned in the x-y-z grid. The scaling of the altitude, z-axis, is the same as the scaling used in the geographic representation. In order to aid the observer in gaining an impression of the horizontal coordinates of each charge, a line is presented which runs from the charge position to its ground level x-y coordinates. The observer is aided in gaining an impression of that height by making that connecting line dashed. A knowledge of h e scaling of the dashes gives a quick indication of the charge's altitude.

3.2.2.3 Depiction of Charge Size and Polarity. The polarity of a representative charge is indicated by color. Currently red is used to label negative charges and white is used to label positive charges. The magnitude of the charge is indicated by the size of the circular marker used to label its position. The scaling currently chosen gives the size of the circle as proportional to the cube root of the charge magnitude. The circle markers give the impression of spheres in the display. With this relation those spheres represent the scaled volume occupied by that charge assuming uniform charge distribution throughout.

3.3 GRAPHICS SOFTWARE EMPLOYED

The software which met all the needs of the current investigation and development was IMSL ™ *exponent* Graphics ™. The versatility and availability of this software made it the only immediate practical choice for the current packages. It is imagined that improvements in this software will be introduced and that other commercial support for graphics imaging will be introduced. Contouring capabilities and 3D plotting are becoming common additions to plotting and spreadsheet software.

3.3.1 SOFTWARE ATTRIBUTES. The version of the software used has the VAX/VMS system as its platform and is easily incorporated into complex programs. It is also compatible with FORTRAN code. These features permitted easy integration of graphics into the package developed.

3.3.1.1 Data Input Versatility. Since this software package can be linked to FORTRAN programs directly there is no need to establish special data files for graphical purposes.

3.3.1.2 Data Output Versatility. The graphics generated by this software can be viewed through several options. The interactive portion of the graphics software directs the image to an appropriate terminal, such as X-Window or Regis. The image can also be filed in a PostScript™ format to be used for producing hard copies in monotone or color..

3.3.2 SOFTWARE LIMITATIONS. This graphics package is versatile but it is not 'friendly' when accepting 3D 'scatter' data. Though this future versions of this software may correct this limitation, the current version is primarily designed to display continuous functions. As a consequence, great care had to be exercised in introducing data and some awkward coding had to be employed. The chief limitation is the software's failure to provide for animation. Time sequenced displays can be achieved through repetitive applications of the software but an unbroken, continuous display of updated results is not a feature of this software.

APPLICATION TO SAMPLE DATA SETS

4.1 EXPERIMENTAL DATA SETS: STORM_A

Data sets obtained from field mill produced by a storm system passing over the field mill grid were chosen to illustrate the packages application to a representative system. A preliminary analysis was carried out and some of the resulting data and graphics are offered as an example of the type of presentations offered by the program and the variety of approaches available for operational or research purpose.

4.1.1 FEATURES OF STORM _A. A storm passing over the KSC/CCAFS region on September 9, 1986 was monitored for an hour and a half. Data from twenty-five electric field mills averaged over one minute intervals was recorded as where readings resulting from several lightning strikes. This record runs from GMT_2126 to GMT_2255 producing a library of eighty-eight data sets of storm activity. Also recorded where the electric field mill readings associated with ten lightning strikes. Readings from these events are stored in a library of data sets prefixed by LIT and carrying the time of occurrence.

4.1.2 ANALYTIC ANALYSIS OF STORM_A. Analysis of all the data sets in both the storm and lightning libraries was carried out using both analytical models, ANALYTIC_D and ANALYTIC_E. All data sets were processed successfully. It is significant that these model packages can deal with charge distributions which cover the region and source charges near but outside the grid boundaries. Analysis results consist of charge distributions, and a calculation of variation C. These results were filed in libraries labeled STORM and STRIKE. This data can be accessed by the graphical portion of the package and is suitable for use in other applications.

4.1.2.1 Variation C. The field generated by the determined charges for each of these data sets was determine as part of the processing. In particular the field at each field mill sight was compared to the actual field mill reading. The operational error for mill readings is taken to be ± 10% of the input value with a minimum of 300 volts/meter. The average value of the variation is labeled as C. Variation C is defined by:

$$C^2 = (N-1)^{-2} \sum_{i=1}^{N} \left((E_i' - E_i) / s_i \right)^2,$$

E_i is the reading of the i^{th} field mill,

E_I' is the value of the field at the i^{th} location as calculated by the model,
N is the number of operational field mills, and

s_i is the operational error associated with the i^{th} mill.

Results for the storm and lightning data sets is as shown below:

STORM_A and STRIKE_A VARIATION C

Data Library	Library Size (data sets)	C Value
STORM_AD	88	3.38 ± 2,77
STORM_AE	88	4.86 ± 2.02
STRIKE_AD	10	0.60 ± 0.25
STRIKE_AE	10	0.93 ± 0.72

4.1.2.2 STORM A Energy. The various charge distribution sets, both for the storm and lightning strikes, used in a calculation of the electrical energy associated with the system. This energy is that of the entire system and includes charges at altitude and ground charges. The energy, Q, is given by the expression:

$$Q = \sum^{20}_{i=2} \sum_{j<i} k\, q_j\, q_i / 2\left((x_j - x_i)^2 + (y_j - y_i)^2 + (z_j - z_i)^2\right)^{0.5},$$

where, $k = 9.0 \times 10^9$ N m^2 / coulomb^2, and the sum is carried out over all charges, q, including 'mirror' charges. This analysis was carried out as an illustration of the type of information that can be gained from knowledge of the charge distribution and the time development shown in figure seven at the end of this section.

4.1.3 GRAPHIC ANALYSIS OF STORM_A. Samples of the graphical files generated by this component are presented in figures 1 and 2. In those figures, all distances are in kilometers. Charge height is indicated by dashed lines. The scaling is such that the distance from dash to dash represents a distance of 1.35 km. A total of 392 different displays are available using data from these four libraries. Samples are given in figures one, two and three of this section.

4.2 CONTROL DATA SETS: STNDRD

The package programs were surveyed using control data sets of charge distributions. This library of control sets was filed in a library labeled STNDRD. The control data sets of charge distributions were transformed into corresponding sets of field mill readings. This was accomplished using the program ELF_MOLD. Thirty-eight sets

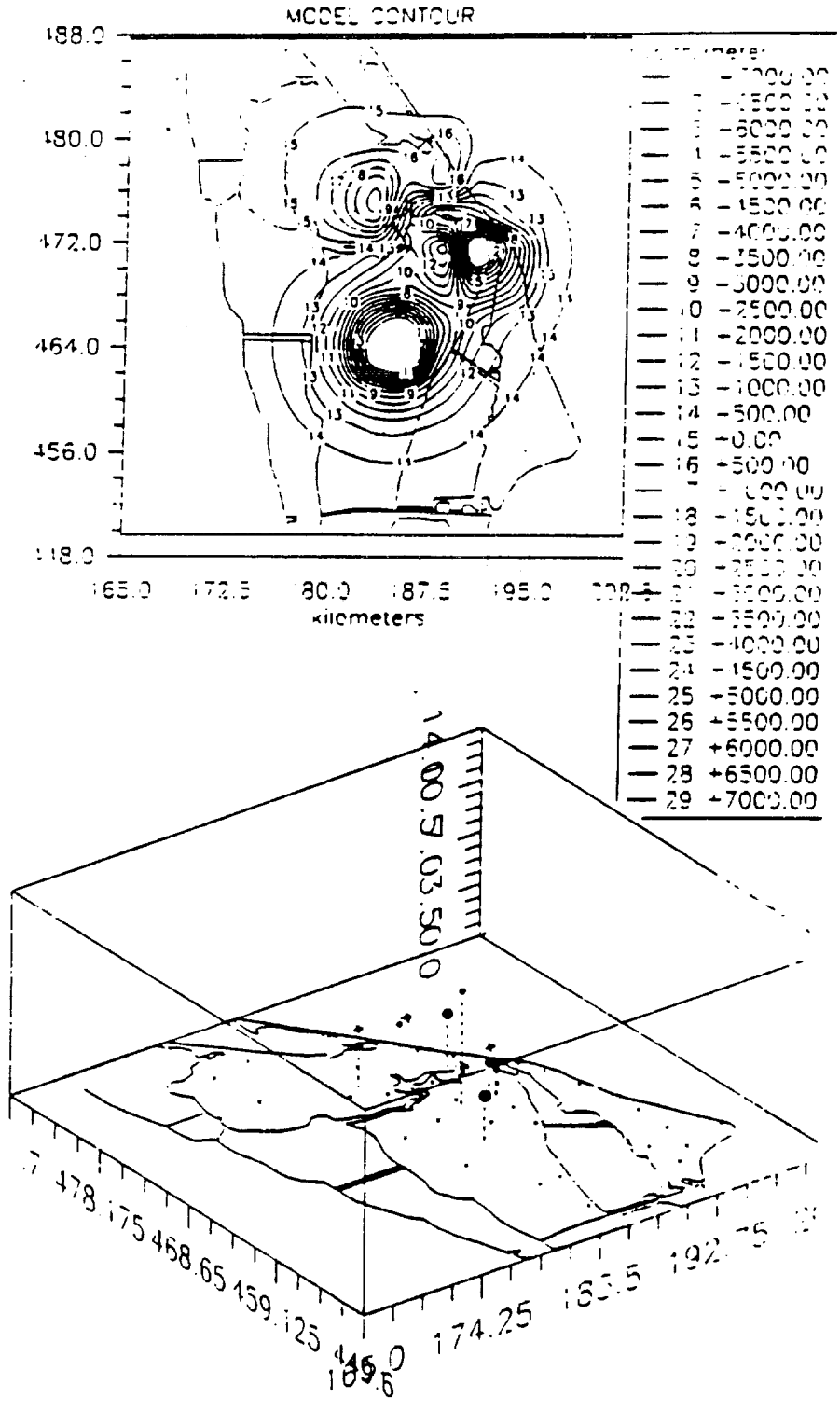

Figure 1. MODEL_D's GMT_2131 .

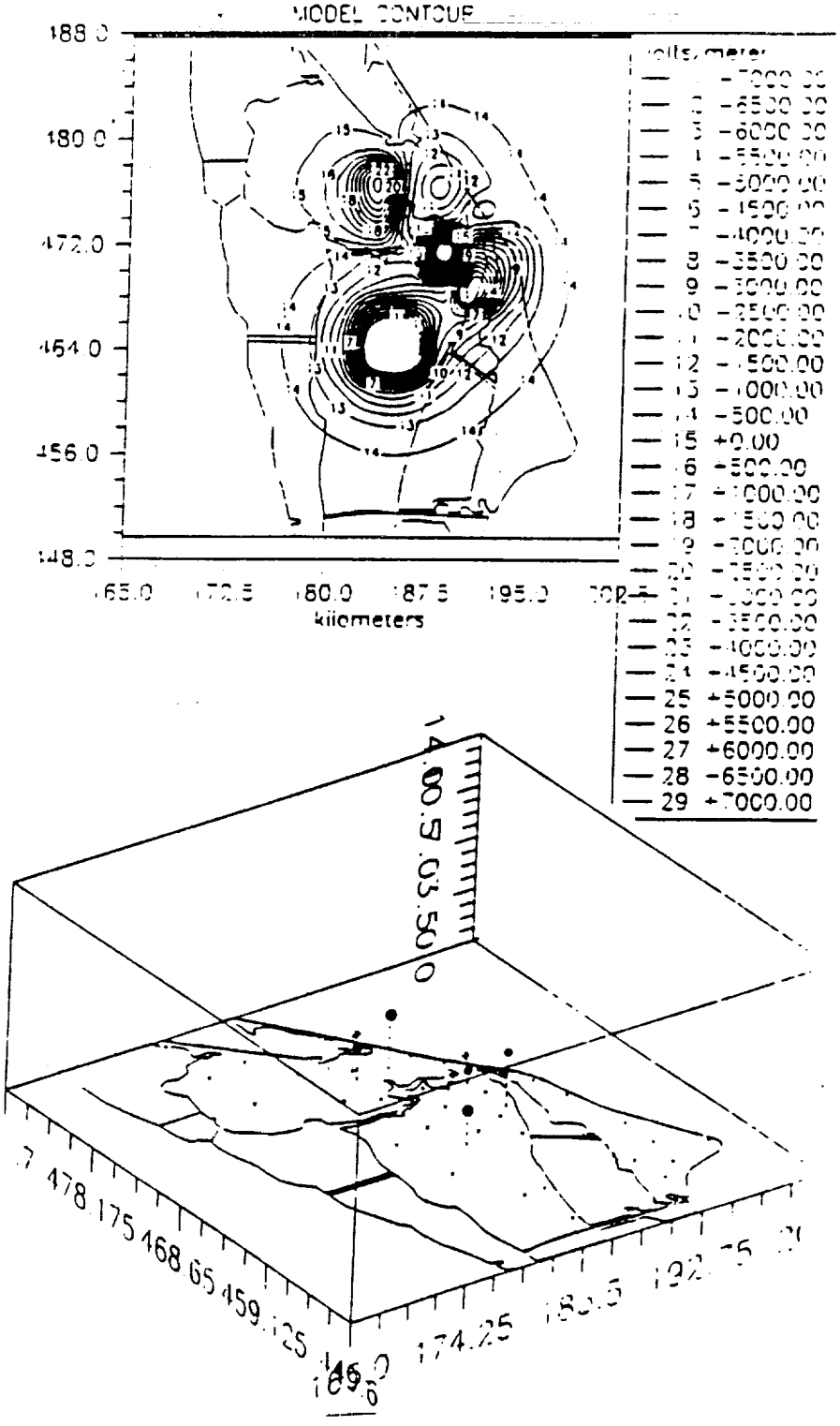

Figure 2. MODEL_E's GMT_2131

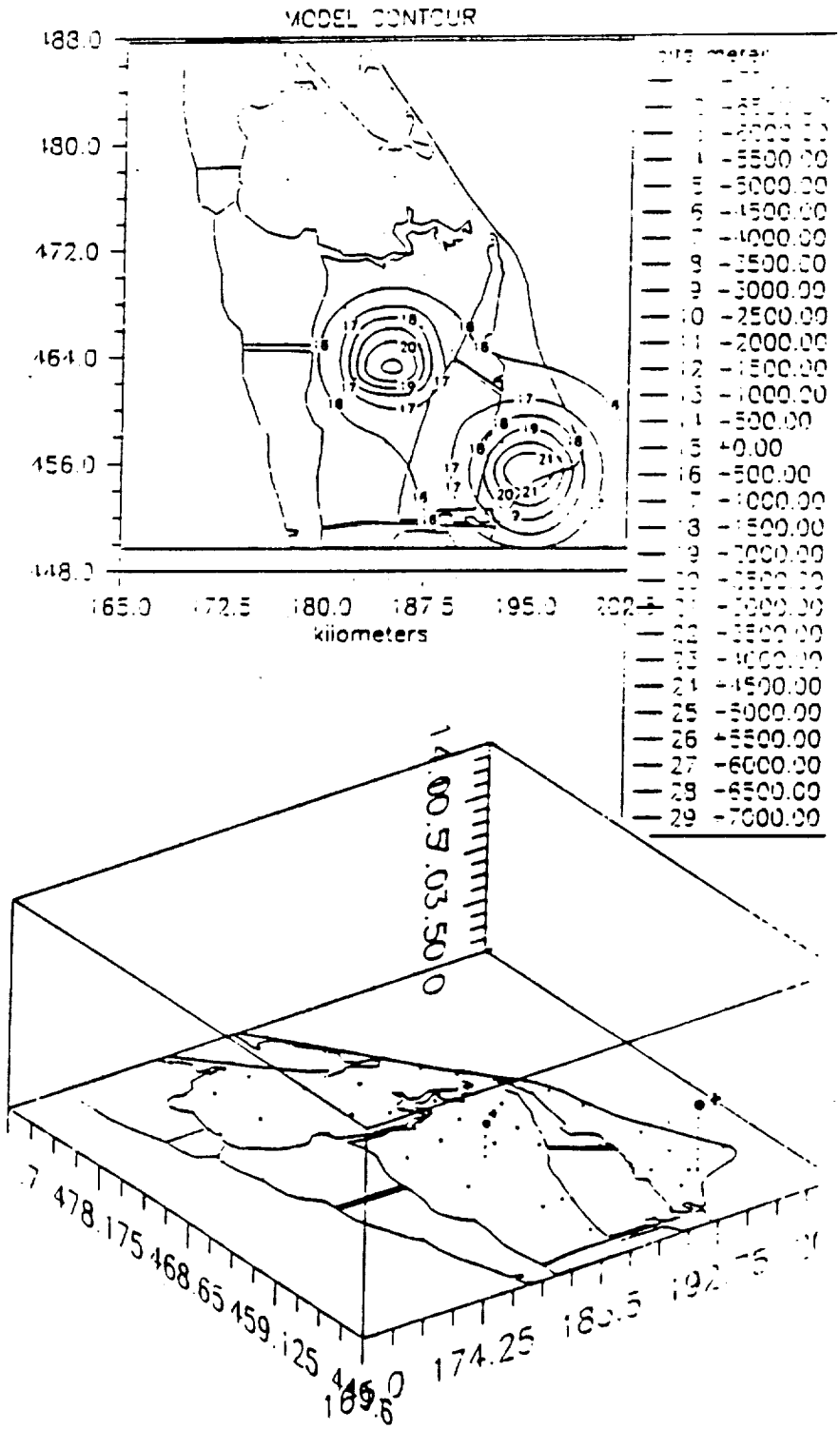

Figure 3. MODEL_D's LIT_2150

of field mill readings carry the prefix TMT. It was these field mill values which were analyzed using the application portion of the package. The results were filed in libraries labeled STNDRD_D and STNDRD_E. These results were compared directly to the control data sets.

4.2.1 ANALYTICAL ANALYSIS OF STNDRD. A variety of situations were considered to give an indication of the ability of the models to reconstruct the input charge distributions. Variations include the number, size and location of charges. A basic test of the models is their capacity to deal with situations where physical system is comprised of fewer than ten charges. Both models are designed not to over-determine the situation and responded favorably to those control situations. Where there is agreement between the number of charges in the control and result sets a statistical comparison is made. In those situations where the models generate a number of charges greater than that in the control set, a comparison of the graphical results is informative.

STNDRD VARIATION C

Data Library	Library Size (data sets)	C Value
STNDRD_D	38	0.52 ± 1.00
STNDRD_E	38	0.54 ± 0.60

4.2.1.1 Monopole Variation in Altitude. As a first test in the ability of the models to determine the altitude of a point charge. A sample charge of fifty coulombs is positioned at fixed central x-y coordinates and a variable z coordinate. Five sets, TMT_1001 through TMT_1005, were generated with altitudes ranging for four kilometers to sixteen kilometers. The results are shown below. Both models show a good ability to follow such variations.

AVERAGE ERRORS ASSOCIATE WITH VARIATIONS IN ALTITUDE

	Charge (coulombs)	Altitude (meters)	X-coordinate (meters)	Y-coordinate (meters)
Model_D	0.098 ± 0.076	9.98 ± 5.10	2.72 ± 3.11	1.78 ± 0.80
Model_E	0.098 ± 0.076	9.98 ± 5.10	2.72 ± 3.11	1.78 ± 0.80

4.2.1.2 Monopole Variation in Magnitude. Five sets of values of field mill readings, TMT_2001 through TMT_2005, were generated to represent the field environment of a point charge which varies in magnitude from ten to ninety coulombs at an altitude of ten kilometers and fixed central x-y coordinates. The results are shown in the table below. Both model were able to locate and determine the size of the charge.

AVERAGE ERRORS ASSOCIATED WITH VARIATIONS IN MAGNITUDE

	Charge (coulombs)	Altitude (meters)	X-coordinate (meters)	Y-coordinate (meters)
Model_D	0.153 ± 0.172	17.3 ± 11.3	4.31 ± 2.89	2.64 ± 1.65
Model_E	0.149 ± 0.173	17.1 ± 11.5	4.36 ± 2.83	2.66 ± 1.61

4.2.1.3 Twin Pole and Dipole Variation in Separation. Ten sets of values of field mill readings, TMT_3001 through TMT_3010, were generated to represent two charges, each with a magnitude of fifty coulombs, at fixed altitudes of ten kilometers and identical x coordinates. The first group of five sets follows twin positive charges as the y coordinate is increased from four kilometers to twenty kilometers. The second group illustrates identical movement of a charge dipole. These variation gives indication of the resolving power of the detection system, the grid of field mills. The results indicate that, along the y axis, the field mill grid can distinguish two charges separated by more than eighteen kilometers. This is illustrated in figure four and the analytic results included in table below.

AVERAGE ERRORS ASSOCIATED WITH CHARGE SEPARATION

	Charge (coulombs)	Altitude (meters)	X-coordinate (meters)	Y-coordinate (meters)
Model_D	0.033 ± 0.022	3.34 ± 2.19	1.62 ± 1.11	3.85 ± 2.48
Model_E	0.042 ± 0.046	4.97 ± 4.19	1.02 ± 0.60	1.675 ± 1.38

4.2.1.4 Crossed Pairs of Charges with Variation in Separation. Ten sets of values of field mill readings, TMT_4001 through TMT_4010, were generated to represent two pairs of crossed pairs of fifty coulomb charges. One pair is orientated along the x axis and the other along the y axis. In the first group of five data sets, all the charges are positive. The separation between the elements of each pair are

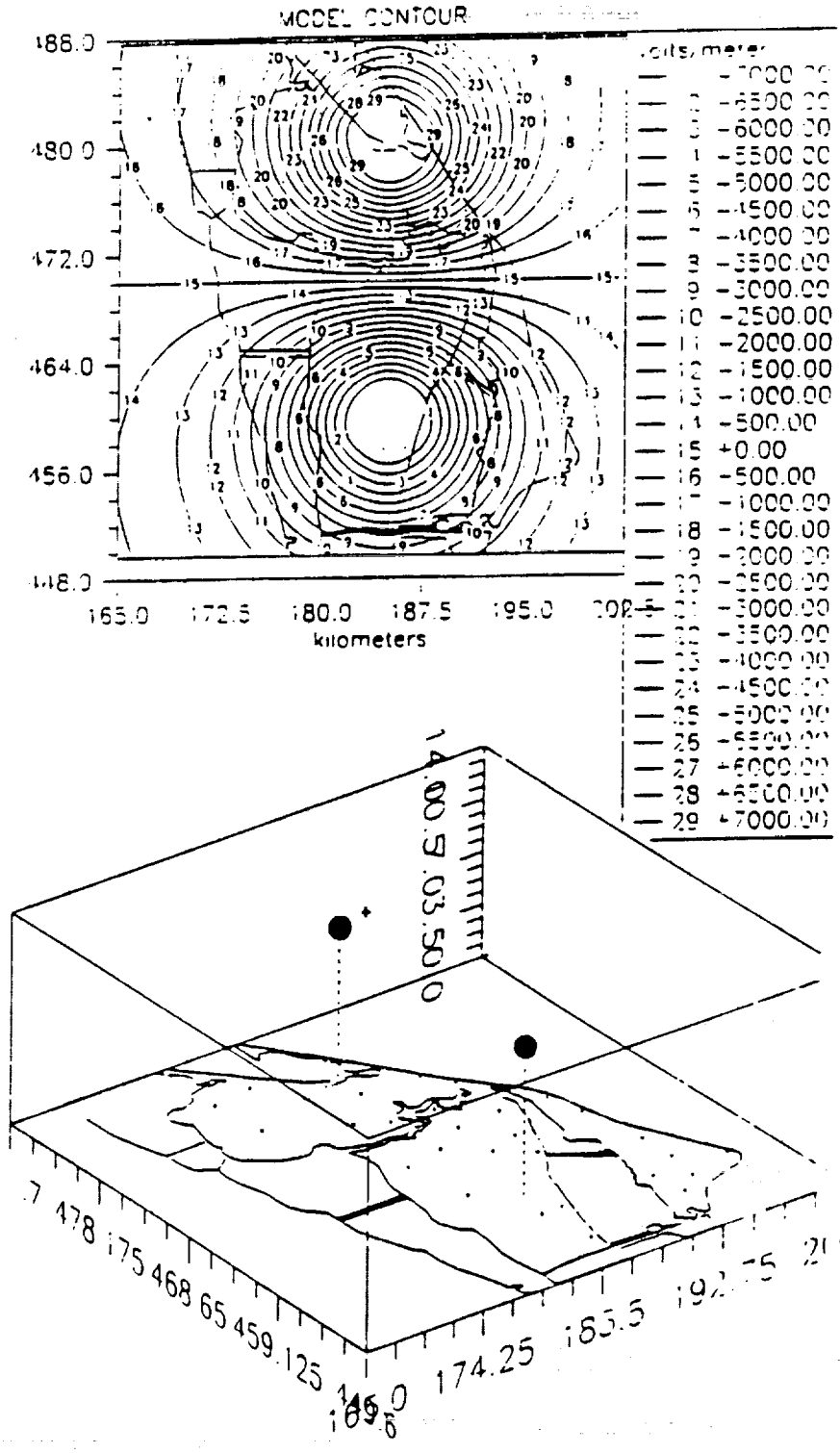

Figure 4. MODEL_D'S TMT_3010

varied from four kilometers to twenty kilometers. The second group of five data sets deals with the same variation applied to two dipoles. The results indicate that the resolution capability of the grid system is less along the x-axis than the y-axis. This is due to the decrease in mill population along the western portion of the region. This is illustrated in figure five.

4.2.1.5 Variation in the Number of Field Mills Used in the Analysis. The data set associated with GMT_2127 was used to generate a group of data sets, TMT_5000 through TMT_5006, in which the number of mills used in the analysis is diminished. The first set of the group represents the full mill complement. In each of the subsequent sets, one mill is removed from the data pool. The mills removed from the data pool gradually spanned the y coordinate of the region. The results of the analysis are presented in figure six.

4.2.2 GRAPHICAL ANALYSIS OF STNDRD. Those variations in charge number, size and position which are described above can be view using the graphic portion of the package. There are over two hundred different graphical displays available using the three control libraries. A full analysis of portion of those libraries is outside space limitation on this presentation. Samples from each library are presented to illustrate the views available. The value of this component of the package is in viewing the development of patterns as charges are separated and noting the relative change in the solutions arrived at by the models. Whereas it is difficult to give a strict analytical comparison between the result and control data sets when the number of charges in each differs, the graphical results show how limitations on the resolving power of the models and the grid are compensated for by the models. In general, this is achieved through the inclusion of small stray charges.

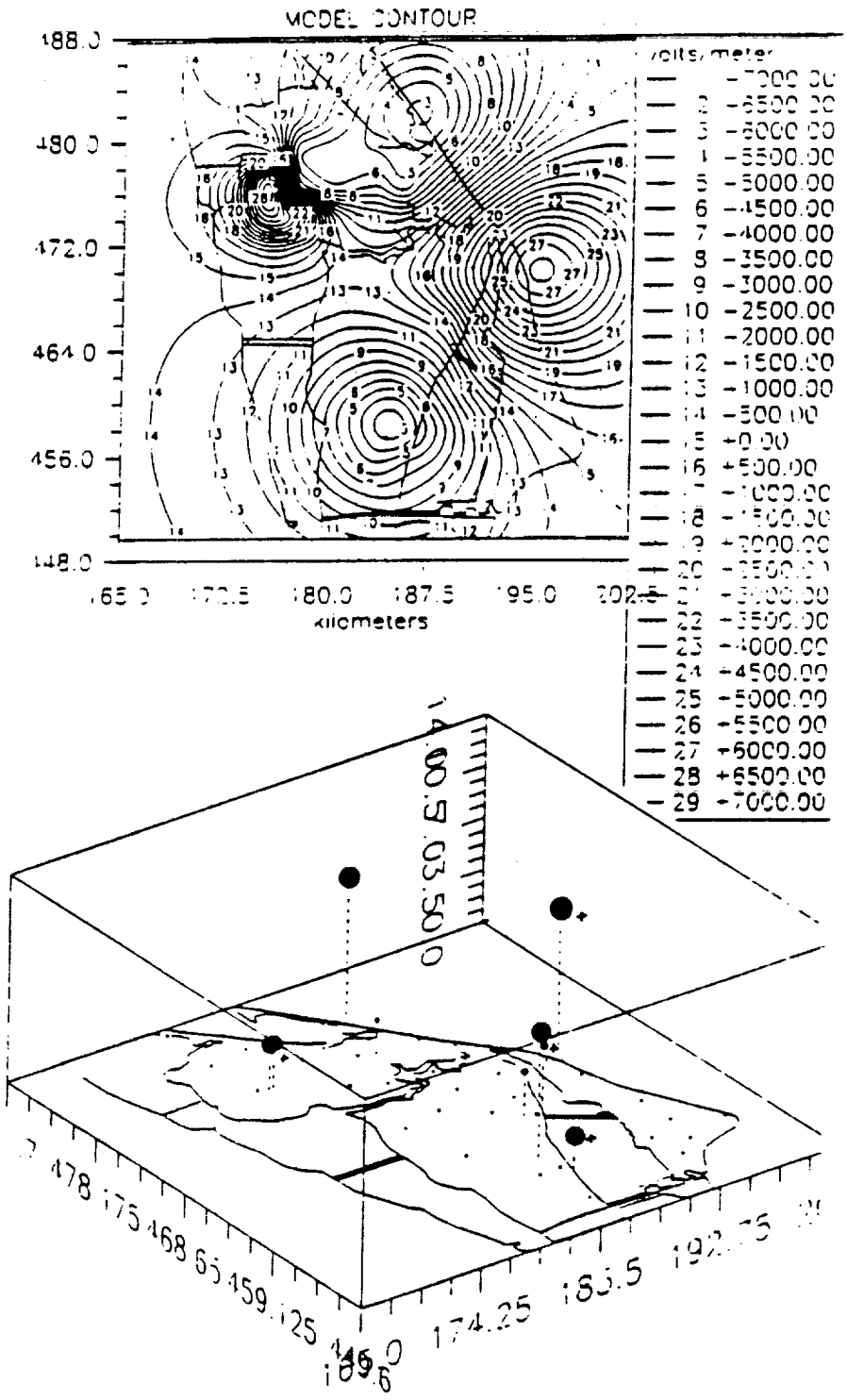

Figure 5. MODEL_D'S TMT_4010

Figure 6. VARIATION C Due to Reduced Mill Population
Data Sets: TMT-5000 through TMT-5006

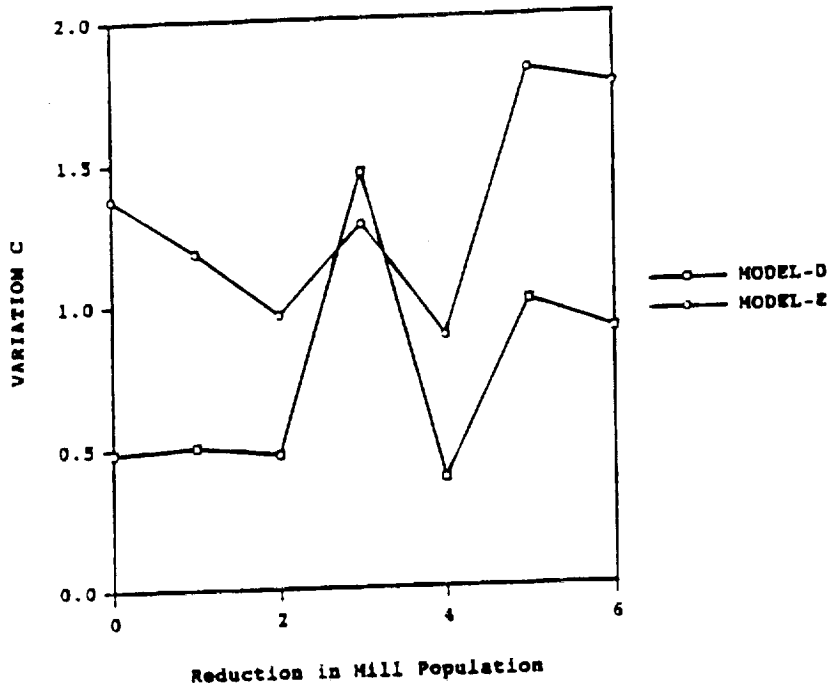

Figure 7. STORM-A and STRIKE-A
MODEL-E ENERGY ANALYSIS

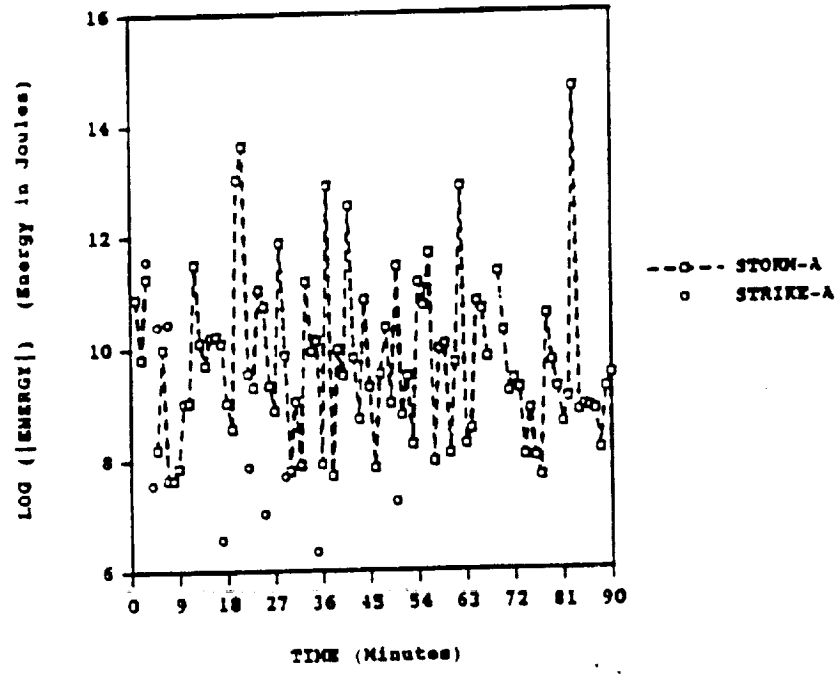

CONCLUDING REMARKS

5.1 ANALYTIC ANALYSIS CAPABILITIES

The analytic portion of the package functions well. Model_D and Model_E are able to establish model sets of charges based on field mill value and limiting constraints. This was accomplished for a wide variety of conditions. The system is able to deal with all calculational anomalies that occur for these conditions. This was verified by its ability to deal with data from a sets sampling actual and controlled situations. Both models demonstrated similar analytic capabilities.

5.1.1 MONOPOLES. The systems showed exceptional accuracy in determining the location and size of monopole charges. This ability was demonstrated repeatedly using controlled input data. This attribute makes the programs extremely valuable in interpreting field change. The system should be able to determining the sign, size, and location of changes in charge density associated with lightning strikes.

5.1.2 RESOLVING POWER. In tests on the ability of the charges to resolve two charges, distinct resolution was not achieved until a dipole separation of about 18 km was reached. Once resolved, the two charges in the control set were characterized with the accuracy demonstrated with monopoles. Until that point the system introduced additional charges. The distinction between the resolving power of the program and that of the field mill grid system was not established.

5.1.3 MODEL FIELD. The model fields generated by the system agreed favorably with input data when weighed against the reliability of that data.

5.2 GRAPHIC ANALYSIS CAPABILITIES

The graphics portion of the package demonstrated its utility as an aid in appraising data set. This was demonstrated when the gradual development of systems was considered as in the gradual resolution of dipoles and the quadrapole control systems. The graphics showed how the analytic portion of the program was sorting out information and the progress being made toward resolution of the poles. It also illustrated the systems dependence on a complete grid system for full information if resolution is to be achieved. As a consequence this portion of the package shows an ability to analyze grid systems.

5.3 RESEARCH AND OPERATIONS APPLICATIONS

The package verified that it is possible to formulate a charge distribution which corresponds to the source charges generating the input data. The strongest limiting factors in achieving a strong correlation between model and source are the

resolving power of the algorithm and that of the monitoring grid.
The programs and the techniques introduced can be used as a mechanism for addressing these limitations. Once accomplished the package can be used in research and operations as projected.

REFERENCES

1. Maier, Launa M., and Thomas R. Strange; Electric Field Mill Training Handbook; Computer Science Corporation; Kennedy Space Center, contract NAS10-11400; KSC-00005; 1988.

2. Jackson, John D.; Classical Electrodynamics; Wiley; 1969.

3. Sadiku, Matthew N.; Elements of Electromagnetics; Holt, Rinehart and Winston; 1989.

4. Rompala, John T.; Algorithms for Contours Depicting Static Electric Fields During Adverse Weather Conditions; 1991 Research Reports, NASA/ASEE Summer Faculty Fellowship Program; E. R. Hosler and M. A. Beymer, eds.; NASA-NGT-60002 Supplement 6; 1991.

5. McCracken, Daniel D.; A Guide to Fortran Programming; Wiley; 1961.

6. Chirlian, Paul M.; Introduction to Structured Fortran; Matrix Publishers Inc.; Portland Oregon; 1979.

7. Etter, D. M.; Structured Fortran 77 for Engineers and Scientists; 3rd ed.; The Benjamin/Cummngs Publishing Co. Inc.; 1990.

8. Uman, Martin A.; Lightning; McGraw-Hill, 1969.

9. Jacobson, E. A., and E. P. Krider; Electrostatic Field Charges Produce by Florida Lightning; *Journal of Atmospheric Science* , vol. 33, no. 1, pp 103-117; January, 1976.

10. Weems, J., N. Wyse, J. Madura, M. Seerist, and C. Pinder; Assessment and Forecasting of Lightning Potential and its effects on Launch Operations at Cape Canaveral Air Force Station and John F. Kennedy Space Center; International Aerospace and Ground Conference on Lightning and Static Electricity, vol II; NASA Conference Publication 10058, 1991.

11. Marcotte, R. A., and A. M. Mulvehill; Detecting and Interpreting Signatures within Electric Field Mill Sensor Data; report to NASA under a contract of Mitre Corp.; February, 1991.

1992 NASA/ASEE SUMMER FACULTY FELLOWSHIP PROGRAM

JOHN F. KENNEDY SPACE CENTER
UNIVERSITY OF CENTRAL FLORIDA

DEVELOPMENT OF A TASK ANALYSIS TOOL TO FACILITATE USER INTERFACE DESIGN

PREPARED BY:	Dr. Jean C. Scholtz
ACADEMIC RANK:	Assistant Professor
UNIVERSITY AND DEPARTMENT:	Portland State University Computer Science Department
NASA/KSC	
DIVISION:	Shuttle Project Engineering Office
BRANCH:	Process Integration Branch
NASA COLLEAGUE:	Arthur E. Beller
DATE:	August 21, 1992
CONTRACT NUMBER:	University of Central Florida NASA-NGT-60002 Supplement: 8

Acknowledgments

I would like to thank Dr. Loren Anderson and Ms. Kari Stiles of the University of Central Florida and Ms. Carol Valdes of the Kennedy Space Center for their efforts in making the NASA/ASEE Summer Faculty Fellowship Program an enjoyable and educational summer. I would also like to thank the many NASA, Boeing and Lockheed personnel who provided answers to a wide variety of questions, demonstrated software systems and provided hardware and software support. The list of names is too long to include here but without the expertise of all this work could not have been accomplished.

I would especially like to thank all the employees in the Shuttle Project Engineering Office for making me feel so welcome during the summer. Having a summer professor in this area was a first but hopefully, will not be the last.

Abstract

A good user interface is one that facilitates the user in carrying out his task. Such interfaces are difficult and costly to produce. The most important aspect in producing a good interface is the ability to communicate to the software designers what the user's task is. The Task Analysis Tool is a system for cooperative task analysis and specification of the user interface requirements. This tool is intended to serve as a guide to development of initial prototypes for user feedback.

Summary

The user interface is an extremely important part of software. Computer users today are not, in general, computer experts but experts in other domains who are dependent on computer software to facilitate their tasks. Developing interfaces for these users is an expensive and time consuming task. It is often difficult for the software developers to understand the user's domain well enough to come up with a usable interface. An iterative design process based on the concept of prototyping is becoming popular today. In this methodology a rapidly developed version of the software is used to obtain user feedback. This version lacks much of the eventual functionality and is used mainly to test out ideas the designers have about how the user interface should look. While the use of prototyping has proven to be valuable in the production of good interfaces, designers are still faced with the problem of developing initial prototypes and incorporating user feedback into the design of the interface.

This work presents a tool to be used in cooperative task analysis. End users and human-computer interaction personnel work together with the Task Analysis Tool to produce a task analysis and a rough sketch of an interface to support these tasks. The tool holds promise as a communication medium between end users and software designers. Better communication means fewer iterations in the interface design while still producing more usable interfaces.

Table of Contents

List of Figures

I. Introduction

1.1 The Design of User Interfaces

An important consideration in software development today is the interaction of the user with the software. This concern has emerged due to the changing nature of users of computer systems and the increasing complexity of current software systems. Today's users are not restricted to "computer hackers" ; they are, in fact, using software systems merely as a tool to aid in different aspects of their jobs. Therefore, the amount of time users have to devote to learning and using the system is limited, as is the amount of frustration they will tolerate. To add to this problem software systems are becoming increasingly complex. This presents a problem for both users and developers. Users often have a difficult time in accessing all the desired functionality. As the interface is essentially the view that the user has of a system, he must be able to clearly see through this interface to the functionality of the software (Shackel, 1988). Instead many of the systems today present a bewildering array of choices for the user. Developers are also faced with maintaining and augmenting complex code. The end result is that dealing with the software either as a user or developer requires a large amount of time and hence is a costly effort.

In order to address these problems an iterative process of software development is stressed. The underlying principle is that changes to the software are easier and less costly to make early in the development cycle. Prototyping is one way of collecting information from the user about the usability of the system early in the software design process (Wilson and Rosenberg, 1988). The user's view of a given software system is determined largely by the interface to that system. That is, system functionality that is not readily accessible in the interface is nonexistent as far as the user is concerned. The software interface should provide a good match with the task that the user must perform with the software. A prototype of the interface is often used to collect users' reactions and feedback to such things as terminology and arrangement of menu items, format of information presented and sequence of movement. This information is then quickly incorporated into the prototype and more user feedback is collected.

Boker and Gronbaek (1991) have studied the use of cooperative prototyping. They contrast this approach to one where designers develop prototypes on their own using information supplied by users. They view cooperative prototyping as a way to overcome problems in developing applications that more closely match user tasks. Initial prototypes are used to make the views of the participants concrete. Prototypes can be refined or replaced as users and designers actively participate in the design process. HCI (human-computer interaction) personnel in this approach need to become familiar with the tasks of the users. Initial prototypes are set up by the designers based on their understanding of the user's tasks. The authors found that both well constructed prototypes which display sample user data and mock-ups which allowed more flexibility in interaction were helpful in obtaining feedback. This approach still relies on an iterative method with the designers having the responsibility for construction of the initial prototype.

1.2 Obstacles to Iterative Design

This iterative procedure results in an interface that the user is pleased with and in timely feedback to the developers. There are, however, several obstacles to an efficient use of such a procedure in the real world. In many instances, software is developed on a contractual basis. This means that the product is agreed upon prior to any design. This agreement usually takes the form of written requirements based mainly on the functionality which the software is to provide. Specifications for the user interface usually do not exist, or if they do, they are merely platform and style specifications. In addition, the requirements are usually generated at the management level. The management level on the developmental side agrees to these. The actual software developers and the actual end users may or may not have participated in this interaction. Therefore, the interface produced often differs drastically from what the users may have expected.

Changes in design are difficult to make in this type of environment. Developers are often removed from the end users both organizationally and physically. Time constraints often make it difficult for the users to schedule large blocks of time or a series of sessions to work with the developers. Therefore, there is little chance for iterative development. Even when iteration exists, the necessary changes may not be incorporated due to the contractual agreement.

Large product development organizations also contain obstacles to user involvement as documented by Grudin (1991). Product development organizations are companies that develop and sell interactive software applications. The development process is separated into two parts: events prior to the start of the project and events during development. Although the time line that separates these processes is difficult to define, budgets and personnel are allocated according to these distinctions. The high level product description used in the early stage generally does not include the user interface despite the fact that it is difficult to draw a line between functionality and the interface. User involvement and interface issues are, therefore, issues that are addressed during development.

Moving some of this involvement to the design phase is a goal of HCI personnel. In Grudin's study rapid prototyping was found to be a useful tool in facilitating cooperative design. Moreover, the need to communicate information about computer use of the user directly to the developer was identified. Therefore, tools and methodologies that can be used to move user involvement to an earlier phase in the software development process are needed. Methods for developing and communicating user interface specifications to software developers are also greatly needed. The work presented here discusses a tool to accomplish this. This tool captures task analysis information directly from the end user and develops a rough initial prototype of the interface.

II. Task Analysis

2.1 Description of Task Analysis

Task analysis is a methodology for describing and analyzing performance demands made on the human element of a system. The goal of task analysis is a total human-machine system consisting of human performance requirements, hardware performance requirements and software performance requirements. Hardware and software requirements are much easier to obtain than are the human performance requirements and their interactions with the rest of the system.

The main objective of task analysis is to explore the relationships between the user's performance and the properties of the system. The focus is on designing a user interface to a system which is efficient and compatible with the view the user has of task performance. Design of dialogs in the interface is also a branch of task analysis. Maddix (1990) states that much dialog is based on an incomplete understanding of what kinds of interaction might take place between a typical user and the system. In doing task analysis the user's interaction with a given system is viewed with respect to the objects in the system and operations that the user performs on those objects. States in the system are changed by performing a sequence of operations on a series of objects. A goal can be described as a certain state within the system. This goal can be achieved by applying sequences of operations to objects in a given state. Guindon (1988) identifies these steps in task analysis:

1. Identify objects
2. Identify operations
3. Identify the sequence of operations used

The human constituents of a system are responsible for recognizing and interpreting states produced by the hardware and software systems. If these states have not produced the desired goals then it is necessary for the human to interact with the software to produce this state. Human error in carrying out these functions can not be completely eliminated but providing systems that are well matched to the users' tasks help in reducing the margin for error.

Don Norman(1986) identifies the gulf of execution and the gulf of evaluation in human-computer interaction. The gulf of execution results when the user is unable to correctly select the necessary sequence of operations to perform in order to produce the desired goal. The gulf of evaluation results from an incorrect interpretation or recognition of the state produced by a sequence of operations. The user bases this interpretation on the feedback produced by the system. The gulf is created by the difference between the user's view of what is happening and what is actually happening in the system. This distance is reduced as the user's view more closely matches the system view. Therefore, the interface and, consequently the dialog, between the user and the system must be the vehicle that maps the user's task into the functional components provided by the software.

A task analysis can be used to provide data about the user component of the system. The major problem then becomes how to map this task analysis data into an interface description that can be used to guide software developers in system design and

implementation. The data produced by a task analysis can take many forms depending upon the purpose for which that data was collected. In the case of this work, the concern is with the user interface so the task analysis will focus on interface items such as data displayed, format of the data, actions or operations on that data and the sequence in which the tasks are performed.

2.2 Obstacles In Performing Task Analysis

In order to produce a task analysis human-computer interaction personnel need to observe the user carrying out the task and to identify the objects, operations and sequences used. Additionally, in carrying out a task analysis for development of a software system, one must keep in mind that the current task will be changed by this automation. This means that the present task analysis must be examined to ascertain the effects that automation will have or that flexibility will have to be built into the system to accommodate future changes in task performance.

Many tasks involve a cognitive aspect. Users choose objects and operation in the system based on domain knowledge. In order to produce an effective interface it is necessary to understand these decisions. As the domains become increasingly complex this presents a larger obstacle to carrying out representative task analyses. Either the human-computer interaction person needs to learn the domain or the domain experts need to learn how to do task analysis.

In addition, domain experts often have difficulty in explicitly stating portions of their task. Portions of any expert's job become routine after a period of time and these routine cognitive tasks become difficult to verbalize. The human-computer interaction personnel is therefore responsible for recognizing missing portions and probing further to extract this knowledge from the expert. This puts additional demand on HCI personnel to understand the domain.

III. The Task Analysis Tool

3.1 Objective of the Task Analysis Tool

The main objective in the development of a tool to use in task analysis is to facilitate communication between the domain expert, HCI personnel , and the software designer. The following is a quote from Walsh, Lim and Long (1988):

> *"Human factors engineers complain that their contribution to iterative systems design is typically sought late, that is following system implementation. Software engineers, in contrast, complain that the human factors contributions to system design are neither timely, appropriate nor implementable. "*

The Task Analysis Tool (TAT) is designed to be used interactively by the domain expert under HCI supervision. Data collected during an interactive session will be analyzed by HCI personnel and given to the software designer to user as a guide to design of the interface. The data collected is saved in two forms: textual information that can be analyzed later for consistency issues within and between interfaces. Additionally, and more importantly for the user, a rough sketch of the interface is generated as information is entered. These screens can then be played back by the end user to help ensure that the displays give complete information in order to accomplish the given task. The Task Analysis Tool can serve as a useful tool to help the end user form a concrete description of his task. As visual feedback is provided immediately the user can match these results to his conceptual model. Corrections can be made to the interface sketch if the user finds that it is incorrect.

The fact that a rough sketch of the interface is produced serves to give a version to the user that is easier to survey for completeness than lists of functional requirements. The rough sketch can be used, in addition to functional requirements, to drive design. Having this sort of information at an early stage of design should mean that a better prototype can be initially developed. This serves in cutting down on the number of iterations that will be needed in obtaining user information. When given to the software developer this rough interface design serves to illustrate the control flow that the user follows. The task analysis tool is also a vehicle for agreement of expectations between users and developers.

3.2 Information Collection in the Task Analysis Tool

There are many definitions of tasks but a general agreement is that a task is composed of a set of human actions that contribute to some objective and ultimately to the output goal of a system. The content of a task can be more specifically defined once the objective of a task is identified.

Drury, Paramore, Van Cott, Grey and Corlett (1987) give the following characteristics useful in defining tasks :

"1. Task actions are related to each other not only by their objective but also by their occurrence in time. One of the concerns of task analysis is to establish and evaluate the time distribution of actions within and across tasks. Task actions include perceptions, discriminations, decisions, control actions, and communications. Every task involves some combination of these different types of cognitive and physical actions.

2. Each task has a starting point that can be identified as a stimulus or cue for task initiation. A cue is often not a single item of data or information. It may consist of several data points, received closely in time or dispersed over a longer time, which together have significance as a cue that an action is to be taken.

3. Each task has a stopping point that occurs when information or feedback is received that the objective of the task has been accomplished.

4. Task cues and feedback may be provided by instrumentation or direct sensory perception, or they may be generated administratively, say, by a supervisor or co-worker.

5. A task is usually, but not necessarily, defined as a unit of action performed by one individual."

The Task Analysis tool captures much of the information deemed characteristic of tasks. Some of this information is included in the sketched interface while other portions of it are included in the data file produced.

Tasks are of three types: discrete or procedural, continuous or tracking, and branching. Discrete tasks require that a series of actions be executed in response to a stimuli or procedure element. A continuous task extends over a long period of time, often cycling through a series of actions. A branching task is determined by the outcome of a certain action within the task.

The prototyped version of the Task Analysis Tool is most useful for discrete or procedural task and continuous tasks. Branching tasks cannot currently be handled but the addition of multiple path links will support this. The example presented in this paper contains an instance of a branching task. Therefore, a link that currently exists in the example might, in reality, not appear.

3.3 Status of the Task Analysis Tool

The Task Analysis Tool (TAT) currently exists in a prototyped version. While there are many features that have already been identified for addition into the system, this prototype should illustrate the usefulness of such a tool. Features suggested for inclusion in a developed version are discussed in section V.

TAT is designed to operate as two side by side displays. The screens that collect information constitute one set of displays. These are presented beside of the interface being sketched. The prototype of TAT was created using Toolbook by Asymetrix (1989) under Windows 3.1.

The figures that are included in this paper were printed using the print facilities of Toolbook. Unfortunately, menu bars do not print out. Therefore these have been separately constructed and included in figures where needed to illustrate the functionality of TAT. The operable version of TAT , therefore, looks slightly different than the version depicted here. In addition, Toolbook does not include the capability to print out dialog boxes. The example indicates which buttons are dialog boxes and describes the choices that are presented. In addition, the sizes of the displays have been adjusted slightly in the printed version in order to accommodate difference in the type size displayed on the screen and the printed type size.

A data file produced from a session with TAT contains information about the task, actions, information displayed and sequencing. Ideally this data could be examined to help in designing interfaces that will accommodate several viewpoints. Moreover, if several applications are to be used concurrently, examination of the data could be used to suggest commodities that should be considered in designing a common user interface. The current file produced is a labeled ASCII file. An example of this data file is included in Figures 14 and 20 and discussed more in section IV.

3.4 Description of the Task Analysis Tool

The Task Analysis Tool asks the user to identify the different tasks used to carry out a given process. These tasks are input as menu items in the constructed interface. A display is created for each discrete task. Figure 1 shows the initial display that is used to collect information about the names and numbers of tasks that makeup the process. Currently, the prototyped version of TAT allows only eight tasks per process. Figure 2 shows the complete set of forms that would be displayed if the user had indicated that eight tasks constituted this particular process. The user is asked to enter the tasks in some sort of meaningful order - either sequentially or in order of frequency of use. This is due to the order in which the items are entered into the menu of the sketched interface.

For each task, a display is presented (see Figure 3) that collects the information to be viewed and the type and format of the information. A task allows for two primary information sources, two secondary information sources and four status indicators. Each task can have up to six actions that are carried out on the information displayed. These actions are presented as sub menu items under the task menu item. The information that the users specifies is to be on the display is roughed out and presented according to the importance (primary, secondary or status) that the user assigns to the information.

Control flow in the system is represented by users specifying the tasks that precede and succeed the current task. These tasks are presented to the user in a dialog box that is constructed using the task names initially input on the first display in TAT. In the interface begin generated the displays for these tasks will be linked in the corresponding fashion so that the user can later play this back to assess if the flow accommodates the process correctly.

Figure 4 contains a template on which each interface display is sketched. For each new task in the process, this page is filled in with information collected from the user.

Figures 5, 6, and 7 are examples of help screens that are provided with TAT. The prototyped version contains no error handling capabilities. Although error detection and more help information will be included in the actual implementation of the software,

more help information will be included in the actual implementation of the software, TAT is intended to be used under the guidance of HCI personnel.

Figure 8 shows the screen that TAT displays when the user has finished typing in the information. At this point in time, the user can exit the system or can run the sketched interface to determine its correctness. If the user chooses to exist at this point, the interface will be saved and can be run later. The name of the data file selected by the user will also be displayed on this screen.

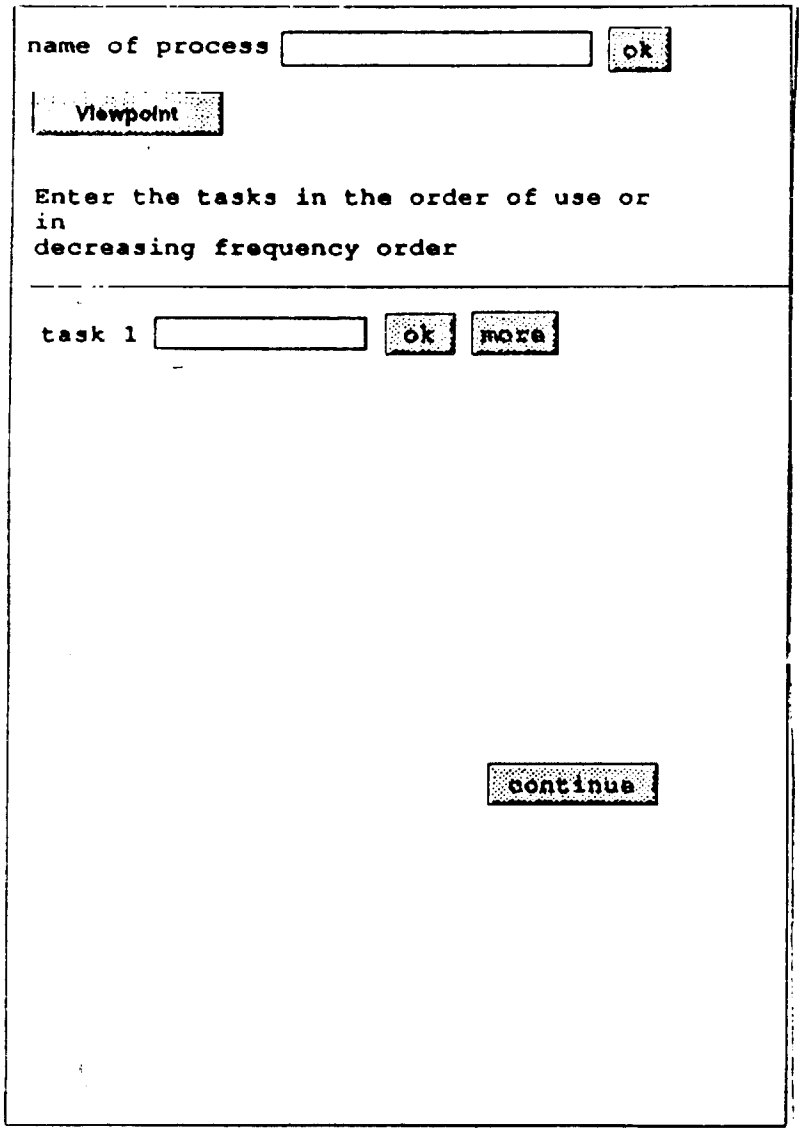

Figure 1: Initial Display of TAT

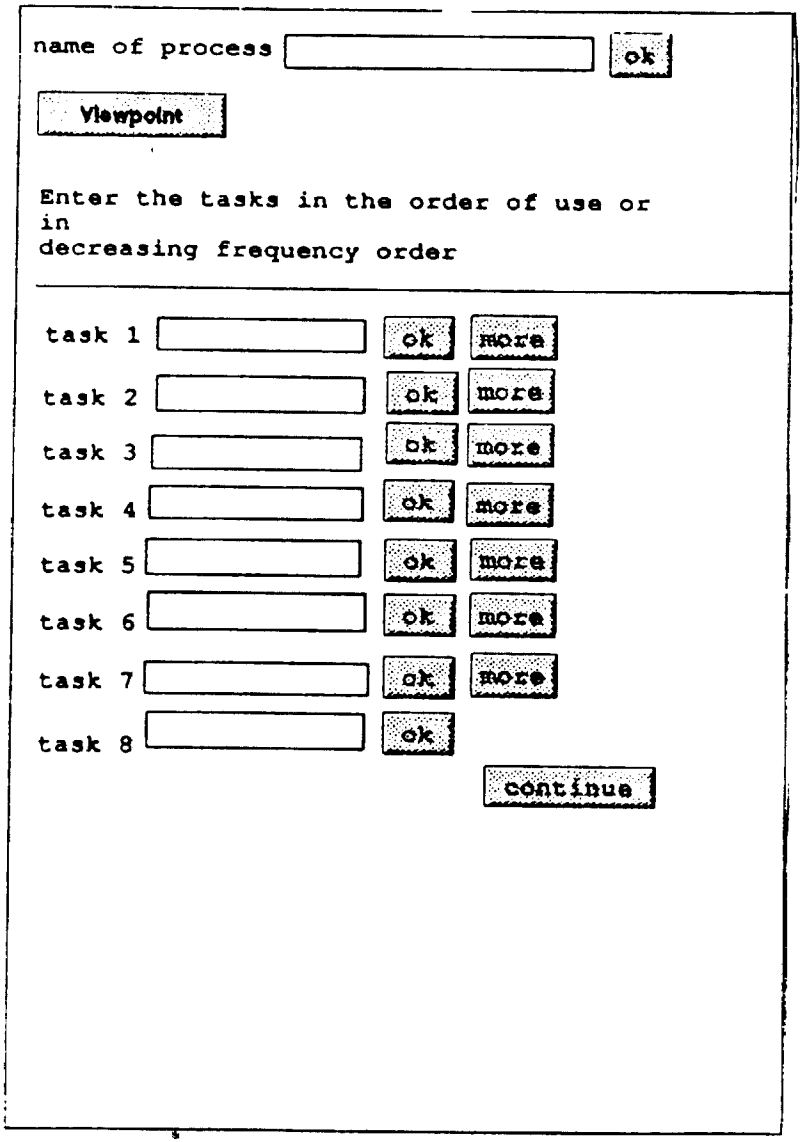

Figure 2: Initial Display of TAT Fully Expanded

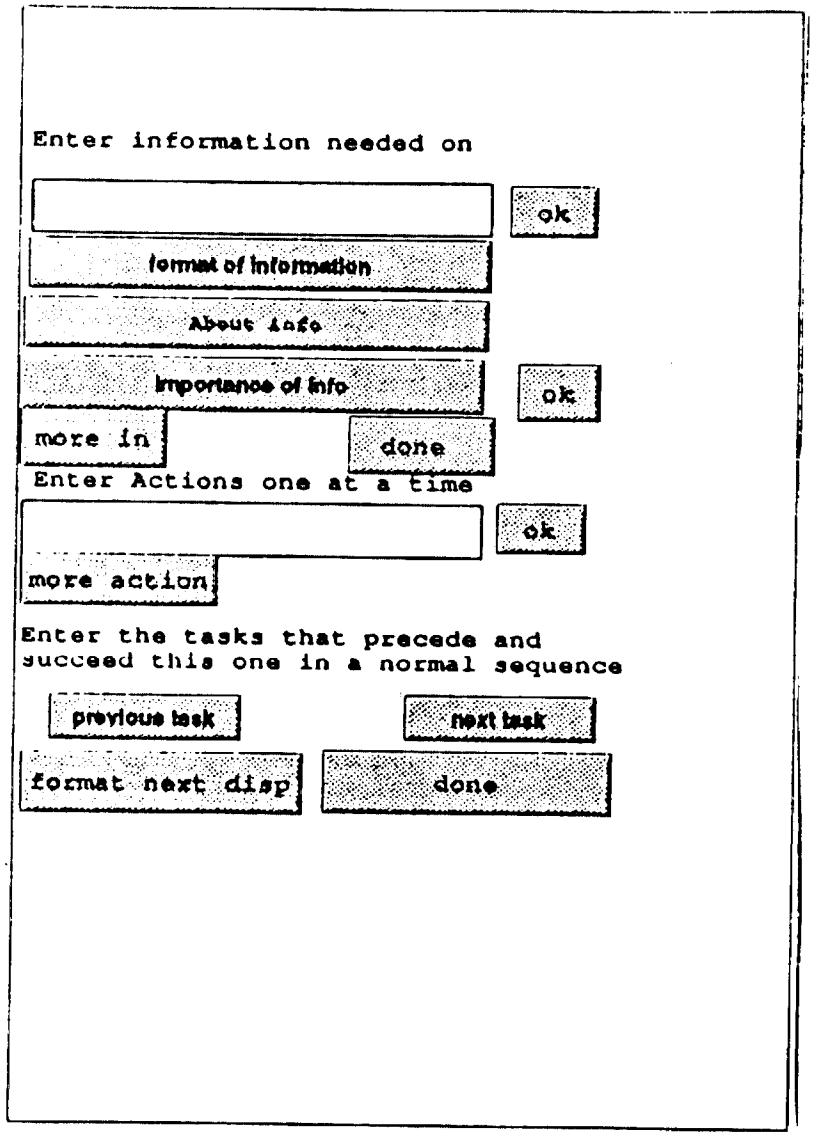

Figure 3: Information Collection Display of TAT

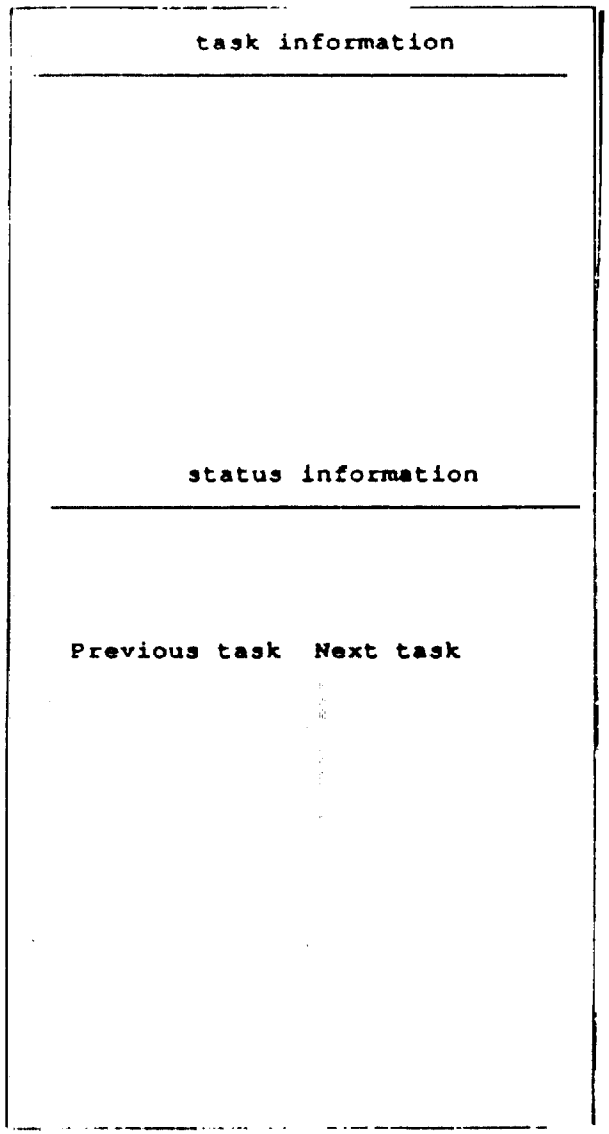

Figure 4: Template for Interface Sketch

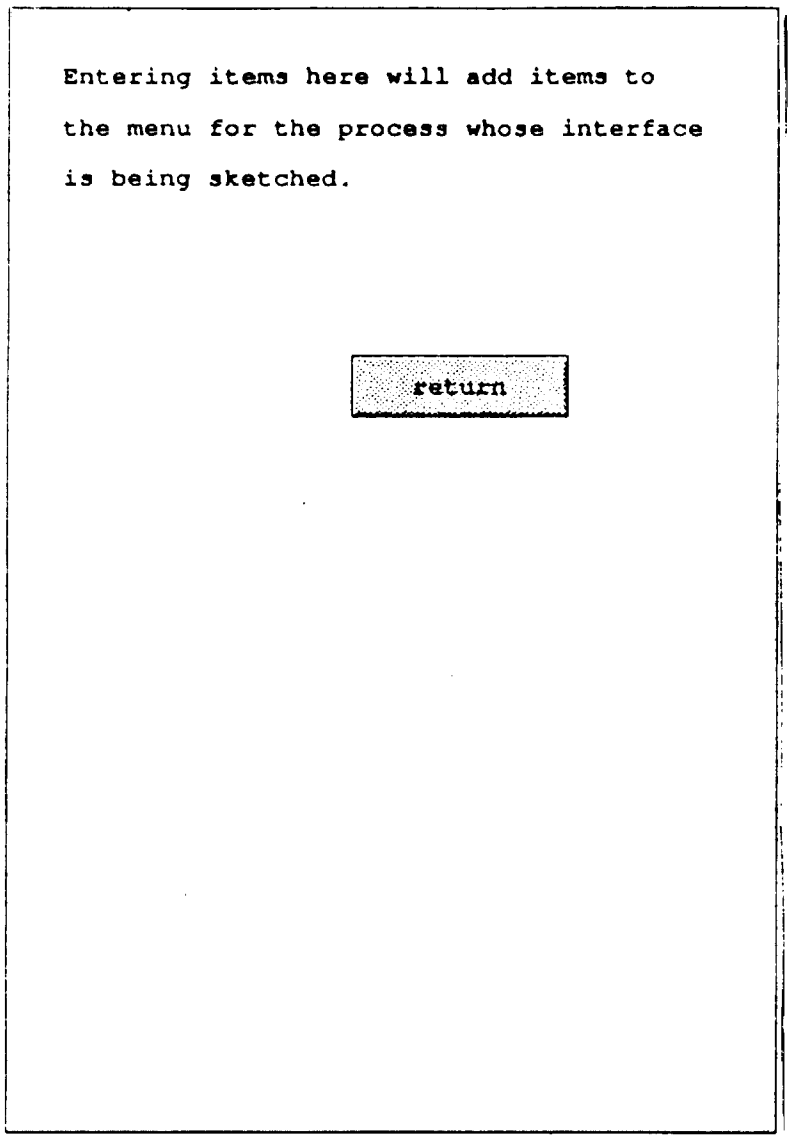

Figure 5: TAT Help Screen

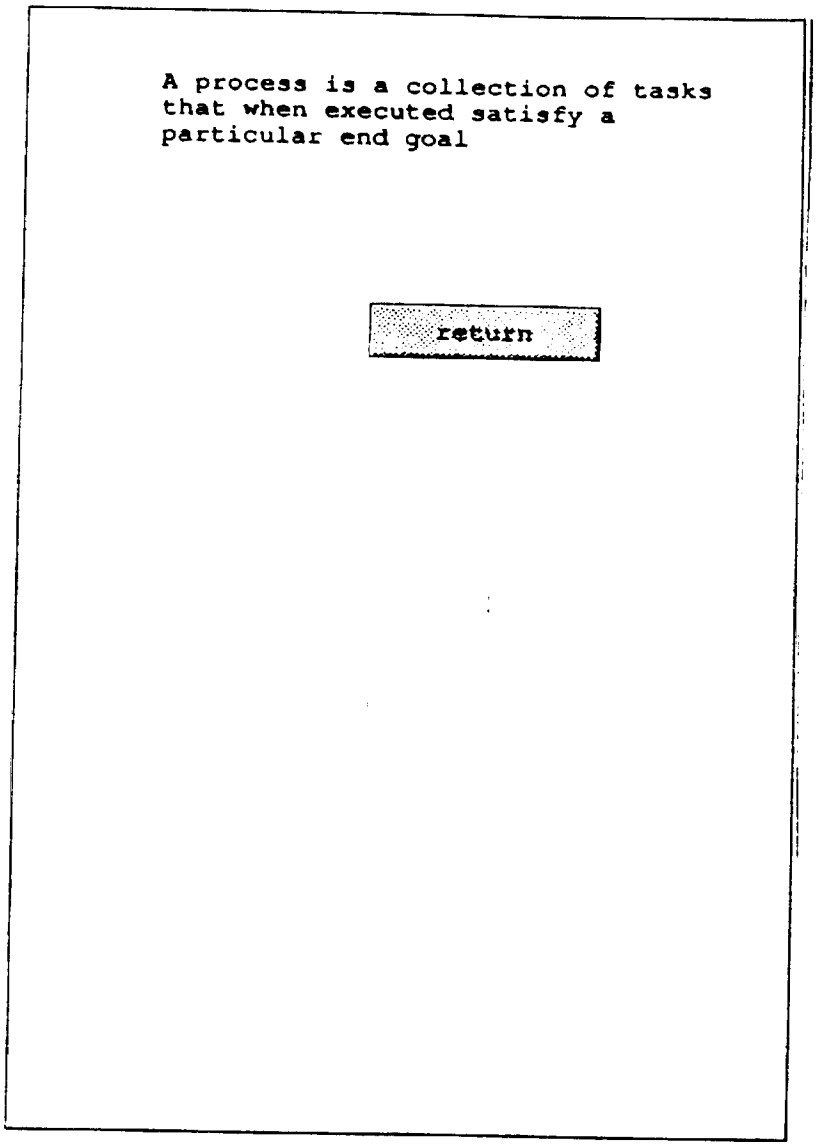

Figure 6: Another TAT Help Screen

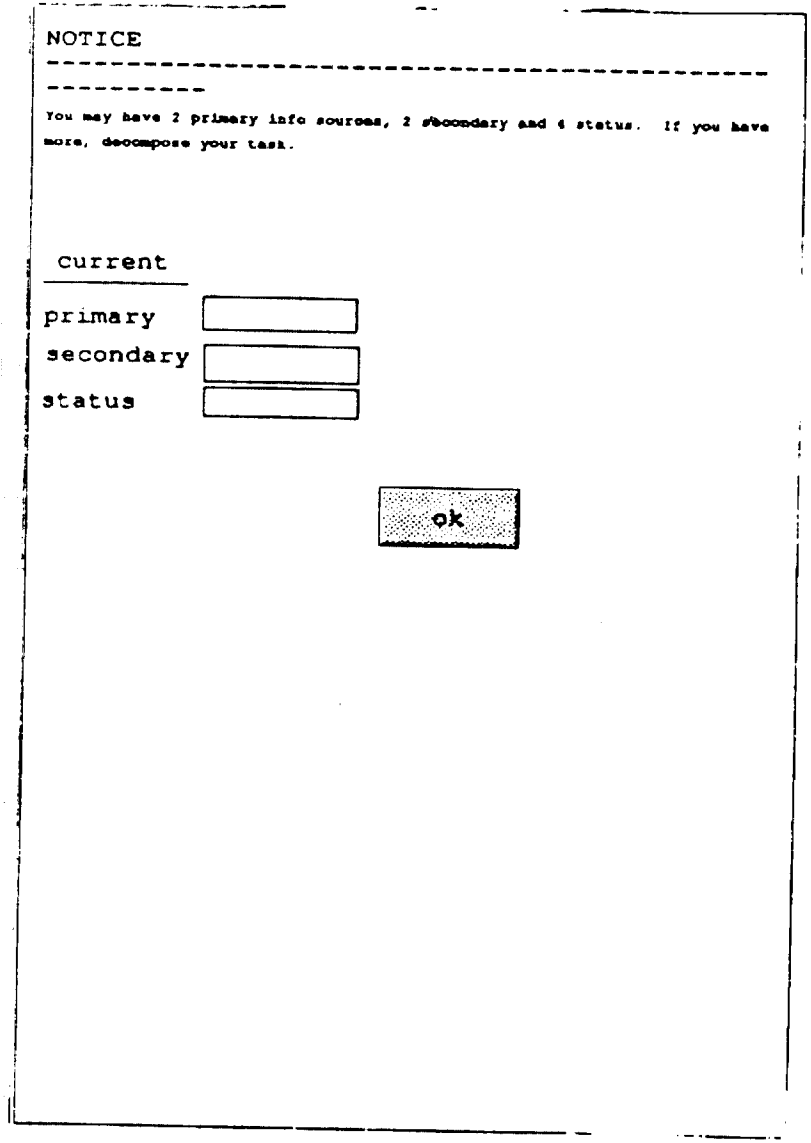

Figure 7: TAT Display for Information Types

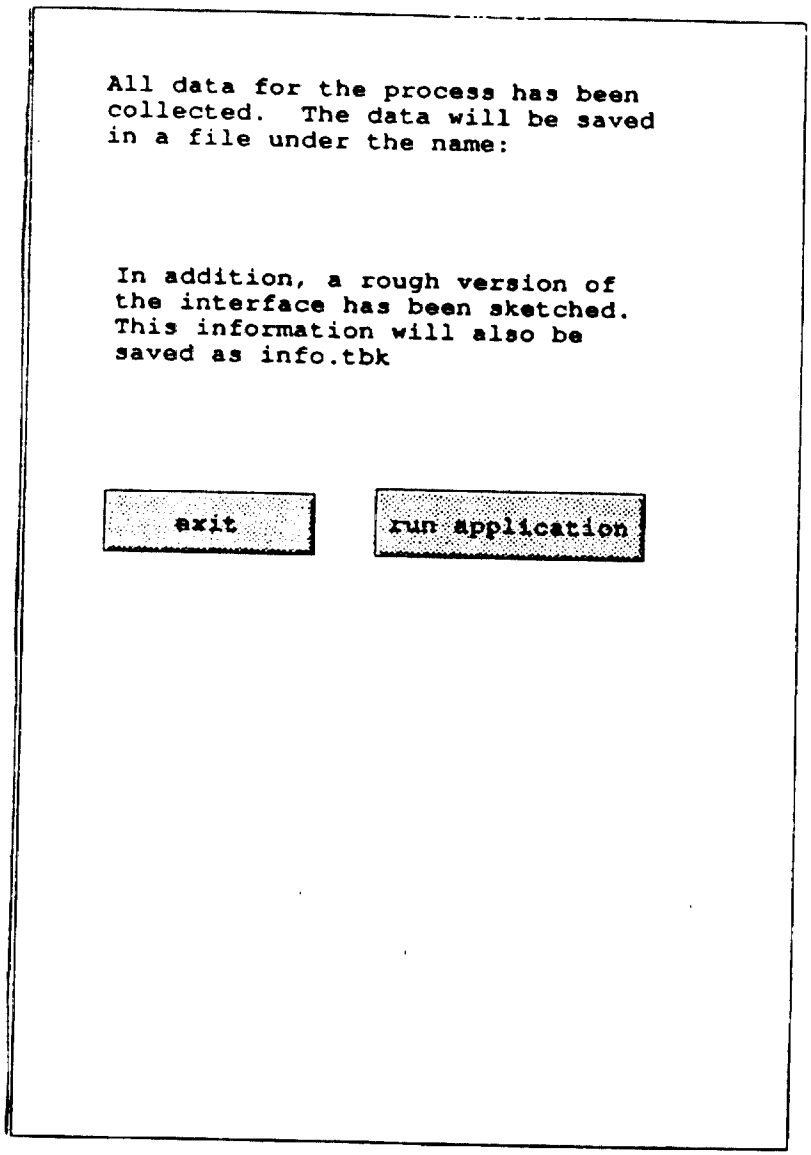

Figure 8: TAT End Display

IV. Example of the Use of TAT

4.1 Description of the Example Task of Electronic Review and Approval

The example presented here is an interface sketch for doing electronic review and approval. The following sections discuss the electronic review and approval process, the example, and an informal collection session using an early paper version of TAT.

In order to make changes to processes in the Shuttle Processing Environment at KSC, change requests must be generated and approved by the systems that are affected. Changes are done at various times before and during any given flow and range in size from large volumes of documentation to changes to a single operation or a change in sequence. A revision to a document is generated by selecting the portions of a master document that are to be used in this particular shuttle flow. Revisions include any changes that were generated previously to operations included in this flow. After a revision has been produced, changes that are made are termed deviations. A deviation may be a change in sequencing or a change to an individual step or steps. Deviations may be temporary. That is, the change is made only for this flow. A permanent deviation means that the change should be incorporated into this operation for all succeeding revisions. Currently these changes (revisions and deviations) are generated by engineering personnel and distributed to NASA personnel and other engineering teams for review and approval.

The review and approval process consists of suggesting changes to the text if necessary, making comments as appropriate or approving the change. During this process a reviewer may wish to see the comments or changes that other reviewers have generated. This procedure is an iterative one as comments and changes may need to be incorporated into the change and the change again distributed to the reviewers.

A computer based version could speed up the process. Reviewers could be notified electronically that a change was ready for review. The individual or group who initiated the change would be able to distribute it to the reviewers without having to either mail or hand deliver hard copies to the various individuals. Comment and changes made by the reviewers would be sent back electronically and could be directly incorporated into the change description. Reviewers would be able to quickly view other comments and the status of the change could be tracked electronically.

4.2 Example of the Process used to Sketch an Interface

The TAT example presented here uses the electronic review and approval process. Two interfaces are sketched here. These interfaces are from two different viewpoints: from the view of an engineering generating the change and from the point of view of a NASA reviewer. The software interface generated must support both views. Soliciting information from both viewpoints will yield data on commonalties that exist and the different emphasis that exists for the different views.

The first viewpoint presented is that of the reviewer. Figure 9 contains the initial information collection display. The name of the process input by the user is used to name the data file that will contain the information collected. The three tasks in the review and approval process are : select, review and approval. As these tasks are

entered by the user, these names appear in the menu bar of the sketched display. This is illustrated in the menu bar of the template for the interface sketch. In addition, a blank display is created on which the interface for each will be sketched. The viewpoint button is a dialog box which queries the user as to his position. In this case, the choices are : engineer, NASA, quality, NASA Test Director, documentation, and other.

Figure 10 contains a portion of the information collected for the task review. Figure 11 contains the interface generated by TAT that corresponds to the data entered in Figure 10. The first field on the display in figure 10 collects of the name of the various sources of information needed on the display. The format of information button is a dialog button that queries the user as to the way information is presented. The choices currently display in this dialog box are graphical, text, labeled data, tabular data and schematic data. The about info and importance of info buttons are a pair. The importance of info is a dialog box that asks whether the user considers a particular piece of information to be of primary or secondary to the task at hand. A third option would be to view the information as status only. TAT contains parameters which limit the number of primary, secondary and status pieces of information that can be concurrently displayed. The limitations in place now are rather arbitrary. In any given domain better limitations could be selected depending on display size , screen resolution and frequency and duration of use. The about info button is linked to a display (see Figure 7) that keeps track of the number of different information types presently selected for a given display. When the importance of information choice has been made and the OK button pressed, a labeled box will be drawn on the interface sketched. The size of the box will differ depending on whether the importance is secondary or primary. The box is also labeled as to how the data will be presented. Status only information appears as a button. If the user wished to enter more information sources, pressing the more info button clears the text field and focuses the cursor there.

When all the information sources have been entered, the user is prompted to enter actions that will be performed. These actions are entered as sub menu items. In order to see these, the user must highlight the task menu item in the sketched interface. The previous task and the next task buttons are dialog buttons that present the user with the list of tasks he has identified as being in this process. In the case of previous task, the list is augmented with start and in the case of next task the list will also contain end. Selecting a choice from these dialog boxes will result in a previous task and next task button being drawn on the interface sketch and in those buttons being linked to the correct display. This facilitates running the application. By pressing the previous or next task button, the user can simulate stepping through the process.

Pressing the format next display button brings up a blank information collection screen for the next task (in the order originally entered by the user on the first display) and a blank template for the interface sketch. After the information has been filled in for all the tasks in the process, the users can select the done button. Several things will then happen. First, information collected will be written to the specified data file. Then the user is asked whether he wishes to run the application just created. If he chooses not to, he can always retrieve this later from the "info.tbk" file and execute it.

Figures 12 and 13 are additional displays generated for the tasks of selecting items to review and approving or rejecting the changes. Figure 14 contains a portion of

the data file that was generated during this session. It contains information about the tasks, the information sources, the actions and the sequence of flow.

Figure 15 shows the initial display that was used to collect the tasks from the engineer's viewpoint. Notice that a task labeled create now exists and is used to initiate the change. In addition a release task exists where notification about an approved change and its incorporate into the master file is accomplished. Figure 16 is the display generated for the task of creating a change.

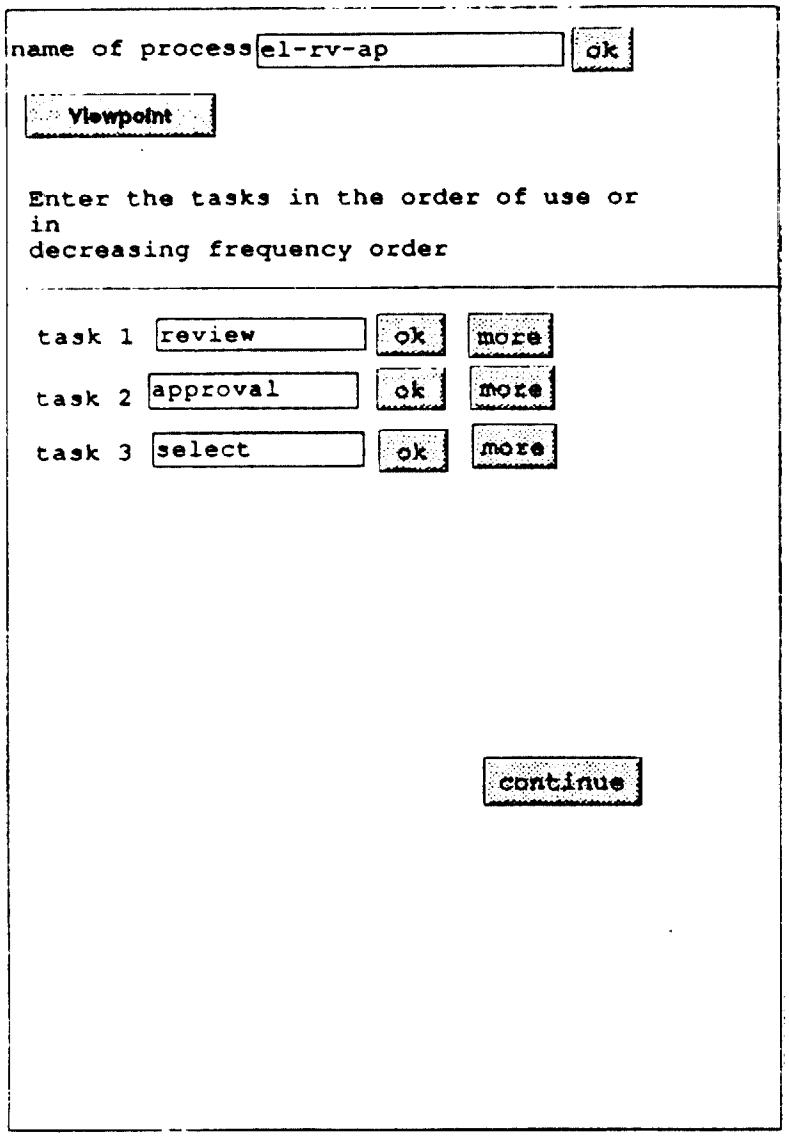

Figure 9: TAT Display for Example and Blank Template for Interface Sketch

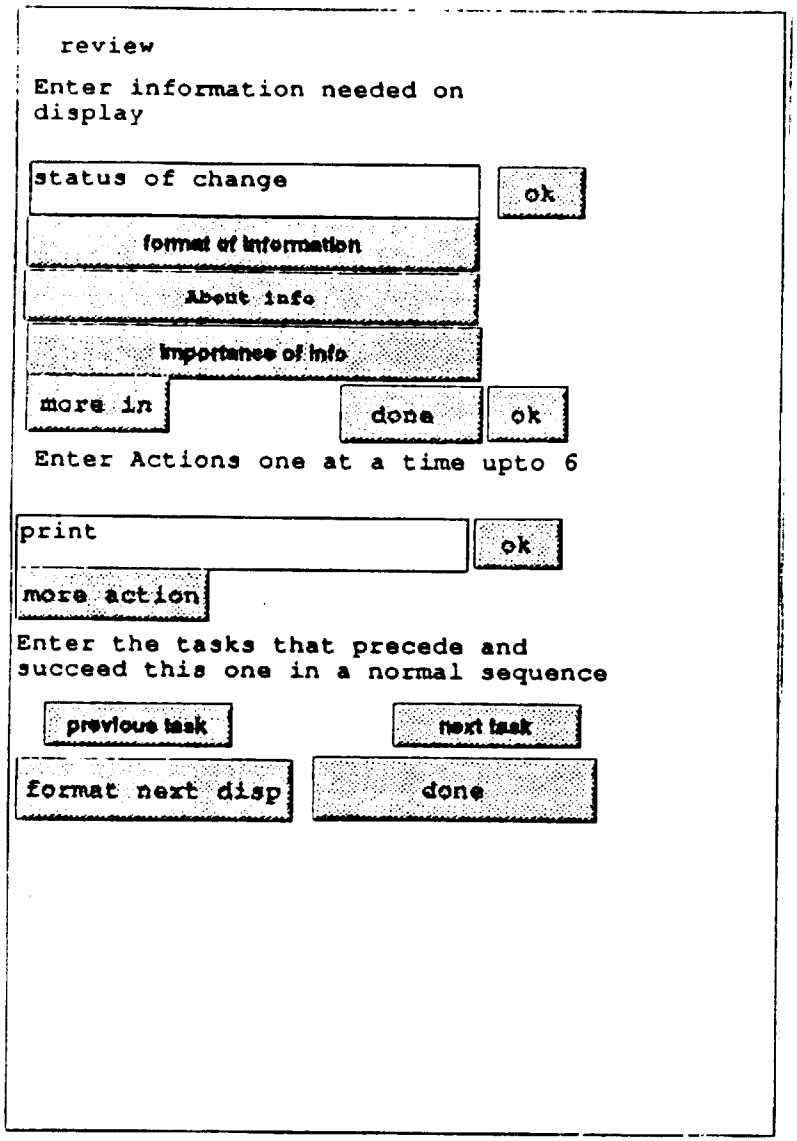

Figure 10: Information Collection Display from TAT for Task "review"

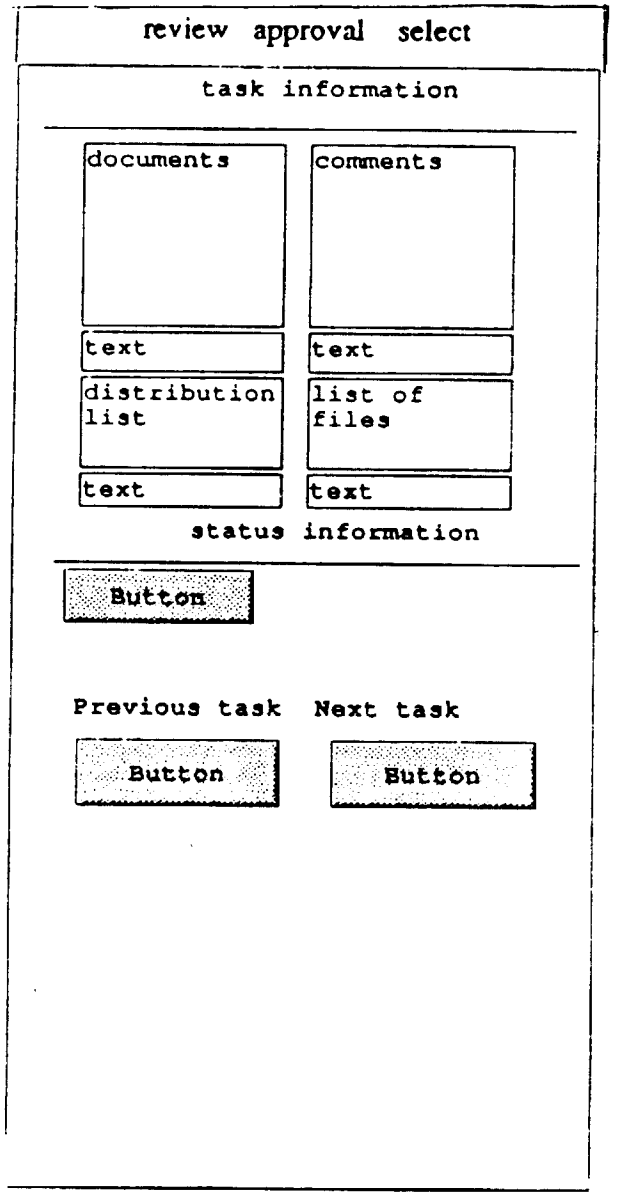

Figure 11: Sketch of Display Generated for "review"

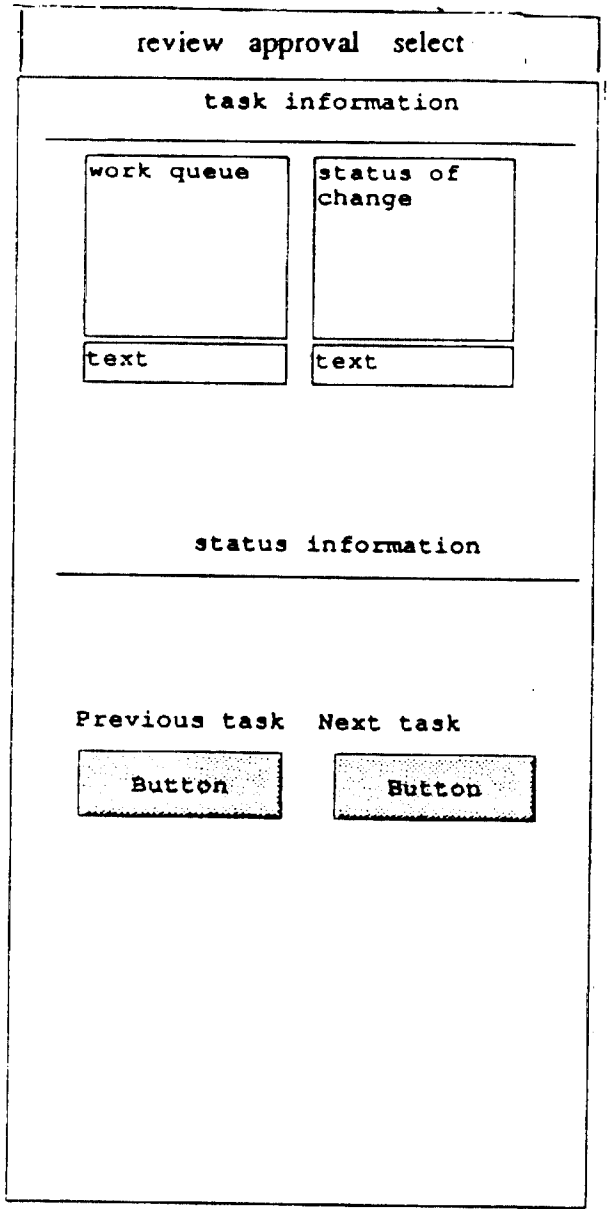

Figure 12: Sketch of Display Generated for "select"

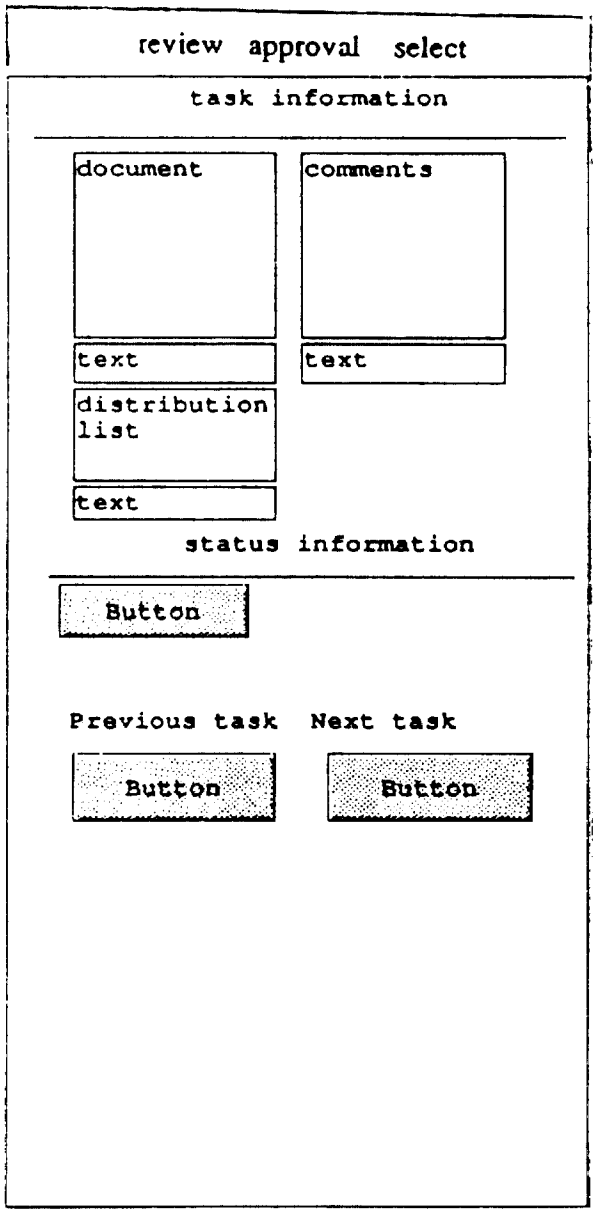

Figure 13: Sketch of Display Generated for "approval"

```
The process being described is:el-rv-ap
this process if from the viewpoint of:NASA
task1 in this process is:review
Task2 is :approval
Task3 is :select
the current task is:review
this information is needed:documents
the information is to be presented as:text
the importance of this information is primary
the current task is:review
this information is needed:comments
the information is to be presented as:text
the importance of this information is primary
the current task is:review
this information is needed:distribution list
the information is to be presented as:text
the importance of this information is secondary
the current task is:review
this information is needed:list of files
the information is to be presented as:text
the importance of this information is secondary
the current task is:review
this information is needed:status of change
the information is to be presented as:text
the importance of this information is status only
the following actions are performed on this info:redline
the following actions are performed on this info:comment
the following actions are performed on this info:distribute
the following actions are performed on this info:display
the following actions are performed on this info:save
the following actions are performed on this info:compare
the following actions are performed on this info:print
the previous task is:select
the task that follows this one is:approval
the current task is:approval
this information is needed:document
the information is to be presented as:text
the importance of this information is primary
the current task is:approval
this information is needed:comments
the information is to be presented as:text
the importance of this information is primary
the current task is:approval
this information is needed:distribution list
the information is to be presented as:text
the importance of this information is secondary
```

Figure 14: Portion of Data Generated for Review and Approval Process

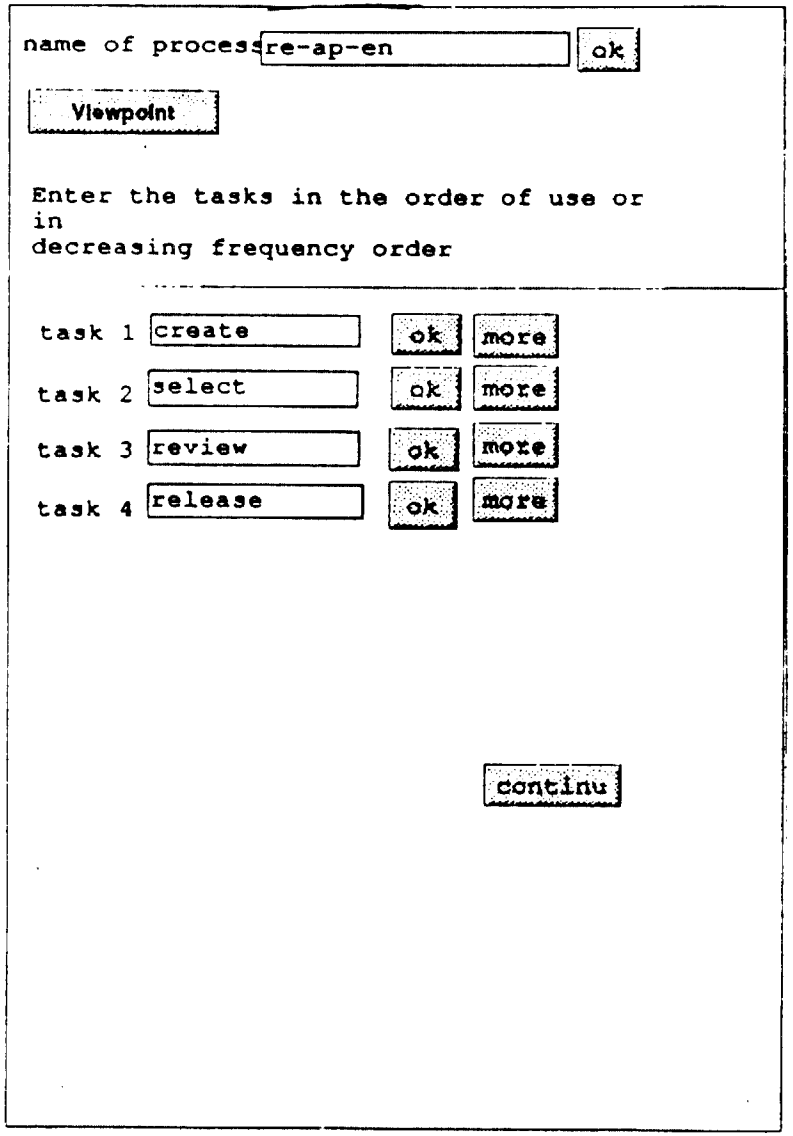

Figure 15: Viewpoint 2: Review and Approval from Engineering View

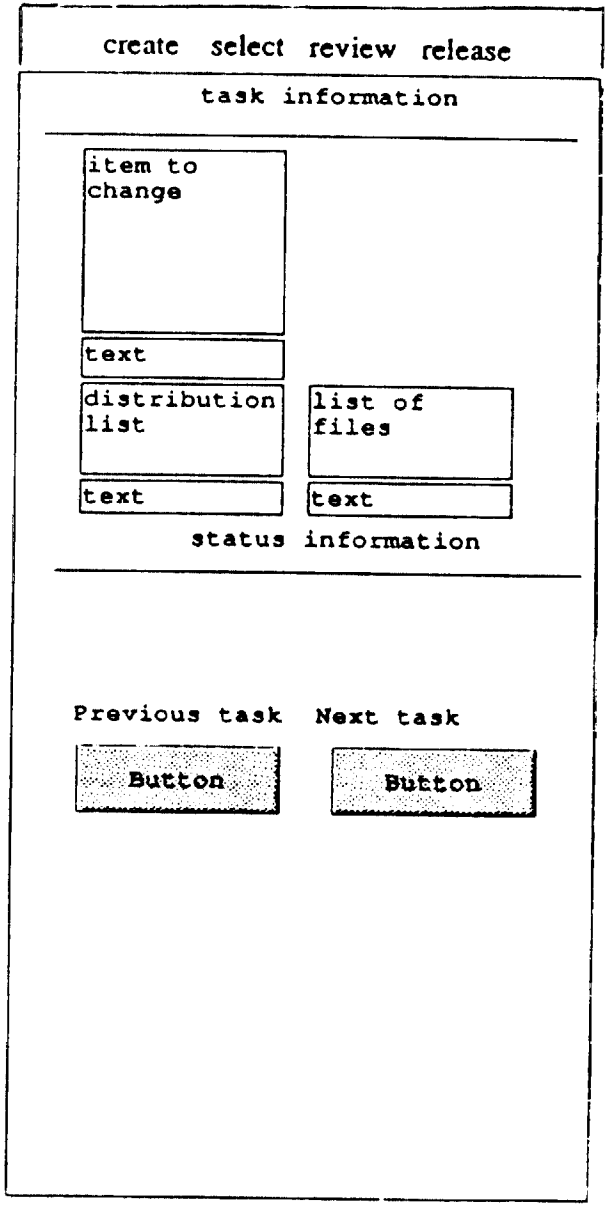

Figure 16: Viewpoint 2: Sketch of Interface for "create"

V. Future Plans for Testing and Using TAT

5.1 Uses for TAT Output

As was previously stated, the TAT output is meant to serve several purposes. First of all, the sketched interface serves to give a more concrete aspect to the task analysis in a form that is easily understood by the user. Using this sketch, the user should be able to assess it for completeness and correctness. The interface could be used in a representative scenario of the process which the user could work through. This sketch should accompany functional requirements given to the developers to facilitate design of the user interface.

Analysis programs could be written to scan the data files generated. This would be particularly useful in the case where several viewpoints are being examined or where several applications are to be run concurrently. The data files can be examined to see conflicts and commonalties in information sources and presentation methods. In particular, common tasks or similar tasks should possess similar actions. Consistency in interface design has been recognized as beneficial to success of software companies (Tognazzini, 1989). Consistency in presentation and actions can be analyzed using the TAT data files.

5.2 Additions to TAT

The prototyped version of TAT is a very rough version. There is much work yet to be done on determining what kinds of information should be collected. Information about feedback desired from a given action seems a likely candidate as does information on the frequency and duration of the task. In order to determine the completeness of information collecting in TAT it will be necessary to try it out in many different domains.

5.3 Functionality Needed

There are many functions that need to be included in a coded version of TAT. The functionality of the current version is limited due to the nature of the prototyping tool used to implement it and the time limitations during which TAT was constructed. Functionality that is seen as needed includes:

1. The ability to display labels on status buttons and task link buttons in the interface sketch.
2. The ability to link up tasks in multiple paths.
3. The ability to save and display sub menu items in the interface sketch. Currently this information is saved in the data file but once the interface sketch is closed, they do not appear in the saved sketch.
4. There should be a way to associate actions with a particular piece of information. This type of knowledge could be useful if deciding to break the task into several displays in the final design of the interface.
5. The user should be able to easily change the choices displayed in the dialog boxes on viewpoint and information type. These choices are

dependent on the domain in which TAT is being used. In addition the user should be able to easily change the parameters concerning the number of tasks and information sources.

5.4 An Initial Test of TAT

The information used in generating this example was produced mainly from informal interviews with personnel involved in Shuttle Flow Processing. This was due mainly to the limited time frame for development of the prototype. However, a paper version was used in one instance to obtain information about the review and approval process. Several observations were made during this process. First, a new step in the review process, that of comparing initial changes and comments to the newly distributed change, was identified. Perhaps this step would have eventually been discovered through further interviews but having to simplify one's thoughts about the task and flow seemed to clarify the process.

The ability to be able to distribute the change to a person other than the originator was identified as was the capability of seeing which jobs were currently being worked when reviewing changes.. While TAT does not currently capture all this information it is rewarding that using this approach elicited this information. This suggests that using TAT along with note taking or audio/video recordings would be a beneficial approach.

5.5 Testing

In order to determine how useful TAT is, it must be used in the development of several prototypes and these compared to the prototypes developed without this tool. In addition, it needs to be determined what kinds of analysis should be performed on the data files and what, if any, other information should be collected that will be useful. It is expected that TAT will evolve as it is used in more varied domains. Testing the benefits of using TAT will be a difficult task. In the best scenario software would be developed with and without using TAT. Performing these kinds of parallel developmental tests in the real work are difficult if not impossible. Therefore, the most realistic situation would be to use it in as many varied situations as possible and use feedback from the users, developers and HCI personnel to determine the benefits.

VI. Conclusions

Development of good interfaces in software means the ability to closely map the user's task to interface elements. This depends on producing a good task analysis and upon an iterative design process. Unfortunately there are obstacles to being able to accomplish both of these. Producing a good task analysis is especially difficult in cases where the domain is complex and in which much user training is needed. The person conducting the task analysis is often given information from the user with no way of assessing its completeness or its relative importance. Moreover, being able to translate this information into an initial prototype is difficult. This is especially the case in situations where no system is currently in place.

In addition it is important to have the ability to communicate to the developer the user's expectations of an interface as early as possible in the design cycle. This helps to reduce the iterative design process and hence lessen efforts and costs.

The Task Analysis Tool is a step in the proper direction. Although simplistic in nature, it serves to obtain feedback from the end user at an early point in the design cycle. This feedback can be easily communicated to software designers to use as a basis for initial prototypes and interface designs. Further refinements of the Task Analysis Tool will be done. Then its benefits in facilitating interface development will be assessed.

VII. References

1. Asymetrix Corporation. (1989). Toolbook. Computer Software.

2. Boker, S. and Gronbaek, K. (1991). Cooperative prototyping: users and designers in mutual activity. *International Journal of Man-Machine Studies*, 34, 453-478.

3. Drury, C., Paramore, B, Van Cott, H., Grey, S and Corlett, E. (1987). Task Analysis. In Salvendy, G. (Ed.), *Handbook of Human Factor*. (pp. 370-401). New York: Wiley and Sons.

4. Grudin, J. (1991). Obstacles to user involvement in software product development, with implications for CSCW. *International Journal of Man-Machine Studies*. 34, 435-452.

5. Guindon, R. (1988). *Cognitive Science and It's Application for Human-Computer Interaction*. Hillsdale, NJ. Lawrence Erlbaum Associates.

6. Maddix, F. (1990). *Human-Computer Interaction: Theory and Practice*. West Sussex, UK: Ellis Horwood Limited.

7. Norman, D. (1986) Cognitive engineering. In D. A. Norman & S. W. Draper (Eds.), *User centered system design*. (pp. 31-61). Hillsdale, NJ: Lawrence Erlbaum Associates.

8. Shackel, B. (1988) . Introduction to the design of end-user interfaces. In N. Heaton and M. Sinclair (Eds.) *Designing end-user interfaces*.(pp. 97-109). Maidenhead Bershire, UK: Pergamon Infotech Limited.

9. Tognazzini, B. (1989). Achieving Consistency for the Macintosh. In J. Nielsen (Ed.) *Coordinating User Interfaces for Consistency*. (pp. 57-74). San Diego, CA: Academic Press.

10. Walsh, P., Lim, K. , Long J. and Carver, M. (1988). Integrating human factors with system development. In N. Heaton and M. Sinclair (Eds.) *Designing end-user interfaces*.(pp. 111-119). Maidenhead Bershire, UK: Pergamon Infotech Limited.

11. Wilson, J. and Rosenberg, D. (1988). Rapid Prototyping for User Interface Design. In M. Helander (Ed.) *Handbook of Human-Computer Interaction*. (pp. 859-875). Amsterdam: Elsevier Science Publishers (North Holland).

N93-19405

1992 NASA/ASEE SUMMER FACULTY FELLOWSHIP PROGRAM

JOHN F. KENNEDY SPACE CENTER
UNIVERSITY OF CENTRAL FLORIDA

TRAINING EVALUATION FINAL REPORT

PREPARED BY:	Dr. Jose A. Sepulveda
ACADEMIC RANK:	Associate Professor
UNIVERSITY AND DEPARTMENT:	University of Central Florida Department of Industrial Engineering and Management Systems
NASA/KSC	
DIVISION:	Personnel Office
BRANCH:	Systems Training and Employee Development
NASA COLLEAGUE:	Carol Valdes
DATE:	August 7, 1992
CONTRACT NUMBER:	University of Central Florida NASA-NGT-60002 Supplement: 8

NASA/ASEE MANAGEMENT SCIENCE FACULTY FELLOWSHIP PROJECT
KSC MANAGEMENT TRAINING SYSTEM PROJECT

TRAINING EVALUATION: FINAL REPORT

José A. Sepúlveda, Ph.D., P.E.

EXECUTIVE SUMMARY

In the area of management training, "evaluation" refers both to the specific evaluation instrument used to determine whether a training effort was considered effective, and to the procedures followed to evaluate specific training requests.

This reports recommends to evaluate new training requests in the same way new procurement or new projects are evaluated. This includes examining training requests from the perspective of KSC goals and objectives, and determining expected ROI of proposed training program (does training result in improved productivity, through savings of time, improved outputs, and/or personnel reduction?).

To determine whether a specific training course is effective, a statement of what constitutes "good performance" is required. The user (NOT the Training Branch) must define what is "required level of performance". This "model" will be the basis for the design and development of an objective, performance-based, training evaluation instrument.

The process of determining training needs and asking from the users "What is the expected result of training? What may happen if no training is given?," is called a "Needs Assessment". Training satisfying the identified needs require a specific, objective, performance-based, training evaluation instruments for each training course.

At KSC, a "Needs Assessment Focus Group" determined training needs and expected results of training. Their answers will help to design a performance-based training evaluation instrument to determine whether training is effective, i.e., whether it meets user's expectations. The evaluations will be accomplished in terms of performance improvement, quality improvement, financial impact, reduction in defectives, team building accomplishments, and less employee turnover. Separate evaluations will be performed when the course ends and a few month later.

A delayed evaluation will ask the supervisor:

* Did training result in improved unit performance?
* Did training result in improved individual performance?
* Would you send somebody else to the same course?

A separate delayed evaluation will ask the trainee:

* Did your performance improve as a result of this course?
* Should somebody else in your unit take the same course?

Scanning equipment and form-processing software are recommended to mechanize the data gathering, analysis and reporting processes.

NASA/ASEE MANAGEMENT SCIENCE FACULTY FELLOWSHIP PROJECT
KSC MANAGEMENT TRAINING SYSTEM PROJECT

TRAINING EVALUATION: FINAL REPORT

José A. Sepúlveda, Ph.D., P.E.

TABLE OF CONTENTS

NASA/ASEE MANAGEMENT SCIENCE FACULTY FELLOWSHIP PROJECT
KSC MANAGEMENT TRAINING SYSTEM PROJECT

TRAINING EVALUATION: FINAL REPORT

José A. Sepúlveda, Ph.D., P.E.

1.0 BACKGROUND

A review of the existing procedures at KSC indicated that the evaluation of training courses is limited to KSC Form 13 (see Appendix). The results are not used for formal reporting. Major problems with this form are:

- Link to KSC's goals and objectives not clear.
- No cost/benefits considered.
- Not used to assess performance improvement.
- Form is processed manually.

Among other characteristics, the proposed Management Training System at KSC was envisioned to have the following evaluation-related properties:

- Linked to KSC Mission, Goals and Objectives.
- Has a performance and values-based focus.
- Sets priorities based on expected results.
- Measures results in terms of performance improvement, benefits, financial impact, quality improvement, team building accomplishments, and less employee turnover.
- Tracks training and performance data.

The evaluations of specific training courses will be accomplished in terms of performance improvement, quality improvement, financial impact, reduction in defectives, team building accomplishments, and less employee turnover.

2.0 THE EVALUATION OF TRAINING

In the area of management training, "evaluation" refers both to the specific evaluation instrument used to determine whether a training course, seminar, presentation, etc., was considered effective, (i.e, whether it met specific, performance-based, objectives); and to the procedures followed to evaluate new training requests.

2.1 The Evaluation of New Training Requests

A Training Branch's objective is to help the Center to achieve all the benefits expected when personnel are prepared to operate in their environments to their full potential. As part of this objective, it is recommended that the Branch:

Participate in Training Needs Assessment and Priority setting

- Perform Needs Analyses
- Perform Method-Means Analyses
- Supervise continuous evaluation and determination of training needs

Evaluate training requests in the same way new procurement or new projects are evaluated

- Examine training requests from the perspective of KSC goals and objectives.
- Determine expected ROI of proposed training program. Does training result in improved productivity (through savings of time, improved outputs, personnel reduction)?

Determine if productivity improves as a result of investment in training.

- Measure results (via a specific, performance-based, evaluation instrument)
- Keep a continuous review of the training results and productivity gains

2.2 The Financial Impact of Training

Training is expensive, however, lack of training could be more expensive! There are a number of costs associated to a training effort:

- direct: materials, instructor, tuition, cost for media, cost of employee travel and per diem, employee salary during training, opportunity cost of foregone production
- indirect: administrative, office space, computers, simulators, depreciation of facilities
- intangibles: cost associated with potential failure of personnel to perform a task or job; savings associated to finishing a job early due to good performance by everybody involved

3.0 PERFORMANCE-BASED TRAINING EVALUATION

3.1 Training Effectiveness

To determine whether training is effective, a statement of what constitutes "good performance" is required. This allows to determine if training produced enough of the desired result as to be considered "effective."

The user (NOT the Training Department) must define what is "required level of performance". This "model" will be the basis for the design and development of an objective, performance-based, training evaluation instrument.

The process of determining training needs and asking from the users "What is the expected result of training? What may happen if no training is given?," is called a "Needs Assessment". Training satisfying the identified needs require a specific, objective, performance-based, training evaluation instruments for each training course.

At KSC, a "Needs Assessment Focus Group" determined training needs and expected results of training. Their answers will help to design a performance-based training evaluation instrument to determine whether training is effective, i.e., whether it meets user's expectations. The evaluations will be performed in terms of performance improvement, quality improvement, financial impact, reduction in defectives, team building accomplishments, and less employee turnover. Separate evaluations will be performed when the course ends and a few month later.

3.2 The Evaluation Procedure

It is not enough to 'pass' a training course. Skill retention and improved performance over time are most important. Separate evaluations will be performed when the course ends and a few month later.

The evaluation at course end will focus on the delivery and content of the course. It will also state the objectives and purpose of the training and ask whether those were addressed in the course.

A delayed evaluation will ask the supervisor who originally approved the training request:

- Considering the following objectives (... here goes what Focus Group establishes as expected results for training...), did this person's performance improve as a result of this course?
- Did training result in improved unit performance (through savings of time, improved outputs, quality improvement, reduction in defectives, team building accomplishments, less employee turnover, or personnel reduction)?
- Would you send somebody else in your unit to take the same course?

A separate delayed evaluation will ask the trainee:

- Considering the following objectives (... here goes what Focus Group establishes as expected results for training...), did your performance improve as a result of this course?
- Would you recommend that somebody else in your unit takes the same course?

Thus, the proposed evaluation procedure will:

* Examine training requests from the perspective of KSC goals and objectives.
* Determine if productivity improves as a result of investment in training.
* Keep a continuous review of the training results and productivity gains.

This will allow the Training Branch to document and report to management and to departments:

- Time and resources needed to provide training
- Employee time and Center resources spent in training
- Evaluation results (aggregate values)

4.0 EVALUATION FORM PROCESSING

It is recommended that the form used to evaluate training courses be modified in such a way that, not only all the necessary information is collected, but that it is done in a mechanized way to speed up processing and reporting and to reduce data entry errors. To do this, the following scanning equipment and software by National Computer Systems are recommended (prices and brochures are attached):

OpScan Model 20 with Dual Ink Read	$9,100
Survey Network Software	$3,000
Freight/Installation	$270
Total	$12,370

The scanner is capable of processing 2,000 double-sided forms per hour. The Dual Ink Read head allows reading black and blue marks. The software permits the design and production (in a laser printer) of custom designed forms.

If purchasing of these is not feasible due to budget constraints, UCF may be able to provide the service of producing and processing the evaluation forms. The results would be dumped in an ASCII file and the statistical analysis would be processed at KSC.

PARTICIPANT'S EVALUATION

S[illegible]NAR

PARTICIPANT'S NAME	ORGANIZATION

MAIL SYMBOL	TELEPHONE NUMBER	DATE(S)

SUPERVISOR'S NAME

PLEASE INDICATE YOUR EVALUATION OF THE SEMINAR IN TERMS OF THE FOLLOWING

	EXCELLENT	GOOD	FAIR	POOR
1. Overall evaluation of seminar.				
2. Seminar content – amount of detail and extent of coverage.				
3. Level of presentation.				
4. Effectiveness of hand-out materials.				
5. Effectiveness of audio/visual aids.				
6. Instructor(s) knowledge of subject.				
7. Instructor(s) effectiveness.				
8. Application to your job.				

IENTS:

SIGNATURE

TITLE

N93-19406

1992 NASA/ASEE SUMMER FACULTY FELLOWSHIP PROGRAM

JOHN F. KENNEDY SPACE CENTER
UNIVERSITY OF CENTRAL FLORIDA

NEEDS ASSESSMENT FINAL REPORT

PREPARED BY:	Dr. Jose A. Sepulveda
ACADEMIC RANK:	Associate Professor
UNIVERSITY AND DEPARTMENT:	University of Central Florida Department of Industrial Engineering and Management Systems
NASA/KSC	
DIVISION:	Personnel Office
BRANCH:	Systems Training and Employee Development
NASA COLLEAGUE:	Carol Valdes
DATE:	August 7, 1992
CONTRACT NUMBER:	University of Central Florida NASA-NGT-60002 Supplement: 8

NASA/ASEE MANAGEMENT SCIENCE FACULTY FELLOWSHIP PROJECT
KSC MANAGEMENT TRAINING SYSTEM PROJECT

NEEDS ASSESSMENT: FINAL REPORT

José A. Sepúlveda, Ph.D., P.E.

TABLE OF CONTENTS

TABLE OF CONTENTS (Cont.)

NASA/ASEE MANAGEMENT SCIENCE FACULTY FELLOWSHIP PROJECT
KSC MANAGEMENT TRAINING SYSTEM PROJECT

NEEDS ASSESSMENT: FINAL REPORT

José A. Sepúlveda, Ph.D., P.E.

1.0 BACKGROUND

1.1 Purpose

The stated purposes of the Management Science Faculty Fellowship Project were:

- Provide a comprehensive analysis of KSC management training for engineers and other management professionals from project/program lead through executive levels.
- Development of evaluation methodologies which can be used to perform ongoing program-wide course-to-course assessments.

This report will focus primarily in the first stated purpose for the project. Ideally, the analysis of KSC management training will build in the current system and efficiently propose improvements to achieve existing goals and objectives while helping to identify new visions and new outcomes for the Center's Management Training Mission.

Section 2 describes the objectives, approach, and specific tasks used to analyze KSC's Management training System. Section 3 discusses the main conclusions derived from an analysis of the available training data. Section 4 discusses the characteristics and benefits envisioned for a Management training System. Section 5 proposes a Training System as identified by the results of a Needs Assessment exercise conducted at KSC this summer. Section 6 presents a number of recommendations for future work.

1.1 Definitions

The following definitions apply to terms as used in this project:

Education:	aggregate of all processes by means of which a person develops abilities, attitudes, and other forms of behavior which are transferable and useful to situations not now known.
Training:	an organized procedure by which people learn knowledge and/or skill and/or attitudes for a definite purpose usually related to a job or task(s) to be performed.
Training for Competency:	goal is to master skills and knowledge to perform. Engineers are trained to competency.
Training for Proficiency:	goal is repeated performance without error. Proficiency implies a mentoring period, practice time, and extra study.

Need:	an observable, measurable, discrepancy between "where we are now" and "where we ought to be". Needs should be justified and documented (including any associated problems).
Needs Assessment:	the formal process of identifying needs and assigning priorities to their analysis and solution. The process identifies performance gaps - an observable, measurable, discrepancy between actual and required level of performance. Implicit in the assessment is the need for a model to determine "required" level. There are three different levels or types of needs assessment: Basic, which looks for gaps at the individual student level of accomplishment; Comprehensive, which focuses at the departmental/project/program level of operation; and Global, which addresses accomplishments at the organizational(NASA) level.
Needs Analysis:	the process of identifying causes or origins of needs and identifying alternative ways to meet them.
Methods-Means Analysis:	specify advantages and disadvantages for each possible situation.
Mission Analysis:	an structured effort to determine where are we going, how will we know we got there, and a plan showing the functions that must be performed along the way.
Function Analysis:	an analysis of each of the elements (functions) in the mission profile. It includes a determination of the possible methods and means to accomplish each function (with a list of relative advantages and disadvantages) and considers constraints, which would preclude the implementation of certain methods and means.

2.0 APPROACH

2.1 Objectives

Specific objectives identified for the KSC management training system project were:

- Identify organization-wide needs and concerns in the area of Management Training
- Identify specific knowledge, skills and abilities important for each individual's performance at different levels of managerial responsibility
- Identify short and long term management skills requirements at different managerial levels

2.2 Procedure

A system approach was used in the analysis. This approach calls for the identification of NEEDS and the requirements for solutions, including identification of alternatives, and methods and means to implement, evaluate and revise the solutions. The approach requires clear and measurable objectives, and a systematic (formal) procedure to reach and periodically review these objectives. The approach is results oriented and flexible, that is, adaptable to dynamic system changes.

2.3 Specific Tasks

2.3.1 The Level of Effort

The first task was to select the level for the Needs Assessment exercise, e.g., basic, comprehensive, or global.[1] A "Comprehensive" level was recommended and adopted for this project: The effort was initially restricted to KSC Management Training.

2.3.2 The Policy Group

A group of people familiar with the situation and with enough "clout" to make decisions was requested. KSC's Policy Group was headed by the Deputy Center Director and included the Directors of the Center' main directorates:

G. Thomas	Deputy Center Director
J. Conway	Director, Payload Management and Operations
J. Honeycutt	Director, Shuttle Management & Operations
M. Jones	Director, Center Support Operations
W. Murphy	Director, Engineering Development
A. Parrish	Director, Safety, Reliability and Quality Assurance
R. Uhrmann	Director, Personnel Office

Alternates:

J. Morgan	Director, Payload Projects Management
R. Sieck	Deputy Director, Payload Management and Operations

[1] See definitions in Section 1.2

2.3.3 The Focus Group

The Policy Group agreed to perform a Needs Assessment at KSC and named twenty managers with vast experience in program and project management at the Center. This group of people is addressed in this report as the "Focus Group". Its composition was the following:

Name	Organization
Earl D. Hopkins	AC-ICO
Thomas E. Clarke, Jr.	AC-RMO-SS
Elliot Zimmerman	CP-PCO
Joe Lackovich	CS-EED-2
Miguel A. Rodríguez	CS-EED-21
Charles McEachern	CS-PPD-2
Floyd Curington	CV-PSD
Saul H. Barton	PM
Dennis Armstrong	PM-TNG
Larry R. Tucci	RM-ENG-1
Terry L. Smith	RO-ORB
Jackie E. Smith	RT
Jim Joyner	RT-ENG
John Dollberg	RT-SOE-1
Doug Polly	SI-IPO
Elgin J. Kirkland	SI-PEC
John Meyer	SI-PEI
Robert Sieck	TM
John C. Van Hooser, Jr.	TP-POD
José García	TV-ETD-2

2.3.4. Needs Assessment

The bulk of the summer effort was dedicated to this task. It included the following activities:

a. Collect internal and external data. Hard data was collected on courses offered since 1965. The analysis focused on two five year periods: January of 1982 through December of 1986 and January of 1986 through December of 1991. A summary of this analysis is included in section 3 of this report.

b. List identified and documented needs. This step includes to revise data and identify potential training needs. A master list of 464 potential management training topics was developed and trimmed to 178 topics for further consideration. These topics were assessed by the "Focus Group" which rated them with respect to importance for the organization, the most likely trainees, when should the training take place and expectations for results.

c. Place needs in a priority order according to organizational level. This list, which is the KSC Management Training System as defined through the Needs Assessment exercise is presented in the section 4 of this report.

d. List and obtain agreement from Policy Group for prioritized needs. The results of the Needs Assessment exercise conducted by the Focus Group were presented to the Policy Group on August 5, 1992. Section 5.4 presents the Policy Group's response.

2.3.5. Mission and Function Analyses[2]

a. Determine mission, function, and detailed performance requirements.

b. Identify possible methods and means. Discuss constraints.

c. Select and implement method-means.

2.3.6. Evaluation:[3]

a. Formulate a process to generate an effective, performance-based, evaluation instrument for each training effort.

b. Determine a mechanism to collect and process data on training effectiveness.

---

2 Due time constraints, this phase was not addressed and is discussed in Section 6, Recommendations.

3 This topic is the subject of an attached report entitled "Training Evaluation".

3.0 INITIAL FINDINGS

After a brief review of the available data on courses offered, dates and attendance, the current training system was described as being mostly "reactive",that is, courses seem to be offered because somebody asks for them specifically, instead of following a specified "curriculum" or planned layout. A system approach is essentially "pro-active", e.g., it identifies needs, seeks a better future response to these needs, and lays a structured foundation to satisfy them.

The current system seems to be focused on an individual's (or his/her supervisor's) unplanned requests. The system approach shifts focus to a global (organizational) concern, developing a training "profile" and helping individuals to go through it, thus preparing them to be successful and contribute to specific organizational ends.

The following are the main conclusions derived from an analysis of the available training data:

From analysis of training database, 1982 through 1991
- Number of courses doubled
- Number of participants doubled
- Average number of participants per session stable
- About 20% of all courses account for 80% of all participants
- Mostly supervisory courses

Reactive situation
- Focused on an individual's (or his/her supervisor's) unplanned requests
- Courses keep changing
- Data flow does not refer to a "curriculum"

Evaluation limited to federal and local forms
- Not used for formal reporting
- Not used to assess performance improvement
- No cost/benefits considered

Limited access
- Geared to engineers and scientists
- Not clear who and why selection for training is made

Link to KSC's goals and objectives not clear

Missing tie to Career Development Plan

4.0 KSC's MANAGEMENT TRAINING SYSTEM

4.1 Characteristics

The KSC Management Training System is envisioned as having the following characteristics:

- A planned and on-going process
- Linked to KSC Mission, Goals and Objectives
- Pro-active
- Responsive to a long-term strategy
- Not a catch-all solution (not every performance need is met through training)
- Responsive to continued feedback on actual performance

- Focused on the word 'system'
  - Aims to improve organizational performance
  - Focuses on organizational needs in a structured manner
  - Links individual development to improve organizational performance

- Considers issues of impact and value
  - Linked to individual progress through organization
  - Sets priorities based on expected results
  - Tracks training and performance data
  - Measures results in terms of costs, benefits and performance improvement
  - has a performance and values-based focus

- Establishes Training Priorities
  - Cost/effectiveness
  - Justifiable funding (investment plan)
  - Accountable

- Translates into Organizational/Departmental/Personal Plans
  - Professional trends
  - Performance indicators
  - Projected competency (Professional Development Assignments)
  - Career paths

4.2 Benefits

- Appeals to individuals
  - Focus on occupational career path
  - Occupational development assignments
  - Occupational leadership
  - Occupational training plan

- Appeals to Supervisors
  - Management involvement
  - Performance plans
  - Performance appraisals

- Skill assessment
- Standardizes and makes objective evaluation method

- Appeals to Departments
  - Needs assessment provides basis for resource allocation
  - Identifies best candidates for promotion or assignment of added responsibilities
  - Considers individual's weaknesses when assessing performance and determining future training needs
  - Helps develop and maintain a balanced work force

- Appeals to Training Professionals
  - Provides framework for discussion, review, and evaluation of training requirements
  - Allows for short/medium/long range planning
  - Justifies resource allocation
  - Individual and organizational evaluation reports
  - Statistical reporting
  - Accountable

- Appeals to Senior Management
  - Framework for justifiable expenditures of scarce training resources
  - Ties training to contribution to organizational performance
  - Focus on team effort, values, leadership and performance
  - Fits into 'NASA/KSC' culture (way of doing things)
  - Consistent with NASA's directives
  - Consistent with OPM's recommendations

4.3 Succession and Development Plan

The figures included in the next two pages describe the approach recommended by the U.S. Office of Personnel Management for an organization-wide Management Training Program. The program is envisioned as offering a set of "Basic Competencies" which should be available to all employees. Later, as a person progresses through the organization ladder, training in first level (supervisor) competencies, mid-level (managerial) competencies, and higher-level (executive) competencies should be provided. The time when training is offered is also important: some may be soon after a person reaches a certain position, on occasions training may wait, and still in other cases, training should take place before the person assumes higher responsibilities.

SUCCESSION AND DEVELOPMENT PLANNING

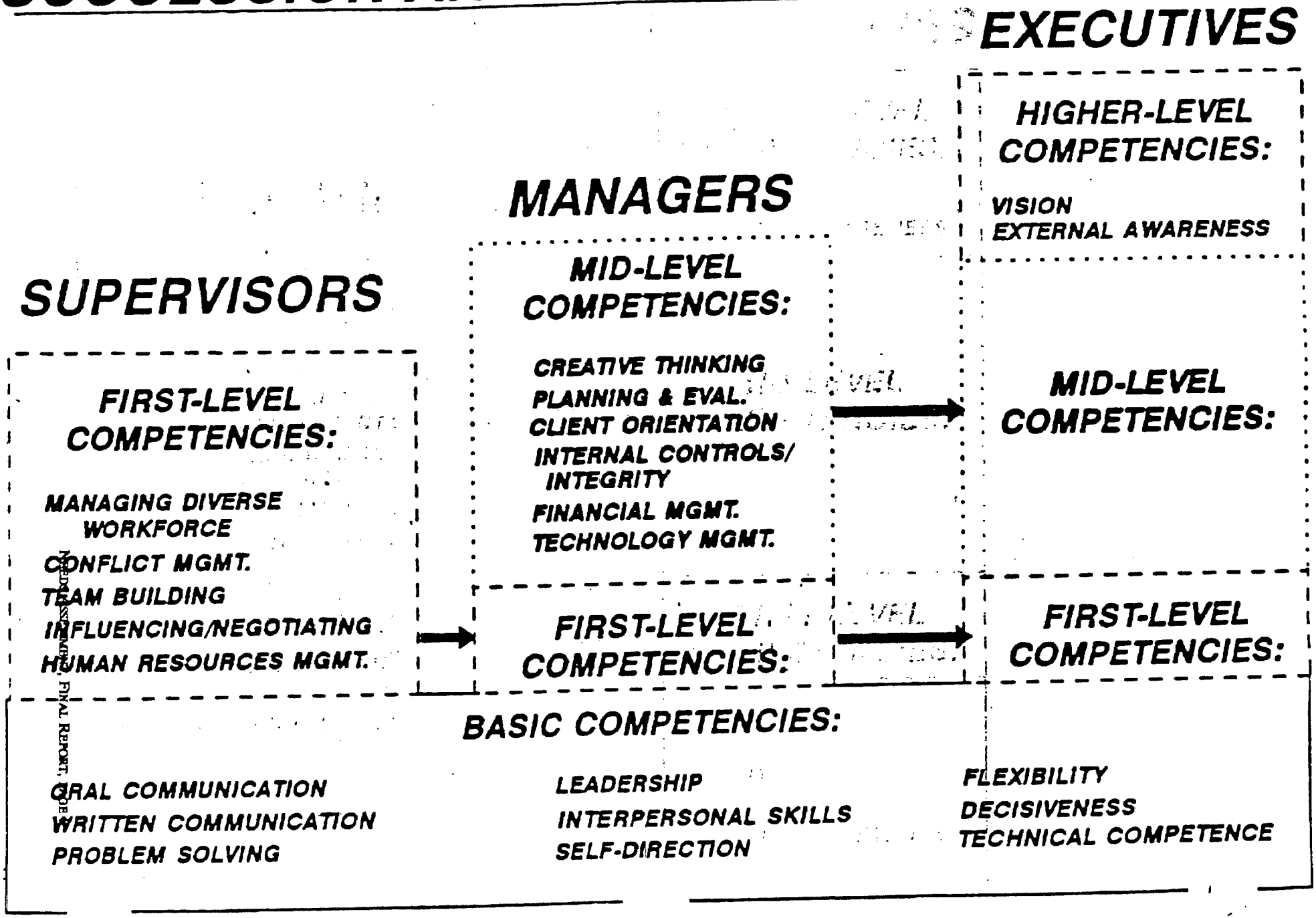

Succession Planning, Final Report, OPE

Attachment 1

OPM CAREER CONTINUUM FOR EXECUTIVE, MANAGEMENT, SUPERVISORY DEVELOPMENT

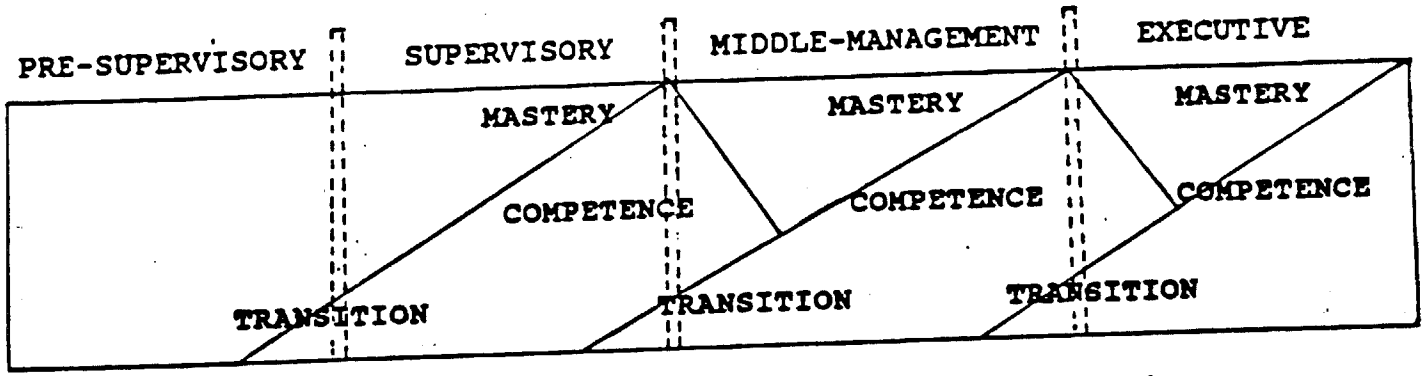

5.0 NEEDS ASSESSMENT

This section presents the Management Training System at KSC as proposed by the consensus of the members of the Needs Assessment Focus Group. The figure in the next page summarizes the recommendations in a manner similar to the one proposed by the Office of Personnel Management (see section 4.3). The figure concentrates only those topics rated as "high priority" (3 and over). Section 5.2 includes all the topics, with their priority, in each level. Section 5.3 lists all the topics rated as "Useful but not essential" or "No Need for Training". Section 5.4 describes the Policy Group's response to the Needs Assessment.

The Appendix presents the details of the Needs Assessment exercise. It includes the complete list of topics; the responses made (by respondent) to each topic (including comments), a summary of the priorities assigned to each topic, the recommended levels, and when to train, and a detailed analysis of the consensus observed in the Assessment.

5.1 Analysis of Consensus

PRIORITY	LEVEL					
	Unanimity	Strong Consensus	Weak Consensus	Disagreement	Totals	Percent
Unanimity	13	22	5	7	47	26.4
Strong Consensus	8	9	3	3	23	12.9
Weak Consensus	13	41	15	21	90	50.6
Disagreement	4	7	2	5	18	10.1
Totals	38	79	25	36	178	100.0
Percent	21.3	44.4	14.1	20.2	100.0	

Notes: Unanimity: All three respondents agreed in assessment
Strong Consensus: Two persons agreed, the third was "close"
Weak Consensus: Two persons agreed, the third person's opinion was very different.
Disagreement: Individual responses were totally different.

The consensus is rated as very high, reflecting the existence of a "KSC Culture". In priority the consensus is about 90 percent. In recommended level, the consensus is less (80%), but still very high by any standards.

SUCCESSION AND DEVELOPMENT PLANNING

SENIOR EXECUTIVES

WITHIN 3 MONTHS IN POSITION

Dealing with media communications

WITHIN 2 YEARS IN POSITION

Strategic planning
Risk assessment methods

MANAGERS

WITHIN 3 MONTHS IN POSITION

Risk/benefit analysis
Increasing departmental dialogue
Managing growth
Organization behavior and development
Sharing power and authority

WITHIN 2 YEARS IN POSITION

The manager as a change agent
Managing large and complex organizations
Risk management
Internal control

SUPERVISORS

IF POSSIBLE, BEFORE ASSUMING THIS POSITION
Incentivizing your work force to come up with better wa
Supervision and personal skills
Cost allocation

WITHIN 3 MONTHS IN POSITION

Accountability in an organization
Coping with continuous change in personnel and technolo
Developing short-range plans
Downsizing (managing shrinking resources)
How to delegate work
Managing resources
Supervision and group performance
Management principles
Staffing: choosing competent people
Budgeting
Career counseling
Developing mid-range plans
Human relations skills
Dealing with issues, mistakes, and conflicts
Effective interviewing
Performance review
Handling disagreements
Handling mistakes
Managing across organization lines
Statistical methods for management
Strategies for mastering change

WITHIN 2 YEARS IN POSITION

Decision support technologies
Establishing work with goals
Involving subordinates
Leadership
Managing Award Fee Contracts
NASA's Mission, Goals, and Objectives
Program management
The budget process
Developing long-range plans
Effective briefings
Management information systems at KSC
OSHA's standards and regulations
Performance-based management

PRE-SUPERVISOR

WITHIN 3 MONTHS IN POSITION

Constant innovation
Cost/Effectiveness analysis
EEO considerations
Encouraging team work
External awareness (customer orientation)
Monitoring progress
Safety and reliability
Sexual harassment
TQM - Total Quality Management
Team approach
Work unit planning
Written communication
Building relationships
How to set and achieve goals
Budget monitoring
Controlling costs
Contract administration
Goal setting and course solutions
Integrity
Process improvement
Effective oral presentations

WITHIN 2 YEARS IN POSITION

Process analysis and control
Productivity measurement and improvement
Project management
Quality and productivity fundamentals
Team building
Communication skills
Coordinating, monitoring, evaluating and
Negotiation/ conflict resolution
Understanding and interpreting human
Accepting criticism
Self-assessment
Encouraging innovation
Finding information
High performing groups
Involving others
Negotiating
Team playing

5.2 Needs Assessment: Topics by Level (Ordered by Priority)

5.2.1 Pre-Supervisor (Basic Competencies)

5.2.1.1 Within 3 months in position

	Priority[4]
Constant innovation	4.10
Cost/Effectiveness analysis	4.10
EEO considerations	4.10
Encouraging team work	4.10
External awareness (customer orientation)	4.10
Monitoring progress	4.10
Safety and reliability	4.10
Sexual harassment	4.10
TQM - Total Quality Management	4.10
Team approach	4.10
Work unit planning	4.10
Written communication	4.10
Building relationships	3.73
How to set and achieve goals	3.73
Budget monitoring	3.40
Controlling costs	3.40
Contract administration	3.37
Goal setting and course solutions	3.37
Integrity	3.10
Process improvement	3.10
Effective oral presentations	3.03
Image and self-projection	3.00
Dealing with difficult people	2.73
Multicultural awareness and diversity in the work place	2.73
Providing support to other persons	2.73
Creative thinking	2.37
Interpersonal skills	2.37
Security	2.10
Representation	2.05
Time management	2.03
Listening skills	1.73
Organizational culture	1.73
Personnel management: hiring, firing, promoting, reward	1.73

---

[4] PRIORITY — Average of answers to "What is the importance of requiring training in this subject matter?"

0.0	There is no need for training in this subject matter
1.1	Useful but not essential
2.0	Helps individual's performance in the future
3.0	Helps individual's performance now
4.1	Helps organizational performance

5.2.1.2 Within 2 years in position	Priority
Process analysis and control	4.10
Productivity measurement and improvement	4.10
Project management	4.10
Quality and productivity fundamentals	4.10
Team building	4.10
Communication skills	3.73
Coordinating, monitoring, evaluating and updating plans	3.73
Negotiation/ conflict resolutions	3.73
Understanding and interpreting human behavior	3.40
Accepting criticism	3.37
Self-assessment	3.37
Encouraging innovation	3.10
Finding information	3.10
High performing groups	3.10
Involving others	3.10
Negotiating	3.10
Team playing	3.10
How to give and take criticism	2.73
Information technologies	2.73
Problem solving	2.73
Superior service to customers	2.73
Planning	2.40
Handling details	2.10
Relationship with management	2.10
Relationship with peers	2.10
Materials management (procurement, transportation, storage)	2.03

5.2.1.3 Anytime before assuming higher responsibilities	
Building consensus on objectives, approaches and success measures	2.40
Building diagnostic skills	2.37
Rewards and recognition	2.37
The individual / organizational fit	2.37
Customer service orientation at NASA	2.10
Managing change	1.73

5.2.2 Supervisors (First Level Competencies)

5.2.2.1 If possible, before assuming this position	
Incentivizing your work force to come up with better ways to do things	4.10
Supervision and personal skills	3.73
Cost allocation	3.10

5.2.2.2 Within 3 months in position

	Priority
Accountability in an organization	4.10
Coping with continuous change in personnel and technology	4.10
Developing short-range plans	4.10
Downsizing (managing shrinking resources)	4.10
How to delegate work	4.10
Innovative management approaches	4.10
Managing resources	4.10
Supervision and group performance	4.10
Management principles	3.73
Staffing: choosing competent people	3.73
Budgeting	3.40
Career counseling	3.40
Developing mid-range plans	3.40
Human relations skills	3.40
Dealing with issues, mistakes, and conflicts	3.37
Effective interviewing	3.37
Performance review	3.37
Handling disagreements	3.10
Handling mistakes	3.10
Managing across organization lines	3.10
Statistical methods for management	3.10
Strategies for mastering change	3.10
Dealing with marginal performers	3.03
Providing performance feedback	3.03
Group dynamics	2.73
Meetings	2.73
Performance analysis/appraisal	2.73
Technical competence	2.73
Training work force for new and changing technologies	2.73
Critical thinking	2.40
Decision analysis	2.37
Developing priorities	2.10
Establishing a motivating environment	2.10
Scheduling and sequencing	2.10
Dealing with hidden agendas	2.03
The procurement process	1.73

5.2.2.3 Within 2 years in position

Establishing work with goals	4.10
Involving subordinates	4.10
Leadership	4.10
Managing Award Fee Contracts	4.10
NASA's Mission, Goals, and Objectives	4.10
Program management	4.10
The budget process	4.10

Developing long-range plans	3.40
Effective briefings	3.10
Management information systems at KSC	3.10
OSHA's standards and regulations	3.10
Performance-based management	3.10
Creating flexible strategies and action plans	2.73
Stress management for professionals	2.73
Utilization of money and equipment	2.73
Cost behavior patterns	2.40
Managing among multiple and conflicting interests, values and demands	2.40
Making decisions	2.37
Economics and decision making	2.10
Influencing others	2.10
Computer models in management	1.73
Productivity issues in a service environment	1.73
Understanding the system	1.73

5.2.2.4 Anytime before assuming higher responsibilities

Decision support technologies	3.40

5.2.3 Managers (Mid-Level Competencies)

5.2.3.1 Within 3 months in position

Risk/benefit analysis	3.73
Increasing departmental dialogue	3.40
Managing growth	3.40
Organization behavior and development	3.10
Sharing power and authority	3.10
Decision making under uncertainty	2.73
Representing, explaining, selling and defending the organization policies	2.73
Finance principles for managers	2.10

5.2.3.2 Within 2 years in position

The manager as a change agent	4.10
Managing large and complex organizations	3.40
Risk management	3.40
Internal control	3.10
Marketing skills	2.73
Information management	2.60
Preparing and defending a budget	2.40
Decision making under risk	2.10
Technology management	2.10
Utilization of human resources	2.03

5.2.3.3 Anytime before assuming higher responsibilities	Priority
Quantitative models in management	2.73
Removing barriers to creative thinking and mental risk	1.73

5.2.4 Senior Executives (Higher Level Competencies)

5.2.4.1 Within 3 months in position	
Strategic planning	2.40
Risk assessment methods	2.03

5.2.4.2 Within 2 years in position	
Dealing with media communications	3.00

5.3 "Useful but Not Essential" & "No Need for Training"

Topic	
Accounting principles for managers	1.10
Building a master activity list and a master schedule	1.10
Challenge of new roles	1.00
Consulting skills	1.37
Dealing with pressure and ambiguity	0.67
Economics and public policy	0.73
Expert systems	1.10
Financial planning	1.40
Honesty, integrity, trust, openness and respect	1.37
KSC organizational information management policies	0.73
Leader/follower roles	0.37
Logistics	1.10
Managing relations with state and local government	1.37
Managing under a labor agreement	1.10
Matrix management	1.37
NASA's past, present and future	1.10
Networking	1.37
Policy analysis and implementation	1.10
Political skills	0.73
Political, economic, social - Future Trends	1.10
Professional ethics and dealing with conflicts of interest	1.10
Professional obligation and rights	1.37
Quality control	1.10
Science and technology in the public sector	0.73
Skill assessment	1.03
Utilizing new technologies	1.10
Work breakdown analysis	1.40

5.4 Policy Group Response

The results of the Needs Assessment exercise were presented to the Policy Group on August 5, 1992. After reviewing the results, the Policy Group decided to give high priority to the training of the following topics:

Managing award fee contracts
Ethics
Procurement
Environmental consciousness
Time management

The Policy Group also recommended that a presentation of the results of the Needs Assessment be made to senior executives; to personnel with "high supervisory potential"; and to lower grade levels and contractors. The possibility of asking lower grades "what does your manager needs?" was also raised. Finally, it was recommended to discuss the issues with the TLP/RMEP programs to see if the fit within their focus.

6.0 RECOMMENDATIONS

The following recommendations are suggested, based on the observations and analyses made through this summer, in the hope that the effort done will be useful to KSC Training Branch's and the Center:

6.1 On the Needs Assessment:

a. Revise list of Training Needs developed and prioritized by the Needs Assessment Focus Group. In particular, make sure that the recommendations of the Policy Group regarding the Needs Assessment are implemented, i.e.:

i. Give high priority to the training of the following topics:

Managing award fee contracts
Ethics
Procurement
Environmental consciousness
Time management

ii. Present the results of the Needs Assessment to senior executives; to personnel with "high supervisory potential"; and to lower grade levels and contractors.

iii. Consider asking lower grades "what does your manager need?".

iv. Consider asking the TLP/RMEP programs to revise the Needs Assessment to see if it fits within their focus.

After the revision, circulate the outcome to let the members of the Focus Group (and other important customers) know you have heard what they said.

b. Use the revised Needs Assessment. Set it as the basis of a "next three-year management training plan". In the future, discuss any new request which includes topics not in this plan. Revise proposed new course descriptions to check if courses fit the plan or modifications (in the plan and/or the courses) are necessary.

c. Perform Needs Analyses and Method/Means Analyses: Develop and implement a (few) training course(s) - an immediate, tangible and visible change that improves training for users and demonstrate that their input was listened to.

6.2 On Evaluation:

d. Evaluate new training requests in the same way new procurement or new projects are evaluated. This includes examining training requests from the perspective of KSC goals and objectives, and determining expected ROI of proposed training program (does training result in improved productivity, through savings of time, improved outputs, and/or personnel reduction?).

e. For existing courses, measure results against user expectations! The Focus Group was also polled for information about their expectations for training (and lack of it). Use these hand-written comments to develop and implement objective, performance-based, assessment instruments for each training effort (course, seminar, video/work book, etc.). Use both immediate and delayed evaluations, and keep constant review of training results and productivity gains.

f. Mechanize course evaluation and develop software to produce standard reports. Modify the form used to evaluate training courses in such a way that, not only all the necessary information is collected, but that it computerized to speed up processing and reporting and to reduce data entry errors. Scanning equipment and form-processing software were recommended to mechanize the data gathering, analysis and reporting processes.

6.3 On Documentation:

g. Keep adequate documentation on cost data (direct, indirect, even "intangible" costs); delivery data (who, how many, where, when); and specific course data (objectives, topics covered, method/means). Even if it means extra effort, it is recommended that an adequate Training Performance Data Base (TPDB) be kept active. It should contain the following data:

- Cost data (NOT in dollars but in hours, units of resources, etc. This will allow for analysis of real expenditures, if needed).
- Delivery data (who, where, how, when, how long, why, what (syllabus), number of attendants, instructor, student's initial and delayed evaluations, supervisor evaluation, comments)
- Performance improvement data (assessment by experts about improved performance, if any. Also by supervisors after a certain time).
- If implemented, make sure the TPDB is linked to Human Resources databases, allows for longitudinal assessment of impact of training program on an employee's performance.
- Specific course data (objectives, topics covered, level addressed, expectations by topic).

6.4 Other Recommendations

h. Apply TQM Principles: Periodically conduct personal interviews with the members of the Focus Group, small group meetings (by branch?), or meetings over lunch with selected managers to find out how do they use what is covered in executive training in their day-to-day business. Ask your customers what they like and dislike about existing training services. Ask what they want for the future.

i. Promote your success. Publicize changes in executive training and illustrate the kind of problems that are being emphasized. Do not forget to give members of the Focus Group feedback on what you are doing as a result of their cooperation. This is an important part of enhancing the Training Branch as a responsive and valuable part of the organization.

N93-19407

1992 NASA/ASEE SUMMER FACULTY FELLOWSHIP PROGRAM

JOHN F. KENNEDY SPACE CENTER
UNIVERSITY OF CENTRAL FLORIDA

STUDY AND DEVELOPMENT OF AN AIR CONDITIONING SYSTEM
OPERATING ON A MAGNETIC HEAT PUMP CYCLE
(DESIGN AND TESTING OF FLOW DIRECTORS)

PREPARED BY:	Mr. Pao-lien Wang
ACADEMIC RANK:	Associate Professor
UNIVERSITY AND DEPARTMENT:	University of North Carolina at Charlotte Department of Engineering Technology
NASA/KSC	
DIVISION:	Mechanical Engineering
BRANCH:	Special Project
NASA COLLEAGUE:	Frank S. Howard
DATE:	August 7, 1992
CONTRACT NUMBER:	University of Central Florida NASA-NGT-60002 Supplement: 8

ACKNOWLEDGMENTS

I would like to thank NASA/ASEE Summer Faculty Fellowship Program, Mr. Willis Crumpler and Dr. Gary Lin of the Kennedy Space Center, Dr. Loren Anderson of the University of Central Florida, for giving me with the opportunity to work on this challenging and rewarding project. Special thanks should be extended to my KSC colleague Mr. Frank Howard for his help, guidance, and encouragement throughout the project. Also my thanks to Mr. Johnny Gay of the Development Testing Laboratory for his support in fabricating and testing of the prototype, without his help I would not be able to complete successfully this summer project. Ms. Kari Stiles's assistance and helpfulness also very much appreciated.

ABSTRACT

This report describes the fabrication, design of flow director, fluid flow direction analysis and testing of flow director of a magnetic heat pump.

The objectives of the project are: (a) to fabricate a demonstration magnetic heat pump prototype with flow directors installed. (b) analysis and testing of flow director and to make sure working fluid loops flow through correct directions with minor mixing.

The prototype was fabricated and tested at the Development Testing Laboratory of Kennedy Space Center. The magnetic heat pump uses rear earth metal plates rotate in and out of a magnetic field in a clear plastic housing with water flowing through the rotor plates to provide temperature lift. Obtaining the proper water flow direction has been a problem. Flow directors were installed as flow barriers between separating point of two parallel loops. Function of flow directors were proven to be excellent both analytically and experimentally.

SUMMARY

The heat pump consists of a rotor turning through four magnetic field area created by permanent magnets. Gadolinium was selected as the working material for this prototype. Rotor was designed to be constructed of flat parallel disks of working material with very small space in between. The rotor rotates in and out of the magnetic field in a clear plastic housing. Water flowing through the rotor plates in the opposite direction to provide heating and cooling effect. It is necessary to divide the fluid flow separately into a cold loop and a hot loop. Separation of fluid loops has been a problem in the model development. Flow directors were installed between two loops at their points of separation to develop enough restriction and properly guide fluid flow through correct path. Both the experimental and computational results prove the validity of the design of the flow director.

For testing and demonstration of flow director performance, magnets were not installed, and rotor plates were constructed with clear plastic instead of gadolinium.

TABLE OF CONTENTS

I INTRODUCTION

The use of Freon gas-cycle to provide refrigeration and space heating has broad application in industry and for domestic in this country. Research has shown that the release of Freon into the atmosphere will deteriorate the ozone layer in the Earth's atmosphere. As a result, research has begun to try to limit or eliminate the use of Freon for refrigeration purposes. One alternative to consider is the magnetic heat pump.

NASA Kennedy Space Center initiated the development of an air conditioning system operating on a magnetic heat pump cycle. The project is being managed by Mr. Frank S. Howard of DM-MED-11. The preliminary study of a laboratory scale demonstration prototype has been completed. The design and engineering drawings were completed during the 1991 NASA/ASEE Summer Faculty Fellowship Program. Fabrication and testing of flow directors of the heat pump are the major tasks for the 1992 summer project.

II DESCRIPTION

2.1 Concept

The rotating magnetic heat pump consists of a rotor of magnetic working material with flow passages to allow heat transfer fluid to move through the rotor in good contact with the magnetic material. The rotor moves in a clear plastic housing with flow ports positioned at the transition between magnetic field change for fluid to enter and exit the housing as shown in Fig. 1. The cycle executed as follows:

(1) Fluid is pumped into the housing at point 1 where the rotor approaching the magnetic field and flows to point 2.

(2) Between points 1 and 2 working material becomes magnetized and heats up. Fluid flowing between 1 and 2, removes most of the heat of magnetization of the working material and transferred to the load (heating loop).

(3) Fluid is pumped into the housing at point 3 flows through the rotor to point 4.

(4) Between points 3 and 4, working material demagnetizes and cooled down. Fluid flowing between 3 and 4, giving away heat to the cold working material and flow to the cooling load (cooling loop).

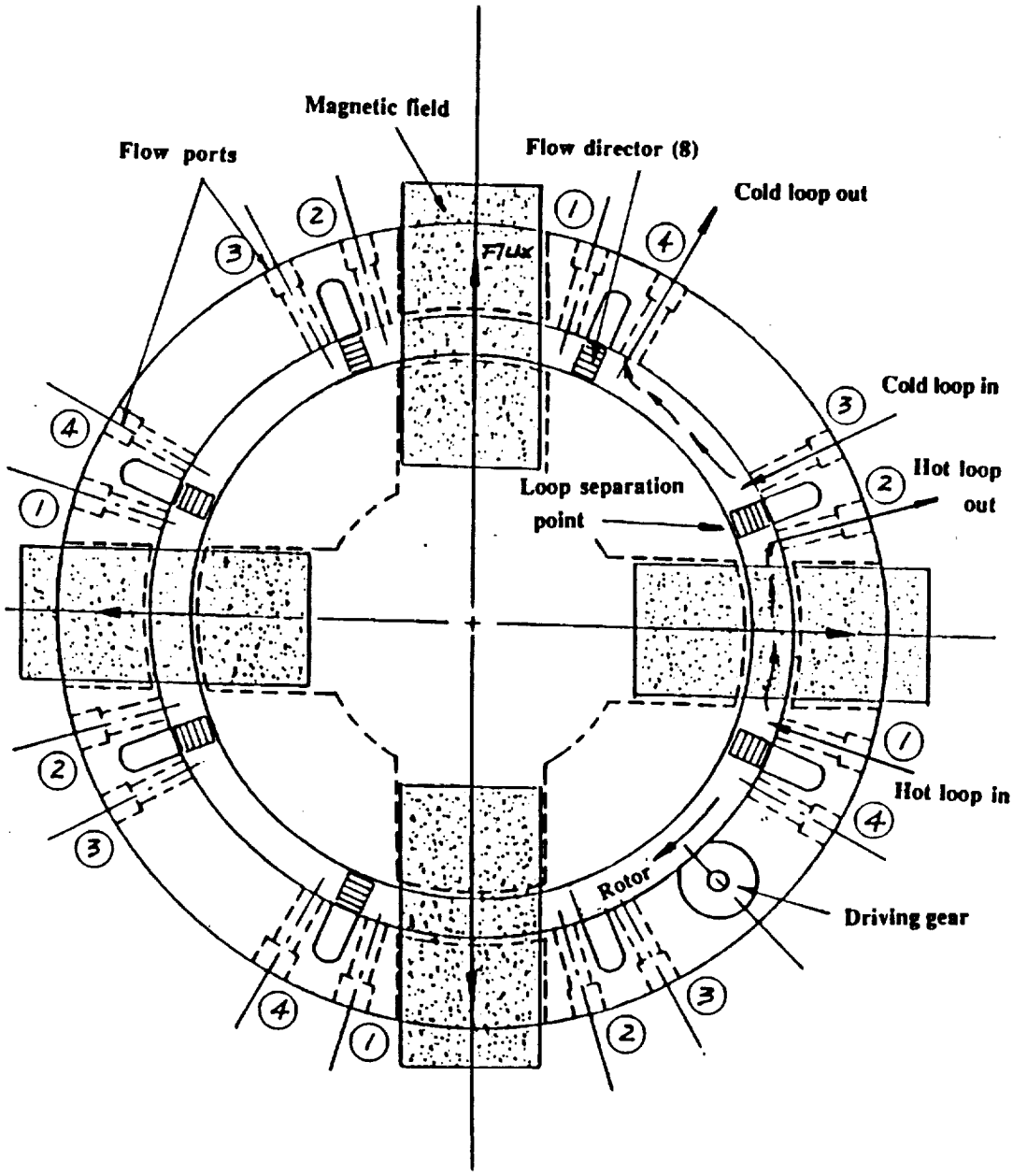

Fig. 1 Housing Assembly

It is necessary to divide the fluid flow into two separate loops, but it was found to be a problem in development of the prototype. To solve the problem, comb shaped flow directors were installed at the separation point between loops, to obtaining proper flow direction.

Summary of design parameters

Core Material: GDTC293
Working fluid: Water
Core Type: Plate
Rotor OD: 0.2159m
Rotor ID: 0.1905m
Core Hight: 0.0397m
Plate Thickness: 0.00159m
Plate Spacing: 0.003175m
High Field: 1 Tesla
Low Field: 0
Rotation Time: 8 Sec/Rev.
Cycle/Revolution: 4

For detail of prototype design, see Ref. 1 and 2

2.2 Flow Director Design

The system demands that fluid flowing in and out of the housing (with rotor rotates in it) must follow two separated loops without mixing. It is very difficult to separate fluid into two loops within the same housing without being mixing (Fig. 1). To solve this problem, Mr. Frank S. Howard suggested to install a comb shaped pieces(called flow director in this report) fitted between the thin rotor plates at the loop separation point (Fig. 2a and 2b), enough restriction would be developed by the comb shaped pieces to properly direct the fluid flow. Calculations from the Darcy's equation indicates that the introduction of Flow Director provides adequate resistance to guide the fluid flow through correct directions with very little mixing.

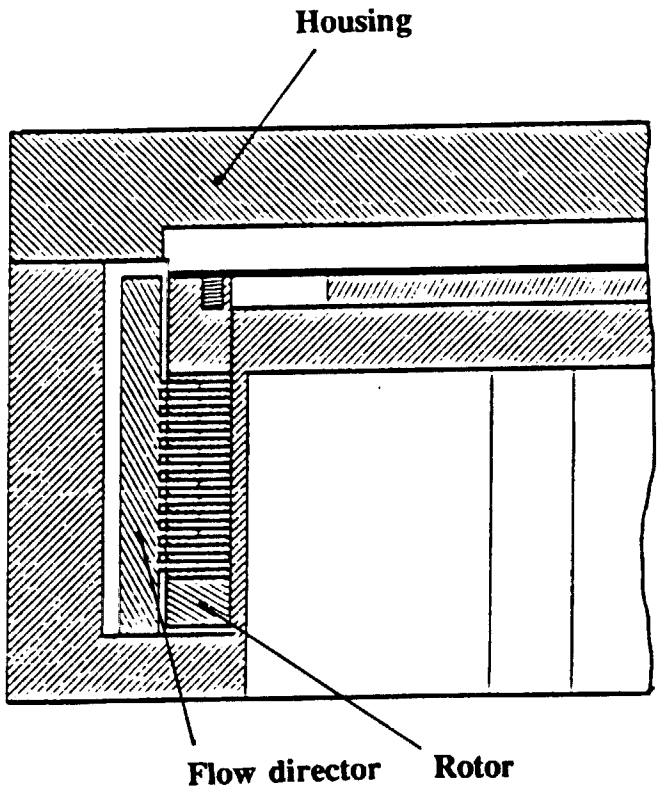

Fig. 2a Flow director assembly

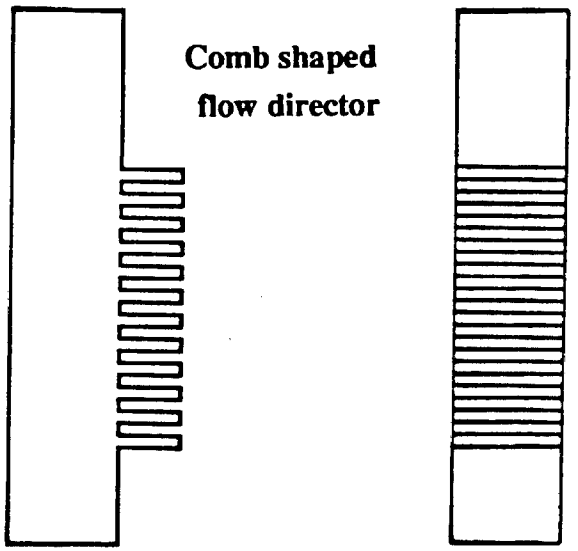

Fig. 2b Flow director

2.3 Calculation of Performance

Fluid entering the housing at point 1 is free to flow through the rotor in either direction to 2 and 4. If there is no barrier at 2, fluid will flow from 2 to 3 and mix with the other loop. Due to the installation of a flow director (comb shaped barrier) between 2 and 3, flow resistance between 1 and 2 is much less than 2 and 3. Thus, most fluid entering at 1 flows to 4 which is the proper direction (see Fig. 3). Calculation indicated that the pressure difference between point 2 and 3 is much greater than between 1 and 2. Most of the fluid entering at 1 flows to the exit port at 4. There are some trace of fluid flow cross the flow director from point 2 to 3 and mix with the adjacent loop, but the quantity was calculated to be very small (only about 6.63 x 10-5 ft3/s/port).

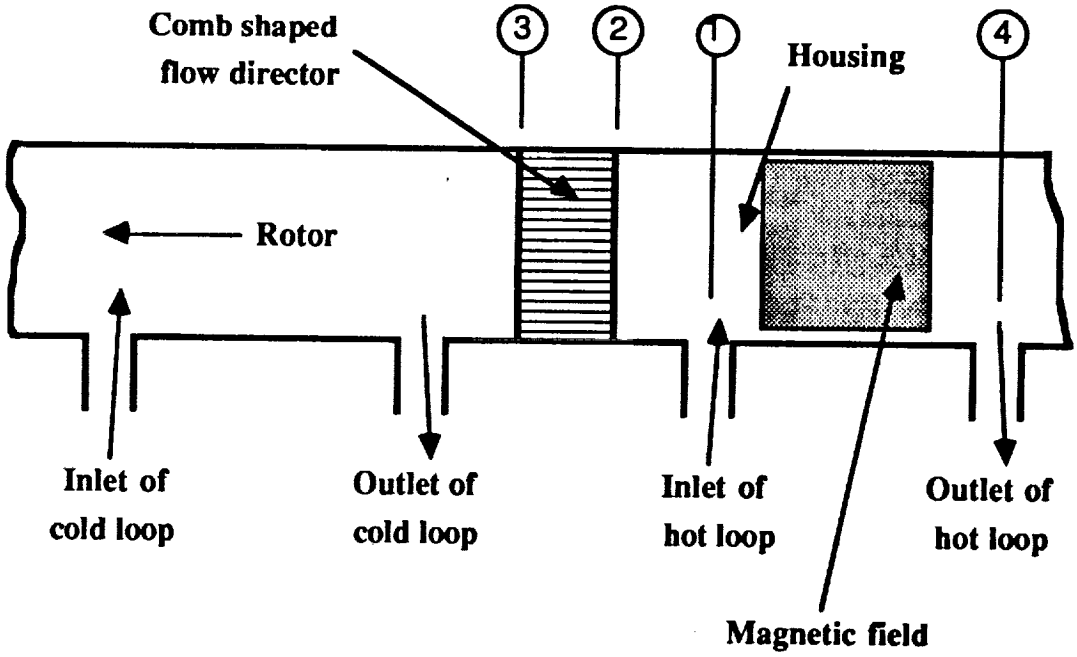

Fig. 3 Schematic for flow director position and loop separation

Calculations are made by using the Darcy formula for laminar flow (Ref. 3)
Reynolds number = 1383 (Laminar flow)

$$\Delta P = 0\ 000668 \frac{\mu L v}{d^2} = 0.1225 \frac{\mu L q}{d^2}$$

For non-circular sections $d = 48\ R_H$, where R_H is the Hydraulic Radius

Where:
- ΔP - Pressure difference between two points (lb/in^2)
- μ - Dynamic viscosity (centipoise)
- R_H - Hydraulic radius (ft)
- L - Length of passage (ft)
- v - Velocity of flow (ft/s)
- q - Rate of flow (ft^3/s)

Pressure differences ΔP and the flow rate through the flow directors q were computed by the ratio of hydraulic radius.

Detailed computations are presented in the Appendix.

III TEST OF FLOW DIRECTORS

3.1 Components and Procedure

The testing prototype consists of the following primary components (Fig. 4);
(1) The housing (with inlet and exit flow ports)
(2) The rotor (with rotor material plates)
(3) Gear driving device and driving motor
(4) Fluid pump and tank for each cold and hot loop
(5) Tygon tubing connecting flow ports to fluid pumps and tanks

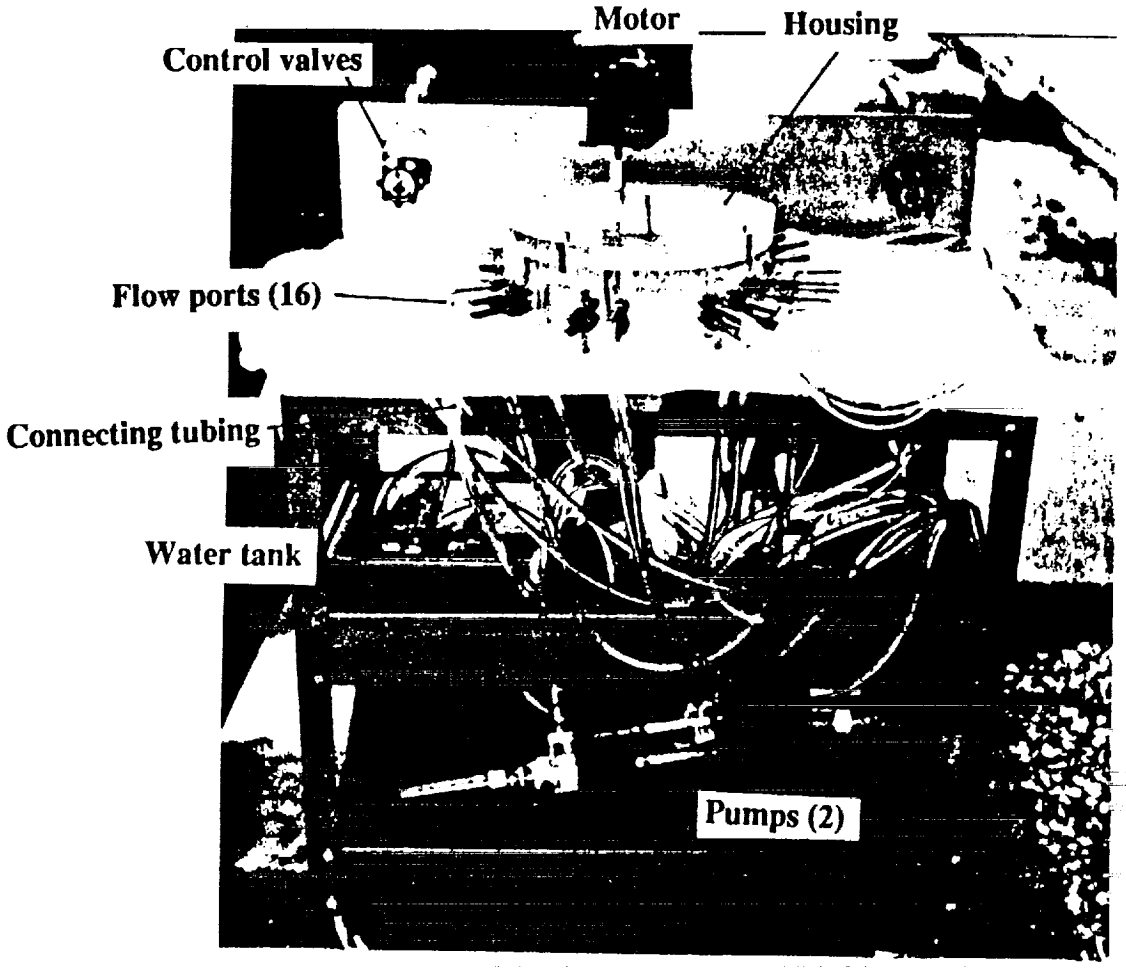

Fig. 4 Photograph of test prototype

Testing procedure:

(1) Turn gear drive motor on, and measure rotor speed in RPM.
(2) Fill fluid tanks with clear water.
(3) Turn pump power on let water run for 15 minutes until water fills housing.
(4) Adjust flow control valves until flow rate of both loops are approximately equal.
(5) Measure flow rate per port with a stop watch and a grade fluid beaker, record flow rate.
(6) Add color fluid into one of the two fluid tank.
(7) Visually inspect path and direction of colored fluid flow, and make sure fluid flow through two separate loops (a clear water loop and a colored water loop).
(8) Exam if any colored water cross Flow Director.
(9) Video tape fluid flow pattern.
(10) Shout down system.

3.2 Result

Analytical Result

1. Computation indicates that the pressure difference between section 2 and 3 is much greater than pressure difference between section 1 and 2. Most of the inlet flow will eventually flow from 1 to 4.

2. Calculation also indicates that the fluid flow through the flow director from 2 to 3 mixing with the adjacent loop quantitatively is very small (about 0.0000663 cubic feet per sec. per flow port).

Test Result

During laboratory testing operation, we found that fluid flow was channeled by the flow director clearly into two separate loops. It matched closely with analytical result (see Fig 5).

The analytical and testing results of the above match satisfactorily.

IV CONCLUSION AND FURTHER DEVELOPMENT

The agreement between analytical and experimental results proved that the project was carried out successfully. The introduction of flow director is a major break through of the magnetic heat pump project, and opened a new era for future research on this subject.

The future tasks for the KSC magnetic heat pump will be:
(1) fabricate rotor with gadolinium,
(2) install four permanent magnets, measuring instruments, and
(3) test for heat pump performance.

V APPENDIX

5.1 Calculations

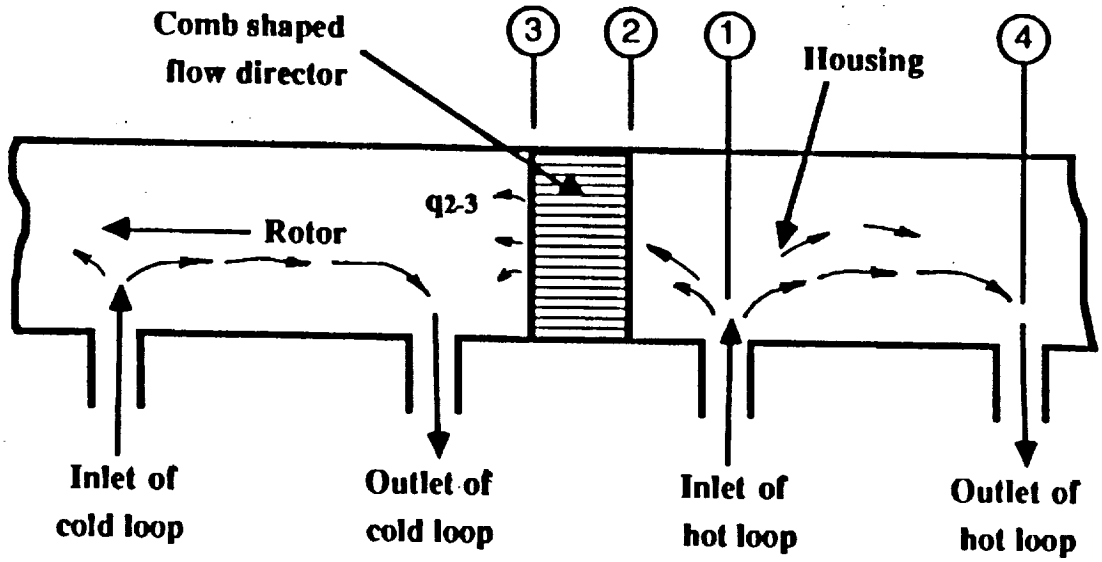

Given (measured):

1. Flow area at section 1 $A1 = 8.64 \times 10^{-4}\ ft^2$
2. Flow area at section 2 $A2 = 2.20 \times 10^{-3}\ ft^2$
3. Wetted perimeter at section 1 $WP1 = 1.52$ ft
4. Wetted perimeter at section 2 $WP2 = 0.86$ ft
5. Hydraulic radius at section 1 $R_{H1} = 5.66 \times 10^{-4}$ ft
6. Hydraulic radius at section 2 $R_{H2} = 2.56 \times 10^{-3}$ ft
7. Flow rate /port $q = 5.3 \times 10^{-4}\ ft^3/sec$
8. Flow velocity at section 1 $v_{1-2} = 0.241$ ft/sec
9. Flow velocity at section 2 $v_{2-3} = 0.616$ ft/sec

Reynolds number

$$R_e = \frac{v(48R_H)}{\nu} = \frac{0.616\ (48)(5.66\times10^{-4})}{1.21\times10^{-5}} = 1383$$

Darcy's formula for laminar flow:

$$\Delta P = 0.000668 \frac{\mu L v}{d^2} = 0.1225 \frac{\mu L q}{d^4}$$

For non-circular flow area $d = 48\, R_H$

Then
$$\Delta P = 0.000668 \frac{\mu L v}{(48 R_H)^2} = 0.1225 \frac{\mu L v}{(48 R_H)^4}$$

Between section 1 and 2

(a) $$\Delta P_{1\text{-}2} = 0.000668 \frac{\mu L_{1\text{-}2} v_{1\text{-}2}}{(48 R_{H_{1\text{-}2}})^2}$$

Between section 2 and 3

(b) $$\Delta P_{2\text{-}3} = 0.000668 \frac{\mu L_{2\text{-}3} v_{2\text{-}3}}{(48 R_{H_{2\text{-}3}})^2}$$

Take (a) / (b) , we have

$$\frac{\Delta P_{1\text{-}2}}{\Delta P_{2\text{-}3}} = \frac{v_{1\text{-}2}}{v_{2\text{-}3}} \frac{(R_{H_{2\text{-}3}})^2}{(R_{H_{1\text{-}2}})^2}$$

$$= \frac{0.24}{0.616} \frac{(5.66 \times 10^{-4})^2}{(2.56 \times 10^{-3})^2}$$

$$= 0.3896 \times 4.89 \times 10^{-2} = 0.0191$$

$$\boxed{\Delta P_{1\text{-}2} = 0.0191\, \Delta P_{2\text{-}3}}$$

Thus, pressure difference between section 2-3 is much greater than pressure difference between section 1-2. Obviously, most fluid flows from section 1 to 4.

Also

$$\Delta P_{1\text{-}2} = 0.1225 \frac{\mu L_{1\text{-}2}\, q_{1\text{-}2}}{(48R_{H_{1\text{-}2}})^4}$$

$$\Delta P_{2\text{-}3} = 0.1225 \frac{\mu L_{2\text{-}3} q_{2\text{-}3}}{(48R_{H_{2\text{-}3}})^4}$$

Since

$$\Delta P_{1\text{-}2} = 0.0191\, \Delta P_{2\text{-}3}$$

$$0.1225 \frac{\mu L_{1\text{-}2} q_{1\text{-}2}}{(48R_{H_{1\text{-}2}})^4} = 0.0191 \left[0.1225 \frac{\mu L_{2\text{-}3} q_{2\text{-}3}}{(48R_{H_{2\text{-}3}})^4} \right]$$

Than

$$\frac{q_{1\text{-}2}}{(R_{H_{1\text{-}2}})^4} = 0.0191 \left[\frac{q_{2\text{-}3}}{(R_{H_{2\text{-}3}})^4} \right]$$

$$q_{2\text{-}3} = q_{1\text{-}2} \frac{(R_{H_{2\text{-}3}})^4}{0.0191 (R_{H_{1\text{-}2}})^4}$$

$$q_{2\text{-}3} = 5.3 \times 10^{-4} \frac{(5.66 \times 10^{-4})^4}{(2.56 \times 10^{-3})^4}$$

$$q_{2\text{-}3} = 5.3 \times 10^{-4} \frac{(5.66 \times 10^{-4})^4}{0.0191 (2.56 \times 10^{-3})^4}$$

$$= \frac{5.3 \times 10^{-4}}{1.91 \times 10^{-2}} \frac{(5.66 \times 10^{-4})^4}{(2.56 \times 10^{-3})^4}$$

$$\boxed{q_{2\text{-}3} = 6.63 \times 10^{-5} \frac{ft^3}{sec} \quad \text{per port}}$$

$q_{2\text{-}3}$ is the quantity of fluid flowing through the flow director mixing with the other loop. It is found to be very small in this calculation.

All calculations are calculated per one flow port.

VI REFERENCE

1. P. L. Wang, "Laboratory Testing of a Supercritical Helium pump for a Magnetic Refrigerator," NASA/ASEE Summer Faculty Research Fellowship Program Research Report, John Kennedy Space Center, Florida, 1988. pp 412-439

2. P. L. Wang, "Study and Development of an Air Conditioning System Operating on a Magnetic Heat Pump Cycle," NASA/ASEE Summer Faculty Research Fellowship program Research Report, John Kennedy Space Center, Florida, 1991, pp 535-553.

3. Engineering Division, Crane Co. "Flow of Fluids through Valves, Fittings, and Pipe," Technical Paper No. 410, Crane Co., New York, 1979, pp 3-1, 3-5.

1992 NASA/ASEE SUMMER FACULTY FELLOWSHIP PROGRAM

JOHN F. KENNEDY SPACE CENTER
UNIVERSITY OF CENTRAL FLORIDA

DESIGN AND EVALUATION OF FDDI FIBER OPTICS NETWORK FOR ETHERNETS, VAX'S AND INGRAPH WORK STATIONS

PREPARED BY:	Dr. M. Chris Wernicki
ACADEMIC RANK:	Associate Professor
UNIVERSITY AND DEPARTMENT:	New York Institute of Technology Electrical Engineering Department
NASA/KSC	
DIVISION:	CAD/CAE
BRANCH:	Data Division
NASA COLLEAGUE:	Ed Bertot Patrick O'Rourke
DATE:	July 31, 1992
CONTRACT NUMBER:	University of Central Florida NASA-NGT-60002 Supplement: 8

ACKNOWLEDGEMENT

The author would like to acknowledge the assistance and cooperation of a number of people at KSC without whom this research effort would not have been possible.

Mr. Hank Perkins for valuable assistance and genuine interest in FDDI project. Patrick O'Rourke and Ed Bertot for valuable support along the way. Bryan Boatright for practical suggestions related to FDDI system design.

Last but not least, I would like to thank Dr. Loren Anderson of U.C.F. who managed the Summer Faculty Program.

Abstract

The purpose of this project is to design and evaluate the FDDI Fiber Optics Network for Ethernets, VAX's and Ingraph work stations.

From the KSC Headquarters communication requirement, it would be necessary to develop the FDDI network based on IEEE Standards outlined in the ANSI X3T9.5, Standard 802.3 and 802.5 topology - direct link via intermediate concentrator and bridge/router access.

This analysis should examine the major factors that influence the operating conditions of the Headquarters Fiber plant. These factors would include, but are not limited to the interconnecting devices such as repeaters, bridges, routers and many other relevant or significant FDDI characteristics.

This analysis is needed to gain a better understanding of overall FDDI performance.

List of Acronyms

KSC - Kennedy Space Center

ANSI - American National Standards Institute

FDDI - Fiber Distributed Data Interface

LAN - Local Area Networks

OSI - Open System Interconnection

OSIRM - Open System Interconnection Reference Model

MAC - Medium Access Protocol

BET - Bit Error Rate

SAS - Single Attachment Station

DAS - Dual Attachment Station

MIC - Media Interface Connections

STP - Shielded Twisted Pair

List of Figures

TABLE OF CONTENTS

1. INTRODUCTION

1.1 General

In today's high pressure business environment, acquiring and distributing information quickly is critical to the functioning of most companies. Networks play an increasingly important role in this process. In this project - choosing the right network, however, is a complicated one. Many factors such as propriety networks, nonstandard applications and single vendor hardware sourcing need to be taken into consideration. Network standards such as Fiber Distributed Data Interface (FDDI) help to simplify this task. The current HQ's ethernet system based on 10 Mbs. standard transmission is going to be replaced by a new LAN operating at 100 Mbs. In such architecture, network systems are designed in layers performing a special set of functions and services. Each layer has it's own protocols, regulating activities within the layer as well across links between stations called nodes, and is independent of each other. The open system interconnection (OSI) with interoperability or open communications supports multivendor communication.

1.2 FDDI Background

The FDDI grew out of the need for high speed interconnections among mainframes, minicomputers and associated peripherials. In October 1982 ANSI committee X3T9.5 was chargered to develop a high speed data networking standard that specified a packet switching LAN backbone that transported data at high throughput rates over a variety of fibers. The FDDI specifications encompass a token passing network enveloping two pairs of fibers operating at 100 Mbs. The 1991-1992 standard covers the first two layers of OSIRM through the MAC sublayer. The optical based FDDI-LAN was designed to enjoy the same type serial interconnection provided by LAN's while providing a high band width, inherent noise immunity, and security offered by Fiber. The FDDI is meant to provide inexpensive connectin-

ity, thus it focuses on the 100 Mbs rates. The FDDI accommodates a synchronous data transmission and is designed as a fiber optic network. The standardization involves duplex optical connectors, fiber characteristics, optical band width, bypass relays and cable assemblies and is designed on overal BER $<10^{-9}$. The network can tolerate up to 11 dBm between the stations, and can support a total cable distance of 100 km around the ring with 500 attachments. The intrinsic topology of FDDI is a counter-rotating token-passing ring. At least part of the reason why FDDI employes a ring topology is based on the characteristics of the optical communication. Bus and passive star topologies would require the optical to be detected at several sources simultaneously. Although, practical fiber optical taps are beginning to become available, the attenuation is still such that number of nodes is relatively limited. Because the fiber optical transmission is best handled with a point-to-point configuration, this aspect is included in FDDI's definition.

1.3 FDDI Standards

Institute of Electrical and Electronics Engineers.

IEEE Std. 802.3 Carrier Sense Multiple Access with Collision Detection (CSMA/CD) Access method and Physical Layer Specifications.

IEEE Std. 802.5 Token Ring access method and physical layer specifications.

IEEE Std. 802.1.a Overview of Local Area Networks (LAN) and Metropolitan Area Networks (MAN) specifications.

IEEE Std. 802.1.d Local Area Networks (LAN's) MAC Transparent Bridging Standards.

IEEE Std. 802.1.i Mac Layer Bridge FDDI supplement.

IEEE Std. 1003.1 Portable Operating System Interface (POSIX).

Ethernet Version 2. A Local Area Network: Data Link Layer and Physical Layer Specification. DEC Intel and Xerox Corp. Version 2.0, Nov. 1982

American National Standard Institute, Inc.

X3.139 FDDI Token Ring Media Access Control Standard

X3.148 FDDI Token Ring Physical Layer Protocol Standard

X3.166 FDDI Token Ring Physical Layer Medium Dependent Standard

X3T9.5 FDDI Station Management (Rev. 6.2)

2. SYSTEM ARCHITECTURE

2.1 Introduction

Network systems are designed in layers. Each layer performs a special act of functions and services. Each layer has its own protocols, regulating activity as well communication and transfer of data between layers and across links. The layers are independent of each other. This layered approach means that designing networks and network functions is easier and networks can provide users with a greater range of accessible and ease-to-use capabilities.

2.2 Open System Interconnection.

OSI is a seven-layer model for an open network atchitecture with high interoperability or open communication. It supports multivendor communication and provides a framework for the development of international standards for computer communication.

The OSI model shown in Fig. 1 was developed by the International Organization for Standardization and InternationalTelegraph and Telephone Consultative Committee.

The physical layer specifies the electrical and physical connections between systems. This layer also translates messages into a form that is compatible with the medium used; for example, fiber or coax cable.

The data link layer introduces control information into messages that are to be transmitted, defines frame construction, addressing error detection and connection to higher layers.

The network layer permits communications between network nodes in an open network, establishes and releases the logical connections for data transfer between communicating nodes and controls the flow of messages between nodes.

2.3 The OSI Model

Repeaters, bridges, and routers link networks together. The simplest network interconnecting device is a repeater (Fig. 2). It acts on the bits transferred between the physical layers of two nodes; it repeats, retimes, and simplifies the bits.

A bridge, called also a data link relay, links similar and dissimilar LANS together to form an extended LAN. (Fig. 3).

Bridges act on the frames transferred between the Data Link Layers of the two nodes, while reactors act on the bits transferred between physical layers.

Bridges are designed to store and then foward frames destined for another LAN and they are also protocol independent. Ideally, bridges are invisible to the cut-stations that are communicating through the bridge. The end-station does not know that the bridge exists or that the message is going through the bridge.

Routers also called an intermediate system, network relay or level 3 relay (Fig. 4) are used to link LAN's. Routers are typically network layer (Layer 3) devices. Routers act on the frames transferred between the Network layers of two nodes. Routers are known to the end-station. Nodes periodically send messages to the routers confirming their existence and their address. The router keeps a record of node addresses and current network status. It forwards a message directly to a local or remote LAN over the route with the least amount of traffic or lowest cost as defined by the network manager. Routers isolate LAN's into subnetworks that can manage and contain network traffic.

2.4 The LAN's Function

LAN - Local area networks connect computers, terminals, and other equipment in the building or on a campus. Bridges connect LAN;s over distances that exceed the capabilities of a single LAN. OSI standards allow different types of LAN's to be linked together. For example two IEE 802.3 networks can be connected with an 802.3/Ethernet bridge.

Fiber Distributed Data Interface is a new multivendor local area network standard developed under ANSI that offers an industry-standard solution for organizations that need flexible, robust, high-performance networks. ANSI has defined the FDDI to be 100 Mbs. LAN featuring the timed-token protocol and supports a dust ring of trees topology. For multimode fiber optic cable used as a transmission medium, the standards specify: optical cable consisting of 62.5/125um, graded index multi mode fibers, a maximum fiber length of 200km with a maximum of 2km between adjacent stations, and a maximum of 500 stations.

2.5 FDDI Topology

An FDDI network consists of physical and logical topologies. The physical topology refers to actual arrangement of the cables and hardware, where the cable can be a line, link, circuit, transmission medium ot channel.

The logical topology refers to the actual path, which varies, depending on traffic flow and the number and location of active stations on the network. Typical configuration for the FDDI is implemented in three ways:

1. As a high-speed backbone connecting mid-speed local area networks.
2. As a high-speed LAN connecting code stations or other devices.
3. As a high-speed connection between host computers.

As FDDI standards, ANSI permits the following topologies:

1. Stand alone concentrator with attached stations.
2. Dual ring.
3. Tree of concentrators.

4. Dual ring of trees.

The stand alone concentrator topology consists of a single concentrator and its attached stations (Fig. 5). These stations can be either single attachment stations (SAS) or dust attachment station (DAS) devices.

This topology can use existing structured fiber optic cable, affording significant cost savings in prewired sites. The dust ring topology shown in Fig. 6 consists of dust attachment stations connected directly to the dust ring. This topology is useful with limited number of users, however, does not easily lend itself to additions, moves or changes.

Because each station is part of the backbone wiring, the behavior of each user is critical to the operation of the ring, and disconnecting a dual attachment workstation causes a break in the ring. In the event of a single failure, a dual ring provides a secondary transmission path, however, multiple failure results in no access to the other rings. In addition, dual, attachment stations require twice the number of connectors and cables, and manual intervention and manipulation of cables results in ring instability in large installations.

The preferred choice when wiring together large groups of user devices is the tree of connectors shown in Fig. 7.

The concentrators are wired in a hierarchical star topology with one concentrator serving as the root of the tree called a HUB. This topology provides greater flexibility for adding and removing FDDI concentrators and stations or changing their location without disrupting the FDDI LAN. The tree configuration connects all stations in a single building or a large number of stations on one floor of a building.

The tree topologies allow network managers to better control access of end-user systems to the network. Inoperative systems can be easily removed from the network by the concentrator, and the network manager can remotely address the concentrator to bypass the device.

In dual ring of trees concentrators cascade from other concentrators connected to a dual ring. Fig. 8.

This configuration places the dual ring where it is needed most - in the campus backbone.

The dual ring of trees is the recommended topology for FDDI. It provides a high degree of fault tolerance and increases the availability of the backbone ring. Also, in this configuration, stations attached to concentrators can be removed from the FDDI LAN as needed. Concentrators can then bypass inactive or defective stations without disrupting the network.

3. REQUIREMENTS

3.1 Introduction

The proposed equipment for the Head Q's (Fig. 9) third floor shall be configured to satisfy specific requirements based on the current KSC networking environment such as:

Local Area Network's (LAN) requirements currently based on 802.3 and 802.5 topologies (ANSI X3T9.5). Direct link shall be provided via intermediate concentrators and bridge/router access. Linking the above networks shall require networking segmentation capabilities including network control, monitoring and management functionality.

3.2 FDDI Concentrator Requirements

3.2.1 Basic Requirements

1. The concentrator shall implement all required sections of the ANSI X3T9.5 FDDI standard including ANSI X3.139, X3.166, X3.148, as well as FDDI Station Management (SMT) version 6.2

2. The concentrator shall be capable of connecting to the FDDI dual counter - rotational ring as a Dual Attached Station (DAS) or as a Single Attached Station (SAS) and support connection in a tree.

3. The concentrators shall display the status of each port, power status, and an operational status indicating whether the concentrator is fully operational. (Using LED's or LCD panels)

4. Physical interface through the Media Interface Connections (MIC) shall support the FDDI duplex plug that terminates the optical fiber from the network with losses less than 1dB for a plug to receptacle.

5. The optical interface - MCI shall support a 62.5/125 or a 50/100 core/clad multimode graded index, 500 MHZ -km fiber duplex connector.

3.2.2 General highly desirable requirements.

1. The electric interface - the concentrator shall provide support for an implementation of FDDI over IBM type 1,2, and 6 shielded twisted pair cabling (STP) for a distance up to 100m.

3.3 Interfacing LAN's

There are many differences among FDDI local area network standards ranging from the type of media to speed of transmission, nodes transmission, size of the single message, nodes encoding of message and distance between nodes.

The FDDI, IEEE 802.3 and 802.5 standards define different topology. IEEE 802.3 is a local bus topology. The 802.5 specifies local ring topology as a single ring topology. A failure on a single ring topology causes the ring to fail. IEEE 802.5 isolates the failure, but does not always recover. FDDI specifies a dual counter-totating ring topology. It also defines the tree and dual ring of trees topology that can be installed as hierarchial star in a structured cable plant. The FDDI dual counter-rotating ring is a robust fault-tolerant structure that ensures data flow in case of failure.

Table I compares the topologies specified by the FDDI, IEEE 802.3 and IEEE 802.5 standards.

Table II does comparison of media for LAN transmission.

Comparison of band width is shown in Table III, where band width is a measure of the amount of traffic the media can handle at one time.

And finally Table IV summarizes the differences and similarities among the FDDI, IEEE 802.3 and the IEEE 802.5 standards.

4. DESIGN, SYSTEM SELECTION AND IMPLEMENTATION OF FDDI

4.1 Introduction

The decision for FDDI depends on the following factors:

1. Type of LAN applications used by organization.
2. Current extent of LAN use.
3. Prediction on the nature of future LAN applications.
4. Predictions on future volume of LAN traffic.

When planning for the backbone system, network planners need to:

1. Choose vendors that provide a platform for a non proprietary open solution.
2. Understand the role and technology of bridges and routers that tie FDDI networks to sub-LAN's, the difference between SAS and DAS devices and advantages of concentrators, the advantage of the dust ring of trees topology.
3. Understand the FDDI management options.

The proprietary solutions-in the backbone systems can be costly because it leads to reliance on a single vendor for networking solutions, and prevents the organization from responding to evolving networking needs. The nonproprietary systems solution includes components from many vendors, and upgrades are done through software changes, thus providing flexibility and investment protection.

In choosing bridges or routers for FDDI, there are distinctly different uses for each LAN-to-LAN connections. Use bridges for the LAN-to-LAN interconnection when the

requirements are for low delay and high throughput. Use routers for the LAN-to-LAN interconnection when longer delay and low performance are acceptable and a high degree of insolation or control is required.

Before implementing FDDI, the questions relating to current LAN use can be answered accurately only by a thorough analysis of current levels of traffic and prediction of future traffic volumes must be based on trend analysis of current traffic patterns.

Appendix A provides a current testing for Ethernet traffic for the third floor Headquarters building, and Fig. 9 shows the space utilization with existing traffic.

4.2 FDDI Implementation

This includes:

1. Determine the configuration and extent of the existing cabling systems.
2. Develop the cable strategy if none exists.
3. Pull the cable within a building.
4. Bring the fiber to the work area on an as needed basis by running fiber optic cable from the wiring closet to the wall outlets in user offices.

Fig. 10 indicates the global plan for KSC FDDI transmission system in Phase I. Based on the Phase I plan for the KSC the Headquarters implementation is shown in Fig. 11. This decision on implementation of FDDI depends on current use and predicted future use, network size, and traffic flow on the network. When choosing components to implement an FDDI network the proprietary solution was avoided.

Bridges and routers both have their place in a network, however, bridges are used for low delay and high throughput, and routers are used when a high degree of isolation or control is required.

DAS workstation connection is used for small workgroups, and SAS and concentrator connections provide manageability reliability and expansion for networks as the demand increases.

The dual ring of trees topology is recommended topology because it protects the backbone from multiple failures, grows as the demand increases, and is easily maintained.

4.3 FDDI System Realization

FDDI is the one technology that consistently meets the latest high-performance corporate networking and communications criteria. The proposed structure for the KSC Headquarters; a nonproprietary implementation shown in Fig. 10 is widely accepted and supported in the industry as the next generation international standard for high-speed multivendor networking interconnections. In such configuration, standard SAS devices such as bridges, systems, and workstations are directly connected to the FDDI LAN through the concentrator, thus providing for the addition or removal of SAS or DAS devices in a nondisruptive manner. The operational integrity of the backbone and midspeed subnetworks is preserved.

4.4 FDDI Products.

4.4.1 The DEC concentrator 500 in modular configuration provides for the attachment of FDDI devices such as workstations, systems and Bridge 500s or other concentrators to the FDDI network.

4.4.2 The DEC bridge 500 provides the interconnection between a midspeed 10MB/s802.3/Ethernet LAN and high speed 100 MB/s FDDI network backbone.

A self-learning intelligent hardware device, it performs standard bridge functions such as filtering and forwarding, and transparent translation of network data between the FDDI and 802.3/Ethernet networks. The DEC Bridge 500, protocol-independent, accomodates multiple protocols.

4.4.3 The DEC FDDI controller 700 provides a direct FDDI connection for a digital high-performance RISC-based work station and brings the speed of FDDI to the desk top, it is a low-cost, high-performance interface option that is implemented as a SAS device. Attaches directly to the FDDI network through the DEC concentrator 500, which provides protection from network disruption and allows configuration flexibility.

5. Conclusion

By selecting Digitals, a nonproprietary solution for a Kennedy Space Center Headquarter's FDDI network, one has selected a secondary generation LAN technology that consistently meets the latest high-performance corporate networking and communications criteria.

Since FDDI is now widely accepted and supported in the industry as a next generation international standard for high-speed multivendor networking interconnection, this selection is most appropriate. The decision to implement FDDI network depends on a current use and predicted future use, network size, and traffic flow on the network. When choosing this realization, the stress was placed on a nonproprietory solution which includes components from a single vendor or from many vendors. In such case, upgrades frequently are done through software changes, thus providing flexibility and investment protection.

6. Future Research Suggestions

In order to maximize performance of the Kennedy Space Center LAN network, one must provide a framework for the management of heterogeneous, multivendor systems. Management functions are used by network - and system - level personnel to monitor, control, maintain the network - A comprehensive network management system provides for configuration, fault, performance, accounting, and security management.

References

1. D. Minoli, "Telecommunications Technology Handbook".
Artech House 1991

2. R. J. Ross, "Fiber Optic Communications Design Handbook".
Prentice Hall 1990

3. T. Edwards, "Fiber Optics Systems - Networks Applications".
J. Wiley 1989

4. G. E. Keiser, "Local Area Networks".
McGraw Hill 1989

5. Digital Equipment Corp., "A Primer to FDDI".
Digital Equipment Corp. 1991

Figures

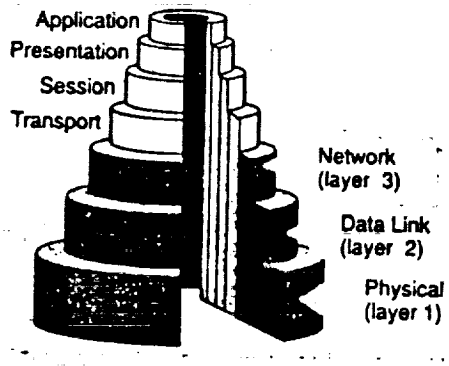

Figure 1 • The OSI model

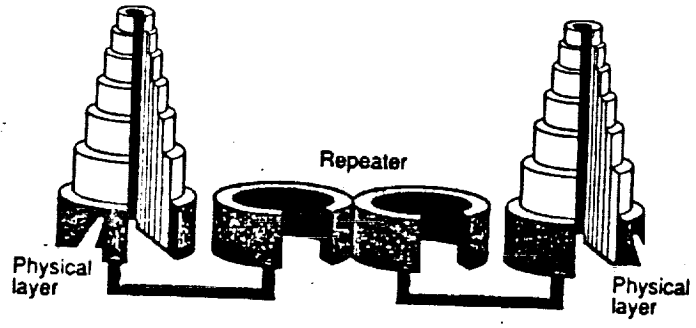

Figure 2 • OSI layer handled by a repeater

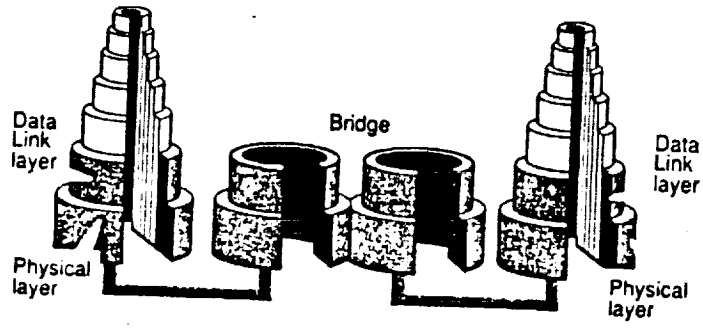

Figure 3 • OSI layers handled by a bridge

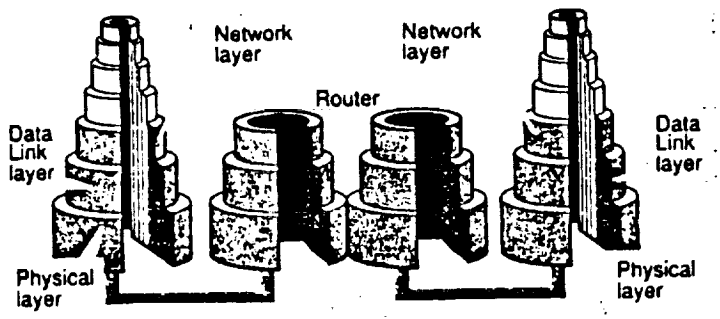

Figure 4 • OSI layers handled by a router

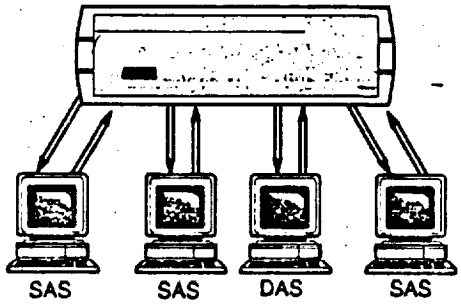

Figure 5 • Standalone concentrator topology

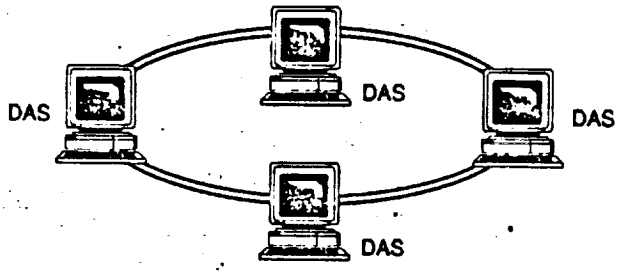

Figure 6 • Dual ring

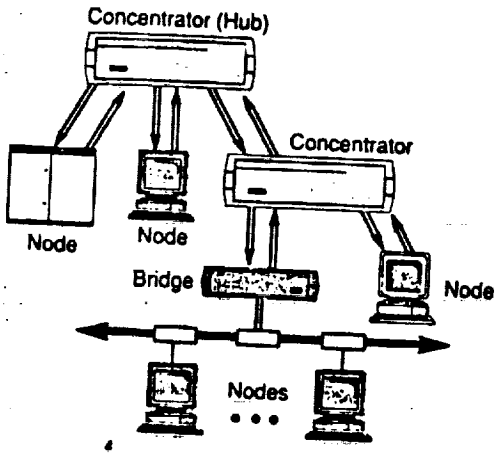

Figure 7 Tree of concentrators wired in a hierarchical star configuration

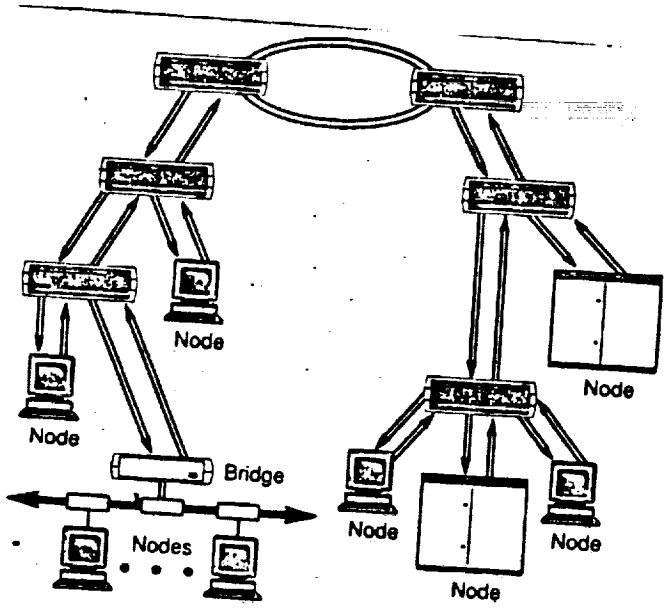

Figure 8 Use of concentrators in the dual ring of trees topology

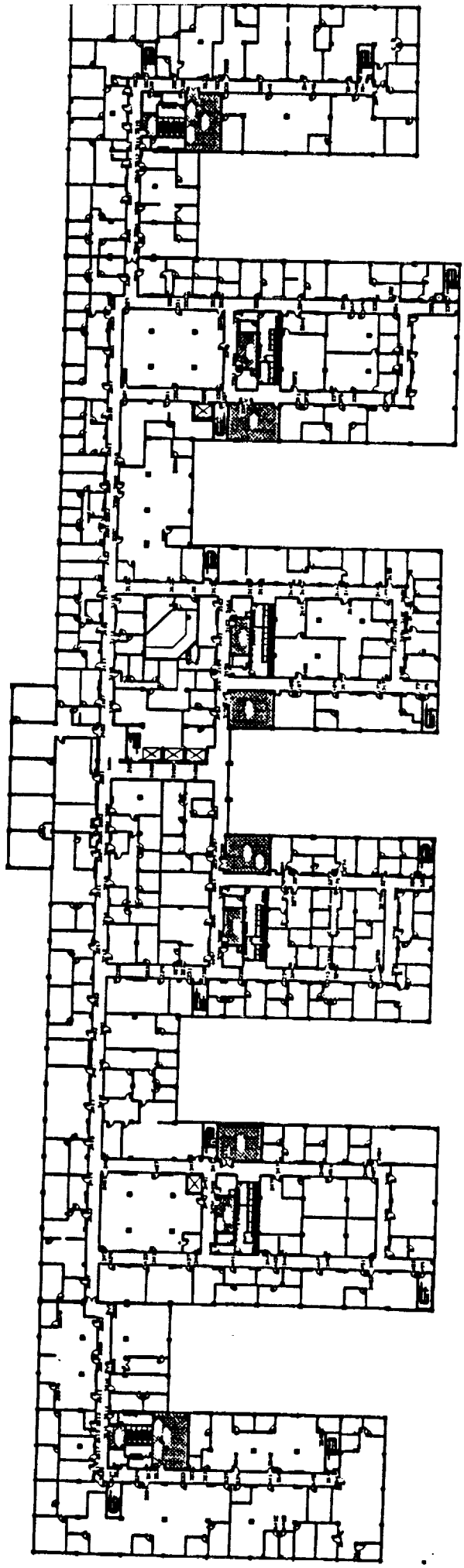

FDDI Transmission System

Preliminary Layout - PHASE 1

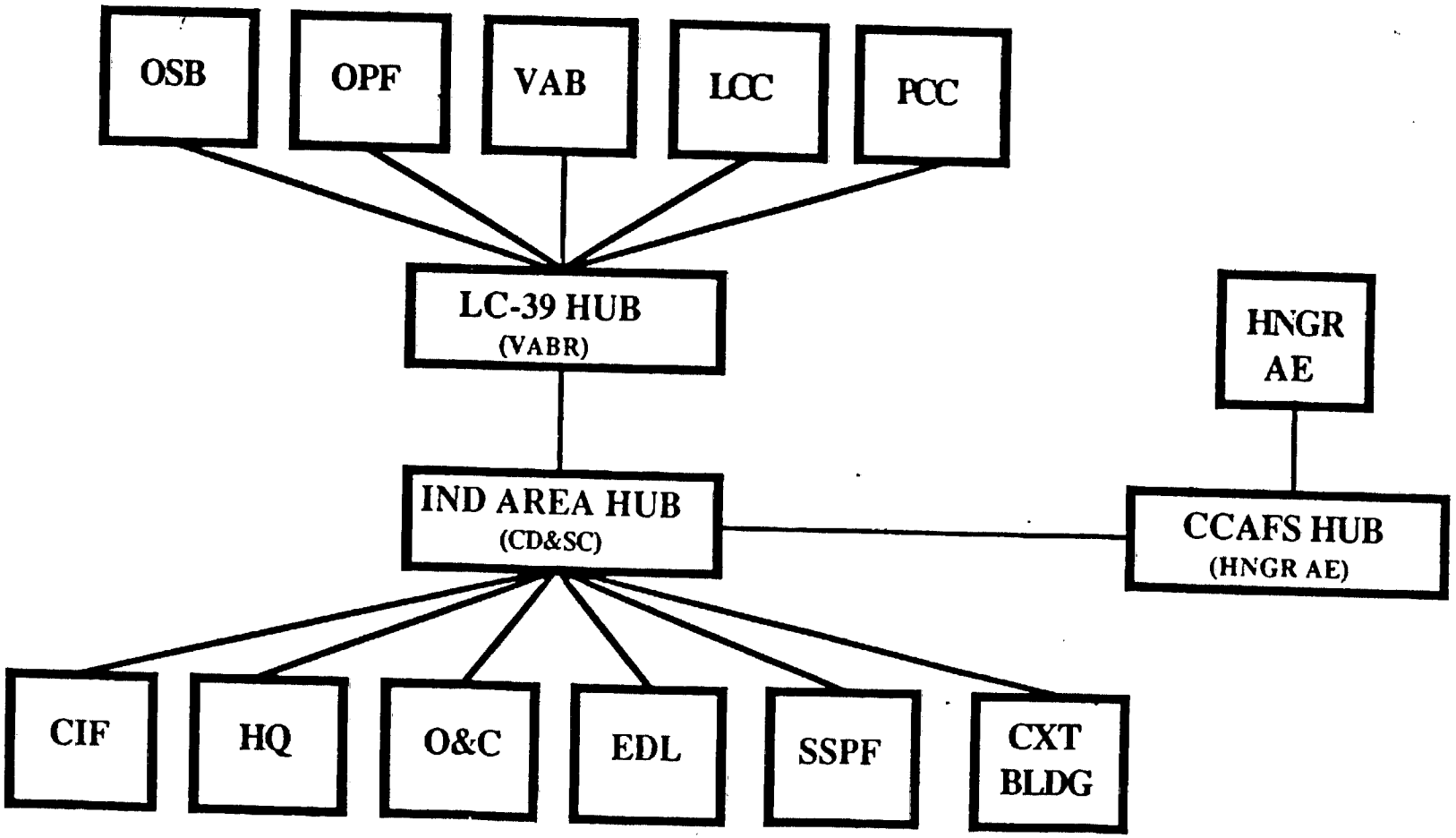

FIG. 10

FIG. 11

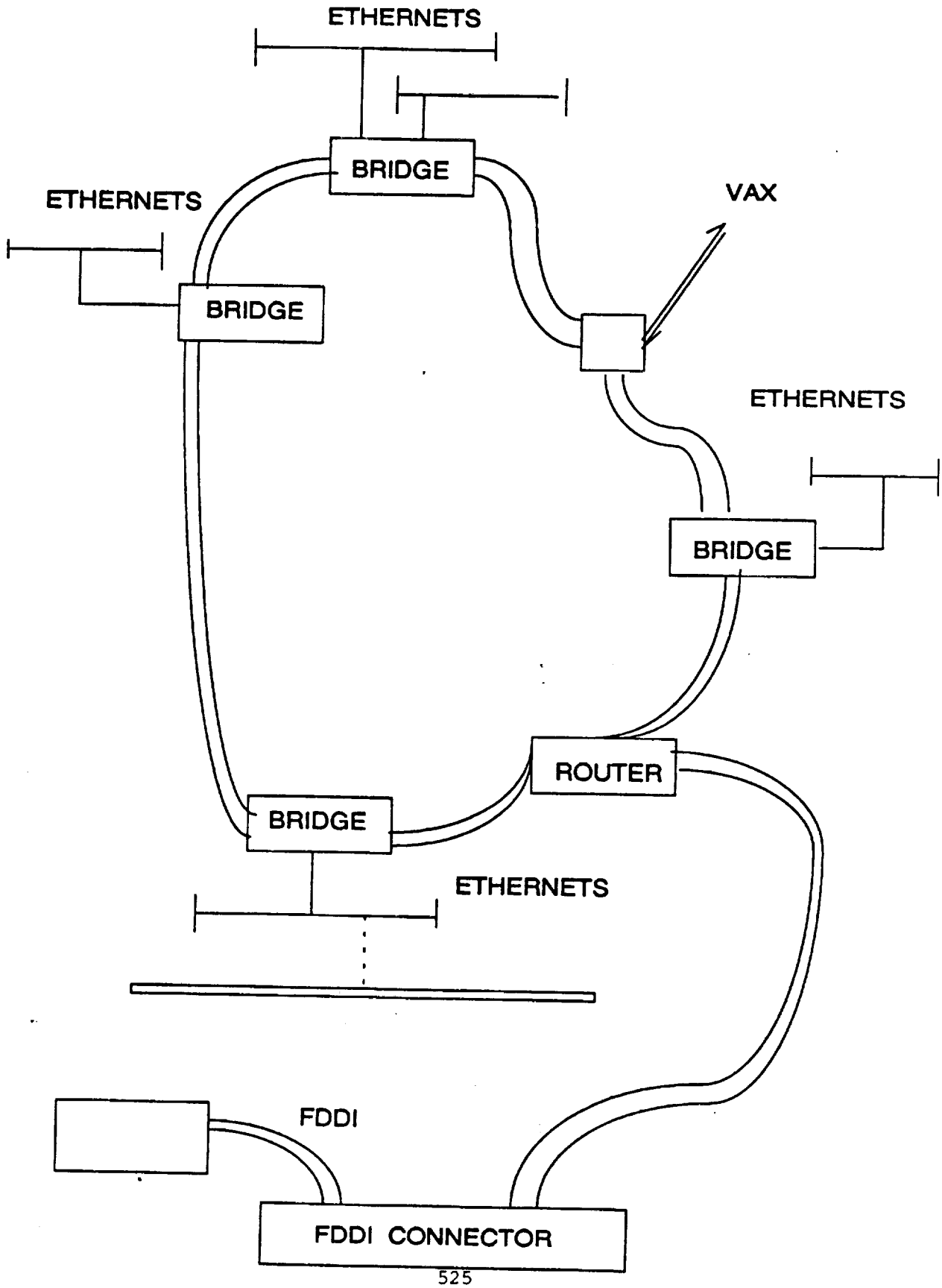
ETHERNETS
BRIDGE
ETHERNETS
VAX
BRIDGE
ETHERNETS
BRIDGE
ROUTER
BRIDGE
ETHERNETS
FDDI
FDDI CONNECTOR

Tables

Table 1 • Comparison of topologies

	FDDI	IEEE 802.3	IEEE 802.5
Logical topology	Dual ring, Dual ring of trees	Bus	Single ring
Physical topology	Ring, Star, Hierarchical star	Star, Bus, Hierarchical star	Ring, Star

Table 2 • Comparison of media

	FDDI	IEEE 802.3	IEEE 802.5
Media	Optical fiber	Optical fiber, Twisted-pair, Coaxial cable, Microwave	Twisted-pair, Optical fiber

Table 3 • Comparison of bandwidth

	FDDI	IEEE 802.3	IEEE 802.5
Bandwidth	100 Mb/s	10 Mb/s	4 or 16 Mb/s

Table 4. • Summary, comparison among standards

	FDDI	IEEE 802.3	IEEE 802.5
Logical topology	Dual ring, Dual ring of trees	Bus	Single ring
Physical topology	Ring, Star, Hierarchical star	Star, Bus, Hierarchical star	Ring, Star
Media	Optical fiber	Optical fiber, Twisted-pair, Coaxial cable, Microwave	Twisted-pair, Optical fiber
Bandwidth	100 Mb/s	10 Mb/s	4 or 16 Mb/s
Media access	Timed-token passing	CSMA/CD	Token passing
Token acquisition	By absorption	Not applicable (CSMA/CD)	By setting a status bit, converts token into a frame
Token release	After transmit	Not applicable (CSMA/CD)	After receive (4) or after transmit (16)
Messages on LAN	Multiple	Single	1 (4 Mb/s rings) muliple (16 Mb/s rings
Maximum frame size	4,500 bytes	1,518 bytes	4,500 bytes (4) 18,000 bytes (16)
Encoding Method	4B/5B NRZ/NRZI	Manchester	Differential Manchester
Number nodes	500	1024	260
Distance between nodes	2 km (1.2 mi)	2.8 km (1.7 mi)	300 m (984 ft) station to wiring closet (4 Mb/s ring), however, 100 m (330 ft) is recommended for both 4 and 16 Mb/s
Maximum network span	100 km (62 mi)	2.8 km (1.7 mi)	Varies with configuration

Appendix

	Time	%Usage
00	Jun 05 13:06:03	3.06
99	12:51:03	11.03
98	12:36:03	5.52
97	12:21:03	4.79
96	12:06:03	2.58
95	11:51:03	6.52
94	11:36:03	1.27
93	11:21:03	4.38
92	11:06:03	3.41
91	10:51:03	3.66
90	10:36:03	5.07
89	10:21:03	8.38
88	10:06:03	7.61
87	09:51:03	8.99
86	09:36:03	3.52
85	09:21:03	9.07
84	09:06:03	4.07
83	08:51:03	4.31
82	08:36:03	12.89
81	08:21:03	8.16
80	08:06:03	6.09
79	07:51:03	9.72
78	07:36:03	11.25
77	07:21:03	7.75
76	07:06:03	8.27
75	06:51:03	5.46
74	06:36:03	3.13
73	06:21:03	1.86
72	06:06:03	1.03
71	05:51:03	0.62
70	05:36:03	0.63
69	05:21:03	0.66
68	05:06:03	0.62
67	04:51:03	0.67
66	04:36:03	0.63
65	04:21:03	0.61
64	04:06:03	0.63
63	03:51:03	0.68
62	03:36:03	0.67
61	03:21:03	0.65
60	03:06:03	0.65
59	02:51:03	0.69
58	02:36:03	0.69
57	02:21:03	0.69
56	02:06:03	1.21
55	01:51:03	2.49
54	01:36:03	2.54
53	01:21:03	2.13
52	01:06:03	1.32
51	00:51:03	2.13
50	00:36:03	1.59

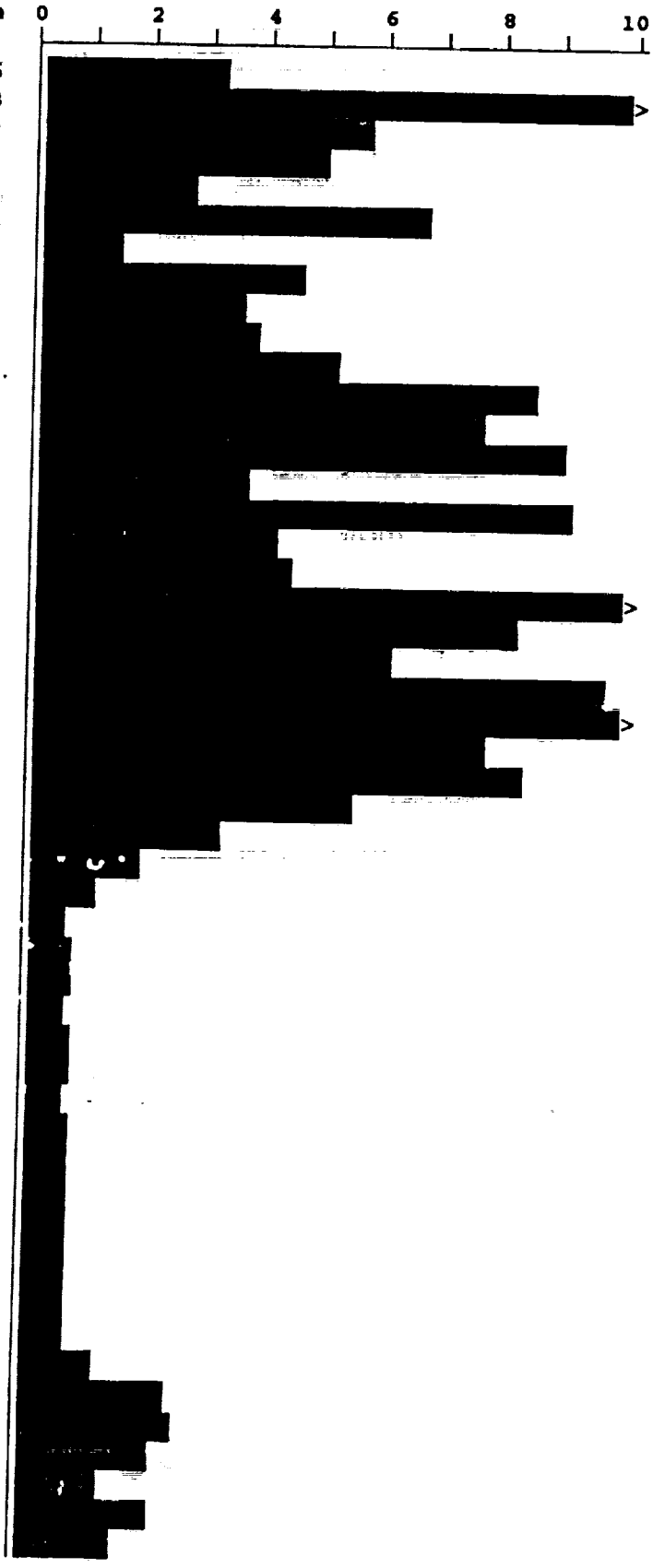

49	Jun 05	00:21:03	1.19
48		00:06:03	0.93
47	Jun 04	23:51:03	1.02
46		23:36:03	1.24
45		23:21:03	1.05
44		23:06:03	3.26
43		22:51:03	3.33
42		22:36:03	4.16
41		22:21:03	2.51
40		22:06:03	3.86
39		21:51:03	4.38
38		21:36:03	4.48
37		21:21:03	4.24
36		21:06:03	3.29
35		20:51:03	2.23
34		20:36:03	3.01
33		20:21:03	2.63
32		20:06:03	4.46
31		19:51:03	5.04
30		19:36:03	5.65
29		19:21:03	5.42
28		19:06:03	5.08
27		18:51:03	4.02
26		18:36:03	3.38
25		18:21:03	3.85
24		18:06:03	1.64
23		17:51:03	0.95
22		17:36:03	1.85
21		17:21:03	2.53
20		17:06:03	1.18
19		16:51:03	2.71
18		16:36:03	4.16
17		16:21:03	5.40
16		16:06:03	4.02
15		15:51:03	8.03
14		15:36:03	3.84
13		15:21:03	4.01
12		15:06:03	4.46
11		14:51:03	4.38
10		14:36:03	2.55
9		14:21:03	5.34
8		14:06:03	3.28
7		13:51:03	2.55
6		13:36:03	2.95
5		13:21:03	3.16
4		13:06:03	3.36
3		12:51:03	3.86
2		12:36:03	8.28
1		12:21:03	5.28

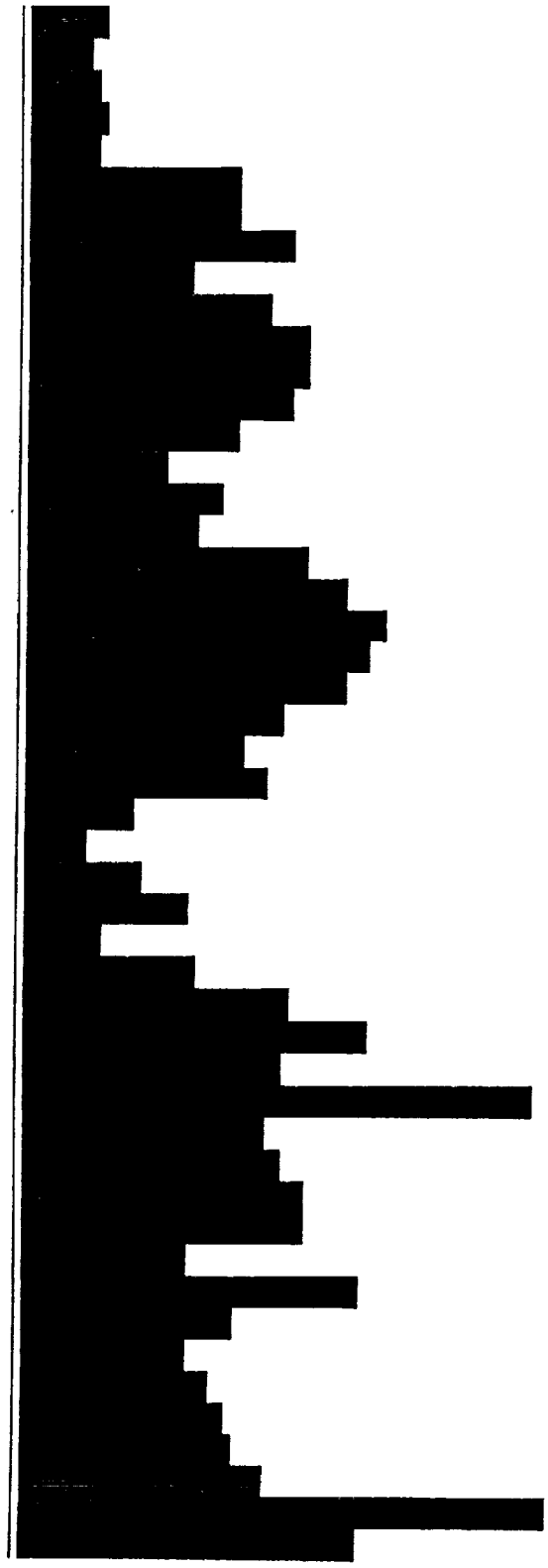

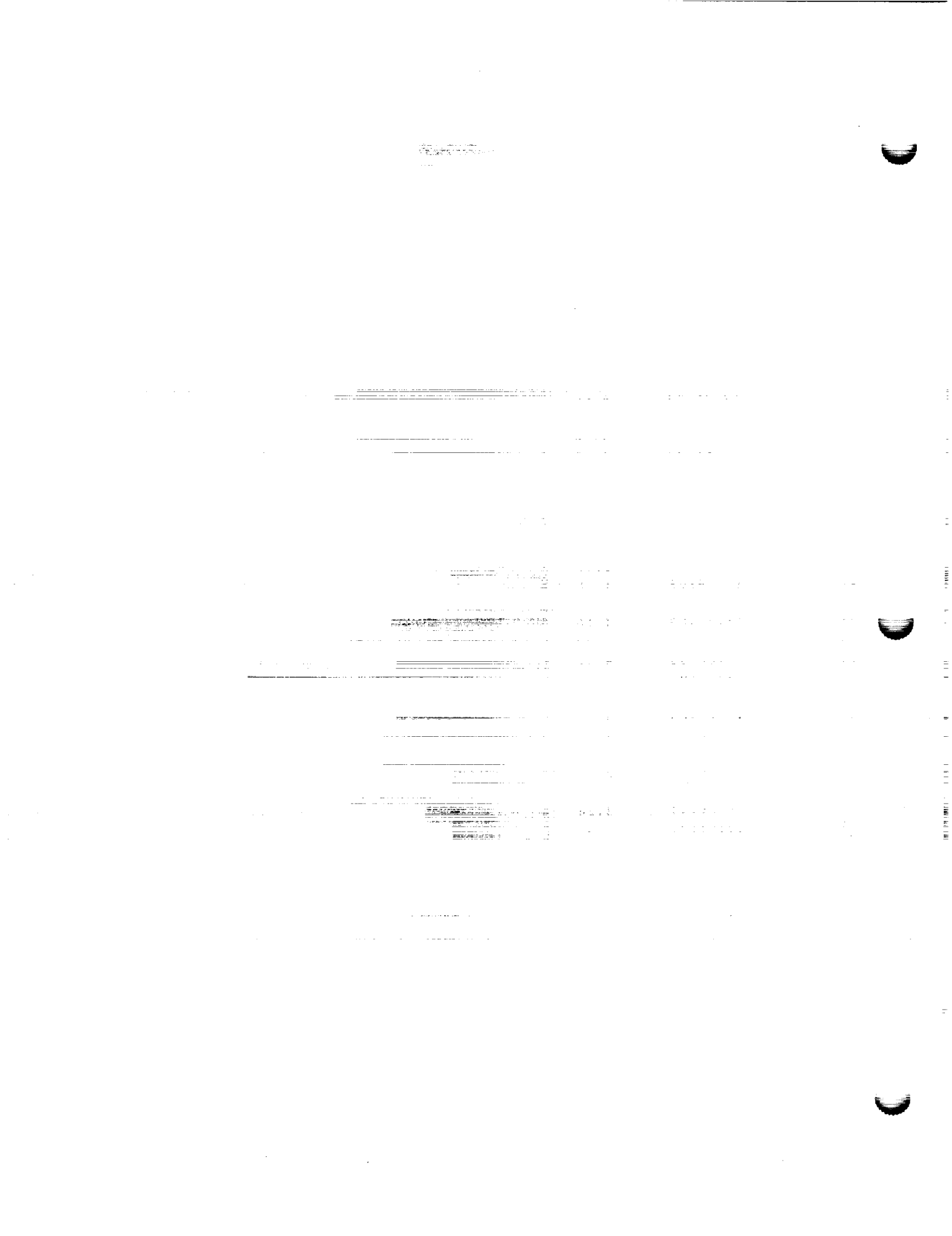

1992 NASA/ASEE SUMMER FACULTY FELLOWSHIP PROGRAM

JOHN F. KENNEDY SPACE CENTER
UNIVERSITY OF CENTRAL FLORIDA

INVESTIGATION OF THE BANDWIDTH OF MULTIMODE OPTICAL FIBERS USED WITH 1550-nm LED AND LASER SOURCES

PREPARED BY:	Mr. Preston A. White III
ACADEMIC RANK:	Professor
UNIVERSITY AND DEPARTMENT:	Southern College of Technology Department of Electrical and Computer Engineering Technology
NASA/KSC	
DIVISION:	Electronic Systems
BRANCH:	Communications
NASA COLLEAGUE:	Larry J. Hand, Jr. Po T. Huang
DATE:	August 21, 1992
CONTRACT NUMBER:	University of Central Florida NASA-NGT-60002 Supplement: 8

ACKNOWLEDGEMENTS:

There are many people whose help must first be acknowledged, for without their help, which was sought so many times and in so many areas, this research effort would not have been possible.

Special thanks to my NASA colleagues Larry Hand for granting me the opportunity to make a small contribution to the fascinating work done within his Video and Data Section, and to my mentor, Po Huang, for his patient counsel and for generously allowing me to take advantage of his vast personal library.

My gratitude to the Fiberoptic Laboratory's support personnel cannot be overstated. I am indebted to Houston Galloway for his work before my arrival to try to ensure that the laboratory would be ready to support this research and for his design and fabrication skills which resulted in the custom-made E/O modules that made some of our studies possible. To Robert Swindle, who was always there, thank you for all of your help with the instrumentation. And to a ready and willing co-op student, Reginald Campos, thanks for all of the help with fabrication and for your patience helping me sort out the laboratory's computing equipment.

Finally, let me add my thanks to that of all of the other faculty researchers to the NASA and UCF people that administered a wonderful summer research program. Carol Valdes arranged a fascinating series of tours (and a VIP launch pass!) that enabled us to better understand the complexity of the mission of KSC. Loren Anderson oversaw our research efforts and helped draw us together with preprogram correspondence and summer newsletters. And Kari Stiles did a such a great job fielding questions and keeping up with the numerous forms required by NASA and UCF.

It's not enough, but thank you all. It's hoped that our efforts have provided at least a small benefit to America's space program and to KSC. I'm proud to have worked with you.

ABSTRACT:

Multimode optical fibers are not intended to be used with 1550-nm sources; however, it is desirable to utilize 1300/1550-nm wavelength division multiplexing (WDM) on some multimode fibers at Kennedy Space Center (KSC). No information from fiber vendors nor from the literature is available to support this use. Preliminary studies at KSC have suggested that these fibers might be usable at 1550-nm if the fibers possessed enough bandwidth when sourced by LEDs.

Detailed bandwidth studies were made on 12 multimode fibers using 1300- and 1550-nm lasers and LEDs. The results showed that the modal bandwidth at 1550-nm was about 50% of the 1300-nm value and that the chromatic dispersion could be predicted by extrapolating the vendor's specifications for wavelengths outside the 1550-nm region. Utilizing these data, predictions of the fiber's optical bandwidth were accurately made. Problems with launch conditions and possible differential attenuation at connectors was noted at 1300-nm but was less significant at 1550-nm.

It appears that the multimode fibers studied will offer adequate performance in the 1550-nm region for a number of current KSC needs. Studies of additional fibers are encouraged to gain more confidence and better understanding of the 1550-nm bandwidth of KSC's multimode optical fibers before committing to 1300/1550-nm WDM.

SUMMARY:

The Fiberoptic Laboratory at Kennedy Space Center is studying the use wavelength division multiplexing (WDM) on its multimode optical fibers using 1300-nm and 1550-nm sources. This appears to be the first time that 1550-nm sources are to be used with multimode fiber, which is routinely used at 850-nm and 1300-nm. Multimode fiber manufacturers do not publish any information about the performance of their fibers at 1550-nm nor have any published studies regarding this application been found in the literature. Preliminary attenuation measurements have shown that multimode fibers installed within the past five years have attenuation at 1550-nm that is low enough to be useful. More recently, a few fiberoptic video test circuits were modified to operate at 1550-nm and have demonstrated that there may also be enough bandwidth for some applications.

Before committing to WDM it was necessary to perform a detailed study to determine the bandwidth that results when the multimode fibers in use at KSC are sourced by 1550-nm LEDs. The research reported herein is the result of numerous bandwidth tests on twelve Corning LDF fibers patched into six loops. The fibers were tested in the 1300- and 1550-nm regions, utilizing both lasers and LED sources, then the results were compared to gain a better understanding of the response of the fibers in both regions.

By using narrow-spectrum lasers as sources, it was found that the modal bandwidth of the LDF fibers at 1550-nm is approximately 50% of that available at 1300-nm. The modal bandwidth measurements are very sensitive to launch conditions; however, the 1550-nm measurements exhibited much less sensitivity. This launch sensitivity may be an operational issue due to the widespread use of non-keyed biconic connectors in the multimode fiber circuits at KSC.

Custom-made LED sources were used to make optical bandwidth measurements. These measurements showed that the LDF fiber's bandwidth was limited at 1300-nm by modal-distortion but was chromatic-dispersion limited at 1550-nm. The chromatic dispersion information available from the vendor appears be valid in the 1550-nm range, eventhough the vendor's specifications exclude this range. By combining these specifications it was possible to make predictions of the optical bandwidth of the test fibers that were within 6% of the measured data.

The results of these tests on twelve fibers lead to the conclusion that WDM of 1300-nm and 1550-nm information onto the multimode fibers at KSC appears promising. Before committing to this technology, the results of this study should be confirmed by making additional measurements on a wider range of installed multimode fibers at the Center.

Table of Contents

List of Figures

List of Tables

1. INTRODUCTION

Kennedy Space Center (KSC) has a long history of utilizing fiberoptic communication technology, beginning when the technology was in its infancy. As the fiberoptics has matured over the past fifteen years, KSC has continued to install even more fiberoptic cables and terminal equipment. Today there are thousands of kilometers of multimode and singlemode optical fibers in multiple-fiber cables that interconnect virtually every facility at the Center. These fibers are used to transport all manner of communication signals including data, video, and voice.

As new advances in fiberoptic technology become available, KSC personnel research the possible uses of these new technologies in support of the Center's present and future communication needs. Those advances that support KSC's mission are quickly put to work. Such is the case with *wavelength division multiplexing* (WDM), a relatively new technology that allows the multiplexing of several independent simultaneous signals onto one fiber by using a different wavelength source for each signal. The use of WDM can allow an immediate increase in information carrying capacity by more efficiently utilizing existing fibers thereby achieving better economy compared to adding more fiberoptic cables. Currently, KSC is gaining experience with WDM to understand how it can be best used to support the various activities conducted at the Center.

1.1 Multimode Fiber Transmission

Optical fibers are categorized as either singlemode or multimode fibers. Singlemode fibers offer the highest performance, having a virtually unlimited bandwidth (information carrying capacity) and the lowest loss. Singlemode fibers allow fiberoptic transmission over distances greater than 100 km or multi-gigahertz bandwidths. The price of this high performance is that singlemode fibers are more difficult to splice or connectorize and usually require laser sources which are themselves fragile and expensive. Therefore, it is attractive to use multimode fibers when these fibers provide adequate performance. For the distances encountered at KSC, many communication applications can be served by multimode fibers sourced by less expensive and easier to maintain LED-based terminal equipment.

Commercial multimode fiber comes in four standard sizes, with the best performance offered by *50/125* fibers (fiber that has a 50-μm diameter core and a 125-μm diameter clad) as shown in Figure 1. These fibers are invariably *graded-index* fibers which are designed to provide excellent optical confinement by continuously refocusing the light toward the fiber centerline. This is done by carefully modifying the glass formulation in the fiber's core so that the index of refraction is reduced away from the centerline. The multimode fibers currently installed at KSC are 50/125 graded-index fibers. The light rays confined in the core travel curved paths which can be called *modes*. There are several hundred modes in 50/125 fiber. Modes close to the center (for example *(a)* in Figure 1) are *low-order modes* and those far from the center (*(c)* in the Figure) are *high-order modes*. The high-order modes are the least strongly confined and often

are lost in poor quality fibers or in fiber paths that have poor connectors, splices, stressful installation or other quality problems.

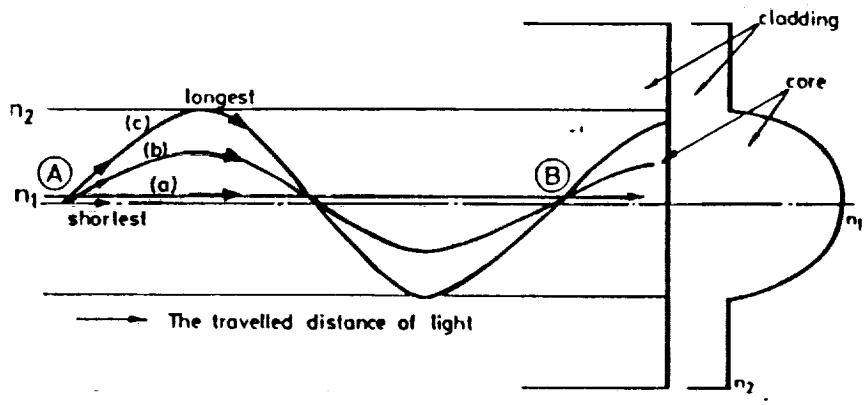

Figure 1. Multimode Optical Fiber

Commercial multimode graded-index fibers have been designed to take advantage of two areas of low attenuation in glass, that naturally occur for light that has wavelengths around 850-nm and around 1300-nm. These areas of high transparency are called *first-window* and *second-window* respectively. Due to the nature of glass, first-window operation is too lossy to be of use over the distances routinely encountered at KSC; therefore, the Center's multimode fibers are sourced by LEDs and lasers that have wavelengths around 1300-nm; that is, by second-window sources.

1.2 Utilization of the Third Window

There is a third window, centered around 1550-nm, which is often used in singlemode fiber systems. However, no fiber vendor offers information on the performance of its 50/125 multimode fibers at this wavelength. Today's WDM devices routinely combine 850- and 1300-nm operation on multimode fibers and 1300- and 1550-nm operation on singlemode fibers.

Since WDM appeared attractive for some applications at KSC and since 850-nm operation was too lossy, some preliminary tests were performed to see if a usable third window existed in KSC's installed multimode fiber. Attenuation tests showed that older fibers were very lossy but fibers less than five years old exhibited a low attenuation window around 1550 nm. This led to the belief that it might be possible to use KSC's 50/125 fibers at both 1300 and 1550 nm, and therefore, WDM might be possible at these wavelengths.

1.3 Necessity of Bandwidth Studies

Given that the multimode fibers exhibited low loss at 1550-nm it is still possible that the bandwidth available in this window might be too low to be practical. The fiber vendors offer

little information on this subject; therefore, tests would need to be made on some installed fiber at KSC to try to understand whether sufficient bandwidth might be available in this window.

A preliminary test was performed by replacing the some of the 1300-nm LEDs with third window LEDs in some of the single-channel video on fiber terminal equipment common at KSC. It was found that most of these modified units still functioned acceptably in third-window operation.

Those encouraging results led to the work reported herein. This research effort seeks to determine the bandwidth that is available in KSC's 50/125 multimode fibers when third window sources are used and to understand the factors that affect third-window bandwidth.

2. FACTORS AFFECTING MULTIMODE FIBER BANDWIDTH

While the 50/125 fiber that is installed at KSC has come from several vendors, the majority of the fiber is from Corning and carries Corning's trade name *Long Distance Fiber* abbreviated LDF. It is this fiber that will be the subject of these studies.

2.1 Modal Distortion

The 50/125 multimode optical fiber common at KSC, allows the propagation of several hundred individual electromagnetic modes as information is guided down the waveguide. Each mode has its own discrete properties including power distribution profile, ray path and propagation delay. The differences between modal propagation delays lead to undesirable distortion manifested as optical pulse broadening, or equivalently, modulation bandwidth limitations. Bandwidth limitations due to this effect are known as *Modal Bandwidth.* Only singlemode fibers are immune to modal bandwidth limitations which is the primary reason that these fibers offer the highest performance.

System designers request one bandwidth parameter that will allow prediction of system performance; however modal bandwidth must be treated as an approximation since it results from a complex interaction of the modes which is influenced by many factors including:

1) the chemical composition and purity of the glass,
2) the indices of refraction of the core and clad and
3) the index of refraction profile

Furthermore, any event that changes the power distribution among the modes will alter the modal bandwidth. Even the small random variations of these parameters, which are inevitable in today's mass-produced fibers, will substantially affect modal bandwidth. Therefore, to be useful in system design, modal bandwidth parameter must be conservatively and cautiously applied.

Graded-index multimode fibers are designed to minimize the modal distortion by differential doping of the host glass to give radial reduction of the core's index as shown in Figure 2. One mathematical parameter can describe the index of refraction reduction function and is called the fiber's *index profile parameter*, α. The figure exemplifies the variation of actual profile of a practical fiber from the design profile.

Dielectric waveguide theory shows that for any one wavelength of light there is one discrete α that causes modal pulse distortion to become negligible. However, since it is not possible to operate a fiber at one wavelength (no monochrome sources exist) and since real fibers have random variations in their profile parameter, practical graded-index fibers always have some significant modal distortion. For today's multimode fibers, α is chosen either to optimize the fiber's modal bandwidth for one window or to give moderately good performance in both first and second windows. Generally, manufacturers optimize 50/125 multimode fiber for second window operation so that the bandwidth is highest in this region. Fiber manufacturers test the modal bandwidth of their multimode products and publish a specification called the

bandwidth•length product that gives the typical modal bandwidth for a one-kilometer continuous length of fiber. Bandwidth•length products are given for first and second window operation but no information is available for third window operation.

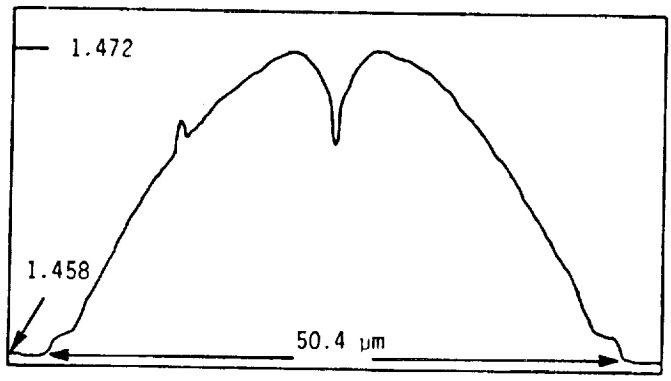

Figure 2 - Index of Refraction Profile

If the fiber's modal bandwidth properties are specified for one kilometer of fiber, it is necessary to know how to scale this specification to the actual lengths of installed fiber; especially, when fiber paths usually consist of a concatenation of several shorter fiber sections. This scaling is usually summarized using the following equation:

$$BW_M = BW_{(l)}/L^{\gamma} \qquad (1)$$

where $BW_{(l)}$the bandwidth•length specification, BW_M is the modal bandwidth of length L (kilometers) of fiber and γ is the *concatenation factor*.

The publishing of a bandwidth•length product should not be interpreted as meaning that the bandwidth is inversely proportional to the length; that is, that $\gamma = 1$. Experiment has shown that γ depends on the axial variability of the optical properties of the fiber which cause an increase of power mixing among the modes. Generally, γ is in the range $0.7 \leq \gamma \leq 1$. Fibers with a lot of variability will have a high degree of mode mixing which leads to a lower γ but high-quality fibers with less variability will have a γ closer to unity. However this analysis is only true for continuous lengths of fiber. Fiber-to-fiber joints (connectors or splices) can cause a very large disruption in the power distribution among the several hundred propagating modes which in turn may cause large variations in modal distortion. For concatenated fiber paths containing many fiber joints, the modal distortion could be quite different from the bandwidth for the same length of continuous fiber. Usually, when concatenated into long paths, even high quality fibers will have a γ less than unity[1].

2.2 Chromatic Dispersion

Except for free-space, all transparent media propagate light waves at speeds that are somewhat dependent on the wavelength of the light. Therefore, different wavelengths of light travel at different speeds and possess different indices of refraction. Transparent materials that exhibit this effect are know as *dispersive materials*. The glass used in all optical fibers is dispersive. Figure 3 shows the dependence of index of refraction on wavelength for Corning's 50/125 LDF fiber[2].

Since fiberoptic sources are not monochromatic, a pulse of light propagating down a fiber will always consist of a group of wavelengths which will possess a range of propagation delays. Mathematically, it is convenient to define the *group index*, N, which is related to the speed at which the wavelength group will conduct information down the waveguide. Group index is related to index of refraction, n, by the following relation:

$$N = n - \lambda(dn/d\lambda) \qquad (2)$$

The group index for Corning 50/125μm LDF is included in Figure 3.

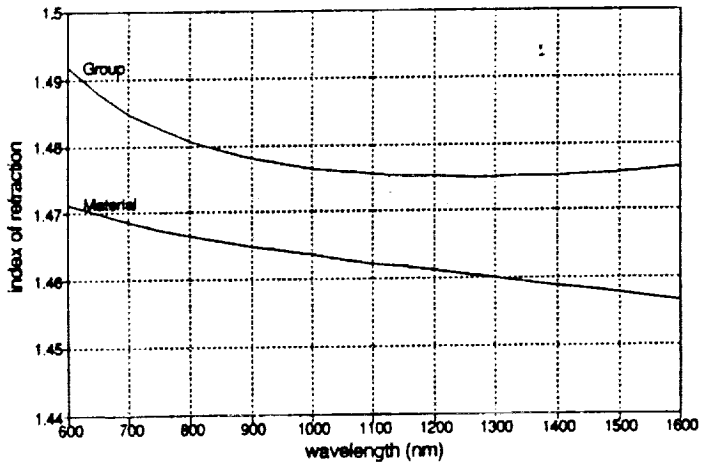

Figure 3. Index of Refraction for Corning LDF

The range of delays in the optical group will broaden optical pulses as they propagate along the fiber. The amount of pulse broadening will be determined by the fiber's material dispersion and the range of wavelengths emitted by the source. It must be reemphasized that since optical fibers are made from a dispersive material, all fibers, singlemode and multimode, exhibit dispersive pulse broadening.

In addition to material dispersion, there is an additional pulse broadening effect due to the confinement of light within a fiber waveguide. This effect is denoted as *waveguide dispersion*. Fiber vendors, knowledgeable of their product's performance and understanding the needs of the

customers publish the *chromatic dispersion*, D, which is the combined effect of material and waveguide dispersions.[3]

Group delay, τ, group index, N, fiber length, L, and chromatic dispersion, D, are related as follows:

$$\tau = LN/c \tag{3}$$

$$d\tau/d\lambda = L/c \cdot (dN/d\lambda) = L \cdot D \tag{4}$$

Figure 4 depicts these relations, for one kilometer of typical Corning 50/125 LDF.

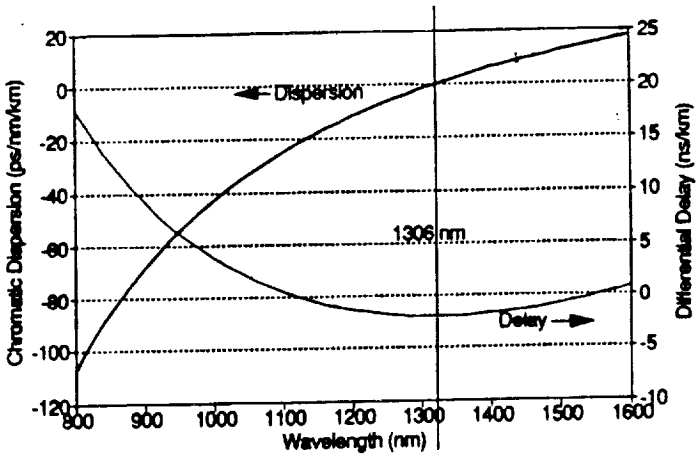

Figure 4. Chromatic Properties of Corning LDF

One standout feature of Figure 4 is that at $\lambda = 1306$ nm chromatic dispersion is zero. This is the *zero-dispersion wavelength*, λ_o, for Corning LDF; however, all ordinary (not dispersion-shifted) fibers have a dispersion graph very similar to the one shown and have a zero-dispersion wavelength in the range $1250 \leq \lambda_o \leq 1350$ nm. It is standard practice for fiber vendors to specify the chromatic properties of their products by giving two specifications: λ_o and S_o which are respectively, the zero-dispersion wavelength and the slope of the dispersion graph at λ_o.

These specifications can be used with the standard mathematical model that adequately describes ordinary fibers to give pulse delay characteristics as follows:[8]

$$\tau = \tau_o + S_o \cdot [\lambda - \lambda_o^2/\lambda]^2/8 \tag{5}$$

$$D = S_o \cdot \lambda \cdot [1 - (\lambda_o/\lambda)^4]/4 \tag{6}$$

Ultimately, system designers require a means to determine the effect of chromatic dispersion on the information carrying capability of installed optical fibers. This is usually done by

determining the pulse broadening, $\Delta\tau$, and the chromatic dispersion bandwidth, BW_D, using the following relationships ($\Delta\lambda$ is the FWHM spectral width of the optical source). For first- and third-window sources

$$\Delta\tau \cong L \bullet \Delta\lambda \bullet D \tag{7a}$$

for second-window sources:

$$\Delta\tau^2 \cong L^2 \bullet [(\Delta\lambda \bullet D)^2 + (\Delta\lambda^2 \bullet S_o/2)^2] \tag{7b}$$

and finally:

$$BW_D = 0.441/\Delta\tau \tag{8}$$

Unlike modal distortion, chromatic dispersion is not affected by launch conditions or fiber joints; therefore, chromatic dispersion bandwidth is inversely proportional to the length of the fiberoptic path. However, as the above relations show, dispersion bandwidth is critically dependent on the spectral characteristics of the fiberoptic source.

2.3 Expected Results:

The specification sheets for the Corning 50/125 LDF include the following information:[4]

Table 1. Properties of Corning LDF

1300-nm:	attenuation:	0.5 to 1.2 dB/km
		(KSC requires $\leq$1.0 dB/km)
	modal bandwidth:	400 to 1500 MHz•km
		(KSC requires $\geq$1000 MHz•km)
Chromatic Dispersion:		
	zero-dispersion wavelength, λ_o:	1297 to 1316 nm
	zero-dispersion slope, S_o	< 0.101 ps/km/nm^2
	dispersion function:	equation (6), $750 < \lambda < 1450$ nm
Index of refraction:	at 850-nm	= 1.4655
	at 1300-nm	= 1.4598

It is expected that the modal bandwidth of the Corning LDF test fibers will be quite high in the second window, since it's optimized for that operation, and somewhat reduced when third-window sources are used. Based upon KSC requirements and Corning specifications, the modal bandwidth•length product should be greater than the KSC minimum 1000 MHz•km when tested close to 1300-nm.

Also, modal bandwidth measurements may be difficult due to modal noise which is present in multimode fiber joints when narrowline lasers are used as sources. It will be important to use a

tightly constrained and overfilled launch condition to fully stimulate all of the modes when testing multimode fibers.[2]

When concatenated links are tested, the modal tests should produce a concatenation factor that is somewhat less than one. It is not known whether this factor will be different for 1300- and 1550-nm operation. The attenuation of the fiber paths under test should be less that 1.0 dB/km in second window operation and slightly lower in third window tests. There may be a relationship between attenuation and modal bandwidth if the fiber joints in the paths under test are subject to differential mode attenuation. In this case, higher loss links may have a higher apparent bandwidth.

Chromatic dispersion effects should be much larger for third window operation than for second. It is expected that the information bandwidth of the 50/125 LDF fibers will be dispersion-limited for third window operation; but dispersion and modal distortion may be equally important for second window tests.

Based upon the Corning's chromatic specifications and assuming an LED source with a FWHM of 65-nm the dispersion bandwidth of one kilometer of fiber should be as shown in Figure 5.

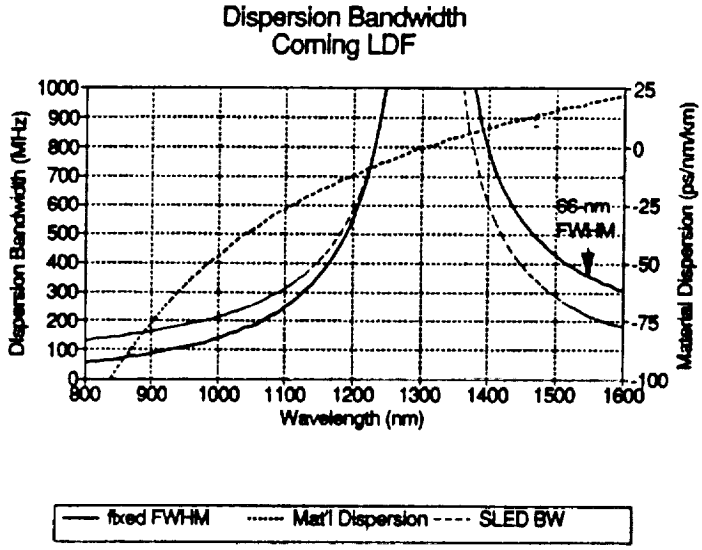

Figure 5. Dispersion Bandwidth for Corning LDF

3. INSTRUMENTATION AND RESEARCH DESIGN

There are twelve Corning LDF fibers that connect the Engineering Development Laboratory (EDL) with the Communication Distribution and Switching Center (CDSC). These fibers are reserved for tests and terminate in the EDL's Fiberoptic Laboratory in biconic connector ports labelled *1* through *12*. In order to allow reliable measurement of a wide range of fiber paths, these 12 fibers were patched into 6 test loops. Four test loops consisted of 4.8-km of fiber looped back at the CDSC. Two test loops consisted of a total of 12.8-km of fiber patched through at the CDSC and looping back at the Banana River Repeater Station (BRRS). Measurements included up to three concatenated CDSC loops. Figure 6 depicts the test loops.

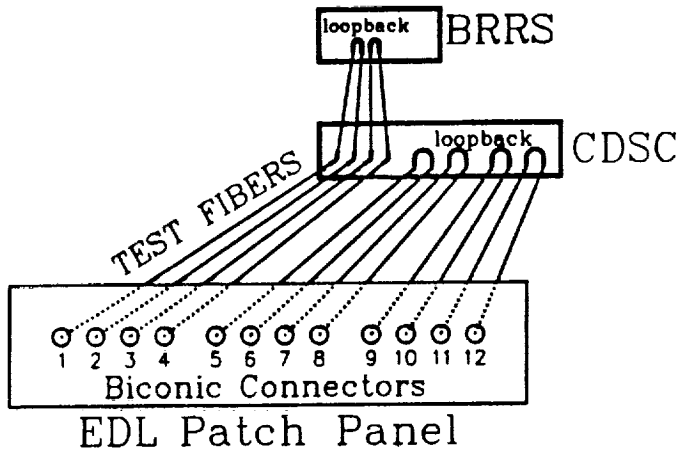

Figure 6. EDL Test Fiber Loops

In support of the wide utilization of fiberoptic technology at KSC, the Fiberoptic Laboratory houses an impressive collection of fiberoptic test instrumentation which allows a complete range of testing of both singlemode and multimode fibers and entire fiberoptic systems. The laboratory's support personnel possess a praiseworthy range of expertize and their aid and counsel made the investigations described herein possible.

Table 2. Test Loop Characteristics

EDL Fiber Numbers	Loop-back Point	total distance (km)	Attenuation (dB)			
			1299-nm		1549-nm	
			forward	reverse	forward	reverse
1-2	BRRS	12.8	16.7	15.8	20.5	19.6
3-4	BRRS	12.8	19.5	18.4	24.6	22.6
5-6	CDSC	4.8	14.7	14.6	15.3	15.8
7-8	CDSC	4.8	8.6	9.7	9.5	10.4
9-10	CDSC	4.8	7.7	6.7	8.5	8.3
11-12	CDSC	4.8	7.4	6.1	7.3	8.9

3.1 Attenuation Measurements

The attenuation of each loop was recorded at 1298-nm and 1549-nm using an EXFO FOT-90 Fiberoptic Test Set. Table 2 summarizes the results of the attenuation tests.

To gain more information on the test loops, each loop was scanned using a Laser Precision TD-9960 OTDR with a TD-861 1300-nm Multimode Optical Module. Figure 7 is an example of one of the OTDR traces.

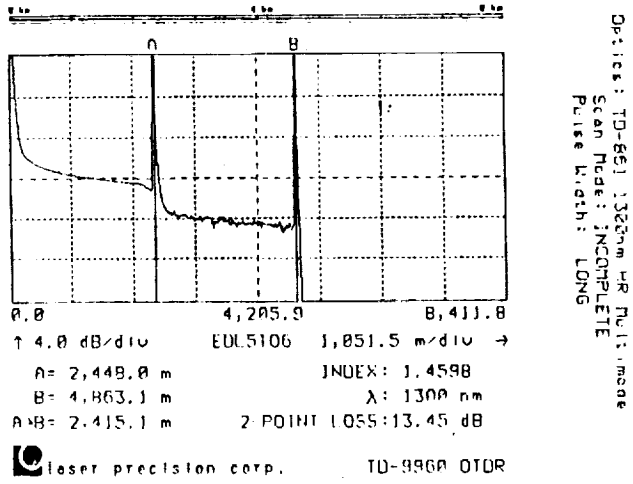

Figure 7. OTDR Trace of Loop *5-6*

3.2 Modal Bandwidth Studies

A recently acquired Hewlett-Packard HP-8702B Lightwave Component Analyzer was used to measure the modal bandwidth of the multimode test fibers. As the block diagram in Figure 8 shows, the HP-8702B is essentially a 300-kHz to 3-GHz microwave network analyzer. By utilizing the calibrated E/O and O/E converters the HP-8702B can make swept-frequency measurements of optical fibers. As the first two rows of Table 3 show, the two Hewlett-Packard laser-based E/O modules had wavelengths of 1309 nm and 1533 nm, chosen to allow fiber measurements in the second and third windows.

Table 3 - E/O Source Modules

E/O Module		Optical Spectrum		Coupled
		peak	FWHM	Power
Name	maker	(nm)	(nm)	(dBm)
83402A	HP	1309	3	+0.4
83403A	HP	1533	5	-1.6
LED-2	custom	1314	65	-12.0
LED-3	custom	1504	62	-14.3

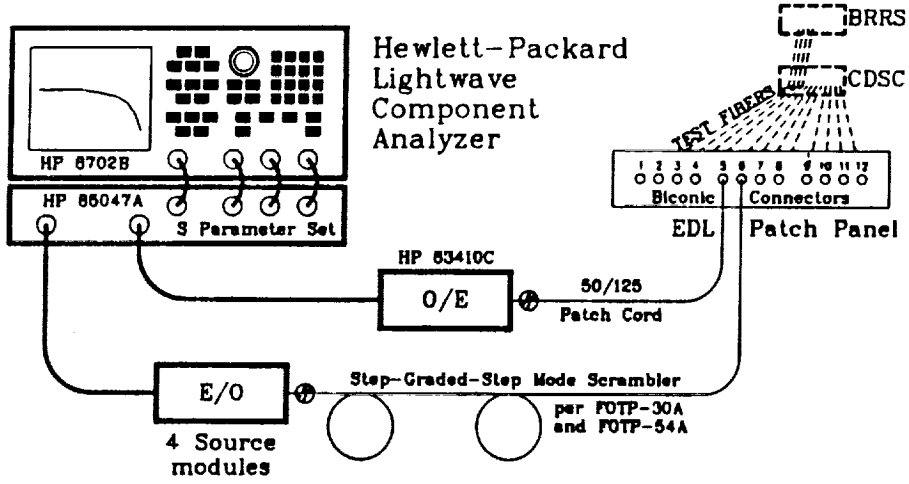

Figure 8. Lightwave Component Analyzer

Modal bandwidth measurements were made in accordance with FOTP-30A[5]. Due to the lengths of the test loops, cladding mode strippers were deemed unnecessary and were not used. In order to enhance measurement reliability, an Anritsu step-graded-step mode scrambler was used at the test fiber loop launch aperture to create a uniformly overfilled launch condition; thus meeting the criteria specified in FOTP-54A[6]. The spectral widths of the Hewlett-Packard E/O lasers were narrow enough so that, according to FOTP-30A, chromatic dispersion effects could be considered insignificant. Thus, the bandwidth measurements made using these E/Os would represent modal distortion bandwidths.

3.3 Chromatic Dispersion Effects

Direct measurements of chromatic dispersion and/or chromatic dispersion bandwidth were not possible with the instrumentation available in the Fiberoptic Laboratory. However, chromatic bandwidth information could be indirectly obtained if bandwidth measurements of the test fibers could be made using a broad-linewidth, LED-based, E/O converter connected to the HP-8702B. Hewlett-Packard does not offer such converters; therefore, the Fiberoptic Laboratory's support personnel designed and fabricated two such modules, one for second-window and one for third-window measurements. The LEDs included in these modules were carefully selected from those available in the laboratory, for high output power, reasonable spectral width and fast risetime. The optical characteristics of these custom-made E/O modules are given in the last two rows of Table 3.

Using the custom E/O modules, swept-frequency response measurements of all of the test loops would be attempted. It was expected that the dynamic range of the Lightwave Component Analyzer would be sufficient to reliably measure the response of two concatenated CDSC loops; however, it was not clear if measurements on three concatenated loops would be possible.

The modal bandwidth measurements obtained from laser E/O modules could be combined with computed dispersion bandwidths obtained using the chromatic specifications published by Corning to obtain an *expected* optical bandwidth. This expected optical bandwidth could then be compared to the measured optical bandwidths obtained using the custom LED E/O modules. It was hoped that a better understanding of factors affecting the third-window bandwidth of the CDSC fibers would result.

Theory suggests that chromatic effects should play a relatively minor role in the second window bandwidth; however, these effects should be a major factor in determining the useful bandwidth limitations when multimode fibers are used with third-window sources.

4. EXPERIMENTAL RESULTS AND DISCUSSION

Using the HP-8702B configured for optical measurements, frequency response plots were obtained for each of the multimode fiber test loops and for as many concatenated paths as possible. The frequency response of each fiber loop was recorded using each E/O source module. All tests were made in both directions. When making optical measurements with the HP-8702B, the electroptical characteristics of the stimulus and response elements (the E/O and O/E module pair and the mode scrambler and patch cord) are stored in the instrument's memory and are used to correct the end-to-end response of the fiberoptic circuit under test so that the display represents the optical performance of the test fiber. Therefore, the fiber's modal optical bandwidth is represented by the -3 dB response point on the plots[7]. A typical set of test plots is shown in Figure 9. As is seen in the Figure, the -3-dB bandwidth of each plot was recorded on the traces.

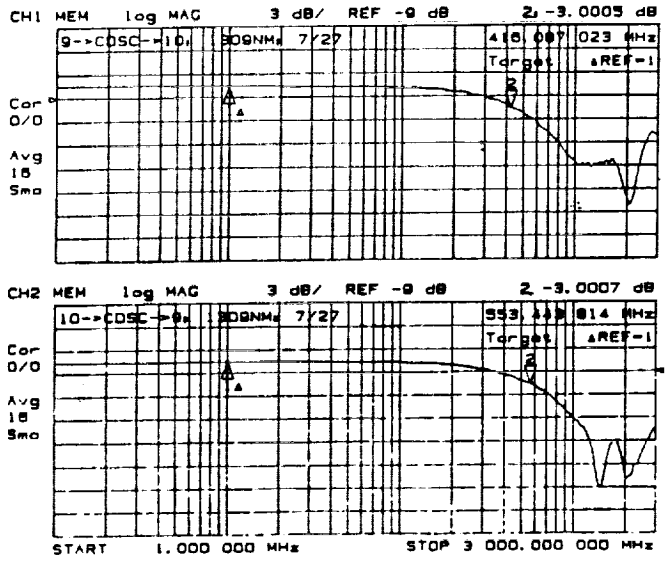

Figure 9. Typical Frequency Response Plot of Test Fibers

4.1 Modal Bandwidth Results:

While performing the modal bandwidth measurements several important observations were made. First, the second-window bandwidth measurements were very sensitive to launch conditions. Since non-keyed biconic connectors were used to interconnect the test equipment and the fiber test loops, the launch conditions could be easily changed. By simply rotating the launch connector a wide range of frequency plots for the same test path could be recorded. Bandwidth differences of as much as 25% were not uncommon. Figure 10 demonstrates this effect by showing two frequency response traces for the same test, where the only difference was that the biconic launch connector was rotated by approximately 60°. As the figure shows, an increase in coupling loss is generally accompanied by an apparent increase in the modal

bandwidth. A reasonable explanation of this effect is that when the launch conditions are changed so that less light is coupled into the fiber, the coupling efficiency of the weakly guided high-order modes is reduced more than the strongly guided low-order modes. Therefore, the higher-loss optical signal consists mostly of low-order modes which have a smaller range of propagation delays resulting in a higher apparent bandwidth.

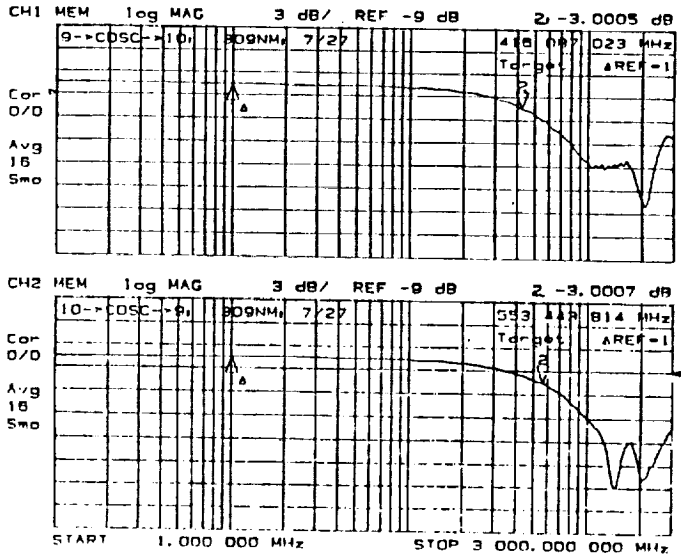

Figure 10. Effect of Launch Connector Rotation on Bandwidth

The third window tests exhibited far less of this launch-condition variability than the second window measurements. This is probably due to the fact that the optical properties of the multimode fiber were tuned to reduce the differential mode delays for second window operation when those fibers have all guided modes stimulated. On the other hand, using the fiber at other than the optimized wavelength produces a bandwidth that is predictably reduced in magnitude but is also reduced in sensitivity to optical path perturbations.

In an attempt to obtain a bandwidth data set that was least corrupted by launch condition variability, two additional steps were included in the test procedure: 1) 1309-nm bandwidth was measured after manipulating the launch connector to give maximum coupling efficiency, and 2) the 1533-nm measurement was then made without disturbing the launch connector.

Figure 11a depicts the results of the modal bandwidth measurements for all four EDL to CDSC test loops. Modal bandwidths are shown using bars and the primary ordinate; and the line and secondary ordinate express the 1533-nm modal bandwidth as a percent of the 1309-nm data. The average data, shown on the right of the figure, were computed without including the 5-6 loop (for reasons described below). As can be seen, the third window modal bandwidth averages 46% of the second window bandwidth; confirming the expectation of a reduction in modal bandwidth for wavelengths away from the optimized second window.

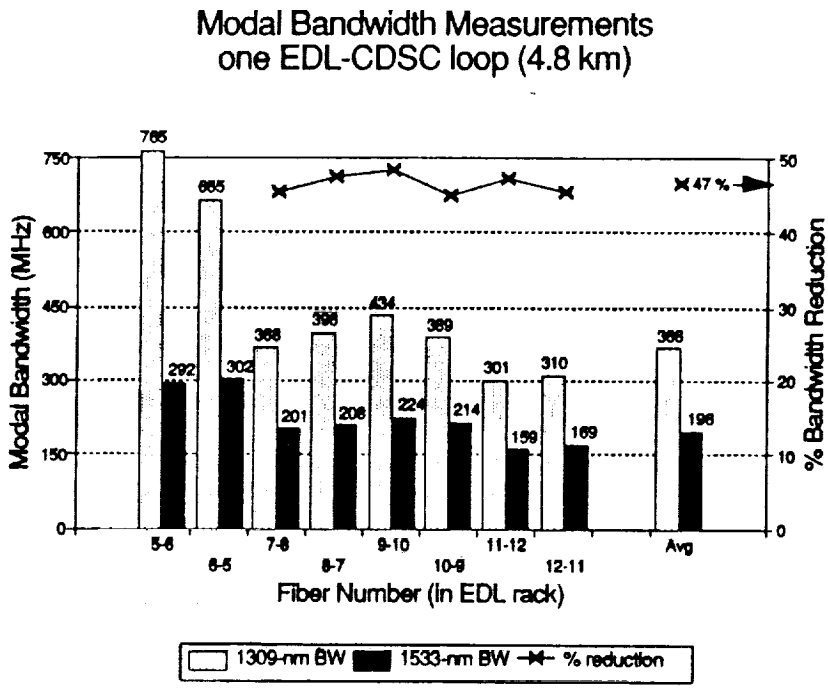

Figure 11a. Measured Modal Bandwidth, Single CDSC Fiber Loops

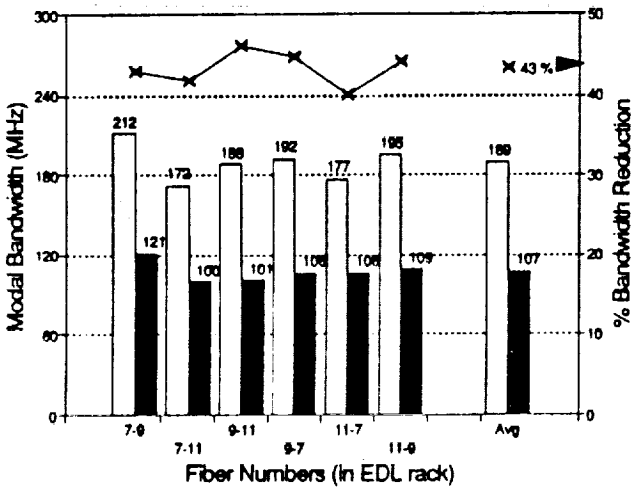

Figure 11b. Measured Modal BW
two concatenated CDSC loops

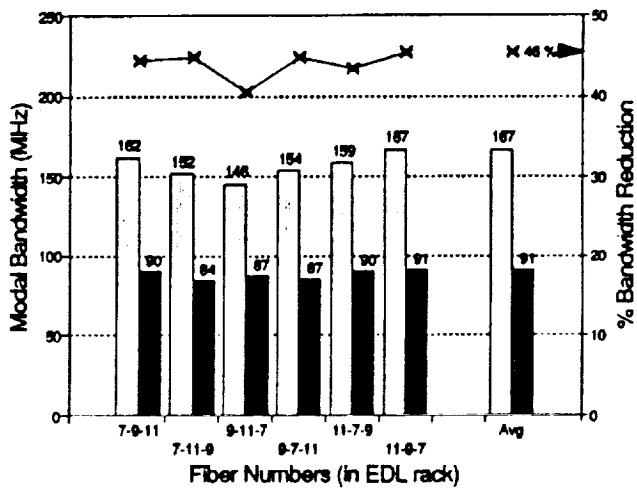

Figure 11c. Measured Modal BW
three concatenated CDSC loops

Reviewing the data of the four CDSC test loops (Figure 11a and Table 2) shows that the loop comprised of fibers *5* & *6* had both a considerably higher bandwidth and attenuation than the other three loops. The bandwidth difference is substantially more pronounced at 1300-nm (95% higher) than in the 1550-nm window (51% higher). This is thought to be another manifestation of the effect of differential attenuation of the higher order modes at one or several connectors along the loops. Also, of the three other loops, loop *11-12* had the lowest attenuation and the lowest bandwidth; possible further evidence supporting this conclusion. Since the transmission characteristics of loop *5-6* were so different from the other three, this loop was excluded from the average comparisons shown on Figure 11a and from the concatenation studies.

Figures 11b and 11c depict the bandwidth and bandwidth reduction information for two and three concatenated CDSC loops. These data compare favorably to the data for the single CDSC loops showing that the third-window modal bandwidth is approximately 45% of that obtained in the superior second-window.

The CDSC loop data for 1309-nm and 1533-nm was subjected to a linear regression analysis in order to find the modal bandwidth-length product and the concatenation factor, γ. Figure 12 shows the results of these analyses.

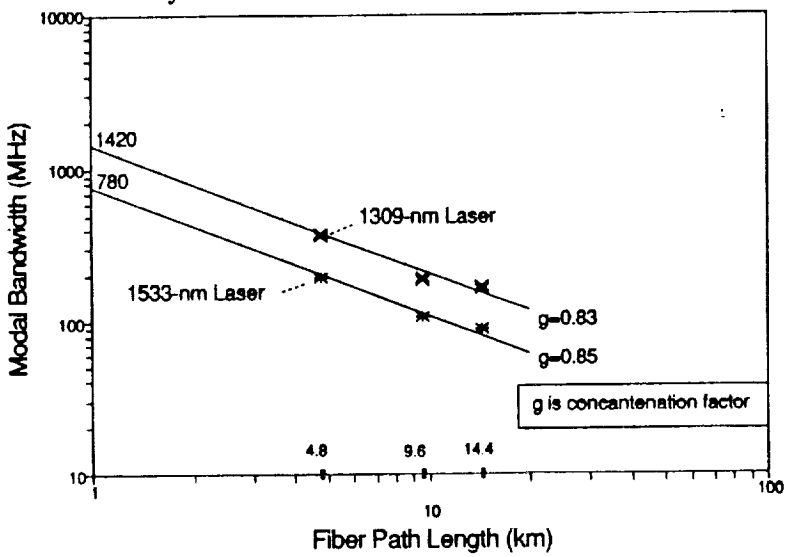

Figure 12. Modal Bandwidth (CDSC Loops) Linear Regression Fit

Figure 13 shows the results of the measurements on the two BRRS test loops using the same format as previously described. An attempt was made to analyze the data from the EDL-BRRS loops similarly; but this was prevented by three additional problems. First, there were only two loops, a very restrictive sample. Second, the test equipment did not have enough dynamic range to allow concatenated measurements on the BRRS loops. Third, these paths contain fibers in two different cables. It is not clear at this time how different these fibers are in modal

characteristics or how these differences would affect the measurements. Limited time caused this study to concentrate on the CDSC loops.

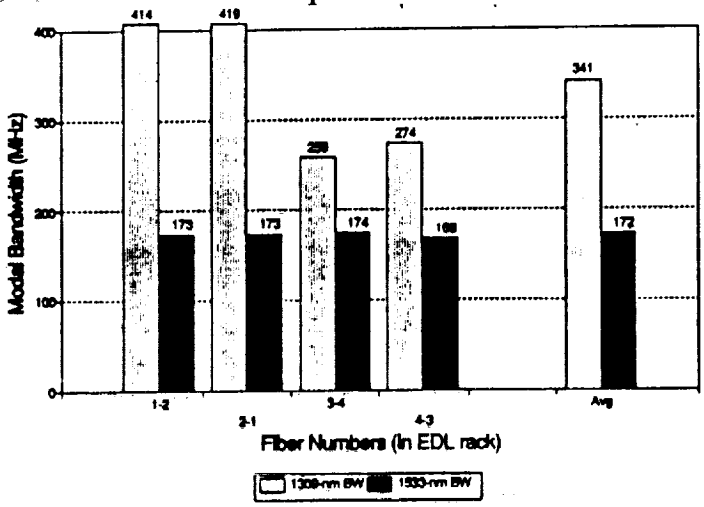

Figure 13 - Modal Bandwidth of Single EDL to BRRS Test Loops

4.2 Dispersion Bandwidth Results:

It was found that the custom made LED-based E/O modules performed admirably making optical bandwidth measurements possible. Using the custom E/O modules, the swept-frequency response measurements of all of the test loops was repeated. The step-graded-step mode scrambler was used on all measurements except those for three CDSC links concatenated. It was determined that, when using the LED-based custom E/O modules, there was very little sensitivity to launch connector alignment, even when the mode scrambler was removed and replaced with a patch cord. Therefore, it was assumed that complete mode excitation was possible without the scrambler when using the LED modules. By removing the scrambler, and its inherent 3.8-dB loss, it was possible to measure bandwidth data for three concatenated CDSC loops.

The results of these bandwidth measurements are shown in Figures 14 and 15. Since the LEDs had spectral widths which were at least twenty times those of the laser modules, these bandwidth measurements would be the result of a combination of both modal distortion and chromatic dispersion effects; that is, the data would represent the *optical* bandwidth. Little chromatic effect was expected for operation close to 1300-nm and this study's data support this expectation. Comparing the second-window bandwidth data for the narrow line laser with the broad spectrum LED data (Figures 11a and 14a) shows that, on average, the LED's optical bandwidth is 10% lower than the laser's modal bandwidth for the single CDSC loops. Since the concatenation factor for the modal bandwidth is less than unity and the factor for dispersion effects is unity, then it would be expected that longer fiber paths would exhibit a larger percent modal bandwidth reduction due to dispersion. It is noted that the data (Figures 11b, 11c, 14b and 14c) support this conclusion.

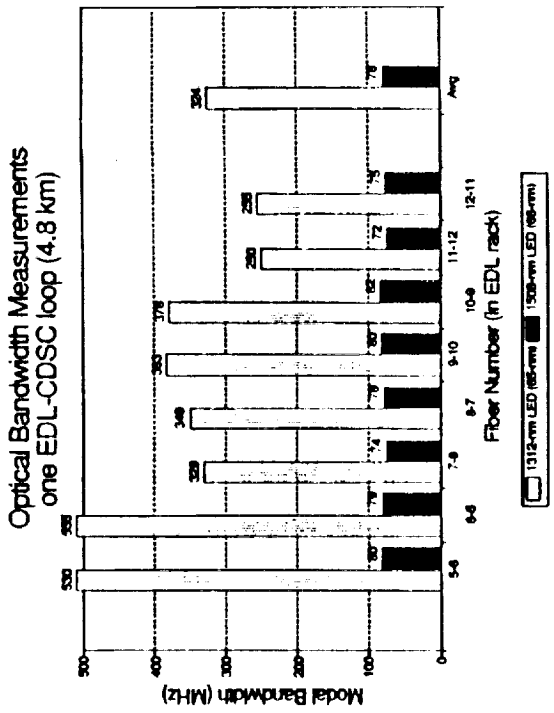

Figure 14a. Optical Bandwidth
Single CDSC Loops

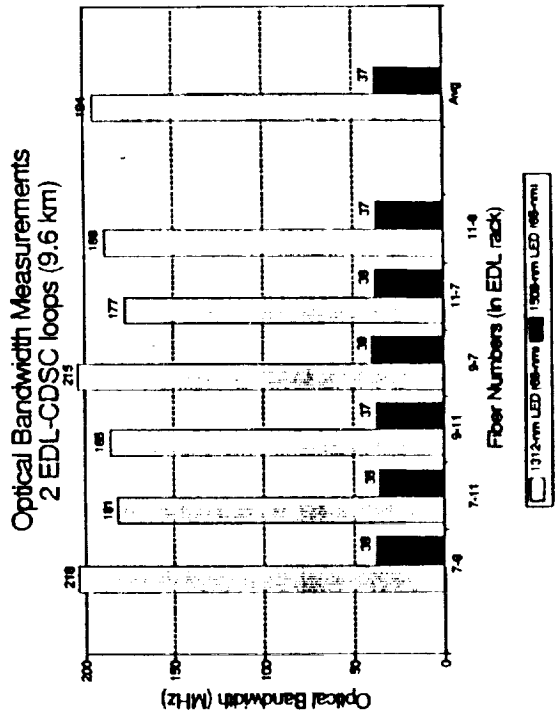

Figure 14b. Optical Bandwidth
Two Concatenated CDSC Loops

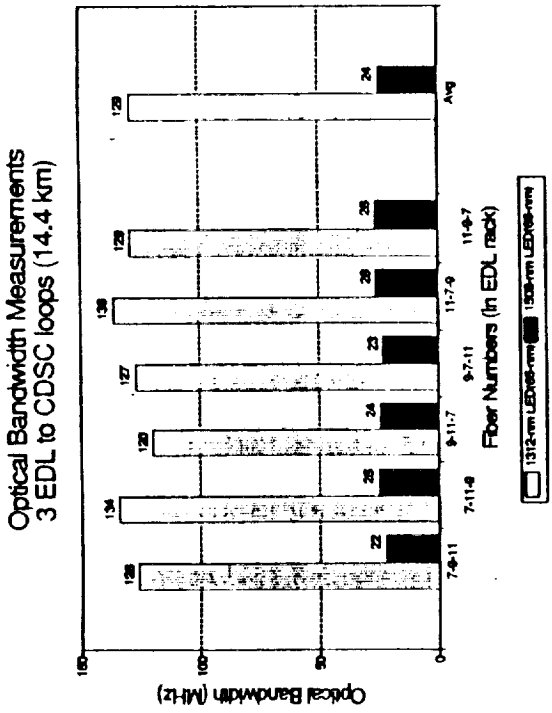

Figure 14c. Optical Bandwidth
Three Concatenated CDSC Loops

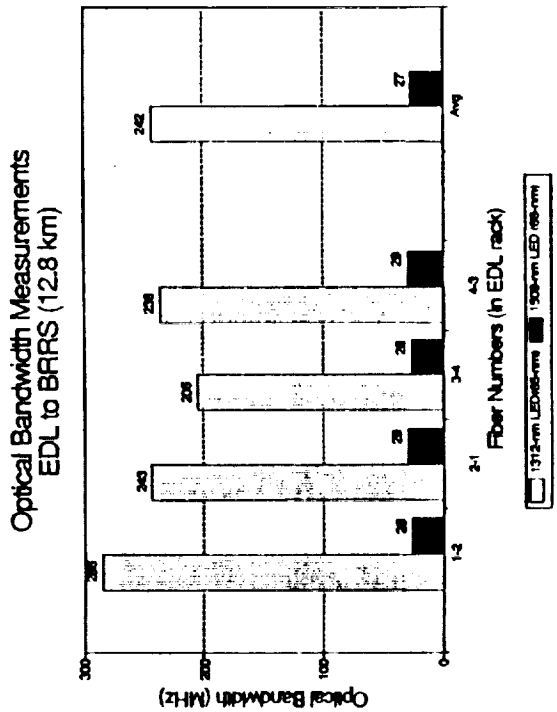

Figure 15. Optical Bandwidth
BRRS Loops

When used with a third-window LED, however, the dispersion effects due to the wide spectral width and the significant chromatic dispersion of the fiber were expected to be comparable to the modal effects. As Figures 11 and 14 show, the third window optical bandwidth of the fibers is approximately one-third of the modal bandwidth and the dispersion effects become even more pronounced at longer distances, as was true with the second-window tests. Therefore, when sourced by a third-window LED, these fibers exhibited a dispersion-limited information transmission capability.

By combining the average measured modal bandwidths with dispersion bandwidth obtained by computation using the Corning chromatic specifications and the spectral characteristics of the LEDs (Table 3) an *expected* optical bandwidth was obtained. Figures 16a, 16b and 16c compare the expected and measured optical bandwidths for all combinations of CDSC fiber loops. It is noted that the relative difference between these two optical bandwidths was 6% or less.. This agreement is quite good especially when the variability of the modal bandwidth measurements and the inherent variability of the fibers themselves are recalled.

4.3 Discussion

As expected, the third window modal bandwidth of the EDL multimode test fibers was reduced to slightly less than 50% of the 1300-nm (optimum) modal bandwidth; that is, from 1400 to 780 MHz•km. At 1300-nm the modal bandwidth measurements were highly dependent on launch conditions; however, the third-window measurements showed much less dependence on launch conditions. The concatenation factor for each window was approximately $\gamma = 0.84$.

While the second-window optical bandwidths were modal-distortion limited, the third-window tests exhibited strong dependence on chromatic dispersion. The expected optical bandwidth, in part based upon manufacturer's chromatic dispersion specifications (λ_o, S_o), agreed nicely with the optical bandwidth measurements made using the LED-based custom-made E/O modules, eventhough the manufacturer did not claim that the dispersion specifications were applicable beyond 1450-nm.

Figure 17 is based upon the average measured modal bandwidth for the CDSC test fibers and Corning's chromatic specifications and shows the expected optical bandwidth for various lengths of EDL test fiber when sourced by 1550-nm LEDs with various spectral widths and by a narrowline laser.

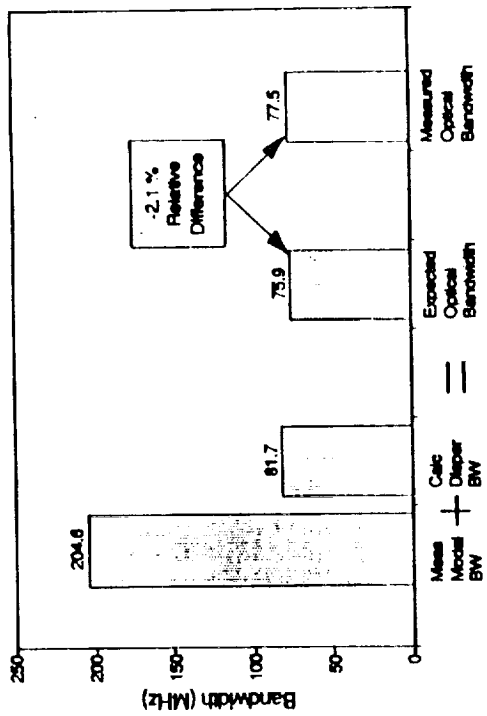

Figure 16a. Expected vs. Measured BW Single CDSC Loop

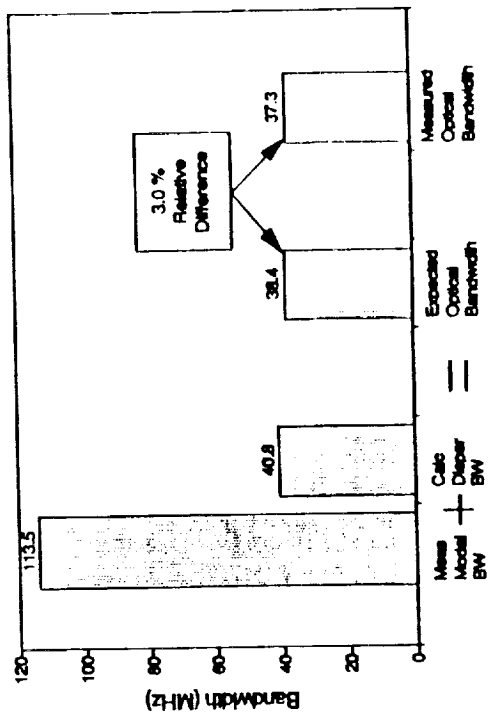

Figure 16b. Expected vs. Measured BW Two Concatenated CDSC Loops

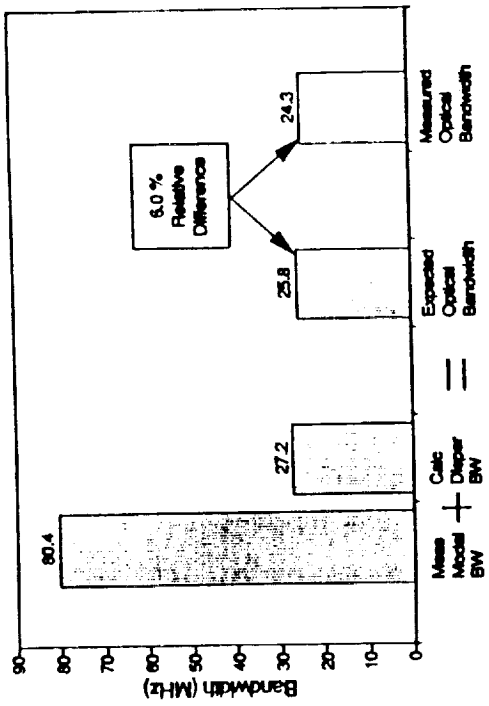

Figure 16c. Expected vs. Measured BW Three Concatenated CDSC Loops

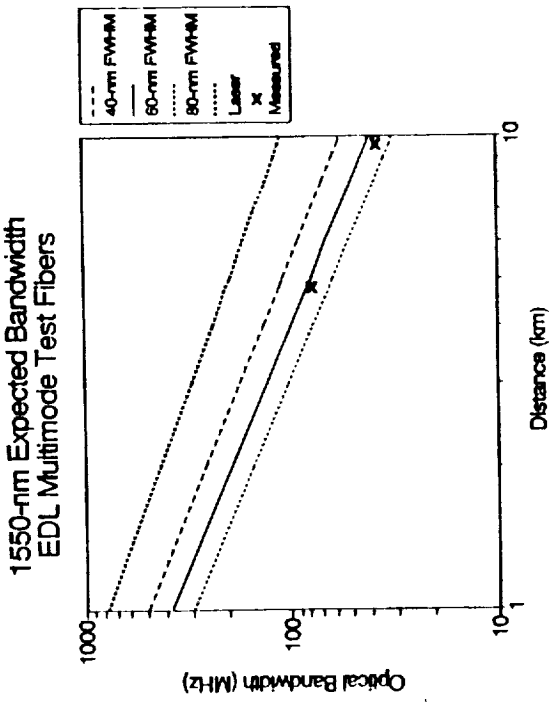

Figure 17. Expected BW LDF Test Fiber

5. CONCLUSIONS AND RECOMMENDATIONS

The results of this study show that the twelve Corning LDF multimode fiber tested have a usable and predictable bandwidth when used with sources in the 1550-nm third window. If the fibers tested are representative of the multimode fibers that have been installed at KSC during the past five years, then WDM on these fibers at 1300- and 1550-nm is an attractive possibility.

The modal bandwidth of these test fibers when used with 1550-nm sources was about 45% of the modal bandwidth expected when 1300-nm sources are used. This bandwidth reduction was true for one 4.8-km test loop but also was valid when or two or three of these loops were concatenated. The tests confirmed that launch conditions can affect the measured bandwidth to a very large degree when 1300-nm sources are used; however, the third-window bandwidth exhibited much less sensitivity.

The bandwidth of these fibers was modal-distortion limited in the second window; but was chromatic dispersion limited when third window LEDs were used. The chromatic dispersion specifications published by the vendor appear to be applicable when extrapolated to third window operation eventhough the vendor excludes wavelengths beyond 1450-nm from these specifications. By utilizing the measured modal bandwidth and the chromatic dispersion specifications, good predictions of the fiber's optical bandwidth were possible.

Before committing to 1550-nm operation, it is recommended that tests similar to those made in this study be performed on a larger sample and a wider range of the installed multimode fibers at KSC. These tests should include fibers of various ages and of various manufacturers. Only by additional testing can it be verified that the 1550-nm window is routinely available on all of the Center's multimode fibers.

If the 1550-nm window is to be used at KSC it is further recommended that, for new fiber cables, the vendors be required to provide chromatic-dispersion information that is valid in the second and third windows. This is especially important since it was confirmed that the optical bandwidth in the 1550-nm window is dispersion-limited.

REFERENCES

1. Refi, J. J. "LED Bandwidth of Multimode Fibers as a Function of Laser Bandwidth and LED Spectral Characteristics." Journal of Lightwave Technology. 4:3, 3/86, p265.

2. Hackert, M. J. "Explanation of Launch Condition Choice for GRIN Multimode fiber Attenuation and Bandwidth Measurements" Journal of Lightwave Technology. 10:2, 2/92, p125.

3. Corning, Inc. "Multimode Chromatic Dispersion". Measruement Method MM-110. 8/90.

4. Corning, Inc. "Corning 50/125 CPC3 Multimode Optical Fiber". Corning Product Information, 7/90.

5. EIA Standard FOTP-30A, "Frequency Domain Measurement of Multimode Optical Fiber Information Transmission Capacity". Electronic Industries Association, Washington, DC, 8/88.

6. EIA Standard FOTP-54A, " Mode Scrambler Launch Requirements for Information Transmission Capacity Measurements". Electronic Industries Association, Washington, DC, 6/85.

7. Verified in a telephone conversation with Sandy Walker of Hewlett-Packard, 7/23/92.

8. EIA Standard FOTP 168, "Chromatic Dispersion Measurement of Multimode Graded-Index and Single-mode Optical Fibers by Spectral Group Delay Measurement in the Time Domain", Appendix A, Electronic Industries Association, Washington, DC, 7/87.

1992 NASA/ASEE SUMMER FACULTY FELLOWSHIP PROGRAM

JOHN F. KENNEDY SPACE CENTER
UNIVERSITY OF CENTRAL FLORIDA

A LOGISTICS AND POTENTIAL HAZARD STUDY OF PROPELLANT SYSTEMS FOR A SATURN V DERIVED HEAVY LIFT (THREE-STAGE CORE) LAUNCH VEHICLE

PREPARED BY:	Dr. E. Dow Whitney
ACADEMIC RANK:	Professor
UNIVERSITY AND DEPARTMENT:	University of Florida Department of Materials Science and Engineering
NASA/KSC	
DIVISION:	Mechanical Engineering
BRANCH:	Propellants and Gases
NASA COLLEAGUE:	James England
DATE:	August 14, 1992
CONTRACT NUMBER:	University of Central Florida NASA-NGT-60002 Supplement: 8

ACKNOWLEDGMENTS

To Dr. Loren Anderson and the other program administrators, I express my appreciation for being selected as a 1992 NASA/ASEE Summer Faculty Fellow. To my NASA colleague, James England, I am particularly indebted for his assistance, guidance and encouragement. The charm and friendliness of Mrs. Kari Stiles and Ms. Carol Valdes in smoothing the transition from Gainesville to KSC is also very much appreciated. Particular thanks to Carol for putting up with a group of unruly professors during the weekly KSC orientation tours.

I am very grateful to all the members of the Propellants and Gases Branch staff, particularly Branch Chief, Roger Hall, as well as David Weidermuth, James Fesmire, and Jamie Hurley, for their advice and support. To James Fesmire, I apologize again for getting lost on Launch Complex 39A just a few days before Space Shuttle Columbia roared off into space.

Special recognition must go to the Branch Secretary, Mary Conklin, for her cheerful assistance and patience, and to Pam Howell, Senior Secretary at the University of Florida, Department of Materials Science and Engineering, who, as always, has transformed my scratching into a very presentable document. As is true with respect to secretaries in any well-run organization, without people like Mary and Pam, this work would never have been completed.

This acknowledgment would not be complete without expressing my sincere gratitude to George Sauro of the Boeing Aerospace Operational Engineering Support Group at KSC for the technical illustrations and graphs which appear in this report.

Finally, to all my friends and colleagues at Kennedy Space Center and the University of Central Florida, thanks again for the opportunity to work on rocket propellants again after some thirty-three years.....it's been a blast!

ABSTRACT

The Bush Administration has directed NASA to prepare for a return to the moon and on to Mars – the Space Exploration Initiative. To meet this directive, powerful rocket boosters will be required in order to lift payloads that may reach the half-million pound range into low earth orbit. In this report an analysis is presented on logistics and potential hazards of the propellant systems envisioned for future Saturn V derived heavy lift launch vehicles. In discussing propellant logistics, particular attention has been given to possible problems associated with procurement, transportation, and storage of RP-1, LH_2, and LOX, the heavy lift launch vehicle propellants. Current LOX producing facilities will need to be expanded and propellant storage and some support facilities will require relocation if current Launch Pads 39A and/or 39B are to be used for future heavy lift launches. No major technical problems are envisioned except for improved noise-abatement measures. Included in the report is a discussion of suggested additional studies, primarily economic and environmental, which should be undertaken in support of the goals of the Space Exploration Initiative.

SUMMARY

As part of the Space Exploration Initiative for the year 2000 and beyond, NASA is planning flights to both the moon and Mars. Initially, eight flights per year are planned; four to the moon and four to Mars. The proposed launch vehicle is a Saturn V derived HLLV (three-stage core) with a four-booster configuration. The payload will be large, 620 Klbs. (281 mt). Lift-off will be accomplished (Core Stage I and four boosters) with seventeen F-1A engines. The propellant system will consist of high grade kerosene fuel (RP-1) and liquid oxygen (LOX) for the first stage and LOX and liquid hydrogen (LH_2) for the second stage.

Although the proposed propellant system represents a technology which is at least thirty years old, the magnitude of the quantity of propellants which will be employed in HLLV launch vehicles presents unique logistics, handling and safety problems. The HLLV will consume 20.6 million pounds of propellant, a 340% increase over propellant consumption of the Saturn V. There are unique problems which must be addressed when handling this quantity of fuel.

Problems addressed during the course of this work period were:

- Petroleum and petrochemical refining/production capabilities of the United States in terms of future HLLV operations and performance goals.
- Present and future LH_2 and LOX production capabilities of the United States in terms of future HLLV operations and performance goals.
- Logistics of transporting large quantities of RP-1, LH_2, and LOX from production sites to HLLV launch sites.
- Storage of large quantities of propellants in the vicinity of HLLV launch sites.
- Safety aspects and possible accident scenarios such as RP-1 emergency dumping, acoustic problems, and fireball and blast effects.

Q-7

TABLE OF CONTENTS

LIST OF ILLUSTRATIONS

Figure

LIST OF TABLES

Table

LIST OF ABBREVIATIONS AND ACRONYMS

AFB - Air Force Base

ASEE - American Society fOR Engineering Education

Btu - British thermal unit

CCAFS - Cape Canaveral Air Force Station

DAF - Directorate of Aerospace Fuels (U.S. Air Force)

dB - decibels

EPO - Exploration Program Office

g - Earth's gravitational constant; 32 ft./sec./sec.

HLLV - heavy lift launch vehicle

KSC - Kennedy Space Center

LH_2 - liquid hydrogen

LOX - liquid oxygen

mt - metric ton; 1,000 kilograms (2204.6 lbs.)

NASA - National Aeronautics and Space Administration

NLS - National Launch System

psi - pounds per square inch

RP-1 - Rocket Propellant - 1 (refined kerosene)

SEI - Space Exploration Initiative

SSC - Stennis Space Center

VAB - vehicle assembly building

VS - short ton (2,000 lbs.)

I INTRODUCTION

On July 16, 1969, the Apollo 11 Spacecraft, freed from Earth's gravity by means of the powerful Saturn V launch vehicle, took man to the surface of the moon for the first time. Over the next three years, this phenomenal feat was to be repeated five more times. In each mission, a Saturn V launch vehicle was used to boost the various Apollo spacecrafts to the moon. The force used to accomplish the first stage of this unparalleled feat was provided by a cluster of five Rocketdyne F-1 rocket engines, each developing over 1.5 million pounds of thrust (1). Since 1972, major activity at Kennedy Space Center (KSC) has centered around the Space Shuttle and Saturn V activity was essentially terminated.

1.1 NATIONAL LAUNCH SYSTEM AND THE SPACE EXPLORATION INITIATIVE

Meeting the demands of the National Launch System (NLS) Program, as well as a directive from the Bush Administration for a return to the moon and exploration of Mars, i.e., the Space Exploration Initiative (SEI), will require the ability to lift huge payloads into low earth orbit. Such payloads may reach the half-million pound range, requiring especially powerful boosters used as strap-ons to a core vehicle (2). In order to accomplish these goals, it has been proposed that future heavy lift launch vehicle (HLLV) designs be based on tried-and-true Saturn V technology employing a new updated version of the F-1, i.e., the F-1A rocket engine (3).

1.2 THE F-1A ROCKET ENGINE

One can make strong arguments for the proposal that future HLLV designs be based upon Saturn V technology. Not only was the F-1 engine the largest, most powerful liquid rocket engine ever built but the performance of this engine was exceptional. Sixty-five F-1's were launched with a 100% flight success rate (4). In addition, the F-1 burned liquid oxygen (LOX) and kerosene (RP-1), a proven technology. To meet the challenge, which will be imposed by future HLLV designs, Rocketdyne not only proposed but has already tested an improved, modernized version of the F-1, the F-1A engine. This engine has the capability of providing 1.8 million pounds of thrust.

1.3 THE HEAVY LIFT LAUNCH VEHICLE

As part of the SEI program, the Exploration Programs Office (EPO) at KSC is considering a number of different designs of future lunar and Mars exploration vehicles. In addition to vehicles, design work is underway on the extension of Launch Pad 39A for SEI Mars capability as well as flame deflectors, new and heavier launcher decks, and enlarged vehicle assembly buildings (personal communication with Donald W. Page, National Launch System - HLLV Office, KSC, Florida, July 9, 1992).

Of the different families of future lunar/Mars vehicles being studied at EPO/KSC, the particular HLLV design considered for this study appeared to be the most ambitious. Thus the rationale for choosing this particular HLLV was that scaling down is easier than scaling up.

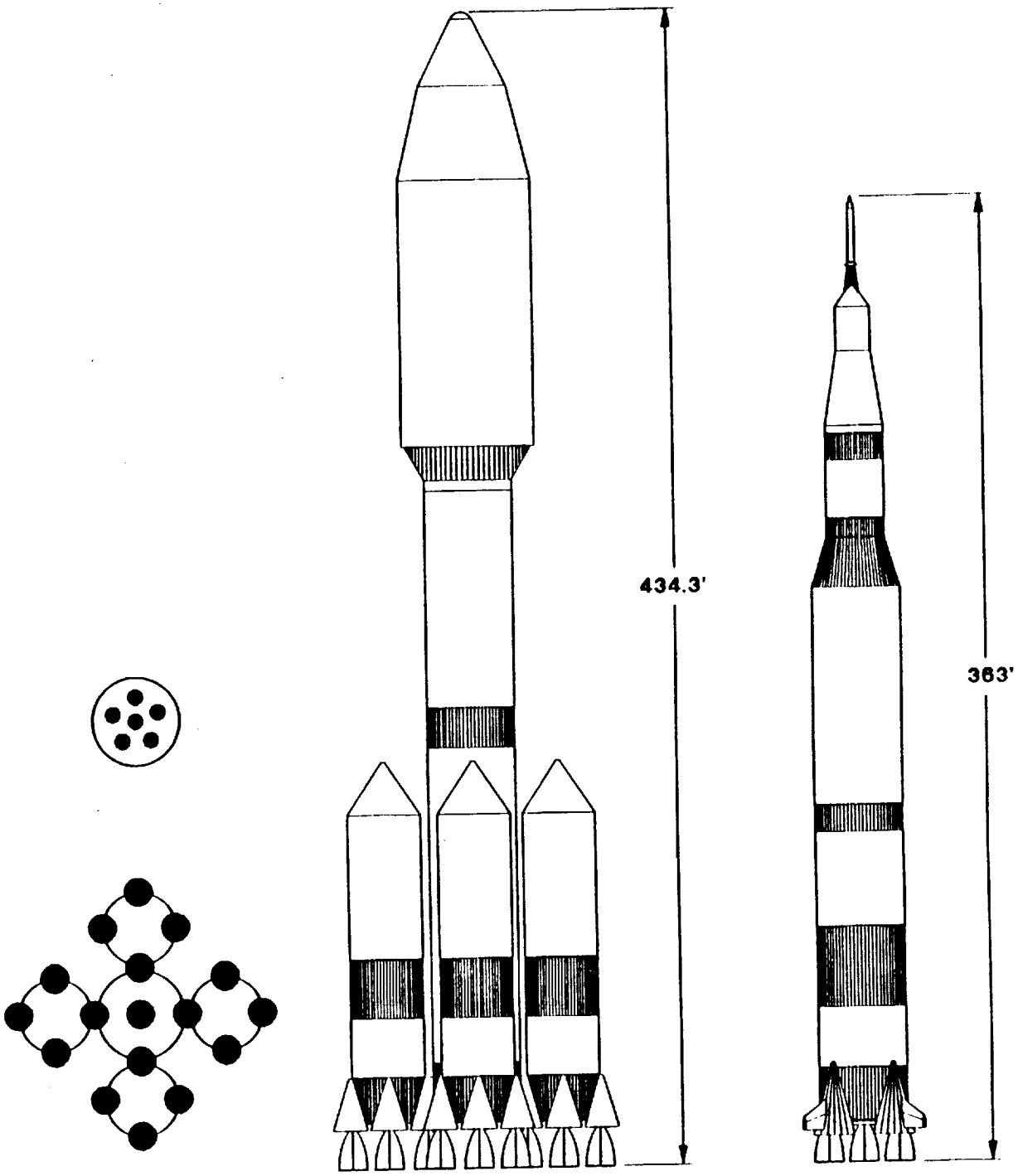

Figure 1-1. Saturn V Derived HLLV (Three-Stage Core), Four-Booster Configuration Rocket. Saturn V Rocket Included for Comparison.

1.3.1 GENERAL FEATURES. In Figure 1-1 is shown a schematic of the Saturn V derived HLLV (three-stage core), four-booster configuration rocket which was used as the basis for this study. Also included in Figure 1-1 for size comparison is a schematic of the Saturn V rocket. To the left of the figure is shown how the seventeen F-1A engines will be positioned in Core Stage I of the rocket (five engines) and in the four strap-on boosters (three engines each), as well as the positioning of the six LOX/LH_2 J-2S engines in Core Stage II.

Although the dimension(s) given in Figure 1-1 for the HLLV are impressive, a better appreciation for its size can be gleaned from Figure 1-2 in which is shown the relative sizes of the HLLV, Saturn V, and Space Shuttle.

In Table 1-1 are given some statistics for the HLLV with particular emphasis on propellant inventory.

TABLE 1-1
SATURN V DERIVED HLLV (THREE-STAGE CORE), FOUR-BOOSTER CONFIGURATION
DESIGN AND PROPELLANT DATA SUMMARY

Shroud
Diameter/Length = 50 ft./175 ft.
Weight = 114,600 lbs.
Cargo Diameter/Length = 46 ft./100 ft.

Instrument Unit Weight = 6,488 lbs.

Core Stage II - (Common Bulkhead Tanks)
Six J-2S Rocketdyne Engines (Thrust = 265,000 lbs. ea.)
Inert Weight = 136,395 lbs.
Propellants = LOX/LH_2
Reserve Propellant = 17,310 lbs.
Burned Propellant = 1,346,279 lbs.

Core Stage I - (Separate Tanks)
Five F-1A Rocketdyne Engines (Thrust = 1,800,000 lbs. ea.)
Inert Weight = 468,467 lbs.
Propellants = LOX/RP-1
Usable Propellant = 5,919,370 lbs.

Boosters (each) - (Separate Tanks)
Three F-1A Engines (Thrust = 1,800,000 lbs. ea.)
Inert Weight = 173,671 lbs.
Propellants = LOX/RP-1
Usable Propellant = 3,442,164 lbs.

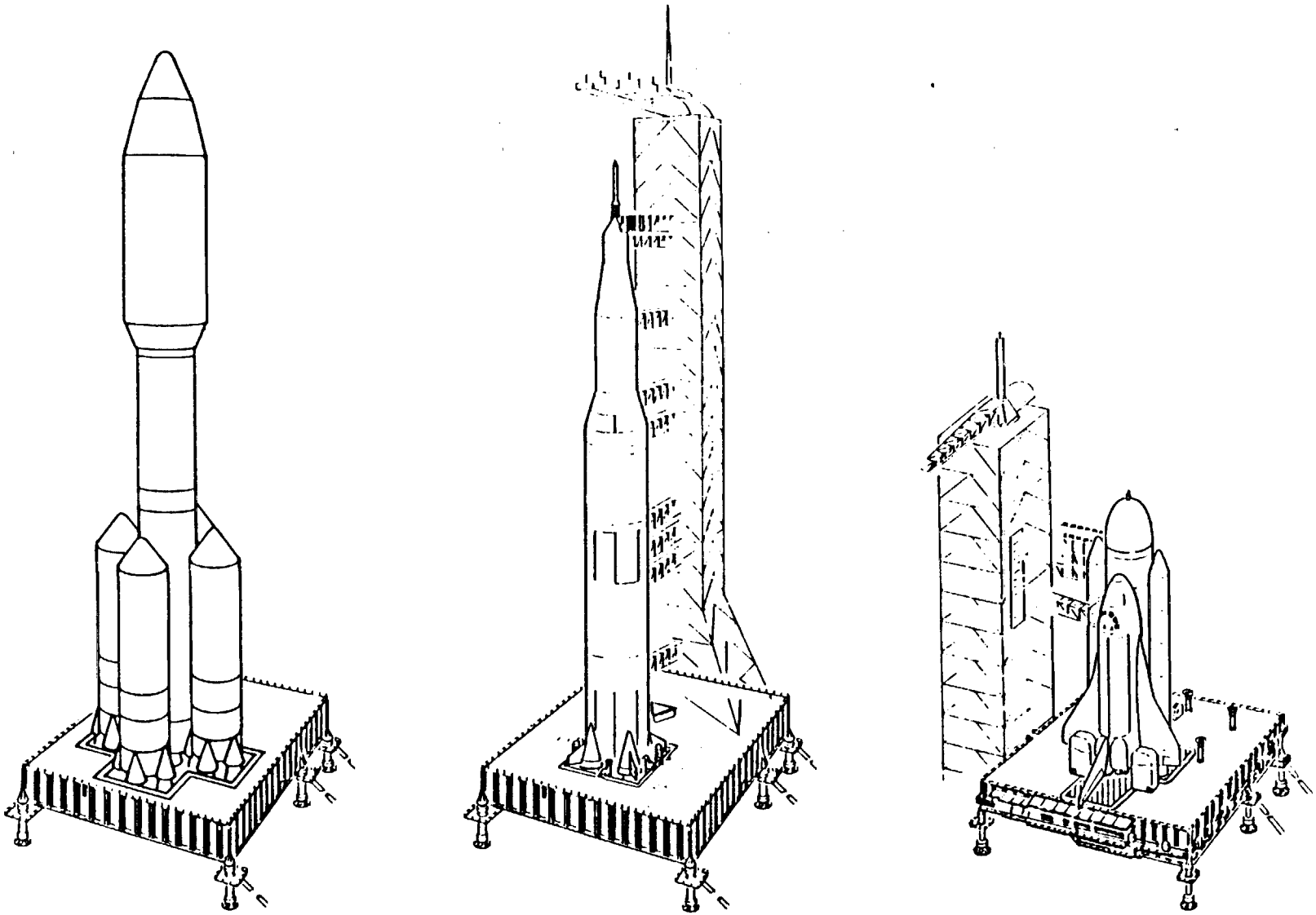

Figure 1-2. Relative Sizes of the HLLV, Saturn V, and Space Shuttle.

1.3.2 PROPELLANT SYSTEMS. Like Saturn V, the HLLV will burn LOX and RP-1 in Core Stage I, as well as in the four strap-on boosters. In Table 1-2 are given calculated values for LOX and RP-1 consumption in the HLLV with its seventeen F-1A engines, along with LOX and RP-1 consumption for the Saturn V launch vehicle (5,6). Total propellant consumption per F-1A engine calculated from the data in Table 1-1 is 1,130,000 lbs./engine, an amount 23% greater than the propellant consumption for the F-1 engine (918,060 lbs.). This value agrees well with the 20% increase in thrust reported by Rocketdyne in upgrading from the F-1 engine (1,500,000 lbs. thrust) to the F-1A engine (1,800,000 lbs. thrust).

TABLE 1-2
COMPARISON OF LOX AND RP-1 CONSUMPTION IN HLLV
(CORE STAGE I AND FOUR BOOSTERS) AND SATURN V

	PROPELLANT					
	LOX		RP-1		TOTAL PROPELLANTS	
VEHICLE	GALLONS	POUNDS	GALLONS	POUNDS	GALLONS	POUNDS
HLLV	1,399,306	13,335,382	870,314	5,874,618	2,269,620	19,210,000
SATURN V	346,960	3,306,526	213,068	1,438,210	560,028	4,744,736

Comparison of the data in Table 1-2 shows that Core Stage I of the HLLV will consume four times the quantity of LOX consumed by the Saturn V first stage and 4.1 times the quantity of RP-1.

Propellants for Core Stage II of the HLLV are LOX and liquid hydrogen (LH_2), the same as in the second and third stages of Saturn V. In Table 1-3 are given calculated values for LOX and LH_2 consumption in the HLLV with its six Rocketdyne J-2S engines, along with LOX and LH_2 consumption for the Saturn V launch vehicle (5,6).

TABLE 1-3
COMPARISON OF LOX AND LH_2 CONSUMPTION IN HLLV (CORE STAGE II)
AND SATURN V (SECOND AND THIRD STAGES)

	PROPELLANT					
	LOX		LH_2		TOTAL PROPELLANTS	
VEHICLE	GALLONS	POUNDS	GALLONS	POUNDS	GALLONS	POUNDS
HLLV	121,071	1,153,806	361,695	209,783	482,766	1,363,589
SATURN V	108,129	1,027,229	350,507	203,294	458,636	1,230,523

Inspection of Table 1-3 reveals that there will be very little difference in the quantity of propellants consumed in HLLV Core Stage II as compared to the combined second and third stages of Saturn V. In hindsight, this is not surprising since HLLV Core Stage II will have six J-2S engines whereas the second and third Saturn V stages also had a total of six J-2 engines.

In terms of propellant consumption, the major difference between HLLV and Saturn V lies in the increased quantities of RP-1 and LOX which will be consumed in the first stage of the former. The logistics of fuel supply for the HLLV is of primary concern with regard to the first stage.

Data presented in Tables 1-2 and 1-3 are summarized in Table 1-4 in which is summarized total propellants (exclusive of hypergolics) consumed in all stages of the HLLV and Saturn V.

TABLE 1-4
SUMMARY OF TOTAL PROPELLANTS CONSUMED IN ALL STAGES OF THE HLLV AND SATURN V

	PROPELLANT							
	LOX		RP-1		LH_2		TOTAL PROPELLANTS	
VEHICLE	GALLONS	POUNDS	GALLONS	POUNDS	GALLONS	POUNDS	GALLONS	POUNDS
HLLV	1,520,377	14,489,188	870,314	5,874,618	361,695	209,783	2,752,386	20,573,589
SATURN V	455,089	4,333,755	213,068	1,438,210	350,507	203,294	1,018,664	5,975,259

1.3.3 PERFORMANCE CHARACTERISTICS. Core Stage I (along with its boosters) of the HLLV with consume 19,210,000 pounds (2,269,620 gallons) of propellants in its seventeen F-1A engines, resulting in a total thrust of 30,600,000 lbs. The oxidizer to fuel ratio is 2.27:1 and exhaust gas composition for the F-1A is known (7). Thus it can be shown that during HLLV first stage burn, the major products of combustion of LOX and RP-1 will be 1,900 metric tons (mt) of CO_2, 2,200 mt of H_2O vapor, and 4,190 mt of CO. Whereas the latter is a poisonous gas, it would not (as with Saturn V launches) pose a hazard since the hot gas is quickly oxidized to CO_2. This oxidation process accounts for the pale blue flame sometimes seen below the yellow/white flame discharge from the F-1 engines during Saturn launches. Total thermal energy output from Core Stage I and boosters will be on the order of 2×10^{10} kilocalories (8×10^{10} Btu). This tremendous energy will lift a payload of approximately 620,000 lbs. (281 mt) into space at a maximum acceleration of 4.9 g's.

Since the incredible energy of the Saturn V booster with its five F-1 engines has been equated to the power output of 85 Hoover Dams (4), the power output of the particular HLLV design which is the subject of this study is on the order of 350 Hoover Dams!

II PROPELLANT LOGISTICS

2.1 RP-1

2.1.1 SOURCE. All RP-1 now utilized in launches at Cape Canaveral Air Force Station (CCAFS), as well as in earlier Saturn V launches at KSC, is procured through the Directorate of Aerospace Fuels (DAF), Propellants Branch, Kelly Air Force Base (AFB), Texas (personal communication with Curtis A. Williams, Fluids Management Group, Technical Operations Division, EG&G Florida, Inc., KSC, Florida, July 28, 1992). DAF is responsible for supplying RP-1 and LOX to U.S. Government Agencies on the East Coast but not responsible for the supply of LH_2. At the present time, the U.S. Air Force is the only customer for RP-1 which is supplied to CCAFS by Howell Hydrocarbons, Inc., of San Antonio, Texas. Howell Hydrocarbons, Inc. serves as a storage and supply source, the RP-1 being produced by local petroleum refineries, although since the termination of Saturn V several suppliers of RP-1 are no longer in business.

Currently, RP-1 is utilized as fuel in the KSC/CCAFS complex only for the first stages of the Delta II launch vehicle at Complex 17 and the Atlas I and II launch vehicles at Complex 36. The Delta booster requires approximately 10,000 gallons of RP-1, the Atlas booster 18,000 gallons, whereas the Saturn V required 213,000 gallons. In calculating RP-1 supply requirements, it has been suggested that a 16% loss of fuel should be assumed (memorandum from Jared P. Sass to James Fesmire, Mechanical Engineering Division, Gases and Propellants Branch, KSC, Florida, dated February 6, 1992). However, this factor has not been included in these calculations on the basis that, particularly with the quantities of RP-1 which will be required for the HLLV, such losses will not be tolerated considering today's tight environmental restrictions.

At 870,000 gallons per launch and eight launches per year (four to the moon and four to Mars) as planned in the SEI program, some 6,960,000 gallons of RP-1 will be consumed. However, in addition to the RP-1 consumed at launch, two to three times this amount will be utilized in required testing and certification of the F-1A engines at NASA Stennis Space Center (SSC) in Bay St. Louis, Mississippi (conference with John Nagle and Michael M. Paul, Directorate of Aerospace Fuels, Propellants Branch, Kelly AFB, Texas, July 30, 1992). SSC, which currently has the responsibility of certifying shuttle engines, is actively planning for the testing and certification of F-1A engines for future SEI vehicles.

Kerosene production in the United States in 1991 amounted to 13,952,000 barrels (585,984,000 gallons) (telephone conversation with Julie Scott, American Petroleum Institute, Washington, DC, July 10, 1992). At first this figure was thought to be of concern to figure HLLV missions since it represents an almost 52% decrease in annual U.S. kerosene production from 1988 to 1991. This decrease is only apparent since during the period 1988 to 1991 some petroleum companies began reporting jet fuel production as a separate entity. Since kerosene and jet fuels fall into the same middle distillate group during the fractional distillation of petroleum, this has the effect of lowering the overall production figures for kerosene (telephone conversation with Alice Lippert, Fuel Oil and Kerosene Sales Data (Annual), Department of Energy, Washington, DC, July 7, 1992). It is obvious from the above figures that, given the demand, refining

capability exists for meeting any future HLLV RP-1 requirements. It is not expected that RP-1 supply will limit future SEI missions involving HLLV's.

2.1.2 TRANSPORTATION. Currently, the RP-1, which is employed in Atlas and Delta boosters, is transported from Howell Hydrocarbons, Inc., in San Antonio, Texas, to Fuel Storage Area 1, CCAFS in 7,000 gallon mobile commercial tankers. The RP-1 is then delivered to launch sites by 5,000 gallon refuelers although future planning provides for a 7,000 gallon KSC mobile tanker and a pumper cart to be refurbished and activated for RP-1 support (personal communication with Irving H. Stenner, Systems Engineering, Technical Operations Division, EG&G Florida, Inc., KSC, Florida, June 23, 1992, and July 22, 1992). During Saturn V activity, RP-1 was delivered to KSC/CCAFS via 10,000 gallon capacity rail tank cars. Today, only one NASA owned RP-1 rail car remains at KSC and is apparently in poor condition.

Since the capacity of a standard size rail car for RP-1 is only 10,000 gallons, this mode of fuel transportation, which deemed practical for Saturn V, will not be practical for meeting RP-1 fuel requirements for the HLLV. A more attractive means of transportation would be by petroleum product barges.

The capacity of commercial ocean-going barges for the transportation of hydrocarbons ranges between 2,500 to 7,500 U.S. short tons (telephone conversation with Roy Walsh, Waterborne Commerce Statistics Center, New Orleans, Louisiana, July 15, 1992) which for RP-1 equates to a liquid capacity of between 740,740 and 2,222,000 gallons. In addition, data from the Maritime Administration confirms that there are a number (more than 300) of tank barges with capacities exceeding 3,000 short tons available for coastline transport of fuel to the KSC/CCAFS complex (telecopier memorandum from Walter Oates, Office of External Affairs, Maritime Administration, Washington, DC, dated July 30, 1992). A petroleum barge of 3,000 short ton capacity equates to a volume capacity of 888,900 gallons of RP-1, just slightly above the HLLV RP-1 fuel requirement. In fact, according to data obtained from the Office of External Affairs of the Maritime Administration, Barge No. 35, designated for petroleum products and operated by Coastal-Belcher Towing Co., identifies Cape Canaveral, Florida, as its operating base. The capacity of this barge is given as 3,125 mt, which translates to a 1,020,648 gallon capacity for RP-1. Since the HLLV requires some 870,314 gallons of RP-1 per launch, Barge No. 35 would appear to be an ideal transportation vehicle for RP-1 fueling of HLLV.

Barge transport of RP-1 to Launch Complex 39A will not involve any new or major construction effort. The KSC Master Plan for Complex 39A shows a barge channel extending as a spur in a northeast direction from the barge channel used to transport the shuttle external LOX/LH_2 tank to the vehicle assembly building (VAB) for mating with the shuttle. This spur cuts through Jack Davis Island and terminates immediately adjacent to Launch Pad A. This channel was used to transport LH_2 by means of barge from Air Products and Chemicals, Inc., LH_2 plant in New Orleans, Louisiana, to KSC during the early days of the Saturn V missions. The LH_2 was off-loaded from barges to storage facilities at the launch complex. Later in the Saturn program, LH_2 was transported by rail tank cars and mobile tankers and barging was discontinued. This channel has probably not been used in the last two decades. However, recent aerial photographs of the Launch

Complex 39A area (taken for vegetation studies) reveal that this channel still exists and appears very distinct in the photographs. Although silting, in all probability, has occurred over the years, the channel has definitely not filled in and would still be serviceable with minor dredging.

In addition, review of the Master Plan for Complex 39B shows that, with the removal of two minor barricades, RP-1 barges could be moved via a waterway which extends from the northern tip of the channel at Pad 39A, proceeds north to the east of the pad, then turns to the west, north of Pad 39A, finally leading, by means of manmade channel, into Gator Hole, which lies to the south of Launch Complex 39B. Thus a route exists for transporting large quantities of RP-1 to Complex 39A and, with a relatively small construction effort, similar quantities to Complex 39B as well.

Some concern has been expressed that, since the channel to Pad 39A has been unused for such a long time, there may be a higher than average number of manatee (*Trichechus manatus*) existing in this waterway today. However, considering how slow a barge tug travels and with the use of suitable propeller guards, it is not expected that the manatee population will be affected in any way.

2.1.3 STORAGE. The only active RP-1 storage facilities existing at KSC/CCAFS today are two above-ground 20,000 gallon bulk storage tanks located at Fuel Storage Area 1, CCAFS. During the Saturn missions, RP-1 was stored in three aboveground 86,000 gallon bulk storage tanks located at both Launch Pads 39A and 39B. Although adequate for Saturn V missions, the total RP-1 storage at each pad (258,000 gallons) would be entirely inadequate for HLLV operations. However, the argument is moot since subject tanks are not double walled, do not meet current environmental standards (8), and therefore cannot be used.

It is proposed that the most practical method of delivering RP-1 to future HLLV boosters is direct off-loading from RP-1 barges. As discussed later in this report (Section 3.3), a preliminary hazards analysis shows that if RP-1 were to be stored in permanent storage facilities adjacent to the launch pads, the separation distance from launch site to fuel storage site will not meet safety requirements for future HLLV operations. Another advantage of barge transport is that the barge can be pulled away from the launch complex area after off-loading of RP-1.

2.2 LIQUID HYDROGEN

2.2.1 SOURCE. Reference to Table 1-4 shows that LH_2 consumption in the HLLV will be essentially the same as was LH_2 consumption in the Saturn V. Using a multiplication factor of three for LH_2 required for HLLV engine certification at SSC and assuming 26% LH_2 transfer losses based on shuttle data, some 9,071,680 lbs. (4,115 mt) or 15,358,354 gallons of LH_2 will be required for the eight planned HLLV launches per year. Production of hydrogen in the United States in 1990 amounted to approximately 148 billion cu. ft. (349,200 mt) (9). Preliminary figures indicate that hydrogen production for 1991 will remain essentially unchanged (10). Thus the annual consumption of LH_2 in future HLLV missions will amount to slightly over 1% of 1990 and 1991 LH_2 production levels in the United

States. However, as is discussed below, there will be a dramatic increase in production levels of LH_2 in the U.S. in the very near future.

Liquid hydrogen utilized at the KSC/CCAFS complex is produced in two plants operated by Air Products and Chemicals, Inc., New Orleans, Louisiana, each plant having a capacity of 32 mt of LH_2 per day. The annual production of these plants is 51,499,456 lbs. (23,360 mt), more than enough to meet future HLLV requirements. In the last year, there has been increased activity in the area of LH_2 production. Air Products and Chemicals, Inc., already the world's largest supplier of LH_2, plans to build, at a cost in excess of $15 million, a new LH_2 facility in Pace, Florida, near Pensacola, as a result of a cooperative agreement with the Spaceport Florida Authority. The plant, with a 30 ton daily production, is scheduled to go on-line in early 1994 (11,12). Besides the space programs, the Clean Air Act is stimulating growth of the hydrogen market (13).

A proposal is also under consideration for the construction of a government-owned LH_2 plant at the KSC/CCAFS complex. The rationale for building such a facility is that LH_2 is currently obtained from private industry by direct contract as distinct from RP-1, which is obtained through DAF. Other than the government wishing to produce its own LH_2 for economic reasons, future HLLV operations would not appear to be limited by LH_2 availability.

2.2.2 TRANSPORTATION. As already noted, the HLLV design used as the basis for this study will essentially consume the same amount of LH_2 as did the old Saturn V vehicles. During the early days of the Saturn projects, LH_2 was barged from Louisiana directly to Launch Complex 39A at KSC. As previously noted, this was the reason the barge channel was constructed to pad 39A. As was done later in the Saturn program, tank trucks or rail tank cars could be used to transport LH_2 from production plants to KSC. NASA owns four LH_2 tank trucks. The older tank trucks have a capacity of 13,000 gallons whereas the newer units have a capacity of between 14,000 and 16,000 gallons. NASA also owns four LH_2 rail tank cars of 34,000 gallon capacity. Considering the fact that new LH_2 production facilities are being planned in Florida, the continued use of tank trucks or rail tank cars for LH_2 transport appears to be even more attractive.

2.2.3 STORAGE. The LH_2 storage facilities at Launch Complex 39A and 39B consist of one 900,000 gallon spherical storage tank at each location. As with the Saturn program, these LH_2 storage facilities will be suitable for HLLV missions except for their present location with respect to future HLLV vehicle launch operations (see Section 3.3 of this report).

2.3 LIQUID OXYGEN

2.3.1 SOURCE. Reference to Table 1-4 shows that, unlike the situation with regard to LH_2, the proposed HLLV will consume more than three times the amount of LOX that was consumed in Saturn V launches. Again using a factor of three to account for LOX requirements for engine testing and certification at SSC and assuming 60% LOX transfer losses based upon shuttle data, some 1,159 million lbs. (525,780 mt) or 121.7 million gallons of LOX will be required for eight HLLV launches per year. Fortunately, as with LH_2, supply of LOX will be no problem. In 1990, the United States produced 462 billion cu. ft. (17,359,000 mt) of oxygen

(9,10). Preliminary indications are that this production figure was slightly exceeded (~2%) in 1991. The proposed HLLV missions would consume annually 3% of all the oxygen that was produced in the U.S. in 1990. Oxygen ranks fourth in total production of all the chemicals produced annually in the United States (10).

Today, most of the LOX utilized at the KSC/CCAFS complex is produced by PRAXAIR (formerly Linde Air, Inc.) in Mims, Florida. This plant, which has since expanded, was constructed in support of the Saturn program and produces 40,000 gallons a day (62,914 mt) annually. Assuming that LOX required for engine testing and certification would come from a source outside of Florida and much closer to the SSC facility, the current LOX production facility at Mims, Florida, would support less than four HLLV launches per year. Fortunately, several LOX plants exist in Orlando, Florida. LOX manufacturing facilities also exist in Tampa and Jacksonville, Florida.

2.3.2 TRANSPORTATION. Because of the close proximity of Mims, Florida, to KSC and CCAFS, mobile tank trucks have always been used to transport LOX to these facilities. However, tank trucks may not be the most practical means for LOX transportation in future HLLV missions, particularly if it will be necessary to transport LOX to KSC from locations further away than Mims. A more practical means of transportation would be by rail tank cars. The volume capacity of a typical LOX rail tank car is dictated by weight and is approximately 19,750 gallons (telephone conversation with Frank Licari, Air Products, Inc., Allentown, Pennsylvania, June 25, 1992).

The argument could be made that considering the quantities of LOX that will be involved in future HLLV missions, barge transfer of LOX from the Mims, Florida, plant to Launch Complex 39A be considered. However, this presents a number of complications. First, the capacity of the Mims plant would need to be more than doubled in order to meet proposed annual HLLV requirements. Since Mims, Florida, is very close to the west bank of the Indian River, LOX could conceivably be barged from Mims south on the Indian River via the Intracoastal Waterway, around Merritt Island and then north via the Banana River and through existing channels to Pad 39A complex. Although the relative economics of barging versus using rail tank cars would have to be made, a safety problem immediately becomes apparent. RP-1 and LOX barges would be using the same channels, a potentially dangerous situation in the event of an accident. Another possible LOX barge route from Mims would be northeast on the Intracoastal Waterway, through Haulover Canal, the southeast away from the Intracoastal Waterway, through Mosquito Lagoon and marshes to Launch Complexes 39B and 39A. However, this route would involve digging of new channels through environmentally sensitive wetlands and would probably never be allowed. All factors considered, the use of rail car transport would appear to be the most practical method for LOX transport. The Florida East Coast Railway provides rail service to the area with a main line through Titusville, Cocoa, and Melbourne. Spur rail lines from the main line at Titusville to Launch Complexes 39A and 39B already exist.

2.3.3 STORAGE. Taking into consideration transfer losses, some 3,800,941 gallons of LOX will be required for each HLLV launch. At the present time, each launch pad has one 900,000 gallon spherical LOX storage tank. To the HLLV launch pad

will need to be added at least three and preferably four more 900,000 gallon LOX tanks. However, as pointed out in Section 3.3 below, the LOX as well as the LH_2 storage tanks will need to be moved further away from the HLLV lift-off site.

III POTENTIAL HAZARDS

3.1 RP-1 EMERGENCY DUMP

Two RP-1 concrete-lined holding ponds exist at each Launch Complex, 39A and 39B. The ponds, constructed for the Saturn V program, were designed to retain spilled RP-1 and discharge water. The dimensions of the pond are 150 feet by 250 feet with a water depth of two feet (14). The two ponds at each launch pad are capable of retaining some 1,122,000 gallons of RP-1, five times the RP-1 capacity of the Saturn V. In order to retain all of the RP-1 from an emergency HLLV dump, the depth of the existing holding ponds will need to be increased by six feet to a total depth of eight feet if we apply the same overdesign factor. This overdesign factor is justified because most certainly spilled RP-1 will be mixed with rainwater in the ponds. Environmental restrictions demand that the petroleum/water mixture be isolated from the environment until the ponds can be pumped out and proper RP-1/water separation processes undertaken.

3.2 ACOUSTIC EFFECTS

Sound pressure levels generated by high-thrust booster engines must be considered. Overall sound pressure levels of 120 to 135 decibels (dB) are important noise levels considered in formulating zoning restrictions. For protection of public property, 120 dB (intermittent) is considered the maximum overall sound pressure level to which the public should be exposed. At 135 dB (intermittent), ear protection is required and some damage to conventional structures may be expected. Sustained exposure to 90 dB will result in hearing damage (15).

According to the KSC Master Plan File for 1972 (conference with Merle D. Buck, Facilities Master Planning Office, Facilities Engineering Directorate, KSC, Florida, July 7, 1992), the Saturn V booster stage produced 135 dB at 4,000 feet, which decreased to 120 dB at 19,000 feet from the launch site. The Saturn V first stage booster was powered by five F-1 engines, whereas the HLLV will employ seventeen F-1A engines. Linear extrapolation gives a calculated 120 dB radius for the HLLV of 64,600 feet. Although large, this number is still considered to be rather modest because the F-1A engines in future HLLV's will be 20% more powerful than the old F-1 engines. In Figure 3-1, the 120 dB level radius associated with a HLLV launch from Complex 39A is shown superimposed (broken line) on a map of the KSC/CCAFS area. Also shown for comparison is the 120 dB radius for the Saturn V (inner broken line). Not only does the 120 dB limit for the HLLV come very close to the City of Titusville, but essentially all of the KSC and CCAFS operational facilities fall within this noise area. Similar calculations show that the 135 dB level for HLLV's will occur at approximately 13,600 feet. Although not shown in Figure 3-1, this level falls just short of the VAB area.

Noise associated with rocket booster lift-offs may be characterized as brief, intense, and predominantly low frequency. In surrounding communities to KSC/CCAFS, launch vehicle noise is usually perceived as a distant rumble. Based on the current launch environment, noise generated by launches, at worst, is considered to be an infrequent nuisance and does not pose a potential health risk

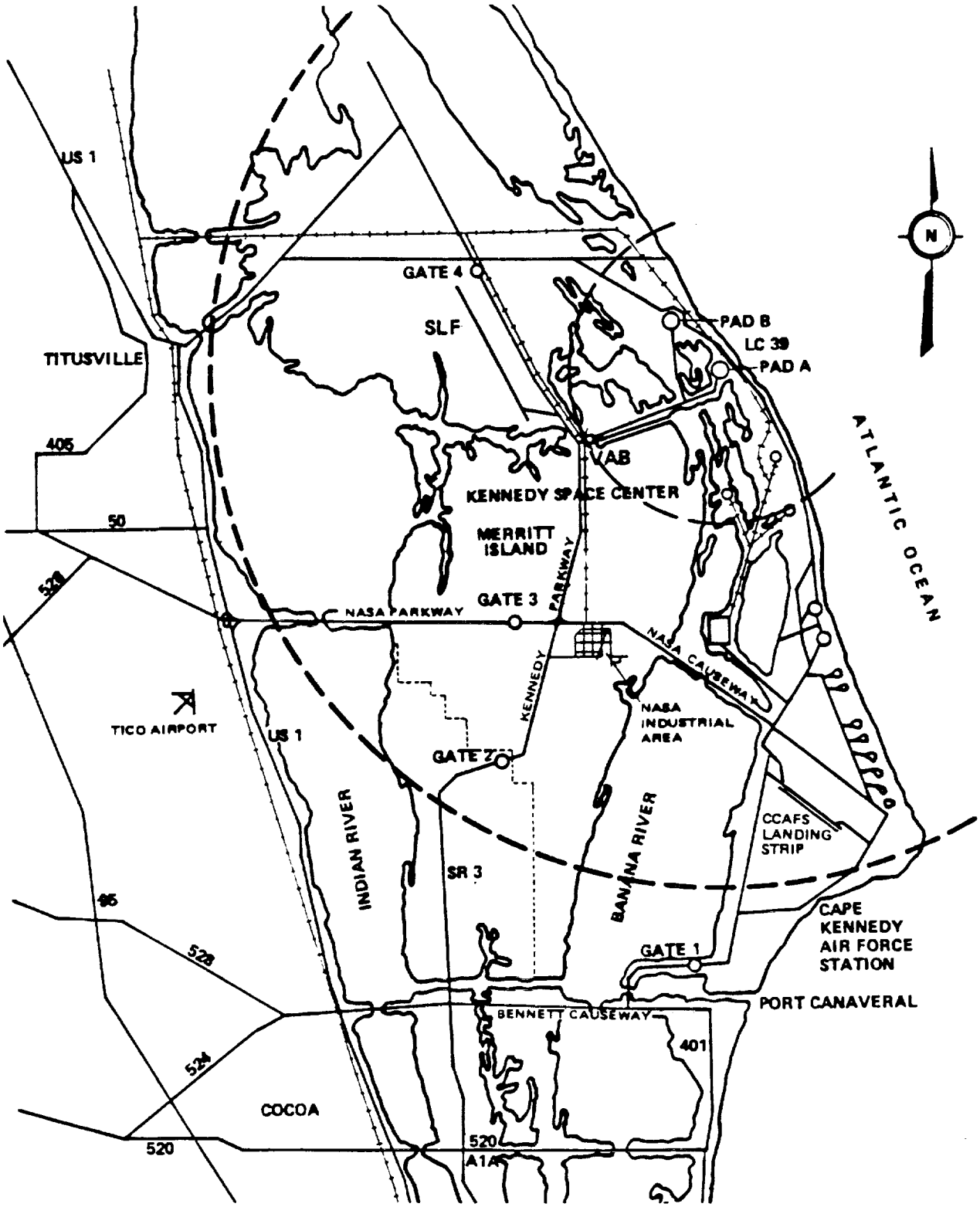

Figure 3-1. 120 dB Noise Level Radii for HLLV (Outer Broken Line) and Saturn V (Inner Broken Line) Superimposed on Map of the KSC/CCAFS Complex. Launches from Pad 39A.

to on- or off-site populations (16). However, this preliminary study suggests that noise associated with future HLLV launches will be more than an infrequent nuisance and may very well pose a potential health risk to both on- and off-site populations. It is almost certain that appropriate noise-abatement measures will need to be incorporated into future HLLV design plans.

3.3 FIREBALL AND BLAST EFFECTS

Studies of hazards associated with liquid propellant explosions must include both blast effects and the thermal environment. Liquid propellant explosions are characterized by a sudden release of a large volume of hot gases, often accompanied by pressure shock. These explosions are considered to be low-order detonations followed by deflagration (burning of the rocket above the launch pad in the event of an accidental failure or deliberate activation of the vehicle destruct system) (17).

Such a study was made for the Saturn V in which was described the thermal environment (the fireball) derived from empirical data and correlation with analytical results (18). For this study, it was assumed that: (1) all the fuel on the Saturn V is consumed in the fireball formation; (2) the fireball expands by deflagration rather than detonation or conflagration (burning of the rocket on the launch pad); and (3) the fireball shape is spherical.

In Figure 3-2 are presented the maximum diameters of fireballs from some experimental tests and missile failures. The following equation was derived by a least squares regression analysis of the data (19):

$$D = 9.82\ W^{0.320} \qquad (1)$$

where D = maximum diameter, ft., and W = weight of propellant, lb.

The fireball duration, derived in a manner similar to that for diameter, is illustrated in Figure 3-3. The least squares fit to the data is as follows:

$$Duration = 0.232\ W^{0.320} \qquad (2)$$

where duration is in seconds.

Using a total HLLV propellant weight of 20.6 million pounds, a maximum fireball diameter of 2,150 feet and a duration time of 51 seconds were calculated from Equations (1) and (2), respectively. These points have been added to Figures 3-2 and 3-3.

Of particular interest in these studies is the observation that both fireball diameter and duration are functions of total propellant mass only and not of the type of propellant.

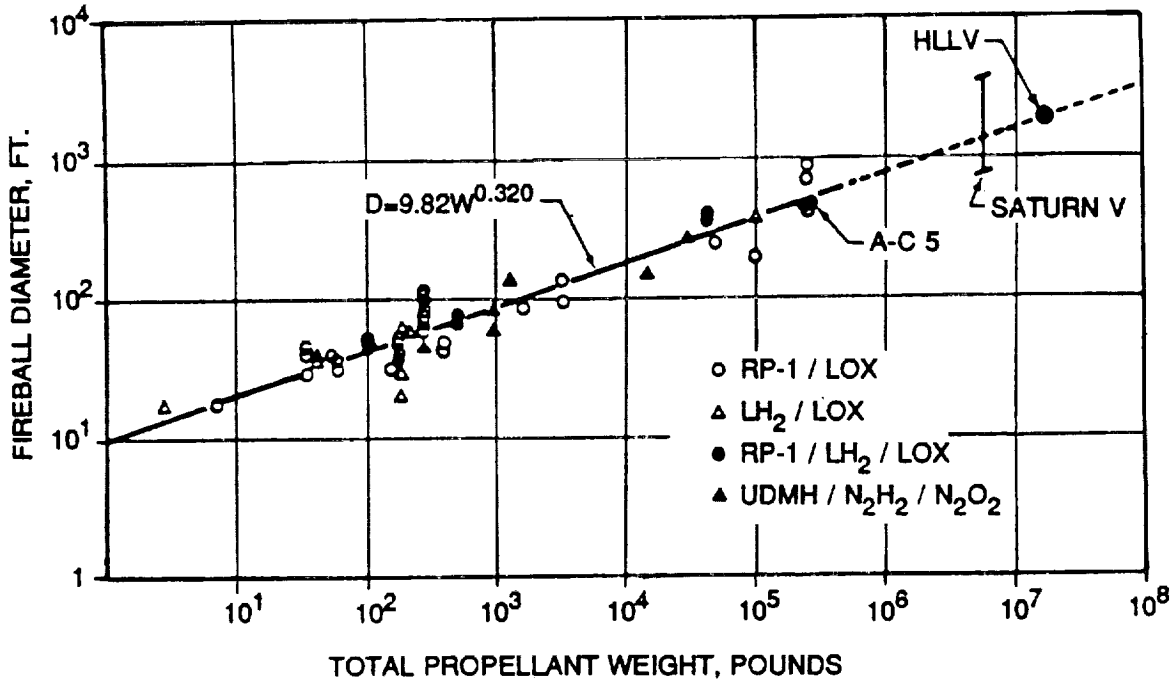

Figure 3-2. Fireball Diameters for Various Weights and Types of Propellants.

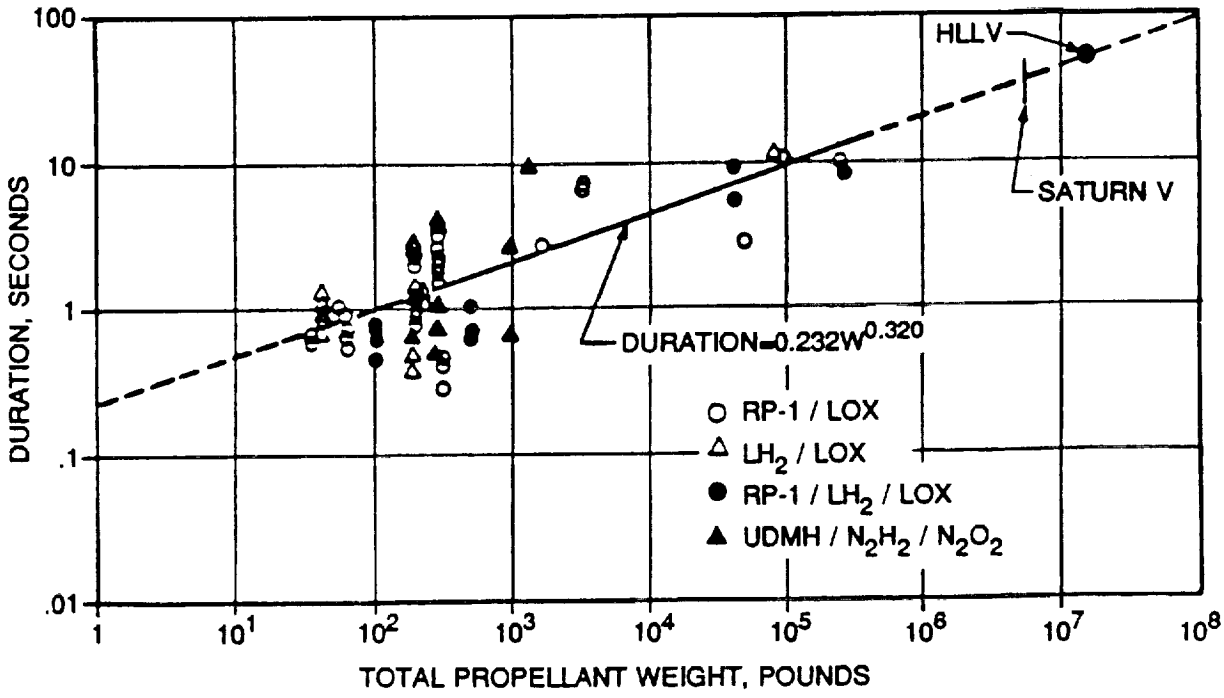

Figure 3-3. Fireball Duration for Various Weights and Types of Propellants.

The effective area covered by the HLLV fireball is shown as a broken circle in Figures 3-4 and 3-5, which are drawings of Launch Pads 39A and 39B, respectively. Inspection of Figures 3-4 and 3-5 shows that the HLLV fireball would come very close to propellant storage facilities on both pads and would spread over most of the maintenance and service operations buildings adjacent to the launch sites. As part of the SEI, various designs are being considered for upgrading and extending the launch pads at 39A and 39B for future HLLV missions. Such reconstruction should also include the relocation of maintenance and service operations buildings considerably outside the sphere of a possible HLLV deflagration.

The complete Saturn V/Apollo configuration contained the explosive equivalent of 1,193,227 lbs. of TNT (1). Based upon relative quantities of total propellants, the HLLV will have a TNT equivalent three times greater (and more than ten times greater than the space shuttle). The KSC Master Plan File for 1972 also outlined safety criteria regarding blast effects. It was determined that at 7,000 feet from a Saturn V detonation, the overpressure resulting from the blast would be 0.65 pounds per square inch (psi). This is the maximum allowable overpressure that ordinary windowless building construction can withstand without damage. All KSC ordinary buildings are designed to withstand a minimum overpressure of 0.28 psi. For the HLLV, this overpressure limit would be extended to 21,000 feet, approximated by the circle indicating the 120 dB noise level radius for Saturn V in Figure 3-1. The VAB area falls just within this limit. It was established that the maximum allowable overpressure to which the Saturn V rocket could be subjected was 0.40 psi. This established the launch danger radius or vehicle protection distance. Launch Complex Pads 39A and 39B are separated at a distance of approximately 8,700 feet, which complies with this criterion. If it is assumed that the 0.40 psi overpressure limit applies to the HLLV as well, then in order to comply with the safety criteria, HLLV's could not be on Pads 39A and 39B at the same time.

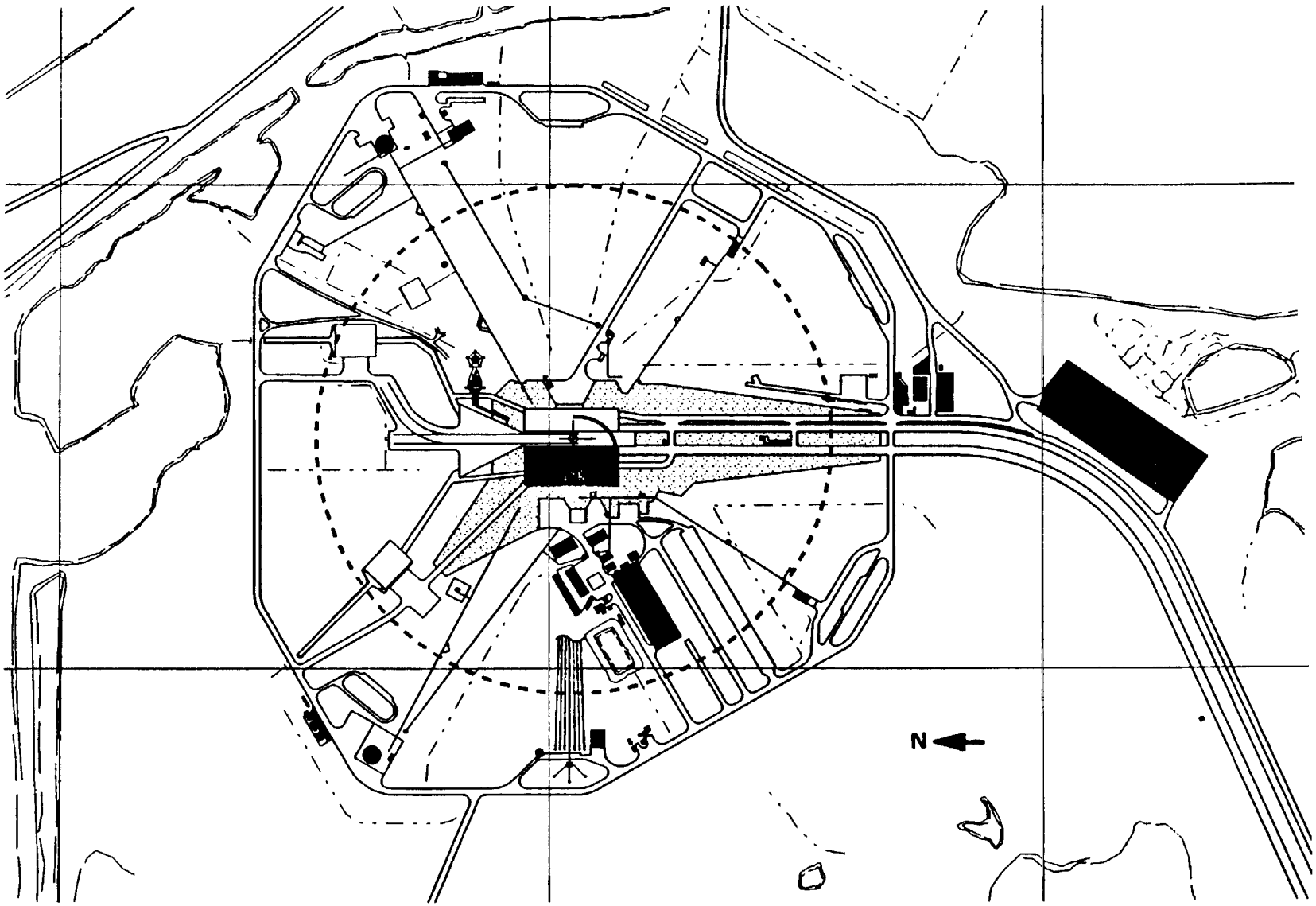

Figure 3-4. Area Covered by HLLV Fireball on Launch Complex 39A.

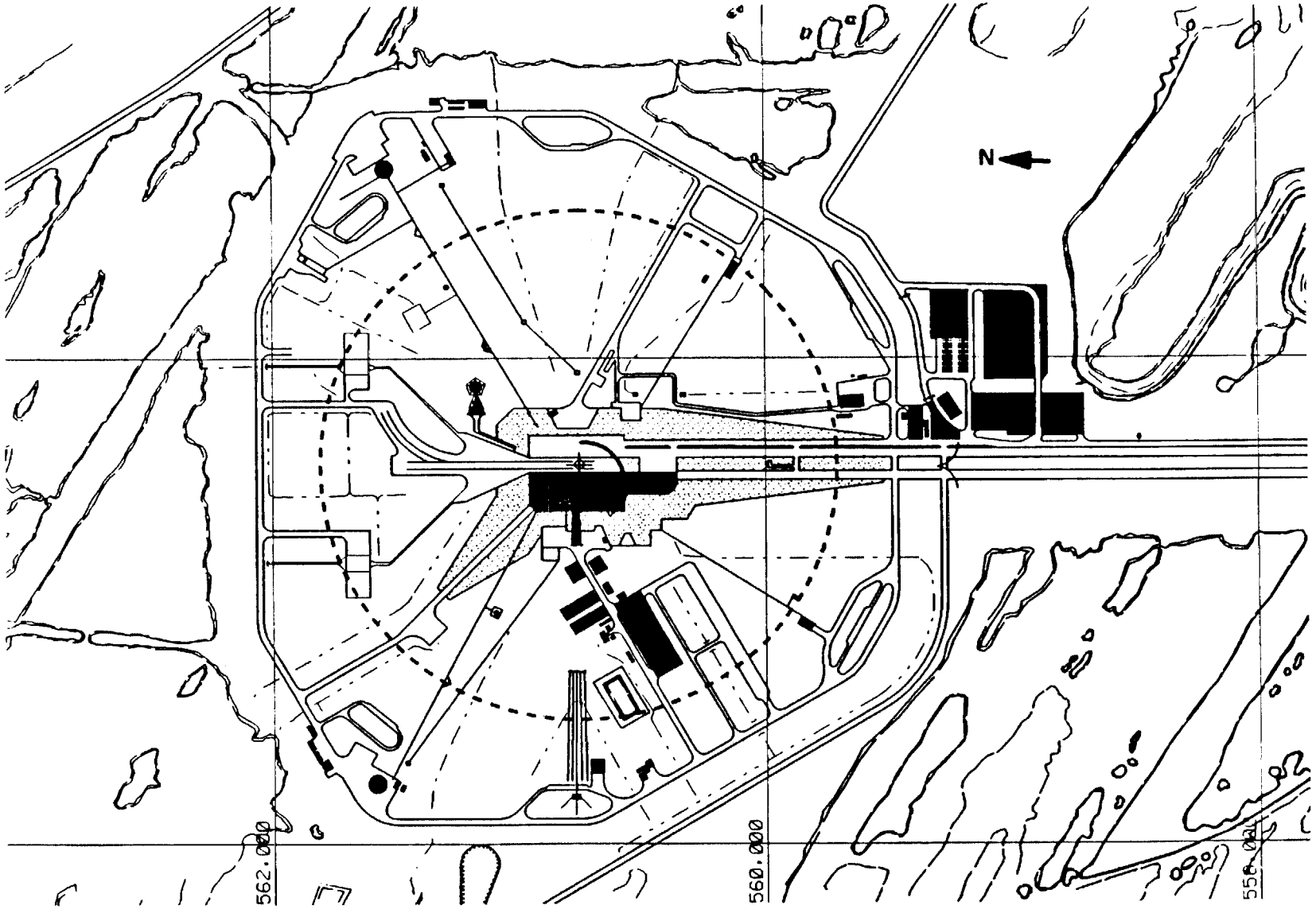

Figure 3-5. Area Covered by HLLV Fireball on Launch Complex 39B.

IV CONCLUSIONS

It is concluded from this study that no major problems should arise with regard to the logistics of securing, transporting, and storage of large quantities of propellants which will be required in future HLLV missions. At the same time, the handling of such large quantities of fuels and LOX should have no serious effect on the KSC infrastructure and, in fact, will be facilitated by reactivation of facilities already present at KSC. Some changes will be necessary, however. The location of some critical facilities, such as operations buildings, RP-1, LH_2, and LOX storage tanks, etc., will need to be relocated further away from the HLLV launch site than they are now in order to avoid a hostile thermal environment (fireball) or blast damage associated with either a HLLV deflagration or detonation.

With regard to specific HLLV propellants, the following conclusions can be drawn:

- Supply of RP-1 should pose no problem. However, the HLLV will require four times (by volume) as much RP-1 as Saturn V, so transportation of RP-1 by either commercial mobile tankers or rail tank cars is not deemed practical. Barge transportation appears most attractive, particularly since a barge channel to Pad 39A already exists. Such a barge could also serve as the storage site since no suitable RP-1 storage facilities exist as KSC today.

- The HLLV will utilize slightly more LH_2 than did the Saturn V. Certainly the supply of LH_2 should pose no problem, particularly since new facilities for LH_2 production are either now under construction or being planned. Since at least one of the new plants will be in Florida and closer to KSC, the continued use of mobile tankers (and possibly rail tank cars) is feasible. Storage of LH_2 is no problem except for the relocation problem discussed above.

- Unlike Saturn V, the HLLV will consume large quantities of oxygen, approximately 3% of the annual production in the United States. Overall this should create no problem, except for the fact that the LOX plant in Mims, Florida, would have to be increased by at least 100% in order to meet future HLLV requirements. However, if necessary, LOX manufacturing facilities in Orlando, Tampa, and Jacksonville could be utilized. Considering the closeness of LOX facilities to KSC, rail tank cars appear to be the most practical means of transportation. Barge transport of LOX from Mims to Launch Pads 39A and/or 39B would either involve LH_2 and LOX barges using the same channels, a potentially dangerous situation, or digging of new channels specifically for LOX barges, an environmentally unacceptable solution.

- Launch pad storage facilities for LOX will have to be increased substantially. At least four additional 900,000 gallon LOX storage tanks (in addition to the 900,000 gallon tank now located adjacent to each pad) will be required for future HLLV missions. Existing tanks must, of course, be relocated.

The one technical problem which must be solved will be that of noise associated with HLLV launches. Unlike previous Saturn V launches or even space shuttle launches today, future acoustic effects associated with the HLLV will be more than just a temporary nuisance. Noise-abatement measures must, and certainly will, be found.

V RECOMMENDATIONS FOR FUTURE WORK

Time constraints did not permit an analysis of either the environmental impact or cost analysis of future HLLV missions. Certainly environmental issues when handling this quantity of propellants must be considered. During the past three decades, new and increasingly stronger regulatory policies for the handling and clean-up of hazardous materials have been promulgated.

Specific objectives which would be addressed in future work are as follows:

- Become cognizant of all standards and regulations: governmental (EPA, OSHA, State of Florida, etc.), non-governmental (ANSI, ASTM, etc.), military and industrial relating to petrochemical-based fuels, LH_2, and LOX.
- Become familiar with the state-of-the-art with respect to RP-1 detection and clean-up techniques.
- Review updated medical data which may have been obtained during the past thirty years with respect to the toxic effects of RP-1.
- Undertake an overall environmental assessment for the HLLV program.

Recently, in compliance with the National Environmental Policy Act of 1969 and the regulations of the President's Council on Environmental Quality, an environmental assessment has been prepared for General Dynamics Space Systems Division for their commercial Atlas IIAS program (16). The results of this study showed that the implementation of the Atlas IIAS program would have no significant environmental impact. It is hoped that the same will hold true for future HLLV projects.

A cost analysis will, of course, be required. A unique aspect of the HLLV propellant system (like Saturn V) is that RP-1, LH_2, and LOX are all derived from starting materials plentiful and inexpensive (petroleum and air). The major expense items are thus processing and transportation, the former item predominating (telephone conversation with Chet Roberts, Compressed Gas Association, Arlington, Virginia, July 7, 1992). The major processing expense is the cost of energy (11). In qualitative terms, the expense of HLLV propellants will be the cost of the energy necessary to extract RP-1, LH_2, and LOX from their starting materials plus the cost of transporting this chemical energy to the launch site. The cost of producing LH_2 and LOX is particularly energy-sensitive and reduction in propellant expense will come primarily through cheaper electrical power, although improved processing methods and more efficient means of transportation will also be important.

New propellant storage separation distances must be determined. Because of transfer losses, some 1.07 million gallons of RP-1, 0.480 million gallons of LH_2, and 3.80 million gallons of LOX will be required for each HLLV launch. These storage facilities cannot be located at existing sites on Pads 39A and 39B, which are 1,450 feet from the pad centers. The basis for calculating safety distances has been established for different classes of explosive, including rocket propellants (20,21).

REFERENCES

1. Saturn V Flight Manual-SA509, Revised Baseline Manual MSFC-MAN-507, National Aeronautics and Space Administration, August 15, 1969 (changed January 1, 1971).

2. Biggs, Bob, "F-1, the No-Frills Giant," published in Threshold-Engineering Journal of Power Technology, No. 8, pp. 20-31, Rockwell International, Los Angeles Basin Data Services Center, Spring 1992.

3. Robertson, Donald F., "Will the Moon Rocket Engine Fly Again?," Space Markets, 7 [5] 2 (1991).

4. Warren, Don, and Langer, C. Steve, "History in the Making - The Mighty F-1 Rocket Engine," Internal Report, Rockwell International, Rocketdyne Division, Canoga Park, California.

5. Saturn V Flight Manual-SA509, Revised Baseline Manual MSFC-MAN-507, National Aeronautics and Space Administration, August 15, 1969 (changed January 1, 1971), pp. 2-14.

6. Saturn V News Reference, National Aeronautics and Space Administration, August 1967.

7. Liquid Propellant Engine Manual, CPIA/M5, Chemical Propulsion Information Agency, The Johns Hopkins University, August 1979.

8. Geyer, Wayne, Bringing Storage Tanks to the Surface, Chemical Engineering, pp. 94-102, July 1992.

9. Industrial Gases - Current Industrial Reports, 1990-Revised. U.S. Department of Commerce, Bureau of the Census Publication MA 28C (90)-1. Issued October 1991.

10. Facts and Figures for the Chemical Industry, Chemical and Engineering News, pp. 32-40, June 29, 1992.

11. Liquid Hydrogen Facility, Aviation Week and Space Technology, p. 11, December 16/23, 1991.

12. Air Products to Build Hydrogen Capacity, Chemical and Engineering News, p. 8, December 16, 1991.

13. Breaking Free at Carbide - Hydrogen Propels Growth of Industrial Gases Unit, Chemical Week, p. 56, May 13, 1992.

14. Saturn V Flight Manual-SA509, Revised Baseline Manual MSFC-MAN-507, National Aeronautics and Space Administration, August 15, 1969 (changed January 1, 1971), pp. 8-13.

15. Industrial Noise (581), U.S. Department of Health and Human Services, Public Health Service, National Institute for Occupational Safety and Health, Cincinnati, Ohio, March 1981, p. 63.

16. Environmental Assessment for the Commercial Atlas IIAS Program, Cape Canaveral Air Force Station, Florida, CH^2M Hill, Inc., Orlando, Florida, August 1991.

17. Fletcher, R.F., Characteristics of Liquid Propellant Explosions, published in Prevention of and Protection Against Accidental Explosion of Munitions, Fuels and Other Hazardous Mixtures, Annals of the New York Academy of Sciences, Vol. 152, Art. 1, October 28, 1968, pp. 432-440.

18. High, Richard W., The Saturn Fireball, published in Prevention of and Protection Against Accidental Explosion of Munitions, Fuels and Other Hazardous Mixtures, Annals of the New York Academy of Sciences, Vol. 152, Art. 1, October 28, 1968, pp. 441-451.

19. Gayle, J.B., Investigation of S-IV All Systems Vehicle Explosion. NASA TM X-53039. NASA Marshall Space Flight Center, April 27, 1964.

20. Jarrett, D.E., Derivation of the British Explosives Safety Distances, published in Prevention of and Protection Against Accidental Explosion of Munitions, Fuels and Other Hazardous Mixtures, Annals of the New York Academy of Sciences, Vol. 152, Art. 1, October 28, 1968, pp. 18-35.

21. Explosives Safety Standards, AF Regulation 127-100, Department of the Air Force, Washington, DC, May 20, 1983.

1992 NASA/ASEE SUMMER FACULTY FELLOWSHIP PROGRAM

JOHN F. KENNEDY SPACE CENTER
UNIVERSITY OF CENTRAL FLORIDA

HURRICANE RISK ASSESSMENT TO ROLLBACK OR RIDE OUT A COST VERSUS LOSS DECISION MAKING APPROACH

PREPARED BY:	Mr. Richard A. Wohlman
ACADEMIC RANK:	Instructor
UNIVERSITY AND DEPARTMENT:	Western Carolina University Mathematics and Computer Science
NASA/KSC	
DIVISION:	Advanced Projects Office
BRANCH:	Atmospheric Sciences
NASA COLLEAGUE:	Jim Nicholson
DATE:	August 7, 1992
CONTRACT NUMBER:	University of Central Florida NASA-NGT-60002 Supplement: 8

ACKNOWLEDGEMENTS

I would like to take a moment to express my gratitude to the UCF folks, Loren Andersen and Kari Stiles for the outstanding support provided me this summer and the unbelievable opportunity this has afforded. Loren for his constant 'hands on' attitude, and to Kari for arranging such a smooth transition from the hills of North Carolina to the flatlands here. Kari, I still owe you Chinese.

Much thanks goes to Jim Nicholson and Jan Zysko without whose guidance my work would have been impossible. Their able assistance in finding a project after termination of RTLP was essential.

Bill, were it not for you wanting me, I'd still be in the hills. Thanks.

A special thanks to the NASA training rep, MS. Carol Valdes for the terrific tours and opportunities to meet people, go places and see things that would have been otherwise impossible. The lead on the sailing class was super.

Support from the Computer wizards here at KSC was fast, freely given and invaluable. Mr. Nick Schultz, Mr. Lloyd Albright and Mr. Rich Neeley had amazing patience with me as I fumbled along with the VAX.

To my fellow colleagues a special heartfelt thanks. Having been around you folks for the last couple of months has been a special treat. Good times, good memories, far too short. Farewell and best of luck in your endeavors.

RAW

ABSTRACT

The potential exists that a hurricane striking the Kennedy Space Center while a Space Shuttle is on the pad. Winds in excess of 74.5 knots could cause the failure of the holddown bolts bringing about the catastrophic loss of the entire vehicle. Current plans call for the rollback of the shuttle when winds of that magnitude are forecast to strike the center. As this is costly, a new objective method for making rollback/rideout decisions based upon Bayesian Analysis and economic cost versus loss is presented.

SUMMARY

There are an average of 8.4 tropical storms each year in the Atlantic Basin with 4.9 of these reaching hurricane strength. Should one of these make landfall at KSC while a shuttle were on the pad, the potential to seriously damage orbiter hardware exists. Protection of the shuttle from the heavy rain and hail is accomplished to a large extent with existing structures which surround the shuttle stack while on the pad, but strong winds are still a major consideration. Current wind limits stand at 74.5 knots sustained winds from any direction. At this point, wind loading on the shuttle stack can cause structural damage to the hold down skirts on the solid rocket boosters which attach the shuttle stack to the launch pad. The potential exists for loss of the vehicle should the attach points fail.

The current plan provides for rollback of the shuttle to the VAB in the event of a hurricane. This procedure requires at least 48 hours leadtime to the onset of 74.5 knot winds. Eight hours are actually required for the movement from the pad to the VAB.

Shuttle managers make the rollback/rideout decision based upon National Hurricane Center forecasts, with input from the Cape Canaveral Air Force Station weather support unit. Managers at present make subjective decisions based primarily on perceived risk of strike.

An analysis of risk based upon cost versus loss could provide managers an objective decision making tool. Using a Bayesian analysis with sequential events and their corresponding probabilities, along with the associated costs of performing each preparation/rollback operation, a decision making tree can be established for selected time critical milestones.

SECTION I INTRODUCTION

1.1 A HISTORY

Between the years of 1886 and 1991, 970 tropical storms spawned in the Atlantic Ocean basin with 614 of these reaching hurricane strength. At Kennedy Space Center, 64 of these tropical storms passed within 75 nautical miles; 26 which were of hurricane strength. Should a hurricane strike the cape while an orbiter were on the pad, damage to the space shuttle and associated hardware could occur. Protection of the Space Shuttle is of prime importance to management.

The Space Transportation System (STS) is made up of the orbiter, external tank and solid rocket boosters. It is stacked in the Vehicle Assembly Building (VAB) and moved to the launch pad some three to four weeks prior to launch where it is exposed to the elements. This exposure is mitigated somewhat by the protection afforded by the Rotating Service Structure (RSS) which encloses the upper surfaces of the orbiter, and the recently installed weather protection system. The weather protection system provides cover to the underside of the orbiter with huge movable panels which move into position from the RSS and block the bottom of the orbiter from exposure to the elements. Under most day to day thunderstorm and shower activity which is so prevalent in this part of the world, these precautions are sufficient to prevent damage to the stack.

Conditions which exist in a hurricane, however, could be beyond the protective capabilities afforded on the launch pad. Wind blown debris could cause damage to the exposed external tank or could damage the orbiter itself. Extreme winds and gusts might cause sufficient swaying in the stack bringing it into physical contact with support structures. In the worst case, the hold down attach points at the aft end of the SRB's could fail due to stack movement causing catastrophic loss of the vehicle.

1.2 HURRICANE PROTECTION PROCEDURES

Current plans provide for rollback from the launch pad of the stack in the event of a hurricane. However, the decision to roll the shuttle back to the VAB must be made long enough in advance for the stack to be secured prior to the onset of hurricane force winds. Signed limits are actually set at 74.5 knots, but for the purpose of this paper, hurricane force winds shall be examined. At present, the leadtime is 48 hours: 40 hours for preparation to rollback, and 8 hours moving to the VAB. A Space Shuttle Vehicle (SSV) Rollback Milestone Schedule is found in the Space Shuttle Hurricane Management Plan, and gives specific timeliness for operations which must be initiated and completed prior to rollback. The document also specifies the makeup and responsibilities of the Hurricane Management Team (HMT) headed by the Deputy Director of Space Shuttle Operations as the primary decision maker. Weather information is provided by a specific weather officer designated by the Cape Canaveral Air Force Station Forecast Facility. The weather officer is charged with providing the HMT all advisories, watches

and warnings issued by the National Hurricane Center (NHC) along with rationale, track error analysis, and model confidence for each of these. The decision maker is faced with making a rollback/rideout choice based upon hurricane strike probabilities which are generally very low beyond the 48 hour point. The decision to rideout will eventually eliminate the possibility to rollback at some point in the decision making process because insufficient time for preparation remains to roll back. Consequently, the rollback decision is kept open until the threat safely passes or until the rollback occurs. Management must continually examine the threat and make decisions based at times upon somewhat subjective forecast information to keep those options open to preclude being overcome by events.

The economics of the situation provides another tool for determining whether to rollback or ride out by using a strict cost versus loss approach. While it is understood that the STS is a national resource whose loss or even damage could adversely affect future operations and public opinion, this study examines only the economics of the decisions involved. Loss costs include both orbiter and typical payload, which can be calculated for each mission. Costs associated with rollback begin when the decision maker halts processing and begins preparation for rollback, and mount with the execution of each rollback preparation procedure. Included in the cost part of the equation is the cost to return the SSV to the state of processing before protection measures were taken. Thus, costs and leadtimes are very dynamic figures. In fact, gathering cost data has proven to be one of the most challenging tasks of this research, and eluded efforts until the final week when a simplified cost figure was found. When the customer whose payload is aboard the Orbiter asks for a launch delay of one day (for example) he is required to pay for the delay. Payment is determined by dividing the yearly operating costs of shuttle operations and immediate support functions by 365. These numbers work out to approximately $1.68 million per day

SECTION II RESEARCH

Several areas required examination before a course of action could be taken. First was a review of previous studies. Next was a scheme which would generate probability changes to be incorporated into the analysis, and finally was the construction of a computer program to allow the weather expert to modify the forecast strike probabilities to reflect the historical data.

2.1 PREVIOUS WORK

2.1.1 STUDIES. In 1968 a study was conducted for the U.S. Department of Commerce titled 'Probability of Tropical Cyclone Induced Winds at Cape Kennedy' by Hope and Neumann which examined the tropical cyclone historical data through 1966. At the time, the critical windspeed was 35 knots which was dictated by safety concerns associated with the Saturn V/Apollo spacecraft. Using a statistical technique to examine storm tracks, Hope and Neumann found that there seemed to be two areas through which storms passed affected the Cape. One of these was in the Western Atlantic just north of the Lesser Antilles, and the other was in the western Caribbean/eastern Gulf of Mexico region. Indications were that the Atlantic storms hit the cape area from the south to south east, while the Caribbean storms arrived from the south to southwest. Storm data was limited to a large part to ship and aircraft reconnaissance reports as satellite data was nonexistent until the mid caribbean's. Conclusions reached were most useful for planning forecasts beyond the 72 hour point.

Neumann in 1975 conducted a study called 'A Statistical Study of Tropical Cyclone Positioning Errors with Economic Applications'. Inaccuracies in storm position and motions have a great affect upon its forecast position. Landfall forecasts are subsequently affected which lead to protection expenditures which were not required, or to damages which could have been avoided had protection measures been taken. Protection costs for the Gulf coast were typically $25.1 million for a 300 nautical mile stretch, and positioning errors of 10nm cost an additional $5 million in 1975 dollars. Building upon techniques used in the earlier paper, methods for storm position error correction and narrowing of landfall forecasts were developed.

A third technical memorandum titled 'The National Hurricane Center Risk Assessment Program (HURISK)' by Neumann consolidated progress made since the 1968 study and expanded upon it. It shall be discussed in some detail in this paper. A detailed description of the HURISK program and its output is discussed in detail in Neumanns paper.

2.2 THE HURRICANE RISK ASSESSMENT PROGRAM

HURISK was designed to be an analysis tool with some long range forecast applicability. The program selects hurricane and tropical storm data from a computer database which

contains data back to 1886. Storms are selected which have passed at some time in their history through a circle with a radius of 75nm centered upon the site of interest. At this authors request, data for the Kennedy Space Center were generated using the HURISK computer program. Its results are described below. The data themselves, charts 1-12, make up Appendix A to this paper.

2.2.1 CHART DESCRIPTION. The first six charts are tabular and graphic data of those selected storms. Chart 1 is a tabular representation of data for each storm. Chart 2 and 3 are maps showing storm tracks for all tropical storms and hurricanes respectively. Chart 4 relates number of storms to the year in which they occurred, and shows some derived numbers: storms per year, hurricanes per year, mean interval, etc Later charts develop specific and detailed analysis of these preliminary data. Chart 5 plots number of occurrences to the date when the storm is nearest the site, and Chart 6 gives the direction from which those storms came. Of particular note here is the confirmation of Neumann's earlier observation of two directions from which storms move through prior to striking the cape area. While the mean direction is from almost due south there appear to be two local maxima, one from the southeast the other from the southwest.

In chart 7, the first of several mathematical models is constructed. Data is plotted for number of storms passing within a specified distance, and a quadratic equation is fitted. This quadratic equation is used in subsequent prediction models. One of these is the Radius of Maximum Wind (RMW) which for KSC is about 25nm for all storms. Again, this average is computed for all tropical storms and not just hurricanes. Chart 8 plots max wind vs. percent of cases and determines a Weibull distribution (an exponential curve) to fit the data. This curve is used in lieu of actual data to calculate the mean return period for a specific maximum wind in Chart 9 which provides perhaps one of the more useful pieces of information from the HURISK program. Since wind limits for STS are set at 74.5 knots, and since gusts (one second duration) are typically 1.25 times magnitude of the maximum sustained wind, enter the table with 60kts (74.5/1.25) and read off approximately 5.3 years for recurrence within the 75nm circle, and about 10 years within 50nm.

Charts 10 and 11 give the probability of x number of storms (1-5) occurring within the 75nm storm circle with respect to the number of years between those occurrences. The last hurricane to move through the 75nm site circle was hurricane David in 1979. To find the probability of having 13 years (1979 through 1992) without a hurricane, enter 13 on the x axis, and move to the right side y-axis and read off about 5%. Similarly, Chart 1 shows that the last tropical storm was in 1988. Using Chart 10, probability of not having a storm for 4 consecutive years is about 9%.

The last two charts 11 and 12 yield gamma distributions for tropical storm and hurricane forward speed respectively. The mean hurricane forward speed is 11.66kts with a standard deviation of 3.53kts. From this chart comes information for making decision circles, those distances at which a decision must be made concerning rollback or rideout

preparations.

2.3 DECISION CIRCLES

Using the timeline from the SSV Rollback Milestone Schedule, a series of decision circles can be constructed. Attachment 1 is the timeline itself. Critical times are shown with their associated actions. These have been developed from a worst case situation (SSV on the pad with cargo aboard nearing the end of launch preparations) so there is some downward flexibility in the schedule. Using the timeline as shown the following table can be generated. The forward velocity of the storm is taken from chart 12 of the HURISK program. Values used are the mean velocity, 11.66kts, and 18.72kts which is the mean velocity plus twice the standard deviation. Note the variability of the first decision circle due to storm forward movement speed. Obviously, should a storm be moving at a much slower rate than the mean velocity, then the decision circles shrink accordingly. When plotted on a map of the region, these circles provide an area which can be used by the decision maker to gauge his time by graphically allowing him to see where he is in the decision making process. It should be noted, however, that quite often that cessation of forward movement signals a change in the intensity of the storm.

Hours to Strike	Diameter @ V=1.66 kts	Diameter @ V=18.72kts
48	560	899
44	513	824
40	466	749
36	420	674
28	326	254
22	257	412
20	233	374
12	140	225
8	93	150

Table I: Decision Circle Diameters

2.4 COST VERSUS LOSS

Decision making based upon probability forecasting is much like placing a bet. To make a good bet, payoffs need to be examined and risk assessment is required. With the STS, total risk avoidance would ground the fleet from June through October because there is a measurable chance a hurricane might hit the center. Acceptance of all risk, on the other hand would leave the STS on the pad during any weather and would ignore the chance of losing the vehicle to extreme hurricane winds. The ideal risk acceptance level lies somewhere between the two extremes. In the absence of a direct willingness or non-

willingness to take risk, this paper assumes that the decision maker is essentially risk neutral; that is, he will make his decision based upon the results of the cost versus loss scheme.

2.4.1 AN EXAMPLE. To help understand the cost versus loss scheme, examine the following example. Suppose that there is a 10% chance that today there will be a severe thunderstorm with damaging hail that will damage your car. Should your car be damaged, it will cost $1500 to repair. This is the loss value. A car cover which will totally protect the car costs $200. The decision is to protect and buy the car cover, or not protect and take the chance that the storm will not damage the car. As Figure 1 shows, there are several possible outcomes. First, if the choice is made to protect, the monetary consequence of that action is $200 regardless of the occurrence or non-occurrence of hail. If the choice is made not to protect, then there are two distinctly different outcomes. First, if there is no hail, the monetary consequence is $0. But, if there is hail, it will cause the loss of $1500. How to choose? Cost vs loss says that if the probability of the event occurring is less than the quotient of the cost divided by the loss then you do not protect. If it is greater, protect. So, based upon this information, the probability of hail (p) is .10, and cost/loss is .13333. Since p<(C/L), do not protect.

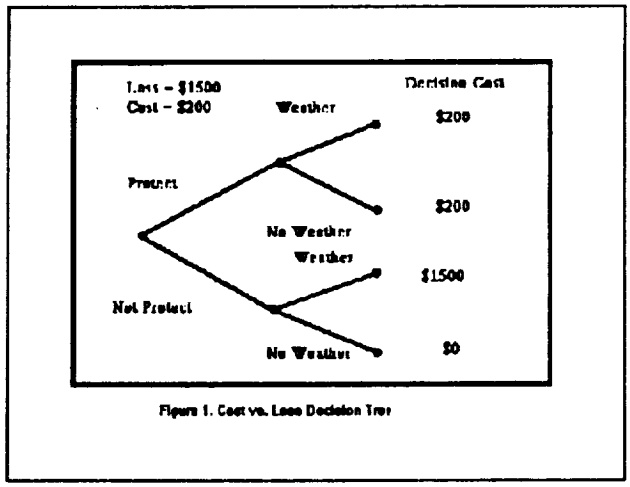

Figure 1. Cost vs. Loss Decision Tree

2.5 BAYES THEOREM

Bayes Theorem takes into account information received subsequent to the forecast being made to yield a new probability. The Theorem itself looks like:

$$(P|y) = \frac{P(E)\,P(y|E)}{P(E)\,P(Y|E) + P(\overline{E})\,P(y|\overline{E})}$$

where:

$P(E|y)$= *probability of event E given event y*
$P(y|E)$= *liklihood of E preceeded by y*
$P(\overline{E})$= *probability of no E occurring*
$P(y|\overline{E})$= *liklihood of y followed by no E*

2.5.1 AN EXAMPLE REVISITED Suppose that in the example above, we subsequently discover that there is a severe thunderstorm directly to our west 40 miles away. Historical records show that when our location received damaging hail, it was preceded by a severe thunderstorm 40 miles to the west. On the other hand, when there was a severe thunderstorm 40 miles to the west, in 10% of the cases our location did not receive damaging hail. Using Bayes theorem, we can examine the effect upon our probability:

$$P(E|y) = \frac{(.10)*(.30)}{(.10)*(.30)+(.90)*(.10)} = .25$$

The probability has changed and we can reenter the decision tree and determine whether protection is required or not. Since p = .25 and C/L = 1.3333, we should protect and buy the car cover.

2.6 DEVELOPMENT OF COMPUTER PROGRAMS

In order to generate probabilities for the Bayesian analysis, an examination of historical data had to be made. Storm data was obtained from the NHC and examined. This effort took considerable time as a computer program to make use of the data was not available and had to be written. The historical master data list itself is a huge ASCII file over 655K bytes long. Data for one storm on the master data list appears in Appendix B.

2.6.1 PROGRAM VECTOR. After running the program VECTOR, data is massaged into several files which are much more manageable. The first of the output files is called TKHDR.DATA. This file is comprised of all track header data from each of the storms as listed in the master data file. Output from one line of this file looks like:

62410 ALMA 5 17 1790 688 11 HR

The number 62140 is the sequence number of the entry in the master data file, ALMA is the storm name, 5/17/1970 is the start date of the storm, 688 is the sequential number of the storm in the data list, 11 is the number of days the storm lasted, and HR means that it reached hurricane strength at some point in its life. The second file that is created is called TRK.DATA, and an example of one storm is shown in Appendix C. The fortran program, VECTOR.FOR is Appendix D. The final output file is called VECTOR.DATA. Data in this file resemble the following:

```
62410  38
62410  16.80 315.59    0.00   25
62410  37.92 309.27   -6.32   25
62410  26.35 297.09  -12.18   25
```

These data represent the following. In the first line, 62410 is the sequence number from the master data list of the header data line in the master data list, and 38 is the number of pieces of data exist for the storm. This is also the number of data lines follows with data of storm 62410. Note that all data lines begin with the same sequence number to tie each to the other. In line 2, the number 16.80 is the distance traveled from the first coordinate given for the storm to the second coordinate. The equation used in the program is the Pythagorean Theorem with the convergence of the longitude lines taken into account for westward (or eastward, as the case might be) motion of the storm. Next is the direction of motion followed by the change in direction since the last position. Since this is the first motion detected, its change is set to zero. Finally is the data for the maximum wind in knots.

2.6.2 PROGRAM CHOOSE. The data is now in a very manageable format, and lends itself nicely to further selection. One selection program, CHOOSE, (Appendix E) allows the user to select storms between certain specified storm sequence numbers. For example, should the user wish to see only data from storms which occurred after 1980 and prior to 1990, by referencing the storm sequence numbers at the beginning and end of the time period (81000 to 90240) he can have those data put into a file named NEWVECT.DATA for further investigation.

SECTION III DISCUSSION OF FUTURE INVESTIGATIONS

Now that the storm data is accessible, new selection programs can be written to allow the user to choose the storms which resemble the storm in progress. By analyzing the vector motion of the selected storms, both based upon time scales and upon distance scales, movement probabilities can be generated for use in the Bayesian analysis. Examination of the vector data yields the behavior of the storms. Questions to be answered could be of the form: given that my storm has turned right 10 degrees in both of the two most recent 6 hour periods, what is the probability that it will a) continue turning right, b) straighten out, or continue on its present heading or c) begin to turn left?

By selecting storms with similar characteristics in terms of windspeed, sea level pressure, forward movement, location and track, or any combination of these, reasonable probabilities can be found.

Once these programs and procedures are complete, they can be easily verified using the historical data. Since the user can de-select specific storms, that storm can be used to test the viability of the model. New insights to storm motion might be uncovered.

Ultimately, once these routines are incorporated into a single program, they should allow the user to gather, select and predict storm strike probabilities for the Center. Using NHC forecasts and analysis, a strike probability can be generated for use in the cost versus loss equation.

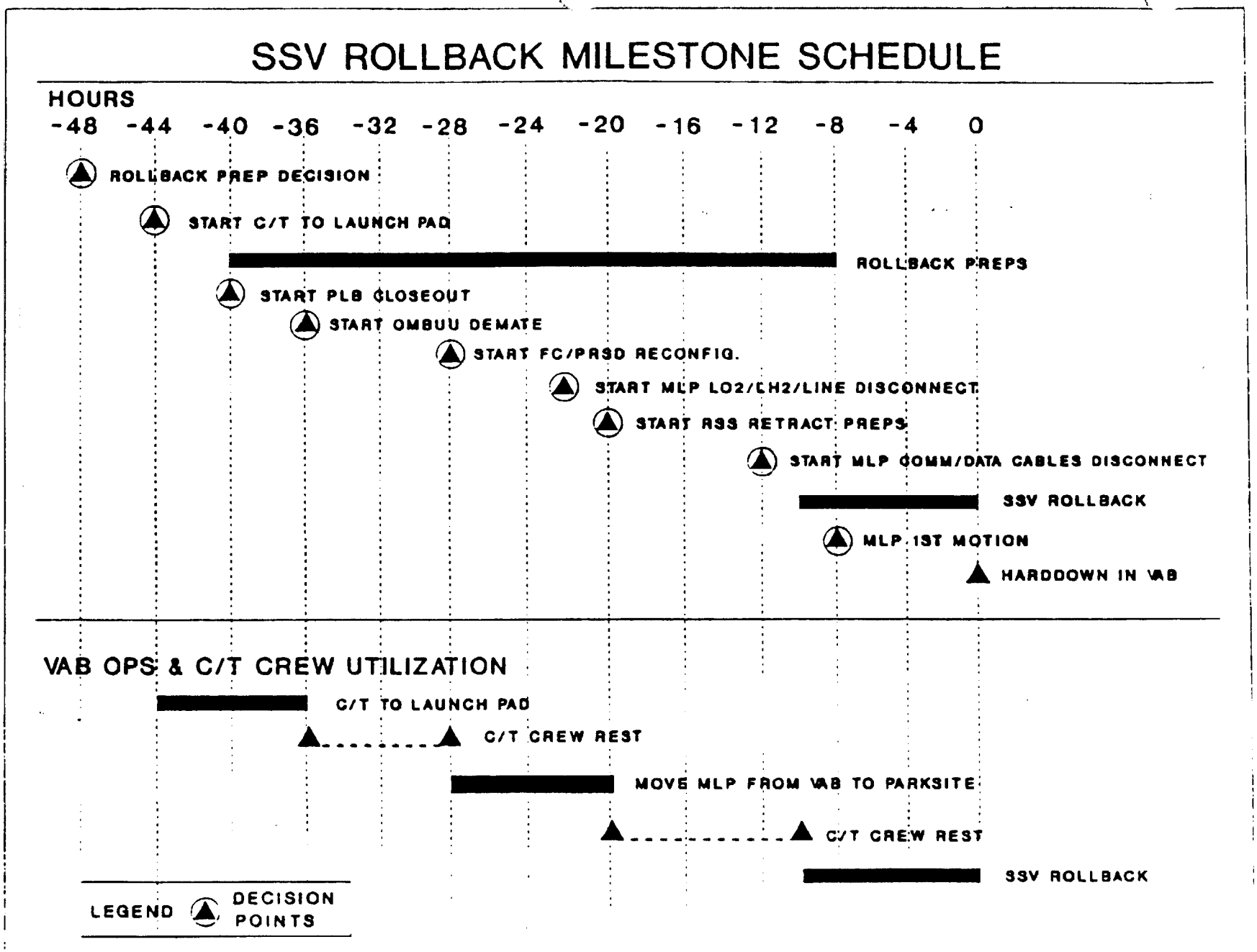

Attachment 1

APPENDIX A

CHARTS 1-12
FROM

HURISK

TROPICAL CYCLONES (1886-1991) PASSING WITHIN 75 N.MI. OF CAPE KENNEDY, FL

STORM INDEX NUMBER	STORM NAME	YEAR	MONTH	DAY (GMT)	STORM NUMBER FOR YEAR	MAXIMUM WIND (KTS) NEAR STORM CNTR AT CLOSEST PT. OF APPROACH	CLOSEST POINT OF APPROACH (CPA) N.MI.	STORM HEADING (DEGS) AT CPA	STORM FORWARD SPEED AT CPA(KTS)
1	NOT NAMED	1886	JUL	19	4	83	73	049	12.5
2	NOT NAMED	1887	AUG	20	4	105	68	356	12.8
3	NOT NAMED	1887	OCT	29	14	96	47	053	27.3
4	NOT NAMED	1889	OCT	5	9	45	66	015	15.8
5	NOT NAMED	1891	OCT	7	7	40	61	030	12.6
6	NOT NAMED	1892	OCT	10	8	35	9	037	8.8
7	NOT NAMED	1893	OCT	25	9	39	36	078	9.9
8	NOT NAMED	1893	AUG	27	6	105	39	332	12.6
9	NOT NAMED	1893	OCT	27	9	95	46	348	11.9
10	NOT NAMED	1894	SEP	26	5	78	31	015	9.4
11	NOT NAMED	1896	OCT	9	5	70	69	045	12.0
12	NOT NAMED	1897	SEP	21	5	35	15	028	11.3
13	NOT NAMED	1897	OCT	19	4	38	31	030	25.7
14	NOT NAMED	1898	AUG	2	1	69	72	290	15.4
15	NOT NAMED	1898	OCT	11	6	40	47	049	13.9
16	NOT NAMED	1899	AUG	14	2	105	47	360	17.5
17	NOT NAMED	1906	OCT	21	6	35	7	202	5.9
18	NOT NAMED	1906	OCT	17	9	35	64	246	15.2
19	NOT NAMED	1909	JUN	29	2	35	59	307	9.3
20	NOT NAMED	1909	AUG	30	6	35	24	345	11.3
21	NOT NAMED	1909	SEP	27	7	35	30	042	9.3
22	NOT NAMED	1910	OCT	18	4	60	55	354	5.3
23	NOT NAMED	1915	AUG	1	6	40	17	319	18.8
24	NOT NAMED	1916	SEP	13	6	35	18	304	10.7
25	NOT NAMED	1921	OCT	26	2	61*	21	087	17.4
26	NOT NAMED	1925	DEC	1	1	65*	18	034	7.0
27	NOT NAMED	1926	JUL	28	6	65*	3	324	11.0
28	NOT NAMED	1928	AUG	9	4	100*	20	317	11.0
29	NOT NAMED	1928	SEP	17	7	85*	58	058	4.0
30	NOT NAMED	1930	SEP	10	5	82*	37	270	10.7
31	NOT NAMED	1933	JUL	31	3	55*	74	306	15.4
32	NOT NAMED	1933	SEP	4	7	80	62	027	15.4
33	NOT NAMED	1934	MAY	26	3	40	49	243	15.4
34	NOT NAMED	1934	JUL	25	4	44	64	299	15.4
35	NOT NAMED	1936	AUG	21	5	40	45	348	13.1
36	NOT NAMED	1937	JUL	30	4	49	44	291	11.3
37	NOT NAMED	1937	AUG	30	7	60*	17	300	12.6
38	NOT NAMED	1939	AUG	12	6	35*	52	236	14.5
39	NOT NAMED	1940	AUG	19	11	66	51	013	12.6
40	NOT NAMED	1944	OCT	24	9	66	60	048	14.5
41	NOT NAMED	1945	JUN	16	4	66	49	056	12.6
42	NOT NAMED	1945	SEP	27	12	66	59	308	9.3
43	NOT NAMED	1949	AUG	5	5	66*	22	026	11.3
44	NOT NAMED	1950	SEP	11	11	67	70	339	11.3
45	EASY	1950	OCT	18	12	61	51	045	17.2
46	KING	1951	OCT	9	5	55	37	054	18.8
47	HOW	1953	OCT	11	12	97	5	027	24.2
48	HAZEL	1954	SEP	5	11	59*	70	346	16.3
49	DONNA	1960	AUG	28	5	100	17	279	11.3
50	CLEO	1964	SEP	10	11	70	67	313	9.7
51	DORA	1964	JUN	9	6	70	33	053	17.2
52	ABBY	1968	OCT	19	8	55	50	048	18.8
53	GLADYS	1968	JUN	25	6	40	47	009	17.2
54	SUBTROP	1974	OCT	7	11	45	11	060	32.9
55	SUBTROP	1974	AUG	20	5	65	6	347	13.3
56	DOTTIE	1978	SEP	4	4	85	45	002	14.0
57	DAVID	1979	AUG	19	4	85	56	260	11.1
58	DENNIS	1981	AUG	25	5	34	60	338	10.0
59	BARRY	1983	SEP	9	10	55	26	302	10.4
60	DIANA	1984	SEP	26	9	45	24	001	10.3
61	ISIDORE	1984	JUL	24	3	53	49	307	11.0
62	BOB	1985	OCT	10	12	41	23	345	27.0
63	ISABEL	1988	AUG	28	3	41	49	049	16.8
64	CARIS	1988	NOV	23	12	38	23		
	KEITH								

CHART 1

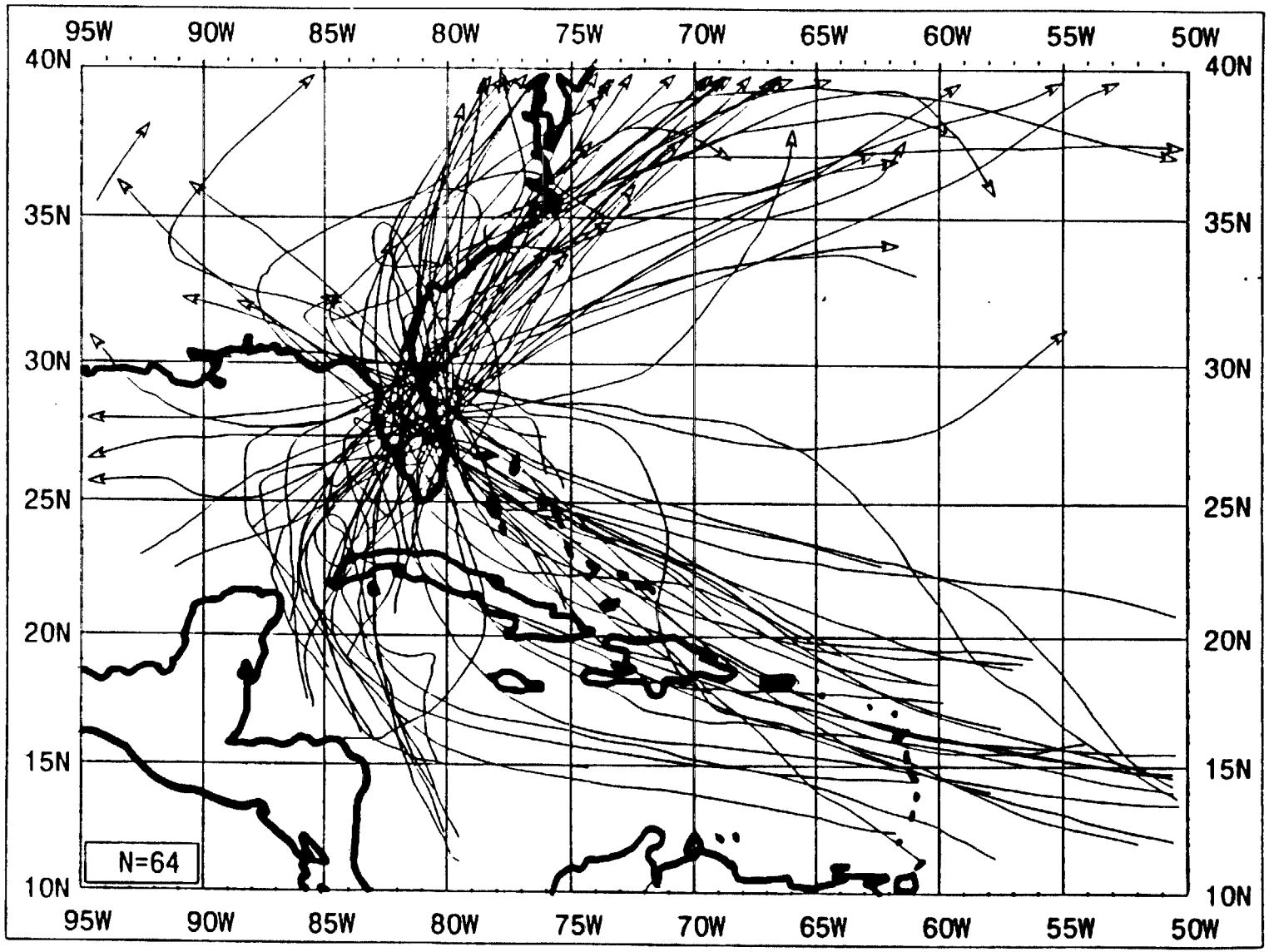

TROPICAL CYCLONES PASSING WITHIN 75 N.MI. OF CAPE KENNEDY, FL 1886-1991

(SITE LOCATION MOVED TO 28.6N, 80.9W)

CHART 2

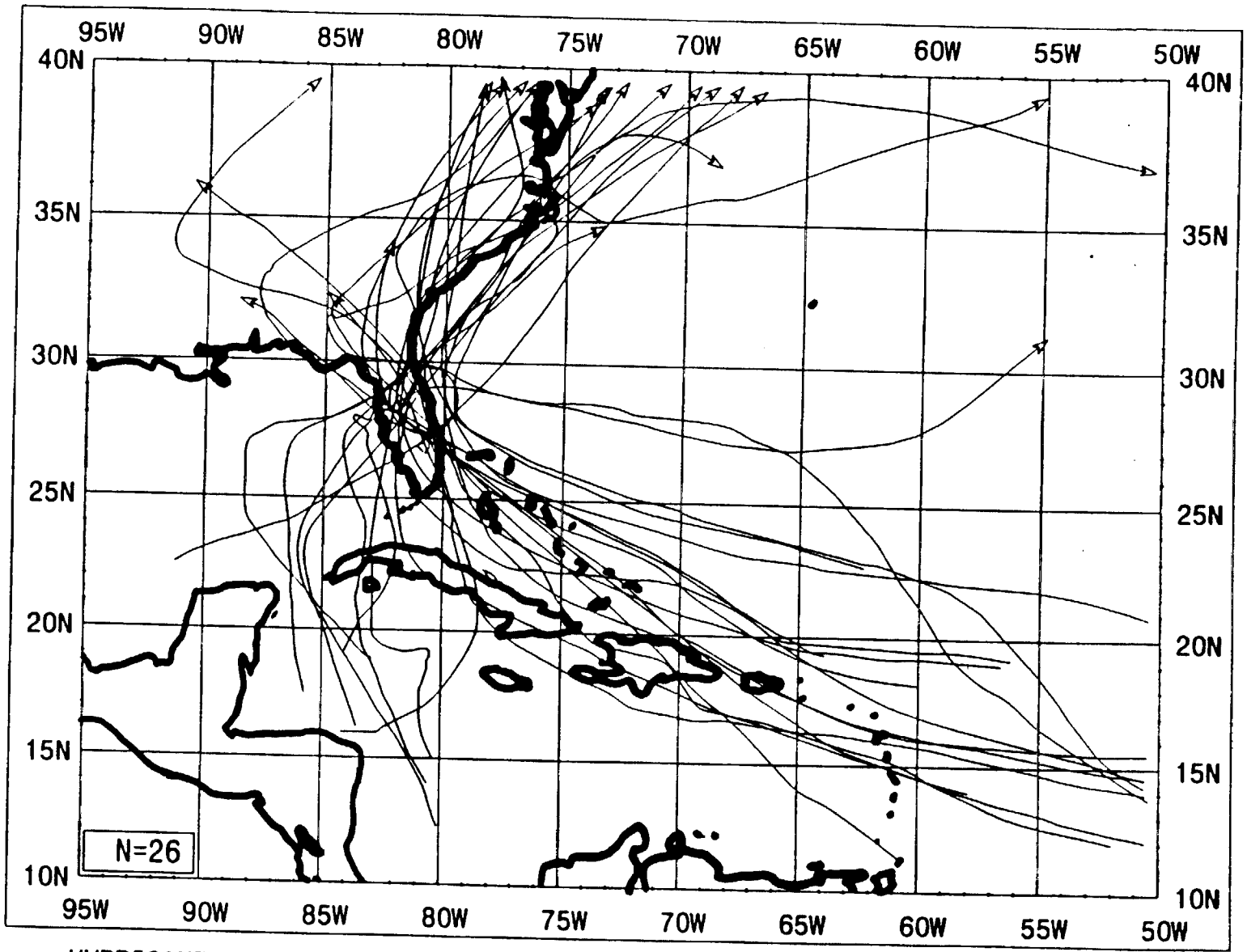

HURRICANES PASSING WITHIN 75 N.MI. OF CAPE KENNEDY, FL 1886-1991

(SITE LOCATION MOVED TO 28.6N, 80.9W)

CHART 3

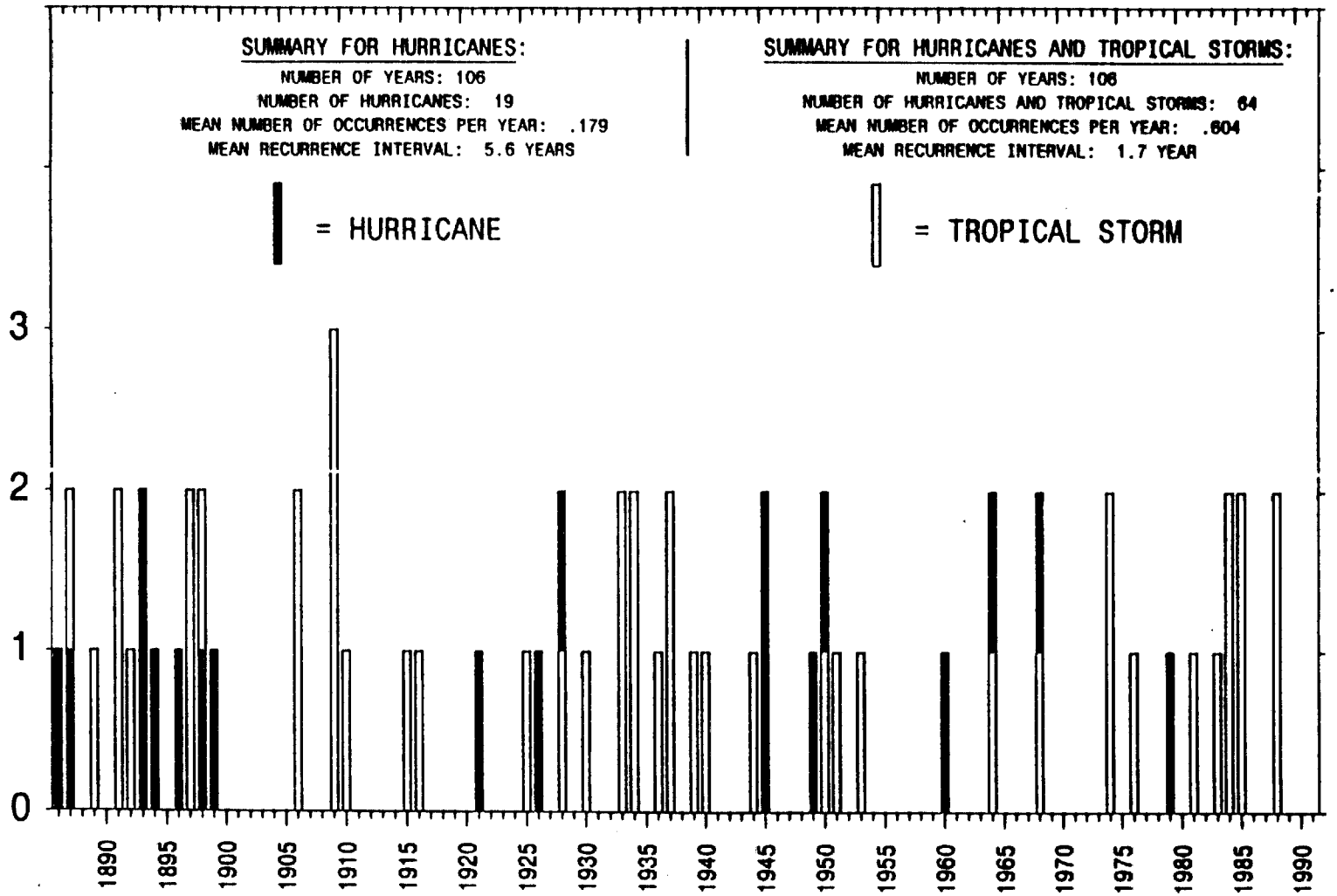

TROPICAL CYCLONES PASSING WITHIN 75 N.MI. OF CAPE KENNEDY, FL 1886-1991

(Note: Storm intensity is determined at time of closest approach to site)

CHART 4

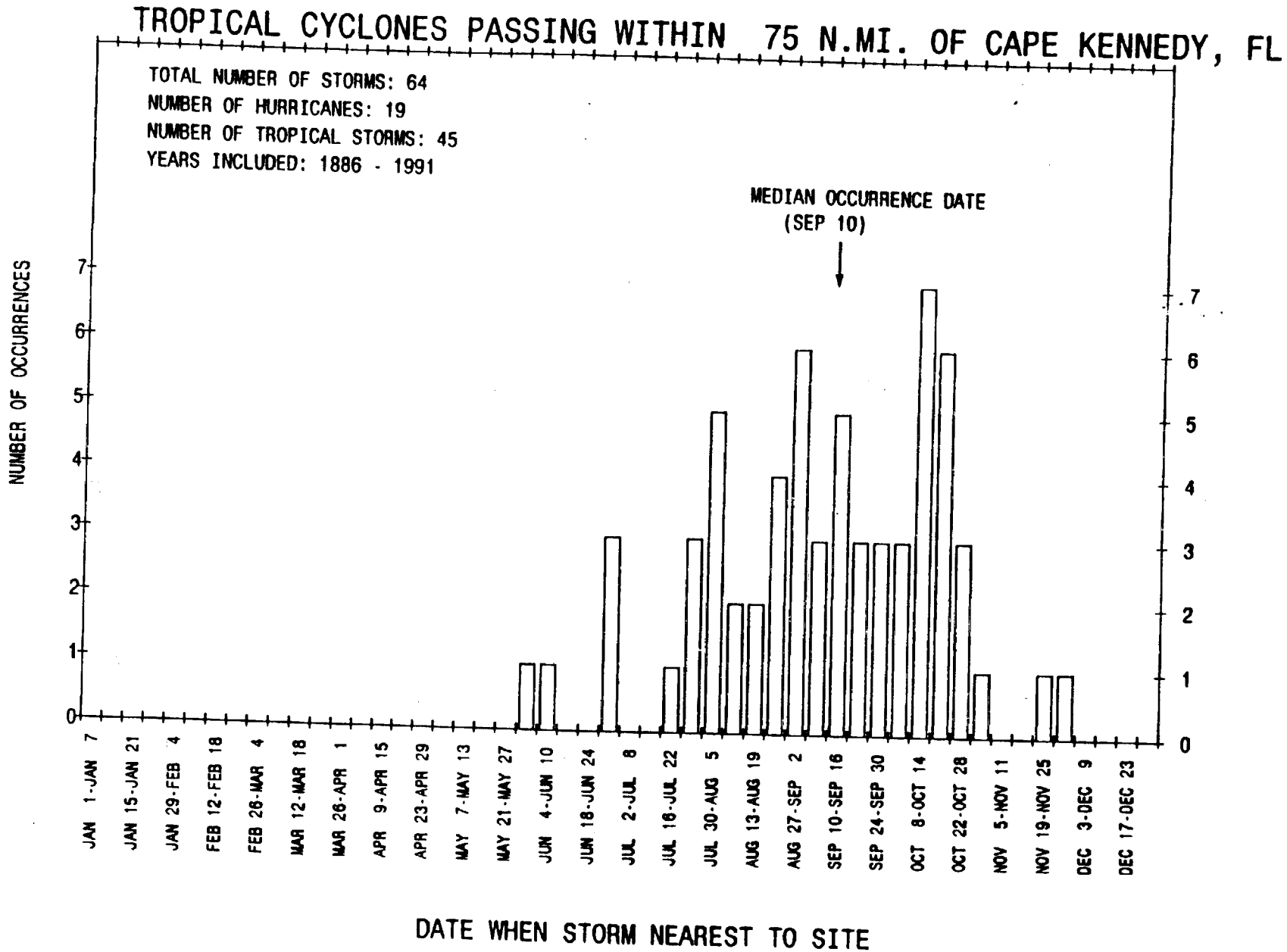
TROPICAL CYCLONES PASSING WITHIN 75 N.MI. OF CAPE KENNEDY, FL
TOTAL NUMBER OF STORMS: 64
NUMBER OF HURRICANES: 19
NUMBER OF TROPICAL STORMS: 45
YEARS INCLUDED: 1886 - 1991
MEDIAN OCCURRENCE DATE
(SEP 10)
NUMBER OF OCCURRENCES
0
1
2
3
4
5
6
7
JAN 1-JAN 7
JAN 15-JAN 21
JAN 29-FEB 4
FEB 12-FEB 18
FEB 26-MAR 4
MAR 12-MAR 18
MAR 26-APR 1
APR 9-APR 15
APR 23-APR 29
MAY 7-MAY 13
MAY 21-MAY 27
JUN 4-JUN 10
JUN 18-JUN 24
JUL 2-JUL 8
JUL 16-JUL 22
JUL 30-AUG 5
AUG 13-AUG 19
AUG 27-SEP 2
SEP 10-SEP 16
SEP 24-SEP 30
OCT 8-OCT 14
OCT 22-OCT 28
NOV 5-NOV 11
NOV 19-NOV 25
DEC 3-DEC 9
DEC 17-DEC 23
DATE WHEN STORM NEAREST TO SITE

CHART 5

DIRECTION DISTRIBUTION FOR STORMS PASSING WITHIN 75 N.MI. OF CAPE KENNEDY, FL

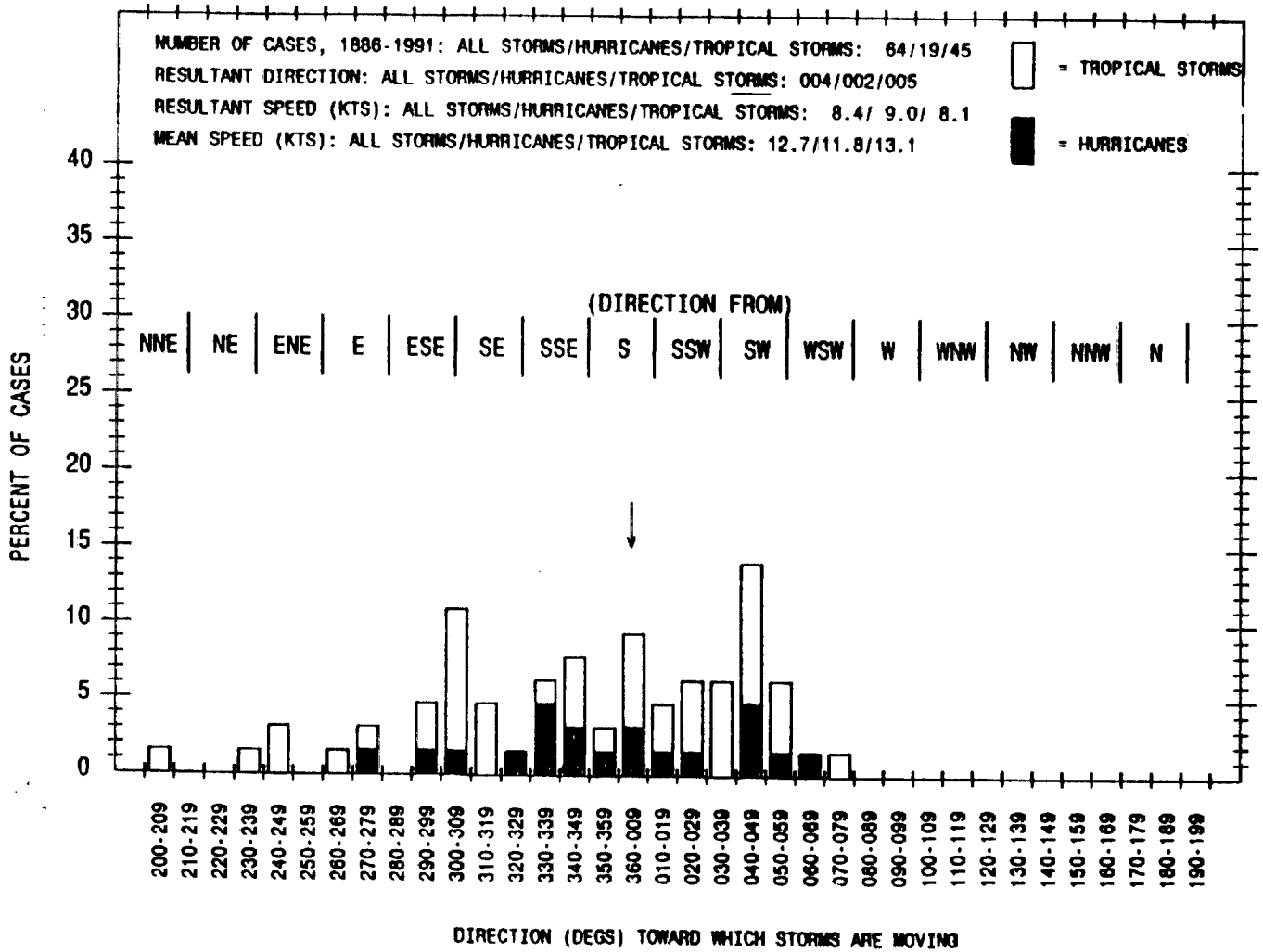

CHART 6

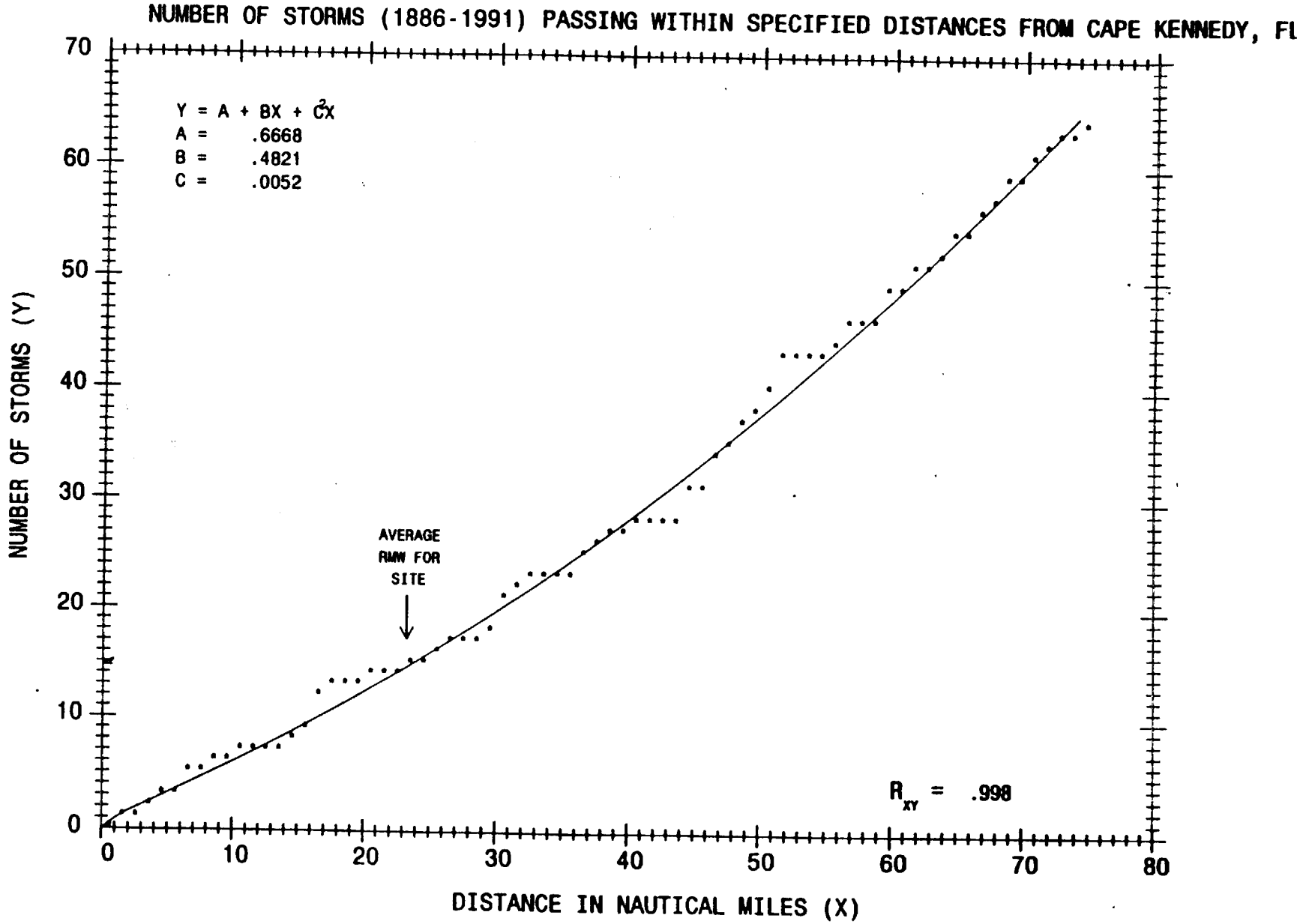
NUMBER OF STORMS (1886-1991) PASSING WITHIN SPECIFIED DISTANCES FROM CAPE KENNEDY, FL
Y = A + BX + CX²
A = .6668
B = .4821
C = .0052
AVERAGE RMW FOR SITE
R_XY = .998
NUMBER OF STORMS (Y)
DISTANCE IN NAUTICAL MILES (X)
0
10
20
30
40
50
60
70
80

CHART 7

WEIBULL DISTRIBUTION FITTED TO HISTOGRAM OF OBSERVED MAXIMUM WINDS

FOR TROPICAL CYCLONES PASSING WITHIN 75 N.MI. OF CAPE KENNEDY, FL

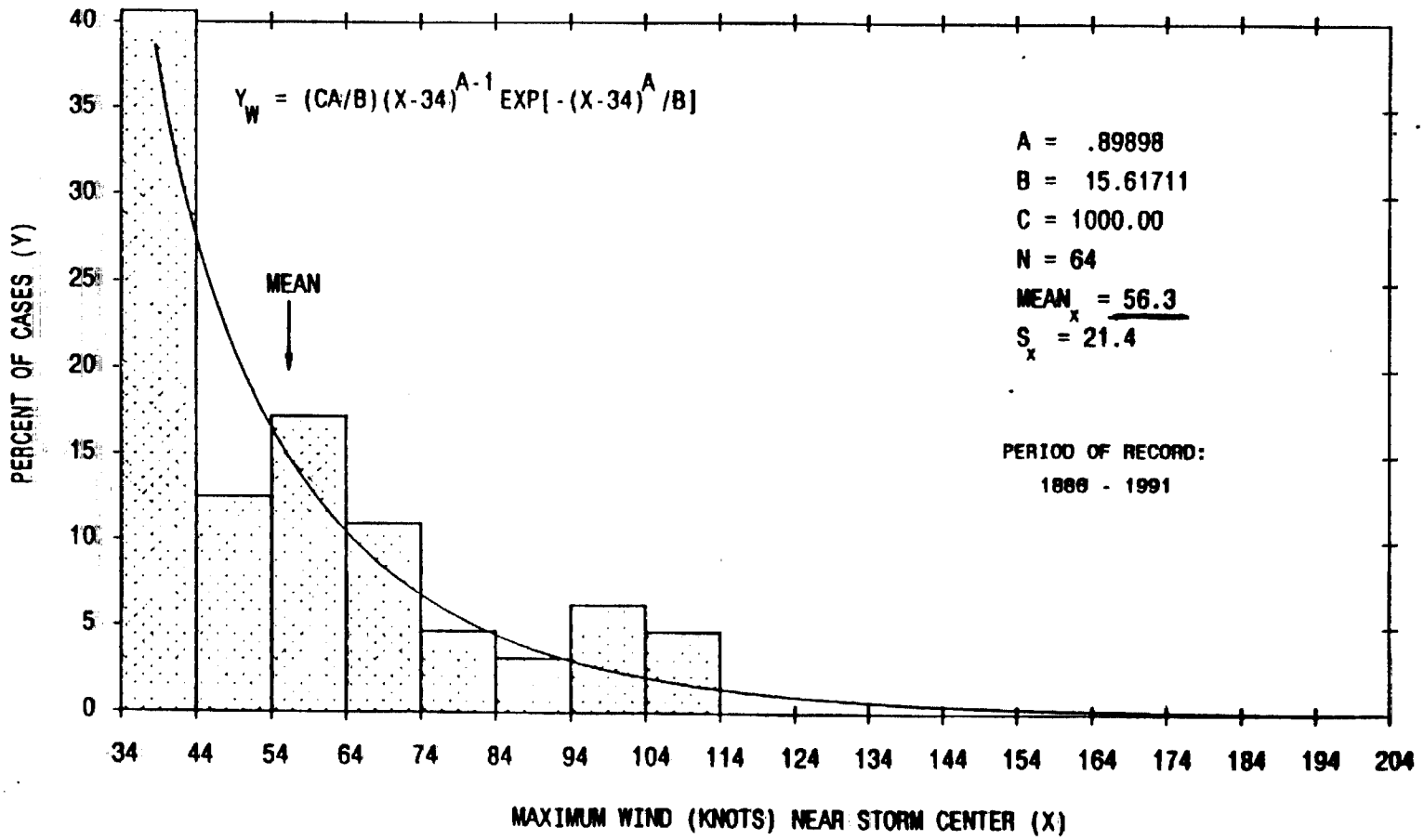

CHART 8

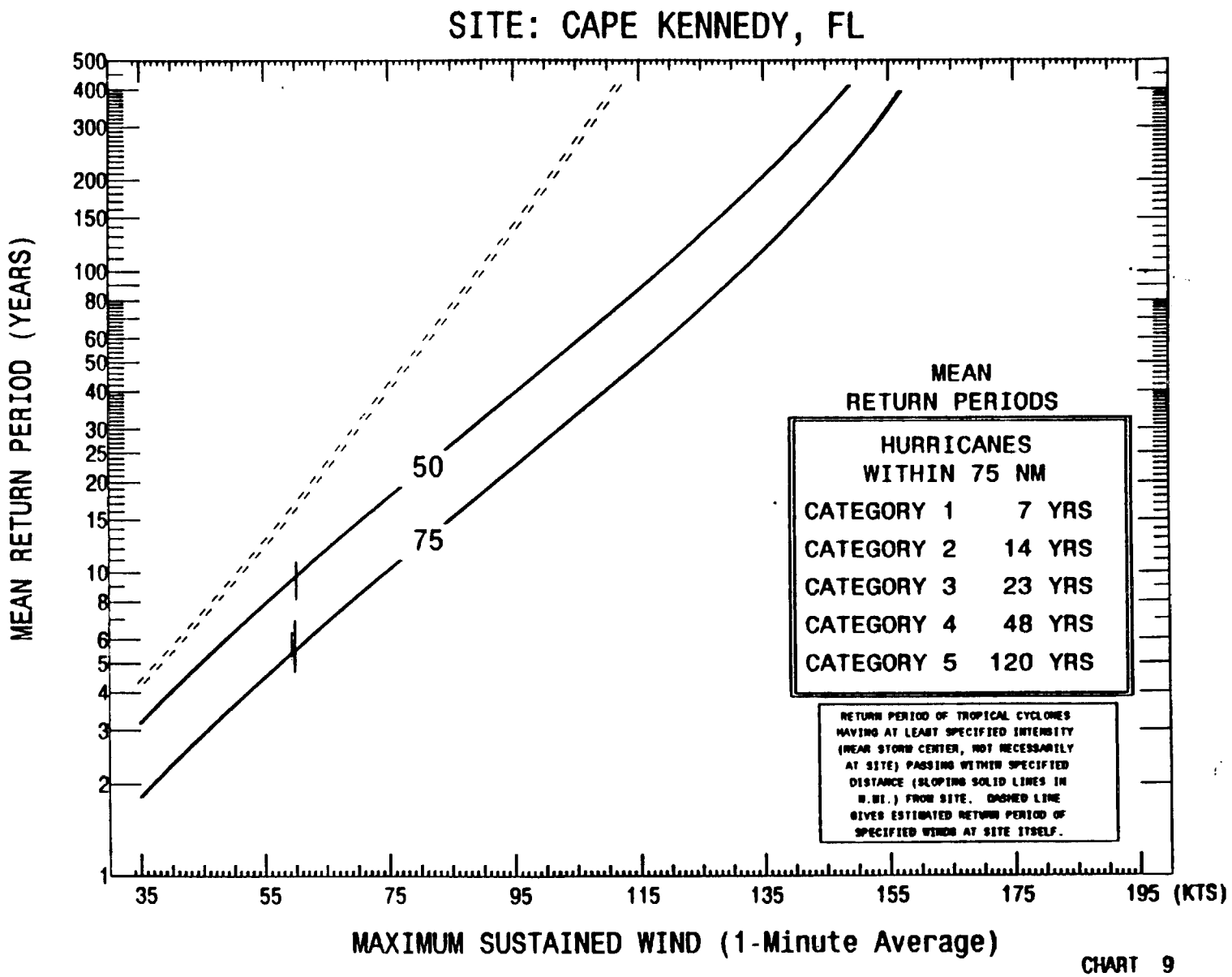
SITE: CAPE KENNEDY, FL
MEAN RETURN PERIOD (YEARS)
500
400
300
200
150
100
80
60
50
40
30
25
20
15
10
8
6
5
4
3
2
1
50
75
MEAN
RETURN PERIODS
HURRICANES
WITHIN 75 NM
CATEGORY 1 7 YRS
CATEGORY 2 14 YRS
CATEGORY 3 23 YRS
CATEGORY 4 48 YRS
CATEGORY 5 120 YRS
RETURN PERIOD OF TROPICAL CYCLONES HAVING AT LEAST SPECIFIED INTENSITY (NEAR STORM CENTER, NOT NECESSARILY AT SITE) PASSING WITHIN SPECIFIED DISTANCE (SLOPING SOLID LINES IN N.MI.) FROM SITE. DASHED LINE GIVES ESTIMATED RETURN PERIOD OF SPECIFIED WINDS AT SITE ITSELF.
35
55
75
95
115
135
155
175
195 (KTS)
MAXIMUM SUSTAINED WIND (1-Minute Average)

CHART 9

PROBABILITY OF AT LEAST X TROPICAL CYCLONES (≥34 KNOTS) PASSING
WITHIN 75 N.MI. OF SPECIFIED SITE OVER N CONSECUTIVE YEARS

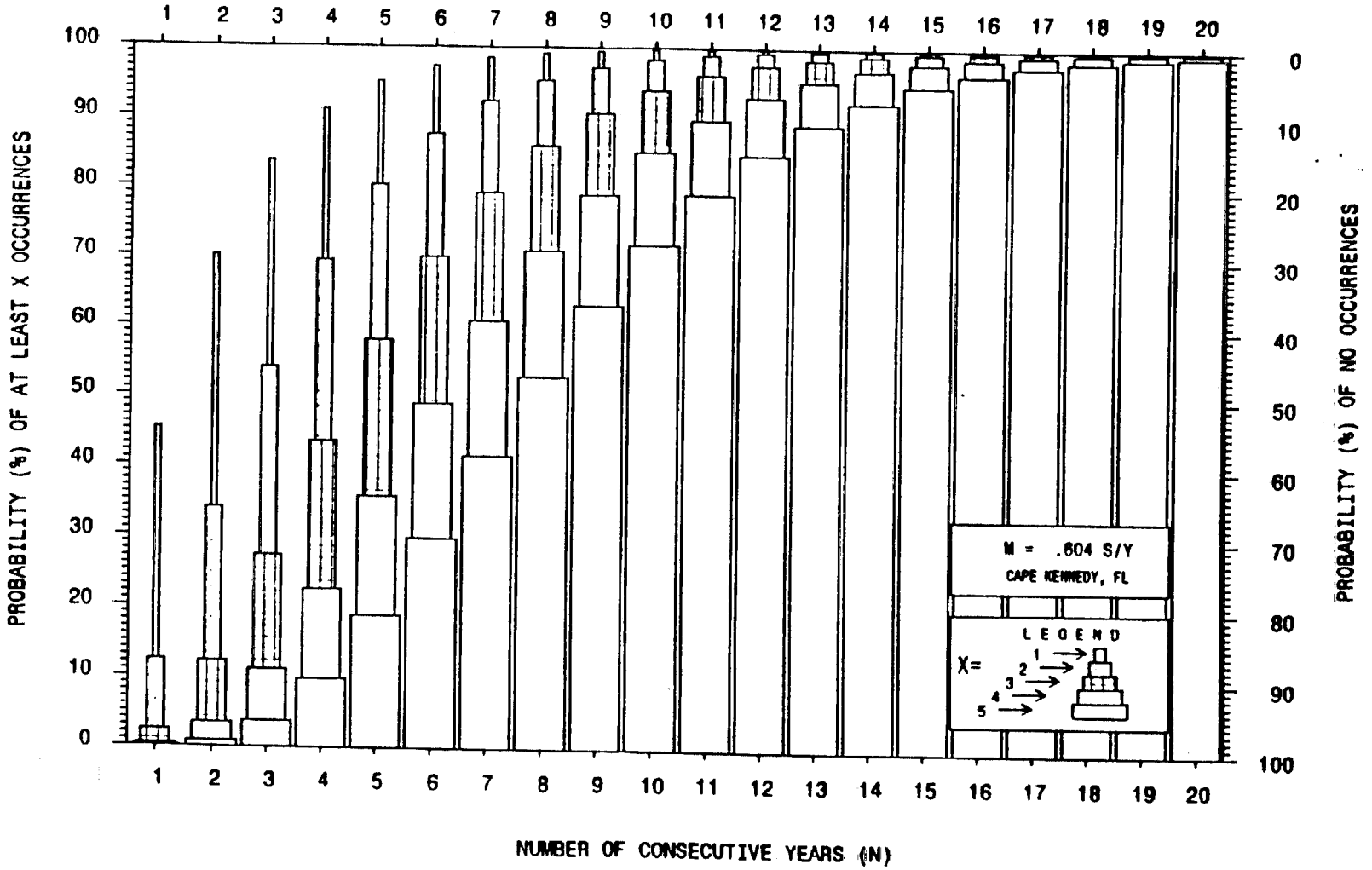

CHART 10

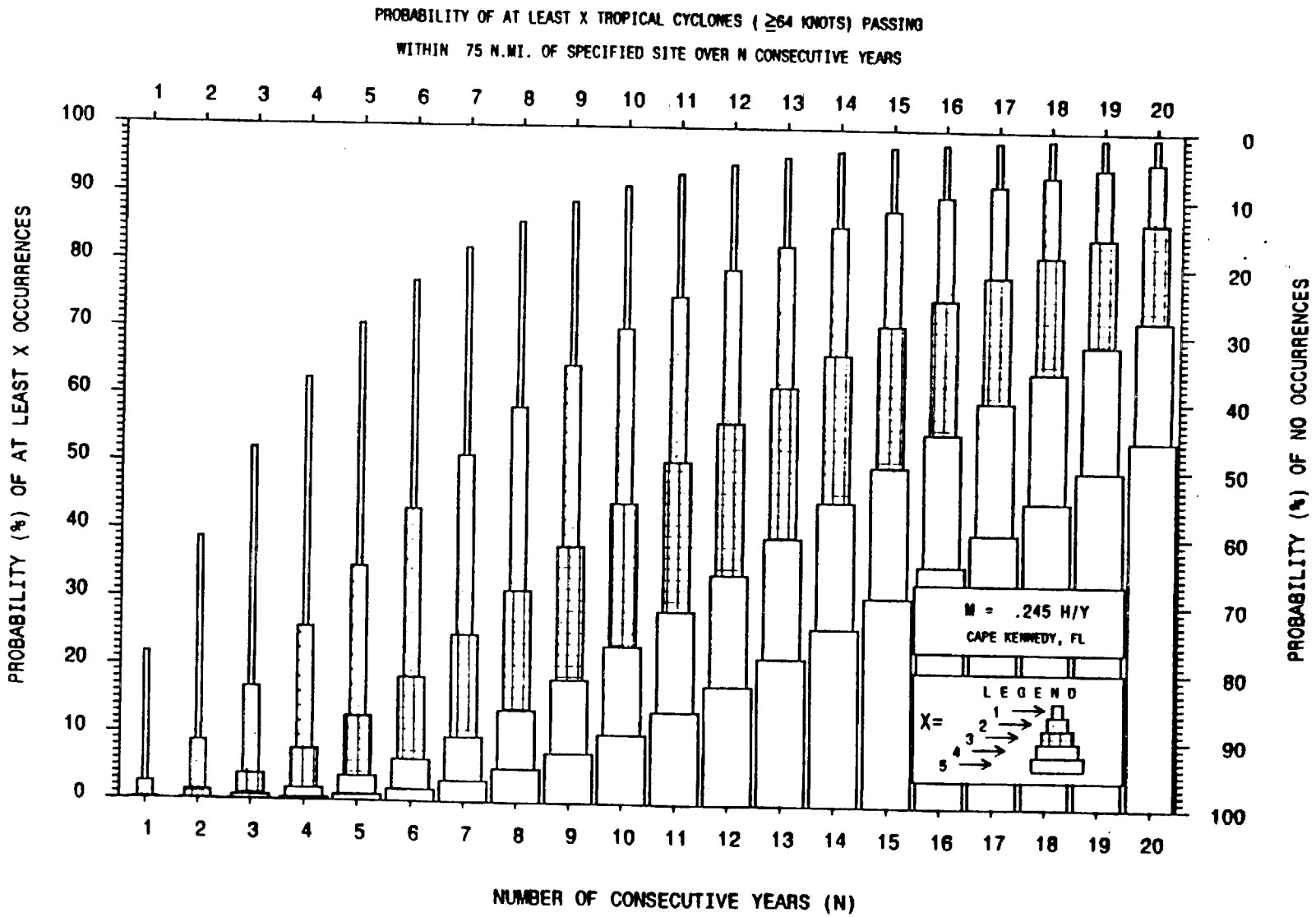
PROBABILITY OF AT LEAST X TROPICAL CYCLONES (≥64 KNOTS) PASSING
WITHIN 75 N.MI. OF SPECIFIED SITE OVER N CONSECUTIVE YEARS
PROBABILITY (%) OF AT LEAST X OCCURRENCES
PROBABILITY (%) OF NO OCCURRENCES
NUMBER OF CONSECUTIVE YEARS (N)
M = .245 H/Y
CAPE KENNEDY, FL
LEGEND
X=

CHART 11

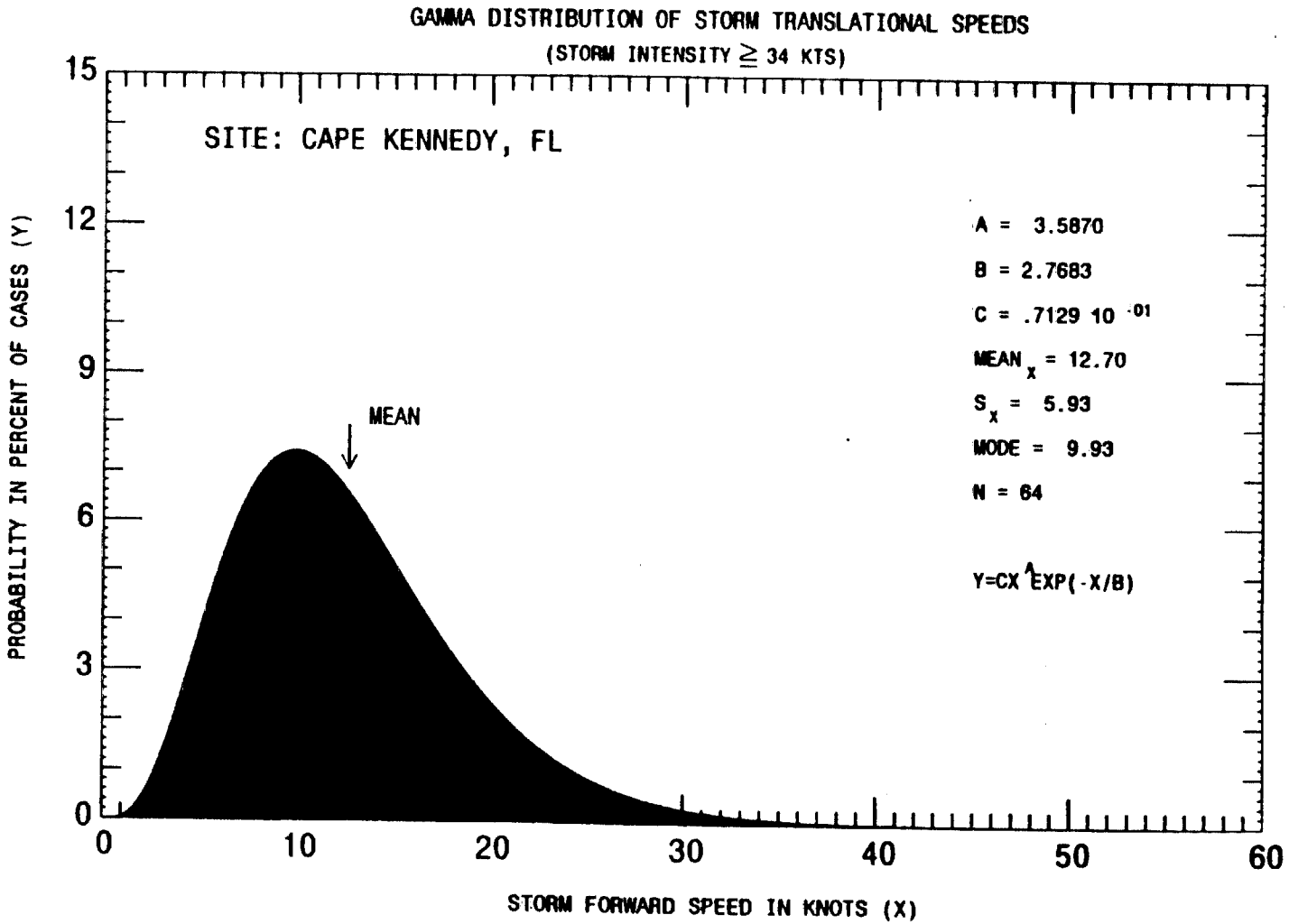
GAMMA DISTRIBUTION OF STORM TRANSLATIONAL SPEEDS
(STORM INTENSITY ≥ 34 KTS)
SITE: CAPE KENNEDY, FL
A = 3.5870
B = 2.7683
C = .7129 10 -01
MEAN X = 12.70
S X = 5.93
MODE = 9.93
N = 64
Y=CX ^EXP(-X/B)
MEAN
PROBABILITY IN PERCENT OF CASES (Y)
STORM FORWARD SPEED IN KNOTS (X)
0
3
6
9
12
15
0
10
20
30
40
50
60

CHART 11

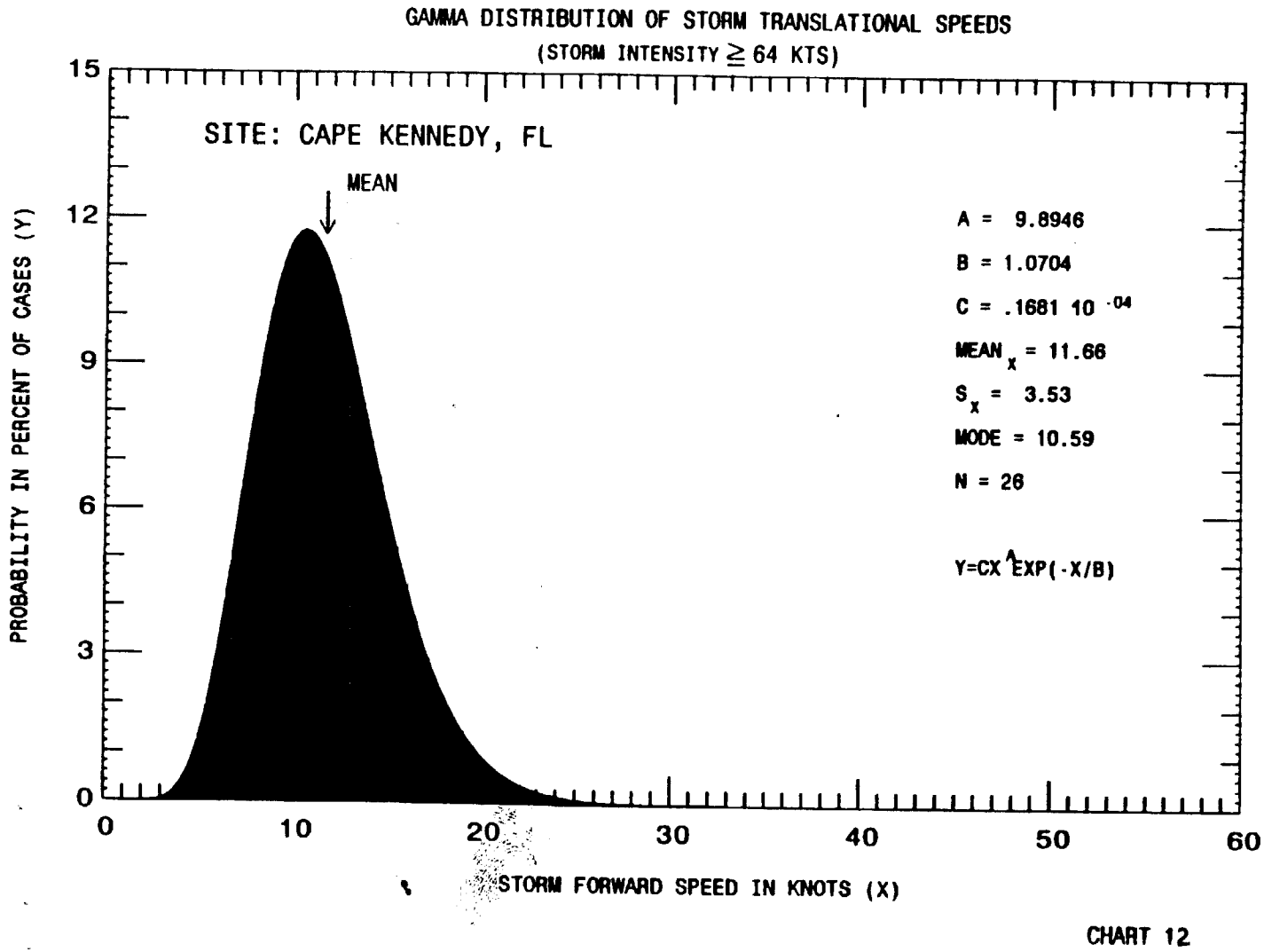
GAMMA DISTRIBUTION OF STORM TRANSLATIONAL SPEEDS
(STORM INTENSITY ≥ 64 KTS)
SITE: CAPE KENNEDY, FL
MEAN
A = 9.8946
B = 1.0704
C = .1681 10 -04
MEAN X = 11.66
S X = 3.53
MODE = 10.59
N = 26
Y=CX^EXP(-X/B)
PROBABILITY IN PERCENT OF CASES (Y)
STORM FORWARD SPEED IN KNOTS (X)
0
3
6
9
12
15
0
10
20
30
40
50
60

CHART 12

APPENDIX B

MASTER DATA LIST

```
62410 05/17/1970 M=11  1 SNBR= 688 ALMA        XING=0
62420 05/17*  0   0   0    0*  0   0   0    0*  0   0   0    0*115 790  25    0*
62430 05/18*117 792  25    0*121 797  25    0*123 801  25 1007*125 805  25    0*
62440 05/19*130 810  25    0*135 815  25    0*140 820  25 1005*145 825  25    0*
62450 05/20*155 825  35    0*162 823  35    0*168 819  65    0*172 816  70  993*
62460 05/21*180 810  55    0*182 803  50    0*185 802  45    0*190 800  40  998*
62470 05/22*196 801  35 1004*193 806  30    0*191 811  30    0*190 818  30 1007*
62480 05/23*192 827  30    0*198 835  25    0*210 839  25    0*219 840  25    0*
62490 05/24*230 840  25    0*240 840  25    0*252 840  25 1008*268 839  25    0*
62500 05/25*283 836  25    0*295 829  25    0*306 822  25    0*318 816  25    0*
62510 05/26*326 812  25 1005*333 807  25    0*348 799  25    0*357 787  25    0*
62520 05/27E365 770  25 1003E370 755  25    0*  0   0   0    0*  0   0   0    0*
62530 HR
```

APPENDIX C

LISTING OF TRK.DAT OUTPUT

62410	38			
62410	16.80	315.59	0.00	25
62410	37.92	309.27	-6.32	25
62410	26.35	297.09	-12.18	25
62410	26.33	297.11	0.02	25
62410	41.91	315.72	18.61	25
62410	41.87	315.77	0.06	25
62410	41.82	315.83	0.06	25
62410	41.78	315.90	0.06	25
62410	60.00	360.00	44.10	25
62410	43.56	15.37	15.37	35
62410	42.73	32.59	17.22	35
62410	29.53	35.65	3.06	65
62410	59.00	35.56	-0.09	70
62410	41.69	73.27	37.71	55
62410	18.88	17.56	-55.71	50
62410	32.08	20.75	3.19	45
62410	36.44	351.06	-29.68	40
62410	33.53	237.53	-113.53	35
62410	30.77	247.04	9.51	30
62410	40.15	261.41	14.36	30
62410	52.42	283.23	21.83	30
62410	57.82	308.51	25.27	30
62410	75.43	342.65	34.14	25
62410	54.29	354.10	11.45	25
62410	66.00	360.00	5.90	25
62410	60.00	360.00	0.00	25
62410	72.00	360.00	0.00	25
62410	96.15	3.22	3.22	25
62410	91.40	10.06	6.84	25
62410	80.85	27.05	17.00	25
62410	75.35	28.85	1.79	25
62410	78.31	23.16	-5.69	25
62410	52.12	22.93	-0.22	25
62410	48.97	30.94	8.01	25
62410	98.40	23.84	-7.10	25
62410	79.83	47.44	23.60	25
62410	95.37	59.78	12.35	25
62410	78.10	67.41	7.63	25

APPENDIX D

LISTING OF PROGRAM VECTOR.FOR

```
C-----------------------------7/22/92-------------------------------------
      PROGRAM VECTOR
C
      INTEGER DATLIN, DATLIN2,DAY,MO,YR,M,SNBR,XING
      INTEGER DLIN(30),MN(30),DY(30)
      INTEGER LAT(30,4),LON(30,4),MAX(30,4),SLP(30,4),MX(120),SP(120)
C
      CHARACTER*1 J1
      CHARACTER*2 J2
      CHARACTER*5 J5
      CHARACTER*6 J6
      CHARACTER*9 NAME,TYPE
      CHARACTER*12 FILENAME
C
      REAL LT(120),LN(120),DIS(120),DIR(120),ADIR(120),PI,DR,XDIS,YDIS
C
      PI=3.141592654
C
C     OPEN (UNIT=10,FILE='NEWTEST.TRK', STATUS= 'OLD',FORM='FORMATTED')
      OPEN (UNIT=11,FILE='TKHDR.DAT',STATUS='NEW',FORM='FORMATTED')
      OPEN (UNIT=12,FILE='TRK.DAT',STATUS='NEW',FORM='FORMATTED')
      OPEN (UNIT=13,FILE='VECTOR.DAT',STATUS='NEW',FORM='FORMATTED')
C
5     WRITE (6,*) 'PLEASE TYPE IN THE NAME OF YOUR STORM FILE.'
      READ (6,10) FILENAME
10    FORMAT (A12)
      OPEN (UNIT=10,FILE=FILENAME,STATUS='OLD',FORM='FORMATTED',ERR=20)
      GOTO 100
20    WRITE (6,25)FILENAME
25    FORMAT (1X,'OOPS, THE DATA FILE ',A12,' DOES NOT EXIST.'
     &  '  TRY AGAIN.',//)
      GOTO 5
100   CONTINUE
C     ---------CLEARS DATA FROM ARRAYS----
C
      DO 150 I=1,30
              DO 160 J=1,4
              LAT(I,J)=0
              LON(I,J)=0
              MAX(I,J)=0
              SLP(I,J)=0
160           CONTINUE
150   CONTINUE
      DO 170 I=1,120
              LT(I)=0
              LN(I)=0
              MX(I)=0
              SP(I)=0
170   CONTINUE
C
C     ---------READING HEADER DATA-----
      READ (10,1000,END=3000) DATLIN,MO,J1,DAY,J1,YR,J2,M,K,J5,SNBR,NAME
1000  FORMAT (I5,1X,I2,A1,I2,A1,I4,1X,A2,I2,I4,A5,I4,1X,A9)
C     ---------READS STORM DATA---------
      DO 2000 I=1,M
              READ (10,1010)DLIN(I),MN(I),J1,DY(I),J1,
     &        LAT(I,1),LON(I,1),MAX(I,1),SLP(I,1),J1,
     &        LAT(I,2),LON(I,2),MAX(I,2),SLP(I,2),J1,
     &        LAT(I,3),LON(I,3),MAX(I,3),SLP(I,3),J1,
     &        LAT(I,4),LON(I,4),MAX(I,4),SLP(I,4)
C
1010          FORMAT (I5,1X,I2,A1,I2,A1,I3,I4,1X,I3,1X,I4,A1,
     &        I3,I4,1X,I3,1X,I4,A1,I3,I4,1X,I3,1X,I4,A1,
     &        I3,I4,1X,I3,1X,I4)
C LN59
```

```
C WHEW! LN129
C       ---------SAVES TO VECTOR.DAT FILE-----
C
                ADIR(1)=0.0
                IF((I-1).EQ.1) GOTO 4740
                ADIR(I-1)=DIR(I-1)-DIR(I-2)
                IF (ADIR(I-1).LT.-270) THEN
                        ADIR(I-1)=ADIR(I-1)+360
                ELSEIF (ADIR(I-1).GT.270) THEN
                        ADIR(I-1)=ADIR(I-1)-360
                ENDIF
4740            WRITE (13,4750)DATLIN,DIS(I-1),DIR(I-1),ADIR(I-1),MX(I-1)
4750            FORMAT (1X,I5,1X,F6.2,1X,F6.2,1X,F7.2,1X,I3)
4700    CONTINUE
C
C       ---------READS STORM MAX INTENSITY---------
        READ (10,1050)DATLIN2,TYPE
1050    FORMAT (I5,1X,A2)
C 140      ---------WRITING DATA TO SCREEN AND FILE---------
C       WRITE (6,1100)DATLIN,NAME,MO,DAY,YR,SNBR,M,TYPE
C       WRITE (6,*)NFIX
1100    FORMAT (1X,I5,1X,A9,1X,I2,1X,I2,1X,I4,1X,I3,1X,I3,1X,A2)
        DO 2500 I=1,M
                WRITE (12,1200)DLIN(I),LAT(I,1),LON(I,1),MAX(I,1),SLP(I,1),
     &                  LAT(I,2),LON(I,2),MAX(I,2),SLP(I,2),
     &                  LAT(I,3),LON(I,3),MAX(I,3),SLP(I,3),
     &                  LAT(I,4),LON(I,4),MAX(I,4),SLP(I,4)
1200            FORMAT(1X,I5,1X,I3,1X,I4,1X,I3,1X,I4,
     &                  1X,I3,1X,I4,1X,I3,1X,I4,
     &                  1X,I3,1X,I4,1X,I3,1X,I4,
     &                  1X,I3,1X,I4,1X,I3,1X,I4)
2500    CONTINUE
        WRITE (11,1100)DATLIN,NAME,MO,DAY,YR,SNBR,M,TYPE
        GOTO 100
C       ---------LOOPS BACK TO BEGINNING OF PROGRAM TO READ NEXT------
C       ---------JUMPS HERE IF READ ENCOUNTERS EOF MARKER IN DATA-----
CLN145
3000    WRITE (6,6000)
6000    FORMAT (1X,/,' ALL DONE!',//,' HEADER DATA IN FILE NAMED ',
     &  'TKHDR.DAT,',/,' STORM DATA IN TRK.DAT,',/,' AND VECTOR DATA',
     &  ' IS IN A FILE NAMED VECTOR DAT.')
        CLOSE (UNIT=10)
        CLOSE (UNIT=11)
        CLOSE (UNIT=12)
        CLOSE (UNIT=13)
        END
```

```
2000    CONTINUE
C
C       ---------STORES STORM DATA IN WORKING FILES-----
C
        DO 4100 I=1,M
                DO 4200 J=1,4
                                LT(4*I-4+J)=LAT(I,J)*.1
                                LN(4*I-4+J)=LON(I,J)*.1
                                MX(4*I-4+J)=MAX(I,J)
                                SP(4*I-4+J)=SLP(I,J)
4200            CONTINUE
4100    CONTINUE
C
C       ---------GETS RID OF ZERO VALUES AT BEGINNING OF ARRAYS-----
C LN78
4500    IF (LT(1).LT.1) THEN
                DO 4550 J=1,(M*4)
                        LT(J)=LT(J+1)
                        LN(J)=LN(J+1)
                        MX(J)=MX(J+1)
                        SP(J)=SP(J+1)
4550                    CONTINUE
                GOTO 4500
        ENDIF
C
C       ---------COUNTS NUMBER OF FIXES-----
C
        NFIX=1
4560    IF (LT(NFIX+1).NE.0.0) THEN
                NFIX=NFIX+1
                IF (NFIX+1.GT.M*4)GOTO 4570
                GOTO 4560
4570            CONTINUE
        ENDIF
C
C       ---------COMPUTES DISTANCE TRAVELED EACH 6HR PERIOD-----
C  LN100
        K=NFIX-1
        WRITE (13,4600)DATLIN,K
4600    FORMAT(1X,I5,1X,I3)
        DO 4700 I=2,NFIX
                XDIS=(LN(I-1)-LN(I))*
     &                  COS(((LT(I-1)+LT(I))/2)*PI/180)*60
                YDIS=(LT(I)-LT(I-1))*60
C
                DIS(I-1)=SQRT((XDIS)**2+(YDIS**2))
C
C110    ---------COMPUTES HEADING TRAVELED FOR EACH 6HR PERIOD-----
C
                IF ((XDIS.GT.0).AND.(YDIS.GT.0)) THEN
                        DIR(I-1)=ATAN(XDIS/YDIS)*180/PI
                ELSEIF ((XDIS.GT.0).AND.(YDIS.LT.0)) THEN
                        DIR(I-1)=ATAN(XDIS/YDIS)*180/PI+180
                ELSEIF ((XDIS.LT.0).AND.(YDIS.GT.0)) THEN
                        DIR(I-1)=ATAN(XDIS/YDIS)*180/PI+360
                ELSEIF ((XDIS.LT.0).AND.(YDIS.LT.0)) THEN
                        DIR(I-1)=ATAN(XDIS/YDIS)*180/PI+180
                ELSEIF ((XDIS.EQ.0).AND.(YDIS.GT.0)) THEN
                        DIR(I-1)=360.0
                ELSEIF (XDIS.EQ.0) THEN
                        DIR(I-1)=180.0
                ELSEIF ((YDIS.EQ.0).AND.(XDIS.GE.0)) THEN
                        DIR(I-1)=90.0
                ELSE
                        DIR(I-1)=270.0
                ENDIF
```

APPENDIX E

LISTING OF PROGRAM CHOOSE.FOR

```
C       -------CHOOSE.FOR------
C       THIS PROGRAM ALLOWS THE USER TO SELECT SPECIFIC STORM OR STORM
C       DATA FROM THE VECTOR.DAT FILE.
C
        PROGRAM CHOOSE
C
        REAL DIS(120),DIR(120),ADIR(120)
        INTEGER MAX(120),N,DATLIN
C
        OPEN (UNIT=10,FILE='VECTOR.DAT',STATUS='OLD',ERR=50)
        OPEN (UNIT=11,FILE='NEWVECT.DAT',STATUS='NEW',FORM='FORMATTED')
        GOTO 80
C
50      WRITE (6,*) ' CANNOT OPEN VECTOR.DAT FILE.  RUN VECTOR FIRST'
        GOTO 5000
80      WRITE (6,*) ' WHAT IS THE FIRST SEQUENCE NUMBER OF DATA?'
        READ (6,*,ERR=70) ISTART
        WRITE (6,*) ' WHAT IS THE LAST SEQUENCE NUMBER? (MAY BE THE SAME)'
        READ (6,*,ERR=70) IFIN
        GOTO 90
70      IF (ISTART.LT.IFIN) THEN
                WRITE (6,*) ' GOT A PROBLEM.  WE SHALL TRY AGAIN.'
                GOTO 80
        ENDIF
90      READ (10,100,END=3000)DATLIN,N
100     FORMAT (1X,I5,1X,I3)
C
C       -----GETS RID OF DATA BEFORE TIME OF INTEREST-----
C
        IF (DATLIN.LT.ISTART) THEN
                DO 500 I=1,N
                        READ (10,150)JUNK1,R1,R2,R3,JUNK2
150                     FORMAT (I5,1X,F6.2,1X,F6.2,1X,F7.2,1X,I3)
500             CONTINUE
                GOTO 90
C
C       -----SAVES DATA OF INTEREST IN NEW DATA FILE-----
C
        ELSEIF ((DATLIN.GE.ISTART).AND.(DATLIN.LE.IFIN)) THEN
                FLAG=1
                WRITE (11,100)DATLIN,N
                DO 1000 I=1,N
                        READ (10,250)JUNK,DIS(I),DIR(I),ADIR(I),MAX(I)
250                     FORMAT (1X,I5,1X,F6.2,1X,F6.2,1X,F7.2,1X,I3)
                        WRITE (11,250)DATLIN,DIS(I),DIR(I),ADIR(I),MAX(I)
1000            CONTINUE
                GOTO 90
C
C       -----GIVES ERROR MESSAGE FOR DATA NOT FOUND.
C
        ELSE
        IF (FLAG.EQ.1) GOTO 3000
        WRITE (6,4000)
4000    FORMAT (/,' COULD NOT FIND ANY OF THOSE IN THE VECTOR.DAT',
     &  ' FILE.',/,' YOU MIGHT WANT TO RERUN "VECTOR" AND MAKE SURE ',
     &  ' OF YOUR NUMBERS.',/,' THEN YOU COULD RERUN THIS PROGRAM. ',
     &  ' BYE!')
        GOTO 5000
        ENDIF
        GOTO 90
3000    WRITE (6,*)
        WRITE (6,*)
        WRITE (6,3500) ISTART,IFIN
3500    FORMAT (//,' GOT IT.  YOUR NEW FILE IS NEWVECT.DAT, AND IT',
     &  ' CONTAINS DATA FROM',/,1X,I5,' TO ',I5,'.')
5000    END
```

REFERENCES

Etter, D. M.; Structured Fortran 77 for Engineers and Scientists; 3rd ed.; The Benjamin/Cummings Publishing Co. Inc., 1990.

Hope, John R., Charles J. Neumann; Probability of Tropical Cyclone Induced Winds at Capt Kennedy; ESSA Techical Memorandum WBTM SOS-1, Silver Spring, MD., 1968.

Martin, J. J.; Bayesian Decision Problems and Markov Chains; John Wiley & Sons, 1967.

McCracken, Daniel D.; A Guide to Fortran Programming; Wiley, 1961.

Murphy, Allan M and Richard Katz editors; Probability, Statistics and Decision Making in the Atmospheric Sciences; Westview Press, 1985.

Neumann, Charles J.; A Statistical Study of Tropical Cyclone Positioning Errors With Economic Applications; NOAA Technical Memorandum NWS SR-82, Springfield, VA., 1975.

Neumann, Charles J.; The National Hurricane Center Risk Analysis Program (HURISK); NOAA Technical Memorandum NWS NHC 38, Springfield, VA., 1987.